CARE-Conf-06-049-HHH

WAMDO 2006

Workshop on
Accelerator Magnet Design and Optimization

3 – 6 April 2006
CERN, Geneva, Switzerland

Proceedings

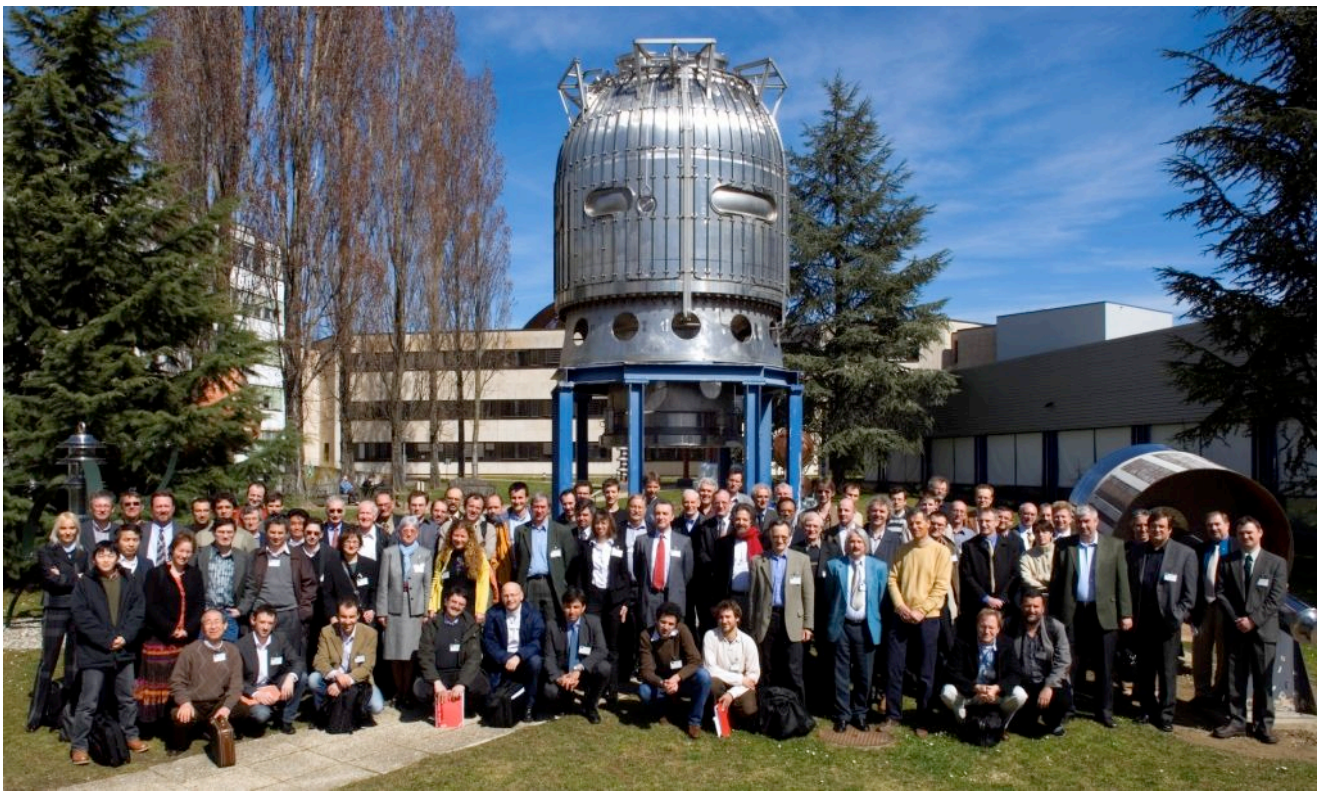

Acknowledgement

We acknowledge the support of the European Community-Research Infrastructure Activity under the FP6 “Structuring the European Research Area” programme (CARE, contract number RII3-CT-2003-506395)

WAMDO-2006

Workshop on Accelerator Magnet Design and Optimization

Organised by :

HHH network /NED JRA of the EU Program CARE
LARP (LHC Accelerator Research Program) – USA

Hosted by the *Accelerator Technology Department - CERN*
CERN, Geneva, 3 - 6 April 2006

After the large effort for the LHC, whose commissioning will take place in 2007, the accelerator magnet community is organizing the post-LHC phase. In Europe, in the frame of EU program CARE (http://esgard.lal.in2p3.fr/Project/Activities/Current/), the network **HHH** - High energy High intensity Hadron beams - (http://care-hhh.web.cern.ch/care-hhh/) foresees a work package dedicated to collaboration for advancement on Accelerator Magnet Technology (**AMT**, http://amt.web.cern.ch/amt/).
The network is synergic to a JRA (Joint Research activity) called **NED** (http://esgard.lal.in2p3.fr/Project/Activities/Current/Quaterly/JRA/) aiming to develop the superconductor and the magnet technology for the construction of a Nb_3Sn model dipole magnet. The network is active both on the high field technology and on the emerging subject of the cycled (Hz range) superconducting magnets, also of interest for the FAIR Project at GSI.

Meanwhile, the American collaboration, organised in the **LARP** (BNL, Fermilab and LBNL for magnets) is pursuing the goal of IR optics design for the LHC luminosity upgrade and of developing superconductors and magnets in Nb_3Sn. A milestone of LARP is to manufacture a test by 2009 high gradient – large aperture quadrupoles models and at least one long quadrupole as demonstrator of the technology in real conditions for field beyond 10 Tesla.

WAMDO builds over the experience of numerous workshops organised by HHH and LARP (http://amt.web.cern.ch/amt/events/workshops/WAMS2004/wams2004_index.htm), namely the previous WAMS2004 and the NED working group on magnet design and optimization. It will provide a convenient forum to host presentations, discussion (and confrontation) on extension of classical designs, novel ideas, numerical modeling and manufacturing issues for advanced superconducting magnets, both for high field (>10 T) and Hz range cycled magnets, as envisaged for GSI or possible improvement of LHC injector chain. Superconductors for high field and Hz regime magnet will also be reviewed, especially in connection with magnet technology.

A few talks will be dedicated to different layouts of IR optics for LHC luminosity upgrade and their implications on magnet design.

Attendance to the workshop is by invitation only (about 100 participants including speakers). If you want to propose colleagues for participation, please inform the organisers. Proposals of talks on various issues are also welcome.

This announcement will be followed by a second one in January 2006 with practical information for registration and accommodation.

W A M D O 2006 @ CERN
List of topics

- Beam Optics and Layout
- Review of ongoing magnet R&D programs
- Design Tools
- Magnet Design: efficiency an FQ (field quality)
- Mechanical design
- Quench Protection
- Magnetization and parasitic effects (snap back, coupling, etc.)
- New concepts

Organizing Committee

Chairmen	Lucio Rossi (HHH)	lucio.rossi@cern.ch
	Steve Gourlay (US-LARP)	SAGourlay@lbl.gov
Scientific Advisors	Luca Bottura (HHH-AMT)	luca.bottura@cern.ch
	Arnaud Devred (CARE-NED)	arnaud.devred@cern.ch
	Steve Peggs (US-LARP)	peggs@bnl.gov
Secretaries	Claudine Bosteels (CERN-ADM)	claudine.bosteels@cern.ch
	Valerie Marchive (CERN-ADM)	valerie.marchive@cern.ch

WAMDO Workshop on Accelerator Magnet Design and Optimization

CERN, 3 – 6 April 2006

Agenda (update 31 March 2006)

3 April 2006

Conference room : Council chamber

Chair : Lucio Rossi **Total 205 minutes**

Schedule	Title	Speaker	Duration	Discussion time
09h00 – 09h05	Welcome	L. Rossi	5′	
09h05 – 09h20	Welcome – CERN programme	R. Aymar	15′	

Beam optics and layout for the LHC luminosity upgrade

09h20 – 09h55	Performance limitations of the present LHC	F. Ruggiero	30′	5′
09h55 – 10h20	IR Layout based on NbTi	R. Ostojic	20′	5′
10h20 – 10h55	Detectors – goals and constraints	D. Denegri	30′	5′
	Coffee break			20′
11h15 – 11h50	IR upgrades using Nb3Sn: report from Pheasant Run	S. Peggs	30′	5′
11h50 – 12h15	Alternative IR solutions	J.P. Koutchouk	20′	5′

Lunch

High Field Superconductors

Chair : Luca Bottura **Total 210 minutes**

14h00 – 14h30	High field superconductor development in the US	A. Ghosh	25′	5′
14h30 – 14h55	Development in high critical current density Nb3Sn strand in Europe for NED and CERN programs	L. Oberli	20′	5′
14h55 -15h20	Nb3Al superconductor development in Japan	K. Tsuchiya	20’	5’
	Coffee break			20′
15h40 – 16h15	Review of Nb_3Sn Instability	L. Cooley	30′	5′
16h15 – 16h40	Cabling issues for Nb_3Sn	D. Dietderich	20′	5′
16h40 – 17h05	Properties of modern Nb3Sn strands and cables	E. Barzi	20′	5′
17h05 – 17h30	HTS relevant for accelerator magnets	J. Schwartz	20′	5′
17h30 – 17h55	HTS in the LHC & in the LHC upgrades	A. Ballarino	20′	5′
17h55 – 18h30	**Discussion and summing up on conductors**		30′	

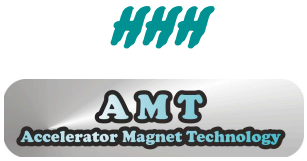

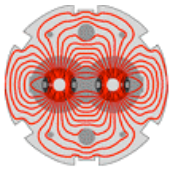

4 April 2006 — Conference room : Council chamber

Design Tools: potential and limitations

Chair : Arnaud Devred — **Total 240 Minutes**

08h30 – 09h10	Magnet design: mechanics and magnetics of the LARP quadrupole TQS01	S. Caspi	35′	5′
09h10 – 09h35	CASTEM for magnet design	J.M. Baze	20′	5′
09h35 – 10h00	ANSYS applications magnet design	S. Farinon	20′	5′
10h00 – 10h30	ROXIE Program Features for the Electromagnetic Design of the Next Generation Accelerator Magnets	S. Russenschuck	25′	5′
	Coffee break		20′	
10h50 – 11h15	Thermal modeling of sc accelerator magnets	I. Novitski	20′	5′
11h15 – 11h40	Energy deposition by radiation: the CERN experience with FLUKA	A. Ferrari	20′	5′
11h40 – 12h05	Heat deposition by radiation/US	N. Mokhov	20′	5′
	LUNCH			

High Field magnets (non-accelerators)

Chair: Bruce Strauss — **Total 240 Minutes**

	Title	**Speaker**	**Duration**	**Discussion time**
14h00 – 14h35	EFDA dipole (design and manufacturing issues and fusion Nb3Sn developments)	E. Salpietro	30′	5′
14h35 – 15h05	Technologies for very high field solenoids at the National High Magnetic Field	J. Miller	25′	5′
15h05 – 15h30	Superconducting Undulators and Wigglers	S. Prestemon	20′	5′
	Coffee break		20′	

High Field magnets (accelerators)

15h50 – 16h25	LARP: Status and Progress	S. Gourlay	30′	5′
16h25 – 17h00	NED and other EU program (CEA-CANDIA-Twente-CERN)	A. Devred	30′	5′
17h00 – 17h35	US core accelerator magnet programs	A. Zlobin	30′	5′
17h35 – 18h00	ILC needs of HF magnets	O. Napoly	20′	5′

5 April 2006 — Conference room : Council chamber

Magnet Design

Chair: A. Zlobin — **Total 170 minutes**

09h00 – 09h35	Scaling law for quadrupoles and dipoles	E. Todesco	30′	5′
09h35 – 10h05	Towards computing training processes in superconducting magnets	P. Ferracin	25′	5′
10h05 - 10h35	Design options for high field Nb3Sn accelerator magnets	V. Kashikhin	25′	5′
	Coffee break		25′	
11h00 – 11h25	Progress in comparison of different high field magnet designs for NED	F. Toral	20′	5′
11h25 – 11h50	Combined function magnets for J-PARC neutrino beam line	T. Nakamoto	20’	5’
	LUNCH			

Magnet Design (continued)

Chair: S. Russenschuck — **Total 245 minutes**

14h00 – 14h35	Scaling pre-stress in dipole magnets and its application using bladders and collars	S. Caspi	30′	5′
14h35 – 15h00	Force for CosT: a parametrization	P. Fessia	20′	5′
15h00 – 15h25	Progress in NED mechanical design	P. Loveridge	20′	5′
	Coffee break		20′	
15h45 – 16h10	Fermi HF dipole and quadrupole: 2D and 3D design issues	G. Ambrosio	25′	5′
16h10 – 16h35	Progress in design at CEA	P. Vedrine	20′	5′
16h35 – 17h05	High field magnet development in Japan	A. Yamamoto	20′	5′
17h05 – 17h30	Discussion and summing up High Field magnet design		60′	

19h00 – 21h00	Cocktail at the Globe of Innovation (CERN)			

6 April 2006 Conference room : Council chamber

Main issue design of cycled (Hz range) magnets

Chair: W. Scandale **Total 140 minutes**

	Title	Speaker	Duration	Discussion time
08h30 – 09h05	Magnet design options for FAIR project	G. Moritz	30′	5′
09h05 - 09h35	Magnet design options for CERN injector chain	G. Kirby	25′	5′
09h35 – 10h00	Strand and cable design for cycled accelerator magnets	A. Verweij	20′	5′
10h00 – 10h25	1Hz Pulsed HTS coil cooled by heat pipes	M. Oomen	20’	5’
	Coffee break		20′	

Field Quality for Accelerators

Chair: Ezio Todesco **Total 75 minutes**

10h45 – 11h15	Field quality for cycled accelerator magnets	L. Tkachenko/ B. Auchamnn	25′	5′
11h15 – 11h40	Field quality of Nb3Sn accelerator magnets	Vl. Kashikin	20′	5′
11h40 – 12h05	Magnetization and instability regimes in Nb3Sn strand cable	M. Sumption	20′	5′
12h05 – 12h30	Magnet test analysis process and feedback to magnet design	S. Feher	20′	5′

LUNCH

New Concepts and Perspectives

Chair: Lucio Rossi **Total 180 minutes**

14h00 – 14h35	Racetrack Magnet Designs and Technologies	R. Gupta	30′	5′
14h35 – 15h10	25 T and beyond	P. McIntyre	30′	5′
15h10 – 15h35	Pipetron use in the LHC	G. de Rijk	20′	5′
15h35 – 16h00	Program on magnet and superconductors under DOE support: a global view	B. Strauss	20′	5′

16h00 – 17h00	**Discussion and SUMMARY**	**60′**	

Table of contents

Contributed papers

Session: Beam optics and layout for the LHC luminosity upgrade **Page**

R. Ostojic	IR Layout based on NbTi	16-18
S. Peggs	IR upgrades using Nb3Sn: report from Pheasant Run	19-24
J.-P. Koutchouk	Alternative IR solutions	25-28

Session: High field superconductors

A. Ghosh	High field superconductor development in the US	30-31
L. Oberli	Development in high critical current density Nb3Sn strand in Europe for NED and CERN programs	32-34
K. Tsuchiya	Nb_3Al superconductor development in Japan	35-37
L. Cooley	Review of Nb_3Sn instability	38-45
D. Dietderich	Cabling issues for Nb_3Sn	46-51
E. Barzi	Properties of modern Nb_3Sn strands and cables	52-55
J. Schwartz	HTS relevant for accelerator magnets	56-60
A. Ballarino	HTS in the LHC & in the LHC upgrades	61-63

Session: Design tools: potential and limitations

S. Caspi	Magnet design: mechanics and magnetics of the LARP quadrupole TQS01	65-67
J.M. Baze	CASTEM for magnet design	68-71
S. Farinon	ANSYS applications magnet design	72-76
S. Russenschuck	ROXIE features and prospects	77-79
N. Mokhov	Heat deposition by radiation/US	80-88

Session: High field magnets (non-accelerators) and (accelerators)

S. Prestemon	Superconducting Undulators and Wigglers	90-92
S. Gourlay	LARP: Status and Progress	93-97
A. Devred	NED and other EU program (CEA-CANDIA-Twente-CERN)	98-101

Session: Magnet design

E. Todesco	Scaling law for quadrupoles and dipoles	103-106
P. Ferracin	Towards computing training processes in superconducting magnets	107-110
F. Toral	Progress in comparison of different high field magnet designs for NED	111-116
T. Nakamoto	Combined function magnets for J-PARC neutrino beam line	117-121
S. Caspi	Scaling pre-stress in dipole magnets and its application using bladders and collars	122-124
P. Fessia	Force for CosT: a parametrization	125-129
G. Ambrosio	Fermi HF dipole and quadrupole: 2D and 3D design issues	130-131
A. Yamamoto	High field magnet development in Japan	132-133

Session: Main issue design of cycled (Hz range) magnets

G. Moritz	Magnet design options for FAIR project	135-143
G. Kirby	Magnet design options for CERN injector chain	144-149
A. Verweij	Strand and cable design for cycled accelerator magnets	150-151
M. Oomen	1Hz Pulsed HTS coil cooled by heat pipes	152-154

Session: Field quality for accelerators

L. Tkachenko & B. Auchmann	Field quality for cycled accelerator magnets	156-158
S. Feher	Magnet test analysis process and feedback to magnet design	159-161

Session: New concepts and perspectives

R. Gupta	Racetrack magnet designs and technologies	163-170
G. de Rijk	Pipetron use in the LHC	171-188
B. Strauss	Program on magnet and superconductors under DOE support: a global view	189-190

Presentations (powerpoint slides)

Session: Beam optics and layout for the LHC luminosity upgrade

F. Ruggiero	Performance limitations of the present LHC	192-203
D. Denegri	Detectors – goals and constraints	204-212

Session: Design tools: potential and limitations

I. Novitski	Thermal modeling of sc accelerator magnets	213-216
A. Ferrari	Energy deposition by radiation: the CERN experience with FLUKA	217-224

Session: High field magnets (non-accelerators) and (accelerators)

E. Salpietro	EFDA dipole (design and manufacturing issues and fusionNb_3Sn developments	225-238
J. Miller	Technologies for very high field solenoids at the National High Magnetic Field	239-245
A. Zlobin	US core accelerator magnet programs	246-252
O. Napoly	ILC needs of HF magnets	253-258

Session: Magnet design

V. Kashikhin	Design options for high field Nb_3Sn accelerator magnets	259-262
P. Loveridge	Progress in NED mechanical design	263-266
P. Vedrine	Progress in design at CEA	267-280

Session: Field quality for accelerators

Vl. Kashikhin	Field quality of Nb_3Sn accelerator magnets	281-285
M. Sumption	Magnetization and instability regimes in Nb_3Sn strand cable	286-296

Session: New concepts and perspectives

P. McIntyre	25T and beyond	297-305

Contributed papers

* * * * *

Session: Beam optics and layout for the LHC luminosity upgrade

UPGRADE OF THE LHC INSERTIONS BASED ON Nb-Ti MAGNETS

R.. Ostojic
CERN, Geneva, Switzerland

Abstract
The superconducting magnet technology based on Nb-Ti cable cooled at 1.9 K has been developed to its full potential for the present generation of LHC magnets. It is generally accepted that a new generation of magnets capable of operating at above 10 T will be required for the next hadron collider, including the upgrade of the LHC. Nevertheless, it is argued in this talk that Nb-Ti (1.9 K) superconducting magnets could be an appropriate intermediate step for the upgrade of the LHC insertions, where for different reasons, the potential of the technology has not been used to its utmost, or where further advances could be made for small-scale magnet production.

1. INTRODUCTION

Superconducting magnets based on Nb-Ti Rutherford-type superconducting cables have been at the forefront of the accelerator magnet science since the Tevatron construction (1980) and well into the 1990s with the SSC and LHC development efforts. Impressive progress has been made in all segments of magnet design and construction, from the superconducting wire and cable development, to the coil design and fabrication techniques, understanding of the dynamics of current sharing, of quench propagation and of protection issues through better modeling and measurement techniques, etc. All these factors contributed to the overall maturity of the field. As from the mid-90s, progress in magnet performance slowed down as attention turned to guaranteeing rather than enhancing performance, which is an essential element of a full scale and affordable industrial production. It is therefore reasonable to say that the Nb-Ti magnet technology has reached its full potential for large-scale production with the development of the LHC main dipoles.

In parallel with the construction of the LHC, the HEP accelerator community has continued to investigate the possibilities for the next generation of hadron colliders. It is generally accepted that a "super LHC", with substantially increased energy reach, will require a new generation of magnets capable of operating at well above 10 T. New magnet designs, based mostly on Nb_3Sn superconductors, have been proposed and discussed in conferences and networking events such as CARE workshops. The present R&D efforts in the US (LARP) and EU (NED), albeit still at a considerably lower level than required for effective advance, have focused recently on a demonstration of the Nb_3Sn technology for magnet parameters required for and in the timeframe compatible with an LHC luminosity upgrade.

In this context, it may be unusual to consider Nb-Ti magnets as an option for an LHC upgrade, as suggested by the title of this talk. Although the basic superconductor is inherently less performing than Nb_3Sn, the Nb-Ti technology is sufficiently mastered that a number of magnet designs can be readily extrapolated from the LHC experience. Furthermore, additional performance advances could be expected for purpose-built magnets. This flexibility opens certain alternatives that have not been fully exploited in the present LHC insertions, which deserve further attention should a change of some of the critical insertion magnets be necessary sooner than it is possible to complete the Nb_3Sn magnet development. In this talk, we sketch out some of the arguments why Nb-Ti magnet technology could provide an appropriate intermediate solution for the upgrade of the LHC insertions.

2. POSSIBLE UPGRADES OF THE LHC INSERTION MAGNETS

The LHC insertions contain several different types of superconducting magnets, most of them based on Nb-Ti conductor cooled at 1.9 K [1]. However, all stand-alone magnets (matching quadrupoles and separation dipoles) operate in saturated helium bath at 4.5 K. Further analysis of the design details shows in fact that superconducting magnets in the LHC do not all belong to the same generation, neither in terms of the superconducting cable performance, thermal and radiation properties of the coils, nor techniques of heat extraction. It is therefore natural to consider in the first instance whether the required performance for magnet upgrade could be achieved by using the LHC main dipole technology. As an example, the upgrade of the matching quadrupoles could be achieved by modifying the cooling scheme so as to operate them at 1.9 K (which is already the case for some of these magnets in the LHC arcs), with significant increase of field gradient. Similarly, the separation dipoles, which belong to the class of 4 T magnets, could be upgraded to 8 T if a design similar to the FRESCA dipole [2] were used. On the other hand, the experience with the present generation of the LHC dipoles and quadrupoles allows a fairly straightforward extrapolation to magnets of similar length or aperture, if so required.

The present LHC low-β triplets were designed and built by Fermilab and KEK as part of the contribution of the US and Japan to the construction of the LHC. The magnets developed by these two laboratories differ in several important features [1]. Nevertheless, they both fulfill the operational requirements of the LHC: they provide the necessary field strength and mechanical and dynamic aperture for the LHC circulating beams at 7 TeV and with a $\beta^*=0.55$ m at the collision points, corresponding to the nominal LHC luminosity of 10^{34} $cm^{-2}s^{-1}$. These quadrupoles also guarantee a safety margin of a factor of 3 with respect to the local peak power generated in the coils by the debris emanating from the *pp* collisions at nominal luminosity. The triplet cooling system enables extraction of 420 W at 1.9 K per triplet, which allows effective cooling of the magnet string up to three times the nominal luminosity. It is therefore possible that the present triplets could operate at the ultimate LHC luminosity of 2.3 10^{34} $cm^{-2}s^{-1}$, however, with a minimal margin.

The lifetime of the inner triplets is estimated as 7 years at nominal luminosity and standard LHC operating scenario [3]. The arrangements with Fermilab and KEK for the supply of the triplets included also one full spare triplet, which was compatible with the available budget and expectations that the work on the second generation of the quadrupoles would follow soon after their completion. Recent discussions on the LHC spare policy indicate that having one spare magnet of any kind, even if it represents a large fraction with respect to the nominal number, is absolutely a bare minimum in view of the relatively long time needed for repair or for the restart of fabrication. Any proposal for the inner triplet upgrade must therefore take the issue of spares into account and provide an appropriate solution.

The present layout of the low-β triplet contains two 6.3 m long MQXA (KEK) and two 5.5 m long MQXB (Fermilab) quadrupoles, all with a coil aperture of 70 mm and operating at 205 T/m in a mirror arrangement [1]. While fulfilling the optical requirements, this arrangement does not optimize the aperture and length of the magnets. Alternative layouts are possible if the aperture and length of the quadrupoles are adapted to their position in the triplet, allowing better use of the potential of the superconductor. Furthermore, use of moderate field gradient quadrupoles having larger apertures becomes possible at the expense of increased length of the magnets. Several possible designs of large aperture quadrupoles based on the existing LHC superconducting cables were recently considered [4]. It was shown that operational field gradients of 150 T/m may be achieved with coil apertures of 90-110 mm. An upgraded triplet requires in this case 8-10 m long quadrupoles, built as extensions of the existing technology.

A quadrupole aperture in the range of 100 mm opens the possibility of reducing β^* to 0.25 m, and hence increasing the luminosity of the LHC. However, as the product of the crossing angle and bunch length (Piwinski parameter) for the LHC beam parameters is already large, the luminosity

(proportional to F/β*, where F is a function of the Piwinski parameter and β*), increases by only a factor of 1.5 when β* is reduced from 0.55 m to 0.25 m. In these circumstances, reducing β* below 0.25 m would lead to ever smaller increase in luminosity at the expense of exponential rise of the quadrupole aperture. A possible remedy is to shorten the bunch length and reduce the Piwinski parameter. Nevertheless, it seems that in a quadrupoles-first scheme a β* of around 0.25 m remains a practical limit for an LHC upgrade. With this in mind, the increase of the coil aperture should be considered primarily as a means to counteract the large heat load that is concomitant with higher collider luminosity. Opening the aperture would also improve the field quality of the magnets and remove the need for higher-order multipole correctors, so that stronger orbit correctors can be included in their place. In this perspective, the reduction of β* to 0.25 m is a measure that is complementary to other factors for increasing the luminosity, rather than its driving element.

Having in mind the present status of the high-field magnet technology, Nb-Ti quadrupoles seem to be an appropriate intermediate solution that could bridge the gap from the initial LHC luminosity runs and 2015, by which time Nb_3Sn accelerator magnets should be fully developed. Although the Nb-Ti technology is mature, a number of design details could still be improved in the framework of small-scale production. For example, the cable insulation and the coil transparency for heat transport could be increased along the lines already studied for the LHC main dipoles [4]. In a more general sense, the engineering of the magnet and its coupling to the 1.9 K heat exchanger could be further optimized. Some improvements in the superconductor performance, or the use of ternary Nb-Ti(Ta) alloy could also be envisaged. These improvements could realistically lead to a 3-4 times larger safety margin than in the present triplets, which would allow regular operation of the low-β triplets at above the ultimate LHC luminosity.

3. CONCLUSIONS

Superconducting magnet technology based on Nb-Ti cable cooled at 1.9 K has reached maturity with the LHC main dipoles. Extensive experience exists in building magnets of different aperture and length, and extensions beyond existing designs seem straightforward. A number of superconducting magnets in the LHC insertions operate at 4.5 K, and in general do not all belong to the same generation. These magnets should in the first place be upgraded by using the technology of the LHC main dipoles. Furthermore, the small number of spare low-β triplets and separation dipoles is a serious concern for normal operation of the LHC. Alternatives are necessary in case the development of the next generation of high-field magnets (Nb_3Sn) takes longer than expected. For the present LHC low-β triplet, options exist which would allow to increase the acceptance by optimizing the length and aperture of each quadrupole. A number of design features of these magnets could still be improved, allowing regular operation of the triplet at above the ultimate LHC luminosity.

REFERENCES

[1] LHC Design Report, Vol. I, CERN-2004-003 (2004).

[2] D. Leroy et al., Design and manufacture of a Large Bore 10 T Superconducting Dipole for the CERN Cable Test Facility, IEEE Trans. Appl. Supercond. 10 1 (2000) 178.

[3] J. Kerby, Functional Specification - Inner Triplet Quadrupole Cryo-Assembly LQXB, LHC-LQX-ES-0006 (CERN EDMS 340672).

[4] C. Meuris et al., Heat Transfer in Electrical Insulation of LHC Cables Cooled with Superfluid Helium, Cryogenics 39 (1999) 921.

IR UPGRADES USING Nb_3Sn – REPORT FROM PHEASANT RUN

S. Peggs
U.S.-LHC Accelerator Research Program (LARP), U.S.A.

Abstract
This report summarizes the activities of the "LHC IR Upgrades Workshop" that took place at Pheasant Run, Illinois, in October 2005 [1]. It closely follows a presentation on this topic that was made at the "Workshop on Accelerator Magnet Design and Optimization" at CERN, in April 2006 [2].

1 INTRODUCTION

The LARP sponsored workshop at Pheasant Run was attended by 55 participants from 7 laboratories (ANL, BNL, CERN, FNAL, KEK, LBNL, SLAC) and 5 universities (Cornell, Kansas, Lancaster, Stony Brook, Texas A&M). There were three working groups:

1. IR optics, energy deposition, magnets; Chair: F. Ruggiero (CERN)
2. Beam-Beam compensation: Chair: T. Sen (FNAL)
3. Crab cavities: Chair: H. Padamsee (Cornell)

The presentations that were made, including closing plenary summaries by the working group chairs, are available on-line [3–5]. Condensed summaries are reported, one by one, below.

2 IR OPTICS, ENERGY DEPOSITION, MAGNETS

2.1 Doublet quads in symmetric optics

Elliptical beams could increase the luminosity by about 30%, with a reduced crossing angle. Symmetric optics require separate channels, for example including dipoles first or very special quads. The beam-beam tune footprints are considerably larger, so this scenario probably requires long range beam-beam compensation using wires. More study is needed!

2.2 Energy deposition in IRs

All IR upgrade scenarios that envisage a luminosity of $10^{35}\mathrm{cm}^{-2}\mathrm{s}^{-1}$ are challenging with respect to energy deposition, because of the linear and total power loads of 100 W/m and 1.2 kW on each side of IP. Simulation results are encouraging, but more study is required! Three aspects need to be addressed simultaneously:

1. Quench limits
2. Radiation damage (magnet lifetime)
3. Dynamic heat load on the cryogenic system

Items 1) and 2) are strongly linked. Nine "Action Items" were identified. Particularly high priority actions were to refine and test scaling laws for IR energy deposition with MARS, and to launch a beam testing R&D program on materials (superconductor and insulation) as soon as possible.

Mokhov concluded that open mid-plane dipoles are very attractive in dipole-first optics with luminosities of order $10^{35}\mathrm{cm}^{-2}\mathrm{s}^{-1}$. Their design accommodates large vertical forces, with 10^{-4} field quality. After 2 years, open mid-plane dipole designs now satisfy magnetic, mechanical, and energy deposition constraints. These designs propose splitting the dipole in 2 longitudinal pieces 1.5 and 8.5 m long, with a 1.5 m absorber in between. With such a design the peak power density in the superconducting coils is ok, the cryogenic heat load is ok, and the radiation damage issues are mitigated.

2.3 Nb_3Sn magnet R&D in the U.S.

The ongoing LARP plan is to develop 90 mm aperture R&D models to address critical design issues - magnetic, mechanical, and quench. LARP is confident that 90 mm results can be scaled over the entire aperture range of interest to LHC IR upgrades. The program currently designs to a 13 T peak field, while the program aims at 15 T or more in the HQ series of high gradient quadrupoles. For calibration: a peak field of 11 T with a 90 mm bore corresponds to a gradient of about 210 T/m.

Table 1: The LARP magnet R&D program

Series		When	Length L [m]	Gradient G [T/m]
Technical Quad	TQ	05-07	1	> 200
Long Quad	LQ	08-09	4	> 200
High grad Quad	HQ	08-09	1	> 250

Novel Nb_3Sn magnets have also been proposed by P. McIntyre, at Texas A&M. These include:

1. an iron-less quadrupole made from structured-cable, nominally to be placed 12 m from the IP, with a gradient of 390 T/m.
2. a 9 T "levitated pole" dipole that uses Nb_3Sn conductor at the pole tips, but NbTi elsewhere.

2.4 Summary by the chair of working group 1 (F. Ruggiero)

It is necessary to model compact IR geometries with novel magnets, particularly with regard to:

- heat deposition and radiation damage
- interference with detector performance

Also needed is a broad examination of the impact of reducing the magnet-free length L^* on the ensemble of issues that affect achievable β^*. Action items include the need for CERN beam physicists to circulate a draft proposal for aperture and field quality requirements, and to assess and compare chromatic performance of any IR solution, including quantitative considerations:

- luminosity
- lifetime
- tune footprints, on and off-momentum

3 BEAM-BEAM COMPENSATION

3.1 Large apertures or beam-beam compensation?

The crossing angle must increase as luminosity rises, because:

- any reduction of β^* implies a larger angular beam spread
- any increase in bunch current and/or number strengthens the beam-beam effect
- potential increases in the interaction length also strengthen the beam-beam effect

Increased crossing angles immediately leads to two painful questions:

1. How large must the upgrade magnet apertures become?
2. Is the geometric luminosity loss acceptable?

How well can beam-beam compensation minimize crossing angle increases?

3.2 Long range beam-beam compensation with wires

Long range beam-beam wires have been installed in the SPS, and used for single beam experiments. They are under construction for installation and studies in RHIC, with elliptic copper bar conductors, air cooled heat sinks, mounted on a vertically movable stand with a 60 mm stroke.

In the SPS experiment it was shown that the deleterious effects of one wire can be successfully compensated with a second wire at nearly the same (effective) phase. The compensation is tune dependent, including current and alignment sensitivity. It was found that the beam lifetime τ depends on the distance between the beam and the wire d as $\tau \sim d^5$, with an exponent of 5 that was lower than expected.

Long range beam-beam studies were performed in RHIC without a wire, with one bunch and one parasitic interaction per beam. Significant effects were seen. The beam current lifetime dropped for beam separations of $d < 7\sigma$, with a strong tune dependence. Not clear in these preliminary studies was the importance of machine nonlinearities and other time dependent effects – did they change with the beam-beam separation? Further studies are planned for RHIC in 2006 without wires, in 2007 with 2 wires powered DC, and in 2008 with 2 wires under pulsed excitation.

There are many challenges to beam-beam long range wires, in operation and under study:

- alignment errors
- current jitter. In study, apply white noise to induce emittance growth.
- optics errors, for example local coupling and spurious dispersion
- phase advance errors between parasitics and wire. In study, scan the longitudinal location of the parasitic collision.
- tune spread of the bunch
- tunes. RHIC and LHC fractional tunes are close. In study, scan the tunes over the limited range available.

The nominal CERN implementation requires the wires to be pulsed at an average rate of 439 kHz, with a turn-to-turn stability tolerance of 10^{-4}. How important are pulsed wires for PACMAN compensation? Is average compensation good enough? More simulations are required. If pulsed wires are required, what is the right frequency – does every PACMAN bunch need a different current?

3.3 Head-on beam-beam compensation with electron lenses

Experience at the Tevatron shows that the tune footprint due to head-on collisions can be efficiently compressed. However, implementation in the LHC would require locations where the horizontal and vertical beta functions are equal. The head-on beam-beam effect is a dominant source of emittance growth in RHIC. An electron lens could help improve RHIC performance. Further beam tests in the Tevatron (without parasitics) would be a useful first step in further studies.

3.4 Simulation challenges

Simulations typically calculate emittance growth rates. The SPS and RHIC experiments measured the variation of beam loss rates with wire currents, tunes and separations, et cetera. It is hard for the experiments to measure emittance changes over the small times studied in simulations. It is hard for simulations to predict beam lifetimes with good statistical accuracy. What is the common observable in experiments and simulations?

3.5 Segue

The compensation of long range beam-beam interactions with wires has the promise of allowing smaller crossing angles, more efficiently using the available aperture, and enabling higher luminosities. Experiments and simulations continue. Compensation of the head-on beam-beam effect with an electron lens

may be implemented in RHIC (following the Tevatron) and studied for LHC. Beam-beam compensation should help to ameliorate the ravages of the beam-beam effect, but it will not be perfect. If beam-beam is ferocious at the highest luminosities, then rapid beam separation will be needed – either dipole first optics or "large crossing angles". Large crossing angle scenarios need crab cavities to compensate for the geometric loss of luminosity.

4 CRAB CAVITIES

The optical matrix element R_{12} measures the appropriateness of a location for crab cavities. It achieves a conveniently large value of 30 -45 m just after the triplet quadrupoles, about 50 m from the IP, where there is about 30 to 60 m of longitudinal free space available in the current IR layout. A large total crossing angle of about 8 mrad – about 20 times the nominal angle – puts the beams about 0.4 m apart at this location, with separate 1-in-1 magnet bores. How transversely close can triplet quadrupoles (especially Q1) and crab cavities be? Gupta has suggested longitudinally staggered quads with the "other" beam in a field-free region just outside coil of "this" beam. In this case crossing angles as small as 4 mrad could be accommodated.

The transverse size of the crab cavity depends inversely on the RF frequency f, so that 800 MHz is much more attractive than 400 MHz. Similarly, the total RF voltage required V also depends inversely on the frequency, through the expression

$$V = \frac{cE}{2\pi e} \frac{\tan(\theta/2)}{f\sqrt{\beta^* \beta_{crab}}} \quad (1)$$

where E is the beam energy and θ is the crossing angle. Thus, higher frequency implementations – at 800 MHz or even 1200 MHz – are desirable in that they would make the system more compact both transversely and longitudinally.

KEK B will soon have operational experience with a 510 MHz crab cavity system. That cavity has a diameter of 0.43 m, but the full diameter of the cryostat is about 1.5 m. Its "squashed" cavity design (not circularly symmetric) has the advantage of raising the frequencies of unwanted HOMs. The KEK B longitudinal filling factor of $< 10\%$ is low for an LHC implementation, which would need a different concept (perhaps using multi-cell structures) with a larger filling factor.

Table 2: Crab cavity parameters for KEK B and for a nominal LHC upgrade

		KEK B	LHC
crossing angle	θ [mrad]	22	8
beam energy	E [TeV]	0.008	7
collision beta	β^* [m]	0.33	0.25
crab beta	β_{crab} [km]	0.1	2
RF frequency	f [GHz]	0.51	1.3
RF voltage	V [MV]	1.4	46

Table 3: Low level RF tolerances required for a nominal 400 MHz LHC crab cavity system (Ohmi & Zimmerman).

Left-Right crab phase tolerance	$\Delta\phi$	0.012^o
Crab-accelerating cavity phase tolerance	$\Delta\phi$	0.012^o
Emittance growth $< 10\%$/hr	$\Delta\phi$	0.008^o
Strong-strong lumi-lifetime $\approx$ 1 day	$\Delta\phi$	0.0015^o
Kick voltage jitter	$\Delta V/V$	0.1%

Table 4: RMS stability requirements for near-future machines

	Amplitude	Phase
SNS, JPARC storage rings	1%	1^o
ILC, LCLS	0.1%	0.1^o
XFELs, ERLs	$\sim$0.01%	0.01^o

Tables 2 and 3 show the tight low level RF tolerances that appear to be necessary for a 400 MHz crab cavity system in the LHC, in comparison with the near-future machines that have the tightest tolerances so far. There is still a way to go!

4.1 Comments from the chair of working group 3

Future studies should take a very hard look at 800 Mhz:

- Is emittance growth due to RF non-linearity ok?
- $R_{12} = 45$ m implies that $V = 37$ MV for $\theta = 8$ mrad
- Can use advanced gradient of 10 MV/m
- The active longitudinal length on each side of an IP is 3.7 m
- With a 30% filling factor, crabs occupy a length of 12 m per side
- The phase tolerance at 800 MHz is a factor of 2 more relaxed than at 400 MHz

ACKNOWLEDGMENTS

I would like to thank all those who contributed to the Pheasant Run workshop, and to apologize in advance to those whose work I may have inaccurately or incompletely represented. In particular, I would like to thank the chairs of the the three working groups – Francesco Ruggiero, Tanaji Sen and Hasan Padamsee.

References

[1] LHC IR Upgrades Workshop, Pheasant Run, Illinois, http://larp.fnal.gov/IR2005 (2005).

[2] S. Peggs, IR Upgrades Using Nb3Sn: report from Pheasant Run, http://wamdo-2006.web.cern.ch/wamdo

[3] Working Group 1 presentations, available at http://larp.fnal.gov/IR2005/showAllTalks.php

1. F. Ruggiero, Summary of WG1 on IR optics, energy deposition, magnets
2. G. Ambrosio, Design for Long Quadrupole
3. M. Bai, AC Dipole for LHC
4. P. Ferracin, IRQ Design comparison: shell-type vs. block type
5. R. Gupta, D1 Dipole Design/IR Magnet Study
6. J.-P. Koutchouk, Possible quad first options for the upgrade
7. P. McIntyre, A Structured-Cable Superconducting Quad for High-Heat-Load Applications
8. P. McIntyre, Levitated-Pole Superconducting Dipole for Use in Beam Separators for LHC
9. J. Johnstone, Doublet IR focusing
10. N. Mokhov, Energy Deposition Issues in LHC IR Upgrades -
11. R. Rabehl, IR Cryogenics and Heat Transfer
12. F. Ruggiero, LHC Upgrade Scenarios and Interaction Region Design
13. F. Ruggiero, Various LHC Upgrade Options
14. A. Valishev, Optics measurements at the Tevatron

[4] Working Group 2 presentations, available at http://larp.fnal.gov/IR2005/showAllTalks.php

1. T. Sen, Working Group 2 Closing Summary
2. W. Fischer, Beam-beam compensation at RHIC - LARP Proposal
3. W. Fischer, Long-range beam-beam interactions in RHIC
4. J.-P. Koutchouk, Beam-Beam compensation with wires
5. J. Qiang, Strong-strong simulation of long range beam-beam effects at LHC and RHIC
6. T. Sen, IR and Beam-Beam
7. T. Sen, Wire compensation proposal
8. J. Shi, Simulation Study of Compensations of Long-Range Beam-Beam Effect in LHC
9. X. Zhang, Use of Electron Lens in Tevatron and LHC

[5] Working Group 3 presentations, available at http://larp.fnal.gov/IR2005/showAllTalks.php

1. H. Padamsee, Working Group 3 Closing Summary
2. R. Gupta, A quadrupole design for crab cavity optics
3. T. Koeth, 3.9 GHz Deflecting Mode Cavity
4. D. Li, X-Ray Pulse Compression Using Deflecting Cavities - Studies at LBNL
5. B. Nash, Crab Cavity Induced Linear Synchrobetatron Coupling Resonances
6. K. Ohmi, Beam Dynamics in Crab Collisions
7. K. Ohmi, Simulations for the LHC to estimate the tolerable level of cavity noise
8. H. Padamsee, Summary of Crab Cavity Ideas
9. H. Padamsee, Super-LHC Crab Ambitions
10. F. Ruggiero, Crab cavities for the LHC Upgrade (by F. Zimmerman)
11. G. Waldschmidt, RF Deflecting Cavity Design for Generating Ultra-Short pulses at APS

SCALING LAWS FOR THE LUMINOSITY REACH OF QUADRUPOLE FIRST LHC LUMINOSITY UPGRADES

J.P. Koutchouk
CERN, Geneva, Switzerland

Abstract
Using a simplified parametric model for the LHC insertion upgrade, the luminosity reach is evaluated versus the distance of the triplet to the IP. The calculation is done for the two magnet technologies (Nb-Ti and Nb_3Sn) that can possibly be considered for the upgrade. The potential of an additional early separation scheme is demonstrated to yield a large luminosity increase, allowing the use of lower beam current. In all cases, the installation of machine magnetic elements within the detectors increases luminosity reach.

1. INTRODUCTION

The present nominal LHC high-luminosity insertion was very carefully optimized, so any significant gain in luminosity will require departing significantly from the baseline solution. For example, the β* function was chosen to yield the best luminosity in the presence of the required beam crossing angle. A simple further reduction of β*, effective in previous colliders, would not yield a significant luminosity increase in the case of the LHC (although such an option was considered when sizing the chromaticity correction system in the arcs, to allow further developments).

A parametric insertion model has been built to investigate the broad parameter dependences for the LHC luminosity upgrade [1].The parameter space being rather large, the goal of the model is to guide and identify potentially interesting solutions. The present version of this model benefits from better estimates of the gradient at quench for Nb-Ti and Nb_3Sn technologies [2] for an inner diameter of 100 mm that looks most suitable. Converted into the quench field at the inner coil diameter, the values assumed are as follows:

Nb-Ti: 9.65 T at inner coil diameter

Nb_3Sn: 14.4 T at inner coil diameter

The goal of this exercise is to estimate the luminosity reach as a function of the distance of the triplet to the crossing point for the upgraded LHC beam (ultimate bunch charge, number of bunches doubled, bunch length reduced by a factor of two). Several quadrupole apertures are considered, and the quadrupole length is assumed to be free. As an alternative, we also consider the luminosity reach of a solution including an optimal early beam separation scheme [1] and only the ultimate bunch charge (bunch number and length nominal).

All solutions used in this study have 20% field margin and "reasonable" optical aberrations. The estimate of the energy deposition is based on a scaling law *including only charged particles*. This conjecture is presently being checked against simulations.

2. RELATIVE LUMINOSITY AND MAXIMUM ENERGY DEPOSITION VS L*

In all the following, the luminosity is expressed in units of the nominal luminosity ($10^{34}cm^{-2}s^{1}$) and the energy deposition in units of the estimated quench level (the usual safety margin of 3 is ***not*** included). As can seen in Fig. 1, the nominal triplet would already yield a significant luminosity improvement by a factor of 4 to 5 if the shielding against the energy deposition from the debris could be improved by a factor of 2×3. Its limited integrated strength does not allow moving it significantly closer to the IP.

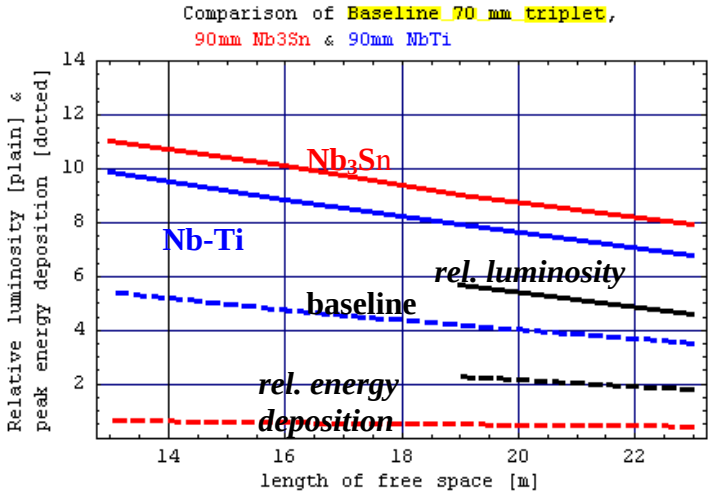

Fig. 1 Comparison of the performance of 70 mm and 90 mm quadrupoles.

At the cost of a moderate increase of magnet length (about 1 m for Nb_3Sn), the luminosity can be increased by 40% when the triplet is moved from its present position (23m) to 13m from the IP. From a purely optical point of view, Nb-Ti technology requires longer magnets that cause a loss of luminosity by 10% to 15%. However, the energy deposition is far above its quench level (4 to 5) ×3. This would require thicker inner shielding, further reducing the effective aperture and thereby the luminosity reach. In contrast, Nb_3Sn technology would offer greater luminosity and feature energy deposition only slightly above quench, requiring attenuation by a factor of not more than 3 to 4.

3. EFFECT OF ENFORCING A CLEARANCE OF 9 MM ON 90 MM APERTURE QUADS

The large energy deposition is likely to require a thicker inner shield. To investigate the consequence, the former cases were run enforcing a 10% aperture clearance to move the beam away from the wall leaving space for a 4.5 mm thick inner shield. It is seen in Fig. 2 that the cost of this 10% clearance is about 10% in luminosity reach. The effect of an inner shield on energy deposition is not yet implemented in the model. In another run, not illustrated here, it was verified that a 100 mm aperture insertion with 10% clearance reproduces rather well the performance of the 90 mm aperture insertion without clearance. The impact of the lengthening of the quadrupoles is small.

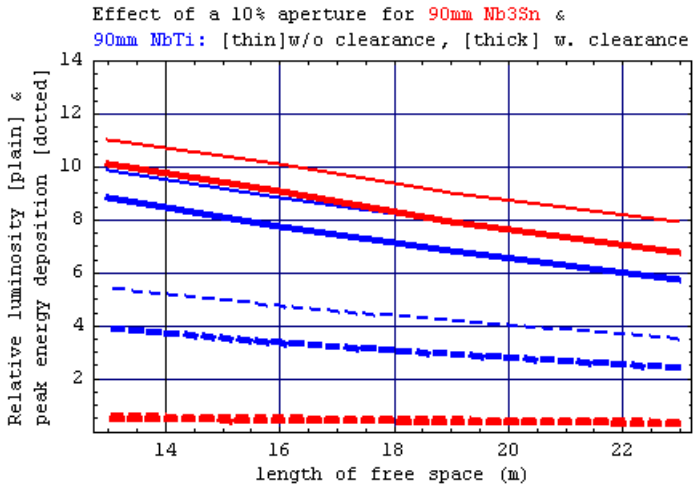

Fig. 2 Effect of a 10% aperture clearance.

4. IDEAL EARLY SEPARATION SCHEME IN IP5

The concept of an early separation was proposed in [1]. The required beam separation at the long-range interaction points is produced as usual by a crossing angle. However, two small dipoles placed deep into the detector kick the beam in such a way as to reduce or cancel the crossing angle at the collision point, while leaving mostly unchanged the beam separation at the long-range interaction points. In this way, the impact of the geometrical loss factor is cancelled or much reduced. For the nominal LHC, the gain would be only 16% in luminosity. For the upgrade however, the gain is typically a factor of 2 and may even reach a factor of 3 for very small β-values reachable with a triplet at 13 m from the IP.

Figure 3 illustrates an early separation scheme with a vanishing collision angle.

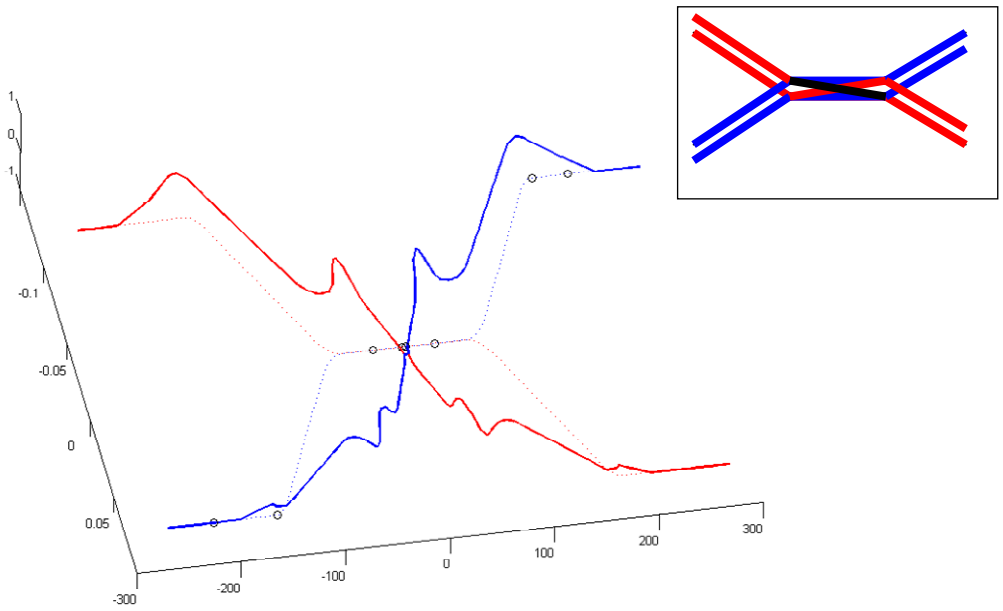

Fig. 3 Principle of the early separation scheme.

5. COMPARISON BETWEEN FULL UPGRADE AND AN EARLY SEPARATION SCHEME

We compare here the luminosity reach of the "full" upgrade as described in [4], namely ultimate bunch current, number of bunches doubled and bunch length reduced by a factor of two, with a scenario using an early separation scheme with vanishing collision angle. In the latter case, the bunch charge is kept at its ultimate value but the number of bunches is not doubled, neither is the bunch length reduced. The triplet technology and apertures are assumed to be Nb_3Sn, 90 mm for the full upgrade and 100 mm for the early separation scheme. This scenario requires 8 Tm dipoles at about 1.5 m from the IP [3]. It eliminates the need for an RF upgrade. As the beam current is significantly reduced, the collective effects and the heat load to the cryogenic system should be only slightly more than in the baseline LHC scenario. As can be seen in Fig. 4, the luminosity reach is remarkable. A consequence, however, is some increase of the event multiplicity with respect to usual upgrade scenarios, partly due to higher luminosity as compared to [4], and partly due to the greater efficiency of the collisions. This issue may be solved by reducing a little the luminosity via the bunch current. The baseline beam current would, for example, lead to a factor of the order of 5 in luminosity.

Fig. 2 Potential of the early separation scheme compared to the "full" upgrade scenario.

6. CONCLUSION

Approaching the triplet to the IP gives up to 40% luminosity increase (l* = 23 m => 13 m). From a purely optical point of view, the Nb-Ti technology requires longer magnets that cause a loss of luminosity of 10% to 15% as compared to the Nb_3Sn technology. However, the anticipated energy deposition is far above the quench level (4 to 5) ×3 for the former. Even with Nb_3Sn technology, the energy deposition must be reduced by a factor of 4, requiring an increase in the quadrupole aperture.

An early separation scheme can change the nature of the upgrade: it becomes possible to reach the luminosity goal with half the beam current, and get a significant increase with the baseline current. This has a major impact on issues like heat load to the cryogenics system, electron-cloud, collective effects - and overall complexity of the machine, which usually influences the integrated luminosity. The price to pay is an increase of the event multiplicity by up to a factor of two and the need to install magnetic machine components inside the detector. The issue of the energy deposition is also drastically modified: quantifying the reduction in the triplet will require more accurate simulations. The potential for increasing luminosity improves as distance to the IP decreases.

ACKNOWLEDGEMENTS

I wish to thank L. Rossi, G. Sterbini, E. Todesco and acknowledge the support of the European Community-Research Infrastructure Activity under the FP6 “Structuring the European Research Area” programme (CARE, contract number RII3-CT-2003-506395).

REFERENCES

[1] J.P. Koutchouk, Possible quadrupole-first options with $\beta^* \leq 0.25$m, CARE-HHH Arcidosso Workshop (2005).

[2] L. Rossi, E. Todesco, About the electromagnetic design of superconducting quadrupoles in particle accelerators (2006) to be published.

[3] J.P. Koutchouk & G. Sterbini, An early beam separation scheme for the LHC, submitted to EPAC 2006.

[4] F. Ruggiero, *ed.*, LHC Luminosity and Energy Upgrade: A Feasibility Study, LHC Project Report 626 (2002).

Session: High field superconductors

HIGH FIELD SUPERCONDUCTOR DEVELOPMENT IN THE US

A.K. Ghosh
Brookhaven National Laboratory, Upton, New York, USA

Abstract
High field superconductor development in the US has been strongly influenced by the needs of the HEP community. US industry has developed high J_c Nb_3Sn strand that has helped achieve 16 T in a dipole magnet. US-DOE Conductor Development Program has been instrumental in helping US industry in achieving non-Cu J_c in Nb_3Sn wire that exceeds 3000 A/mm2 at 12T. However these strands are intrinsically unstable to flux jumps at low field because of the large effective filament size. US industry has been developing strands with increasing number of sub-elements to lower the filament diameter and hence improve stability. In other superconductors, OST has developed Bi-2212 strands that are suitable for magnets exceeding 16 T. The relatively new MgB_2 is also being developed in wire form suitable for magnet coils. As yet MgB_2 wire has failed to realize the high field potential of this superconductor.

1. INTRODUCTION

The US Conductor Development Program funded by the High Energy Physics Office of DOE has been instrumental in the development of high-J_c Nb_3Sn wires. This program is augmented by the SBIR (Small Business Innovative Research) programs, one of which assists small companies in developing strands for HEP magnet needs. At the last WAMS meeting (2004), R. Scanlan described these programs and the goals of the development, one of which is the achievement of critical current density, J_c, in the non-Cu region of the wire >3000 A/mm^2 at 12 T. Oxford Superconducting Technology, OST has made wire with this record high J_c, using the Rod Re-stack Process, RRP. Target CDP goals and the current progress for Nb_3Sn is summarized in Table 1. This report describes the progress of development in US industry of Nb_3Sn, Bi-2212 and MgB_2.

Table 1
Target specifications for the HEP conductor

Long Range Goals	Progress
J_c (non-Cu, 12 T, 4.2 K) = 3000 A/mm^2	Achieved in RRP
J_c (non-Cu, 15 T, 4.2 K) = 1600 A/mm^2	Achieved in RRP
D_{eff} = 40 microns or less	Achieved in split sub-elements, J_c is lower
Piece length: > 10,000 m	>6000 m in RRP
Heat treatment: < 200 h	150-180 h
Cost: < $1.50/kA-m (12 T)	$ 5.50/kA-m (RRP)

2. Nb_3Sn

2.1 Oxford Superconducting Technology

OST has been producing the 54/61 design RRP internal-Sn strand for several years. During the last year, they processed 250 kg under the LARP and CDP programs. 93% of the lengths delivered were greater than 1 km, with more than 50 % in lengths > 3 km. The average J_c of the strands was ~2900 A/mm^2 at 12 T and > 1500 A /mm^2 at 15 T. This was achieved for a reaction of 50 h at 665 C.

The average RRR of the strands was ~ 180 indicating that the Nb barrier does not react through - which can lead to Sn-contamination of the stabilizer and a reduction in RRR.

The work by Peter Lee (ASC'04, EUCAS'05) has shown that the higher J_c in these strands are a result of higher Nb_3Sn content as well as a higher layer J_c than the ITER or early MJR wire.

OST has also made several R&D billets with higher number of re-stack elements, 91, 108 and 217 filaments to reduce the effective filament size. With increasing number of re-stacks, the processing becomes more difficult as the non-tin parts work-harden. In addition the increased number of surfaces introduces bonding problems which reduces the yield due to wire breakage. Although high J_c can be achieved in these wires, there seems to be a trend of lower J_c with decreasing filament size.

OST has also been developing strands with Ta-dividers to effectively lower the filament size. This was successfully demonstrated for a 37-filament billet where the effective filament diameter was calculated to be ~ 40 μm from magnetization measurements (ASC'04).

Overall, OST has been by far the leader in high J_c development and this is the main reason that its wire is the "baseline" strand for the magnets being developed in the LARP program.

2.2 Outokumpu Advanced Superconductors

OKAS has been developing high-J_c wire for HEP. The development has been slow, with strands that are still considered R&D material; J_c ~ 2400 A/mm2 has been achieved. The 0.8 mm wires contain 37 sub-elements with individual barriers similar to RRP wire, and have filament diameters of ~ 100 μm.

2.3 Supercon

Supercon has been developing powder-in-tube (PIT) wire using Nb and NbTa tubes under an SBIR program. To date their wires have achieved ~ 1300 A/mm^2 - much lower than that of SMI in Europe.

3. Bi-2212

This HTS is useful for magnets, as it can be fabricated in wire form. OST has been the leading company for this material in the US and has developed 0.8 mm strands that show an engineering Je (10 μV/m criterion) at 25 T of 400 A/mm2 and an n-value of 17. For magnets with fields > 20 T, this wire becomes very attractive compared to Nb_3Sn. Prototype Rutherford cables have been fabricated and are undergoing reaction trials. Braided ceramic yarn has enabled manufacture of layer-wound, wind-and-react coils. A successful wind-and-react coil technique has produced a 1 T insert in a 19 T background, and shows good potential for future high field insert coils. The precursor composition strongly affects J_e, and the performance at 20 K is substantial, with potential for improvement. Bi-2212 wire offers unique benefits over other HTS materials as round or rectangular wire can be made which shows no anisotropy. Lengths are available today that are suitable for cable and coil development. With continued R&D there is good reason to expect substantial performance improvement and cost reduction.

4. MAGNESIUM DIBORIDE

This superconductor (MgB_2) is the latest in a long line of potential high field superconductors. Although thin film work shows that this 39 K superconductor has the potential for an upper critical field of 40 T that still remains to be demonstrated for a wire. One needs to introduce sufficient doping in the high T_c phase to raise the H_{c2}, and secondly, since wires are usually made using powder technology, the issue of connectivity remains a major issue. Nevertheless, HyperTech under SBIR and other programs have produced long lengths of wire by the CTFF process which carries 200 A at 1T. At present this superconductor seems to be a suitable wire for low field applications at temperatures in the range of 4-10 K. There has been steady progress in wire development. The challenge is to increase the fill factor, and the connectivity of grains.

DEVELOPMENT OF HIGH CRITICAL CURRENT DENSITY Nb_3Sn STRAND IN EUROPE FOR NED AND CERN PROJECTS

L. Oberli
CERN, Geneva, Switzerland

Abstract
In the framework of the CARE (Coordinated Accelerator Research in Europe) project, the Next European Dipole (NED) activity has started to assess the suitability of Nb_3Sn technology to prepare for a luminosity upgrade of the Large Hadron Collider in the insertion regions. One goal of the NED activity is to promote the development of high performance Nb_3Sn strands and cables in collaboration with European industry, aiming at a non-copper critical current density of 1500 A/mm^2 at 4.2 K and 15 T. After establishing specifications for strand and cable, CERN issued a call for tenders in June 2004 and, in November 2004, awarded a contract to two firms, Alstom-MSA in France and Shape Metal Innovation (SMI) in Netherlands to develop the NED conductor. This is being done in the framework of the NED activity funded by the EU-FP6 program. A contract, funded by CERN, was also awarded in April 2005 to Luvata (formerly OUTOKUMPU) in Finland. We report here on the status of Nb_3Sn conductor development presently being carried out in Europe.

1. INTRODUCTION

The NED activity at CERN started with a preliminary magnetic design for a large bore, high field Nb_3Sn dipole magnet [1] that was initially aimed at deriving meaningful Nb_3Sn strand and cable specifications. Preliminary investigations of the layered $\cos\theta$-type, 88 mm bore dipole led to the definition of a 26 mm wide Rutherford cable, made from 40 strands of 1.25 mm in diameter. The strands consist of Nb_3Sn filaments with a maximal effective diameter of 50 μm embedded in a copper matrix. The strand has to reach a minimum critical current of 1636 A at 4.2 K and 12 T. The main characteristics of the strand are given in Table 1.

Table 1
Main characteristics of the NED strand

Parameter	Value
Diameter	1.250 mm
Effective filament diameter	< 50 μm
Cu to non-Cu ratio	1.25 ± 0.10
Minimum critical current at 4.2 K	1636 A at 12 T 818 A at 15 T
Non-Cu critical current density at 4.2 K	3000 A/mm^2 at 12 T 1500 A/mm^2 at 15 T
RRR after full reaction	> 200

2. CONDUCTOR DEVELOPMENT PLAN

After discussion with CERN, a conductor development plan made of two R&D stages was established with each firm to develop systematically the NED conductor. The first development stage (referred to as step 1) aims at the qualification of the initial strand design, while step 2 is for the qualification of the final strand design. These two steps will be followed by the establishment of a viable industrial process for strand and cable production. The potential of each billet design and that of its eventual industrialization were also discussed in detail between each Contractor and CERN.

3. STATUS OF STRAND DEVELOPMENT

3.1 Status of strand development for SMI

For SMI, whose manufacturing process is based on the powder in tube technology, step 1 is devoted to reach a non-copper critical current density larger than 2500 A/mm^2 at 4.2 K and 12 T based on an existing 192 filaments strand design while step 2 is devoted to develop the NED strand with 50 μm filament diameter and to scale up to a larger size billet. SMI produced two billets B201 and B205 during step 1 with a different powder composition as compared to an existing billet B179 that had produced 2250 A/mm^2, adding more tin in the powder to react a larger fraction of the Nb-7.5%Ta wall. The two billets were drawn without breakage to a diameter of 1 mm to get 50 μm filament diameter. However, severe tin leakage occurred at the melting point of tin during the heat treatment of the strand leading to a lower critical current density than expected. SMI launched an effort to optimise the critical current density of the billet B179. The duration of the heat treatment at 675 ^{o}C was extended to 84 hours and a critical current density of 2410 A/mm^2 at 4.2 K and 12 T was obtained. Based on this result, SMI launched a new billet (B207) design to get a strand of 1.25 mm in diameter with 50 μm filament diameter by using Nb-7.5%Ta tubes identical to billet B179 and with the same powder composition. The strand reaches a high critical current (~ 1300 A at 4.2 K and 12 T, thus only 20 % below the 1636 A target value) but a rather low critical current density (2077A/mm^2). This lower than anticipated critical current density is attributed to a problem in the powder preparation which underwent by mistake an additional heat treatment. Stability current measurements carried out by INFN-Milano did not show any flux-jump induced quench for field sweeps around 15 mT/s and currents up to 1600 A. The magnetization measurements performed at INFN-Genova confirm that the wire exhibits few flux jumps and that the effective outer diameters of the Nb and Nb_3Sn tubes are conform to expectations: 58 μm for the Nb tubes and 46 μm for the Nb_3Sn tubes. Finally, the strands were deformed mechanically by rolling to study the strand sensitivity to unidirectional deformation and to evaluate if the strands are capable of being cabled. Whereas the filament layout of the billet B179 rolled to a deformation level of 28 % was severely affected showing shear fracture planes crossing the filaments, the filament layout of the billet B207 was able to sustain the high unidirectional deformation.

SMI has launched the fabrication of another billet with an identical filament layout as for B207 to achieve at least the critical current density obtained with the billet B179 and to qualify the strand design by relevant cabling tests.

3.2 Status of the strand development at Alstom-MSA

For Alstom-MSA, which promotes the Internal Tin Diffusion (ITD) technology, step 1 is devoted to develop the ITD fabrication process based on cold drawing and to study the influence of relevant parameters on workability and performance. For step 1, Alstom-MSA launched the fabrication of five types of strand, with the aim of determining the optimum design to get high critical current. All sub-element billets suffered from an excessive number of breakages, except a sub-element billet with a central tin core which was successfully drawn to restacked dimension. Alstom-MSA has identified the origin of the breakages which were due to a lack of cohesion between the different elements. The manufacturing process has since been improved by Alstom-MSA. In agreement with CERN, Alstom-MSA has produced with a modified process three additional sub-element billets which were drawn

without breakage to the restack dimension. The main issues related to the problems of workability in the manufacturing of sub-element billets have been solved by Alstom-MSA. The development program now proceeds through step 2, concentrating on the manufacturing process of the final billet.

3.3 Status of the strand development at Luvata

The manufacturing process of Luvata is based on Internal Tin Diffusion technology. The development plan has been discussed thoroughly with CERN and two different manufacturing processes were chosen for step 1. For both processes the billet design for the sub-elements is based on a central tin core layout, whereas the final billet will either be manufactured by a double stacking or by a quadruple stacking process. The optimum strand design derived from step 1 will be chosen to continue the development of the NED strand during step 2.

4. CONCLUSION

The technical challenges to develop a strand fulfilling the NED specification are numerous. After little more than a year of development, it can be seen that significant progress has already been made. SMI should reach shortly a critical current density of at least 2400 A/mm^2 at 4.2 K and 12 T for a NED-type strand. Alstom-MSA has also made a vigorous effort to develop the NED strand, and very encouraging results have been obtained.

REFERENCES

[1] D. Leroy and O. Vincent-Viry, Preliminary magnetic designs for large bore and high field magnets, CERN/AT 2004-22 report (2004).

Nb_3Al DEVELOPMENT IN JAPAN

K. Tsuchiya, C. Mitsuda
High Energy Accelerator Research Organization (KEK), Tsukuba, Japan
T. Takeuchi, A. Kikuchi
National Institute for Material Science (NIMS), Tsukuba, Japan

Abstract
NIMS has been devoting its energies to the development of the RHQ processed Nb_3Al wires for a number of years and KEK has also started an R&D program several years ago in collaboration with NIMS. This paper describes the present status of the RHQ Nb_3Al wires in Japan.

1. INTRODUCTION

At present, Nb_3Sn wire is chosen for the development of high field accelerator magnets in terms of the properties, availability, and cost. However, it is a brittle compound, and thus requires special handling and processing. Compared to this material, Nb_3Al has a better strain tolerance and has shown promising high field characteristics compared to Nb_3Sn when processed by a Rapid Heating /Quenching (RHQ) process. This conductor could therefore become an interesting candidate for use in future high field magnets and/or high field NMR magnets. For this reason, we have been developing Nb_3Al wire for a number of years [1].

In this process multifilamentary Nb/Al precursor wires are prepared by a conventional Jelly-Roll (JR) process. The starting monofilament is assembled by rolling Nb and Al foils around a pure Nb core, and then extruded and drawn to a wire. The monofilament wires are restacked into a multifilament billet, and the billet is drawn to a wire of the final size. For the extrusion and drawing processes, the billet is encased in a Cu sheath to make the size reduction process smooth, but the Cu must be chemically removed for the RHQ process. Thus, the multifilamentary wire has a Nb-matrix structure. In RHQ operation, these precursor wires are rapidly heated up to about 2000 °C by ohmic heating of a constant current passed through a section of the wire, which was moving at a constant velocity, between a Cu electrode pulley and a molten Ga bath, then subsequently quenched in a Ga bath at about 50 °C. Through this process, the Nb/Al composite filaments are converted into a Nb/Al supersaturated bcc solid solution. The RHQ condition is an essential processing parameter that determines the critical characteristics of the Nb_3Al. On the surface of wires treated by the RHQ operation, Ga and Nb oxide layers are present. These were filed off mechanically and then the stabilizing copper is attached on the surface of the wire by a special plating technique.

2. KEK ACTIVITY

The major development items at KEK are to increase the non-copper J_c and to find a good stabilization method [2]. For the former item, several wires with different Nb-matrix ratios (1.0, 0.8 and 0.6) were fabricated, and the effects of the Nb-matrix ratio and area reduction conditions after the RHQ treatment were studied. By decreasing the Nb-matrix ratio, we could increase the non-Cu J_c, but the best J_c was obtained in samples with a Nb-matrix ratio of 0.8, not in samples with a Nb-matrix ratio of 0.6. Figure 1 shows the non-copper J_c of stabilized Nb_3Al wires. The highest non-Cu J_c achieved so far was 2156 A/mm^2 at 10 T and 4.2 K, corresponding to a superconductor current density of 3881 A/mm^2.

For the latter item, a special copper electroplating technique to deposit a thick Cu layer on the surface of the wire was developed and the mechanical bonding strength and the electrical characteristics of the Cu layer were studied by bending and drawing the wire, and by measuring the

resistance. Although the present piece length of the Cu stabilized Nb_3Al wire is about 40 cm, we can draw and reduce the wire down to 60% of the original diameter without damaging the bonding of the Cu stabilizer. In order to scale up the technology, we have constructed a pilot plant that can produce a long copper stabilized Nb_3Al wire and started the commissioning recently.

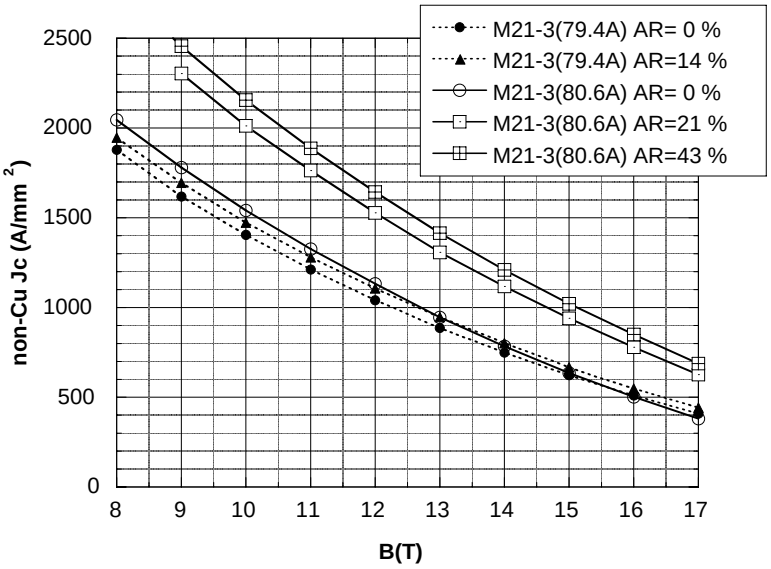

Fig. 1 Non-copper J_c of Nb_3Al wire.

3. NIMS ACTIVITY

One of the major development items in NIMS is the scale up of the wire fabrication. The target is to increase the piece length more than 2 km for the wire of 1.35 mm diameter. For this purpose an assembling technique of a large multi-billet with 140 mm diameter and 450 mm length (about 50 kg) was developed and 2.6 km long wire was successfully fabricated from the billet. In addition to making a long-length Nb/Al precursor, a uniform RHQ treatment along the long-length precursor wire is very importance for the scale up. NIMS had prepared a new reel-to reel apparatus that had a capacity of RHQ processing for 3 km long wire and they succeeded to fabricate a long-length RHQ Nb_3Al wire. Now they entered the stage to study the quality of the long-length wire by making a solenoid with a reasonable size.

Next development item is a development of the stabilization technique. They developed a Cu iron-plating technique to destroy a Nb oxide layer on the surface of the wire and to obtain a good bonding between copper stabilizer and the RHQ processed wire [3]. To date they have produced 1.2 km long copper stabilized Nb_3Al wire.

Recently NIMS started a trial fabrication of 27-strand Nb_3Al Rutherford cable in collaboration with Fermilab. Figure 2 shows the cross section of the cable, and Table 1 lists the main parameters of the strand used for the cabling test. The cross-section is about as expected, but some separation of the copper can be seen at the edge of the cable. This problem must be solved in the near future.

Fig. 2 Cross-section of the Nb_3Al Rutherford cable. The packing factor of this cable is 90.1%.

Table 1
Main parameters of the Nb_3Al strand used for cable fabrication

Strand diameter	1.03 mm
Number of Nb_3Al filament	144
Filament diameter	50 μm
Cu / non-Cu ratio	0.65
I_c @ 15 T, 4.2 K	380 A

4. SUMMARY

Compared to the recently developed high J_c Nb_3Sn wires, the non-Cu J_c of the Nb_3Al wire is a little lower, however, it has a very attractive feature of high strain tolerance. Therefore NIMS and KEK have been developing the RHQ Nb_3Al wires suitable to the future high field magnet for a number of years. The highest J_c achieved so far is 2156 A/mm^2 at 10 T and 1021 A/mm^2 at 15 T. We will continue the effort to increase the non-Cu J_c.

For the stabilization technique of the wire, both laboratories have developed their own method. Up to the present time it cannot be said which of the two is better. Although the bond between Cu stabilizer and the Nb_3Al wire is fairly good, it would be preferable to make it stronger.

A trial fabrication of Nb_3Al Rutherford cable has just started in collaboration with Fermilab. A study of various properties, e.g. mechanical and superconducting characteristics, will be performed soon, with the aim of producing suitable cable for future high field accelerator magnets.

ACKNOWLEDGEMENTS

We are very grateful to CERN and Prof. Yamamoto for their continuous support and encouragement in this development. The authors would like to express our thanks to the Tsukuba Laboratory of the NIMS for providing a chance to use the high-field magnet facilities.

REFERENCES

[1] T. Takeuchi and K. Tsuchiya, Proceedings of the Workshop on Accelerator Magnet Superconductors (WAMS 2004) 122.

[2] K. Tsuchiya et al., MT-19, IEEE Trans. Appl. Supercond. 16 2 (2006) 1204.

[3] A. Kikuchi et al., ASC2004, IEEE Trans. Appl. Supercond. 15 2 (2005) 3376.

INSTABILITIES IN Nb_3Sn WIRES

L. Cooley and A. Ghosh
Brookhaven National Laboratory, Upton, New York, USA

Abstract
High current density Nb_3Sn strands made by internal-tin routes are not stable against flux jumps at low fields. Since flux jumps release heat, they can initiate quenching if thermal conductivity to the liquid helium is poor. To make matters worse, tin is a potent contaminant of copper, and reaction of strands to maximize performance leads to the loss of thermal conductivity. We discuss how the root of a solution of this problem lies in optimizing two parameters, *RRR* and J_c, instead of J_c alone. An important workaround for magnet designers is controlling the balance between performance and stability by reducing the temperature or time of the final heat treatment step. This provides ample J_c while also keeping *RRR* high. Under these conditions, the instability current density threshold J_s is higher than J_c. Additional factors are also available to improve the management of instabilities, including new strand designs with smaller sub-elements or divided sub-elements.

1. INTRODUCTION

We review recent work to understand and overcome instabilities in high-J_c Nb_3Sn strands developed for high-field dipole and quadrupole magnets. A general specification by magnet programs is for strands to have very high critical current density J_c, such as the 3,000 A mm^{-2} target of the U.S. HEP R&D program. This presents two central problems to the operation of a stable magnet. First, the tendency to maximize critical current density leads to consolidation of filaments into a single mass and substantial reaction of the Nb diffusion barrier, creating an effective diameter that is equal to the diameter of the subelement itself. Second, the tendency to react substantial fractions of the diffusion barrier brings the tin perilously close to or in contact with the copper stabilizer, resulting in contamination of the copper and loss of its electrical and thermal conductivity. In combination, these problems can prevent the operation of an accelerator magnet because flux jumps initiate quenches in the low-field portions of the magnet.

There are several strategies to work around these problems, which we outline in this report. Foremost is the implementation of less aggressive reaction heat treatments, which preserve the stabilizer and, rather remarkably, produce current densities almost as high as the maximum that can be obtained. In addition, we discuss progress in other strategies, including subdividing the sub-element to reduce the effective diameter of the superconductor, increasing the number of sub-elements to reduce their diameter at given wire diameter, and varying the ratio of sub-element perimeter to its area. We also discuss measurements and diagnoses.

2. KEY FEATURES OF MODERN ACCELERATOR MAGNET STRANDS

Almost all internal-tin wire designs now being used greatly restrict the amount of inter-filamentary copper to maximize the sub-element fraction that is converted to superconductor after reaction. This increases the non-copper J_c. As a result, filaments merge into a solid mass during the reaction heat treatment, producing a large characteristic size over which magnetization and transport currents flow (the effective diameter).

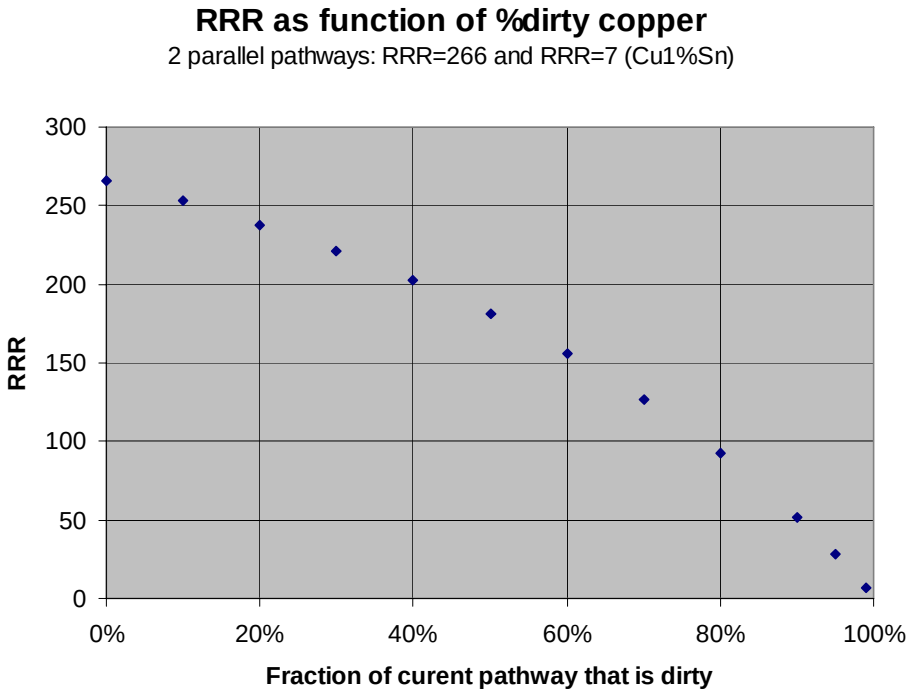

Fig. 1 RRR calculated for a bimetal composite strip, consisiting of a fraction *f* of "dirty" copper (RRR ~ 7, resistivity at room temperature = 1.88 μΩ cm) and a remainder (1-*f*) of "clean" copper (RRR = 266, resistivity at room temperature = 1.00 μΩ cm), as a fraction of the dirty copper.

In addition, wire manufacturers have found it beneficial to wrap each sub-element restack with its own diffusion barrier, instead of using a single diffusion barrier around the entire filament pack (as is used in many wires for the ITER). A significant fraction of the diffusion barrier is subsequently reacted; this is *intended* in the design of most strands. Since the diffusion barrier forms an annulus around (and often merged with) the filament pack, its partial reaction can produce a large effective diameter. Even if the filaments are tightly packed, the modern reaction prescriptions are quite successful at distributing tin throughout the sub-element during low-temperature steps of the reaction, and it is difficult to avoid reaction of diffusion barriers made from Nb. Other barrier materials, such as Ta and V, are not as ductile and are prone to thinning or rupture.

As pointed out by Wilson [1], an adiabatic stability threshold is crossed when the magnetic energy stored within the critical state exceeds the heat capacity of the superconductor and its thermally bonded copper. Given that sub-element diameter $d_s = d_w\ [N(1+R)]^{-0.5}$, where N is the number of sub-elements and R is the stabilizer to non-stabilizer area ratio, typical values of d_s are ~100 μm for wire diameters d_w of approximately 1 mm. For a 100 μm sub-element carrying a current density of 3,000 A mm^{-2} at 12 T and 4.2 K, the heat capacity of a strand (~1,000 J m^{-3} K^{-1}) and the ~15 K operating margin barely meet this stability criterion against small disturbances. This means that flux-jump instabilities are essentially inevitable at low fields, due to the faster-than-linear increase of J_c with decreasing field. So far, all internal-tin strand designs exhibit flux jumps at low fields.

Since flux jumps deposit heat into a magnet, management of the heat is an important task to ensure safe operation. Here, however, the potency of tin for scattering electrons in copper is an obstacle. According to Fickett [2], even as little as 0.1% Sn (atomic %) is sufficient to reduce the residual resistivity ratio RRR of copper to 7. This contamination level is well below that which can be reliably detected by micro-chemical analyses, which are sensitive to 0.5%. Any drop in RRR from its value of ~300 for oxygen free high-conductivity copper signals significant contamination. For example, if two parallel copper pathways are considered, one with RRR = 266 and the other with RRR = 7, Fig. 1 shows that a significant fraction the total electrical pathway must consist of the contaminated portion by the time a decrease of RRR to ~100 occurs.

Reaction heat treatments often produce the maximum J_c value by maximizing the area fraction of the sub-element that is converted to Nb_3Sn. Since Nb diffusion barriers have the best ductility and produce the most uniform sub-elements, this means that partial reaction of the barrier is intended, bringing the tin supply close to and then in contact with the copper stabilizer. Thus, maximum J_c is correlated with tin reaching the copper and a reduction of RRR. So, while magnet R&D programs have emphasized maximizing J_c to provide headroom for solving other problems, they also facilitate loss of electrical and thermal conductivity of the copper matrix. This reduces both heat conduction to the liquid helium bath and inductive coupling to retard the flux jump. The specific behavior, which obeys complicated sets of coupled nonlinear thermo-electromagnetic equations [3], is beyond the focus of our review. What is essential is that the two problems above can combine to initiate quenches in the low-field portions of magnets.

3. STABILITY CURRENT DENSITY

During the past 4 years, new test mandrels and new testing procedures have reduced the tendency for Nb_3Sn strands to quench during standard critical current measurements. Key improvements include control of strand motion, support for transport current across transition zones, and lengthening of the current input region. These improvements now make it routine to attain stable voltage vs. current curves (*V-I* plot) at fields above about 8 tesla, where critical currents can approach 1,000 amperes, which allow the extrapolation of a critical current criterion through the measured data. Below this field range, quenches of the strand often occur well below the critical current. Flux jumps can be triggers for these quenches. Significant efforts at Fermilab and at Berkeley have mapped out in detail the quench thresholds for various regimes of field, strand diameter, sub-element number, and so on, and the observed boundaries appear to be consistent with stability calculation.

However, the multiple potential quench triggers in a short-sample experiment, let alone in a magnet, make it difficult to decipher whether in fact flux jumps initiate quenching or whether other sources, such as mechanical motion, become active as the testing current increases. This distinction is important, because flux-jump instabilities are intrinsic to the properties of the strand itself, whereas other triggers are related to the quality of test fixture or magnet assembly. Magnetization measurements, in which the sample is free from mechanical binding, definitely show that all internal-tin strands used in HEP programs experience flux jumps at low fields. Here, the magnetic moment of the sample is monitored while the magnetic field is swept with the sample held at constant temperature. Since vapor cooling is typically used in magnetometers, these experiments are conducted at a lower stability than for samples immersed in a coolant bath.

Our recent work [4-6] outlines an experimental technique to determine the maximum current density that can be passed through a strand experiencing a flux jump and still able to recover. Like magnetization experiments, the sample is held at constant temperature under a field sweep. However, this is conducted while the sample also carries a constant transport current and while it is immersed in the liquid helium bath. The transport current is at or below the current used to generate successful a *V-I* plot at higher fields, making other triggers of flux jumps unlikely. The resulting plot of voltage versus field (*V-H* plot), such as that in Fig. 2, typically shows numerous voltage spikes, which are generated by flux jumps as the current and field profiles inside the strand alter to accommodate the external field change. Since the strand J_c can be very high in this field range (0 to 4 tesla), the critical current lies far above the transport current, and there is ample capacity to accommodate current transfer between the sub-elements. It is also important to recall that even though the transport current can be carried by a small fraction of the total number of sub-elements at low field, all sub-elements are fully carrying induced magnetization currents if the field has been ramped over an interval larger than the penetration field, typically < 1 T. The central question is whether the thermal perturbations caused by the current and flux rearrangements can escape to the coolant bath without quenching the strand.

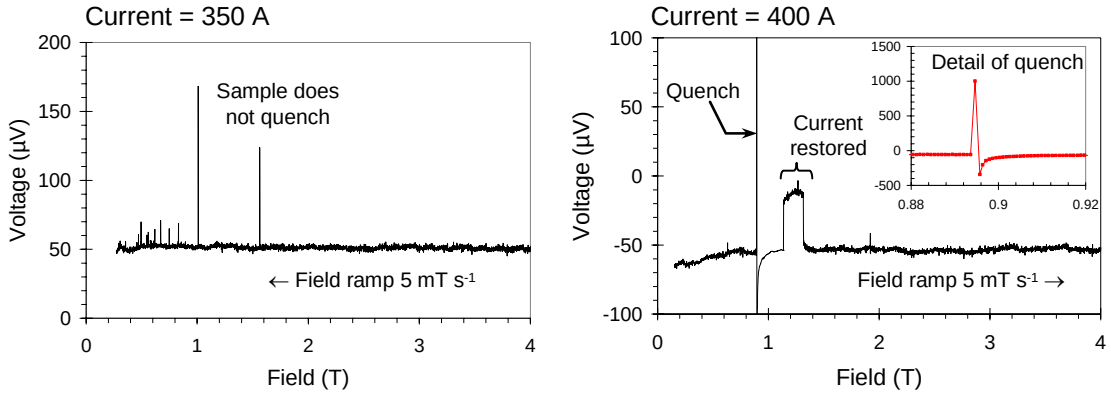

Fig. 2 *V-H* plots for two settings of constant applied current. On the left, a current of 350 A is below the threshold where heat released by flux jumps causes the strand to quench. On the right, a current of 400 A produces a quench that drives the conductor above the critical temperature, tripping the power supply.

After measuring a number of *V-H* curves at different applied currents, it is typically seen that the applied current is correlated with the likelihood that a flux jump will quench the strand. This correlation allows a stability current density threshold, J_s, to be defined by the maximum current at which flux jumps do not result in quenching of the strand. In fig. 2, this threshold current is between 350 and 400 A, yielding J_s of ~1400 A mm^{-2} for this 0.8 mm diameter strand (50% copper stabilizer).

4. BALANCING J_C, J_S, AND RRR

As mentioned earlier, a nearly complete reaction of the diffusion barrier is intended in most internal-tin strand designs, following from a strategy of maximizing superconductor area while just avoiding tin contamination. However, since Nb_3Sn wire fabrication is complex, it is very difficult to design a barrier thickness that is just enough to ensure reaction of all of the Nb filaments while also avoiding tin contamination for a given reaction sequence. Instead, the optimum heat treatment matrix is determined empirically.

Reducing the time or temperature of the reaction reduces the amount of filament and barrier area that is converted to Nb_3Sn, effectively trading performance to better ensure copper purity. A key question, then, is to what extent is J_c reduced by limiting the final reaction duration? Before about 2003, work on modified jelly-roll strand designs indicated that the falloff could be quite large, perhaps 30%. A second question is whether the stability current density is correlated with RRR at all.

In 2004, we conducted experiments to probe explicitly these questions. Fig. 3 summarizes the results, as published recently in [4]. The strands used for this experiment are 54-subelement Restacked-Rod Process (RRP) wires from Oxford Instruments-Superconducting Technology (OI-ST), which are the progenitors of the present LARP strand design. First, as final reaction duration increases, there is a steep falloff of RRR, indicating that there is substantial diffusion of tin into the copper even after 24 hours. For reference, final reaction times for modified jelly-roll wires could be as long as 200 hours. Second, there is a strong correlation between J_s and RRR, indicating that the loss of thermal conductivity indeed causes a reduction in the strand's ability to survive flux-jump instabilities. Third, there is very little variation of J_c with reaction time, where 90% of the maximum J_c is reached already at only 24 hours. Fourth, and most importantly, J_s falls below J_c when the final reaction step exceeds about 45 hours. This indicates the crossover for operation of a magnet, because the load-line passes through an instability region at low fields. In other words, flux jumps in the low-field portions of the magnet will produce quenches when $J_s < J_c$.

While for this particular strand the onset of unstable magnet operation appears to occur for RRR of ~20, this value should not be used as a guideline. Instead, the moral of this experiment is that

modern strands are provided with tin activity that is so high as to permit short reactions and high *RRR* values without sacrificing performance too greatly. Moreover, since the duration and temperature of the reaction heat treatment are parameters controlled by the magnet designer, the inter-relationship of J_c, J_s, and RRR provide the means to adjust the stability of the magnet at the laboratory. For the experiment described in Fig. 3, the extra work in preparation of additional strands, testing, and the implementation of *V-H* plots as a standard characterization tool provided a much more complete knowledge base for magnet construction.

5. OTHER PARAMETERS AFFECTING PERFORMANCE VS. STABILITY BALANCE

5.1 Perimeter-to-area ratio

The RRP conductor design uses barriers around each sub-element, often called the distributed barrier approach. In this design, a copper thermal pathway lies next to each potential heat source, connecting it with the coolant bath (if the copper stays clean). This makes the purity of the inter-sub-element copper extremely important. When tin contaminates the thin copper regions between sub-elements, the direct thermal link is broken. Heat generated in an interior sub-element must diffuse through neighboring sub-elements instead, greatly reducing the strand's ability to shed heat and recover. Thus, tin contamination changes the effective ratio of thermal transfer perimeter to heat generating area from one determined by the dimensions of the sub-element to one determined by the dimensions of the strand. That is, the thermal transfer coefficient becomes worse by a factor of approximately $N^{1/2} \sim 7$. This may explain why J_s falls so quickly with reduction of an an awe R.

To explore this hypothesis further, we measured *V-H* data for a high current-density strand design with a single barrier surrounding all of the sub-elements. The strand chosen was an Outokumpu Advanced Superconductors (OKAS) design with 19 sub-elements and a Ta diffusion barrier. Despite having RRR of 235, *V-H* data showed that J_s was only 566 A mm^{-2}. This is only 2/3 the J_s of an RRP strand with RRR of only 7 in fig. 3. Although the sub-elements are larger in the OKAS strand than in the RRP strand, and therefore the heat released by flux jumps is higher than in the RRP strand, the huge difference in J_s clearly points to the significant roles played by the higher perimeter-to-area ratio and the presence of clean inter-sub-element copper in the RRP designs.

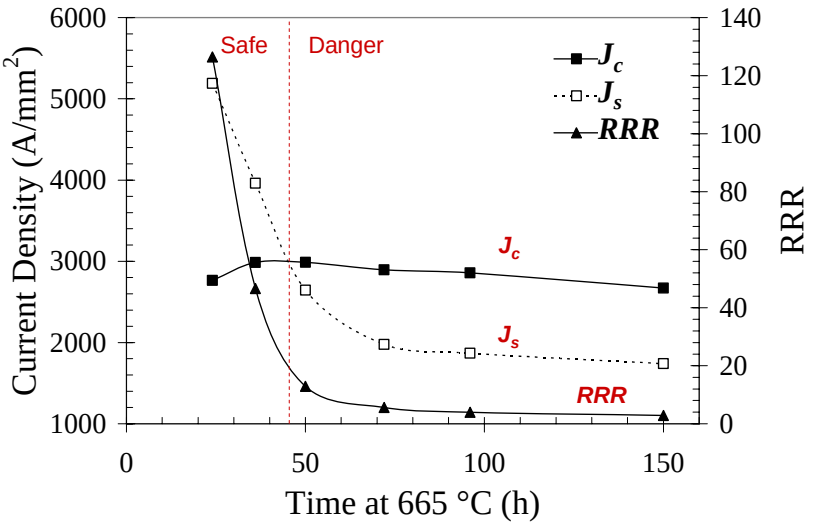

Fig. 3 Summary of experiments to determine the optimum balance between performance and stability. The duration of the final stage of the strand reaction is given on the x-axis. For time > ~ 45 hours the stability current density J_s falls below the critical current density J_c and recovery from flux jumps may not be possible.

5.2 Sub-element diameter and division

An interesting question is whether it is possible to produce sub-elements that are inherently stable against flux jumps. At the very least, strands that are closer to this stability limit should exhibit better tolerance of tin contamination, due to the smaller amount of heat released by a flux jump. To explore this goal, and to move closer to the DOE-HEP target of 40 μm sub-element diameter, OI-ST has produced RRP conductors with up to 216 sub-elements. As discussed earlier, the sub-element diameter scales with $N^{-1/2}$ for constant copper fraction (which is usually close to 50% of the strand area). For a 0.8 mm strand and 50% copper fraction, N = 216 yields a sub-element diameter of 38 μm.

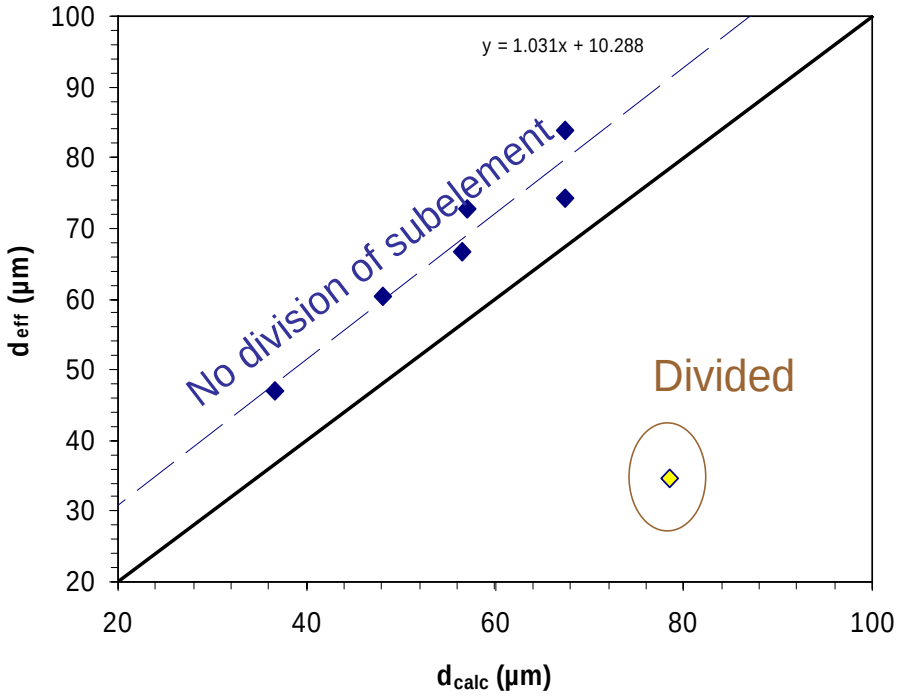

Fig. 4 Effective filament diameter (determined from magnetization and extrapolated transport measurements) plotted against the calculated sub-element diameter (determined by wire diameter, sub-element number and copper fraction). The solid line denotes $d_{eff} = d_{calc}$. Increasing the number of sub-elements produces data with a comparable slope (dashed line) but offset due to distortion of the sub-element shape.

However, the ductility of strands with high sub-element number is not as good as for lower sub-element number. The materials science beneath this observation is at an early stage. The difficulties in drawing the strand have two important effects on stability. First, distortion of the sub-element shape produces regions where the diffusion barrier is thin, increasing the potential for tin contamination of the copper. Our tests showed a reduction of RRR despite no visible points of tin break-through by scanning electron microscopy for a 126-sub-element design, suggesting that controlling tin contamination is more subtle. Second, distortions of the sub-element shape increase the dimension over which magnetization currents flow, adding to the magnetization. These distortions produce effectively larger filament diameters than those calculated for a round sub-element (see Fig. 4).

Significant improvement has come from strategies to divide the ring of filaments that make up the sub-element. OI-ST described processes for inserting foils or spacers in published work. As seen in Fig. 4, this approach is much more successful at reducing the effective filament diameter than increasing the sub-element diameter has been. The drawback is the reduction in superconductor area, since about 10% of the sub-element area (and sometimes more) is taken up by the dividers.

5.3 Estimating RRR

Measurements of RRR can be routinely done as part of testing. At BNL we record the sample resistance as the helium boils away overnight following a series of testing experiments. A new probe has been set up to measure multiple samples simultaneously. However, the need not revolve around the schedule of the test facility. After comparing ~50 different samples with a wide range of RRR, we observed a strong correlation between RRR and the value of residual resistance determined at liquid nitrogen temperature (Rr = resistance at 300 K divided by the resistance at 77 K):

$$RRR = 0.47 \exp (0.81\ Rr).$$

The quality of this estimation is shown in Fig. 5 for a number of RRP strands.

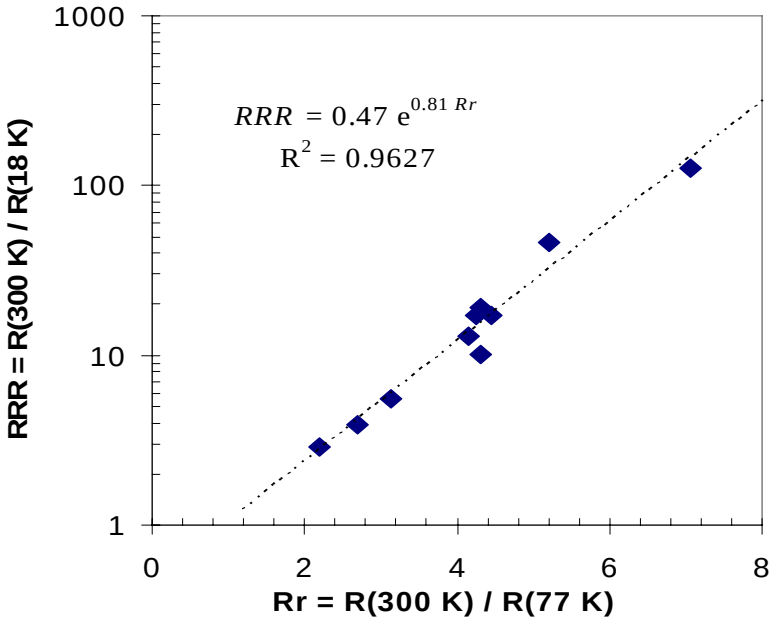

Fig. 5 Measured valu of RRR plotted against the residual resistance at liquid nitrogen temperature (Rr). The dashed line indicates the fit by RRR = 0.47exp(0.81Rr), which has a high quality regression as indicated.

5.4 Effects of reaction temperature

Besides limiting the duration of the final reaction stage to preserve high *RRR*, it is possible to reduce the reaction temperature for comparable time to achieve the same effect. Based on data for reaction rates of high-tin bronze composites, the growth rate of the Nb_3Sn layer roughly doubles for every 50 °C increase in temperature near 700 °C. This means that a 24-hour reaction at 695 °C (as specified by the manufacturer) could be lengthened to 48 hours at 650 °C to obtain roughly the same non-copper area of Nb_3Sn. The advantage of longer time at lower temperature is a wider window to detect and control the onset of tin contamination, providing a better ability to optimize both J_c and *RRR*.

We have explored the effects of time and temperature on strand properties over a wide range of reaction parameters using the same RRP wire. These results are summarized in Fig. 6 for the LARP strand design (OI-ST billet 8220-4 at 0.7 mm diameter). There are several points to note. First, increasing the reaction temperature generally drives down *RRR* regardless of the reaction duration. Second, there is a rather wide temperature range, at least 50°C, which can be used to obtain J_c close to 3000 A mm^{-2} at 12 T, 4.2 K. In these circumstances, better combinations of J_c and *RRR* are seen for reactions at 650 than at 665 or 680 °C. For these reasons, we now favour lower reaction temperatures.

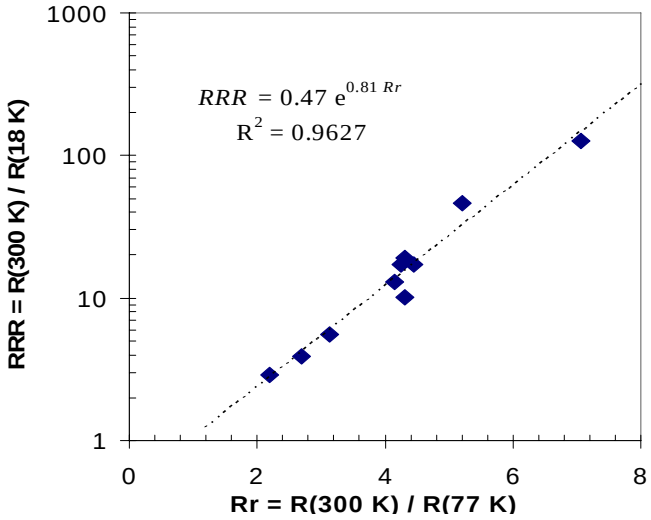

Fig. 6 Critical current density and RRR as a function of reaction temperature during the final heat treatment. Reaction times range from 48 to 150 hours at 635 °C and 24 and 48 hours at 680 °C. While J_c is optimum for the 665 °C, 72-hour reaction, the 650 °C reaction gives a good combination

6. SUMMARY

Flux-jumping problems are difficult to avoid due to metallurgical issues associated with ductility, shape control, piece length, and design of Nb_3Sn strands. Since almost all existing Nb_3Sn strands display flux jumps, magnet designers should take this into account, and take steps to manage the heat released. An important factor is the balance between performance (J_c) and stability (RRR and J_S). It was shown that a necessary condition for safe magnet operation is $J_s > J_c$, which is ensured by keeping RRR high. Recent strand designs provide some flexibility in choosing the reaction heat treatment, because J_c reaches high values quickly, so the sacrifice in performance to preserve stability is small.

New methods were developed to probe flux-jump instability. In particular, the *V-H* plot has become a standard measurement in our laboratory. This technique determines the instability current threshold with less ambiguity than current-voltage measurements as it reduces problems associated with current injection into the strand and mechanical motion. Simplification of the measurement of RRR by using a liquid-nitrogen measurement was also discussed.

Our experiments also revealed a tendency for reactions at temperatures above 650 °C to degrade RRR, even for short reaction time (24 hours) in the final stage. A better combination of high RRR and good J_c was found for reactions completed at 650 °C. Because the stability-performance balance involves two parameters, reactions at lower temperature (650 vs. 695 °C) are now preferred for LARP.

REFERENCES

[1] M. N. Wilson, Superconducting Magnets (Oxford University Press 1983).

[2] F. R. Fickett, Cryogenics 22 (1982) 135.

[3] See for instance A. V. Gurevich and R. Mints, Rev. Mod. Phys. 59 (1987) 941.

[4] A. K. Ghosh, E. A. Sperry, L. D. Cooley, A. R. Moodenbaugh, R. L. Sabatini, and J. L. Wright, Supercond. Sci. Technol. 18 L5 (2005).

[5] A. K. Ghosh, L. D. Cooley, and A. R. Moodenbaugh, IEEE Trans. Appl. Supercond. 15 (2005) 3360.

[6] A. K. Ghosh, L. D. Cooley, A. R. Moodenbaugh, J. A. Parrell, M. B. Field, Y. Zhang, and S. Hong, IEEE Trans. Appl. Supercond. 15 (2005) 3494.

DESIGN AND FABRICATION OF RUTHERFORD-TYPE CABLES FOR HIGH FIELD MAGNETS

D. R. Dietderich, H. C. Higley, and R. M. Scanlan
Lawrence Berkeley National Laboratory, Berkeley, USA

Abstract
The Superconducting Magnet Group of LBNL has been fabricating cables for numerous superconducting applications for over 15 years. The cabling parameters (wire diameter, cable thickness, cable width, pitch length, and keystone angle) that are acceptable for various strands with different internal structure, composition, and fabrication methods are discussed. An empirical model is presented to guide in the cabling process to minimize or eliminate strand damage. The evolution of the cable parameters are placed in context with a discussion of the cables developed for the record high field magnets (Cos θ magnet D-20, common coil magnet RD-3, and block magnet HD-1) fabricated at LBNL.

1. INTRODUCTION

Magnets for High Energy Physics (HEP) applications require the highest critical current densities to obtain the highest magnetic fields. To that end, the Rutherford laboratory in England developed a rectangular cable that bears its name [1]. The rectangular geometry of the cable provides the highest packing density, also called packing or compaction factor, of the strand, plus the flexibility for winding magnets of various types: Cos θ, Cos 2 θ, and racetracks coils.

For over 15 years the Superconducting Magnet Group (SMG) of Lawrence Berkeley National Laboratory (LBNL) has been fabricating cables. During this time over 900 cables of Nb_3Sn, NbTi, and Bi-2212 have been produced, some in very long lengths, while others have been short prototypes. This paper summaries the experience at LBNL and presents guidelines for the fabrication of damage- free cables.

2. CABLE DESIGN

LBNL has established certain guidelines when making rectangular cables from strand of internal tin (IT) or powder-in-tube (PIT) wire. Due to the difference in mechanical properties of the wire components, i.e. core materials (i.e. Sn or Sn alloy or Nb-Sn powers) and the Nb-Cu matrix, they cannot be as deformed to the same extent as NbTi strand. Cables made of Nb_3Sn strand always (except perhaps for Nb_3Sn bronze-processed wire) need to be made wider than cables made of NbTi strand for the same cable parameters (i.e. number of strands, strand diameter, cable pitch length).

The development of a cable for a magnet of the SMG is an iterative process. A magnet designer proposes a cable for a particular magnet design (i.e. cross section). These initial parameters (i.e. number of strands, strand diameter, cable width, cable thickness and keystone angle) are used as a starting point for prototype cable development. The initial parameters are modified so that minimal or no critical current reduction of the strand occurs and the cable is mechanically stable for winding coils.

3. CABLING EQUIPMENT

The cabling machine at LBNL consists of a stiff, large diameter wheel that can hold up to 60 spools of wire. Magnetic brakes on each spool, plus one additional capstan brake controls the wire tension. The strands are guided into the aperture of the Turk's head by a guide ring and mandrel with a tip shaped for that particular type of cable. The upper and lower rolls of the Turks head are powered and each is driven with a DC motor. This aids the "caterpuller" belt drive that pulls the cable from the Turk's head. The powered rolls reduces the cable tension to ~20 kg from over ~200 kg, for a non-power mode of operation, on the cable during the cabling process and thus prevents collapse of wide cables when the tension is too high.

The dimensions of the cable are measure with a hydraulic driven assembly that loads both faces and edges of the cable so that the cable size (width, thickness, and keystone angle) is determined. The LVDT's on the measuring machine have been calibrated using a gage block with the approximate dimensions of the cable being produced. The measurements are pressure dependent, so the pressure in the hydraulic system has been standardized to 17 MPa for Nb_3Sn cables. This is much less that the pressure used for NbTi cables. Table 1 gives the typical values for cabling tension and strand parameters that are important for cabling.

A typical LBNL mandrel tip has a width about 2 strand diameters less than the calculated cable width and a thickness about ¾ of a wire diameter. Special mandrels for adding cores to a cable are produced by cutting a slot in the top of the mandrel along its length. This permits a ribbon core of various materials (e.g. stainless steel, Ni-Cr, MgO paper etc.) to be fed from a spool into the center of the cable.

Table 1
Typical Values of Cable and Wire Parameters

Item	Nb_3Sn
Strand twist	Right hand 0.5-1 twist/cm
Strand spring back	350 - 750 deg.
Strand tension	2.0 - 2.5 kg
Turks head load	59 kg
Planetary ratio	-0.57:1
Overall compaction	
Cable residual twist after anneal and re-roll	< 20 deg.

4. LBNL CABLING PROCEDURES

To improve the mechanical characteristics of cable for magnet winding and to remove part of the contraction that a cable undergoes during heat treatment LBNL has implemented a double rolling procedure for our last several magnets [2-5]. The initial cable is fabricated to the desired width but made 50 - 75 μm over-size in thickness. After the cable has been annealed at 200°C for 4-6 h the cable is rolled to the desired thickness but the width is not narrower than the initial width. During the annealing step the cable becomes thicker, wider and shorter [6, 7]. The anneal reduces the residual stress in the strand that develops during wire fabrication. The anneal removes about one half (0.2-0.25%) of the overall longitudinal contraction that a cable will undergo during a complete heat treatment cycle to about 650°C.

This annealing plus re-rolling procedure has three functions: One is to reduce the dimensional changes that would take place during coil heat treatment. The second is to give the cable a little higher overall compaction (an increase of 2 - 3 %) such that the engineering critical current density is increased slightly. The third, and perhaps the most important, is to provide a more mechanically stable cable for magnet winding due to better interlocking of the strands, plus a relatively flat cable with less than 20% residual twist.

5. MATERIALS

NbTi – The most robust of the superconducting strands that is presently being cabled. The high strength of the NbTi filaments, good bonding between the components due to hot working, and the absent of Sn permits it to be highly deformed to greater than 95% compaction without significant loss of critical current.

Nb_3Sn – The state of the art fabrication processes produce a composite that has components with very different mechanical properties. For example, the Sn formation of the Nb_3Sn is supplied by a high tin content core. All of the processes supply Sn via a phase with a high tin content, with the internal Sn processing being almost a pure Sn core, while the PIT process uses an inter-metallic powder. The low shear strength of the core material places limits on the amount of deformation that a strand can undergo without degrading the superconducting properties of the strand.

6. CABLE PARAMETER CALCULATIONS

Recently LBNL departed from just using the overall compaction of a cable to calculate fabrication parameters. LBNL has decoupled the width and thickness deformations in determining the final dimensions. The overall compaction is still useful in terms of how efficiently the cable was fabricated in terms of overall current density (i.e. the higher the compaction the higher the cable current density). A simple calculation can show that for the same cabling parameters (i.e. number of strands, strand diameter, and pitch length) one can obtain two cables with the same cross-sectional area (i.e. compaction) for different ratios of width to thickness. For example, by increasing the cable width by 0.40 mm from 16.00 to 16.40 mm and decreasing the cable thickness by 0.035 mm from 1.435 to 1.400 mm one can obtain the same packing factor. However, these two cables are not the same regarding the deformation of strands at the edge. The narrower one could potentially have damaged strands.

There are two configurations for strands at the edge of a cable and both can be seen in the images of a cable cross -section (Fig. 1). The strands in Fig. 1(a) on the left produce a rectangular configuration and are in what I call an “in-phase” arrangement. As one follows a strand along the cable axis into the paper one will come to the configuration shown in Fig. 1(b) on the right. The strand that was on the bottom layer of the cable has gone around the edge and is midway between the top and bottom layers. This is the widest strand configuration of the cable and it is the section from which the un-compacted dimensions are calculated. The two configurations of Fig. 1 are only 2-3 mm apart along the cable axis.

Even within the same strand family (internal-Sn and PIT) variations in mechanical properties occur. This requires that one use these initial cabling parameters as the first iteration in fabrication of a cable for a magnet and then finalize the magnet dimensions. The high-critical current density strand now beginning produced does not yet have the uniformity of the large production billets of NbTi or that of Nb_3Sn for the ITER program. For years LBNL, and others, have used the overall compaction of a cable as a guide for its fabrications and deformation. However, this does not provide guidance regarding the deformation of the width relative to the thickness. The two dimensions must be decoupled.

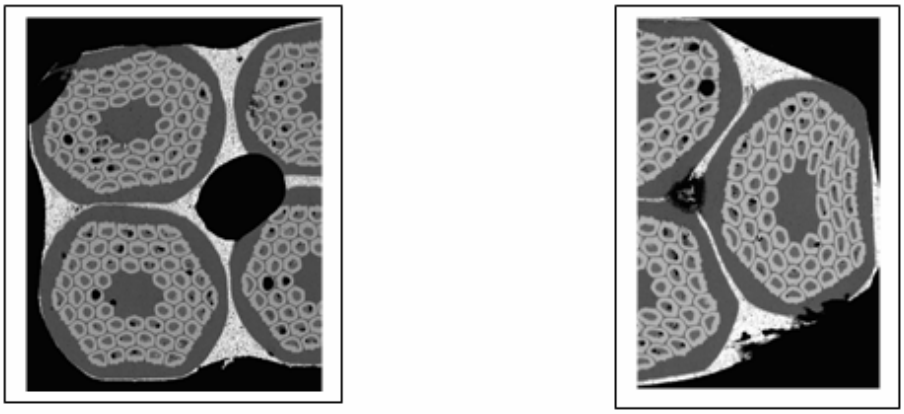

(a) (b)

Fig. 1 Scanning Electron Microscope images of a polished cross-section of reacted cable. The two photographs show the strand configuration at the edge of a cable. Image (a) shows the symmetric orientation of strand on the top and bottom of the cable. Image (b) shows the asymmetric orientation of the strands. To go from the strand configuration in (a) to that in (b) a strand rotates around the perimeter of the cable.

With the early keystone cable R&D runs for D-20, and its final production cable runs, the importance of the deformation at the edge of the cable began to be recognized (Fig. 2). By making the cable too narrow, strands are highly deformed at the cable edge and are severely deformed and potentially damaged.

LBNL has developed a simple empirical formula for determining an acceptable cable width for the odd strand configuration. The input to this formula is the number of strands in the cable (N), the strand diameter (d), and the cable pitch angle (PA). The Width Parameter (WP) for a cable is defined as the difference between the cables as fabricated width and W divided by the W. The "theoretical width of the cable" (W_{th}), or un-compacted cable width, is defined by the following formula:

$$W_{th} = d \cdot (N/2) \cdot [\text{cosine } (PA)]^{-1},$$

and the Width Parameter, $WP = (w - W_{th})/W_{th}$. A value of $WP > 0$ means that a cable has been fabricated wider than its theoretical width and the opposite is true for values of WP less than zero.

In slide 13 of my WAMDO presentation there is a factor added ($0.732 \cdot d$) that is included when calculating the cable width for fabrication. For simplicity of comparison of various cables it is has not been included in the Width Parameter and Thickness Parameter deformation plots. This factor arises from the fact that a strand must go from the top of the cable to the bottom by going around the edge but there is interference between the strands which requires that the cable be wider than one would expect from the Width Parameter.

The Thickness Parameter (TP) is easier to define since the un-compacted cable thickness is just twice the wire diameter (2d). Therefore, the Thickness Parameter, $TP = (t - d)/2d$. For a rectangular cable TP is always less than zero. However, for a keystoned cable TP is least at the minor edge (thin edge) and greatest at the major edge (thick edge). Due to the thickness variation across the cable the TP on the major edge could have a positive value. This could lead to a cable being mechanically unstable. To alleviate this possibility one must over-compact the width of the cable, which concentrates the deformation at the thin edge and could produce strand damage.

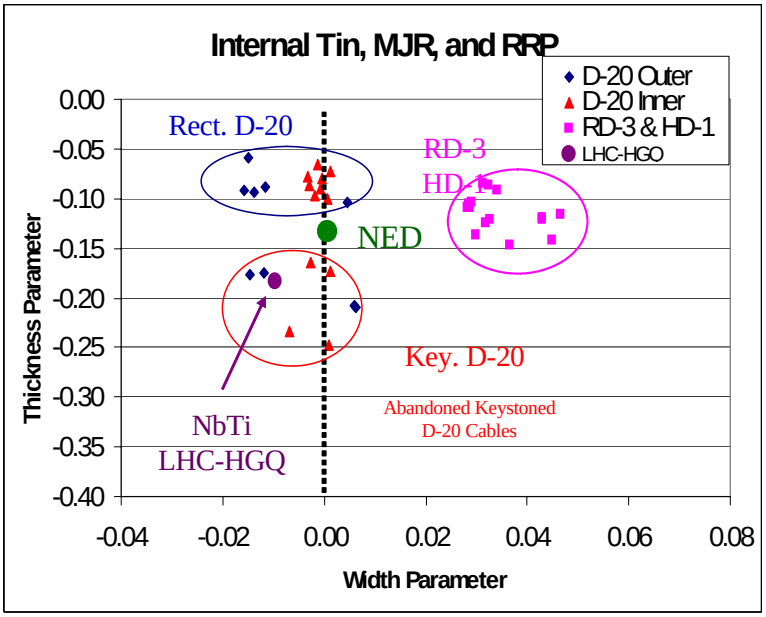

Fig. 2 Parameter space for prototype and production cables made for several LBNL magnets. Prototype cables made for D-20 had rectangular and keystoned versions. The final D-20 magnet design used rectangular cable. All of the RD-3 magnet series and HD-1 magnet were made with rectangular cable.

7. D-20 HISTORY

The first magnet cross-section designs for D-20 (a four-layer dipole magnet) were for keystoned cable. These early cables were found to have damaged sub-elements and reduced critical current performance. In Fig. 2 these appear in the lower left quadrant. To better understand the Width Parameter vs. Thickness Parameter plot of Fig. 2 one just needs to know that cables in the lower left quadrant are made thinner and narrower than those in the upper right quadrant, and that cables on the left are narrow than those on the right while those at the bottom are thinner than those at the top.

D-20 was ultimately fabricated with rectangular cable noted in Fig. 2. The cables for LBNL's more recent magnets, RD series and Hd-1, were made wider and thinner in accordance with our present cabling philosophy.

If one adds a data point for the inner cable for LHC HGQ (High Gradient Quadrupole), which is made of strands of NbTi with a diameter of 0.808 mm, to the plot of cable width vs. cable thickness one sees that it appears in the lower left corner of the graph. The strands in this cable undergo more strain than high-Jc Nb_3Sn strands can withstand without severe damage.

The NED cable has been added to the plot using the proposed cable parameters. It is a little narrower than the LBNL cable calculator would propose. If one adds in the factor of $0.732 \cdot d$ to W_{th} then the NED point moves further to the left (i.e. narrower and more edge compaction).

8. CONCLUSIONS

The work at LBNL has shown that the most important aspect of cabling strands of Nb_3Sn is the deformation at the edge of a cable. Due the dissimilar mechanical properties of the components within the strands of the internal-tin type and powder-in-tube type conductors the amount of strain that a wire can withstand is significantly less than that of for NbTi or bronze type Nb_3Sn strands. The lack of hot working of the composite may also contribute to cabling limitations due to reduced bonding between the components. The biggest mistake made in cabling of Nb_3Sn strand is to treat the strand as if it was like NbTi strand as shown in the "thickness vs. width" deformation plot.

It is highly recommended that a prototype cable with the initial parameters used in the magnet design be made prior to finalizing the coil cross section and dimensions.

ACKNOWLEDGEMENTS

This work was supported in part by the U.S. Department of Energy under Contract No. DE-AC03-76SF00098. The authors would like to thank N. Liggins and L. Sun for aid in cable fabrication and metallography.

REFERENCES

[1] G.E. Gallagher-Daggett, “Superconducting Cables for Pulsed Dipole Magnets,” Rutherford Lab. Report RHEL/M/A25 (1972).

[2] A. D. McInturff, et al., “Test results for a high field (13T) Nb_3Sn dipole,” Proc. Part. Accel. Conf. (1997) 3212. Available via http://www.JACoW.org/

[3] A.F. Lietzke et al., “Fabrication and test results of a high field Nb_3Sn racetrack dipole,” Proc. Part. Accel. Conf. (2001) 208. Available via http://www.JACoW.org/

[4] A.F. Lietzke et al., “Test results of RD-3c, a Nb_3Sn common-coil racetrack dipole magnet, *IEEE Trans. Appl. Supercond*., vol. 13 (2003) 1292.

[5] D.R. Dietderich et al., “Dimensional Changes of Nb_3Sn, Nb_3Al, and $Bi_2Sr_2CaCu_2O_{8+d,}$ Conductor during Heat Treatment and the Implications for Coil Design,” *Adv. in Cryogenic Eng*., vol. 44B, Plenum Press (1998) 1013.

[6] N. Andreev et al.,"Volume Expansion of Nb_3Sn Strands and Cables during Heat Treatment", *Adv. in Cryogenic Eng*., vol. 48B (2001) Plenum Press, 941.

PROPERTIES OF MODERN Nb_3Sn STRANDS AND CABLES

E.Barzi for the Superconductor R&D Group
Fermi National Accelerator Laboratory, Batavia, USA

Abstract
The ongoing superconductor (SC) effort at FNAL focuses on the endeavor of making state-of-the-art magnets for present and future accelerators out of brittle materials. The infrastructure, including test facility, cable fabrication, and reaction and impregnation sites, was built upon this need with the mission to serve as an interface between materials and magnets as a leading center for conductor technology. The characterization of each step of the process that leads a flawless round strand to become part of a cable first, and of a coil next, including heat treatment, transport tests of strands and cables, and microscopic analysis of cable damage, has helped manufacturers to understand where their round strand weaknesses reside, and to improve their design for magnet applications.

1. INTRODUCTION

Studies of superconductor technology for high field magnet applications include:

i) measurement of properties of round strands;

ii) cable development and assessment of the impact of cabling on strand properties;

iii) measurement of the effect of preload and Lorentz forces;

iv) feedback to Industry based on strand and cable performance;

v) feedback to magnet design based on the effect of conductor properties on magnet performance.

2. STRAND PROPERTIES

2.1 Critical current density

The critical current density over the non-Cu area of a strand, J_c, has made substantial progress in time. For strands the critical current, I_c, is typically determined from the V-I curve using the 10^{-14} Ω·m resistivity criterion. A highest J_c of 3300 A/mm^2 was obtained by OST in a 0.7 mm wire of RRP design with 60 spaced sub-elements in a 61 restack array [1]. High performance is typically achieved by packing as much niobium and tin as possible in the non-Cu area. A rule of thumb is that about 50 at.% Nb is needed for a J_c of 3000 A/mm^2. In addition, alloying with Ta and/or Ti is known to improve the upper critical field, H_{c20}. A flux-pinning model in granular A-15 superconductors based on Josephson-coupled arrays and anisotropic flux pinning by grain boundaries, which suggests that the critical current of these materials could be largely improved by elongating their grain structure or by introducing longitudinal microstructures in the strand, can be found in [2].

2.2 Effective filament diameter

The d_{eff} is obtained from 13-10-13 T magnetization loops by measuring $\mu_0 M(12T)$ per total strand volume and $I_c(12T)$, and considering the filaments round. The d_{eff} is typically larger than the average geometric size [3]. For procedures of filament size optimization see Bibliography. It is well known that the effective filament diameter, d_{eff}, determines the level of magnetic instabilities and field quality in SC accelerator magnets (see for instance [4,5]). Several groups worked on improving stability [6-9],

and it was experimentally shown that a d_{eff} of excessive size reduces the transport current at low field to ≤ 20% of its expected I_c value [8]. Collaborating with strand manufacturers to reduce d_{eff} is therefore important. In [10] the d_{eff} onset for instability was experimentally determined to be below 65 μm for strands with J_c(12 T) of ~2000 A/mm^2. This translates to an upper limit of 40-45 μm for a strand with a J_c(12 T) of ~3000 A/mm^2. By extrapolating from d_{eff} measured as a function of the filament (or sub-element) number in Nb_3Sn strands of various designs, a 217-filament strand would provide a d_{eff} of 24 μm for a 0.7 mm wire and of ~34 μm for a 1 mm wire.

2.3 Instability current

In light of the renewed phenomenon of magnetic instability [6-9], measuring the minimum quench current, or stability current, I_S, in the presence of a magnetic field variation has become part of strand and cable characterization [11]. This is done through V-H tests. The current is first ramped to a fixed value, and the field is swept up and down with ramp rates of 5 to 17 mT/s in the field range 0-4-0 T. If no quench is observed the current is increased and the test repeated. A phenomenological model that has been so far consistent with data can be found in [4]. Also J_s has made continuous progress in time. For instance, in high J_c RRP round strands by OST, J_s is now greater than 5000 A/mm^2 as opposed to values below 3000 A/mm^2 in 2003. It was shown that for round strands in the d_{eff} range 70-110 μm, the I_s normalized to I_c, as measured at the various US Labs, varied between 7 and 20% as a function of RRR [12].

3. CABLE PROPERTIES

The I_c of a Nb_3Sn virgin strand in the high field range can be substantially degraded during cabling due to plastic deformation, and during magnet fabrication and operation due to precompression and Lorentz forces. In addition, cabling has an effect also in the low field range, as filament deformation can worsen the instability current.

3.1 Effect of cabling on high field performance

The effect of cabling degradation was systematically studied using short samples of 28-strand Rutherford cable with aspect ratio ~8, and packing factors (PF) in the 85 to 95% range [13]. The sample set included keystoned and rectangular geometries, cables made with and without a stainless steel core and cables made with different cabling machines. There was no observable difference between rectangular and keystone cables having the same PF. The level of degradation depends on the strand design, *i.e.* its ability to withstand plastic deformation, and on PF. For instance, a substantial improvement in performance was obtained by SMI in the PIT design by replacing hexagonal tubes with round ones, which eliminated the original shearing.

Cables with 88-90% PF that were tested using facilities at CERN (B<10 T, 1.8-4.2 K), BNL (B<7 T, 4.3 K), and FNAL (B<2 T, 2.8-4.5 K) were consistent with their extracted strand test results. Cable tests confirmed instability by producing quench currents well below the expected critical surface at fields below 8 T [14].

3.2 Filament deformation

It was shown that filament size distributions in a strand change after the cabling process [10]. The average filament size increases, as well as the width of the distribution.

3.3 Effect of cabling on low field performance

Filament deformation explains why the low field transport current for round strands is always larger than for cabled strands. In addition, in cables and extracted strands I_s and RRR (as averaged over the whole Cu area) are not as reproducible as in round strands. The effect on instability of current imbalances in the presence of discontinuities (*i.e.* splices) in a 5-pitch long cable was investigated and found negligible [15].

3.4 Effect of transverse pressure

The effect of transverse pressure was measured for cables with aspect ratios ~8 made of 1 mm Nb_3Sn strands of various technologies [16]. The large spread that was found for PIT results is consistent with what was found in magnets. For a typical 100 MPa load on FNAL dipole models, the I_c degradation of PIT magnets at 10 T varied within 10-40%. Studies of transverse pressure degradation determine stress limits for the various conductors used in magnet design.

4. FEEDBACK TO INDUSTRY

In the process that leads a flawless round strand to become part of a cable first, and of a coil next, the same cabling process affects strands of different kinds in different ways, from filament shearing to sub-element merging to composite decoupling. To better understand the role of d_{eff} in instabilities and to simulate cabling deformations, the same strands to be used in the cables can be rolled down to decreasing sizes to cover an ample range of relative deformations. The behavior of rolled and cabled strands can then be compared through microscopic analysis as well as macroscopic measurements.

4.1 Microscopic analysis

Microscopy is used for damage analysis, which includes measuring filament size distributions of the deformed strands, and counting defects at each stage of the deformation. An adequate statistics has to be used to tailor uncertainty to the accuracy needed by the phenomenon under study. RRP and PIT materials behave very differently under deformation. For instance, RRP deformed strands show some merging between sub-elements. This phenomenon, which is seen in rolled strands and also in cables, can be quantified by measuring the number of merged sub-element as a function of relative deformation.

4.2 Macroscopic measurements

These include magnetization. In contrast with cabled strands, where the merging between sub-elements is a local effect, in rolling the deformation is continuous along the length of the strand. This produces a measurable and reproducible number of merged sub-elements as a function of deformation, as mentioned above. In this case, merging can be observed through magnetization measurements. Whereas for powder-in-tube (PIT) magnetization of increasingly thinner strands decrease as expected (in a configuration where the thin edge is perpendicular to the field), consistently with a negligible merging, for RRP the magnetization amplitude decreases down to 20% deformation, but starts increasing above this threshold.

To reduce cabling impact on sub-element merging, OST [1] produced a new billet with increased Cu thickness between sub-elements. The next step in this R&D is to increase Cu thickness in a billet with larger number of sub-elements.

5. FEEDBACK TO MAGNET DESIGN

By knowing conductor properties J_c and d_{eff}, the magnet peak field allowed by magnetic instabilities can be predicted [17]. The more unstable is the strand, the larger the peak design field has to be. The predicted peak fields obtained by using properties of strands used in magnets are all consistent with magnet data. Vice versa, minimal strand requirements can be established by entering the desired magnet peak field.

ACKNOWLEDGEMENTS

I wish to thank Daniele Turrioni, Al Rusy, Tom VanRaes, Marianne Bossert and the numerous students who contributed to different phases of these studies. I also wish to thank the High Field Magnet group for continuous and invaluable feedback.

REFERENCES

[1] Jeff Parrell et al., FNAL R&D proposal with OST, 2005-2006.

[2] J. McDonald et al., A Model for J_c in Granular A-15 Superconductors, IEEE Trans. Appl. Supercond. 11 1 (2001) 3884.

[3] M. D. Sumption et al., Analysis of Magnetization, AC Loss, and d_{eff} for Various Internal-Sn based Nb_3Sn Multifilamentary Strands with and without Sub-element Splitting, Cryogenics 44 (2004) 711.

[4] V. V. Kashikhin et al., Magnetic Instabilities in Nb_3Sn Strands and Cables", IEEE Trans. Appl. Supercond. 15 2 (2005) 1621.

[5] V. V. Kashikhin et al., Correction of the Persistent Current Effect in Nb_3Sn Dipole Magnets, IEEE Trans. Appl. Supercond. 11 1 (2001) 2058.

[6] D. Dietderich et al., Correlation Between Strand Stability and Magnet Performance, IEEE Trans. Appl. Supercond. 15 2 (2005) 1524.

[7] A. Ghosh et al., Dynamic stability threshold in high-performance internal-tin Nb_3Sn superconductors for high field magnets, Supercond. Sci. Technol. 18 (2005) L5-L8.

[8] E. Barzi et al., Instabilities in Transport Current Measurements of Nb_3Sn Strands, IEEE Trans. Appl. Supercond. 15 2 (2005) 3364.

[9] D. Turrioni et al., Study of Nb_3Sn Cable Stability at Self-field using a SC Transformer, IEEE Trans. Appl. Supercond. 15 2 (2005) 1537.

[10] E. Barzi et al., Effect of Temperature and Deformation on Nb_3Sn Strands Instabilities, Advances in Cryogenic Engineering 52 (2006) 566.

[11] E. Barzi et al., Round and Extracted Nb_3Sn Strand Tests for LARP Magnet R&D, IEEE Trans. Appl. Supercond. 16 2 (2006) 319.

[12] Workshop on Low Temperature Superconductors, Nov. 15-17, 2004, Monterey, CA.

[13] E. Barzi et al., Development and Study of Rutherford-type Cables for High-field Accelerators Magnets at Fermilab, Superconductor Science and Technology 17 5 (2004) 213.

[14] G. Ambrosio et al., Measurements of Critical Current and Instability Threshold of Rutherford-type Nb_3Sn Cables, IEEE Trans. Appl. Supercond. 16 2 (2006) 1160.

[15] J. McDonald et al., Fast Algorithm for Computing Inductive Voltages in a Network Model of a Rutherford Cable, IEEE Trans. Appl. Supercond. 15 2 (2005) 1625.

[16] E. Barzi et al., Sensitivity of Nb_3Sn Rutherford-type Cables to Transverse Pressure, IEEE Trans. Appl. Supercond. 15 2 (2005) 1541.

[17] A. V. Zlobin et al., Effect of Flux Jumps in Superconductor on Nb_3Sn Accelerator Magnet Performance, IEEE Trans. Appl. Supercond. 16 2 (2006) 1308.

BIBLIOGRAPHY

Progress of Nb-Based Superconductors, printed Feb. 18, 2005, by Maeda printing Co., LTD, Editors K. Inoue, T. Takeuchi, A. Kikuchi.

HIGH TEMPERATURE SUPERCONDUCTORS FOR ACCELERATOR MAGNETS

J. Schwartz
Florida State University, Tallahassee, USA

Abstract
The development of high temperature superconductors for magnet applications has progressed to the stage where multiple conductor options may become suitable for accelerator magnet applications. In this paper, the conductor options are first presented in terms of their technical properties for magnets. Subsequently, some of the primary issues for magnet engineering are discussed, including electromechanical performance quench behavior and the effects of quenching on I_c-strain. It is found that high temperature superconductors behave differently from low temperature superconductors in a number of ways, and as a result a retrofit approach to magnet design will not be optimum. Key design issues for high temperature superconductor magnets are summarized.

1. INTRODUCTION

Since their discoveries in the late 1980s, high temperature superconductor (HTS) technology has progressed significantly and a variety of magnet applications are beginning to appear. These materials offer a number of potential advantages over metallic low temperature superconductors, including high critical temperature, which results in potentially higher operating temperature and/or large energy margins for quenching, and high upper critical field, which results in very high critical current density at fields as high as 45 T. At present, however, HTS materials have serious drawbacks compared to LTS materials, including significantly higher cost, relatively poor mechanical properties, inhomogeneity along the length and a limited database of material properties. In this paper, the various HTS conductor options are reviewed from a magnet standpoint. Key magnet issues include conductor selection, critical current density (J_c) as a function of magnetic field, temperature, strain and fatigue, coil manufacture (wind&react and react&wind), stability (energy margin), quench detection and protection. These are discussed in relation to the design optimization processes.

2. HTS CONDUCTOR OPTIONS

Three HTS conductors have emerged as legitimate magnet conductors for future magnet systems. Each has distinct advantages and disadvantages that will influence the magnets and applications for which they are preferred. Two of these conductors are based on $Bi_2Sr_2Ca_{n-1}Cu_nO_{2n+4}$, the other is based upon $YBa_2Cu_3O_7$.

2.1 $Bi_2Sr_2CaCu_2O_{8+x}$ and $Bi_2Sr_2Ca_2Cu_3O_{10+x}$

$Bi_2Sr_2CaCu_2O_{8+x}$ (Bi-2212) and $Bi_2Sr_2Ca_2Cu_3O_{10+x}$ (Bi-2223) have critical temperatures of 90 K and 110 K, respectively, and are manufactured by the powder-in-tube (PIT) process with a combination of Ag and Ag-alloy sheathing. Typically, the ceramic powder is packed into a Ag tube and drawn into a wire. The wire is then cut, restacked, and sheathed within a AgX tube. Depending upon the number of filaments desired, more than one restack is possible. Silver is used for the initial sheathing material because it plays a key role in the processing that is necessary to obtain high J_c. It also provides ductility during wire drawing and rolling, allows rapid oxygen transport, which is essential for proper phase evolution during heat treatment, is chemically compatible with the superconductor, and reduces

the oxide melt temperature, thereby introducing surface texturing during recrystallization. AgX is used for the outer sheaths because it offers superior mechanical properties to pure silver.

There are essential differences between Bi-2212 and Bi-2223 that directly impact their potential for magnets. While both conductors require a high degree of uniaxial texture to have high J_c, in Bi-2212 this is achieved through a partial-melt process. Thus, after deformation is complete, the Bi-2212 conductor is heat treated above the peritectic melt temperature, at which point the Bi-2212 phase has decomposed into a liquid phase and a solid phase. It is then cooled and the Bi-2212 reforms with the grains growing predominantly parallel to the Ag interface. Bi-2223, however, is not taken into a partial-melt state and derives its texture from a thermo-mechanical process which alternates between heat treatment and mechanical deformation (rolling). Due to these differences, Bi-2212 can be used with either react-and-wind or wind-and-react magnet construction, while Bi-2223 is limited to react-and-wind magnets. Furthermore, Bi-2223 is only capable of carrying high J_c in the form of a wide, thin tape conductor, which is highly anisotropic, while Bi-2212 carries high J_c in either a wide, anisotropic tape or an isotropic round wire. Current production lengths by industry are ~1.2 km/batch of Bi-2223 by American Superconductor Corp. and ~200 m/batch of Bi-2212 by Oxford Instruments.

2.2 $YBa_2Cu_3O_7$ Coated Conductors

$YBa_2Cu_3O_7$ (YBCO) conductors, which have a critical temperature of about 95 K, are formed into coated conductors through deposition processing on a NiW or Incoloy substrate. This is necessary because YBCO requires biaxial texture and does not readily deform mechanically like Bi-2212 and Bi-2223, which are micaceous. There are two general approaches to introducing texture in YBCO coated conductors. In one approach, the metallic substrate is processed such that it has the required biaxial texture. Ceramic buffer layers are then deposited onto the substrate; the YBCO is deposited upon the buffer layers, and then covered with a protective Ag layer. In the other approach, the buffer layers are deposited with texture upon an untextured substrate. The rest of the process is then similar. Typically a layer of Cu stabilizer is added to either the Ag side of the conductor, or around the entire conductor. In both cases, the thin buffer layers are present as a chemical buffer between the YBCO superconductor and the Ni-based substrate and as a template for textured growth of the YBCO layer. Typically the metallic substrate is 50-100 μm thick, the buffer layers are about 0.1 μm thick, and the YBCO layer is 1 μm thick. Thus the fraction of superconductor in the conductor is very low. As with Bi-2223, it is only possible to form YBCO in wide tapes, although the tapes can be slit to less-wide conductors (currently 4 mm). Also like Bi2223, YBCO conductors are anisotropic and are limited to react-and-wind magnets. The present longest lengths of conductor are about 200 m in length. An industrial capacity of 300 km/year is targeted for the end of CY 2007 [1].

3. CONDUCTOR COMPARISONS

3.1 Overview

A general comparison of the three conductor options is shown in Table 1. The potential for W&R magnets, which has distinct advantages for strain management, and the existence of round wires, makes Bi-2212 the preferred conductor for high field, low temperature (4.2 K) magnets. It is also important to note the potential differences in conductor cost between the three options. The cost/performance for Bi-2212 and Bi-2223 are roughly similar, varying primarily with their electrical performance and thus primarily driven by the field and temperature of the magnet. While it is reasonable to expect that the performance of Bi-2212 and Bi-2223 will improve, cost reductions are limited by the high price of Ag. YBCO, on the other hand, has the potential to be much less expensive than Bi-2212 and Bi-2223 because the cost of Ni-based alloys is much less than that of silver. However, YBCO cost reductions are likely to be limited by the complexity of the deposition processing. If chemical-based deposition processes progress (as opposed to physical vapor deposition processes), the price could decrease substantially.

Table 1
Summary of HTS Conductors for Magnets

Conductor	Conductor Processing	Multifilamentary	Geometry	Isotropic	n-value	Coil Winding
Bi-2212	PIT	Yes	Tape or wire	Yes or no	Low	R&W or W&R
Bi-2223	PIT	Yes	Tape	No	Medium	R&W
YBCO	Deposition processing	No	Tape	No	High	R&W

3.2 Electromechanical Behavior

An important similarity between the HTS conductors is that they are all metal matrix composites with a ceramic superconductor [2]. Thus, because of the potentially large stresses and strains in a superconducting magnet, it is important to understand their electro-mechanical behavior in single cycle and in fatigue. Figures 1 and 2 show a stress-strain curve and a normalized I_c(4.2 K)-strain curve for Bi-2212 tape conductor, and Figs. 3 and 4 show a stress-strain curve and a normalized I_c(77 K)-strain curve for a YBCO coated conductor. Comparing Figures 1 and 3, the differences between a Ag-alloy matrix and a Ni-alloy matrix are clear. The Ni-alloy matrix remains linearly elastic to a much higher strain value, and the transition to plastic is sharp and clear. Comparing the stress-strain curves to the I_c-strain curves, it is also seen that the yield point of the conductor corresponds to the strain at which I_c begins to decrease. After reaching this critical strain, the failure is rapid. Thus, the mechanical behavior of the composite is dominated by the ductile matrix, but the electro-mechanical behavior is indicative of a brittle superconductor. This implies that to better understand the electrical failure limits of these materials, statistical approaches are necessary [3-8].

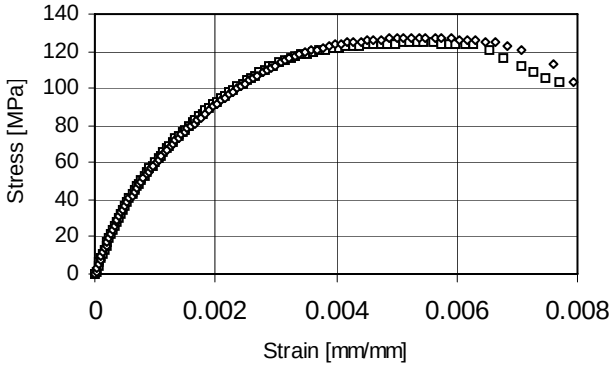

Fig. 1 Stress-strain curve for Bi-2212.

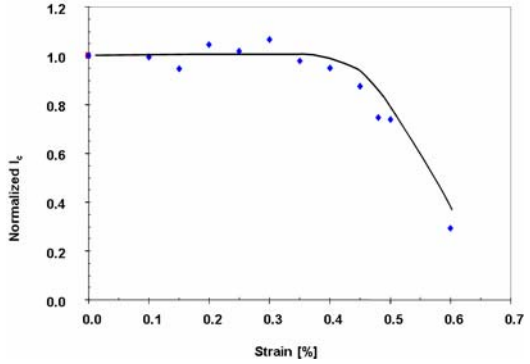

Fig. 2 Ic(4.2 K, s.f.)-strain curve for Bi-2212.

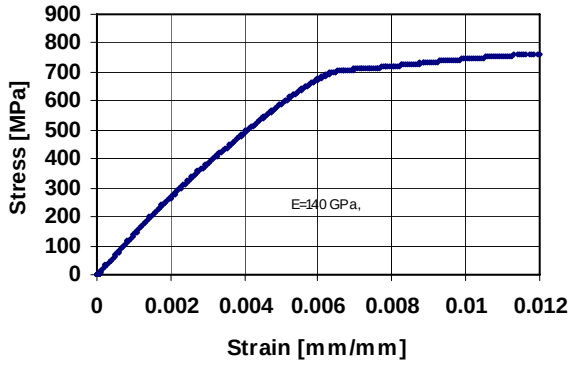

Fig. 3 Stress-strain curve for YBCO.

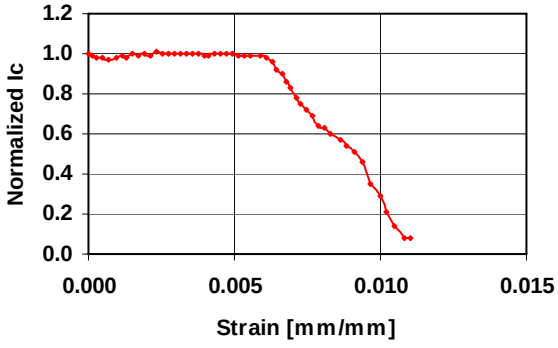

Fig. 4 Ic(77 K, s.f.)-strain curve for YBCO.

3.3 Stability and Quench Behavior

An important topic for accelerator magnets for which there are significant differences between the use of LTS and HTS is stability and quench behaviour. HTS has a distinct advantage in that the minimum quench energy is much greater, but it has the disadvantage that the quench propagation velocity is much slower [9-12]. It is clear that HTS magnets will quench when exposed to a sufficiently high heat load [13]. Whereas for Nb-Ti and Nb_3Sn, the maximum hot spot temperatures are known and quench detection and protection systems are designed accordingly, information as to what is necessary to damage or destroy an HTS conductor during a quench is relatively sparse.

Figure 5 shows an HTS sample mounted and instrumented for quench studies. A Nichrome wire is mounted at the center of the conductor and is used as a heat source using pulsed current. On each side of the Ni-Cr wire, alternating voltage taps and temperature sensors are installed along the length of the conductor. A steady-state transport current, below its critical value, is applied to the HTS conductor. A current pulse (300 ms) is then passed through the Ni-Cr wire. The energy is varied through the pulse amplitude, and voltage and temperature are monitored along the conductor. For small heat pulses, the voltage rises and then recovers. Above a critical heat value, the voltage rise continues and the conductor quenches. The propagation velocity is determined using the voltage taps. After the quench, the voltage taps are used to measure conductor I_c versus location and to determine if the conductor is damaged. Results for a YBCO conductor damaged during a quench are shown in Fig. 6. The upper curve shows peak temperature during the quench. The two lower curves show critical current versus location before and after the quench. Clearly the conductor has been damaged, and the damage correlates with the peak in temperature. What remains unknown is the physical mechanism of the damage and whether it is driven by peak temperature or temperature gradient.

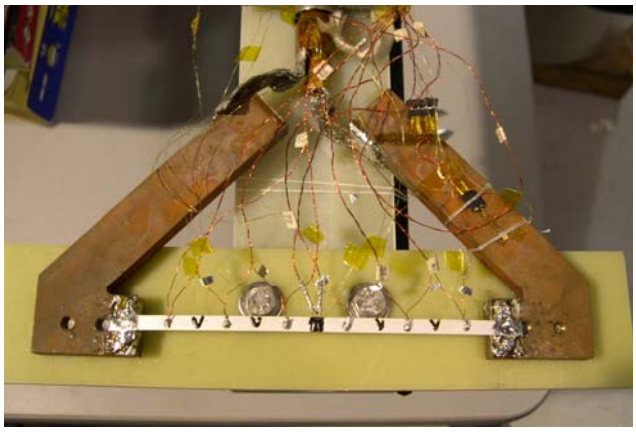

Fig. 5 Sample holder with HTS sample mounted for quench studies.

4. CONCLUSION

The development of HTS materials has great potential for accelerator magnets, particularly because of the increased energy margin and temperature margin, which will be particularly beneficial for high heat flux magnets. With the proper selection of materials, radiation resistant magnets may become feasible. When designing an HTS magnet, however, it is important to address the intrinsic differences between LTS and HTS conductors. Magnet design optimization must be done based upon the unique properties of the HTS conductors. For example, it may be beneficial to operate an HTS magnet at an elevated temperature (e.g., 20 K), in order to take advantage of the increased heat capacity and thus greater energy margin, despite the decrease in critical current density. In this example, however, the quench propagation velocity will be slow and quench protection may be a challenging issue. Understanding these trade-offs, and the quench-related failure limits, will be essential for optimizing magnets that take advantage of HTS properties.

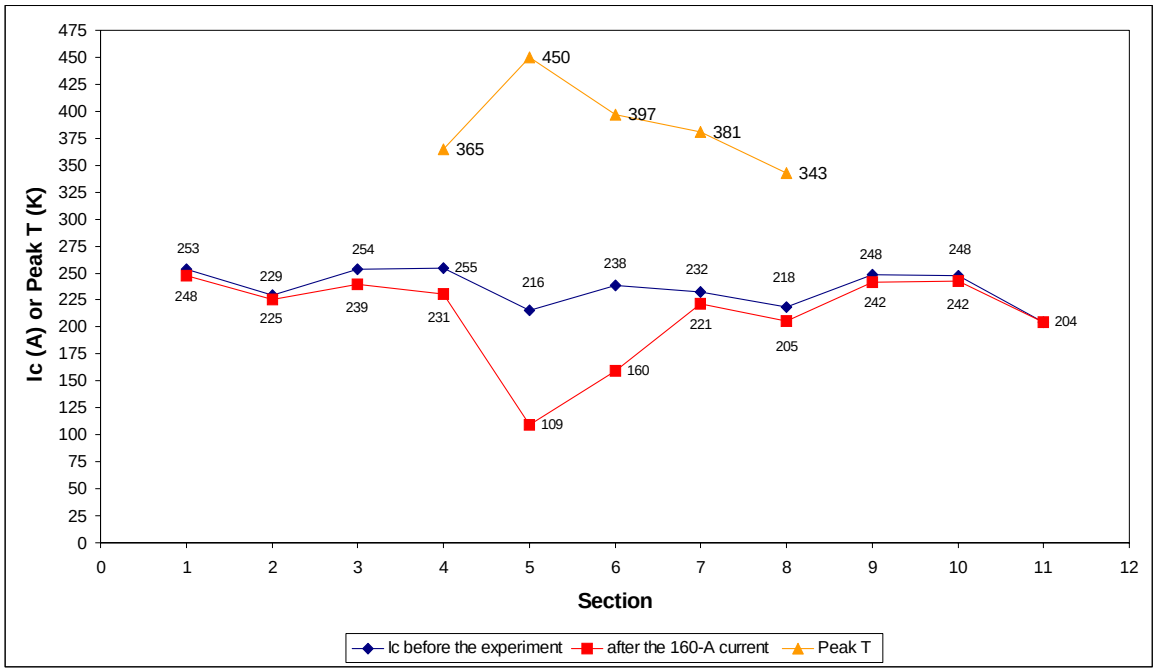

Fig. 6 Temperature during a quench and I_c-location before and after a quench for a YBCO coated conductor.

ACKNOWLEDGEMENTS

The author thanks A. Mbaruku, U.P. Trociewitz, X.R. Wang, H.W. Weijers for many useful discussions and experiments that contributed to this paper.

REFERENCES

[1] A.P. Malozemoff, presented at the 2006 Spring Meeting of the Materials Research Society, San Francisco (2006).

[2] H. Sekine et al., *Journal of Applied Physics* 70 (1991) 1596.

[3] J. Schwartz et al., IEEE Transactions on Applied Superconductivity 7 (1997) 2038.

[4] B.C. Amm et al., Advances in Cryogenic Engineering 44B (1998) 671.

[5] Y. Viouchkov et al., IEEE Transactions on Applied Superconductivity 10 (2000) 1134.

[6] Y. Viouchkov and J. Schwartz, IEEE Trans on Appl. Superconductivity 11 (2001) 3062.

[7] A. L. Mbaruku et al., IEEE Transactions on Applied Superconductivity 13 (2003) 3522.

[8] A.L. Mbaruku et al., Advances in Cryogenic Engineering Materials 50B (2004) 700.

[9] E.E. Burkhardt et al., IEEE Transactions on Applied Superconductivity 5 (1995) 393.

[10] F. Trillaud et al., Cryogenics 43 (2003) 271.

[11] F. Trillaud et al., Advances in Cryogenic Engineering Materials 50B (2004) 852.

[12] X.R. Wang et al., IEEE Transactions on Applied Superconductivity 15 (2005) 2586.

. [13] H.W. Weijers et al., Superconductor Science and Technology 17 (2004) 636.

HTS IN THE LHC & IN THE LHC UPGRADES

A. Ballarino
CERN, Geneva, Switzerland

Abstract
CERN is a major user of High Temperature Superconducting (HTS) material due to its incorporation into many of the current leads for the LHC project. There are already clear applications for HTS in the earliest upgrade scenarios, and thanks to its acquired expertise in the domain, CERN is well placed to extend the efficient use of these materials.

1. INTRODUCTION

CERN is an important player in the field of the application of High Temperature Superconductors (HTS). The use of HTS for the current leads in the LHC is one of the most important industrial applications of this material. By incorporating HTS material the heat conducted into the helium bath is reduced by a factor of ten, and the corresponding power consumption by a factor of three [1]. This saving was not the only benefit. By reducing the cryogenic load, it became reasonable to envisage independent powering of the quadrupole magnets in the matching sections, leading to increased flexibility in the optics of the machine. The HTS industry was also looking for a visible, commercial application of their technology, and the CERN current lead project was vitally important. It can be expected that HTS will play an increasing role in the work of consolidating and upgrading the LHC, and by virtue of its experience, CERN is well placed to take advantage of this emerging technology.

2. HTS FOR LHC: THE LHC CURRENT LEADS

When the possibility of incorporating HTS material in the current leads was first proposed, it was not clear exactly which technology would be most appropriate, neither was it clear how best to make use of the cryogenic system that had already been adopted for cooling the LHC [1]. The technology finally chosen was multi-filamentary Bi-2223 tape with a gold-doped silver alloy matrix. While work on prototypes had led to an improved bulk material incorporating stabilizing alloy (that is now used commercially for some applications), it was decided that, due both to its fragility and the difficulty of making very low resistance joints, the use of bulk HTS (Bi-2212, Bi-2223 or YBCO) was not appropriate for the LHC. Moreover, industry was starting to make Bi-2223 tape on a large enough scale to give confidence that their quality control would ensure reliable material and deliveries.

At the LHC, about 3 MA of current are transported via more than 3200 current leads (see Table 1). This is the largest current lead project ever undertaken. The initial intention was to apply HTS to the low current leads, but small cryogenic savings and severe geometric constraints on their integration led to a decision - following good results of tests - to adopt HTS for the higher currents.

Table 1
Type and Number of LHC current leads (excluding leads for the low-beta insertions)

Quantity	Current rating (A)	Magnets	Type
64	13000	Main dipole and quadrupole chains	HTS
258	6000	Matching sections magnets	HTS
708	600	Corrector quadrupole, sextupole and spool pieces	HTS
520	120	Dipole correctors in matching sections	Resistive
1504	60	Dipole correctors in arcs	Resistive

A typical Bi-2223 tape carries about 100 A in self-field at 77 K. However, at this temperature, it is very sensitive to magnetic field, and by restricting the maximum operating temperature to about 50 K one can get significantly better performance. In order to reduce the heat conductivity, a silver alloy with 5 % wt. gold replaces the customary silver matrix. This fraction of gold is found to provide the technical-economic optimum for the application.

The Bi2223 tape is extremely fragile. It was therefore decided to assemble the tapes into the more robust form of stacks of about eight tapes [2]. We initially thought we could use sintered stacks from American Superconductor (AMSC), but on analysis some samples were found to have cracks, and a CERN-developed technique of soldering was adopted as being more reliable.

The tape was specified, and over 30 km was purchased, following competitive tendering, from two suppliers (AMSC and EAS). Tape was delivered on spools in lengths of up to 300 m, inspected on reception, cut into 0.35 m pieces, and assembled and vacuum soldered (Sn-Ag eutectic) into stacks. The stacks are all characterized at 77 K (via a contract with CESI) before delivery to the lead manufacturers, where they are vacuum soldered (Sn-Pb) onto a stainless steel cylinder according to CERN procedures. The project requires about 10000 stacks. The HTS material was delivered on time and is of good quality. No material was rejected for insufficient current carrying capacity, and the stability of dimensional tolerances has been remarkable. Only a few percent of the cut lengths were deemed unacceptable due to visible bubbling. The critical current of the HTS stacks varies from 350 A (stacks from EAS tape) to about 630 A (stacks from ASC tape). All stacks were measured at 77 K in self-field, according to the 0.1 μV/cm, 1 μV/cm and 2.5 μV/cm electric field criteria. Some stacks were measured at different temperatures (from 77 K to 65 K) and in the presence of external magnetic field, parallel and perpendicular to the tape, of up to 0.5 T. Several samples of tape were irradiated using fast neutrons to verify their radiation resistance properties [3].

The tape is typically 4 mm wide and 0.2 mm thick. The filling factor is about 30 %. Each spool was electrically characterized by the manufacturer at liquid nitrogen temperature. The average critical current is about 79 A for the EAS and more than 100 A for the AMSC tape. The average n-value, at 77 K and in self-field, is 25. Four short samples per each production unit underwent mechanical tests. The minimum bending radius is 50 mm, and yield strength is 100 MPa (EAS tape reinforced with Mg) and 50 MPa (AMSC tape).

The LHC current leads were conceived, designed and specified at CERN. Prototypes were built in-house, and after validation purchased according to build-to-print specifications. To save time, an initial series of each lead type was manufactured in the CERN workshops. The leads are currently being manufactured by Cecom (13 kA) and BINP (6 kA and 600 A). They are all tested in nominal operating conditions at ENEA (13 kA and 6 kA) and at the University of Southampton (600 A). Presently about two thirds of the leads are available at CERN.

Thanks to the material studies undertaken at CERN and the contacts with the companies involved, CERN has acquired considerable understanding regarding the application of HTS in its different forms, including skill in the associated calculations and the practical issues of handling and characterization. We have become acquainted with the manufacturers and users of HTS material, both for leads and for other applications. Because of this network, CERN help is now solicited by other laboratories for the design of HTS leads, not only for quasi-dc operation (as in LHC) but also for pulsed use. In addition, work is being done in parallel to characterize material with regard to use in superconducting switches, leads and buses – and possibly in magnets too. Besides the practical work on the leads, the preparatory work for future development involves theoretical and practical studies of quench propagation, ac losses and eddy currents in HTS.

3. HTS AND LHC UPGRADES

3.1 Consolidation of the baseline LHC

Before moving to upgrades, it is likely that there will be at least two applications for HTS in the programme of Operations Support, Maintenance and Consolidation of the baseline LHC. There are magnets and bus-work in the cleaning insertions that risk being vulnerable to heating due to radiation. Suitable replacement magnets are identified, but these will benefit from purpose-designed leads and bus-work using HTS material. There is also a need for a long multi-strand HTS bus.

3.2 Intermediate low-beta upgrade

There may be the demand for an intermediate upgrade of the high-luminosity low-beta insertions. This is clearly the easiest way to improve luminosity should there be problems with increasing beam intensity. Moreover, due to the addition of the beam screen through the present quadrupoles, their aperture is smaller than that which was originally planned. The work presented by R. Ostojic (these proceedings) addresses this issue. The characteristics of the present leads and lead box should not constrain the optimization of the magnet system. Based on experience with the baseline LHC, ideas exist for improved types of leads and feed box that we could consider integrating into the system.

3.3 Injector upgrades

At the request of other laboratories, the possible use of HTS leads for pulsed use is being addressed.

3.4 Major low-beta upgrade

Clearly there will eventually be the need for a substantial upgrade of the low-beta insertions. Studies in progress suggest that the layout could undergo a quite radical change, including the integration of dipoles. It may well be advantageous to use HTS in at least some of these magnets. HTS material offers higher temperature margin and good radiation resistance. At the last Magnet Technology Conference, experts were optimistic about the future of HTS, forecasting regular improvement in its current-carrying capacity. This should be followed carefully and it may be interesting to develop some “react-and-wind” designs that use, or could use, HTS material. Thanks to the expertise and renown it has gained with the current lead project, CERN is well placed to follow up this line, in a complementary fashion to the upgrade magnet work being undertaken in the US LARP program.

4. CONCLUSION

It is widely acknowledged that CERN is at the forefront as regards the application of HTS. For identified consolidation work on the baseline machine, as well as for an intermediate upgrade there are already potential uses of HTS. The work that is in progress on the optimization of HTS leads for pulsed operation will be directly applicable to the powering of a possible superconducting injector. CERN should also include HTS in the thinking for a major upgrade of the magnet systems for high luminosity insertions. Finally, it should be remembered that consolidation and upgrades do not only concern magnets, but also essential ancillary equipment that should be optimized together with the magnet systems. HTS is an important component of this equipment, as well as having the potential of being a conductor for future magnets.

REFERENCES

[1] A. Ballarino, Application of High Temperature Superconductors to Accelerators, Seventh European Particle Accelerator Conference, Vienna (2000), and LHC Project Report 420.

[2] A. Ballarino, S. Mathot, D. Milani, 13000 A Current Leads for the LHC: from Conceptual Design to Prototype Validation, Proc. EUCAS 2003, Sorrento, and LHC Project Report 696.

[3] T. Taylor, A. Ballarino, A. Ryazanov et al, Effect of Fast Neutron Irradiation on Transport Properties of HTS Material, Proc. EUCAS 2003, Sorrento, and CERN/AT 2004-6.

Session: Design tools: potential and limitations

MAGNET DESIGN: MECHANICS AND MAGNETICS OF THE LARP QUADRUPOLE TQS01

S. Caspi
Lawrence Berkeley National Laboratory, Berkeley, USA

Abstract
This talk covers the design, analysis and preliminary cool-down results of LARP quadrupole TQS01. The main features of the quadrupole are as follows: 2-layer Nb_3Sn coils with 10 mm wide, 27-strand cable (0.7 mm MJR strand) having expected short sample performance at 4.2 K of 11.2 T (field), 220 T/m (gradient) and 12.4 kA (current). The accumulated azimuthal Lorentz stress is -123 MPa and the accumulated axial force is 350 kN (4 quadrants).

1. MAGNET PRODUCTION AND ASSEMBLY

Magnet production and assembly goes through the following sequence of work:

- Coil winding
- Coil reaction
- Instrumentation
- Impregnation
- Coil sub-assembly
- Structure sub-assembly
- Final assembly
- Axial pre-stress using rods and piston
- Azimuthal pre-stress using bladders and keys

A series of photographs demonstrating each step are included in the presentation.

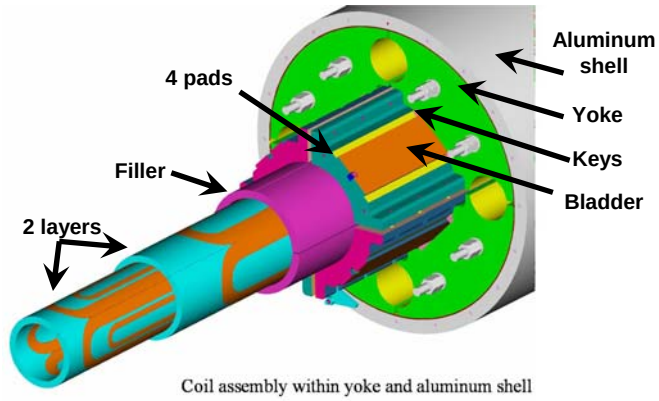

.

Fig. 1 Schematic view of the short racetrack quadrupole.

The magnet design (see Figs. 1 and 2) and analysis took full advantage of the integration between CAD (ProEng), magnetic analysis (TOSCA) and structural analysis (ANSYS). The design addressed two major requirements: 1) No azimuthal separation at the pole, 2) No axial separation in the end. Based on these two rules, the modeling, which included friction, provided sufficient information both for the assembly procedure and to forecast the stress-strain behavior on cool-down and excitation.

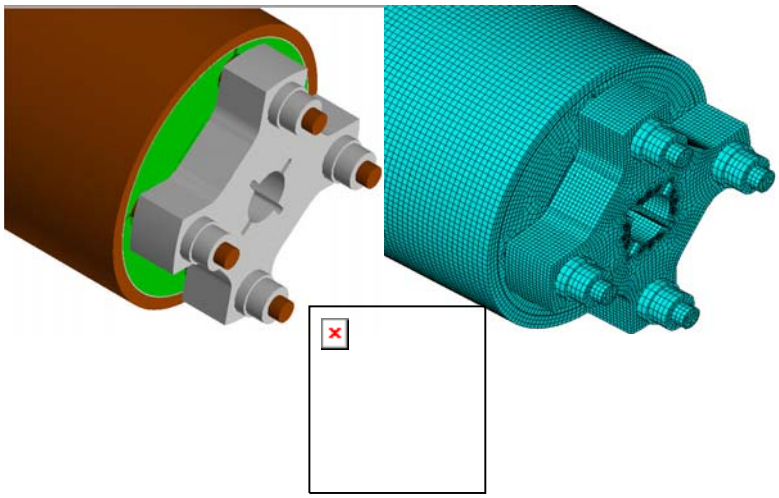

Fig.2 Integrated design of TQS01.

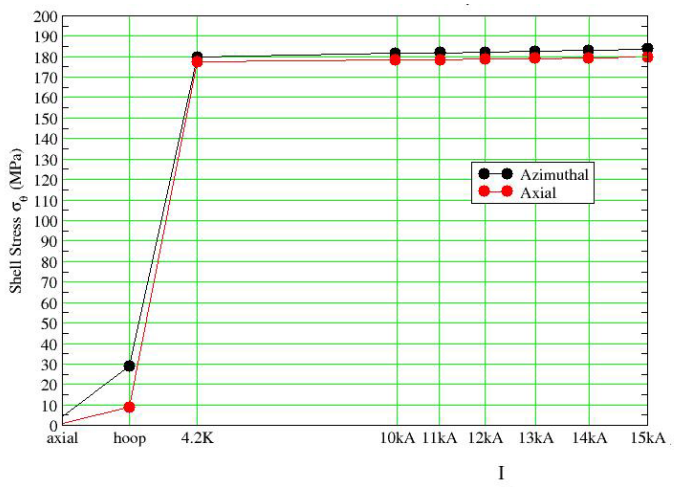

Fig 3 Shell azimuthal stress -shell and yoke are with a friction factor of μ=0.6; other friction surfaces, μ=0.2.

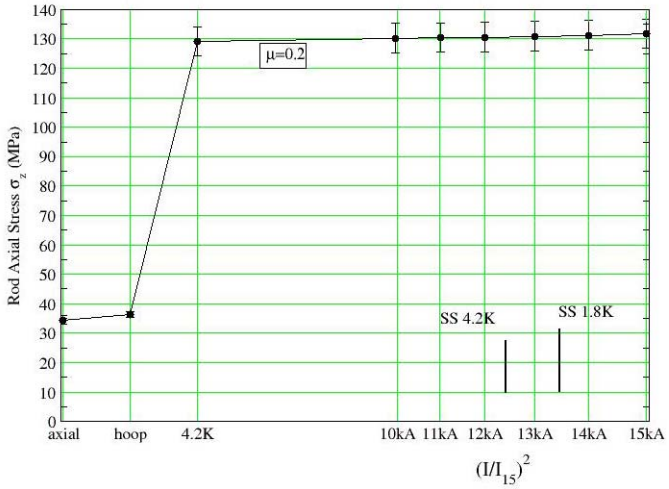

Fig. 4 Stress in the axial rods during assembly, cool-down and excitation.

One of the most important lessons learned during the ANSYS analysis was a possible source of magnet training. Two similar (yet different) training mechanisms were identified with the straight section and the magnet end (see Fig. 5).

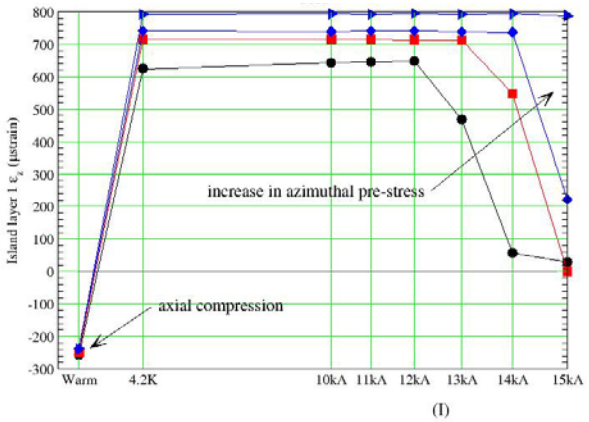

Fig. 5 Strain release in the pole-island with excitation.

1.1 Straight section

Axial tensile strain in the pole island, held by friction, releases when the coil pulls away due to insufficient azimuthal pre-stress.

1.2 End section

Sliding and tarring occurs between the coil and the island due to insufficient axial pre-stress.

The inter-relation between the axial and azimuthal strain in the coils, island and shell needs to be better understood. As the formulation suggests axial stress between the island and the pole turn INCREASES when the azimuthal stress between the two surfaces decreases. This surprising result (yet to be measured) is strongly dependent on friction and the fact that in the straight section axial strain does not change much with excitation (see Fig. 6).

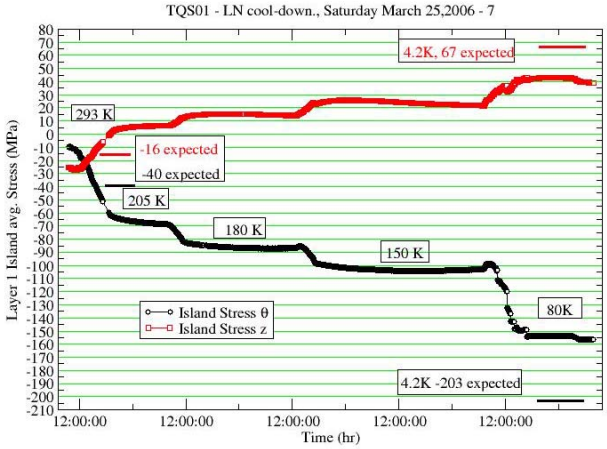

Fig. 6 Measured strain in pole island with cool-down to 80K indicates azimuthal compression and axial tension.

2. CONCLUSION

- TQS01 is the most “engineered” magnet we ever built.
- We have analyzed every component from assembly through cool-down and excitation and pushed Nb3Sn technological to new limits.

With a test to follow in a few weeks the design expectations are:

- To reach short sample prediction (field, current, stress);
- To get there with minimum training.

CAST3M FOR MAGNET DESIGN

J.M. Baze
CEA, CEN Saclay, France

Abstract
The Finite Elements simulation code CAST3M has been used extensively in DAPNIA since early 1990 to help in designing superconducting or conventional magnets. It offers an integrated tool dealing with all coupled topics involved in such design: electromagnetic and thermal studies, as well as solid and structure mechanics. A short description of its possibilities, a list of magnets for which this code has been widely used and work engaged about quadrupole head design are presented here.

1. SHORT PRESENTATION OF CAST3M CODE

1.1 Overview

CAST3M is a finite element code built and enriched over 35 years in the Nuclear Reactor Division of CEA (French Atomic Authority) in the Dept. of Mechanical and Thermal Engineering (DEMT) [1].

Conceived as a tool box dealing with all geometric and mathematical objects handled with finite element techniques, it provides an integrated software package allowing to couple a great range of problems such as solid and structural mechanics, heat transfer, many diffusion models, flow circulation (EF and VF), magnetostatics, eddy currents in some configurations, linear or non-linear behaviour, etc. For each of these topics the code offers a wide range of possibilities.

The code is organised in 2 levels of programming:

1. Lower layer for development (Fortran C++) reserved to code designers;
2. Upper layer using a simple purpose-built interpreted language (Gibiane) that allows users to tailor their own application using operators.

This allows for easy exchange of mesh and others information with most commercial FE codes and CAD software.

1.2 Main features of the upper level language

1.2.1 Generalities

Execution works in data flow, the user build a data base containing objects named at his convenience by applying operators on already defined objects

Object2 = Object1 **OPERATOR** operand(s)

All objects are given automatically a type according to the used operator. This allows verification of syntax during execution and correction on line during interactive runs.

1.2.2 Procedures

The normal version of Cast3M provides a wide set of ready-made procedures dealing with conventional problems encountered by design engineers. Gibiane allows user to writes sequences using logical operators loops, etc., and to arrange their ‘routines’ in ‘procedures’ that may be stored and accessed as operators which offers a very convenient and fast tool for peculiars developments.

Full information about the tool can be obtained at the following address:

http:\www-cast3m.cea.fr

2. SPECIALIZED OPERATORS FOR MAGNET DESIGN

In the early 1990s, mechanical engineers designing magnets in our laboratory had real difficulties to obtain a thorough definition of the distribution of the magnetic forces for introducing into CAST3M mechanical simulations. So a set of magneto-static procedures have been developed, using a derivation of operators normally devoted to thermal problems, which allow treating and coupling most of the topics encountered in designing conventional or superconducting magnets, either in 2-D or 3-D.

2.1 2-D Vector Potential

Table 1
procedures for 2-D computation

Result	Name of procedure
Vector Potential	POT_VECT
Current map description	DESCOUR
B Computation	INDUCTIO
Forces by contour integral	FORCONT
Forces by surface integral	FORBLOC
Harmonic analysis	DDFOUR
A and B Projection on regular grid	PROI POLY

2.2 3-D Scalar potentials (Reduced and Total) [2],

2.2.1 Computation of source field

2.2.1 .1 Operator BIOT

This operator adapted from a program already used in the laboratory [3] for the computation of induction or vector potential with no iron in the vicinity, given by coil described as arrangement of bars, rings, arcs of rectangular or trapezoidal cross section (semi analytical integration).

2.2.1 .2 Procedure BIOVOL

This procedure computes induction or the vector potential given by any kind of finite element if the current density is known at integration points, which can be achieved easily by solving a potential problem on meshed coils using standards operators. This way is very time consuming and must be reserved to configurations where the BIOT operator cannot be used.

2.2.2 Procedures

Table 2
Procedures for 3-D computation

Fonction	Name of procedure
Scalar potentials (reduced _ total)	POT_SCAL
Reading coils characteristics	LEC_BOB
Biot-Savart Field computation	CHAMBOB
Forces distributed on coils	S_IVB
Forces on iron parts	EFF3D

The procedure LEC_BOB is a layer above the BIOT operator. Its use is as follows:

- To read in a simple way the geometrical characteristics of coils;
- To allow to ask for a mesh of the coil (which is not necessary to compute the field) and to build the coil current density in order to obtain Laplace forces;
- To store all sub-components of coil description in a structured and preconditioned object handled by CHAMBOB, S_IVB, EFF3D making easy local post processing.

2.3 Common procedures for 2- and 3-D

Table 3
Common 2-D and 3-D procedures

Fonction	Name of procedure
Definitions of (B-H) curves	H_B
Potential Non linear material iterations	MAG_NLIN

2.4 Eddy currents

It is also worth noting that a finite element devoted to compute eddy currents on thin shells, developed during the conception of TORE-SUPRA, has been incorporated [4] in CAST3M, i.e. element ROT3. This can be useful for designing shields or vessels around superconducting magnets.

3. MAGNETS ENGINEERED IN DAPNIA WITH CAST3M

Since the early 90s CAST3M has been used extensively in DAPNIA to achieve mechanical design of many superconducting magnets such as (see presentation for illustrations):

- LHC quadrupole;
- Cebaf 0.6 m aperture quadrupole Q1;
- Clas (Cebaf) 4.6 T solenoid with active shielding,
  inner bore: 0.240 m; outer diameter ~1 m;
- CMS 4 T solenoid,
  inner bore: 6.4 m ; length: 12.5 m;
- ATLAS Toroid 8 race track coils,
  outer diameter: 20 m; length: 26 m;
- R3B spectrometer with active shielding arrangement of
  12 superconducting coils, overall size ~ 3 m x 3 m.

For all these magnets we have had to confront the usual range of problems, namely:

Non-isotropic material behaviour;

Shrinkage during cool down;

Efficiency of cooling system;

Action of huge magnetic forces;

Difficult structural mechanical challenges.

4. ONGOING WORK FOR QUADRUPOLE HEADS

In 2005 work has started on providing a convenient specialised tool that allows easy variation about the significant parameters in the design of quadrupole heads. The first step of this operation has consisted of writing a chain of procedures that can produce from a reduced set of geometrical data all the necessary ingredients. The resulting model provides a database where all physical components are

stored as structured and preconditioned objects. From this database different models of increasing complexity can be run, going from a simple bulk model (material continuity over all components) to a model including joints element providing different interfaces, e.g. unilateral contact, contacts with friction, etc. These difficult simulations must be now fed with data coming from experimental test programs on conductors and prototypes of heads.

5. CONCLUSION

The mechanical conception of superconducting magnets presents an increasingly difficult challenge due to the physics requirements for thorough dimensional stability at the same time as increasing the field level. It is a great advantage for engineers to be able to perform all the necessary computations using a single tool that allows the handling and passing of information in the most appropriate form between the various disciplines. The CAST3M suite of programs provides this possibility.

REFERENCES

[1] P.Verpeaux, A.Millard, T.Charras. A.Combescure, A modern approach of large computer code for structural analysis, Structural Mechanics in Reactor Technology N°10, Los Angeles (1989).

[2] J.Simkin and C.Trowbridge, Three-dimensional non-linear electromagnetic field computation using scalar potentials, Proc. IEE 127 6 (1980).

[3] C. Lesmond, Biot and Savart computation, CEA internal report.

[4] J.Blum, L.Dupas, C.Leloup, B.Thooris, Numerical simulation of the Eddy currents in the thin shells of a tokamak, Actes du colloque: Modelisation et calcul en électromagnétisme MODELEC 22-24 (1984)

ANSYS APPLICATION IN MAGNET DESIGN

Stefania Farinon
INFN- Sezione di Genova, Italy

Abstract
The INFN-Genova experience in using ANSYS for magnet design started in 1994. From that period on, the ANSYS software was greatly enhanced, following the outstanding evolution of computational and graphical tools of these years. This paper will point out a few distinguishing features which make ANSYS particularly worthy of being adopted for magnet design.

1. INTRODUCTION

ANSYS [1] is a general purpose finite element code that can be used in a wide range of physical fields - structures, heat, electromagnetism, aerodynamics, biomechanics, etc. - and also in many multi-aspect simulations in one, two or three dimensions. The best way to project an idea of its remarkable capabilities is to give a few examples that illustrate some of its special features.

2. ELECTROMAGNETIC ANALYSIS

2.1 Magnetic field accuracy

When designing electromagnetic devices, it is often of basic importance to make very accurate calculations of the magnetic field distribution. In these cases, it could be critical to estimate the grade of accuracy of the finite element analysis. To that extent, ANSYS gives the user a very powerful tool that is the possibility to reproduce the same simulation in several different formulations. Among them, the basic ones are the Magnetic Scalar Potential Formulation (MSP), which uses the magnetic scalar potential (MAG) as a degree of freedom for the analysis, and the Magnetic Vector Potential Formulation (MVP) which uses the three components of the magnetic vector potential (AX, AY and AZ) as degrees of freedom. It can be demonstrated that the MSP formulation converges to the exact energy from above, whilst the MVP formulation converges to the exact energy from below. This means that, when accuracy is a critical factor, the best way to tackle an electromagnetic analysis is to run both the formulations: the difference between the two is the best measure of the accuracy.

As an example, let us consider the magnetic field produced by a CMS-like solenoid in air (internal radius 3.18 m, external radius 3.46 m, length 12 m, ampère-turns $44 \cdot 10^6$). If we compare the finite element analyses with the analytical expression for the field along the magnet axis (Fig. 1), it is verified that the vector potential formulation gives an approximation of the magnetic field that is low, whilst the scalar potential formulation gives an approximation that is high.

2.2 Optimization using a genetic algorithm

Another interesting feature of the ANSYS program, showing its high degree of flexibility, is the possibility to use it as a mere subroutine of any other external program. Parameters can be either directly passed or exchanged via external files.

As the ANSYS internal optimization techniques are not particularly efficient, a typical example is the implementation of the ANSYS program in an external optimization algorithm. In particular, we implemented ANSYS in an existing genetic algorithm, written in Fortran, where ANSYS is only a mathematical operator able to calculate the objective function. Let us consider the RHIC-like dipole shown in Fig. 2, made up of 4 blocks, of respectively 9, 11, 8 and 4 turns, and able to produce a central field of 4.5 T. The parameters taken into consideration for the optimization are 9, describing the angular position of the blocks (6 parameters) and the position of the hole inside the iron (2

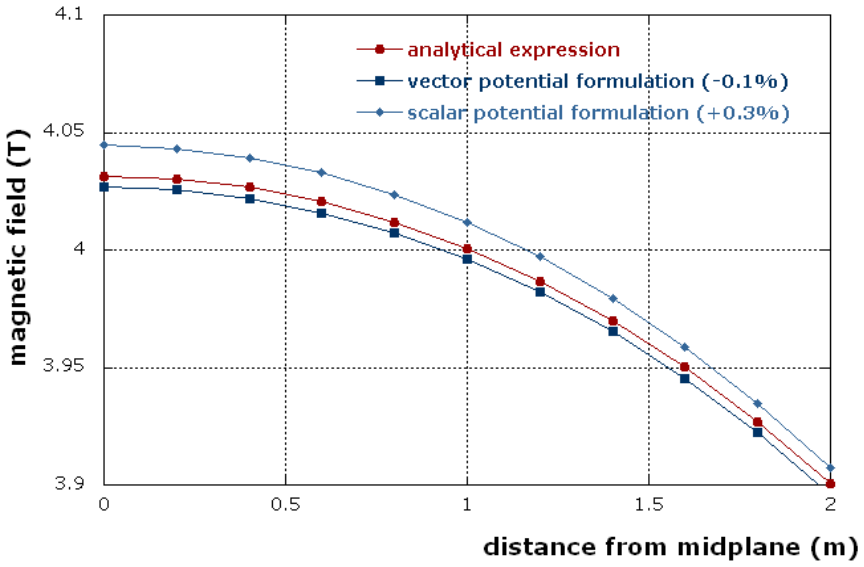

Fig. 1 Magnetic field along the axis of the CMS magnet near the midplane: comparison among MSP formulation, MVP formulation and analytical expression.

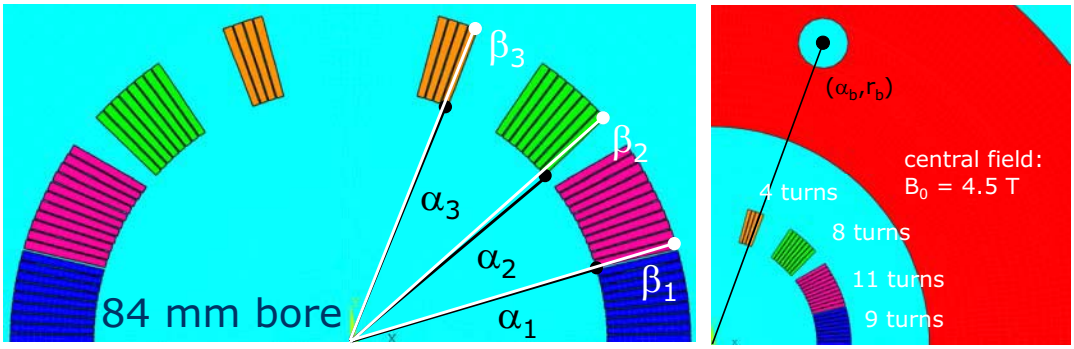

Fig. 2: Schematic section of a RHIC-like dipole, showing the optimization parameters used in the genetic algorithm.

parameters). Having as optimization function the sum of the first 4 non-zero harmonic components of the magnetic field calculated at a reference radius of 30 mm, in only 56 generations we found a satisfactory solution: b3=0.08 units, b5=0.66 units, b7=1.22 units and b9=0.24 units.

3. STRUCTURAL ANALYSIS

3.1 Large deformation of plastic materials

Analysis involving large deformations of plastic materials is usually very complicated, and often gives rise to problems of convergence for finite element codes. In this regard, ANSYS has developed a very efficient method to generate elements for modeling solid structure that can effectively handle analysis involving plasticity, large deflection, and large strain, even in the presence of contact.

As an example, consider the Nb_3Sn un-reacted internal tin wire for the NED experiment made by Alstom and shown in Fig. 3 together with the finite element model used for the analysis. In the model, all the mechanical material properties are represented by bi-linear stress-strain curves. Contact elements have been modeled between the walls and the external surface of the wire. Let us suppose to

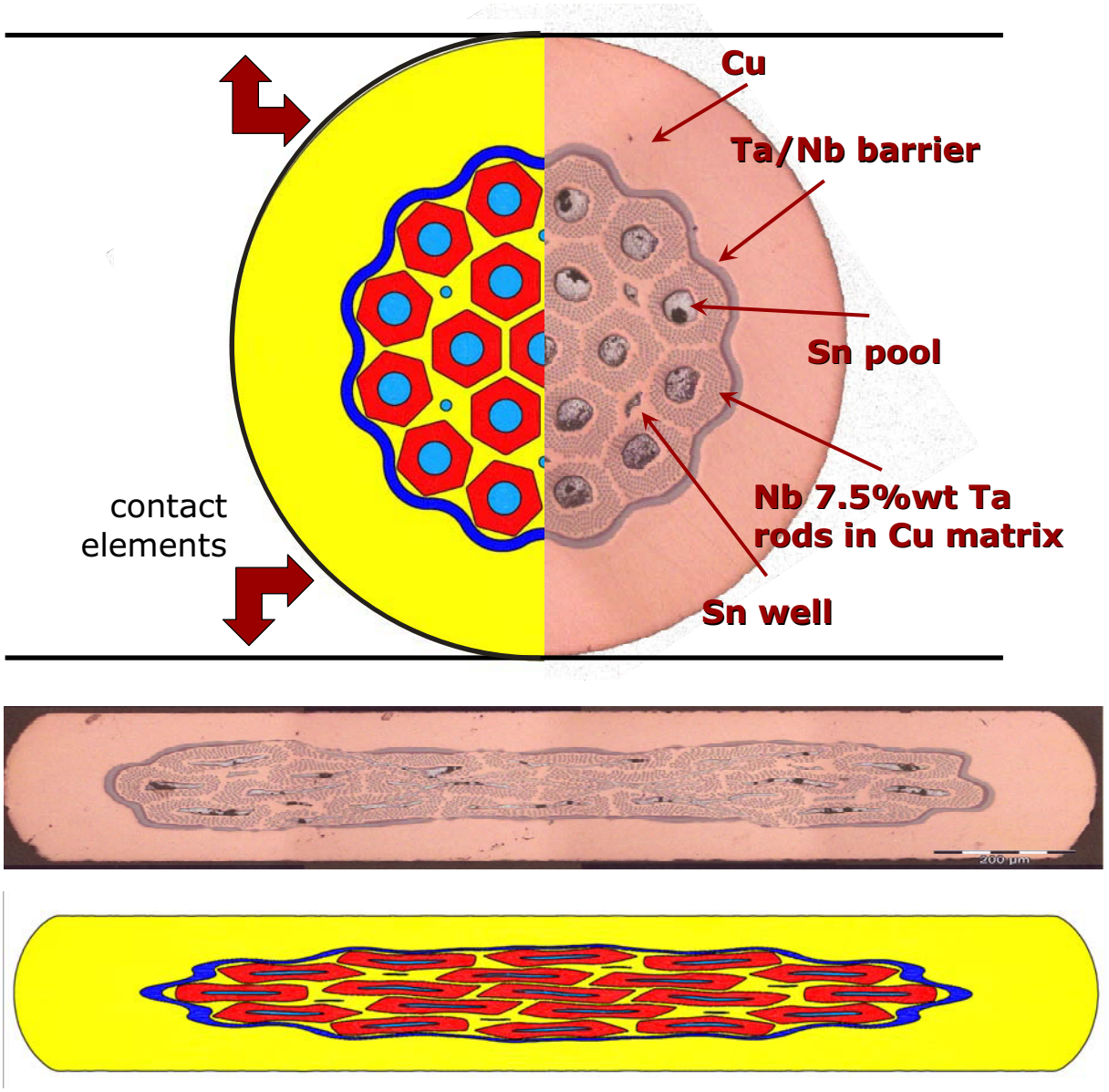

Fig. 3: Nb_3Sn un-reacted internal tin wire for the NED experiment made by Alstom: comparison between measurement and finite element analysis for 75% reduction of wire diameter.

squeeze the wire between two rigid and parallel walls. In Fig. 3 there is a comparison between a real experiment and the calculation corresponding to a total reduction in diameter of 75%. The agreement is not completely good, but clearly, the limit of this kind of analysis is the fact that it cannot take into account rupture and mixing up of material, as evidently occurs in this case. In any case the goal was not to simulate exactly the stress status of a largely deformed wire, but rather to set up a method allowing the comparison of the mechanical behavior of different layouts.

4. MULTI-ASPECT SIMULATIONS

4.1 Coupled thermal electric transient analysis

An example of a rather complicated coupled thermal electric transient analysis is the simulation of the thermal behavior of a superconducting magnet during a quench. The only input needed for this kind of analysis, besides the appropriate material properties, is the rule of the current decay after the quench is detected.

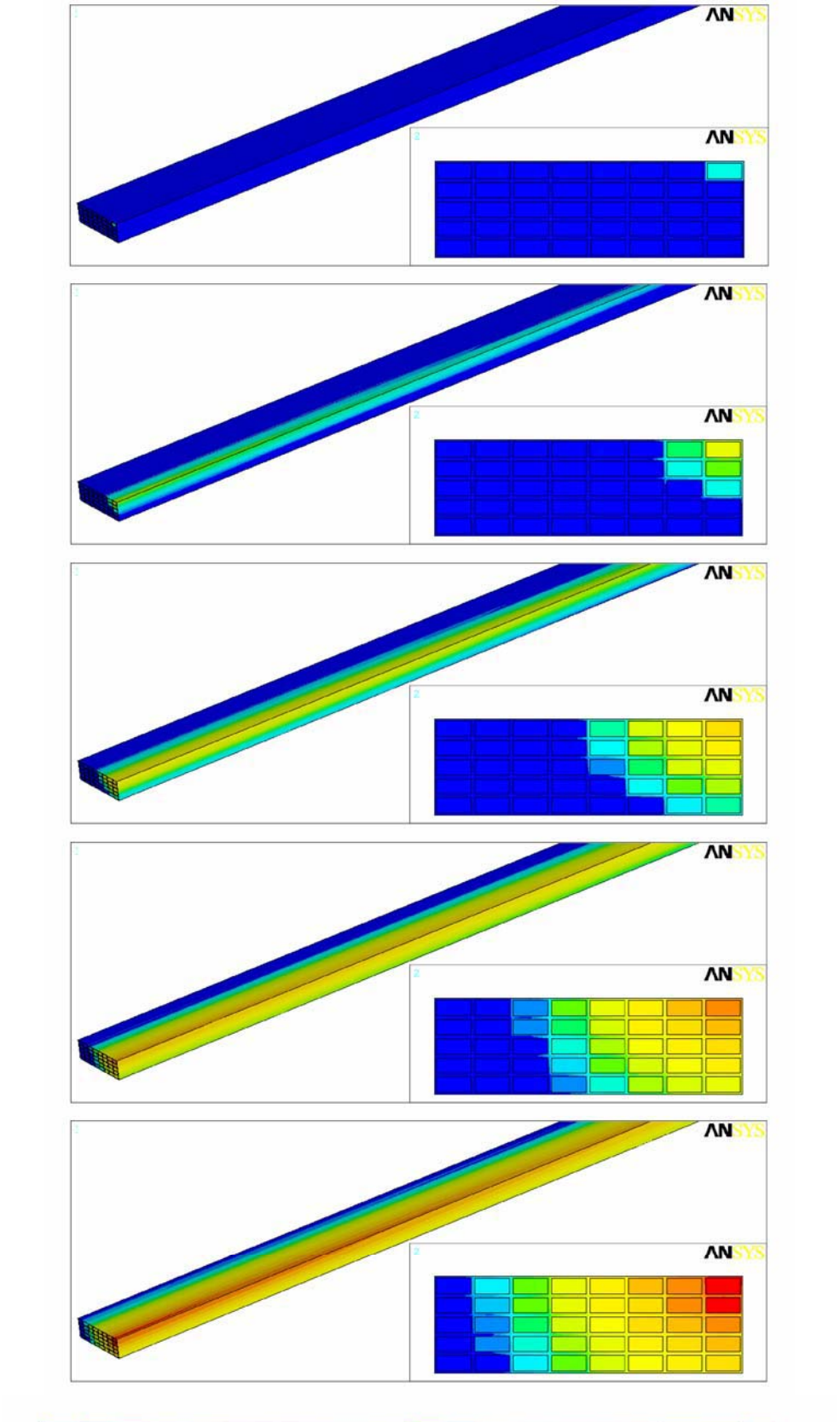

Fig. 4 Example of a thermal electric transient analysis: temperature profile as function of time in a rectangular winding. At $t=0^{+}$, the temperature of the right top conductor has been raised to 10 K. The system is assumed to be adiabatic.

If we consider a basic protection circuit, an external resistance R_e in parallel to the superconducting magnet, when a quench is detected the current starts to decay with a simple exponential law:

$$I(T,t) = I_0 e^{-\frac{R_e + r_i(T,t)}{L}t} \tag{1}$$

where L and $r_i(T,t)$ are respectively the inductance and the internal resistance as function of temperature and time of the superconducting magnet. Next step is to define a logical algorithm for this analysis. Let us start from an initial situation in which the internal resistance is zero, the circulating current is the operating one and the temperature is the operative one everywhere but the region where the quench starts, where the temperature is arbitrarily set to a higher value. Due to the raise of temperature, it happens that the internal resistivity grows, so that we have a corresponding decay of the current circulating in the magnet, and due to that a new value of resistivity. So, the basic idea is that the values of resistance at time t, simply obtained as the ratio between the dissipated power and the current circulating at the time t, allows calculating the loading conditions at the time t+Δt, that is the new values of the operating current and resistivity.

An example of how this procedure works is shown in Fig. 4, corresponding to the thermal transient of a rectangular winding made of 40 insulated turns. The resistivity of the conductors is represented by Eq. (2):

$$\rho(T) = \begin{cases} \rho_{SC} & T < T_g \\ \rho_{SC} + \rho_{Cu}(T)\dfrac{T - T_g}{T_C - T_g} & T_g < T < T_C \\ \rho_{Cu}(T) & T > T_C \end{cases} \tag{2}$$

where ρ_{SC} is the resistivity of superconductor (nearly zero), $\rho_{Cu}(T)$ is the resistivity as function of temperature of copper (RRR 100), T_C is the critical temperature of superconductor, and T_g is the sharing temperature, defined as: $T_g = T_C - (T_C - T_0) I_{op}/I_C$.
At time $t=0^+$, the temperature of one face of the top right conductor is raised up to 10 K. No cooling is present, that is the temperature diffusion is supposed to be adiabatic. Fig. 4 represents the evolution in time of the temperature profile in the winding.

What is most interesting is the potential of this analysis. First of all, it is possible to take into account any kind of boundary conditions, the presence of possible cooling, or potential source of thermal disturbances, by simply adding the desired loads to the finite element model. Second, it is possible to solve the problem in case of a different protection circuit or un-detected quench, by only changing the law of current decay. And finally, as time by time ANSYS computes the temperature distributions; these distributions can be used as input loads for structural analysis, in such a way to calculate the stress maps as functions of time during the quench propagation process.

5. CONCLUSION

I think that the ANSYS program has been widely demonstrated to be a powerful tool for magnet design. Its main advantage consists in the fact that it continuously evolves following the progress of calculation tools and the needs of the users.

REFERENCES

[1] ANSYS®, Inc., revision 10.0 (www.ansys.com)

ROXIE FEATURES AND PROSPECTS

S. Russenschuck
CERN, Geneva, Switzerland

Abstract
The paper describes the features and the planned developments for the CERN field computation program ROXIE for the design and optimization of (not only superconducting) magnets for (not only) accelerators.

1. INTRODUCTION

The design and optimization of superconducting accelerator magnets is dominated by the requirement of an extremely uniform field, which is mainly defined by the layout of the superconducting coils. For the field calculation it is necessary to consider even very small geometrical effects, such as those produced by insufficient keystoning of the cable, insulation, coil deformations (due to collaring, cool down, and electromagnetic forces) and grading of the current density in the cable due to different cable compaction. If the coils had to be modeled in the finite-element mesh, as is the case in most commercial field computation software, it would be difficult to define the current density as this would require a further subdivision of the cables into a number of radial layers.

For the 3-D case in particular, commercially available software was found to be ill-suited for the design and field optimization of superconducting magnets for the LHC. The ROXIE (**R**outine for the **O**ptimization of magnet **X**-sections, **I**nverse field calculation and coil **E**nd design) program package was therefore developed at CERN, and is now being increasingly used in other institutes.

2. FEATURES

In collaboration with the Technical University of Graz, Austria, the program was extended to include the possibility of calculating iron saturation effects using a reduced vector-potential method. ROXIE also includes the method of coupled boundary/finite-elements, which was developed at the University of Stuttgart, Germany, and which is specially suited for the calculation of 3-dimensional effects in magnets. The advantage of both methods is that the coils do not need to be represented in the finite-element mesh and can therefore be modeled with the required accuracy.

The development of the ROXIE program was driven by the following main objectives:

- To write an easy-to-use program for the design of superconducting coils in two and three dimensions considering field quality, quench margin, and hysteresis effects due to persistent currents in the superconductors.
- To provide for accurate field calculation routines that are specially suited for the investigation of superconducting magnets, i.e., accurate calculation of the field harmonics, the field distribution within the superconducting coil, superconductor magnetization etc.
- To integrate the program into a mathematical optimization environment for field optimization and inverse problem solving.
- To integrate the program into the engineering design procedure through interfaces to Virtual Reality, to CAD/CAM systems (for the making of drawings and manufacturing of end-spacers for the coil heads), and
- via interfaces, to commercial structural analysis programs.

The modeling capabilities of the ROXIE program, together with its interfaces to CAD/CAM and its mathematical optimization routines, have inverted the classical design process wherein numerical field calculation is performed for only a limited number of numerical models that only approximate the actual engineering design. ROXIE is now used as an approach towards an integrated design of superconducting magnets. The steps of the integrated design process are as follows:

- Feature-based geometric modeling of the coil and yoke, both in two and three dimensions using only a number of meaningful input data to be supplied by the design engineer. This is a prerequisite for addressing these data as design variables of the optimization problem.
- Conceptual design using a genetic algorithm, which allows the treatment of combined discrete and continuous problems (e.g. the change of the number of cables per block) and the solving of material distribution problems. The applied niching method provides the designer with a number of local optima which can then be studied in detail.
- Subject to a varying magnetic field, currents that screen the interior of the superconducting filaments are generated. The relative field errors caused by these currents are highest at injection field level and have to be calculated to allow subsequent partial compensation by the introduction of controlled geometrical field errors.
- Deterministic search algorithms are used for the final optimization of the coil cross-section.
- Minimization of iron-induced multipoles using a finite-element method with a reduced vector-potential formulation (developed at IGTE Graz, Austria) or the BEM-FEM coupling method (developed at ITE Stuttgart and Robert Bosch GmbH, Germany).
- Calculation of the peak voltage and peak temperature during a transition from the superconducting to the normal conducting state (quench).
- Sensitivity analysis of the optimal design through Lagrange multiplier estimation and the set-up of payoff tables. This provides an evaluation of the hidden resources of the design.
- Tolerance analysis by the calculation of Jacobian matrices, and estimation of the standard deviation of the multipole field errors.
- Generation of the coil-end geometry and shape of the so-called end-spacers using methods of differential geometry. Field optimization including the modeling and optimization of the asymmetric connection side, ramp and splice region as well as external connections.
- 3-D field calculation of the saturated iron yoke using the method of coupled boundary elements and finite-elements, BEM-FEM.
- Production of drawings by means of a DXF interface for both the cross-sections and the 3-D coil-end regions.
- End-spacer manufacture by means of interfaces to CAD/CAM (DXF, VDA), rapid prototyping methods (laser sinter techniques), and computer controlled 5-axis milling machines.
- Tracing of manufacturing errors from measured field imperfections, by the minimization of a least-squares error function using the Levenberg-Marquardt algorithm.

3. FUTURE PROSPECTS

While the design process described above is well established for superconducting accelerator magnets, the methods implemented in the code can also be applied to other fields of magnetic technology, including large air-coil (detector) magnets, solenoids, conventional magnets etc. Clearly, the ROXIE user interface has been designed with accelerator magnets in mind. This, however, does not preclude

the creation of numerical models for devices such as actuators or electrical machines. Recently added features include:

- Calculation of the working point considering fit-curves for the critical surface.
- Inter-filament coupling currents.
- Inter-strand coupling currents.
- Eddy currents in copper wedges of finite length (not connected at the magnet ends)
- New material database structure.
- A virtual reality interface.

Future extensions will include refined methods for

- Quench calculation.
- Hysteresis modeling using Preisach formalism.
- A BEM-FEM solver based on methods of Discrete Electrodynamics, i.e., employing discrete differential forms.

As calculations can only be as good as the input data provided, the ROXIE team would highly appreciate if the community could establish a common database of material characteristics, including critical surfaces of superconductors, thermodynamic properties of materials used in accelerator magnets, and B(H) curves for iron yokes (including hysteresis measurements). It would also be extremely useful to have a database of numerical models of built magnets (including their magnetic measurements).

BIBLIOGRAPHY

More information on the licensing, download, and use of the program can be found on the web pages http://cern.ch/at-mel-em/.

The eBook: Electromagnetic Design and Mathematical Optimization Methods in Magnet Technology can be downloaded from http://russ.home.cern.ch/russ. It has in its 3.3 version about 600 pages and lists more than 250 references.

REDUCING RADIATION LOADS IN IR QUADRUPOLES FOR LHC UPGRADES

N.V. Mokhov, I.L. Rakhno
Fermilab, Batavia, IL 60510, USA

Abstract
Challenging beam-induced energy deposition issues are addressed for the next generation of the LHC high-luminosity interaction regions based on Nb_3Sn quadrupoles. Detailed MARS15 Monte Carlo energy deposition calculations are performed for various coil diameters, thicknesses and materials of the inner absorber at a field gradient of 200 T/m. It is shown that using the inner absorber made of tungsten-based materials can make the final focus superconducting quadrupoles compatible with a luminosity of 10^{35} cm^{-2}s^{-1}.

1. INTRODUCTION

The superconducting (SC) magnets of the Large Hadron Collider (LHC) under construction at CERN are based on NbTi superconductor. The high-gradient quadrupoles for the interaction region (IR) inner triplets have been developed and manufactured by KEK and Fermilab [1]. These quadrupoles with 70-mm coils, provide a field gradient of 200 T/m and will allow one to achieve the nominal luminosity of 10^{34} cm^{-2}s^{-1}. As a result of thorough optimization of the IP1/IP5 layouts and low-β quadrupole design, the system was designed and built to protect the IR SC magnets against debris generated in the pp-collisions as well as to protect magnets and detectors against beam halo and a missteered beam coming to the IP. The system includes a set of absorbers in front of the inner triplet (TAS), inside the triplet aperture and between the low-β quadrupoles, inside the cryostats, in front of the D2 separation dipole (TAN), and between the outer triplet quads as well as a complex system in IP6 and tertiary TCT collimators for the incoming beam. Their parameters were optimized over the years in detailed energy deposition calculations at Fermilab to provide better protection consistent with the engineering constraints [2].

Several possible upgrade paths are under consideration to achieve a luminosity capability of 10^{35} cm^{-2}s^{-1} at the LHC interaction points (IP) [3, 4]. Recent progress in the development of Nb_3Sn superconductor enables one to consider Nb_3Sn magnets as possible second generation quadrupoles for the LHC IRs [5]. One of the most serious limitations here is the luminosity-driven energy deposition in the IR magnets. The quadrupole fields sweep the secondary particles from pp-collisions at the IP into the SC coils along the vertical and horizontal planes, giving rise to a local peak power density ϵ_{max} that can substantially exceed the quench limits and reduce component lifetime, with kW-level radiation loads on the inner triplet cryogenic system [6].

This study is a continuation of our first look [7] at energy deposition issues for the new IR magnets. We address the dependence of radiation-induced energy deposition in the Nb_3Sn magnets on coil diameter, thickness and material of the inner absorber at a field gradient of 200 T/m by doing comprehensive energy deposition calculations with the MARS15 Monte Carlo code [8, 9]. A configuration compatible with the luminosity of 10^{35} cm^{-2}s^{-1} is proposed.

2. INNER TRIPLET MODEL

The calculation model of the IR is presented in Figs. 1-2. A longitudinal structure of the inner triplet region corresponds to the LHC lattice v6.5. The updates consist in replacing the quadrupoles based on NbTi superconductor with larger bore ones based on Nb_3Sn. The four magnets in the region–Q1, Q2A, Q2B, and Q3–differ only in length while their radial structure, excluding the inner absorber (liner), is

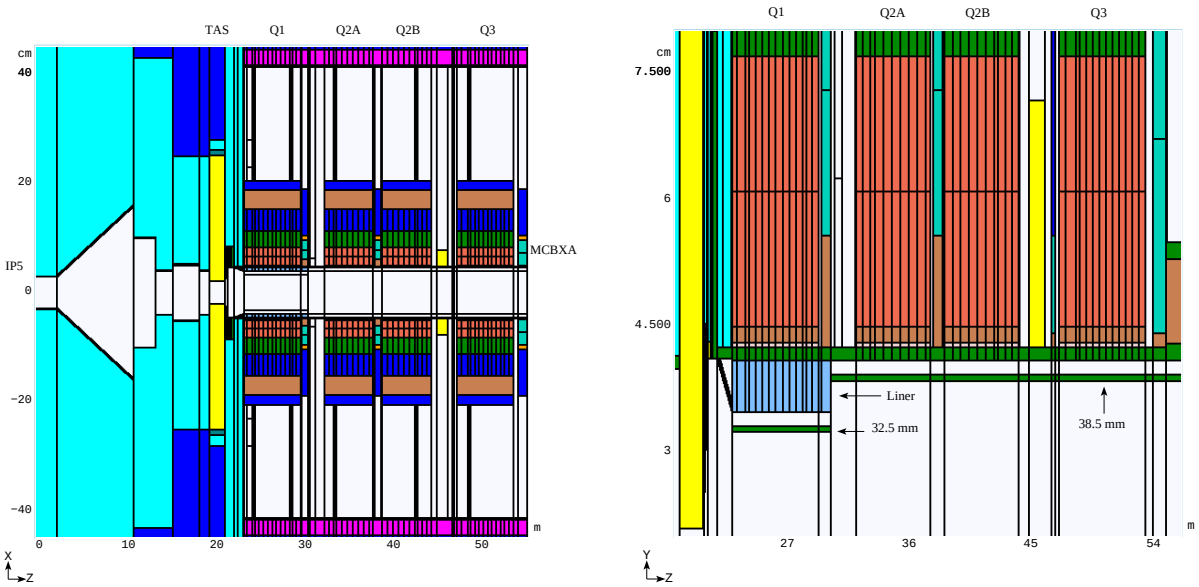

Fig. 1: Schematic view of the IP5 model with key elements labeled (left) and fragment of the inner triplet geometry with a baseline liner (right).

assumed to be the same. In this model, the baseline thickness of the liner is 6.2 mm in the region of Q1 quadrupole with no liner all the way downstream of Q1.

According to manufacturer's specifications, the cold cable contains 50% bronze and 50% Nb_3Sn with a specific density of 5.4 g/cm^3. A nominal field gradient of 200 T/m is used. A half crossing angle of 212 μrad and 21-mm TAS1 aperture were assumed in the calculations performed with the MARS15 Monte Carlo code [8, 9]. Although some details of the model are specific to IP5 (horizontal crossing and detector-machine transition), results are applicable to both high-luminosity interaction regions, IP1 and IP5.

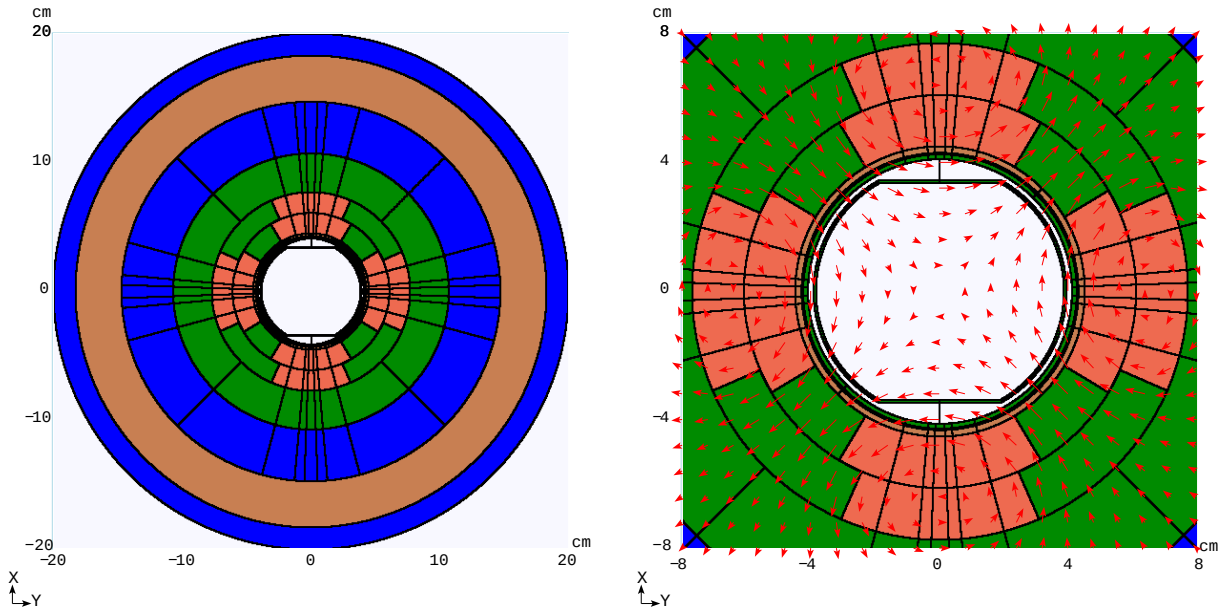

Fig. 2: MARS15 geometry model of a 90-mm Nb_3Sn inner triplet quadrupole: cross section (left) and fragment showing more details as well as magnetic field distribution (right).

In this study we address the following two major problems relevant to beam-induced energy deposition in the LHC IR quadrupoles: peak power density and dynamic heat load. The former quantity enables one to determine if a magnet design under consideration is safe with respect to quenches. It is also directly related to the peak dose accumulated in the SC coils; this allows one to estimate their lifetime. The overall performance of the cooling system of the magnets should correspond to the heat load. The normalization of the data presented below corresponds to a luminosity of 10^{35} cm^{-2}s^{-1}. The design goal used below in connection with the peak power density has been calculated taking into account the quench limit for Nb_3Sn magnets of 5.0 mW/g [6, 10], with a safety factor of three on top of that [2]. It gives us 1.7 mW/g for the maximum power density in the SC coils as the design goal.

3. PEAK POWER DENSITY IN SC COILS

3.1 Coil aperture

A calculated distribution of peak power density, ϵ_{max}, in the inner triplet SC coils is shown in Fig. 3 (left). Here a baseline stainless steel inner absorber is used. One can see that the peak power density exceeds the design goal significantly. We have studied the dependence of ϵ_{max} on coil diameter. In our model developed for this purpose the radial position of each layer, including the beam screen, was adjusted appropriately while its thickness was kept the same (see Fig. 2). Due to lack of calculated magnetic field maps for coil diameters other than 90 mm, we apply a scaling procedure to the only existing field map. Namely, the two-dimensional distribution of the magnetic field developed previously for 90-mm Nb_3Sn magnets [11] is adjusted in the following way: given B_x and B_y for a two-dimensional grid $\{x_n,y_k\}$, we apply a multiplication correction factor of $D(mm)/90$, where D is inner coil diameter, to the coordinates of every single point of the grid as well as to the corresponding field components. Being an approximation the described procedure enables us to keep the field gradient constant.

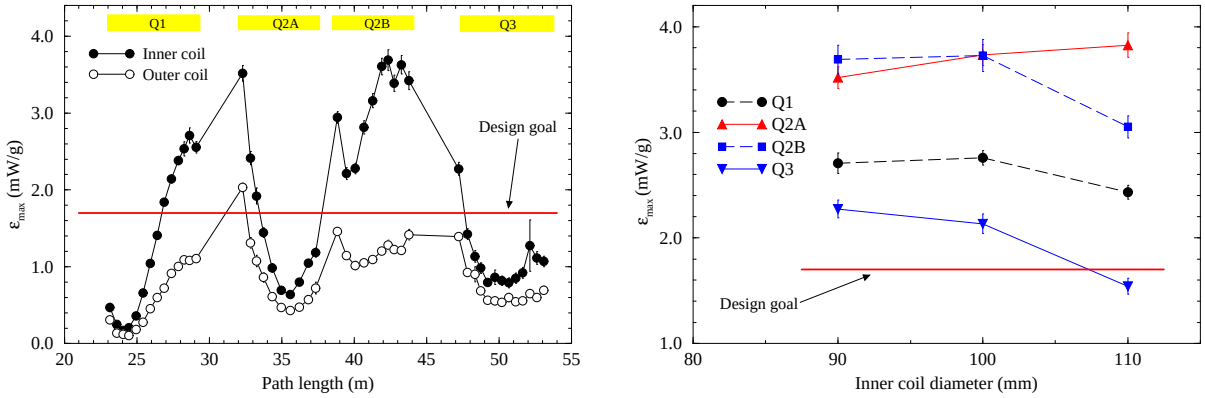

Fig. 3: Distributions of peak power density along the inner triplet for 90-mm quadrupoles with a baseline stainless steel liner (left) and its dependence on inner coil diameter calculated for a baseline stainless steel liner (right).

The calculated dependencies of maximum peak power density on coil diameter are shown in Fig. 3 (right). One can see that at a fixed gradient, increasing the coil diameter from 90 to 110 mm one decreases ϵ_{max} in all the quadrupoles except Q2A, where ϵ_{max} is slightly up due to the reduced shielding effect of Q1. Power density is still unacceptably high. In order to understand qualitatively the dependencies shown in Fig. 3, we have examined partial energy deposition contributions to the hottest spot in the Q2B coil made by various shower components. A built-in tagging technique as well as histogramming [8, 9] were used for this purpose. The analysis revealed that more than 90% of the total energy deposition at the hottest spot is due to electromagnetic showers induced by $\pi^0 \rightarrow 2\gamma$ decays (see also below). The neutral pions are generated in inner regions of the system (beam screen, liner, cold bore) by charged hadrons coming from the IP. When increasing the coil diameter, two opposing factors come into play: (i) increased distance between the coil and beam gives rise to a reduction in energy deposited in the coil;

(ii) to keep the same field gradient, one has to increase the magnetic field itself which, in turn, gives rise to an increase in charged hadron hit rate over the inner regions and, therefore, an increase in neutral pion production. The two factors acting together give rise to the distributions shown in Fig. 3.

3.2 Liner thickness

In order to reduce the peak power density in the quadrupoles, one can increase the liner thickness d. A dependence of ϵ_{max} as a function of d has been calculated for 100-mm quadrupoles (see Fig. 4). For 90-mm ones there is not any extra room for the absorber from Q2A through Q3 because the beam screen is at 38.5 mm (see Fig. 1) and this is exactly the spatial limitation imposed by beam optics for β^* = 0.25 m [5]. For 100-mm quadrupoles one has the extra room to fit a liner up to 5 mm in thickness. One can see from Fig. 4 that even with a liner of increased thickness, ϵ_{max} in Q2B goes a bit beyond the design goal. Therefore, one has to rule this option out, at least for 90-mm and 100-mm quadrupoles.

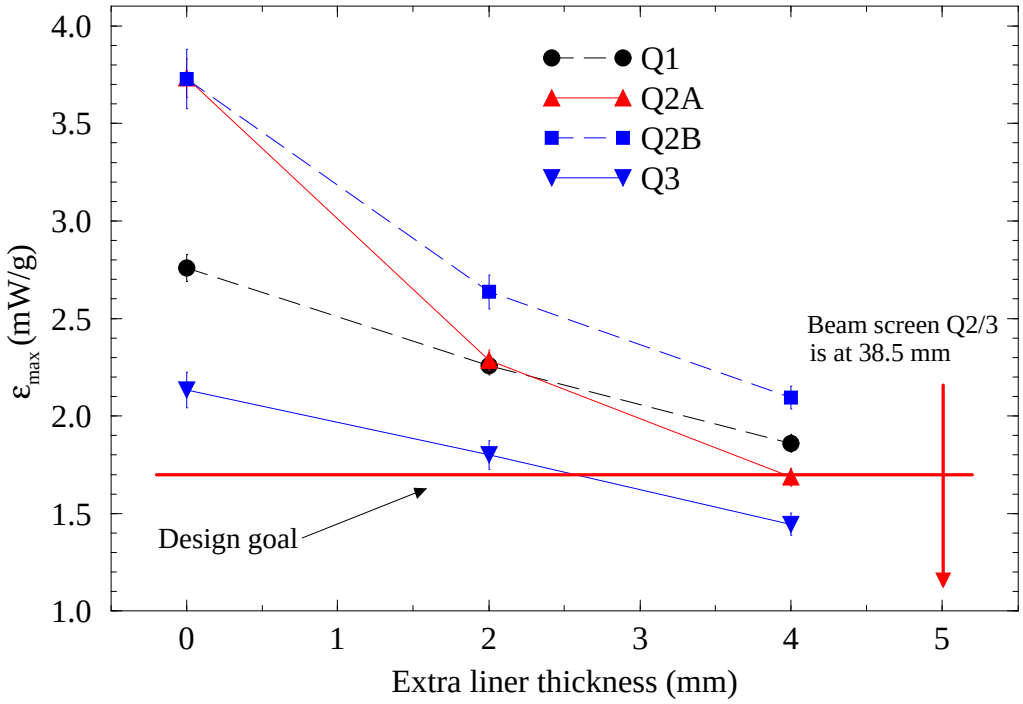

Fig. 4: Peak power density in the Nb_3Sn quadrupoles with inner coil diameter of 100 mm *vs* extra thickness of the stainless steel liner, Δd. Total thickness of the liner, d, is equal to d_0 + Δd, where d_0 is the baseline liner thickness.

3.3 Spacers in SC coils

Another option that could help to reduce the peak power density in the coils is replacing the superconductor in the hottest spots along the entire magnet length with a low-Z material. This has the advantage of providing decreased collision density and spreading the power density peak over a bigger volume. Aluminum and graphite were studied. A model and sample power density distribution are shown in Fig. 5. One can see that ϵ_{max} in the Q2B inner and outer SC coils is about 1.8 mW/g, slightly above the design goal.

One could further reduce the peak power density using the spacer approach by choosing one of the following options: (i) increasing the size of the spacers and extending them through the outer coil; (ii) using other material–more dense than aluminum; (iii) using a combination of the described aluminum spacers with a steel liner of increased thickness (see previous Section). This approach has never been tested in practice. There are some difficulties with the coil design in this approach. It is also clear

that there will be some effect on the field quality with the spacers, thus requiring magnet optimization studies. It seems that this approach could be considered as an auxiliary one that might be useful under other circumstances.

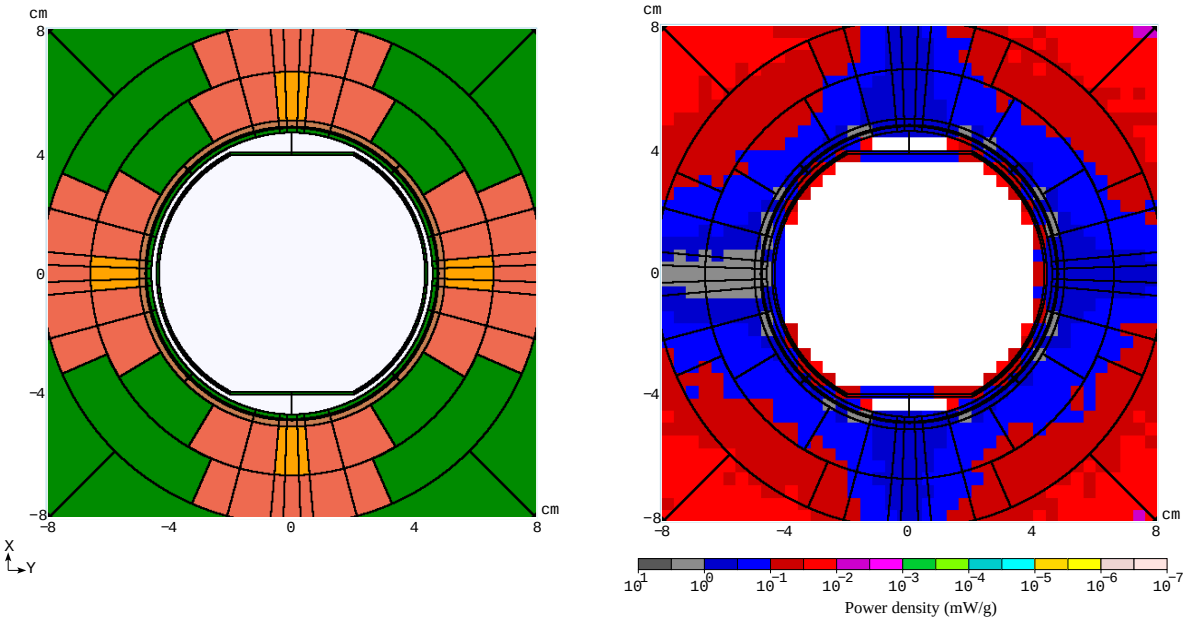

Fig. 5: Cross section of a 100-mm Q2B quadrupole with aluminum spacers and corresponding power density isocontours.

3.4 High-Z inner absorber

As described earlier in the paper, more than 90% of the energy deposition in the hottest spots of the SC coils is due to electromagnetic showers. Fig. 6 (left) shows the energy spectra of electrons and photons for the hot spot in Q2B. One can see that about 50% of all photons in the region have energies from

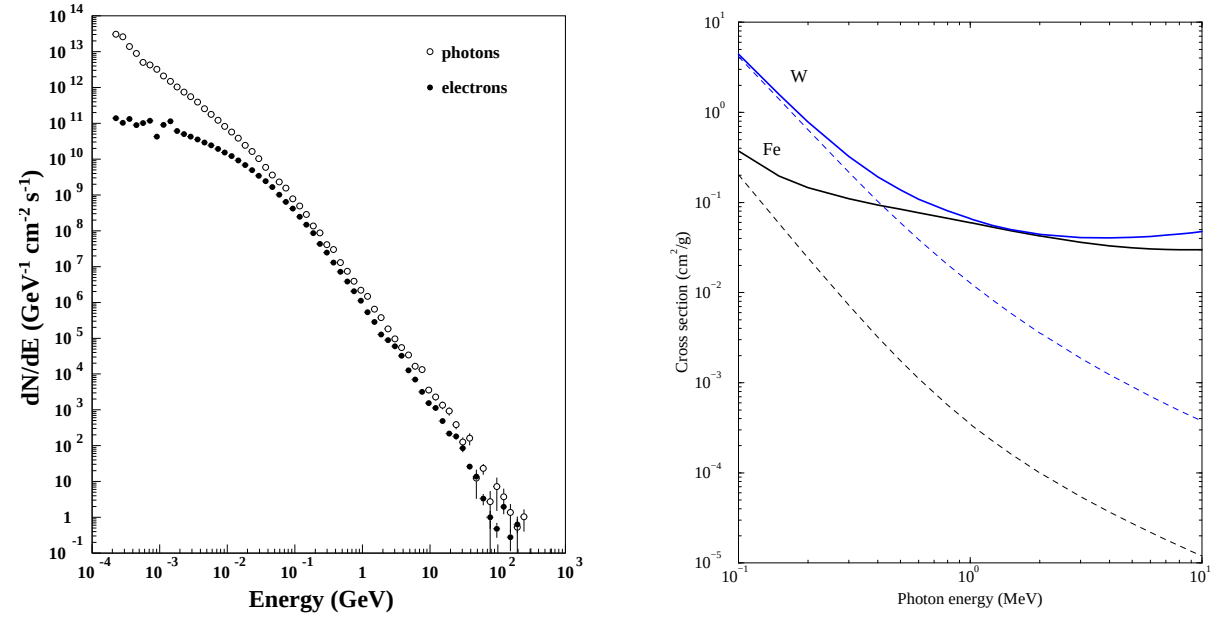

Fig. 6: Energy spectra of electrons and photons averaged over the hottest spot in the inner Q2B coill (left) and photon total (solid) and absorption (dashed) cross sections for iron and tungsten [12] (right).

200 to 400 keV. Therefore, a promising way to optimize the liner is to replace the stainless steel with a high-Z material. In such a case one can take the advantage of very strong photoabsorption that, at low energies, scales with the atomic number as $\sim Z^5$ (see Fig. 6 (right)). A good candidate is a commercially available tungsten-rhenium alloy, W25 Re, that contains 75% tungsten [13]. MARS15 calculations have revealed that, other things being equal, the W25 Re liner provides substantial absorption of low-energy photons and, therefore, a significant reduction of ϵ_{max} in all the quadrupoles (see Fig. 7). It should be noted that in our model the W25 Re is used to replace both the steel liner and the 1.5-mm steel cold bore adjacent to the liner (see Fig. 1). The design goal is reached with a W25 Re liner 7.2-mm thick in Q1 and 1-mm thick in the rest of the triplet.

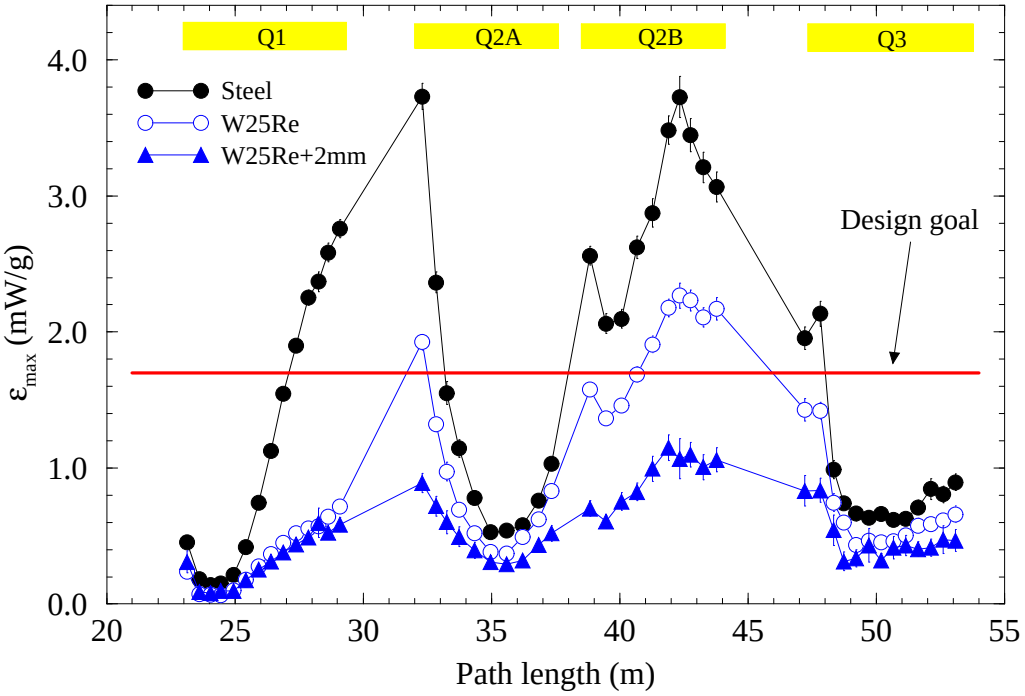

Fig. 7: The peak power density in the inner coil of the 100-mm Nb_3Sn quadrupoles calculated for the baseline thickness of stainless steel, W25 Re liners, and for a W25 Re liner of increased thickness. W25 Re is used to replace both the steel liner and 1.5-mm steel cold bore adjacent to the liner (see Fig. 1).

4. DYNAMIC HEAT LOADS

In order to design an adequate cooling system for the inner triplet at a luminosity of 10^{35} cm^{-2}s^{-1}, dynamic heat loads on the magnets are of primary importance. Results calculated for the liner and superconducting coils of the IR quadrupoles are shown in Fig. 8.

One can easily see the effect of increased energy deposition in the W25 Re liner when compared to the steel one. It follows from Fig. 8 that the W25 Re liner provides for an overall better protection for the superconducting coils in the inner triplet. It also mitigates the local huge spike at the IP end of the Q2A quadrupole observed when using the steel liner. At the same time, the total dynamic heat load (see Fig. 9) does not vary significantly with liner because the liner is responsible mostly for an internal re-distribution of the energy deposited in the system.

The integral of the dynamic heat load is presented in Table 1. It should be noted that: (i) the data given in the second column of the Table refers to the energy deposited not only in the liner itself but also in the beam screen (see Figs. 1 and 2); (ii) in addition to the beam screen, liner, and superconducting coils, the other parts of the quadrupoles also contribute to the total heat load presented in the last column of the Table.

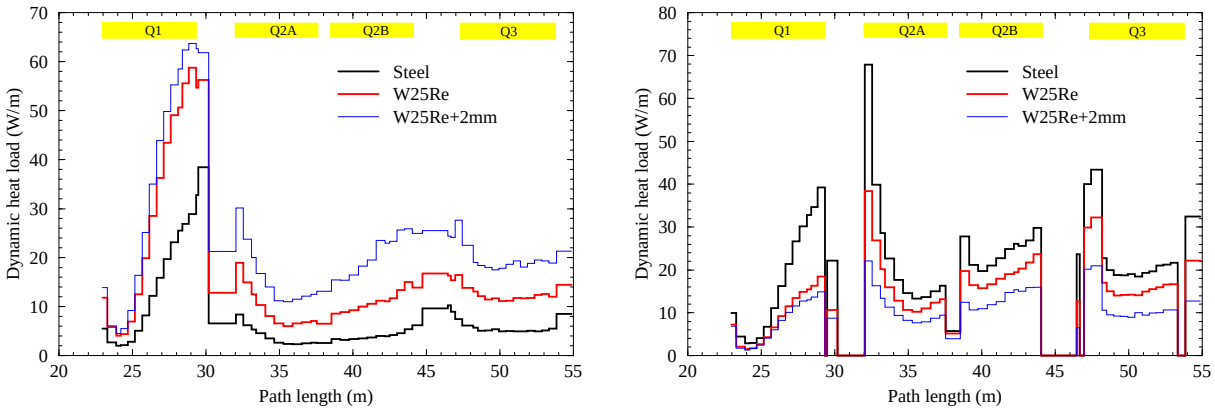

Fig. 8: Dynamic heat load to the liner (left) and superconducting coils (right) of the 100-mm Nb_3Sn quadrupoles and correctors calculated for the steel and W25 Re liners of baseline thickness as well as for a W25 Re liner of increased thickness. W25 Re is used to replace both the steel liner and 1.5-mm steel cold bore adjacent to the liner (see Fig. 1).

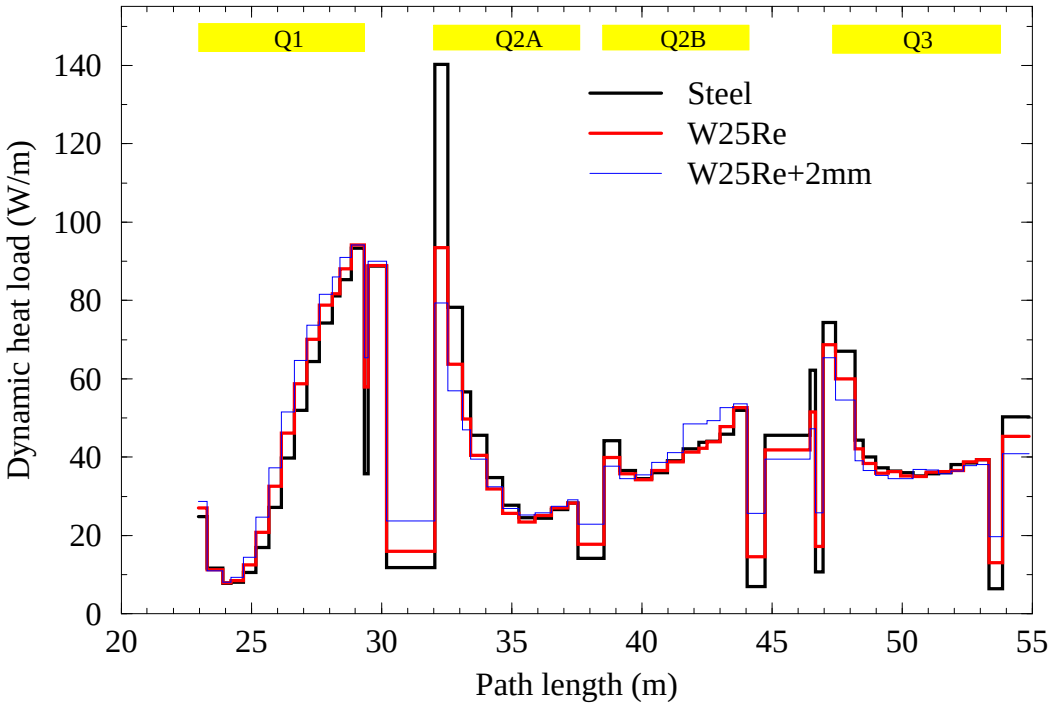

Fig. 9: Distribution of total dynamic heat load in the 100-mm Nb_3Sn quadrupoles calculated for the steel and W25 Re liners of baseline thickness as well as for a W25 Re liner of increased thickness.

Since the total dynamic heat load scales with luminosity and the modifications discussed above to the quadrupoles do not give rise to significant variation, the heat load remains the outstanding constraint on the cooling system capability and the cryoplant cost. One can see from Fig. 8 that a separate cooling system for the liner, maintained at liquid nitrogen temperatures, could provide for a solution to this problem and should be studied in detail. With such a separate cooling system and a W25 Re liner of increased thickness, the dynamic heat load to the superconducting coils would not exceed 20 W/m with a total heat load to the coils of 307 W.

Table 1: Integral data on the dynamic heat load (W/m) for the inner triplet with 100-mm Nb_3Sn quadrupoles at an ultimate luminosity of 10^{35} $cm^{-2}s^{-1}$. Steel and W25 Re liners of baseline thickness as well as a W25 Re liner of increased thickness are considered.

Component	*Liner*			*Coil*			*Total*		
	S[a]	W[b]	W2[c]	S[a]	W[b]	W2[c]	S[a]	W[b]	W2[c]
Q1	81	175	203	109	56	49	268	287	304
Q2A	22	52	88	132	91	62	259	217	209
Q2B	21	60	112	134	105	74	228	225	239
Q3	35	79	127	155	117	76	280	269	261
Correctors and TASB	85	146	211	117	78	46	259	271	296
Total	244	512	741	647	447	307	1294	1269	1309

[a] Model with a stainless steel liner of baseline thickness.
[b] Model with a W25 Re liner of baseline thickness.
[c] Model with a W25 Re liner of increased (by 2 mm) thickness.

5. CONCLUSION

The calculated data on peak power density and dynamic heat load to the LHC inner triplet with Nb_3Sn quadrupoles is presented at an ultimate luminosity of 10^{35} $cm^{-2}s^{-1}$. In order to reduce the peak power density to an acceptable level, various options were studied: (i) increasing inner coil diameter (90, 100, and 110 mm); (ii) increasing thickness of the inner absorber (liner); (iii) replacing the material of the liner with a tungsten-based alloy (W25 Re) instead of stainless steel; (iv) using spacers in the hottest spots of the SC coils. A W25 Re liner of increased thickness (7.2 mm in the Q1 region and 1 mm from Q2A through Q3) provides for the most effective shielding and allows us to reach the design goal of 1.7 mW/g for 100-mm Nb_3Sn quadrupoles. The calculated total dynamic heat load to the inner triplet is about 1300 W. In order to cope with the heat load at that level, a separate cooling system for the inner absorber, maintained at liquid nitrogen temparatures, might be required.

6. Acknowledgements

The authors are thankful to C. Brown for useful comments. This work was supported by the Universities Research Association, Inc., under contract DE-AC02-76CH03000 with the U. S. Department of Energy.

References

[1] N. Andreev *et al.*, IEEE Trans. Appl. Supercon., v. 11, No. 1, March 2001, p. 1558.

[2] N.V. Mokhov, I.L. Rakhno, J.S. Kerby, J.B. Strait, "Protecting LHC IP1/IP5 Components Against Radiation Resulting from Colliding Beam Interactions", Fermilab-FN-732 (2003); LHC Project Report 633, CERN (2003).

[3] J.B. Strait, M. Lamm, P. Limon *et al.*, "Towards a New LHC Interaction Region Design for a Luminosity Upgarde", PAC2003 Proc., p. 42; Fermilab-Conf-03/098 (2003), LHC Project Report 643 (2003).

[4] J.B. Strait, N.V. Mokhov, T. Sen, "Overview of Possible LHC IR Upgrade Layouts", Fermilab-Conf-05/007-AD-E-T (2005).

[5] T. Sen, J. Strait, A. V. Zlobin, Proc. 2001 Part. Accel. Conf., Chicago, June 2001, p. 3421.

[6] N.V. Mokhov, D.R. Chichili, S.A. Gourlay *et al.*, "Superconducting Magnets in High-Radiation Environment at Supercolliders", Fermilab-Conf-06/244-AD (2006).

[7] T. Sen, V.V. Kashikhin, P. Limon *et al.*, "Beam Physics Issues for a Possible 2nd Generation LHC IRs", *Proc. of EPAC 2002 Conf.*, Paris, pp. 371-373 (2002).

[8] N.V. Mokhov, "The Mars Code System User's Guide", Fermilab-FN-628 (1995); http://www-ap.fnal.gov/MARS/.

[9] N.V. Mokhov, K.K. Gudima, C. James *et al.*, "Recent enhancements to the MARS15 code", Radiation Protection Dosimetry, v. 116, pp. 99-103 (2005), Fermilab-Conf-04/053 (2004).

[10] A.V. Zlobin, Private communication, Fermilab (2006).

[11] V.V. Kashikhin, Private communication, Fermilab (2002).

[12] http://physics.nist.gov/PhysRefData/.

[13] http://www.matweb.com/.

Session: High field magnets (non-accelerators) and (accelerators)

SUPERCONDUCTING UNDULATORS AND WIGGLERS

S. Prestemon, D. R. Dietderich, S. Marks, R. D. Schlueter
Lawrence Berkeley National Laboratory, Berkeley, California, USA

Abstract
Superconducting undulators and wigglers are being developed as the next generation of synchrotron radiation sources. We discuss the motivation and performance advantages of superconducting insertion devices, and review the research undertaken at Lawrence Berkeley National Laboratory for the development of Nb_3Sn based undulators over the last few years, culminating in the successful test of a 14.5mm period prototype that reached its short-sample limit in four quenches.

1. INTRODUCTION

Superconducting undulators and wigglers are magnetic structures introduced in the path of high-energy charged particles, usually electrons, with the purpose of generating intense synchrotron radiation [1]. Typically the radiation is in the X-ray wavelength, dictated by the particle energy and the field and period length of the device. Although the first superconducting insertion devices were used in early experiments on free-electron lasers (FEL's; see for instance the HEPL experiment at Stanford [2] and SuperACO at Orsay [3]), the use of undulators and wigglers became common only in the 1980's when permanent magnet structures (Halbach arrays [4]) were introduced.

The significant increase in superconductor performance, and improved design and fabrication processes, has lead to recent renewed interest in superconducting insertion devices. Superconducting wigglers are now installed on many light sources, as well as in damping rings, such as the CESR wigglers [5]. A number of light sources are currently pursuing the development of superconducting undulators to enhance the performance of existing storage rings. For a given field and period, higher peak field implies a larger spectral range available to the user; similarly, by shortening the period the performance can be used a) to attain higher energies, thereby providing access to new wavelengths, and/or b) to enhance the number of periods in a given device length, hence increasing the flux and brightness of the radiation.

2. UNDULATOR R&D

Superconducting undulators and wigglers are under active development in a number of laboratories around the world (see [6] for a sampling of ongoing R&D). However, a number of technical issues must be addressed before these devices can replace the existing permanent magnet insertion devices, which have proven to be reliable sources for users. Key technical issues include:

1. superconductor stability and system protection,
2. magnetic and structural design considerations,
3. phase error minimization e.g. by minimizing fabrication tolerances and by passive and/or active shimming,
4. accurate magnetic field measurements for phase error determination in a cryogenic environment,
5. mitigate performance impact from beam-based thermal loads, and accurate prediction of these loads, ideally based on calorimetric measurements,

Motivated by the general interest in higher performance insertion devices, Lawrence Berkeley National Laboratory initiated an R&D effort in 2002 to consider issues associated with NbTi and Nb_3Sn superconducting undulators, particularly as they relate to application in a storage ring. First, in order to benefit from recent developments in high-critical current conductors such as APC NbTi and Nb_3Sn, very high

copper current densities must be accommodated due to the low-field, high J_c operating conditions. Lowering the Cu current density through increased Cu fraction would defeat the benefit of high J_c material. Second, undulator radiation is characterized by a harmonic structure that requires very high field quality be maintained through the structure. Third, the design and fabrication must be sufficiently well understood to reliably produce devices capable of attaining a performance specification for users.

2.1 Copper current density

The first LBNL prototype, prototype I, focused on protection considerations. A 30mm period device, it addressed the high J_{cu} issue by incorporating Nb_3Sn and using a passive diode protection scheme designed by WangNMR, Inc. The device was tested at LBNL, and demonstrated that Cu current densities in excess of 4kA/mm2 could be reliably protected against [7]. Detailed voltage signals from quenches during testing suggested flux jump instabilities may have been limiting the device performance. Furthermore, physical inspection showed signs of epoxy cracking, which could also have generated premature quenches due to heat deposition.

During this R&D effort it became apparent that Nb_3Sn is the best candidate material for this application, having the highest J_c performance in the 4-6T range typically encountered, and having much higher tolerance to temperature fluctuations than NbTi. Under most application scenarios the device will be subjected to some heating associated with the electron beam; uncertainties in the amplitude of the heating is a key concern for the application of SCU's to storage rings (see for instance [8], [9], [10]).

2.2 Phase error correction

The LBNL Prototype II was designed to address phase error correction. Undulator radiation is generated by superposition of in-phase radiation emanating from an electron as it proceeds through consecutive bends; variations in the path length taken by an electron result in phase errors that can destroy the coherence and hence the brightness of the generated radiation. A second year of LBNL funding allowed for the fabrication of a second Nb_3Sn prototype, designed with a 14.5mm period and incorporating simple shim coils on pole tips to provide a $> 1\%$ field kick independent of the background field for phase-error correction of the device [11]. A concept was developed wherein such correction coils could be used as part of a system to provide active correction to a full device to provide high brightness radiation.

2.3 Latest test results

In 2005 the Advanced Photon Source at Argonne National Laboratory asked the LBNL team to demonstrate the Nb_3Sn technology on a 14.5mm prototype, to serve as a demonstration coil for a future superconducting undulator on a funded APS beamline. The resulting device, prototype III, was designed with a single strand Nb_3Sn wire so as to reduce the operating current below $1kA$, and incorporated design modifications based on experience with the first two prototypes, including elimination of large regions of epoxy by adding endshoes on each coilpack and increasing dynamic stability through enhanced RRR (from ~ 20 to ~ 100 by reducing reaction temperature and time). The device reached short-sample on the 4^{th} quench, demonstrating that the fabrication process is now reasonably well understood. Furthermore, the successful operation of the Nb_3Sn magnet in a low-field, high current density regime demonstrates that judicious use of dynamic stability can reliably overcome the low-field instability issue recently of such interest to the high-field accelerator magnet community [12].

3. CONCLUSION

Superconducting undulators and wigglers are under active development in a number of laboratories around the world. To be competitive with existing permanent magnet devices, very high operating current densities are needed. An R&D effort at LBNL has demonstrated that state-of-the-art Nb_3Sn supercon-

ductors can be used for this application, despite the relatively low operating fields. Nb_3Sn material has the further advantage of providing larger temperature margin than is available with NbTi.

Although phase correction has been partially addressed, a number of technical issues remain to be resolved, including sufficiently accurate field measurements in a cryogenic environment. Lastly, the issue of beam-induced image current heating is an area of concern that would strongly benefit from a collaborative effort among multiple facilities.

ACKNOWLEDGEMENTS

I would like to thank the workshop organizers Lucio Rossi and Steve Gourlay for their successful efforts in hosting a very productive gathering of specialists in the accelerator magnet community.

References

[1] R. D. Schlueter, in "Synchrotron Radiation Sources - Technical Primer", H. Winick, Ed., World Scientific Publishing Co., 1994

[2] L. R. Elias and J. M. Maday, Rev. Sci. Instr. 1979.

[3] D. A. G. Deacon et al., IEEE Trans. on Nuclear Science, Vol. NS-28, No.3, June 1981.

[4] K. Halbach, Nuclear Instr. and Methods, 169, 1980.

[5] J. A. Crittenden, A. Mikhailichenko, A. Temnykh, PAC,2003.

[6] ESRF Workshop on Superconducting Undulators, June, 2003.

[7] S. Prestemon et al., Proc. PAC 2003, Portlan, Oregon.

[8] B. Podobedov, ESRF Workshop on Superconducting Undulators, June, 2003.

[9] E. Wallen, ESRF Workshop on Superconducting Undulators, June, 2003.

[10] R. D. Schlueter et al, Synchrotron Radiation News, January/February 2004, Vol. 17, No. 1.

[11] S. Prestemon et al., IEEE Transactions on Applied Superconductivity, June 2005

[12] D. Dietderich et al, to be presented at ASC2006, Seattle, Washington.

LARP: STATUS AND PROGRESS

S. A. Gourlay for the LARP Collaboration)*
Lawrence Berkeley National Laboratory, Berleley, USA

Abstract

In 2004, the US DOE established the LHC Accelerator Research Program (LARP) with the goal of developing a technology base for future upgrades of the LHC. The focus of the magnet program, which is a collaboration of three US laboratories, BNL, FNAL and LBNL, is on development of high gradient quadrupoles using Nb_3Sn superconductor. Other program components address issues regarding magnet design, radiation-hard materials, long magnet scale-up, quench protection, fabrication techniques and conductor and cable R&D. This paper presents an overall view of the program with emphasis on the current quadrupole project and outlines the long-term goals of the program.

1. INTRODUCTION

The Large Hadron Collider (LHC) is designed for the collision of proton beams in four interaction regions (IRs) with a nominal energy of 7 TeV per beam and two high-luminosity IRs of 10^{34} $cm^{-2}s^{-1}$. The first generation low-beta quadrupoles for the LHC IR inner triplets, based on NbTi superconductor, have been developed and are being fabricated by KEK and Fermilab in collaboration with CERN [1]. They provide a nominal field gradient of 205 T/m in a 70-mm bore and operate at 1.9 K in a high radiation environment.

The U.S. LHC Accelerator Research Program (LARP) is a follow-on activity to the U.S. LHC Accelerator Construction Project, a collaboration of LBNL, BNL, and FNAL [2]. Participation in this program builds on the previous investment in the construction project and ensures continued development of domestic accelerator science and technology. The multi-year program includes participation in commissioning the accelerator and U.S.-provided components, design and construction of state-of-the-art beam instrumentation, accelerator physics studies, and design and technology development required for an upgrade of the interaction region magnet systems to increase luminosity.

The start of LHC operation is planned for 2007. However, preliminary studies of possible scenarios for future LHC upgrades have already been started at CERN and in the U.S. [3] aimed at increasing the luminosity to 3-10 × L_{nom} or reaching the highest possible beam energy E = (1.5-2) × E_{nom}. The ranges in both parameters reflect the uncertainties in actual LHC performance as well as unknown technical limitations.

The projected lifetime of the current IR magnets is six to seven years at full luminosity. Combined with cost considerations, this makes replacement of the IR magnets an obvious scenario for an initial upgrade.

The US National Laboratories (Berkeley Lab, Brookhaven and Fermilab) are now positioned to develop the next generation of high performance magnets for the IRs of the LHC, which can, by themselves, double or triple the luminosity, and which will be compatible with operation at full performance at a luminosity as high as 10^{35} $cm^{-2}s^{-1}$. The same magnet technology also has the

*) This work was supported under contract DE-AD03-76SF00098 by the Director, Office of Energy Research, Office of High Energy Physics, U.S. Department of Energy.

potential to allow a new machine to be built in the LHC tunnel with up to a factor of two increase in beam energy.

Steady improvements in the application of Nb_3Sn technology have been made over the last several years [4]. The LARP magnet program is charged with answering the question of whether it can now be considered a viable material for practical high field accelerator magnets. High gradient, large aperture quadrupoles operating under high radiation induced heat loads, require superconductor with performance parameters provided by Nb_3Sn. Development of a Nb_3Sn-based technology that can be industrialized will require a long-term, aggressive R&D program. In addition to basic magnet development, the program outlined in this paper includes parallel development of ancillary technology to address issues that are crucial for operation of the magnets. Examples are; heat load due to secondary particles and synchrotron radiation, vacuum, quench protection, injection field quality and long coil fabrication.

The LHC luminosity upgrade provides a unique opportunity to operate magnets using Nb_3Sn technology in an accelerator. LARP will also help to strengthen collaborative ties amongst the US Labs as well as with CERN and the international community.

2. PROGRAM STRUCTURE

2.1 Program Goals

The above issues and others that emerge during the course of the R&D program are addressed by the general goal of the program to "demonstrate by 2009 that Nb_3Sn magnets are a viable choice for an LHC IR upgrade." This goal has three components that are implemented by a combination of model magnets with specific targets.

2.1.1 Predictable and reproducible performance

The viability of any new technology application is judged on the consistent reproducibility of performance and operating parameters. This component of the program is expressed through the construction of a series of "Technology Quadrupoles" (TQs). The TQs are based on a two-layer, cos-theta geometry with a 90 mm bore. The first series uses Modified Jelly Roll (MJR) conductor with a J_c of approximately 2,000 A/mm^2 at 12 T and 4.2 K. The expected maximum gradient is 215 T/m at 4.2 K (235 T/m at 1.9 K). The TQs are also used to compare two support structure designs; TQC01, based on stainless steel collars supported by an iron yoke (Fig. 1) and thick stainless steel skin and TQS01, a shell-based structure using bladders for precise, low-level pre-stress control and interference keys to retain the pre-stress, allowing bladder removal (Fig. 2). A tensioned aluminum shell compresses internal iron and coil components developing substantial pre-stress on cool-down [5, 6].

2.1.2 Long magnet fabrication

Development of fabrication, handling and assembly techniques required for the construction of long magnets will begin with scale-up of simple racetrack coils. A nominal length of 4 meters was chosen for the "long racetrack" (LR) coils, and later adjusted to 3.6 m so that the magnet would fit in available vertical test dewars at both BNL and Fermilab. The LR coils are based on a well-developed 2-layer design, contained in a simple aluminum shell-type structure used extensively in the LBNL magnet program and similar to that used for TQS01 [8,9,10], Fig. 3. Successful completion of this program will be followed by construction of a long (3.6 m) cos-theta quadrupole (LQ) based on the TQ cross section.

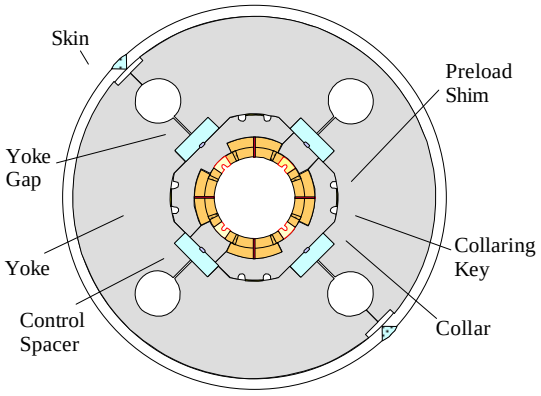

Fig. 1 TQC mechanical structure.

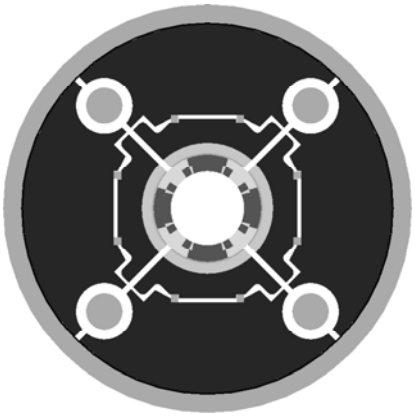

Fig. 2 TQS mechanical structure.

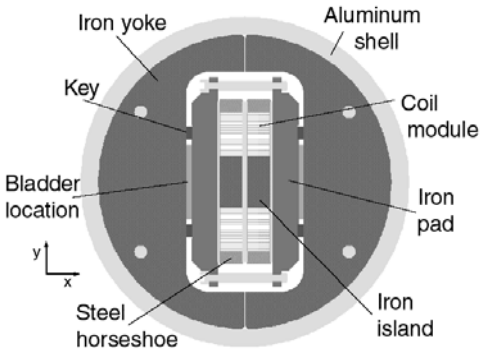

Fig. 3 Sub-scale magnet cross section.

2.1.3 High gradient in a large aperture

In FY06 work will begin on the conceptual design of a "High gradient quadrupole" (HQ) that will explore the ultimate performance limits in terms of peak fields, forces and stresses. The HQ design will be selected based on analysis of different options as well as feedback from ongoing studies in the areas of materials, model magnet and supporting R&D. A 90 mm aperture over a 1 m length was deemed sufficient to investigate the critical design and technology issues while being cost-efficient and offering good compatibility with existing tooling. It is expected that the HQ design will provide coil peak fields of the order of 15 Tesla, corresponding to gradients of about 300 T/m in the 90 mm aperture. At a minimum, each phase should result in a magnet that performs to within a significant fraction of the conductor potential, and which shows no significant retraining after a thermal cycle. A summary of the program is shown in Table 1.

Table 1
Phase I LARP Magnet Program Summary

Model Magnets		**Type**	**Length (m)**	**Gradient (T/m)**	**Aperture (mm)**	**FY05**	**FY06**	**FY07**	**FY08**	**FY09**
Series	Description									
TQ	**Technology Quad**	Cos-2theta	1	> 200	90		$3_N + 1_R$	$2_N + 1_R$		
LQ	**Long Quad**	Cos-2theta	4	> 200	90				1_N	1_N
HQ	**High Gradient Quad**	Cos-2theta	1	> 250	90					2_N
Supporting R&D		**Type**	**Length (m)**	**Peak Field (T)**	**Aperture (mm)**	**FY05**	**FY06**	**FY07**	**FY08**	**FY09**
Series	Description									
SQ	**Sub-scale**	block	0.3	10 – 11	110	$1_N + 1_R$	$1_N + 1_R$	$1_N + 1_R$	1_N	
SR	**Short Racetrack**	block	0.3	10 – 12	N/A		1_N	1_N	1_N	
LR	**Long Racetrack**	block	4	10 - 12	N/A			2_N		
N = New Magnet										
R = Revised Magnet using existing coils										

2.2 Program Organization

The above activities are integrated and organized around four general areas; Design Studies, Model Magnet R&D, Supporting R&D and Materials. They form the basis of a Work Breakdown Structure and are functionally represented by working groups, made up of members of the collaborating laboratories. The working groups are coordinated by "Level 2" managers who also oversee the various tasks in their respective areas. The responsibility for coordination and execution of a particular task resides with specific "Task Managers."

2.2.1 Design Studies

The Design Studies activity is generally intended to provide input on magnet parameters and lay the groundwork for the program. It covers a broad range of activities; conceptual magnet designs, radiation deposition studies, cryogenic and cooling issues and provides an interface for communication with the Accelerator Physics section of LARP.

2.2.2 Model Magnet R&D

Model Magnet R&D integrates input from the other three areas to produce model magnets that directly apply to the program goals. The current focus is on the TQs and it will eventually house activities to build the LQs and HQs.

2.2.3 Supporting R&D

Supporting R&D covers a wide range of technical issues, primarily related to fabrication and operation. The largest task in this area is long magnet scale-up. Other tasks include sub-scale

quadrupoles (SQs) to study performance-related issues, verify analysis models, incorporate rad-hard materials and support structure development.

2.2.4 Materials

Conductor is a critical component of the program. The responsibility of the Materials activity is two-fold; provide sufficient quantities of well-characterized strand for magnet development and carry on the necessary R&D to support development of material that will ultimately be used for the upgrade.

3. CONCLUSION

The US LHC Accelerator Research Program has launched an aggressive program to develop accelerator magnet technology for upgrades that will enhance the physics potential of the LHC. The LARP is an excellent opportunity to extend high field accelerator magnet technology, and to create and strengthen national and international collaboration that will continue into future projects.

THE LARP MAGNET COLLABORATION

G. Ambrosio, N. Andreev, M. Anerella, E. Barzi, R. Bossert, S. Caspi, D. R. Dietderich, S. Feher, P. Ferracin, A. Godeke, S.A. Gourlay, R. Gupta, A. Ghosh, R. Hafalia, C. R. Hannaford, V.S. Kashikhin, V.V. Kashikhin, A.F. Lietzke, A.D. McInturff, N. Mokhov, F. Nobrega, I. Novitsky, R. Rabehl, G.L. Sabbi, J. Schmazle, D. Turrioni, P. Wanderer, R. Yamada, A.V. Zlobin

REFERENCES

[1] R. Ostojic, M. Karppinen, CERN; R. Bossert, J. Dimarco, S. Feher, J. Kerby, M. Lamm, T. Nicol, Fermilab; N. Kimura, T. Nakamoto, KEK, Production and installation of the LHC Low-Beta Triplets, MT-19, IEEE Trans. Appl. Supercond. 16 2 (2006) 437.

[2] R. Kephart et al., The U.S. LHC Accelerator Research Program: A Proposal, http://www-td.fnal.gov/LHC/USLARP.html.

[3] A comprehensive bibliography can be found at http://care-hhh.web.cern.ch/carehhh/publications.htm.

[4] S.A. Gourlay, High Field Magnet R&D in the USA, MT-18, IEEE Trans. Appl. Supercond. 14 2 (2004) 333, and SC-MAG #813, LBNL-53128, 6/24/2003.

[5] R.C. Bossert et al., Development of TQC01, a 90 mm Nb_3Sn Model Quadrupole for LHC Upgrade Based on SS Collar, MT-19, IEEE Trans. Appl. Supercond. 16 2 (2006) 370.

[6] S. Caspi et al., Design and Construction of TQS01, 1 90 mm Nb_3Sn Model Quadrupole for LHC Luminosity Upgrade Based on a Key and Bladder Assembly, MT-19, IEEE Trans. Appl. Supercond. 16 2 (2006) 358.

[7] S.E. Bartlett, S. Caspi, D.R. Dietderich, P. Ferracin, S.A. Gourlay, C.R. Hannaford, A. Hafalia, A.F. Lietzke, S. Mattafirri, G. Sabbi, An R&D Approach to the Development of Long Nb_3Sn Accelerator Magnets Using the Key and Bladder Technology, ASC2004, IEEE Trans. Appl. Supercond. 15 2 (2005) 1136, and LBNL-54893.

[8] S. Caspi, L, Chiesa, M. Coccoli, D.R. Dietderich, S.A. Gourlay, R. Hafalia, A.F. Lietzke, J.W. O'Neill, G. Sabbi, R.M. Scanlan, An Approach for Faster High Field Magnet Technology Development, IEEE Trans. Appl. Supercond. 13 2 (2003) 1258, and SC-MAG #773 LBNL-49918.

[9] P. Ferracin et al., Assembly and Test of SQ01b, a Nb_3Sn Racetrack Quadrupole Magnet for the LHC Accelerator Research Program, IEEE Trans. Appl. Supercond. 16 2 (2006) 382.

HIGH-FIELD ACCELERATOR MAGNET DEVELOPMENT IN EUROPE

A. Devred
CEA/Saclay, France, & CERN, Geneva, Switzerland

Abstract
This paper presents a short review of ongoing high field accelerator magnet R&D programs in Europe.

1. INTRODUCTION

Compared to the situation in the United States, the efforts in Europe for the last 10 to 15 years have been mainly devoted to, and focused on, building the LHC. As a result, R&D programs aimed at high field accelerator magnets have been very limited and have suffered from severe lack of resources. The CARE/NED Joint Research Activity, approved by the EU in the summer of 2003 and launched in January 2004 was meant to revive these R&D efforts by promoting synergies among the various partners, but its funding was capped to 25% of the requested budget and had to be significantly scaled down. In spite of this difficult environment, some serious work is nevertheless being carried out at various European Laboratories and the end of LHC magnet production may offer new opportunities.

2. ONGOING PROGRAMS

2.1 Overview

The main high field magnet R&D programs presently ongoing in Europe are: (1) a collaboration between Twente University (TEU, The Netherlands) and CERN on a large-aperture dipole magnet model, (2) a collaboration between CEA/DSM/DAPNIA and Alstom/MSA (France) on a technology-demonstrator quadrupole magnet model, (3) the EU-FP6 CARE/NED Activity and (4) the CANDIA program supported by INFN in Italy. Discussions have already started regarding the continuation of NED and the preparation of FP7 proposals.

2.2 TEU/CERN Collaboration

Following the success of the 1-m-long, 50-mm-aperture dipole magnet model MSUT, which, in 1995, reached a record field of 11 T on its first quench at 4.4 K, Twente University and CERN signed in 1998 a second collaboration agreement to develop a 1-m-long, 88-mm-aperture dipole magnet model delivering a nominal field of 10 T. One of the goals of the collaboration was to support the development of Nb_3Sn wires by the Powder-In-Tube (PIT) process with a filament size of ~20 μm and a non-Cu $J_C > 2000$ A/mm^2 at 4.2 K and 10 T at ShapeMetal Innovation (SMI) in The Netherlands.

After some difficulties, SMI succeeded in producing a 0.9-mm, binary Nb_3Sn PIT wire with 20-μm filaments and a non-Cu J_C of 2200 A/mm^2 at 4.2 K and 10 T that could be made into a Rutherford-cable with less than 5% degradation (it also succeeded in producing a ternary $(Nb–Ta)_3Sn$ wire that achieved 2000 A/mm^2 at 4.2 K and 12 T). Unfortunately, the collaboration ran out of resources and only 3 out of 4 cable unit lengths have been manufactured. Twente University has carried out the detailed design of the magnet model and has produced one dummy pole, but the program is now on hold.

2.3 CEA/Alstom Collaboration

DSM/DAPNIA at CEA/Saclay and Alstom/MSA are collaborating since 1996 on the development of a technology-demonstrator, Nb_3Sn quadrupole magnet model. This model is based on the design of the LHC arc quadrupole magnets, where the NbTi coils are replaced by Nb_3Sn coils. It relies on very

conservative wire specifications based on ITER HPI (19-μm effective filament diameter and non-Cu J_C of 765 A/mm^2 at 4.2 K and 12 K) and is expected to achieve a gradient of about 210 T/m in a 56 mm aperture at 4.2 K.

Alstom/MSA has, for some time, delivered 5x60-m-long cable unit lengths (4 poles plus one spare), but the magnet model manufacturing was only started at the beginning of 2005 to severe lack of human resources at CEA. The manufacturing is now well underway. Two dummy poles and two out the five final poles have been wound, heat-treated and vacuum-impregnated with epoxy resin. Both dummy poles have been cut into pieces and used for collaring trials.

The manufacturing of the five poles is expected to be completed by mid-September 2006. The collaring will be carried out at ACCEL, in Germany, in the fall and the coldmass should be integrated at CEA/Saclay by the end of the year. The cold test in a horizontal cryostat is scheduled for early 2007. A second test in a vertical cryostat and with a background solenoidal field of up to 4.5 T is foreseen in the fall of 2007. This second test, which is funded by the EUROTEV Design Study, is meant to reproduce the operating conditions of the final focusing quadrupole magnets for the ILC (small crossing-angle IR scenario).

2.4 CARE/NED JRA

2.4.1 Introduction

The EU-funded CARE/NED JRA is presently articulated around four Work Packages and one Working Group: (1) Management & Communication (M&C), (2) Thermal Studies and Quench Protection (TSQP), (3) Conductor Development (CD), (4) Insulation Development and Implementation (IDI), and the Magnet Design and Optimization (MDO) Working Group. It involves 7 institutes (8 laboratories): CCLRC/RAL in the UK, CEA in France, CERN, CIEMAT in Spain, INFN/Genoa and INFN/Milan, Twente University in The Netherlands and Wroclaw University of Technology in Poland. The total budget is around 2 M€, while the EU grant amounts to 979 k€ (over a 3-year period).

2.4.2 TSQP Work Package

The TSQP work package includes two main Tasks: (1) development and operation of a test facility to measure heat transfer to helium through Nb_3Sn conductor insulation (carried out by CEA and Wroclaw University of technology, under the leadership of CEA), and (2) quench protection computation (carried out by INFN/Milan).

The first part of the heat transfer measurement Task was to design and build a new He-II, double-bath cryostat. The cryostat was manufactured by Kriosystem in Poland under the supervision of Wroclaw University according to specifications written by CEA. The cryostat was delivered to CEA on 20 September 2005 and has been tested to helium superfluid. Problems with a LHe level sensor are delaying the measurements which are expected to start in June 2006.

Regarding the quench computation Task, INFN/Mi has carried a detailed analysis of the thermal and electrical behavior of NED-like magnets during a quench. The computations were focused on the reference 88-mm-aperture, $\cos\theta$, layer design and show that, magnets up to 10 m long can be operated safely, thereby justifying the choice of conductor parameters made early on. The Task is completed and a final report has been issued.

Since the start of NED, two complementary efforts have been launched at CERN: (1) analysis of available LHC magnet test data at high ramp rate to determine how well the heat-transfer measurements at CEA correlate with actual magnet data, and (2) review of magnet cooling modes to estimate, on the cryogenics system point of view, what are the limitations on power extraction and to provide guidance on how to improve cooling of magnet coils (preliminary conclusions indicates that NED-like magnets may have to be operated in superfluid helium).

2.4.3 CD Work Package

The CD work package includes two main Tasks: (1) conductor development (under CERN supervision), (2) conductor characterization (with participations from CEA, CERN, INFN/Genoa and INFN/Milan, coordinated by Twente University) and (3) FE wire model to simulate cabling degradation (developed by INFN/Milan with an active CERN support).

Details on the conductor development Task can be found in L. Oberli's contribution to these proceedings. This Task is carried out through two industrial subcontracts awarded by CERN to Alstom/MSA in France ("Internal Tin" process) and SMI in The Netherlands ("Powder In Tube" process). It is complemented by a 3rd contract, awarded to Luvata ("Internal Tin" process), outside the realm of NED and funded directly by CERN.

NED conductors are characterized by performing critical current and magnetization measurements. The critical current measurements offer a real challenge, given the expected performances of NED wires (*e.g.*, ~1600 A at 4.2 K and 12 T on a 1.25-mm-Ø wire, compared to ~200 A presently achieved on 0.8-mm-Ø ITER wires). To validate sample preparation and measurement processes, CEA, INFN/Milan and Twente University have carried out an extensive cross-calibration program and have now achieved a reasonable convergence. Magnetization measurements are performed under the supervision of INFN/Genova using three different techniques: SQUID, Vibrating Sample Magnetometer (VSM) and AC susceptibility magnetometer. The measurements are carried out as a function of field (to assess effective filament diameter and flux jumps) and temperature (to study the nature and size of the different superconducting phases present in the wire).

Regarding the FE Task, INFN/Genova has been working on a mechanical model (based on ANSYS®) to simulate the effects of cabling on un-reacted, Nb-Sn wires. To feed the simulations, CERN has supervised and/or carried out a series of nano-indentation and micro-hardness measurements to determine the mechanical properties of the materials making up the wire in the cold-work state in which they exist prior to cabling. The model is under evaluation and should soon provide useful tool to compare the sensitivity of different billet layouts.

2.4.4 IDI Work Package

The IDI work package includes two main Tasks: (1) studies on "conventional" insulation systems relying on ceramic or glass fiber tape and vacuum-impregnation by epoxy resin (carried out by CCLRC/RAL) and (2) studies on "innovative" insulation systems relying on pre-impregnated fiber glass tapes and eliminating the need for a vacuum impregnation (carried out by CEA).

With regard to the conventional insulation, CCLRC/RAL is evaluating a polyimide-sized glass fiber tape that is able to sustain the required Nb_3Sn heat treatment without degradation and which seems a promising solution for this type of insulation.

The innovative insulation Task is built upon an ongoing R&D program at CEA, which has demonstrated the feasibility of such a system, but which has been on hold for a year due to a lack of human resources; the program has now restarted and is getting up to speed.

2.4.5 MDO Working Group

The MDO Working Group is made up of representatives from CCLRC/RAL, CEA and CERN and is coordinated by CIEMAT. Its main charge is to address the following questions: (1) How far can we push the conventional, $\cos\theta$, layer design in the aperture-central-field parameter space (especially when relying on strain-sensitive conductors)? and (2) What are the most efficient alternatives, in terms of performance, manufacturability and cost?

A number of magnetic configurations have been selected and are presently being evaluated. In parallel, CERN has pursued the electromagnetic optimization of the baseline, 88-mm-aperture, $\cos\theta$ layer design with respect to conductor geometry, iron shape (to reduce saturation effects) and

ferromagnetic shims (to compensate magnetization effects). This optimization led to the definition of a Reference Design Version 2.

2.5 INFN/CANDIA Project

INFN has approved on 30 November 2004 a research project called CANDIA (Italian acronym for CAvi in Niobio-stagno per DIpoli ad Alto campo or niobium-tin cables for high field dipoles), involving teams from Frascati (LNF), Genoa and Milan (LASA). The main goal of CANDIA is the development of a Nb_3Sn conductor according to NED-like specifications. A call for tender was issued in fall 2005 and a contract for the manufacture of 1500 m of wire was awarded on 15 December 2005 to Outokumpu Copper Superconductor Italy (OCSI). The chosen technology is internal tin and the expected delivery is fall 2007. It is evident that close ties are maintained between CANDIA and NED.

3. WHAT'S NEXT?

Ten European Group Leaders/Managers and 2 US-LARP Managers have co-signed a contribution to the CERN Council Strategy Group in charge of elaborating a strategy for high energy physics in Europe. This document outlines a program for European superconducting accelerator magnet R&D aimed at LHC luminosity upgrade, and promotes the manufacturing of NED (in complement to LARP) and some well-focused R&D on cycled NbTi accelerator magnets. This document will serve as a basis for a letter of intent to the European Strategy Group on Accelerator R&D (ESGARD) for FP7 proposals (due on 28 April 2006) and could be extended to outline a world-wide program.

Session: Magnet design

SCALING LAWS FOR THE ELECTROMAGNETIC DESIGN OF SUPERCONDUCTING DIPOLES AND QUADRUPOLES

E. Todesco, L. Rossi
CERN, Geneva, Switzerland

Abstract
We have derived equations for computing the critical field (gradient) for a superconducting dipole (quadrupole) in the case of a sector coil. We show that these equations agree well with the actual results corresponding to coil lay-outs of several magnets that have been built for particle accelerators. The equations can be used to estimate the coil thickness needed to obtain a given field (gradient) for a given aperture and superconducting material.

1. INTRODUCTION

The aim of this paper is to derive an analytical approximation for the critical field (gradient) that can be achieved in a superconducting dipole (quadrupole) based on a superconducting material with a linear critical surface such as Nb-Ti. Scaling laws have been studied since long ago (see for instance Ref. [1]). In [2,3] the case of a $cos\theta$ dipole has been analyzed in detail, including aspects related to forces that are neglected here. We base our analysis on a sector coil with uniform current density, with one wedge to set to cancel the first two field harmonics. The goal is to have a formula that allows carrying out a parametric analysis of the electromagnetic design of a superconducting dipole or quadrupole. A complete analysis of the quadrupole case summarized here can be found in [4].

2. DIPOLES

2.1 The scaling law for the critical field

Let B_c be the critical field of a superconducting dipole, i.e. the magnetic field that can be reached in the center of the aperture when the conductor is at the short sample limit. We propose the following analytical expression

$$B_c \sim \frac{\kappa c B^*_{c2} \gamma_0 w_{eq}}{1 + \kappa c r \lambda \left(\frac{w_{eq}}{r} \right) \gamma_0 w_{eq}} \tag{1}$$

where

- B^*_c and c are the *superconducting parameters of the material*: we assume that the critical surface (j_c,B) of the material is linear

$$j_c(B) = c(B - B^*_{c2}) \tag{2}$$

  and therefore B^*_{c2} is the critical field at zero current in tesla (e.g., 10 T for Nb-Ti at 4.2 K, or 13 T at 1.9 K) and c is the slope in A/mm^2/T (600 A/mm^2/T for Nb-Ti).

- *Parameter of the cable*: κ is the filling factor (non-dimensional), i.e. the ratio between the cross-sectional surfaces of the superconductor and the insulated coil. It includes the dilution due to the Cu:SC ratio in the strands (1.2 to 2 for most strands), that due to voids in the cable (around 15%), and that due to the insulation (around 15%). When all is included, it usually ranges from 0.35 to 0.25.

- *Parameters of the coil lay-out*: r is the aperture radius [mm], and w_{eq} is the equivalent width defined as follows: for a 72º sector coil, with a wedge between 48º and 60º, the area A_s of the coil is related to the width of the sector and to the aperture radius through

$$A_s = \frac{2}{3}\pi[(r+w)^2 - r^2] = \frac{2}{3}\pi r^2\left[\left(1+\frac{w}{r}\right)^2 - 1\right] \tag{3}$$

The equivalent width is the width of the sector coil whose area is equal to the coil area A:

$$w_{eq} \equiv \left(\sqrt{1+\frac{3A}{2\pi r^2}} - 1\right) r \tag{4}$$

The quantity λ is the ratio between the peak field in the coil and the field at the centre of the aperture; it is a function of the ratio between the equivalent coil width and the aperture radius. We used the following fit

$$\lambda = a_{-1}\frac{r}{w_{eq}} + a_0 \tag{5}$$

- *Constants*: are derived for the case of a 72º sector coil with one wedge between 48º and 60º; γ_0 =0.000663 [T mm^2/A], a_{-1}=0.070, a_0=1.

2.2 Critical field versus coil width

For a lay-out with w_{eq}>>r, the critical field tends to B^*_{c2}. The dependence of critical field on coil width for different values of the aperture derived from Eq. (1) is given in Fig. 1 for Nb-Ti at 4.2 K, with a filling ratio of 0.35. Also plotted is the case of an ideal $cos\theta$ coil, with γ_0 =0.000628 T mm^2 /A,, and a_{-1}=0, a_0=1 (i.e. independent of r). One observes that for smaller aperture radii the same coil width leads to a higher critical field, and that it tends to the results of the $cos\theta$ coil.

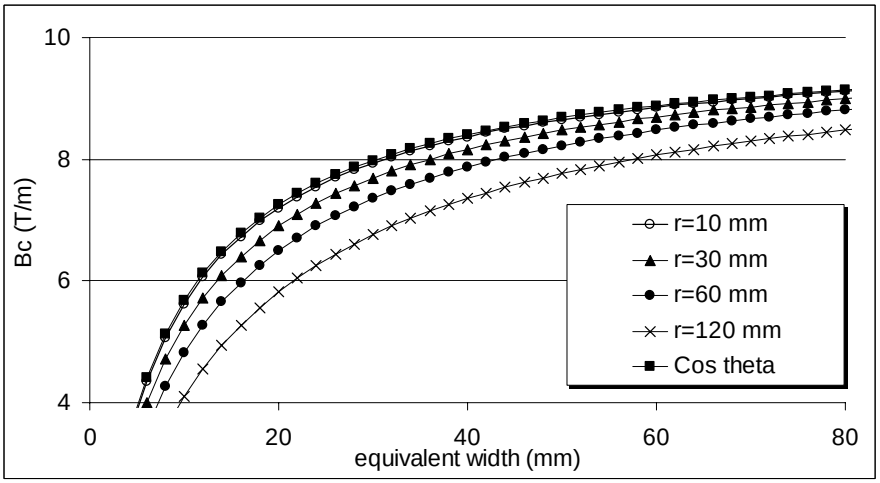

Fig.1 Critical field versus equivalent coil width as given by Eq. (1) for different apertures, for the case of Nb-Ti at 4.2 K, and with a filling factor of 0.35.

2.3 Comparison with existing dipoles

We used Eq. (1) to estimate the critical field of the coil lay-out of 5 existing Nb-Ti dipoles. We found an agreement within 4% for all cases, including that ones with current grading.

3. QUADRUPOLES

3.1 The formula for the critical gradient

Let G_c, be the critical gradient of a superconducting quadrupole, i.e. the gradient that can be reached when the conductor is at the short sample limit. We propose the following analytical expression

$$G_c \sim \frac{\kappa c B_{c2}^{*} \gamma_0 \log\left(1+\frac{w_{eq}}{r}\right)}{1+\kappa c r \lambda\left(\frac{w_{eq}}{r}\right)\gamma_0 \log\left(1+\frac{w_{eq}}{r}\right)} \tag{6}$$

where

- B^{*}_{c} and c are the *superconducting parameters of the material*: (see previous section)
- *Parameter of the cable*: κ is the filling factor (see previous section).
- *Parameters of the coil lay-out*: r is the aperture radius [mm], and w_{eq} is the equivalent width defined as follows: for a 36º sector coil, with a wedge between 24º and 30º, the area A_s of the coil is related to the width of the sector and to the aperture radius via the same Eq. (3), and the equivalent width is the width of the sector coil whose area is equal to the coil area A (Eq. 4).

  The quantity λ is the ratio between the peak field in the coil and the field gradient times the aperture radius; it is a function of the ratio between the equivalent coil width and the aperture radius. We used the following fit

$$\lambda = a_{-1}\frac{r}{w_{eq}} + a_0 + a_1\frac{w_{eq}}{r} \tag{7}$$

- *Constants*: are derived for the case of a 36º sector coil with one wedge between 24º and 30º; γ_0 =0.663 [T mm^2 /(A m)], a_{-1}=0.042, a_0=1, and a_1=0.113.

A simplified expression for λ is $\lambda \sim \lambda_0$=0.165, that provides a handier formula

$$G_c \sim \frac{\kappa c B_{c2}^{*} \gamma_0 \log\left(\sqrt{1+\frac{3A}{2\pi r^2}}\right)}{1+\kappa c r \lambda_0 \gamma_0 \log\left(\sqrt{1+\frac{3A}{2\pi r^2}}\right)} \tag{8}$$

where we also replaced the definition of equivalent coil width with the coil lay-out area A as in (4).

3.2 Estimate of the maximum critical gradient versus aperture

For a lay-out with $w_{eq} >> r$, the critical gradient tends to zero since λ is proportional to w_{eq}(see Eq. 7). Therefore, there is an optimum coil width that maximizes the critical gradient G_c. The maximum critical gradient G_c^{max} versus the aperture radius r computed according to Eq. (6) is given in Fig. 2 for Nb-Ti at 1.9 K, for a typical filling factor of 0.35. A comparison is given with the naïve estimate $G_c^{*} = B_{c2}^{*}/r$. One finds that in the range of aperture radii (10 to 100 mm) analyzed one obtains from 30% to 20% less, and that one approaches the naïve limit for very large apertures.

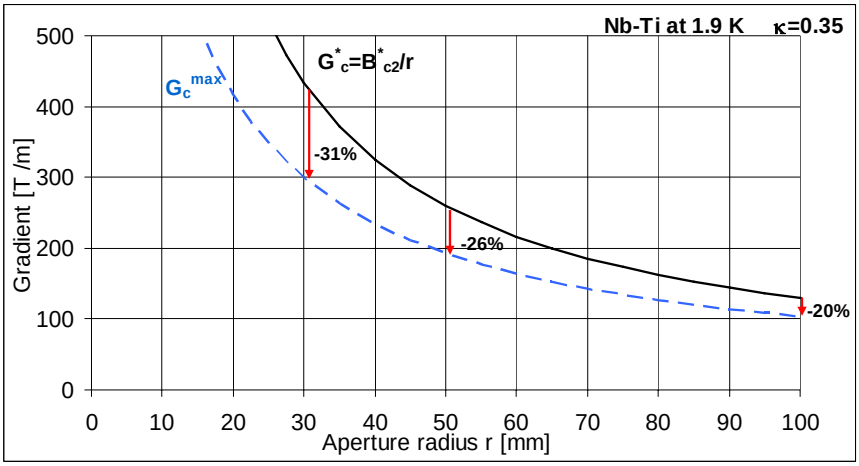

Fig. 2 Maximum critical gradient as estimated from Eq. (6) vs. aperture radius, for the case of Nb-Ti at 1.9 K, and with a filling factor of 0.35. The gradient derived from the naïve assumption $G_c^* = B_{c2}^*/r$ is shown for comparison.

3.3 Comparison with built quadrupoles

We used Eq. (6) to estimate the critical gradient of the coil lay-out of 13 Nb-Ti quadrupoles. We found an agreement within 4% for 10 cases without current grading, whereas three cases with grading give up to 9% more.

4. CONCLUSION

We propose two equations for computing the critical field (gradient) in superconducting dipoles (quadrupoles), when the critical surface can be approximated by a linear fit. These equations depend on the superconducting properties of the material, on the dilution of the superconductor in the coil, and on the area of the conductor. All the other details of coil lay-out, such as the number and the size of the conductor blocks and the number of layers, are neglected. Notwithstanding this rather crude approximation, the equation agrees well with the actual values. For the case of the dipole, it proves to be rather close to the $\cos\theta$ formula for aperture radii smaller than 30 mm, but it gives different results for very large apertures (see Fig. 1). These equations have been derived for a simple sector coil, and can be used as a benchmark to judge the efficiency of the different types of coil lay-outs. Moreover, they can be used to derive the maximum critical gradient that can be achieved for a superconducting quadrupole of a given aperture, and the thickness of the coil needed to get a given field (for dipoles) or gradient (for quadrupoles). A detailed analysis of the quadrupole case is given in [4].

ACKNOWLEDGEMENTS

We wish to thank J.P. Koutchouk and T. Taylor for useful discussions and comments.

REFERENCES

[1] G. Ambrosio, et al., Preliminary proposal of a Nb_3Sn quadrupole model for the low beta insertion of the LHC, INFN Report/TC **95/25** (1995).

[2] S. Caspi, P. Ferracin, Limits of Nb_3Sn accelerator magnets, Particle Accelerator Conference, JACoW (2005) 107.

[3] S. Caspi, P. Ferracin, S. Gourlay, Graded high field Nb_3Sn dipole magnets, MT-19, IEEE Trans. Appl. Supercond. 16 2 (2006) 354.

[4] L. Rossi, E. Todesco, Electromagnetic design of superconducting quadrupoles, submitted to Phys. Rev. STAB (2006).

TOWARDS COMPUTING TRAINING PROCESSES IN SUPERCONDUCTING MAGNETS

P. Ferracin
Lawrence Berkeley National Laboratory, Berkeley, USA

Abstract
In the last years the Superconducting Magnet Program at Lawrence Berkeley National Laboratory has been developing 3D finite element models of superconducting magnets for particle accelerators, with the goal of analyzing and interpreting magnet test results, as well as studying quench initiation and training. The model allowed investigating the deformation of the support structure, the stresses in the coils, and the displacements of the conductors, in particular with respect to the pole and the end spacers. We present here a new analysis, where the energy dissipated during magnet excitation due to mechanical motions is computed, and its consequent temperature rise evaluated. Furthermore, non-reversible processes like ratcheting and training are modeled. The results are compared with the experimental measurements performed on the magnet SQ02.

1. SQ02

1.1 Magnet design

The design of the subscale quadrupole magnet (Fig. 1, left) consists of four subscale coil modules. The cables are composed of 20 Nb_3Sn strands with a diameter of 0.7 mm, and insulated with a 0.1 mm thick woven sleeve of fiberglass. Each coil module was wound around an iron pole (island) in a flat racetrack double-layer configuration and confined within a stainless steel horseshoe. The coils are placed around a square aluminum bore with a clear aperture of 110 mm and a square side of 128 mm (coil aperture).

The Lorenz forces in the straight section are directed towards the magnetic mid-plane, in the direction perpendicular to the wide surface of the cable (azimuthal direction), and towards the center of the magnet, in the direction perpendicular to the narrow surface of the cable (radial direction). The required azimuthal and radial pre-stresses are 70 MPa and 5 MPa respectively. Along the longitudinal direction, due to the high energy stored in the magnet, a significant axial force of 96 kN pushes outwardly each coil end, corresponding to an unsupported tension in the straight section of 100 MPa.

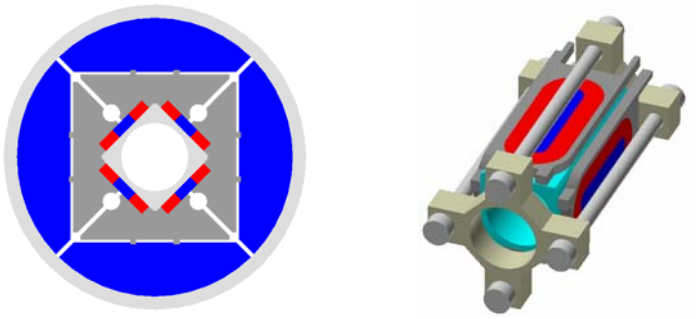

Fig. 1 Cross-section (left) and axial support (right) of SQ02.

The support structure comprises several components: aluminum bore, stainless steel pads, iron yokes, and aluminum outer shell. As a first step in the assembly, the four coils were placed around the aluminum bore. The functions of the bore are providing an initial alignment structure to position the coils, and supporting the conductors under the action of radial Lorentz forces. The coil-bore assembly was then surrounded by four stainless steel pads, and inserted into a structure composed by a four-piece iron yoke and an aluminum shell. Alignment between the shell and the yokes and between the yokes was ensured by 12 keys.

A 5 mm gap between pads and yokes provided room for inserting four pressurized bladders, which generated the primary force needed to spread the yoke apart, apply tension to the shell and pre-compress the coil-pads subassembly. Once the structure was locked by interference keys, the bladders were deflated and removed. During cool-down, the shell generated further pre-load on the coils, due to the different thermal contractions of aluminum and iron.

In order to reduce the conductor motion in the end region resulting from axial Lorentz forces, a longitudinal support system, was included in the design (Fig. 1, right). Four aluminum rods, with a diameter of 25 mm, were inserted in the four holes of the pads, and bolted to two 50 mm thick stainless steel end plates. The rods were pre-tensioned with an axial piston at room temperature, and, similarly to the outer shell, they significantly increased their stress during cool-down.

1.2 Test results

The magnet performance is given in Fig. 2, where the fraction of short sample current (9.9 kA) for each quench is plotted as a function of the quench number. All the quenches were located in the pole turn.

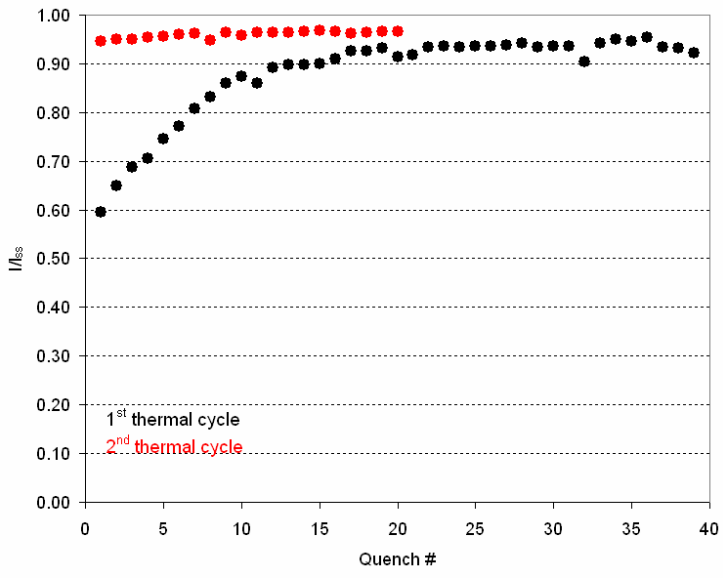

Fig. 2 Training performance of SQ02.

2. FRICTIONAL ENERGY DISSIPATION

In order to interpret the SQ02 test results, we computed the energy dissipated during excitation. Assuming a friction factor μ between the coil and the pole, we evaluated the sliding distance δ due to axial Lorentz force and the generated shear tension σ. The energy dissipated due to sliding with friction can therefore be obtained at each excitation step from δ and σ.

In Fig. 3 we show the frictional energy (J/m^2) dissipated from 8000 A to 9000 A in the contact area between the coil and the pole.

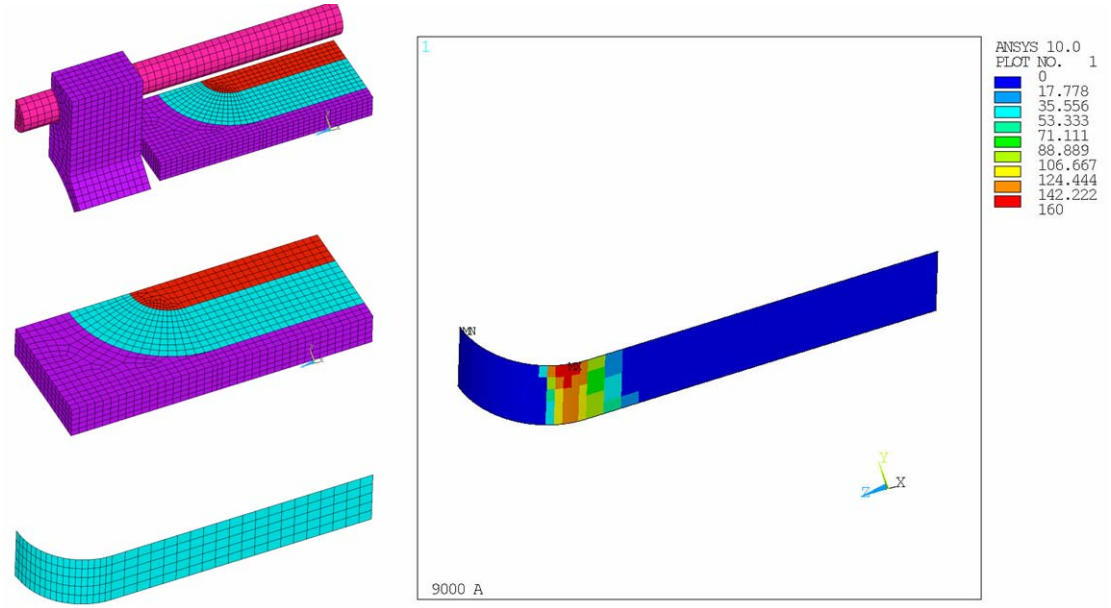

Fig. 3 Frictional energy (J/m^2) dissipated from 8000 A to 9000 A.

3. RATCHETING

We define as ratcheting the increase of coil length as Lorentz forces are cycled. The axial Lorentz forces tend to pull the coil ends outwardly, and after an excitation cycle the coil does not return to its original length, due to friction between the components. This phenomenon has been observed in several magnet [1]-[5], as well as in SQ02 (Fig. 4, left). By performing loading-unloading consecutive computations, we noticed that the model can reproduce a non-conservative system, where energy is dissipated due to friction, and the numerical results are path dependent (Fig. 4, right).

As well as the coil axial displacement, also the dissipated energy features a path dependent behavior.

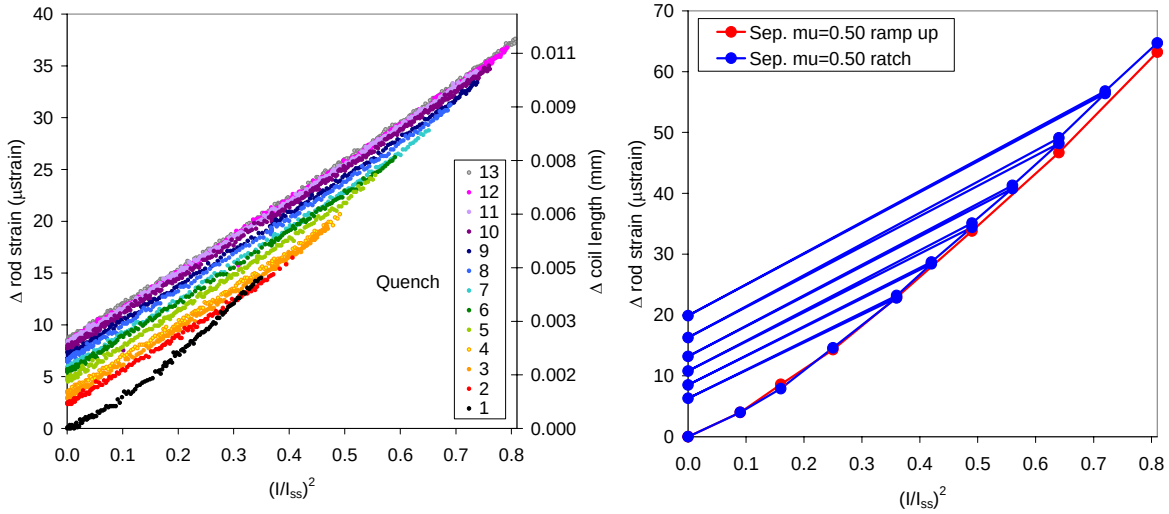

Fig. 4 Measured (left) and computed (right) coil ratcheting.

4. THERMAL AND TRAINING MODEL

By combining the dissipated energy analysis with the ratcheting computations, it possible to evaluate the temperature rise characteristic of each loading cycle, compare it with the coil temperature margin (Fig. 5, left), and finally estimate a training curve (Fig. 5, right).

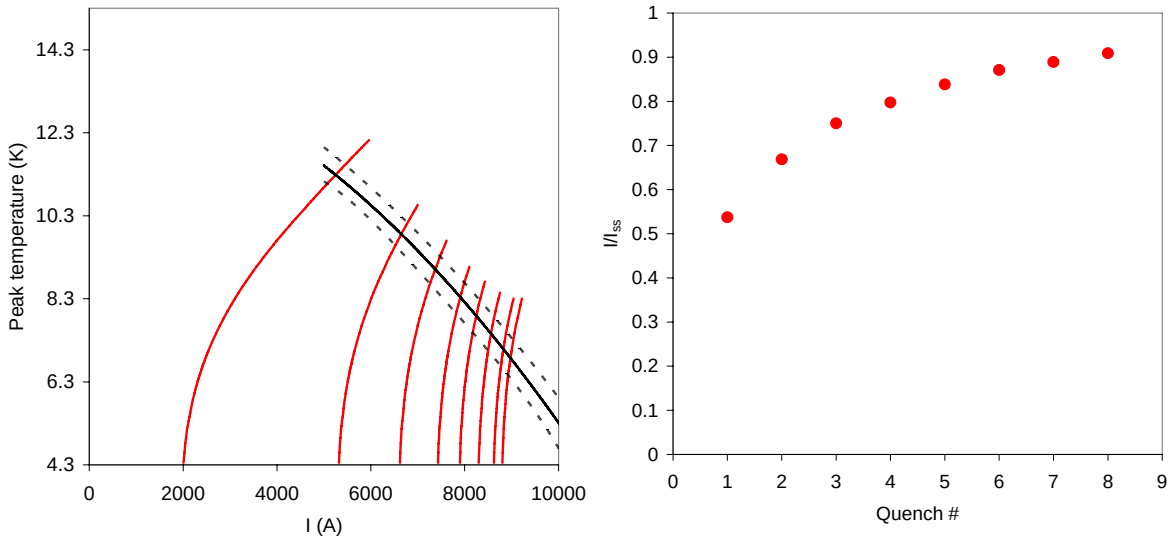

Fig. 5 Peak temperature and critical temperature (left), with estimated training curve (right).

REFERENCES

[1] J. Strait et al., Tests of full scale SSC R&D dipole magnets, IEEE Trans.Magnetics, 25 2 (1989) 1455.

[2] J. Buckley et al., Mechanical performance of a twin-aperture 56 mm bore 1 m long dipole model made with SSC type cables, IEEE Trans. Magnetics 32 4 (1996) 2136.

[3] A. Devred et al., About the Mechanics of SSC Dipole Magnets, AIP Conf. Proc. 249, 2 (1992) 1367.

[4] K. Artoos et al., Measurement and analysis of axial end forces in a full-length prototype of LHC main dipole magnets, IEEE Trans. Appl. Supercond. 10 1 (2000) 69.

[5] S. Mattafirri et al., Performance analysis of HD1: a 16 T Nb3Sn dipole magnet, IEEE Trans. Appl. Supercond. 15 2 (2005) 1156.

PROGRESS IN THE COMPARISON OF DIFFERENT HIGH FIELD MAGNET DESIGNS FOR THE "NEXT EUROPEAN DIPOLE" (NED)

*F. Toral *)*
CIEMAT, Madrid, Spain

Abstract
A Working Group on Magnet Design and Optimization within the NED collaboration is exploring the use of layered cos-θ designs for large aperture (88-160 mm), very high field (up to 15 T) dipoles, and efficient alternatives. Coil configurations include common coil, motor-type, ellipse-type, slotted cos-θ and double helix. Common starting parameters have been set, as have figures of merit for comparison. This report indicates the advantages and drawbacks of designs based on ongoing 2-D magnetic calculations.

1. INTRODUCTION

The NED collaboration [1] has set up a Working Group on Magnet Design and Optimization, with participants from four Institutes: CEA/Saclay, CERN, CIEMAT and RAL, to study:

- How far can we push the conventional, cos-θ layer, design in the aperture vs. central field parameter space (in particular when having to rely on strain-sensitive conductors)?
- What are the most efficient alternatives in terms of performance, manufacturability and cost?

The approaches selected for study are: slotted cos-θ (CERN), motor-type (CIEMAT), ellipse-type (CEA), common coil (CIEMAT) and double helix dipole (RAL). The conventional layered cos-θ is studied both at CERN and RAL. Table I shows the common starting parameters for the studies. The strand is that proposed for the NED specification, i.e. diameter 1.25 mm, Cu to SC ratio 1.25.

Table 1
Common starting parameters for the magnet design optimization

Peak field in conductor	15	T
Aperture	88-130-160	mm
Reference radius	29-43-53	mm
Superconductor Jc	3000 (1500)	A/mm^2 @ 4.2K and 12 T (15 T)
Cu to non-Cu ratio	1÷2	
Operating margin	10÷20	%
Filling factor of cable	87	%
Insulation thickness	0.2	mm per conductor face
Cabling degradation	10	%
Multipole content	a few 10^{-4}	@ 2*aperture/3
Overall coil length	1.3	m
Peak stress	150	MPa
Max coil deformation	<0.05	mm (due to Lorentz forces)
Peak temperature	300	K (at quench)
Peak voltage to ground	1000	V (quench)

*) On behalf of the NED Magnet Design and Optimization Working Group.

2. COS-θ DESIGN

The cos-θ layer configuration has been optimized at CERN (see Fig. 1). The last iteration design is the so-called Reference Design 2 [2]. Table A1 in the Appendix shows the salient features of the 88 mm aperture dipole. Two independent studies [3, 4] have shown that the stresses on the coil mid-plane are above 150 MPa for 130 and 160 mm aperture dipoles, which become unfeasible. As part of the optimization, an elliptical iron yoke is proposed to decrease the large variation of b_3 along the load line. Ferromagnetic shims have been introduced in the cable core to compensate for the effect of persistent currents. Harmonic optimization has been done at CERN using Roxie and at RAL with Opera, using a different algorithm, with similar results. The outstanding advantages of this design include low peak-to-bore field ratio, good superconductor efficiency, low stored energy and small overall magnet size. The only disadvantage is the high mid-plane stress in the coil.

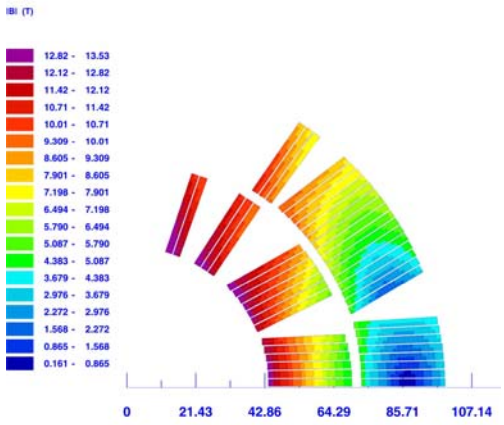

Fig. 1 Magnetic field map at the coils of the 88-mm cos-θ dipole.

3. ELLIPSE-TYPE DESIGN

It is well-known that a uniform elliptical current density creates a uniform dipole field. CEA/Saclay has studied an optimal ellipse-type design (see Fig. 2). The salient features of the results are given in Tables A1 and A2. While the ratio of peak to bore field is low, and homogeneity is good, stored magnetic energy (and self-inductance), is greater than that of the cos-θ version. The horizontal component of the Lorentz force is large, and internal support is necessary to prevent the coils from bending, decreasing the useful aperture for a given inner coil radius. Further investigation is needed to check the feasibility of non-planar coil ends (3-D mechanical computation, winding techniques).

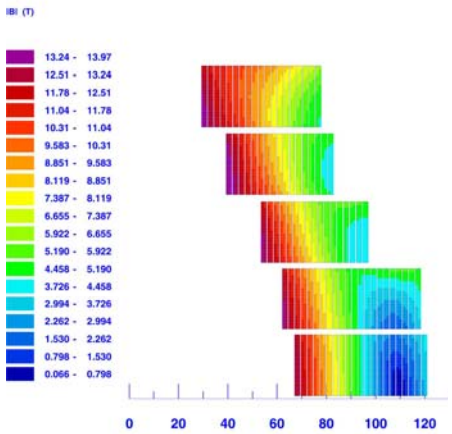

Fig. 2. Magnetic field map at the coils of the 88-mm ellipse-type dipole.

4. MOTOR-TYPE DESIGN

This magnet design resembles a toroid. The main advantages are the simplicity of the coil geometry and the low coil mid-plane stress. The most outstanding drawbacks are the fringe field and the large number of turns, due to a reverse field created by the outermost coil blocks. An additional coil block has been introduced at the outer radius, but with opposite current polarity. This addresses both problems: the overall number of turns is reduced by a factor of 2, by cancelling the anti-dipole field; and the fringe field is reduced, as the magnetic moment is small. However, the latter is still high in the vicinity of the coils, and cannot be reduced by means of an iron screen (which even enhances its level). The magnet assembly is complex, and the coil end design is still a challenging problem (see Fig. 3). Finally, the stored magnetic energy is large, the peak-to-bore field ratio is not as low as in the previous designs and Lorentz forces are large. The field quality has not been fully optimized (ROXIE requires some additional design variables). Tables A1 and A2 summarize the 2-D magnetic results.

Removal of the outermost coil blocks of the motor-type design yields the cos-θ slot dipole. The

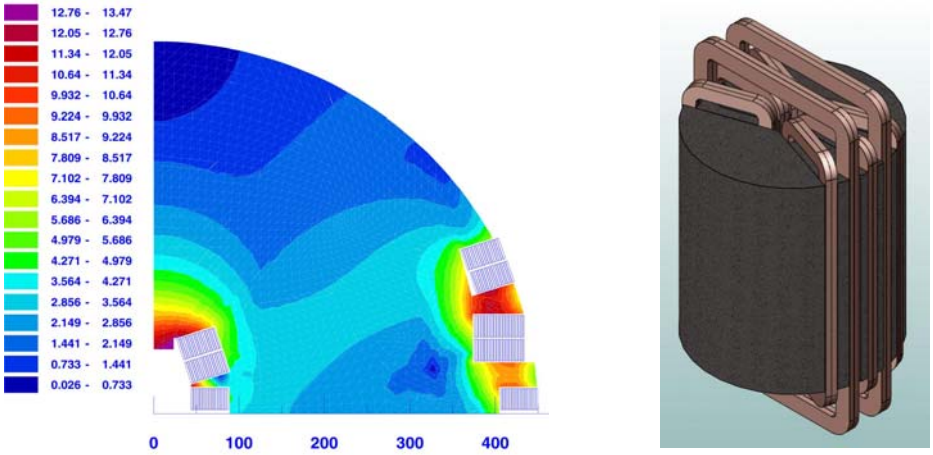

Fig. 3 Magnetic field map at the coils of the 88-mm motor-type dipole, and model magnet assembly.

problems concerning the fringe field and the high number of turns disappear, but the coil end design becomes quite complex. This coil configuration will also be studied in the near future.

5. COMMON COIL DESIGN

The inherent feature of this configuration is the two-in-one iron yoke. The peak to bore field ratio and the cross-talk are very sensitive to the distance between both apertures. In the present design, this distance is about 350-400 mm (depending on the aperture), and it seems to be small. The peak to bore field ratio is poor as the field line density is high between the apertures. To get good field quality, the most effective ampere-turns must be replaced by spacers. In the near future, that distance should be increased. Nevertheless, the overall size is still smaller than that of other designs. A longer distance also enhances the superconductor efficiency, as the cross-talk decreases. The main results are given in Tables A1 and A2. The field quality is not completely optimized, due to insufficient design variables. The stored magnetic energy is large, as are the Lorentz forces. Average coil stresses seem acceptable, but further detailed calculations are necessary. Obviously, coil fabrication is very simple.

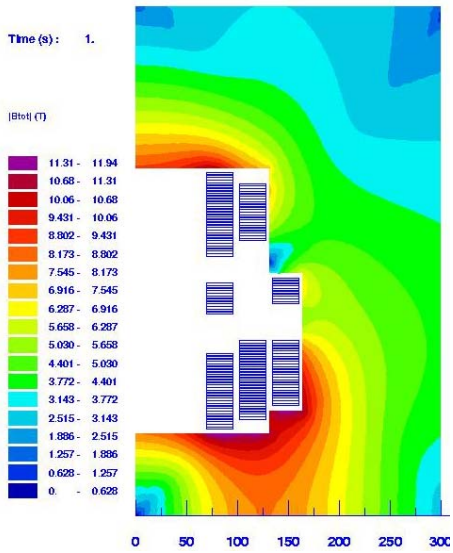

Fig. 4. Magnetic field map at the coils of the 88-mm common coil dipole.

6. CONCLUSIONS

For the 88 mm aperture, the cos-θ layer design is the best possible one. However, for large apertures (130÷160mm), the coil mid-plane stresses become too high in the cos-θ layer design. The NED Magnet Design and Optimization Working Group are studying a number of alternative magnet designs. The Working Group has established essential common starting parameters and agreed upon a set of figures of merit in order to ensure a fair comparison of the alternatives. This report summarizes the ongoing 2-D magnetic field calculations. All the coil configurations studied to date have both strong and weak points, and the next steps of the programme, i.e. detailed 2-D mechanical calculations, to be followed by full 3-D analysis, are crucial for the design of a very high field magnet with a large aperture.

REFERENCES

[1] A. Devred et al., Status of the Next European Dipole (NED) activity of the Coordinated Accelerator Research in Europe (CARE) project, EUCAS 2005, Proc. to be published (2006).

[2] N. Schwerg, Electromagnetic Design Study for a Large Bore 15T Superconducting Dipole Magnet**,** Diploma Thesis, Berlin TU (2005).

[3] J.M. Rifflet, Final Report of Contract EFDA/04-1201 (2005).

[4] D. Leroy, O. Vincent-Viry, Preliminary Magnetic Designs for Large-Bore and High-Field Dipole Magnets, CERN Report CERN/AT/2004-22 (2004).

APPENDIX – COMPARISON OF PARAMETERS OF HIGH FIELD DIPOLES OF THE VARIOUS TYPES UNDER INVESTIGATION

Table A1
Salient features of the various dipole types with 88mm aperture

	Cos-θ type	Ellipse-type	Motor-type	Common coil	
Aperture	88	88	88	88	mm
Area of bare conductors / aperture	10647	16761	34382	15495	mm^2
Area of insulated conductors / aperture	12711	20165	41332	18626	mm^2
Number of strands per aperture	7200	11856	24320	10960	
Outer iron yoke	475	500	450	600/800	mm
Current	26.2	20.243	26.7	26.95	kA
Margin on load line	10.00	10	9.93	10.16	%
Bore field	13.11	13.54	12.95	12.20	T
Peak field	13.53	13.974	13.49	13.43	T
Peak field/bore field	1.032	1.032	1.042	1.10	
Peak field at 0% on load line	15.03	15.49	14.98	14.95	T
Multipole content					
b3	0.402	0.136	0.066	-6.120	units
b5	0.069	0.2635	4.184	-8.407	units
b7	0.078	0.661	-8.839	6.181	units
b9	1.699	0.247	-6.109		units
b11	2.686	-0.007	-1.933		units
a2				-2.290	units
a4				6.883	units
a6				-0.797	units
Engineering current density	371.02	313.2	392.8	396.4	A/mm^2
Self inductance /aperture /unit length	4.387	10.71	9.193	7.998	mH/m
Stored energy / aperture / unit length	1.505	2.19	3.277	2.904	MJ/m
Stray field					
- at 50 mm from the outer iron radius	0.03	0.06	2.1	1.8	T
- at 1 m away from the magnet center	0.006	0.015	0.055	0.07	T
Magnetic forces					
- Fx per side of aperture	13.382	19	12.044	7.265	MN/m
- Fy per quadrant	-3.233	-3.54	-2.873	1.954	MN/m
- Max. accumulated membrane stress perp. to broad face of the conductor	124.3	107	97	112.1	MPa
- Max. accumulated membrane stress parallel to broad face of the conductor			103	112.8	MPa

Table A2
Salient features of possible 130mm and 160 mm aperture dipoles

	Ellipse-type		Motor-type		Common coil		
Aperture	130	160	130	160	130	160	mm
Area of bare conductors / aperture	20629	27291	40716	50669	18096	20132	mm^2
Area of insulated conductors / aperture	24818	32833	48946	60910	21754	24201	mm^2
Number of strands per aperture	14592	19304	28800	35840	12800	14240	
Outer iron yoke	680	820	450	500	700/900	700/1000	mm
Current	19.983	18.281	26.4	26.2	26.45	26.5	kA
Margin on load line	10.1	10.8	10.11	10.01	10.01	10.66	%
Bore field	13.32	13.375	12.68	12.42	11.07	10.34	T
Peak field	13.976	14.03	13.49	13.53	13.50	13.38	T
Peak field/bore field	1.049	1.049	1.064	1.089	1.22	1.29	
Peak field at 0% on load line	15.52	15.69	15.01	15.03	15.00	14.98	T
Multipole content							
b3	0.004	0.09	1.659	-0.439	0.531	-6.120	units
b5	0.004	-0.05	-0.762	2.115	-5.721	-8.407	units
b7	-0.0008	0.008	7.031	4.746	21.614	6.181	units
b9	-0.05019	-0.00337	-4.241	-7.157			units
b11	-0.2474	0.0163	-3.006	-4.659			units
a2					-0.716	-6.585	units
a4					3.422	3.497	units
a6					-8.160	-9.082	units
Engineering current density	309.2	282.8	388.4	385.5	389.1	389.8	A/mm^2
Self inductance /aperture /unit length	16.92	30.16	14.456	22.636	11.901	14.806	mH/m
Stored energy / aperture / unit length	3.38	5	5.036	7.768	4.162	5.200	MJ/m
Stray field							
- at 50 mm from the outer iron radius	0.018	0.022	2.5	3.4	1.92	2.5	T
- at 1 m away from the magnet center	0.008	0.015	0.092	0.2	0.11	0.16	T
Magnetic forces							
- Fx per side of aperture	23.25	28.67	12.0178	14.272	7.385	7.423	MN/m
- Fy per quadrant	-4.3	-5.59	-3.757	-4.243	3.190	3.314	MN/m
- Max. accumulated membrane stress perp. to broad face of the conductor	115	124	103	121	110.6	129.7	MPa
- Max. accumulated membrane stress parallel to broad face of the conductor			125	125	117.0	118.2	MPa

SUPERCONDUCTING COMBINED FUNCTION MAGNETS FOR THE J-PARC NEUTRINO BEAM LINE

T. Nakamoto
KEK, Tsukuba, Japan

Abstract
A single type of superconducting combined function magnet will be utilized for the 50 GeV, 750 kW proton beam line for the J-PARC neutrino experiment. The magnet is designed to provide a dipole field of 2.6 T combined with a quadrupole field of 19 T/m in a coil aperture of 173.4 mm at a nominal current of 7345 A. Two full-scale prototypes and the first two magnets, of the required production run of twenty-eight units, have been built and tested, confirming that the magnet performance fulfills the specification.

1. INTRODUCTION

A second generation of long-baseline neutrino oscillation experiments has been proposed as one of the main projects at the J-PARC [1, 2] and the construction of the facility is in progress. Superconducting combined function magnets, SCFMs, will be utilized for the 50 GeV, 750 kW proton beam line for the neutrino experiment. The magnet is designed to provide a dipole field of 2.6 T combined with a quadrupole field of 19 T/m in a coil aperture of 173.4 mm at a nominal current of 7345 A. A series of 28 magnets in the beam line will be operated DC in supercritical helium cooling below 5 K [3]. Since the main accelerator will be operated at 40 GeV at the beginning, the SCFM was designed for use with proton beam energies of both 40 and 50 GeV. The parameters of the conductor are listed in Table 1, and the main design parameters of the SCFM are shown in Table 2.

Table 1
Parameters of the conductor

Superconducting Strand	
Diameter & twist pitch, Z	0.825 mm & 15 mm
Cu/SC ratio	1.95
Filament diameter	6 μm
Superconducting Cable	
Width & middle thickness	15.1 mm & 1.480 mm
Keystone angle	0.9°
RRR of Cu	> 70
Cabling pitch, S	100 mm
Number of strands	36
Critical current	>12240 A @6 T, 4.2 K

Table 2
Main design parameters* of the SCFM

Physical & magnetic length	3630 & 3300 mm
Coil inner & outer diameter	173.4 & 204.0 mm
Yoke inner & outer diameter	244 & 550 mm
Shell outer diameter	570 mm
Dipole & quadrupole field	2.59 T & 18.7 T/m
Peak field in coil	4.7 T
Load line ratio	72 %
Nominal operating current	7345 A
Inductance &.stored energy	14.3 mH & 386 kJ
Number of turns:	
Left side: 2 blocks	35, 6
Right side: 5 blocks	6, 5, 10, 13, 7
Magnetic force on a coil:	
F_x & F_y left side	-618 & -360 kN/m
right side	434 & 114 kN/m

*For 50 GeV operation

Prior to the fabrication of production magnets, the magnet design was confirmed through an R&D program in which fabrication tooling and assembly procedures were established and two full-scale prototype magnets were built. The program was successfully completed and it was verified that the magnet performance fulfilled the specification [4-9].

Following competitive tendering, the contract for the series production of the magnet system was awarded to Mitsubishi Electric (MELCO). Technology developed for the prototype magnets has been transferred to MELCO and the first two production magnets have been successfully completed.

2. DESIGN AND FABRICATION

2.1 Design Overview

A unique feature of the SCFM is the left-right asymmetry of the coil cross-section: the current distributions for superimposed dipole and quadrupole fields are combined in a single layer coil. Another design feature is the adoption of glass-fiber reinforced phenolic plastic spacers for electrical insulation to reduce the labor and inspection costs associated with classical ground plane insulation.

The most appropriate 2D coil arrangement to generate the required field was determined using ROXIE [10]. As shown in Fig. 1, the coil is divided into 2 blocks for the left (high field, HF) side and 5 blocks for the right (low field, LF) side to provide the appropriate combined field. The effective pole is rotated by about 20° towards the high field side (left side in this figure). The shape of the coil ends was also modeled using ROXIE, which provided CNC files for the manufacture of G10 end spacers. The 3-D magnetic field was calculated using Opera-3D (TOSCA). Magnetic length was calculated to be 3350 mm for the dipole field. The relatively large value of b_3 is mainly due to the shape of the coil ends and cannot be eliminated. Beam optics calculations confirmed that the design magnetic field of the SCFM, with a tolerance of 10^{-3} at a reference radius of 50 mm, was sufficiently acceptable.

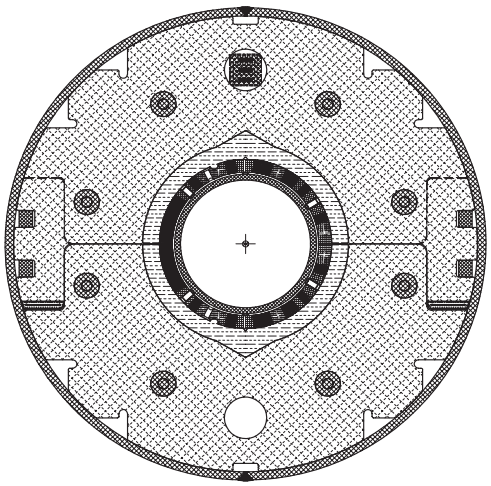

Fig. 1 Cross-section of the superconducting combined function magnet (SCFM) for the 50 GeV proton beam line serving the J-PARC neutrino experiment.

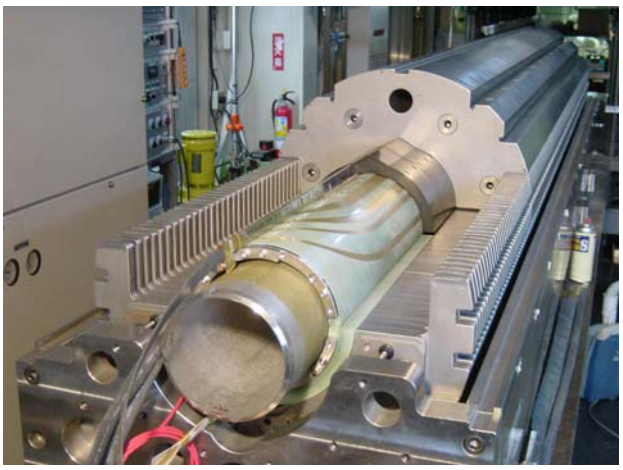

Fig.2 Magnet being prepared for yoking.

The coil is mechanically supported by a keyed yoke made of fine-blanked iron laminations. The iron yoke also functions as a magnetic flux return. The plastic spacers are placed between the coil and the iron yoke. The coil pre-stress of 80 MPa is produced by the yoking process. Both coil ends are longitudinally fixed by end plates.

2.2 Coil Winding

The Rutherford type NbTi/Cu superconducting cable that was used for the outer layer of the LHC main dipole magnet was simply adopted for the SCFM to reduce the cost of cable development. The end spacers and the wedges are made of GFRP (G10 and G11). They were precisely made by CNC machining. Size control of the wedges is very important to achieve good field quality and adequate pre-stress. The tolerance of the wedge size is set to be 0.1 mm.

The coil is wound like a dipole coil and cured in a thick forming shell at 400 K for 5 hours. An appropriate combination of several shims for the curing was carefully chosen to achieve the design coil stress of 80 MPa during yoking and to avoid displacement of the effective pole due to unbalanced coil size. During curing, median plane shimming ensures correct control of asymmetric coil over-size.

2.3 Yoking

A picture of the magnet prepared for the yoking process is shown in Fig. 2. The glass-fiber reinforced phenolic plastic spacers are placed between the coil and the iron yoke. The plastic spacers function as not only electrical insulation but also to align the coil with respect to the iron yoke: a triangular feature at the top fits into the notch of the iron yoke and a circular shaped key on the inner diameter fits into the groove on the pole spacer of the coil, as shown in Fig. 1.

The keyed iron yoke technology was transferred from the MQXA [11]. The “fixing yoke” sheet is 5.8 mm thick and has grooves for keying at claws on both sides while the “spacer yoke” sheet, 6.0 mm thick had no claw. The upper- and lower-yoke assemblies are compressed at their shoulders up to ~13 MN by a hydraulic press and are locked by keying. The yoke gap is closed at the median plane by the keying. With the keys installed, we achieve both the desired cross section of the structure and the coil alignment with appropriate pre-stress.

2.4 Shell welding, and work on the ends

The helium vessel is formed by two halves of an SUS304L shell covering the yoked magnet. The shell has 4 holes at 5 points along the magnet length, 20 holes in total. The yoked magnet is rotated 90° and the top and bottom are longitudinally welded by two automatic welding machines with the yoke shoulder aligned via the holes using the hydraulic press. A backing strip is not permitted for the shell welding, due to Japanese high-pressure regulations. Instead, pre-formed inserts of SUS308L are set between two halves of the shell and are completely welded at the first (of a total of 11) welding pass.

Fifteen alignment targets are precisely fixed on the shell at 0, 90, and 180° with respect to the yoke shoulder and then all holes are welded over with caps. The targets are used for the magnet alignment in the following process.

Ferrules of SUS304L, so called “end-rings”, transversely welded at both ends of the shell function to fix the end plates. Each coil end is longitudinally compressed to ~ 40 kN by studs on the end plates. Leads from the upper and lower coils are connected by using 96Sn-4Ag solder with a non-activated flux (Kester #135) and then the lead spice is enclosed in a G10 case fixed to the end plate.

3. TEST RESULTS

As mentioned above, two prototypes and two production magnets have been fabricated so far. In addition, the first prototype was rebuilt for the further quench protection studies. In total, five cold tests have been carried out in a 9 m vertical cryostat filled with liquid helium at 4.2 K [7], [9], [12].

3.1 Quench Characteristics

All magnets successfully reached the nominal current of 7345 A at a ramp rate of 5 to 20 A/s without a spontaneous training quench. Furthermore, they were successfully excited up to 7700 A, i.e. 105 % of nominal current. The prototypes were also energized at different ramp rates and no quench occurred up to the nominal current even at the maximum rate of 750 A/s. The first prototype had no training

quench after a full thermal cycle. Full energy dump tests were carried out for the production magnets on which the quench protection heaters were fully installed and the quench protection heaters were verified to protect the magnets safely. In fact, all magnets have shown excellent quench performance.

3.2 Field Quality

Magnetic field measurements were performed with a 500 mm-long rotating printed circuit board on which 5 radial rectangular coils were arranged in parallel. The rotating board was vertically scanned along the magnet in the warm-bore tube. Analogue bucking with a combination of radial coils was adopted to obtain higher order harmonics. In this measurement system, it is difficult to determine the dipole field with good accuracy because an off-centered rotating axis induces a "feed-down" effect due to higher order harmonics. This significantly affects measurement of the dipole field because of the large quadrupole component. In the following data, therefore, the magnetic field is analyzed with the average of the skew quadrupole component along the magnet straight section equal to zero.

Figure 3 shows the distribution of the dipole and quadrupole components along the magnet axis for the production magnets at a current of 7460 A. The measurements generally reproduce calculations using OPERA-3D (TOSCA) for both components. There is, however, a small discrepancy in the dipole field. This is probably induced by a "feed-down" effect. The field integrals over the length of the magnet at 7345 A and at 50 mm radius are ~8.73 Tm (dipole) and ~3.07 Tm (quadrupole) and vary little from magnet to magnet. These values are to be compared with those calculated with 8.711 Tm and 3.119 Tm respectively calculated with OPERA-3D. The apparent systematic difference of 1 to 2 % for the integrated quadrupole appears to be due to the magnet ends, and the effect is being investigated.

Figure 4 shows the field integrals of higher order harmonics at a current of 7345 A. The calculations reproduce reasonably the measurements for each multipole component. It was confirmed that the field quality met the specifications for all magnets.

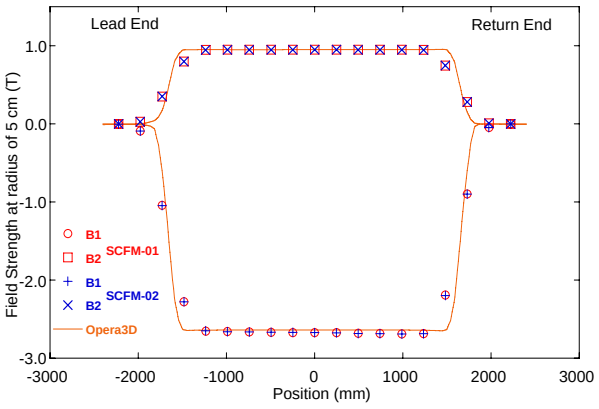

Fig. 3 Dipole and quadrupole components distribution along the magnet axis at a current of 7460 A.

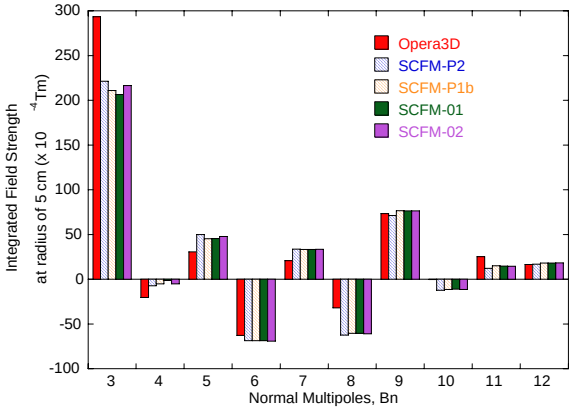

Fig. 4 Field integrals of higher order harmonics at a current of 7345 A.

4. SUMMARY AND FURTHER PLANS

Two full-scale prototypes and two production magnets have been successfully completed. All magnets showed excellent excitation performance, with field quality fulfilling the specifications.

A full-scale prototype cryostat containing two magnets has been assembled by MELCO. It will be tested at the horizontal test stand at KEK [13]. The first series of 6 production cryostats with 12 magnets will be built in 2006. The complete magnet system for the neutrino beam line should be ready by 2009.

ACKNOWLEDGEMENT

The author thanks CERN for assistance and technical suggestions on the procurement of components.

REFERENCES

[1] Y. Itow et al., The JHF-Kamioka neutrino project, hep-ex/0106019

. [2] M. Furusaka et al., The joint project for high-intensity proton accelerators, KEK Report 99-1; JAERI-Tech 99-056; JHF-99-3 (1999).

[3] T. Ogitsu et al., Superconducting magnet system at the 50 GeV proton beam line for the J-PARC neutrino experiment, MT-18, IEEE Trans. Appl. Supercond. 14 2 (2004) 604.

[4] T. Ogitsu et al., Superconducting Combined Function Magnet System for J-PARC Neutrino Experiment, ASC2004, IEEE Trans. Appl. Supercond, 15 2 (2005) 1175.

[5] T. Nakamoto et al., Design of superconducting combined function magnets at the 50 GeV proton beam line for J-PARC neutrino experiment, IEEE Trans. Appl. Supercond. 14 2 (2004) 616.

[6] T. Nakamoto et al., Development of a Prototype of Superconducting Combined Function Magnet for the 50 GeV Proton Beam Line for the J-PARC Neutrino Experiment, IEEE Trans. Appl. Supercond. 15 2 (2005) 1144.

[7] T. Nakamoto et al., Development of Superconducting Combined Function Magnets for the Proton Transport Line for the J-PARC Neutrino Experiment, Proc. 2005 Part. Accel. Conf., Knoxville, (2005), and http://accelconf.web.cern.ch/AccelConf/p05/PAPERS/TOAA006.PDF

[8] T. Tomaru et al., Alignment in Warm Measurement of the J-PARC Combined Function Magnet, MT-19, IEEE Trans. Appl. Supercond. 16 2 (2006) 1338.

[9] K. Sasaki, Test Results of Superconducting Combined Function Prototype Magnets for the J-PARC Neutrino Beam Line, IEEE Trans. Appl. Supercond. 16 2 (2006) 158.

[10] S. Russenschuck, ROXIE: routine for the optimization of magnet x-sections, inverse field calculation and coil end design, CERN 99-01 (1999).

[11] T. Nakamoto et al., Production and performance of the LHC interaction region quadrupoles at KEK, ASC2002, IEEE Trans. Appl. Supercond. 13 2 (2003) 1321.

[12] K. Sasaki, Test results of superconducting combined function magnets for the J-PARC neutrino beam line, to be presented at the Applied Superconductivity Conference 2006.

[13] K. Sasaki, to be presented at Applied Superconductivity Conference 2006.

SCALING PRE-STRESS IN DIPOLE MAGNETS AND ITS APPLICATION USING BLADDERS AND COLLARS

S. Caspi
Lawrence Berkeley National Laboratory, Berkeley, USA

Abstract

The presentation focuses on the relation between coil size, bore size and stress in Nb_3Sn cos-θ dipole magnets. It reveals that a dipole field depends on the coil radial width only (and not on the bore size). The accumulated azimuthal Lorentz stress on the mid-plane does depend on the bore size. Using realistic engineering current density the overall stress decreases with field, due to the increase in coil thickness to compensate for the decrease in current density. The analysis proceeds to include the option of coil grading.

1. CURRENT DENSITY, COIL SIZE AND STRESS

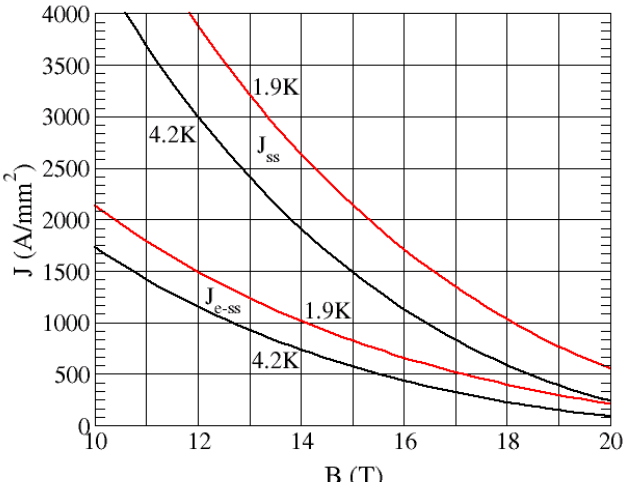

Fig.1 Current density of Nb_3Sn and engineering current density used in modeling, based on 3000 A/mm^2 at 12 T and 4.2 K.

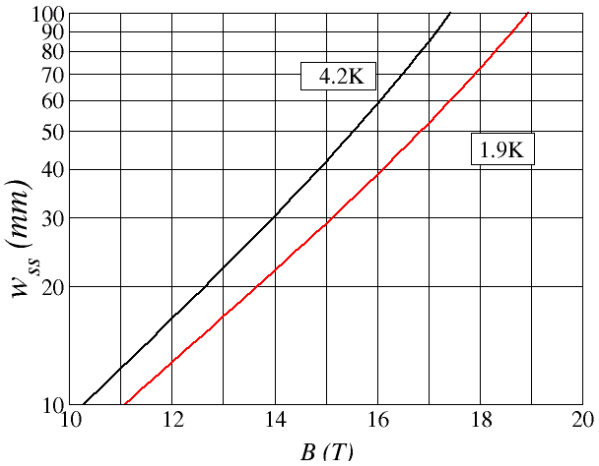

Fig. 2. Minimum coil thickness required to generate a dipole field.

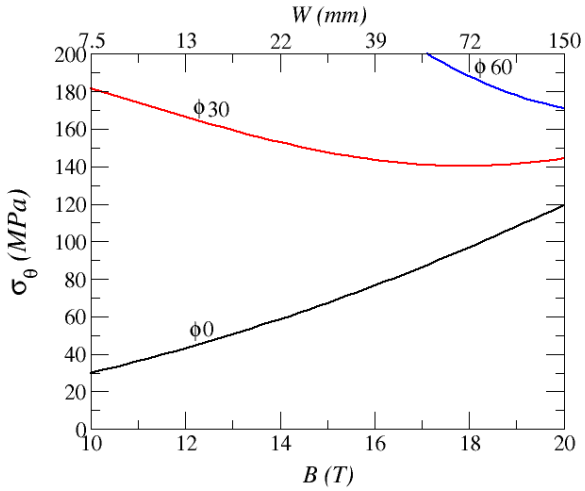

Fig 3 For a given field B, a coil thickness W is needed, which in turn yields a Lorentz stress. The decrease in stress for a given bore is a consequence of the increase in coil size needed to generate higher fields.

2. ASSEMBLY AND PRE-STRESS

In this part of the report we compare the assembly and applied pre-stress using conventional collars with that based on the concept of keys and bladders introduced for the high field program at LBNL.

The advantages and limitations of collars are as follows:

- Advantages
  1. Coil assembly
  2. Coil alignment
  3. Pre-stress
  4. Cost effective
  5. 35 years of experience
- Requirements and limits
  1. Press
  2. Over pre-stress during collaring
  3. Self supporting ~< 10 T
  4. Modeling issues (ANSYS)
  5. Instrumentation

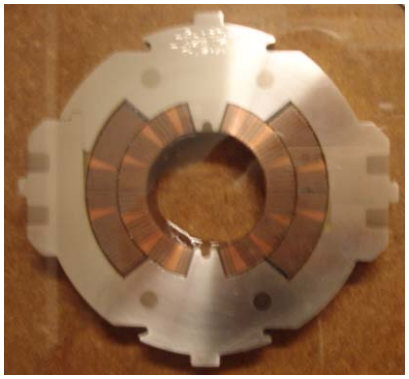

The advantages and limitations of the keys and bladders approach are:

- Advantages
  1. Coil assembly
  2. No pre-stress limit (~20 T)
  3. Low RT pre-stress
  4. Low over pre-stress
  5. Fine stress control
  6. No press , cost effective
  7. Modeling (3-D ANSYS)
- Requirements and limits
  1. Alignment
  2. 5 years of experience
  3. Bladder technology

Fig. 4 Bladder with an inlet tube and housing. This design allows the manufacturer to laser weld the block to the top sheet of the bladder. After the block is attached, the top and bottom sheets can be laser welded together without the tube obstructing the machine path.

The bladder is inserted between the pads and yoke and then pressurized, widening the gap between them. The process strains the shell and compresses the coils. When the measured azimuthal strain on the shell reaches its design value keys are inserted between the yoke and pads, the bladder deflated and removed.

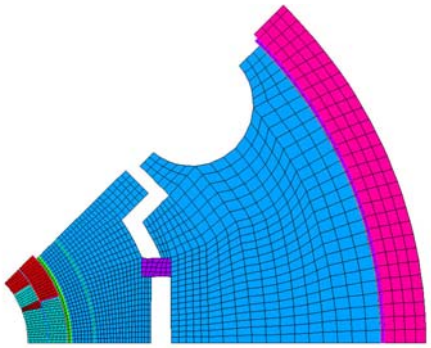

Fig. 5 Cross-section of quadrupole TQS01 showing the gap between the pads and the yoke. The key (in purple) bridges the gap after the bladders have been removed.

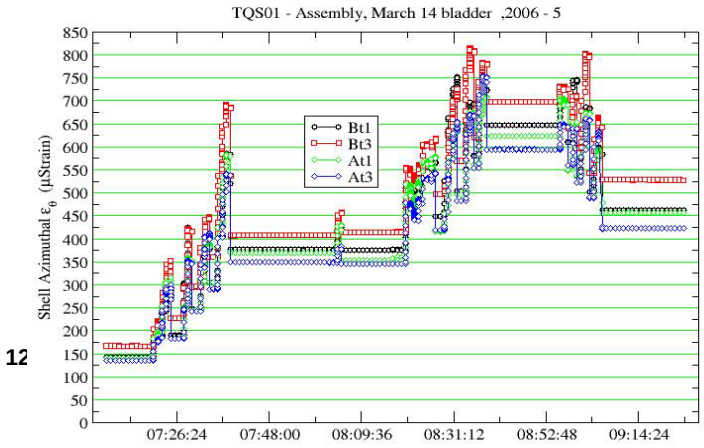

Fig. 6 Measured azimuthal strain in the .shell during assembly. Displacement shims are shown in microns.

3. SUMMARY

- Parametric dependencies exist between field, coil size and stress in Nb_3Sn dipoles
- The bore size has little impact at very high fields
- Very high field dipoles are feasible but probably not yet affordable for accelerators
- A 2-layer graded magnet reduces its thickness by 10% at 12 T and 42% at 20 T
- Grading may increase the outer layer stress to an unacceptable level
- Stress management can be confined to the outer layer only
- At high fields collars or pads are only a tool to assemble and align the coils
- High pre-stress must involve the structure
- Bladders and keys provide excellent pre-stress control
- An external aluminum shell permits low pre-stress during assembly and delivers an additional high pre-stress during cool-down
- Cool-down pre-stress can be based on analysis.

PARAMETRIC ANALYSIS OF FORCES AND STRESSES IN SECTOR WINDING SUPERCONDUCTING QUADRUPOLE COILS

*P. Fessia, F. Regis *, E. Todesco*
CERN, Geneva, Switzerland

Abstract
This paper first presents a review of the existing analytical approximations of the field in the coils for a sector winding quadrupole configuration. It focuses on evaluating to which extent these formulae are usable as a first estimation of the resultants of the electromagnetic forces and the consequent stress distributions. The profile of the forces on the coil edges are analysed in order to evaluate a-priori the loads on the mechanical structures intended to contain the coils. The results deriving from the analytical formulae are then compared to those obtained numerically using an FE model of one octant of the quadrupole coil. We also analyse the evolution of the forces in function of the maximum admissible field gradient.

1. INTRODUCTION

One octant of a quadrupole winding has been considered, with aperture radius r_i, thickness w and angular extension α_0 equal to 30^o. The surrounding air has been modeled up to 45^o for reason of symmetry, while the current density J feeding the magnet has been set as a constant. The magnet has been rigidly constrained along the radial edge thus simulating a collar of infinite stiffness, while along the mid plane the constraints has been placed to respect the mechanical continuity with the lower coil octant. No iron yoke has been introduced and no azimuthal pre-stress as well.

2. ANALYTICAL APPROXIMATIONS OF THE MAGNETIC FIELD AND FORCES

In order to define the magnetic field inside the coil and the derived variables (Lorentz forces and stresses) two analytical approximations can be taken into consideration:

1. $cos\phi$ current distribution [1];
2. constant current distribution [3].

The first formulation has been originally derived form the expansion series of the scalar potential, while the second results from the vector potential, both expanded respect to the centre of the aperture and to infinite; the field inside the magnet is then given by the sum of the magnetic field expression within the useful aperture and outside the coil, by imposing that they are null at the outer and inner radius respectively.

The sector coil formulation matches very well with the numerical results even if only the first term of the expansion series is used (Fig. 1a); on the other hand, the magnetic field distribution inside the coil shows a large discrepancy respect to the numerically computed values (Fig. 1b). An analysis of the magnetic energy U_m reveals that the sector coil approximation provides an estimation differing from the numerical by about 4%, while $cos\phi$ shows a constant error of about 20%.

The Lorentz forces F_x and F_y have been computed, and compared to the results from a parametric numerical analysis (radius varying from 14 to 196 mm and coil width from 5 to 40 mm).

*) Sponsored by ASP (Associazione per lo Sviluppo Scientifico e Tecnologico del Piemonte) and Compagnia di San Paolo, Turin, Italy.

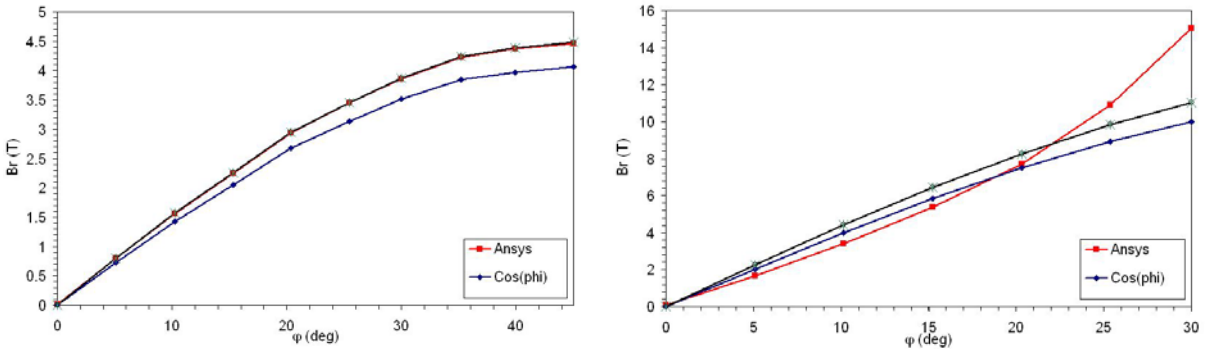

a) *Br* inside the useful aperture @ r constant. b) *Br* inside the coil @ r constant.

Fig. 1 Radial Magnetic field *Br* in a sector winding (r_i = 84 mm, w = 20 mm, J = 1000 A/mm^2).

The differences in evaluating the magnetic forces (see Fig. 2) between the two analytical approximations are constant and equal to:

$$\frac{F_{x,sector}}{F_{x,\cos\varphi}} = \frac{\cos\alpha_0 \sin\alpha_0}{9\pi} \tag{1}$$

$$\frac{F_{y,sector}}{F_{y,\cos\varphi}} = \frac{4\sin\alpha_0}{\pi} \tag{2}$$

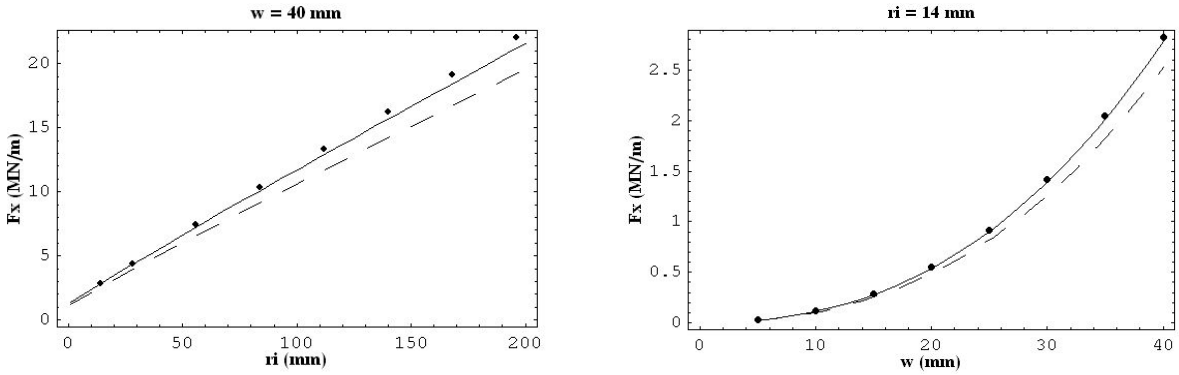

a) F_x varying r_i @ w constant = 40 mm. b) F_x varying w @ r_i constant = 14 mm.

Fig. 2 Radial Magnetic force F_x as a function of the geometric parameters (J ~ 1000 A/mm^2).

Vertical magnetic and horizontal force distribution F_y,, compressing the coil mid-plane, and F_x behave similarly, varying almost linearly with the aperture radius but parabolically with coil width.

3. STRESSES ON COIL MID PLANE AND COLLAR CONTACT PROFILE

3.1 Azimuthal stress p_φ and radial stress p_r

From the balance of forces acting on an infinite coil element [2], neglecting shear stress, one can derive the azimuthal stress p_φ at the coil mid-plane, by integrating F_y over θ in the interval $(0,\alpha_0)$:

$$p_\varphi = -\frac{j^2 \mu_0 \sin 2\alpha_0}{8\pi r^2}\left[r^4 - r_i^4 + 4r^4 \ln\left(\frac{r_i + w}{r}\right)\right] \tag{3}$$

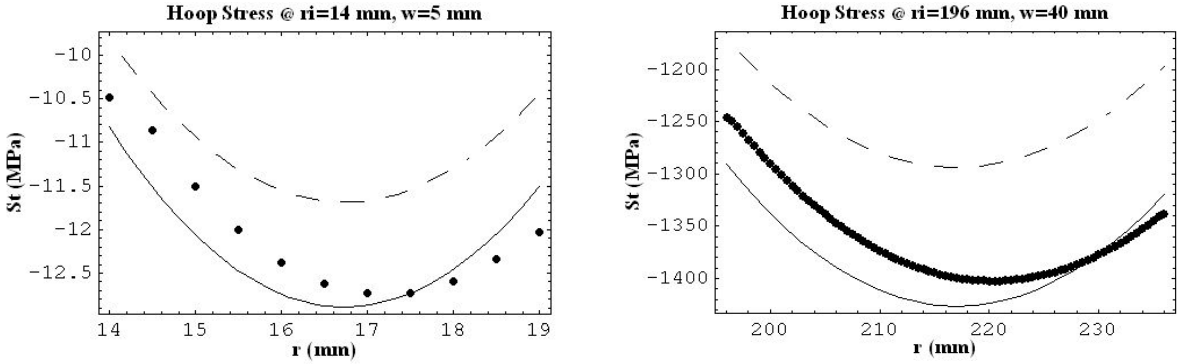

a) p_φ @ r_i = 14 mm, w = 5 mm. b) p_φ @ r_i = 196 mm, w = 40 mm.

Fig. 3 p_φ on coil mid plane as a function of the geometric parameters (J ~ 1000 A/mm^2). The stress values obtained in case b) are not realistic, as J = 1000 A/mm^2 > maximum critical current distribution for that aperture.

The differences between the analytical and numerical distributions come from not considering shear stress, so the coil material does not influence the stress distribution on the coil edges (Eq. (3)). The same considerations apply to distribution of stress on the collar edge, where the radial stress is:

$$p_r = -\frac{j^2 \mu_0 \sin 2\alpha_0}{36\pi \cdot (r_i + w)^2} f_{pr}\left(r_i^4, w^4\right) \tag{4}$$

with

$$f_{pr}\left(r_i^4, w^4\right) = -w\left(12r_i^3 + 42r_i^2 w + 28r_i w^2 + 7w^3\right)\cos 2\alpha_0 + \\ + 9w(2r_i + w)\left(2r_i^2 + 2r_i w + w^2\right)\cos 2\varphi + 12r_i^3 (r_i + w)(\cos 2\alpha_0 - 3\cos 2\varphi)\ln\left(\frac{r_i + w}{r_i}\right) \tag{5}$$

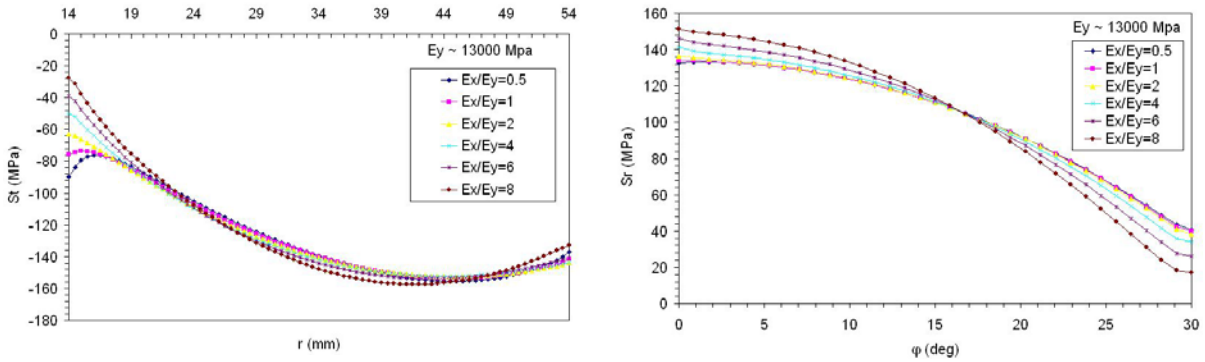

a) p_φ @ r_i = 14 mm, w = 40 mm. b) p_φ @ r_i = 196 mm, w = 40 mm.

Fig. 4 Effect of material anisotropy on p_φ (J ~ 1000 A/mm^2).

3.2 Influence of the material anisotropy

In order to better investigate the influence of mechanical properties of the windings on the stress distribution, numerical simulations have been performed varying the ratio E_r/E_φ in the range [0.5-8], with E_φ set at ~13 GPa [5]. No significant variation on the distribution values can be observed; the peak of the azimuthal stress p_φ is not affected by the anisotropy, nevertheless a considerable influence can be observed at the inner radius.

4. CRITICAL CURRENT DENSITY AND ITS IMPACT ON THE LORENTZ FORCES

4.1 Critical current density parameterization

The parameterization of the critical surfaces for NbTi and Nb_3Sn cables are given in Table 1 [4].

Table 1
Parametric laws for the critical current density $J_{c,sc}$ and main values.

	NbTi		**Nb_3Sn**	
Parametric Critical Surface	$J_{sc,c}=c\cdot(B^*_{c2}-B)$		$J_{sc,c}=c\cdot(B^*_{c2}/B-1)$	
Temperature (K)	4.2	1.9	4.2	1.9
B^*_{c2} (T)	10	13	22.3	26.3
c (A/(T mm^2))	600	600	3400	2500

The formulae for $J_{sc,c}$ take into account cable features (Cu to SC ratio, insulation and voids) by a dilution factor *k*. The distribution of the Lorentz forces and stresses have been computed for the sector coil approximation only. The magnetic forces are proportional to J_c^2: for a case of inner radius 30 mm and width 30 mm, the ratio between the magnetic force F_x for a NbTi cable and a Nb_3Sn cable is 0.6

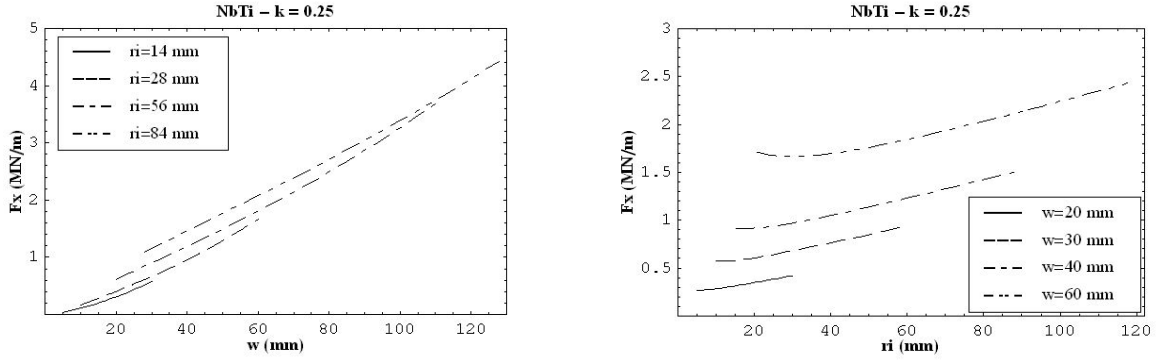

a) *Fx* for a NbTi cable @ J_c, keeping the aperture radius constant for each curve.

b) *Fx* for a NbTi cable @ J_c, keeping the coil width constant for each curve.

Fig. 5 Magnetic axial force *Fx* computed at J_c. The dilution factor $k = 0.25$ characterizes the LHC MQ.

4.2 Minimum azimuthal stress analysis

The stress on the coil mid plane has been analyzed in order to define the distribution of the peak stress as a function of the geometric parameters and of the material properties. Representing the peak stress as a function of the coil width (r_i const.), a minimum can be observed for a certain coil width and for a set aperture (Fig. 6-a). In terms of critical gradient G_c, the larger the aperture, the lower is the gain of G_c if the coil width is increased beyond the point of minimum stress. Moreover, beyond this point, the peak stress itself increases rapidly as G_c saturates to a given value depending on the critical field $B^*_{c2}$and on r_i (Fig 6-b). The analytical results are confirmed by the numerical simulations. The analysis of the stress at the outer radius reveals a trend similar to the peak stress: since the function of $p_\varphi(r_o)$ is simpler, the behaviour of such a function can be studied, thus extending the results to the peak stress. Finally, the presence of a minimum stress depends also on the superconductor properties, i.e. on *k* factor; a mathematical analysis reveals that the radius r_i, beyond which is possible a minimization of the stress, is a linear function of the dilution factor. The corresponding coil width has been found to be equal to $0.55r_i$ in all the cases analyzed. The same considerations hold for a Nb_3Sn quadrupole magnet.

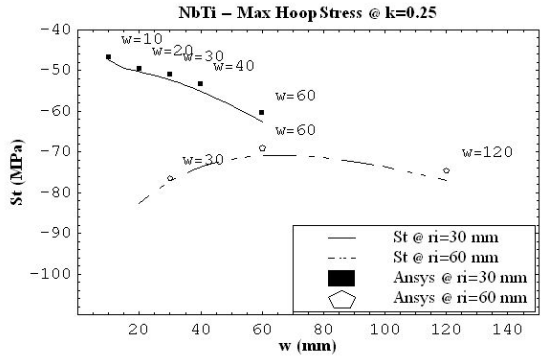

a) p_φ for a NbTi cable @ J_c, keeping the aperture radius constant for each curve

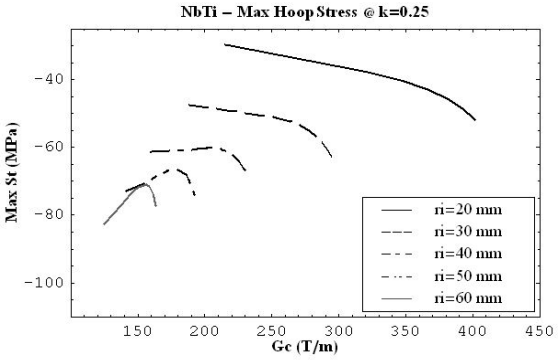

b) p_φ for a NbTi cable as a function of the critical gradient G_c.

Fig. 6 p_φ for a NbTi cable computed at J_c. One can observe the minimum point from an aperture of 40 mm on, while the trend is almost linear for $r_i < 40$ mm, with $k = 0.25$.

5. CONCLUSIONS

Despite of the imprecision in predicting the maximum field inside the coils, analytical approaches provide a good estimate of forces and stresses if an appropriate estimate of the peak field is used [4]. An analytical approach to define the stress distribution leads to reliable results even if the shear effect is neglected; moreover an anisotropic material does not affect the stress distribution at the coil edges. In order to define the magnetic forces and related stresses, a parameterization of the critical current density has been introduced. By analysis of the stress distribution at the coil mid plane as a function of a given current density (J_c in our case), a minimum peak stress can be found, by proper selection of the aperture and the coil width, starting from certain cable features. Finally, since the peak stress exhibits almost the same behavior than the stress at the outer radius, the latter can be studied as a substitute for the peak stress, with a corresponding simplification of the mathematics.

REFERENCES

[1] R. Meuser, Magnetic field for thick cos$n\theta$ winding, Engineering Note M5254, LBL (1978).

[2] R. Meuser, Stresses in a thick cos$n\theta$ winding, Engineering Note M5256, LBL report (1978).

[3] A. Asner, Cylindrical aperture multipoles with constant current density sector windings, CERN Internal Report, SI/Note MAE/69-15, (7-10-1969).

[4] E. Todesco, Electromagnetic design of superconducting quadrupoles, submitted to Phys.Rev. STAB

[5] O. Bruning, et al., LHC Design Report v.1: The LHC Main Ring, CERN 2004-003-VI, 2004

[6] A.V. Zlobin, V.V. Kashikhin, J.B. Strait, Aperture limitations for 2nd generation Nb_3Sn LHC IR quadrupoles, PAC 03, JACoW (2003) 1975.

[7] S. Caspi, P.Ferracin, Limits of Nb_3Sn Accelerator Magnets, PAC'05, JACoW (2005) 107.

BIBLIOGRAPHY

G. Genta, Principi e Metodologie della Progettazione Meccanica (Levrotto e Bella, Torino, 1989).

F.M. Asner, High Field Superconducting Magnets (Oxford Science Publications, 1999).

FERMILAB HF DIPOLE & QUADRUPOLE: 2D & 3D DESIGN ISSUES

G. Ambrosio
Fermi National Accelerator Laboratory, Batavia, USA

Abstract
This report reviews the design of HFDA (dipole) and TQC (quadrupole) developed at Fermilab using Nb_3Sn superconductor. The focus of the report is on lessons learnt during the design of these magnets and on interesting developments in the design process. The main points can be summarized as: (i) superconducting magnet design is a continuous effort and feedback from all phases of magnet R&D should be taken into account; (ii) the closer we get to material limits (for instance transverse pressure), the more careful and detailed should be the FEM analysis and mechanical modeling.

1. DIPOLE DESIGN

R&D for the HFDA dipole series started about eight years ago under the Fermilab high field magnet project (HFM) and several models have been built. The main features of the HFDA design are:

- Use of ceramic Insulation with ceramic binder (CTD 1008x);
- No interlayer splice (each double-layer coil is wound with a continuous cable);
- Spacers between coils and yoke are used instead of collars;
- The gap between the two iron yoke halves remains always open;
- Coil pre-stress is provided by aluminum clamps and skin (welded or bolted).

Two versions have been developed. The first version has a 28-strand cable with 1-mm strand diameter, the second a 39-strand cable with 0.7-mm strand diameter. The cables had the same width (14.2 mm) in order to have the same coil volume and use the same mechanical structure. The maximum field in the 43.5-mm aperture is about 12 T with a J_c of 2000 A/mm^2 at 4.2 K, 12 T. More details about design and fabrication are given in Refs. [1-2], and recent results are shown in Ref. [3].

1.1 Feedback to the Design

The most interesting feedback into the design from fabrication and test of the dipole models has been:

- Fine tuning of the FE models due to measurements of material properties on samples fabricated as close as possible to the real coils, and due to measurements on mechanical models, and on real coils during magnet assembly and test;
- Modification of magnet assembly procedure in order to keep maximum coil stress below 125 MPa during all stages of fabrication and test, due to measurement of PIT (Powder In Tube) conductor degradation under transverse pressure;
- Very positive feedback about the use of a ceramic binder for coil fabrication;
- Change of splice region design and splicing procedure: extension of the lead-end saddles leaves more space for the Nb_3Sn cable to lead splice and support of the cables during splicing;
- Conductor design: the choice of the conductor (strand and cable) and of its reaction process have to be carefully made taking into account the stability limit of the conductor compared with magnet operating current. The effect of flux jumps on field quality require further study;

- Turn displacements due to fabrication process are larger in Nb_3Sn than in NbTi magnets. Causes should be identified and possibly corrected.

2. QUADRUPOLE DESIGN

The R&D for the TQC (Technological Quadrupole using collars) started about two years ago under LARP (LHC Accelerator Research Program). The first model should be tested in summer 2006. The main feature of the mechanical design is the use of collars, which provide partial pre-stress (70 MPa peak stress). Total pre-stress (140 MPa peak stress) is obtained after skin welding, and remain the same during cool-down (150 MPa peak stress). More details about the design can be found in [4].

2.1 Feedback and 3D Mechanical Analysis

Several mechanical models have been assembled and tested in order to verify the concept, and optimize the mechanical design. The mechanical models showed that collars can be used to reach 70 MPa coil pre-stress without overloading and maintaining stress distribution within +/- 5 MPa, by using tapered keys and a multi-step (more then 4) collaring process.

A small asymmetry was found in the practice coils used for a mechanical model. Investigations are in progress in order to understand if the asymmetry is due to coil fabrication process or to previous tests performed on the same practice coils.

A detailed 3-D ANSYS model of the magnet return-end (non lead end) has been created and is generating the first results. This model has several interesting features such as the use of coordinate systems following each turn along the end in order to allow using orthotropic cable properties with the correct orientation in all parts of the model; and the use of the ANSYS birth-and-death element capability to simulate the cracking of epoxy under load and the crack propagation. Several parameters (axial module of collar pack, bond strength between conductor and end parts, coil thermal contraction, coil/collars friction coefficient) have been experimentally measured on samples as close as possible to the real magnet. Preliminary results show the opening of a gap between the pole and the pole-turn on the second layer at different currents depending on end pre-load.

ACKNOWLEDGEMENTS

The design, fabrication, and test of the magnets presented in this report are the result of the excellent work of the whole High Field Magnet group at Fermilab.

REFERENCES

[1] G. Ambrosio, et al., Development of the 11 T Nb_3Sn Dipole Model at Fermilab, IEEE Trans. Appl. Supercond. 10 1 (2000) 298.

[2] D. Chichili, et al., Fabrication of the Shell-type Nb_3Sn Dipole Magnet at Fermilab, IEEE Trans. Appl. Supercond. 11 1 (2001) 2160.

[3] A.V. Zlobin, G. Ambrosio, N. Andreev, E. Barzi, R. Bossert, R. Carcagno, D.R. Chichili, L. Elementi, S. Feher, V.S. Kashikhin, V.V. Kashikhin, M.J. Lamm, I. Novitski, Yu. Pischalnikov, C. Sylvester, M. Tartaglia, R. Yamada, Development and Test of Nb_3Sn Cos-θ Dipoles Based on PIT Strands, IEEE Trans. Appl. Supercond. 15 2 (2005) 1160.

[4] R. Bossert, et al., Development of TQC01, a 90mm Nb_3Sn Model Quadrupole for the LHC Upgrade Based on SS Collars, MT-19, IEEE Trans. Appl. Supercond. 16 2 (2006) 370.

HIGH FIELD ACCELERATOR MAGNET DEVELOPMENT IN JAPAN

A. Yamamoto
High Energy Accelerator Research Organization (KEK), Tsukuba, Japan

Abstract
An advanced accelerator magnet development program is being carried out, in Japan, with focusing on Nb3Al superconductor to be applied for high field magnets expected in the LHC accelerator upgrade program. The general plan and progress are presented.

1. INTRODUCTION

Based on the success of the CERN-KEK cooperative work for superconducting quadrupole magnets for the LHC beam interaction regions [1], further cooperative work is planned on basic research and development for high field magnets (> 10 T) expected in the LHC luminosity upgrade program. The current interaction region quadrupole magnets may need to be replaced with new ones, possibly within 10 years of operation in the high radiation environment. A luminosity upgrade is to be expected in this timeframe, and new quadrupole magnets with large aperture (90~100 mm) and high field gradient (> 200 T/m) will be required. The maximum field in the coil will reach 12~15 T. Advanced superconductors having greater critical current density in higher fields and better mechanical stability will be inevitably required. We aim to develop Nb_3Al superconductor and model magnets to establish the technology for the high field superconducting magnets for the LHC luminosity upgrade.

2. DEVELOPMENT OF Nb_3Al CONDUCTOR

Nb_3Al conductor has better strain tolerance and will exhibit promising high-field characteristics, if the critical current density can be improved in a field region of 12–15 T and the stabilizer can be appropriately attached [2]. We have been developing the Nb_3Al conductor, as an interesting candidate for future high-field accelerator magnets, in cooperation with National Institute of Material Science (NIMS) [3]. The critical current density has been improved, as summarized in Table 1, by using a new method, the so-called Rapid-Heating and -Quenching (RHQ) technique originally developed at NIMS [2]. Various optimization studies of the wire parameters and heat treatment conditions have been performed using wires of ~0.8 mm in diameter with relatively small filaments size (~50 μm). We plan to further improve the current density to ~2000 A/mm^2 at 12 T in the coming few years.

Table 1
Critical current density of Nb_3Al superconductor

	Year 1998	Year 2005
J_c at 10 T (A/mm^2)	1334	2150
J_c at 12 T	1000	1650
J_c at 15 T		1000

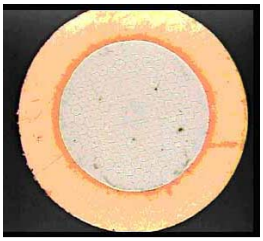

Fig. 1 Cross-section of Nb_3Al conductor stabilized with Cu.

For the stabilization of the superconductor, we have developed an electroplating technique and succeeded to deposit a copper layer on the surface of the wire. Figure 1 shows a cross-section of the copper-stabilized Nb_3Al wire. We plan to extend the unit length to ~100 m by using a newly developed electroplating machine, and Rutherford cable will be made with the Cu-stabilized strands.

3. RACE-TRACK COIL DEVELOPMENT

A series of short race track coils will be developed to evaluate the cable performance in the field level of 15 T. The coils are to be assembled with iron yoke in a common coil configuration [4] to maximize the peak field in the coil, with a very compact hybrid coil configuration consisting of Nb_3Al and NbTi coils. The design parameters of the model magnet are summarized in Table 2, and the conceptual cross section of the model magnet, with flux lines, is shown in Fig. 2.

Table 2
Race-track coil parameters

Coil Layers	2 (Nb_3Al) + 3 (Nb-Ti)
Turns / layer	35
Coil cross section (h x v)	7.4 mm x 82.5 mm
Coil outer dimensions	250 mm x 500 mm
Peak field in the coil	> 14 Tesla
Current density in the coil (non copper)	2000 A/mm2
Cable dimension	1.25 x 7.4
No strand	20
Strand diameter	0.7 mm

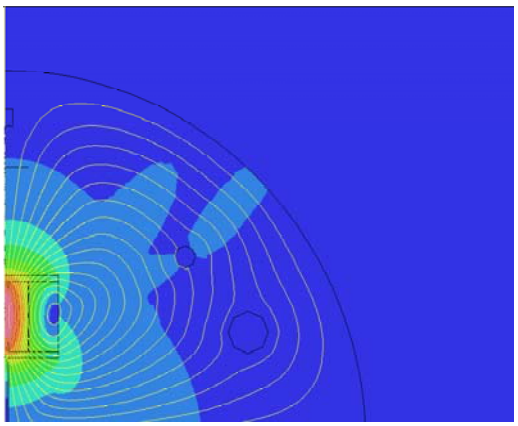

Fig. 2 Cross-section of the race-track, common coil model magnet.

4. SUMMARY

We are planning to develop high field superconducting magnet technology for the LHC accelerator luminosity upgrade with a focus on Nb_3Al superconductor, which has certain advantages relating to its tolerance concerning mechanical stress, and features a relatively higher critical current density in the field level of 15 Tesla. The program is in to be carried out via a series of development studies - for the Nb_3Al strand with copper stabilizer, cabling, and model magnet fabrication with race-track coils in a common coil configuration. Future scope will include the development of high-field superconducting magnets for the LHC beam interaction region, with fields of up to 15 Tesla in the coil. The basic R&D program is to be completed within 3 years, in order to prepare for this further development.

ACKNOWLEDGEMENTS

The author wishes to thank Dr. R. Gupta of BNL for his kind cooperation and various discussions on the design of both race-track coils and common coil magnets.

REFERENCES

[1] Y. Ajima et al., The MQXA Quadrupoles for the LHC Low-Beta Insertions, Nucl. Inst. and Meth.,A 550 (2005) 499.

[2] T. Takeuchi, Nb_3Al Conductors for High-Field Applications, Supercond. Sci. Technology 13 (2000) R101.

[3] K. Tsuchiya et al., Nb_3Al Wire Development for Future Accelerator Magnets, MT-19, IEEE Trans. Appl. Supercond. 16 2 (2006) 1204.

[4] R. Gupta et al., Common Coil Magnet Program at BNL, ASC-2000, IEEE Trans. Appl. Supercond. 11 1 (2001) 2168.

Session: Main issue design of cycled (Hz range) magnets

MAGNET DESIGN OPTIONS FOR FAIR PROJECT

G. Moritz
GSI, Darmstadt, Germany

Abstract

Up to now only one synchrotron (Nuclotron at JINR, Dubna) has been equipped with fast-pulsed superconducting magnets. The demand for high beam intensities leads to the requirement of fast-pulsed, periodically cycling magnets for synchrotrons. An example is FAIR (Facility for Antiproton and Ion Research) at GSI, which will consist of two synchrotrons in one tunnel and several storage rings. The fast field ramp rate and repetition frequency introduce many magnet design problems and constraints in the operation of the accelerator. Persistent currents in the superconductor and eddy currents in wire, cable, iron and vacuum chamber reduce the field quality and generate cryogenic losses. A magnet lifetime of 20 years is anticipated, resulting in up to 10^8 magnet cycles. Therefore special attention has to be paid to material fatigue problems. R&D work is being done in collaboration with many institutions to reach the requirements mentioned above. Model dipoles were built and tested. The results of the R&D are reported.

1. INTRODUCTION

GSI plans to construct a new accelerator complex, the international "Facility for Antiproton and Ion Research" (FAIR) [1], which will provide high intensity primary and secondary beams of ions and antiprotons for experiments in nuclear, atomic and plasma physics. It will consist mainly of 2 synchrotrons, SIS100 (100 Tm rigidity) and SIS300 (300 Tm rigidity), in one tunnel, and several storage rings. Figure 1 gives an overview of the facility.

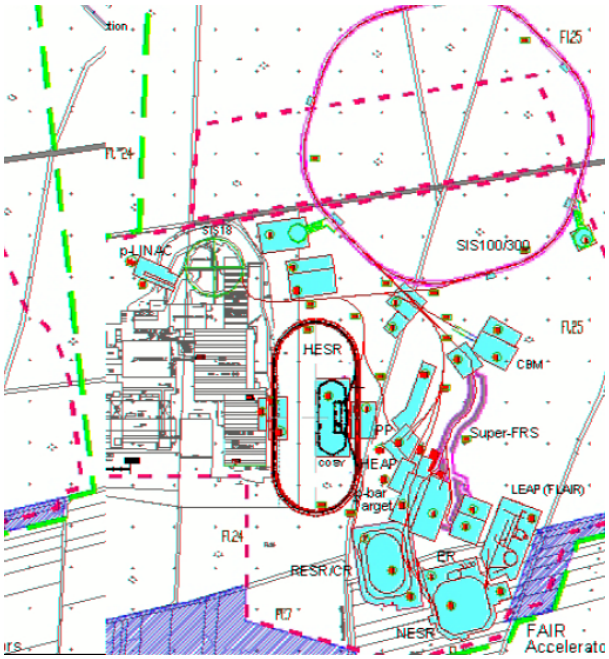

Fig. 1 Topology of FAIR.

The SIS100 is the heart of the facility. It will accelerate ions and protons at a high repetition rate and either send them to the targets for Radioactive Ion Beam (RIB) or Antiproton Beam production or to the SIS300 for further acceleration to higher energies. The CR storage ring complex will cool the secondary beams and accumulate the antiprotons. HESR and NESR are the experimental storage rings for antiprotons and ions, respectively.

In order to reach the required high intensities, the magnets of the synchrotrons have to be rapidly pulsed at a high repetition frequency (AC-operation). The required dipole ramp rate is 4 T/s for SIS100 (at about 1 Hz) and 1T/s for SIS300, with a duty cycle of 50%. All storage rings except the NESR/RESR will be operated as DC rings. The NESR/RESR maximum dipole ramp rate will be 1 T/s, because of the short life time of the decelerated radioactive ions.

This paper deals only with rapidly-cycling superconducting accelerator magnets needed for FAIR. R&D policy was to restrict the activities at GSI to design and coordination work and to the operation of a test facility for model and prototype magnets. Collaborations were established with institutes having experience with magnets similar to those of FAIR, concentrating at the beginning on dipole R&D and transferring the results to quadrupoles, afterwards. At the earliest possibility, industry should be involved in the R&D.

As SIS100 and SIS300 are to be installed in the same tunnel, their different rigidities lead to different requirements for the magnets, which are compiled in Table 1. Consequently, different design approaches are necessary. These are described later on.

Table 1
Main superconducting magnets of the synchrotrons.

	Number of magnets	Aperture (mm)	Magnet length (m)	Max. field / Max. gradient	Max. ramp rate
SIS100:					
Dipoles	108	130 × 60 (gap height 66)	2.8	2.1 T	4 T/s
Quadrupoles	168	135 × 65	1.1	32 T/m	61 T/m/s
SIS300:					
Dipoles	108	86 (circular) (coil inner diameter:100)	2.9	6 T	1 T/s
Quadrupoles	156	86 (circular) (coil inner diameter:100)	0.9	90 T/m	15 T/m/s

2. R&D TOPICS

Fast cycling of magnets in the Hz-range leads to special problems, which are to be adressed by the R&D. The R&D is directed towards the most critical issues. These are:

- Eddy and persistent currents;
- Mechanical structure and lifetime of the magnets.

Further R&D is compiled under other topics.

2.1 Eddy and persistent currents

Due to the changing magnetic field, eddy currents are created in the coil, yoke, structural elements, and the beam pipe. These eddy currents affect the field quality and create large steady-state AC losses. First, it is necessary to minimize these effects. Second, good heat removal is necessary, to remove the non-avoidable losses.

The SIS100 main magnet losses are dominated by the dynamic load, which amounts to approximately 75% of the total load. The following magnet parts contribute to the losses:

- Yoke (hysteresis and eddy current loss);
- Structural elements (hysteresis and eddy current loss);
- Beam pipe (eddy current loss);
- Strand:
  - hysteresis loss ~ filament diameter d → reduce filament size
  - filament coupling loss ~ tp^2/ρ → reduce twist pitch tp, increase matrix resistivity
- cable (Rutherford or similar):
  - strand coupling loss due to R_a → increase R_a (coating)
  - strand coupling loss due to R_c → increase R_c (cored cable)

Besides reducing the AC losses in the conductor and the cable, one has to provide appropriate cooling and allow for local current redistribution in the cable. All 3 measures together must allow an appropriate temperature margin, under AC operating conditions. The R&D is therefore directed at development of small filament size wires (2 to 3μm) and a cored cable.

2.2 Mechanical structure and lifetime of the magnets

The fast cycling requirement leads to an enormous number of cycles during the planned lifetime of 20 years. 200 million cycles are expected for SIS100, 1 million cycles for SIS300. Therefore, the movement of any magnet part during cycling is to be minimized. R&D on material fatigue and crack propagation for critical parts is to be performed.

2.3 Other topics

- Magnet quench protection requires special measures because of the high ramp rate, which requires a high charging voltage of the magnet strings. Therefore, stacks of diodes or warm bypass elements are necessary.
- Because the iron yoke of the magnet is at cryogenic temperature, one has to look for a yoke material with the best compromise between a high saturation flux density and low hysteresis losses.
- Since field quality is ramp rate dependent, measurements of the field quality during ramping are needed.

3. SUPERCONDUCTING MAGNETS FOR SIS 100

These superferric magnets are very similar to those of the Nuclotron ring at JINR, Dubna [2]. The conductor ('Nuclotron-cable') was especially designed to cool large steady-state head loads of rapidly cycling magnets through the use of two phase helium, flowing through a copper-nickel-tube with low hydraulic resistance. The strands, wound around the outside of the tube, are indirectly cooled.

R&D goals are:

- Improvement of DC field quality (2D / 3D);
- Guarantee of long term mechanical stability ($2 \cdot 10^8$ cycles);
- Reduction of eddy / persistent current effects (may affect field quality, losses).

Since these magnets are iron dominated, no influence of the eddy/persistent currents on field quality was observed. However, large cryogenic losses occurred in the original Nuclotron magnets (dipole coil 30%, dipole yoke 70%). The yoke losses consist of hysteresis losses in the iron and eddy current losses in iron and structural support elements of the magnet. Figure 2 shows the reduction of the losses during the R&D phase [3].

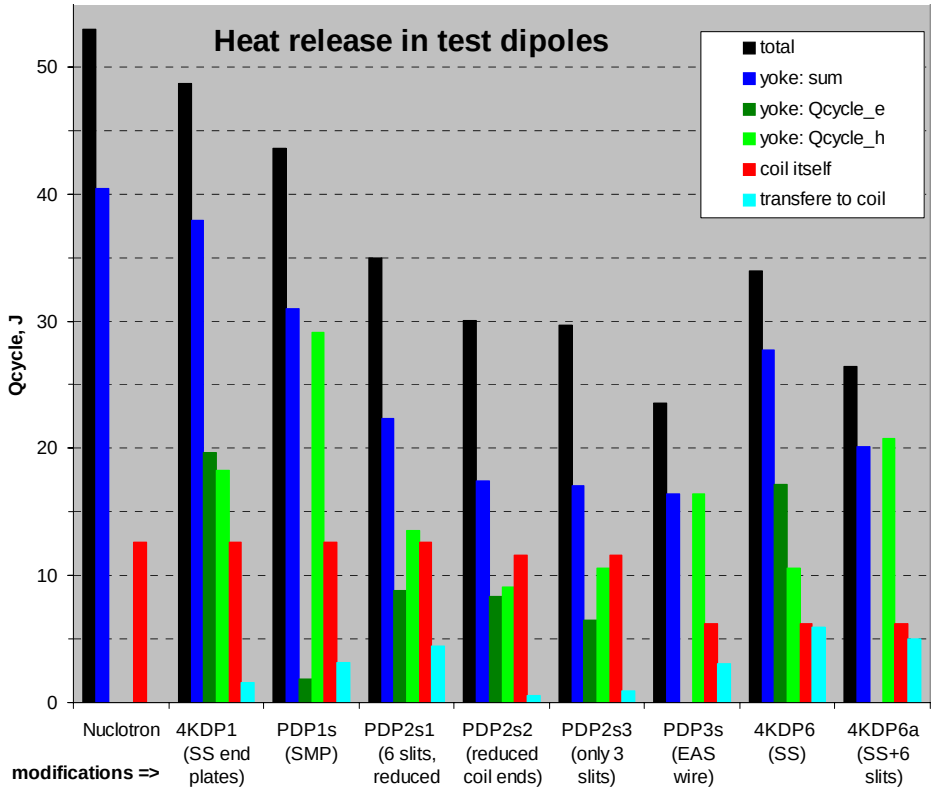

Fig. 2 Loss reduction during R&D phase for the triangular cycle 1Hz, 2T.

Detailed investigations were made in order to guarantee the 20-year lifetime of the magnet. The use of a conductor support structure (under development, Fig. 3) will reduce the previously existing high point-to point loads between adjacent conductors, due to Lorentz forces, and allow accurate positioning of the conductors [4].

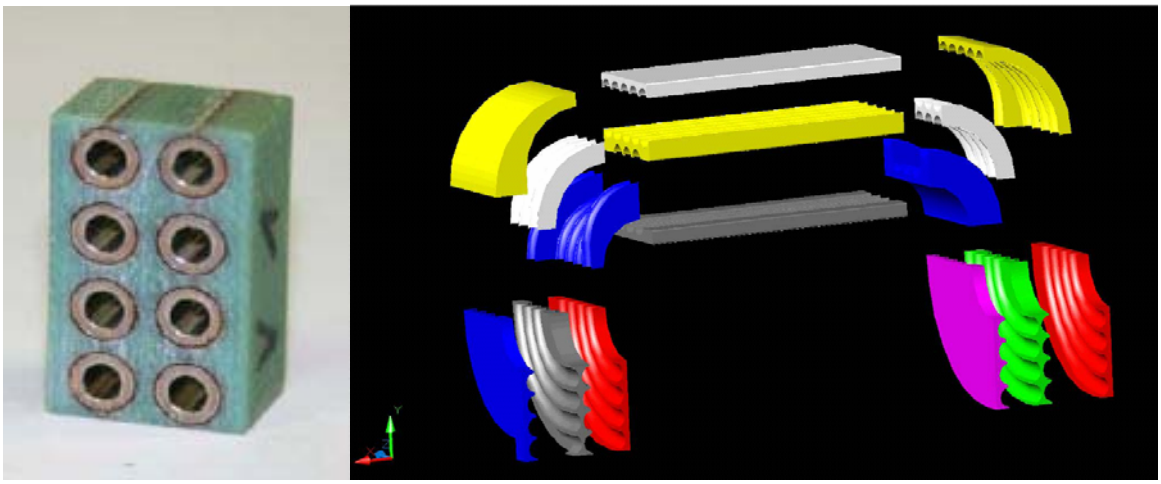

Fig. 3 coil support structure of SIS 100 dipole

Figure 4 shows the lamination cross section of the SIS 100 quadrupole. The slits improve field quality and reduce the eddy currents due to longitudinal field components of the fringe field.

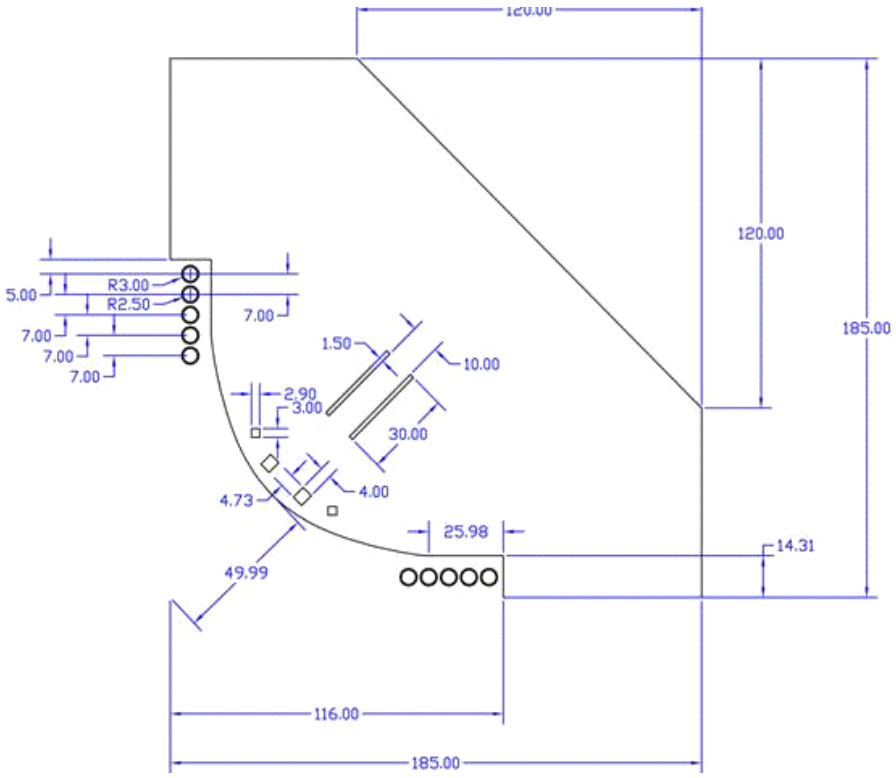

Fig.4 Lamination cross section of SIS 100 quadrupole.

The load line in Fig. 5 shows that these superferric magnets operate at a high saturation level. This is not a problem from the power consumption point of view, but the operating margin is reduced.

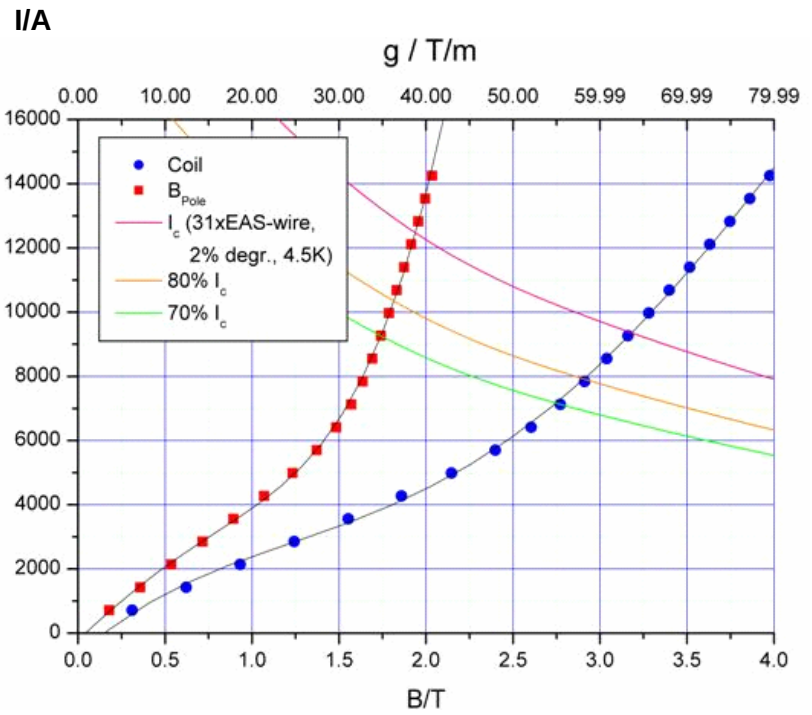

Fig. 5 Load line of the SIS 100 quadrupole.

4. SUPERCONDUCTING MAGNETS FOR SIS 200 / 300

4.1 Dipole GSI 001

R&D was started at BNL with the construction of a 4T, 1 T/s dipole, called GSI001, built very similarly to the RHIC dipole. It was designed to demonstrate the feasibility of a rapidly cycling cosθ dipole and to investigate related topics such as quench behaviour, AC field quality, and cryogenic losses [5,6].

Table 2 shows the difference between the RHIC dipole and GSI 001.

Table 2
Parameters of RHIC dipole and GSI 001.

	RHIC dipole	RHIC type dipole GSI 001
Superconducting wire	NbTi-Cu (1:2.25) filament diameter 6 mm twist pitch 13 mm no coating	NbTi-Cu (1:2.25) filament diameter 6 mm twist pitch 4 mm Stabrite coating
Rutherford cable	no core	2 x 25μm stainless steel core
Coil	phenolic spacer Cu wedges	stainless steel collar (G-11CR keys) G-11CR wedges
Yoke	H_c = 145 A/m 6.35 mm laminations	H_c = 33 A/m, 3.5% Silicon 0.5 mm laminations, glued

4.1.1 Ramp rate limitation of the quench current

Figure 6 shows only a small degradation of the quench current in the region of interest (1 T/s), due to moderate AC heating. This is because of good heat removal. Current redistribution is possible due to the low adjacent resistance of the cored Rutherford cable.

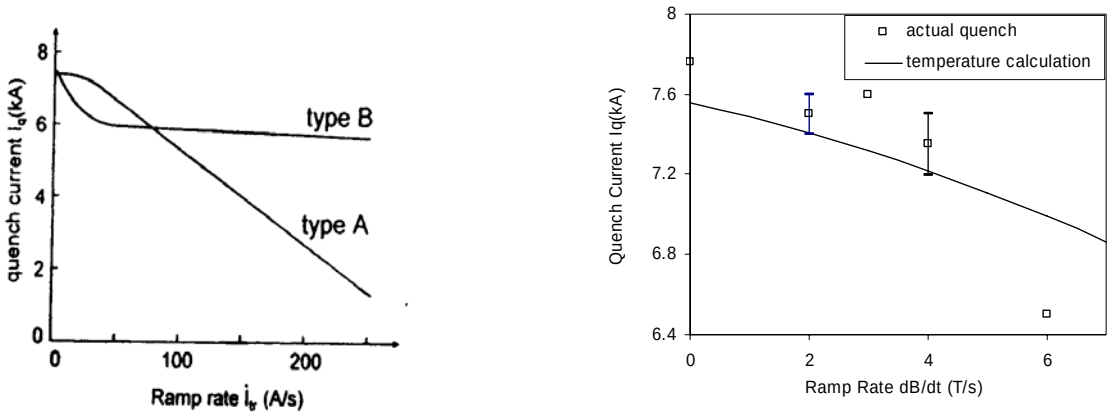

Fig. 6 Type definition of ramp rate behavior (left) and measured ramp rate dependence of GSI 001 (right).

4.1.2 Cryogenic losses

Cryogenic losses at the 4K level were measured with the V-I method as a function of the ramp rate and the maximum field during a triangular cycle (Figure 7). The lines show calculated losses, using experimental values of wire and cable resistances, effective filament diameter and iron hysteresis [7]. The hysteresis part is in good agreement, while the measured eddy current contribution (slope) is higher than calculated, especially at higher field levels. Most probably we have here an unknown eddy current contribution.

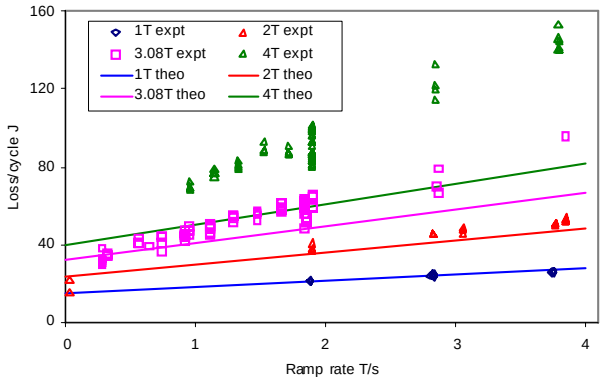

Fig. 7 Cryogenic losses of GS I001 for a triangular cycle.

4.1.3 AC field quality

BNL has developed a stationary harmonic coil system, which allowed a measurement of the field harmonics during the ramp. Figure 9 shows the allowed harmonic b3 (difference between down and up) as a function of the ramp rate up to 4 T/s.

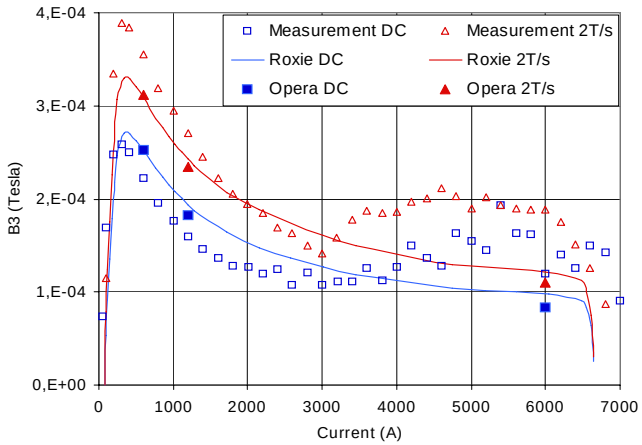

Fig. 8 Transient behaviour of the normal sextupole harmonic of GSI 001.

ROXIE and VF Opera 2D code were extended to implement AC effects. Figure 8 shows good agreement between the measured and calculated sextupole component B3 [8].

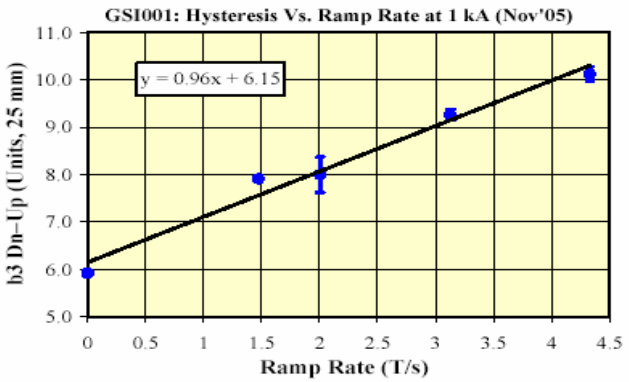

Fig. 9 Comparison of measured and calculated b3 at radius of 25 mm.

DC skew terms are small. However, large AC skew terms a_2 and a_4 were measured, indicating a top-down asymmetry. Simulations are underway to explain this effect. The magnet GSI 001 will be tested next month in the new test facility at GSI, cooled with forced flow single phase helium.

4.2 SIS 300 dipole

A conceptual design study was made at IHEP, Protvino based on the design of the UNK dipole. The main assumptions / results were:

- cooling: one phase supercritical Helium @ 4.4 K, with internal re-cooling;
- temperature margin: 1.0 K with the option of lowering the helium temperature;
- collared coil supported by iron shell (taking part of the load);
- strand diameter: 0.825 mm;
- filament size: 3.5 μm;
- Rutherford cable: 36 strands with core (LHC dipole outer layer cable dimensions);
- quench protection: magnet not self-protecting - needs heaters.

Meanwhile, the technical design (2D/3D magnetic design, FEM mechanical analysis, thermal analysis, quench analysis) is almost finished. Figure 10 shows the 2D coil design and the FEM model for mechanical analysis. The maximum operating temperature of the conductor is 4.76 K (see Fig. 11). The minimum critical temperature (at 6 T) of the turn closest to the pole is 5.7 K, so the temperature margin is ~ 0.9 K.

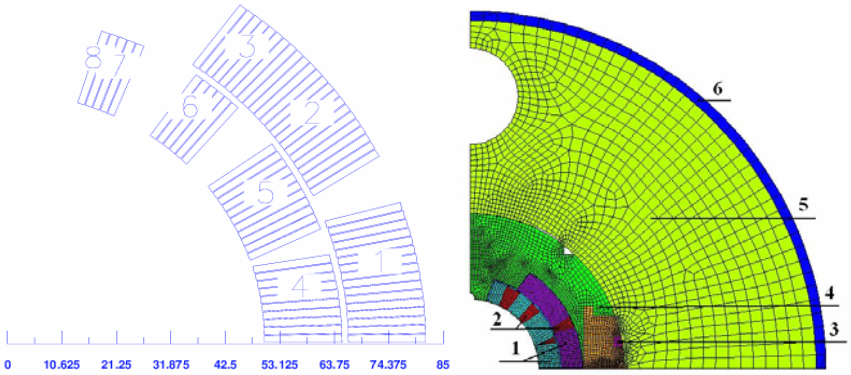

Fig. 10 2D coil design (left) and FEM model for mechanical analysis of SIS300 dipole (right).

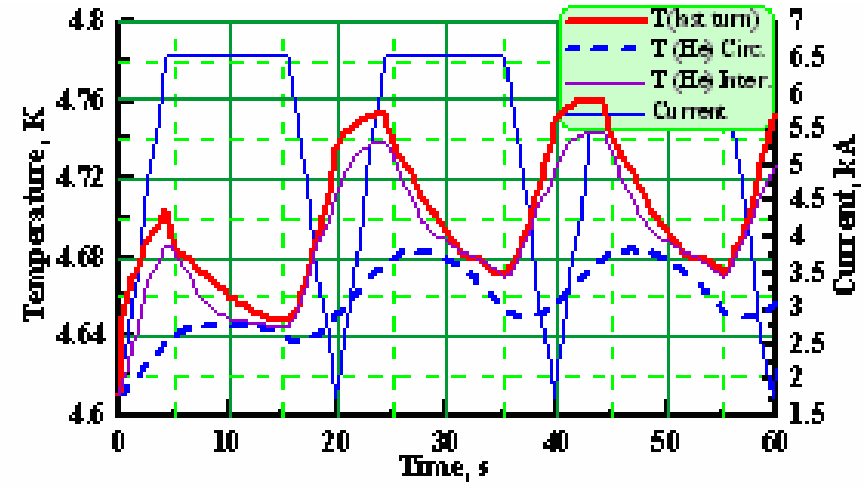

Fig. 11 Highest temperature in a magnet of SIS 300 dipoles during ramping.

4.3 Further work for SIS 300 magnets

Dipole: tooling design and production

winding test of a short model coil

construction and test of model dipoles (cold masses)

prototype construction and test (project 'Disco-Rap', INFN)

Quadrupole: Work packages/milestones are defined within a project 'SupraPulse' by CEA Saclay

5. SUMMARY

Rapidly cycling sc magnets are foreseen for the synchrotrons of FAIR. The R&D to develop these magnets, including low loss conductor, is under way. First dipole models have been built and tested.R&D continues on quadrupoles and full size magnets.

ACKNOWLEDGEMENTS

I am greatly indebted to all members of the collaborations, to our consultants, and to the members of the GSI magnet group for their dedicated work.

REFERENCES

[1] FAIR- Facility for Antiprotons and Ion Research, www.gsi.de

[2] A.M.Baldin et al., Superconducting fast cycling magnets of the Nuclotron, IEEE Trans. Appl. Supercond. 5 (1996) 875.

[3] A. Kovalenko et al., New Results on Minimizing AC Power Losses in a Fast Cycling 2T Superferric Dipole with a cold Yoke, IEEE Trans. Appl. Supercond. 16 2 (2006) 338.

[4] EU FP6 'DIRAC secondary Beams', 1st Annual Report, Annex 3: Design report on structural analysis (Deliverable 53 of task 22)

[5] P. Wanderer et al., Initial Test of a Fast Ramped Superconducting Model Dipole for GSI's Proposed SIS 200 Accelerator, PAC'03 JACoW (2003) 2162.

[6] A.K. Ghosh, Cable Design for Fast Ramped Superconducting Magnets (Cos-θ Design), WAMS2004, Archamps

[7] M.N. Wilson et al., Measured and Calculated Losses in Model Dipole for GSI's Heavy Ion Synchrotron, IEEE Trans. Appl. Supercond. 14 2 (2004) 306

[8] G. Moritz et al., Recent Test Results of the Fast-Pulsed 4 T Cosθ Dipole GSI 001, PAC'05 JACoW (2005) 683.

[9] I. Bogdanov et al., Final Report on the Research and Development Contract: Design of 6 T Superconducting Dipoles for the SIS 300, MT-INT-Bogdanov-2003-001

MAGNET DESIGN OPTIONS FOR THE LHC INJECTION CHAIN

G. A. Kirby
CERN, Geneva, Switzerland

Abstract
The report presents some initial results from a study looking into the design requirements for a fast ramped dipole magnet that could form the main magnet used in the upgrading of the CERN SPS. It gives a broad look at the parameters that would need to be addressed, and identifies the direction that the R&D would be required to take if this type of magnet were to be needed.

1. INTRODUCTION

The design objectives used for the present study are summarized in Table 1.

Table 1
Tentative design objective for a superconducting SPS magnet

Peak field	4.5 T
Good field region (diameter)	80 mm
Field quality	± 2 units
dB/dT [T/s]	1.5 T/s
Number of cycles (20 years)	1 M Cycles
Radiation load [W/m]	10 W/m
Peak radiation load [W/m]	30 W/m
Duration of a cycle [seconds]	12 s
Time of exposure	60 k hours
Typical refrigeration power W/m	10 W/m
Effective duty-cycle	0.4
Magnet length [m]	6 m
Number of dipoles	750
Maximum voltage	1 kV

The typical operational cycle is shown in Fig. 1.

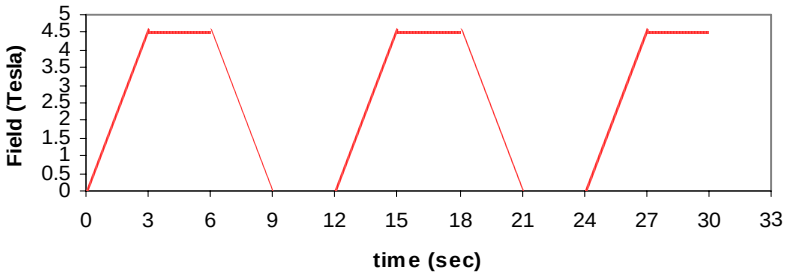

Fig.1 Typical cycle.

2. CONDUCTOR

The type of cable we may consider using is shown in Figs. 2 and 3. For use in this magnet the cable losses must be minimized, and to do that the following parameters should be kept as small as possible: filament diameter, strand diameter, filament twist pitch (this is approximately limited to 6 times the strand diameter), cable twist pitch (this is approximately limited to 7 times the cable width). The conductor development program must include a chapter on minimizing the twist pitches. The control of R_c and R_a is also important, and good results have been obtained by introducing a foil in the center of the cable. If a high resistance coating is developed the foil could possible be removed. Cooling is important, so an open structure will be helpful. A low cable edge compaction could help improve cooling. An open as possible cable would also help cooling, with the constraint that the cable must not collapse. The cable width plays a major role in the losses, as do the exact composition and layout of the constituent strands. Comparing designs of magnet with a Cu matrix as a function of magnet aperture, it is found that the losses reduce from 6.8 to 5.9 and 2.8 W/m as one passes from 100 mm diameter to 80 mm and 60 mm. The heat loss per meter is reduced from 6.8 to 3.8 W/m for the 100 mm diameter aperture magnet with the introduction of a CuNi matrix and a "fragmented" strand design, i.e. one in which the copper required in the strand for protection is cut into small blocks separated by relatively resistive walls.

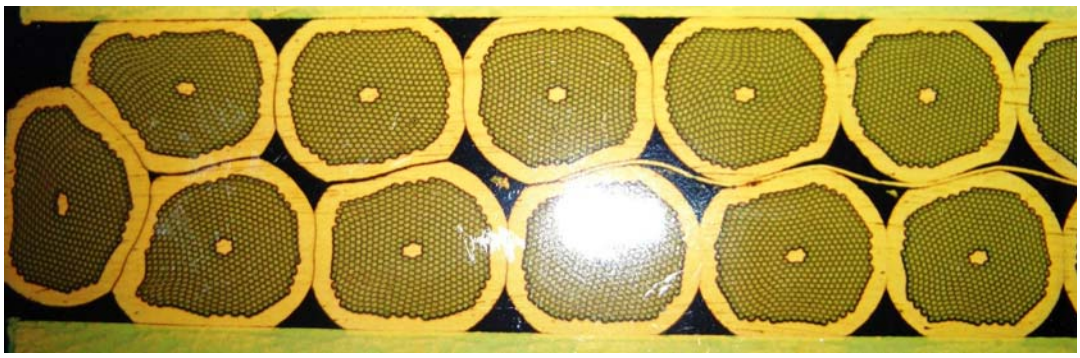

Fig. 2 High compaction - not much space for helium cooling. 0.95 compaction factor.

Fig. 3 Open cable, with 0.78 compaction factor. We also see the foil in the center of the cable.

The target value for the losses is 5 W/m. As the aperture could be about 80 mm, it is clear that a resistive matrix design strand should be developed. R_c and R_a are still not well under control and variations with time due to cycling will force the development of a resistive matrix strand. Radiation losses may increase the aperture further this must be studied.

3. MAGNET DESIGN

It is instructive to compare the merits of 1- and 2- layer designs. If we consider a magnet with 100 mm diameter aperture, the main point is that the losses for the 2-layer magnet are 4.6 W/m compared with 9.0 W/m for the single layer. This is for a Cu matrix: if a CuNi matrix is used the values are reduced further. The argument against a twin layer design is that it needs about 4 times the voltage to drive it at 1.5T/s, requiring about 134V for a single 6m long magnet. As the heat load will certainly be the major technical challenge and the power supply voltage appears to be acceptable, two layers would seem to be the way to go.

3.1 Heating of the winding

The basic assumption is that the cables are cooled by conduction through the insulation on the inner edge of the cable only. Later we will investigate the magnet cooling in more depth. The development of temperatures during a ccle is shown in Fig. 4. The plot shows that most of the heat is generated at low field. The start temperature is recovered after about 1.5 seconds after the end of the ramp. This is important to know, as if it had not, the cable temperature would continue to increase with subsequent cycles. Clearly with a larger temperature difference more heat would be extracted but the cable would finally run at a higher average temperature (assuming it remained superconducting). The peak temperature rise occurs at the end of the down ramp. This is not critical, as with no current the magnet cannot quench. The important moment is at the end of the up ramp.

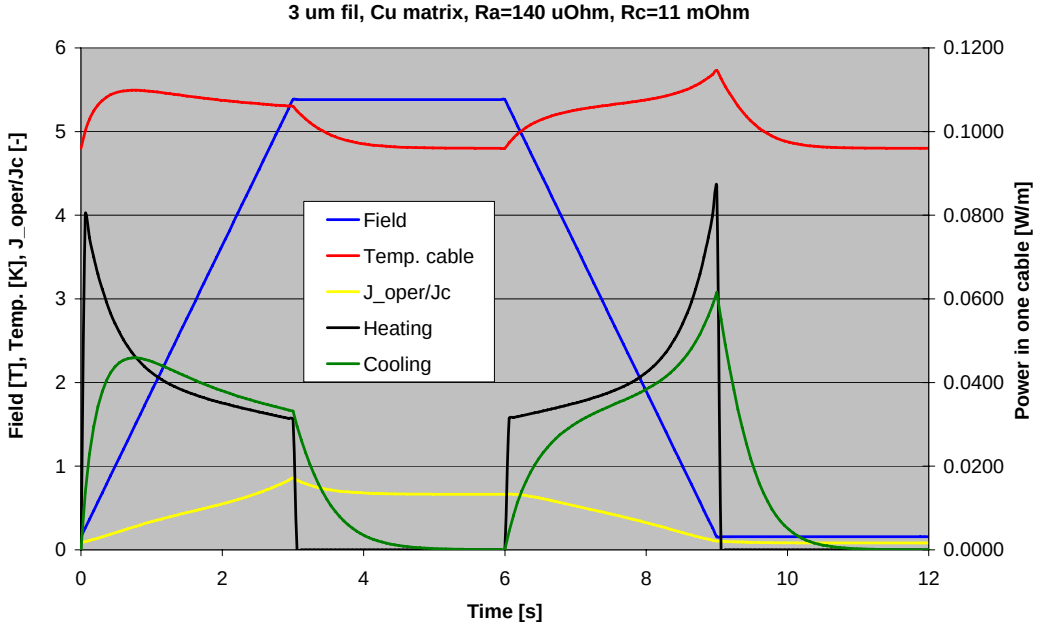

Fig. 4 Plot showing the evolution of temperature in the winding during a cycle.

This plot is a good tool to understand the process. The final cycle profile is of course likely to change. The final temperature margin will depend on cooling that can be achieved and what the final radiation heating is. This must be added into the model.

3.2 Field quality during ramping

In the PowerPoint presentation there is a short film showing the changing field quality during ramping, from injection, assumed to be at 6.6% of maximum field, up to 4.5 T, and down to injection. Each change of color represents 1 unit or $1x10^{-4}$ with respect to the main field. It can be seen that as the field starts to reduce the "good" area actually increases in size for a moment due to errors momentarily canalling out. Clearly field quality is only important when the beam in present.

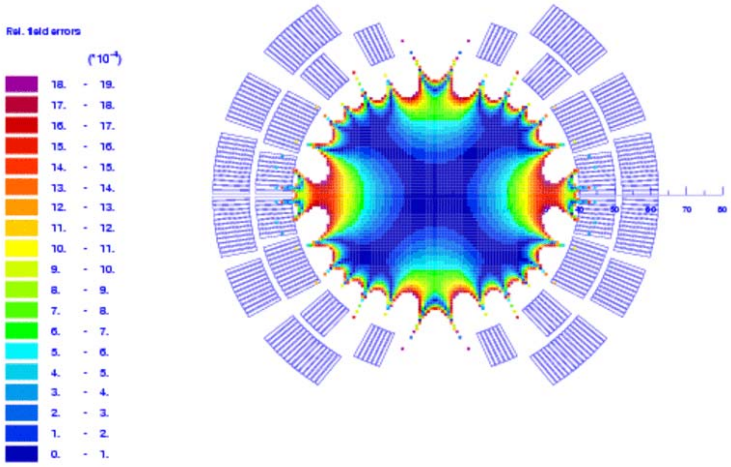

Fig. 5 Example of display of field quality during ramping.

3.3 Comparison of cooling modes

To extract 10 Watts per meter we may investigate two possible modes:

1) Forced convection of supercritical helium (~1–10 W/m) at 2.2 K to 5 K;
2) Static pressurized He II LHC (~1–10 W/m) at < 2.2 K.

Forced convection of supercritical helium between 2.2 and 5 K is the preferred cooling mode. He II at 1.8K is considered due to the high heat extraction through the superfluid. However due the uncertainty of the internal cable resistances R_c & R_a that will finally set the cable working temperature range, He II can be excluded for the now. This is because if the temperature were to rise above 2.2 K then the high cooling conduction through the super-fluid would be lost. This, coupled with the lower C_p of the materials would mean that the temperature rise on the strand would be greater. If we were to lose the super-fluid state the system would fail. For these reasons it is suggested that further work should be concentrated on forced convection in pressurized supercritical helium between 2.2 and 5K.

3.4 Extracting the heat

The magnet must have channels in the coil that allow the helium to convect the heat up to a heat exchanger. The plot in Fig. 6 shows where the heat is generated in the coils Cooling channels will have to be designed accordingly. In the next study we intend to check if natural convection is sufficient to remove the heat, as it could be that this process is too slow to get the heat from the coils to the heat exchanger, in which case the temperature rise would be too high. If this is so, a different design should be made in which helium is pumped through the coils.

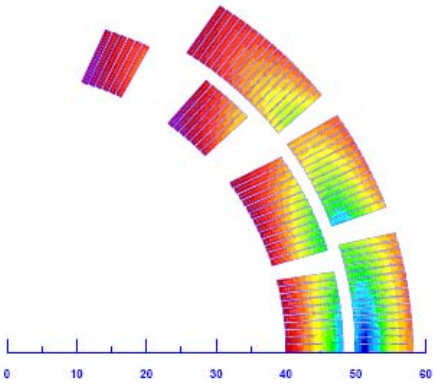

Fig. 6 Coil temperature.

3.5 Choice of material for the wedges

Eddy currents in the wedges would affect the internal heating and field quality. We considered the use of three metals and glass fiber reinforced plastic (GFRP):

- copper with resistivity 1.7 10^{-10} Ohm.m
- bronze with 3.0 10^{-8} Ohm.m
- stainless steel with 5.0 10^{-7} Ohm.m
- GFRP – very big – 10 10 $^{+(20 \text{ or } 30)}$

The losses were calculated to be:

- copper: 22.03 W/m
- bronze: 0.125 W/m
- stainless steel: 7.49 mW/m

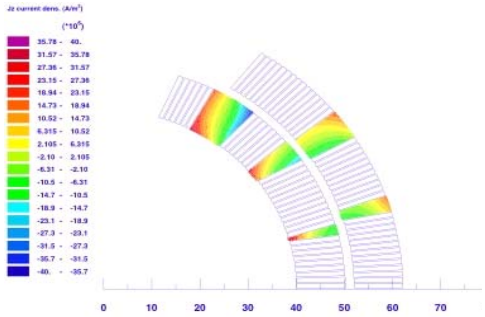

Fig. 7 Heating due to eddy currents.

The impact on field quality is not negligible for copper. The eddy-current density is at about 1/10 of the transport current density in the cables, giving Δb_3 of about 2 units. For the other materials the eddy-currents do not affect the field quality.

The conclusion is that the wedges should preferably be GFRP.

3.6 Mid-plane gap

A mid-plane gap may be needed to allow radiation to exit without overheating the coils. The size of the gap for this magnet is not yet known, however to try to understand the effect on the field quality and strength a number of designs were made. It was found that the area of good field quality was significantly reduced for a gap 2 to 3 mm from the mid-plane: this is illustrated in Fig. 3. More work is needed to correctly size the gap - if it is needed.

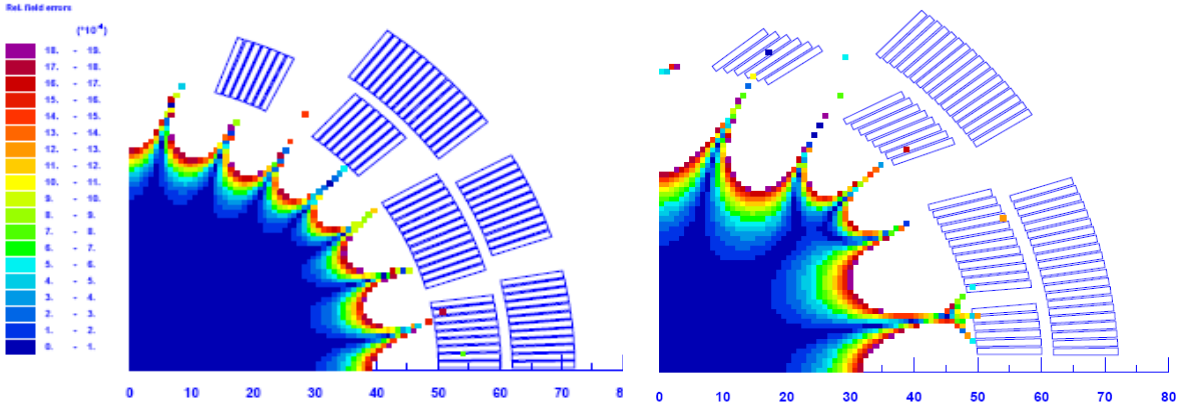

Fig. 8 Effect on field quality of introducing a mid-plane gap.

3.7 Quench simulation

Using the standard LHC quench heaters to protect the coil and typical LHC quench detection times. This particular single 6 m long magnet seemed to be over-protected with only a small temperature rise (see Fig. 9). It is clear that the design of the magnet must take into account the quench performance from the initial design stage. As for this particular design if the copper was reduced the strand could be smaller and so save on heating during operation yet still survive quenching. Quench detection time must be studied as the higher driving voltages may make detection slower.

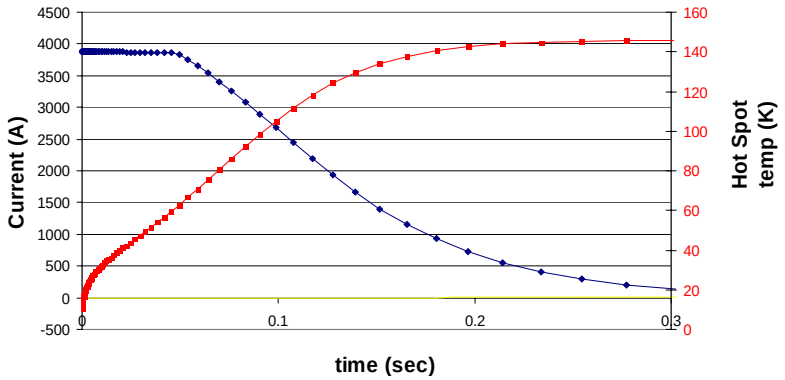

Fig. 9 Current decay and hot spot temperature.

3.8 Mechanical design

As it is required to be able to extract high heat flux from the coil, an open design is needed. The traditional ground insulation forms a tight seal around the coil that would reduce cooling flow of helium. This can be circumvented by using Phenolic spacers. Such spacers are cheap to produce and fast to assemble, so also help keep the cost down. However some development is needed to achieve the tolerances.

3.8.1 Fatigue

Designing the magnet to withstand the fatigue of millions of cycles is important. The failure stress is improved with reduction of temperature. Careful design using finite elements and accelerated testing will be important to achieve a design that can survive. Fermilab was forced to repair several magnets then modify all the remaining undamaged magnets due to a fatigue failure after only 10^5 cycles. Our target is $5x10^6$…

Fig. 10 Effect of fatigue.

3.9 Timescale

An important point not covered in the presentation is the estimate of the time needed to develop such a magnet. If LHC were to decide on this magnet it would be several years before installation could start. About three 3 years should be allocated for development: the time will be spent on the strand design, how to control the R_c and R_a , and life testing (a year or so for each design - possibly several designs in parallel). Then to prepare for production would take about 2 years – to build the tooling and prototype debugging. Then to make the 750 magnet 3 to 4 years... That is, to be realistic, 9 to 10 years from the start. And we have not started!

SUPERCONDUCTING STRANDS AND CABLES FOR CYCLED ACCELERATOR MAGNETS

A. Verweij
CERN, Geneva, Switzerland

Abstract
Calculations have shown that superconducting Nb-Ti strand and Rutherford cable can be used for cycled accelerator dipole magnets in the range of 1-10 T/s and for fields up to about 5 T. This layout has certain advantages with respect to obtaining the most compact magnet (given the high overall engineering critical current density in the coils), which usually results in cost savings and AC loss reduction. A description is given of the general layout of the conductors that will be required to reduce the AC loss to an acceptable level, and the most important issues for R&D are identified. The main focus is on Nb-Ti conductors, as other commercially available superconductors are both very much more expensive and difficult to use

1. INTRODUCTION

It has been demonstrated that, from an AC loss point of view, superconducting Nb-Ti strand and Rutherford cables can be used for cycled accelerator dipole magnets in the range of 1-10 T/s and having fields of up to about 5 T. This approach is conducive to achieving a compact magnet because of a high overall engineering critical current density in the coils, and usually results in cost savings as well as AC loss reduction. Furthermore, this approach benefits from existing experience and available tooling and software.

The purpose of this presentation is to describe the general layout of conductors when it is required to reduce the AC loss to an acceptable level, and to identify the most important issues for R&D. It is clear that the final conductor can only be decided upon after several iterative steps incorporating magnet design and manufacturing possibilities of both magnet and conductor.

The focus is on Nb-Ti conductors. Other commercially available superconductors are very difficult to use due to their brittleness: they are also much more expensive. However, a study on other type of magnets and/or cables should be performed in order to fully understand the possible advantages and drawbacks of alternative designs.

2. CONDUCTORS FOR CYCLING MAGNETS

Assuming some standard features of cos-θ dipole magnets, general conclusions can be drawn with regard to the strand and cable layout.

2.1 Strand layout

For relatively low rates (around 1 T/s) a Cu-matrix strand could be foreseen with filaments of about 2-3 μm. Preliminary tests (by drawing an LHC strand down to half its size) have shown that such a strand has almost no I_C degradation as compared to the 'normal' Nb-Ti strands and can be developed in relatively short time.

Applications at higher rates (2-10 T/s) require not only smaller filaments (0.3-2 μm) but also a resistive matrix, such as Cu-Mn or Cu-Ni, and (especially for the highest rates) an anisotropic central ring and possibly resistive outer shell. Almost no experience exits in industry on such strands and

development has to be done in close collaboration with industry and will take considerable time and several trial billets per company.

A extensive R&D phase is required to study and measure the following attributes of strands:

- Workability during production (including bonding between the different materials, twisting, number of breaks);
- Filament distortion, magnetization and the proximity effect;
- Inter-filament coupling loss;
- Critical current;
- Effect of the resistive matrix (and other resistive parts) on the stability of the strand. It should also be verified if the presence of copper in-between the filament bundles (in a multi-stack assembly) could improve the stability.

2.2 Cable layout

Suppression of the inter-strand coupling currents requires minimum values for the contact resistance R_c in the 1-100 mΩ range, i.e. several orders of magnitude larger than for the LHC dipole cables. Restrictions on R_a are much less severe, and values in the range 10-100 μΩ are sufficient. Both conditions can be met by applying highly resistive coatings on the strand, or by applying moderate coating in combination with an internal resistive strip. The latter is possible due to the allowed anisotropy between adjacent and crossing contacts. Which way to proceed depends mainly on the possibilities for high resistive coating, the workability during cabling and coil winding of cables with internal strips, and the stability. Development for reduction of the inter-strand loss will require major R&D; experiments on cables and possibly coils are needed for validation.

The conclusions given above are in general valid for cos(θ) dipole magnets. Optimization of the conductor layout requires of course a joint approach together with the magnet design. The following aspects of cable design are especially important:

- The minimum amount of copper (and its RRR), needed to safely protect the magnet against burn-out in case of a quench. Any reduction in the amount of copper will reduce the strand diameter and hence significantly reduce the inter-filament losses end eddy current losses;
- The required operating margin, both in terms of temperature and current;
- The number of layers of the magnet, where a double layer magnet can be made with significantly smaller losses, but will result in much larger inductance and hence voltages during ramping;
- The orientation of the conductors, which can easily change the inter-strand coupling losses by a factor of 2;
- The need for special thermal drains which will reduce the peak temperature in the conductor but reduces of course the overall engineering current density;
- The possibility and effectiveness of a multi-strand joint (in stead of a cable-to-cable joint) in order to homogenize the transport current and reduce the BICCs.

Finally it is important to note that loss calculations and predictions often turn out to be significantly different from the real losses. Variations in the magnetization loss, inter-filament loss and inter-strand loss of up to 20%, 100% and 1000% respectively are no exception. It is therefore very important to measure the losses in single strands, cables, but also in the magnet and have a fast feed-back to the conductor design.

HTS COILS COOLED WITH 30 K HEAT PIPES FOR GENERATING CONSTANT AND PULSED MAGNETIC FIELDS

M. P. Oomen, V. Hussennether, N. Prölss, M. Leghissa, H.-W- Neumüller
Siemens AG, Corporate Technology, Erlangen, Germany

Abstract
Siemens is developing rotating machinery with high-temperature Superconductor (HTS) coils operating at around 30 K, which offer lighter weight, smaller volume and less energy consumption than conventional machinery. Research topics are the DC properties of HTS, AC loss, stability and quenching, complex coil geometries, high-current conductors and cooling concepts. The report illustrates these topics by describing the manufacture and test of a 1-Hz pulsed HTS coil cooled by a Neon heat pipe system. HTS can be used to produce DC fields of several tesla and pulsed fields of hundreds of mT in a compact and efficient way. The results are relevant also for accelerator applications.

1. INTRODUCTION

Siemens AG is developing industrial applications for high-temperature superconductors (HTS). Presently the main focus is on rotating machinery: motors and generators. The most advantageous concept is a synchronous machine with superconducting rotor. In a synchronous machine the magnet field rotates with the rotor; so the rotor coils see a constant field and carry DC current. The HTS coils in the rotor form a multipole magnet configuration. The rotor is cooled with liquid Neon in a closed cycle: evaporated Neon is recondensed by GM refrigerators outside the machine. The rotor is mounted inside a rotating vacuum cryostat. The surrounding conventional stator comprises iron and copper windings, using AC current to generate the rotating field.

In 2005 a 4 MW motor / generator with HTS rotor was successfully tested in the Siemens A&D LD systems test facility in Nuremberg. This 2-pole machine operates at 60 Hz, 3600 rpm, generating 10.6 kN of torque [1]. The rotor coils are wound with Bi-2223/Ag/AgMg tapes. In operation the rotor requires 50 W of cooling power at 28 K. Redundant GM coolers can be exchanged if necessary without warming up the rotor. Compared to conventional machines of the same power rating, HTS motors and generators have smaller volume, lower weight and less energy consumption.

2. RESEARCH TOPICS

For this application the following topics are investigated:

2.1 DC properties of HTS tape under operating conditions

HTS-tape manufacturers usually characterize and optimize their tapes at 77 K in self-field. The critical current I_c and the N-value are much higher at operating temperatures around 30 K. Operating fields of several T again decrease I_c. Manageable loss density in compact windings requires operation at ≈0.1μV/cm, clearly below I_c. The dependence of I_c on temperature T and magnet field B should be known in order to design an efficient device.

2.2 AC loss in the HTS tape

Ideally, the HTS tapes in the rotor only see DC current and field. However, imperfect excitation of the rotor causes an AC ripple on the rotor current. Imperfect stator current supply (converter) causes disturbances in the rotating stator field, which lead to field changes on the rotor that are not

completely screened by the damper screen. The frequency spectrum of these variations may be complex. Load changes require fast changes in rotor current. The loss density from these causes should be kept small since the dissipated heat has to be removed from a compact winding structure without large temperature rise. In the literature there are few AC-loss measurements and little theory for combinations of DC+AC current with DC+AC field. Therefore experiments are necessary.

2.3 Stability and quench

Load changes lead to increased dissipation in the coils for a short time. Replacement of a refrigerator (e.g. for maintenance) decreases the cooling power for a short time. Finally, the machine should be able to survive a short in the stator, which causes huge alternating field components on the rotor for several seconds. Thermal and electromagnetic models are therefore required that can answer the general question: by how much and for how long can the current, field and temperature exceed the operating point, without a quench of the HTS coils? From experience, Bi-2223 HTS tapes with their highly conducting Ag matrix usually survive quenches at 77 K. However, at 30 K this is not certain.

2.4 Coil geometry

HTS are usually produced in tape form. Flat racetrack coils are relatively easy to wind, but compact machines require the coils to wrap around the drive shaft. This requires saddle coils with heads are bent in a 3D shape, similar to accelerator dipoles that are bent over the beam pipe. First experiments show that within certain limits, such coils can be produced with HTS, without degradation of the tape.

2.5 High-current conductors

Large machines like power-plant generators will require rotor currents of several kA, much higher than the critical current of a single HTS tape. Several insulated tapes can be combined in a transposed Roebel-type cable, like a conventional transformer cable. In-plane bending of the tapes without degradation requires large bending radius, to the transposition pitch of the cable is typically several m. In this way, conductors of >1 kA at 77 K and several kA at operating conditions are produced.

2.6 Cooling concepts

The heat load in an HTS machine must be transferred from a compact rotating coil set to a stationary refrigerator system. Possible concepts are a cryogen bath (which is expensive with Neon and may be hazardous in case of quench), heat pipes or cooling loops (whose functioning depends on their orientation), or cryogen-free cooling by conduction only. The aim is a reliable and easy-to-operate cooling system that is “invisible” to the customer.

3. 1-HZ PULSED HTS COIL COOLED BY HEAT PIPES

3.1 Coil design and manufacturing

Some of the above-mentioned topics (DC properties, AC loss, stability and quench, cooling concept) were investigated using a specially produced HTS double-pancake coil cooled with Neon heat pipes. The coil is designed to produce 0.2 T of pulsed field at 1 Hz, with 50 ms ramp time, in an inner bore of 200 mm. The compact coil has 370 mm outer diameter and 58 mm thickness. It can be placed in 0.2 T background field, parallel or perpendicular to its self-field. The coil is cooled by a single GM refrigerator that provides 41 W at 27 K. Eddy currents, AC loss, heat transfer to the Neon heat pipes and Lorentz forces were critical points in the design of the coil.

The coil layout is described in detail in [2]. The two identical pancake windings each have 130 turns of insulated Bi-2223/Ag tape. Both current leads are on the inside; a current bridge connects the windings on the outside. A steel heat-pipe system is thermally connected to the upper plane of the coil. The 6 turns of pipe come together in a manifold at the 0° position: each turn is interrupted at the 180° position in order to prevent eddy currents around the pipes. During operation the coil is tilted by a few degrees, with the 180° position lowest, to make the liquid Neon flow downwards in the pipes to this

position. The current leads are at the 180° position. The lower pancake is cooled only via conduction through the upper one. The whole is encased in a rigid GRP former that supports the Lorentz forces.

The heat-pipe system is first soldered together, and tested at 25 bar pressure and under vacuum. It is then embedded in grooves in the top half of the GRP former. The contact plane between heat pipes and winding is filled with Stycast, then mill-cut in order to provide a smooth winding plane and good thermal contact. The first pancake is wet-wound between this plane and a temporary Teflon disc. This disc is removed when the resin has hardened. The second pancake is then wet-wound between the first pancake and the Teflon disc. Finally the bottom half of the GRP former is added.

3.2 Coil testing

Tests at 77 K are performed in a liquid nitrogen bath. For 30 K tests, the coil is suspended in a vacuum vessel, surrounded by a heat shield with super-insulation. A GM refrigerator mounted on the lid of the vacuum vessel cools down a double condenser for two separate Neon heat-pipe systems. One system is connected to the coil; the other one cools the heat shield, where also the current leads, voltage taps and thermometer wiring are thermally anchored.

Test results are described in detail in [2]. At 77 K the critical current is 48 A, slightly better than expected. No degradation of the HTS tape has occurred during coil winding or cool-down to 77 K. At 30K the critical current is 240 A. From 25 K to 35 K the critical current is about 15% lower than predicted with a model that accounts for the temperature distribution in the winding. There may have been some degradation due to non-uniform thermal stresses during cool-down to 30K.

The AC loss with pulsed current is measured with a calorimetric method. At 27 K the design current of 250 A, 1 Hz, can be applied for an indefinite time without quench. The AC loss is then about 20 W, which is removed by the heat-pipe system with a temperature rise less than 2 K in the winding. Several waveforms and combinations of AC and DC are tested. The measured AC loss is compared to predictions from a model developed by Siemens CT [3]. The model tends to under-predict the loss with pure AC and over-predict the loss with DC+AC. The average error is about 25%.

At 27.5 K, where the critical current is 245 A, the coil can carry 260 A stably. The cooling system then removes 22 W locally. At 265 A, with 35 W of local power dissipation, the coil quenches. The quench propagates quickly (fraction of a second) through a large portion of the winding.

CONCLUSIONS

In general the HTS test coil performed as expected. HTS coils operating around 30 K can generate DC fields of several T and pulsed fields of several hundred mT at frequencies of a few Hz. Complex coil geometries are possible and cabled conductors for several kA can be produced. Possible applications for HTS are rotating machines, but also special magnets for accelerators. The AC loss occurring inevitably at several hundred mT/s can be removed much more efficiently at 30 K than at 4 K. Compared to low-T_c superconductors, the larger thermal margin and higher heat capacity at 30 K give increased stability. Premature quenches and training are not usual for HTS coils. Finally, cooling concepts are possible with little or no liquid cryogen.

REFERENCES

[1] W. Nick, presented at SCENET Workshop, Finland (2005).

[2] M.P. Oomen, P. v.Hasselt, N. Prölss, M. Leghissa, M. Kruip, S. Lister, A. Atkins and G. Gilgrass, A pulsed HTS coil cooled by heat pipes as part of a pre-polariser magnet system, MT-19, IEEE Trans. Appl. Supercond. 16 2 (2006) 1519.

[3] M.P. Oomen, R. Nanke and M. Leghissa, Modelling and measurement of AC loss in BSCCO/Ag tape windings, Superconductor Science and Technology 16 (2003) 339.

Session: Field quality for accelerators

FIELD QUALITY IN CYCLED MAGNETS

B. Auchmann, L. Tkachenko
CERN Geneva, Switzerland and IHEP Protvino, Russia

Abstract
The simulation of field quality needs to take into account geometrical effects, the non-linear iron yoke and persistent currents. In cycled machines we also have to consider eddy-current effects such as interfilament coupling currents, interstrand coupling currents or eddy currents in conductive elements of the magnet structure. In order to be ready for these challenges, new tools have been implemented into ROXIE. Their results have been compared to measurements.

1 INTRODUCTION

Two projects currently draw the community's attention to cycled magnets: GSI's FAIR project, and possible upgrade scenarios for the LHC injector chain. In the simulation of field quality for cycled magnets eddy-current effects need to be taken into account. In a superconducting magnet we distinguish between two kinds of effects: (1) eddy currents in the cables: interfilament coupling currents (IFCCs), interstrand coupling currents (ISCCs), boundary induced coupling currents (BICCs); (2) eddy currents in conductive structural elements, such as wedges, rods, protection sheets or the beamscreen liner.

We will present calculations of ISCCs and IFCCs for the FAIR project and eddy-current calculations in the wedges of a dipole in a potential upgrade scenario for the SPS.

2 EDDY CURRENTS IN THE CABLE

The SIS300 dipole magnet will be powered either in a cycled mode (1.6 T - 6 T - 1.6 T at 1 T/s ramp rate) or in a so-called stretcher mode (slow ramp followed by constant excitation). The more challenging operating mode is the cycled one. Eddy-current induced field perturbations and losses need to be controlled. To come to a deeper understanding of these phenomena, a model magnet has been built, based on the RHIC dipole design. The field quality of the magnet was measured under different conditions (DC, 2 T/s and 4 T/s ramp rates) and the losses per cycle were recorded. The goal of this exercise was to use numerical tools in order to reproduce and thus understand the measured field quality and losses.

2.1 Modes for IFCCs and ISCCs

For IFCCs the following semi-analytical model is used in ROXIE, compare Fig. 1 (left):

$$M_\mathrm{f} \quad = \quad \lambda_\mathrm{w}\, \partial_t B\, \frac{l_\mathrm{w}}{2\pi}\, \underbrace{\frac{1}{\rho_0 + \rho_1 B}}_{\rho_\mathrm{eff.}}\,.$$

The user is required to provide the wire filling-factor λ_w, the wire twist-pitch l_w and the effective resistivity $\rho_\mathrm{eff.}$ which consists of a constant part ρ_0 and a coefficient due to magneto resistance ρ_1.

Two different models are implemented in ROXIE for ISCCs: (1) An electrical network model, compare Fig. 1 (right), and (2) a semi-analytical equivalent-magnetization model:

$$M_\mathrm{c}^\perp = \frac{1}{120}\,\frac{\partial_t B^\perp}{R_\mathrm{c}}\, l_\mathrm{c}\, N(N-1)\,\frac{c}{b}, \quad M_\mathrm{a}^\perp = \frac{1}{3}\,\frac{\partial_t B^\perp}{R_\mathrm{a}}\, l_\mathrm{c}\,\frac{c}{b}, \quad M_\mathrm{a}^\parallel = \frac{1}{8}\,\frac{\partial_t B^\parallel}{R_\mathrm{a}}\, l_\mathrm{c}\,\frac{b}{c}.$$

The user provides the cable twist-pitch l_c, the contact- and adjacent resistances, $R_\mathrm{c},\ R_\mathrm{a}$, and the cable dimensions b (narrow side) and c (broad side). It is known that the resistivities in the above models have large variations and cannot be determined precisely.

Fig. 1: Left: Sketch of filaments in a strand, courtesy of A. Verweij. Right: Electrical network representing a Rutherford-type cable, courtesy of R. de Maria.

2.2 Matching Measurements and Simulations

Figure 2 (red and orange curves) shows field quality measurements in the GSI001 magnet. An effort was made to reproduce these results in simulations. The use of nominal values for the resistivities in IFCC- and ISCC-models yielded the correct orders of magnitude, but not the qualitative behavior, compare Fig. 2 (left). The exercise thus consisted in finding material parameters that would also reproduce the qualitative behavior. The result is shown in Fig. 2 (right). The simulation with adapted parameters also yields losses that correspond more closely to the measured values, compare Fig. 3.

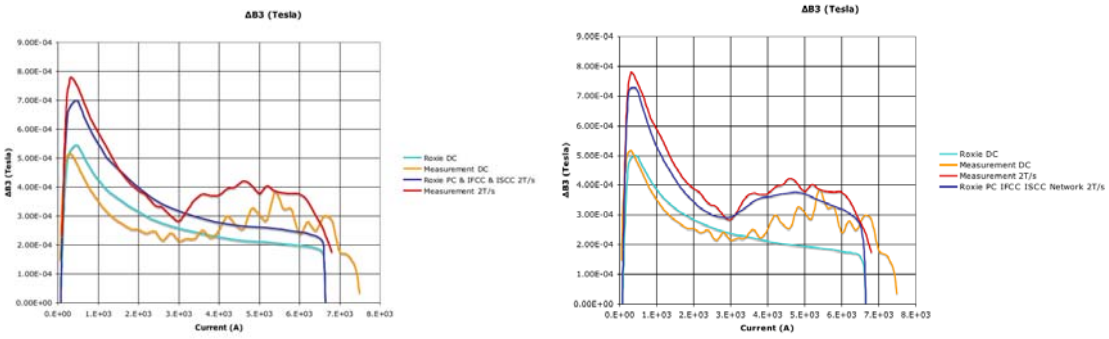

Fig. 2: Difference in absolute B3 (T) between up- and down-ramp at a reference radius of 25 mm. Left: Simulation using nominal resistivity values. Right: Simulation using adapted resistivities.

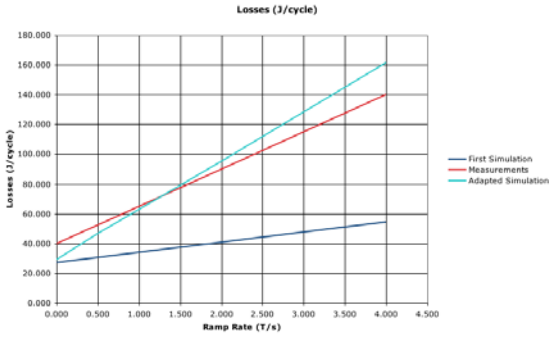

Fig. 3: Comparison of losses/cycle between measurements and calculation. The calculated values are given in J/(m cycle), whereas the measurements are given for the entire GSI001 dipole with a length of about 1.2 m.

3 EDDY CURRENTS IN THE WEDGES

3.1 Theory

When we use a 2D finite element (FEM) calculation to simulate eddy currents, we assume an infinitely long geometry with all fields constant along the longitudinal coordinate. The fields are either directed longitudinally or transversally. It is common knowledge that this assumption implies a Maxwell-gauge of the magnetic vector potential ($\mathrm{div}\,\mathbf{A} = 0$). It is rarely mentioned, that this assumption also implies that the electric scalar potential is constant over the entire domain of interest ($\varphi = \mathrm{const.}$), effectively short-circuiting all conductive elements at infinity. The magnetic flux between any two conductive elements is linked in a loop that closes at infinity. Large eddy currents that flow from one conductive element to the other. This behavior generally does not represent the real application.

The FEM algorithm needs to be adapted. We need to introduce one additional degree of freedom per conductive element into the system of equations: see red coefficients in (3.1 a). These degrees of freedom represent longitudinal electric voltages. Furthermore the additional equations ensure that the Faraday law is obeyed. The net eddy-current flow in each conductive element can now be specified, e.g., set to zero on the right-hand side of (3.1 b).

$$[\mathrm{D}^1][\mathrm{M}^1_\nu][\mathrm{D}^0]\{A_\mathrm{z}\} + [\mathrm{M}^1_\kappa]\{\partial_t A_\mathrm{z}\} - [\mathrm{K}^2_\mathrm{C}]\{\tau\}G'U' = \{\jmath_\mathrm{S}\} \quad (3.1\,\mathrm{a})$$

$$-\{\tau\}^\mathrm{T}[\mathrm{K}^2_\mathrm{C}]^\mathrm{T}\{\partial_t A_\mathrm{z}\} + U' = R'I \quad (3.1\,\mathrm{b})$$

3.2 Results

Eddy-current losses in the conductive wedges of a main dipole were calculated for an upgrade study of the SPS, presented by G. Kirby at the WAMDO 2006 workshop. The results are displayed in the below table for a ramp rate of 1.5 T/s. We find that only pure copper produces significant losses. The eddy-current density in copper is of the order of the transport current. The eddy currents therefore have a sizable impact on field quality.

Material (4 K)	Resistivity (Ohm.m)	Losses (W/m)	Δb_3
pure copper	$1.7\ 10^{-10}$	22.03	3.1
bronze	$3.0\ 10^{-8}$	0.13	0.01
stainless steel	$5.0\ 10^{-7}$	$7.5\,10^{-3}$	$5\ 10^{-3}$

4 CONCLUSION

We have shown that numerical tools can be used to simulate eddy currents in both, superconducting cables and conductive structural elements of a magnet. Due to the large uncertainty of resistivity values in IFCC- and ISCC-models, we have to gauge our models with measured field-quality- and loss-curves. We have further shown that FEM-based eddy-current calculations get somewhat involved when several conductive elements are electrically isolated from each other. The problem can be overcome and simulations indicate that stainless steel is an option for a wedge material in cycled magnets.

MAGNET TEST ANALYSIS PROCESS AND FEEDBACK TO MAGNET DESIGN

S. Feher for the HFM group of Fermilab
Fermi National Accelerator Laboratory, Batavia, USA

Abstract
Magnet tests are an important part of the magnet design and fabrication optimization process. Through two examples this importance is described in the presentation. This paper summarizes the main points of the presentation.

1. INTRODUCTION

In the past ten years US significantly contributed to the world wide effort of developing the next generation of Nb_3Sn accelerator magnets. Fermilab alone has built and tested 14 Nb_3Sn magnets: 5 cosθ dipoles, 5 mirror dipoles, 3 race track dipoles, 1 double aperture common coil dipole, 2 small race track coils. Fermilab has also developed a detailed and thorough approach to testing Nb_3Sn magnets by introducing comprehensive test procedures and new magnet diagnostics tools. It is important to realize that tests provide timely feedback to the design team and it can explore and probe issues that are hard to analyze and calculate.

2. TEST, ANALYSIS AND FEEDBACK

Magnet tests in general can be divided into two major branches. The first branch consists of the R&D tests, perhaps better called experiments since the outcome of the test is predicted but not known. The main goal of these tests is to verify design and fabrication goals and to measure key parameters which feeds back into the design and fabrication process. Isolating and characterizing design and fabrication issues are also important.

The other branch is that of the production tests. In this case we deal with well-established parameter values. The main goal for these tests are to verify design and fabrication goals and measure key parameters, which feeds back into the design and fabrication process. It is also important to provide magnet parameters which are relevant for accelerator operation.

In the case of R&D magnet experiments and tests, every magnet goes through checkout procedures and some mechanical tests during and right after it has been fabricated. The most significant tests are the room temperature mechanical measurements. The usefulness of the results is strongly coupled with Finite Element Modeling, as it is important to predict and measure deformation and stresses. The main purpose of the other room temperature tests (inductance, resistance, ringing, HV tests, magnetic measurements) is quality assurance.

Cold experiments and tests are the most important part of the magnet R&D program. These include electrical tests, mechanical measurements (strain gauge studies), quench performance and quench protection studies, and magnetic measurements. In order to execute these measurements the magnet needs to be instrumented with diagnostic tools including voltage taps for localizing quenches, spot heaters for initiating and measuring quench velocities, temperature sensors for measuring Ic by warming up the coil using spot heaters in DC mode, strain gauges for mechanical analysis and a quench antenna which uses pick up coils to get more information about quench locations (can only be used when theI magnet has a bore).

Fermilab has developed a standard test plan which utilizes test procedures in a systematic way. This approach for testing was critical during our R&D effort since it allowed us to compare efficiently

all of the different magnet test results. This plan was also adopted by the US LARP collaboration. The test plan has two Test Cycles. Between test cycles the magnet goes through full thermal cycling between 300K and 4.5K. Usually most of the tests are performed in the first test cycle. The second test cycle is reserved for tests which we were not able to perform in Test Cycle I . Occasionally it was found that some of the tests have a great importance and thus were repeated in the second test cycle.

Test Cycle I contained the following tests:

- Quench training – 4.5K, 20A/s
  - Quench locations (V-taps, Quench Antenna)
  - Voltage spikes
- Current Ramp Rate Dependence
- Magnetic Measurements
- Temperature Dependence
  - Training the magnet first at 2.2K (20A/s)
  - Quenching at different temperatures
- Quench heater
  - Strip heater – quench protection
  - Spot heater – quench velocities, quench integral, DC heating
- AC losses
- Splice Resistance
- RRR

In Test Cycle II the minimum is to re-train the magnet or to check whether it remembered its training.

One of the most important analysis processes is to verify the critical quench current limit of the magnet. The goal is to do this by using experimental data, and not to rely on short sample measurements. The pure experimental approach became more important for Nb_3Sn magnets than for NbTi since the Nb_3Sn magnets critical current value is more unpredictable: even if a witness sample is placed in the furnace during the heat treatment the witness sample might have not experienced the same heat treatment; or we don't have an exact pressure dependence data so that the error on the actual prediction from short sample measurement is quite large. Obviously determining experimentally the critical quench current limit is not a straightforward measurement since it is almost impossible to measure micro-volt changes for the voltage across the whole magnet coil, which would be necessary to observe the reversible transition of a superconductor from superconducting to normal state. The method we developed is based on collecting many pieces of evidence that all point toward the fact that the conductor within the magnet reached its critical current limit. If all of the following criteria are satisfied there is a high probability that the magnet has reached its critical current limit:

1. Clear evidence that the magnet reached a quench current plateau for quenches collected at a nominal 20A/s ramp rate and 4.5K LHe bath temperature;
2. Quench locations are in the high field region;
3. Temperature and ramp rate dependence has a smooth function at low ramp rates and around 4.5 K;
4. After training the magnet at low (typically at 1.8 – 2.2K) and returning to 4.5K the quench current remains at the same level as it was prior to low temperature quenches. For this criterion it is also important that at lower temperatures the magnet reached higher quench current values so we are sure that the magnet was exposed to high Lorentz forces prior to returning at 4.5K quenches. This confirms that the magnet finished its training so it is quite unlikely that there are any mechanical limitations;

5. Measuring quench velocity is important since it can point toward uniformity issues. If the quench velocity has a high value and it changes monotonically we expect no issue with uniformity. This also means that it is quite unlikely that the critical quench current limit is a local phenomenon for this magnet.

As an example, the quench performance of two tested magnets can be seen in the presentation.

The other important analysis process and design feedback is to identify quench current limitations. Premature quenching can occur for several reasons:

1. Mechanical instability is the most common source. Conductor movement under high pressure and magnetic field can generate enough heat to quench the coil. Inadequate mechanical support can also be the reason of large spontaneous energy release due to epoxy cracking;
2. Splices are not appropriate or other conductor damage occurred;
3. Conductor instability can be two folded. In a strand level the most common cause is a sudden Flux jump. On a cable level uneven current distribution also can cause a significant quench current degradation.

In order to identify or to narrow down the cause many tests should be performed:

- Quench locations and velocities;
- Ramp rate dependence studies;
- Temperature dependence studies;
- Temperature margin measurements;
- Voltage spike and flux change studies;
- AC loss measurements;
- Magnetic measurements.

Several iterations of design and fabrication changes based on test results feedback was necessary in order to be able to figure out the exact cause of magnet quench performance limitations. As an example, the Fermilab experience with designing, building and testing Nb_3Sn accelerator magnets is shown in the presentation. For figures and tables see the presentation itself [1].

3. CONCLUSION

This paper is a summary of the Powerpoint presentation made at the WAMDO workshop. The talk emphasized the importance magnet testing and its importance in the design and fabrication process.

REFERENCES

[1] S. Feher, Power point presentation at the WAMDO conference.

Session: New concepts and perspectives

RACETRACK MAGNET DESIGNS AND TECHNOLOGIES*

R. Gupta
Brookhaven National Laboratory, Upton, New York, USA

Abstract
This paper presents a review of racetrack coil magnet designs and technologies for high field magnets that can be used in LHC upgrade. The designs presented here allow both "Wind & React" and "React & Wind" technologies as they are based on flat racetrack coils with large bend radii. Test results of the BNL 10.3 T "React & Wind" common coil magnet are also presented. A possible use of High Temperature Superconductors (HTS) in future high field accelerator magnets is examined.

1. INTRODUCTION

All conductor dominated accelerator magnets are currently based on the conventional "cosine theta" designs. Magnets based on flat racetrack coils offer an alternative to these "cosine theta" designs. "Racetrack coil designs" are particularly attractive for "high field magnets" with "brittle conductors" (a) because of the way large Lorenz forces can be resolved in a magnet structure and (b) because of the simple flat racetrack coil geometry that minimizes the stress and strain degradation on brittle conductors. A number of designs have been developed with large bend radii that permit the use of both "Wind & React" and "React & Wind" technology and are also attractive for using HTS in accelerator magnets. These designs include the "common coil design" for "energy upgrade", the "open midplane dipole design" for "dipole first optics" and the "modular quadrupole design" for "luminosity upgrade". As shown in the following sections, these designs produce field quality that satisfies the requirements of accelerator magnets and is as good as that produced in conventional "cosine theta" designs. It is shown that commercially available HTS starts becoming competitive in performance with the Nb_3Sn superconductor currently specified for LARP (LHC Accelerator Research Program) interaction region magnets at an operating field of ~14 T or above.

2. MAGNET DESIGNS

2.1 Common Coil Design

The common coil magnet design has been proposed [1, 2] for 2-in-1 dipoles where the apertures are over and under with the desired beam spacing in the vertical direction. In the basic design (see Fig. 1), the main coils are common to both apertures. This allows the use of flat racetrack coils with large radii. The basic concept was later extended to a 4-in-1 dipole [3] to allow the injector to be included in the same cryostat and magnet system. As shown in Fig. 2 and Fig. 3, it is possible to design such racetrack coil magnets that produce good field quality in both body and end regions [4]. The common coil magnet design can be used for an LHC energy upgrade. The proposed 4-in-1 magnet will incorporate a lower energy injector in the same cryostat to fit within the present LHC tunnel. The common coil design also offers a cost-effective and rapid turn around approach for carrying out a systematic magnet R&D program [1, 4].

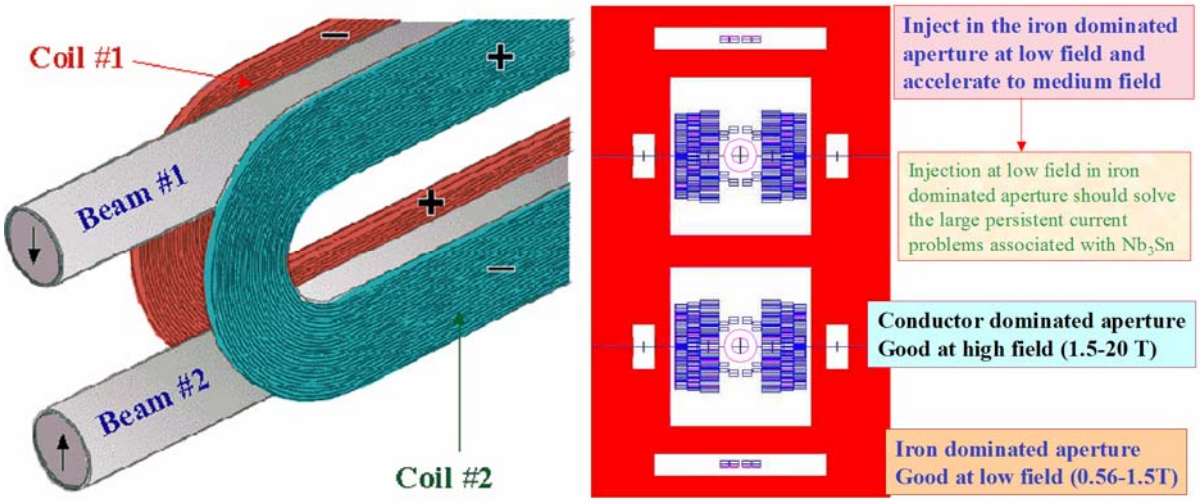

Fig. 1 Common coil design concept for 2-in-1 magnet (left) and for 4-in-1 magnet (right).

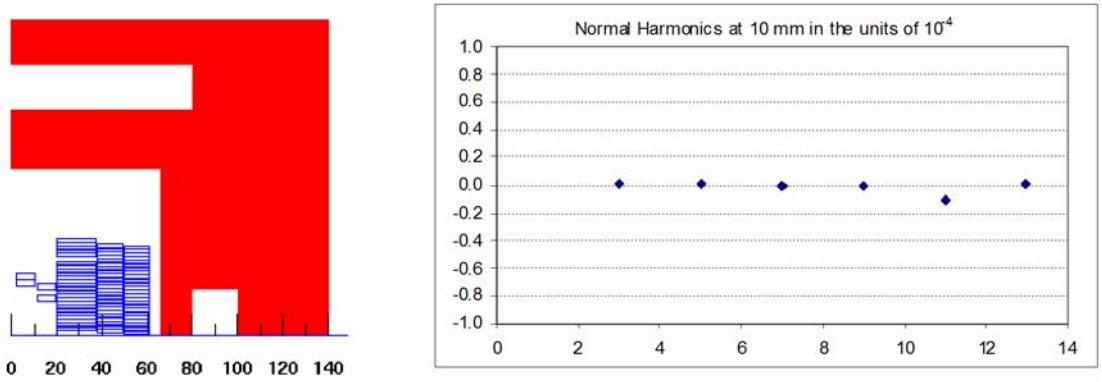

Fig. 2: Field harmonics in a 40 mm aperture common coil magnet design (left) at a 10 mm radius (right). The geometric harmonics are better than 1 part in 10^5 which satisfies the requirements of most particle accelerators.

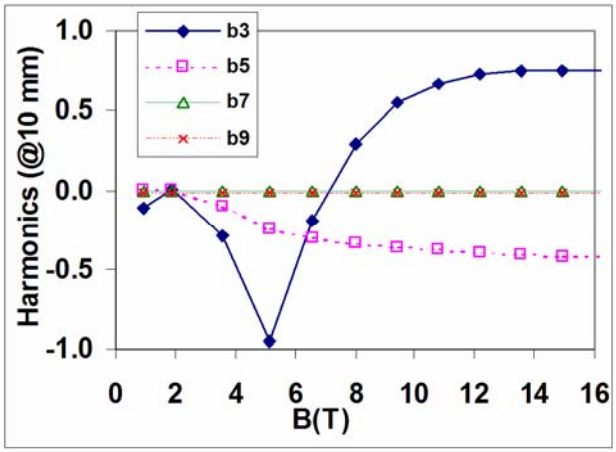

End Harmonics in Unit-m

n	Bn	An
2	0.00	0.00
3	0.01	0.00
4	0.00	-0.03
5	0.13	0.00
6	0.00	-0.10
7	0.17	0.00
8	0.00	-0.05
9	0.00	0.00
10	0.00	-0.01
11	-0.01	0.00
12	0.00	0.00
13	0.00	0.00
14	0.00	0.00
15	0.00	0.00
16	0.00	0.00
17	0.00	0.00
18	0.00	0.00

Fig. 3 Saturation induced (left) and end-harmonics at a 10 mm radius in a 40 mm aperture common coil dipole. 2-d and 3-d optimization of above common coil design was carried out with ROXIE [5].

2.2 Open Midplane Dipole Design

The dipoles on the either side of the interaction regions in the "dipole first optics" of the LHC IR upgrade are subjected to a large spray of particles from the interaction point. Energy deposition from these particles gets highly concentrated on the midplane and may limit the lifetime and quench performance of these magnets. Moreover, the cost of removing this energy at 4 K will be very high. To overcome these challenges, an open midplane dipole design is proposed where most of the heat load is removed at ~80 K. The design concept is shown in Fig. 4. It has been discussed in more detail elsewhere [6]. The magnetic design can be optimized such that it produces the desired field quality (relative field error a few parts in 10^{-5} on midplane, see Fig. 4). Moreover, the design can be developed in such a way that the blocks closer to midplane experience the Lorentz forces away from midplane and thus requiring a little structure between the upper and lower halves of the coils at midplane. Energy deposition calculations by Mokhov [7] show that these designs significantly reduce the heat load on the coils and allow a safe operation of the magnet for over ten years.

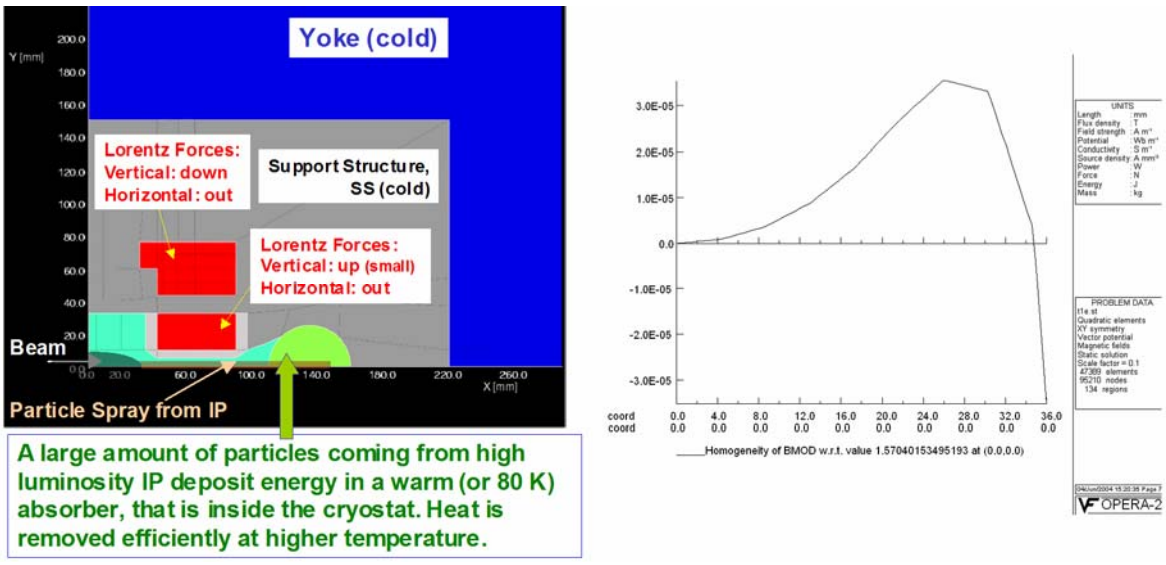

Fig. 4 Open midplane dipole design concept (left) and relative field errors on the midplane in an optimized design (right). The magnet design was optimized with RACE2dOPT [8].

2.3 Modular Quadrupole Design

The magnetic design of quadrupoles differs significantly from that of dipoles because, unlike the dipole, the strength of a quadrupole does not increase linearly as a function of conductor width. Moreover, for a high gradient design, the conductor must be at or very close to the aperture (radius) and at the midplane. However, most quadrupole designs with flat racetrack coils tend to put conductors near the aperture (radius) at or near the pole and away from the midplane. Thus, for the same conductor (same critical current), those type of quadrupole designs with flat racetrack coils have significantly lower maximum gradients irrespective of the amount of conductor used. A modular quadrupole design with flat racetrack coil and large bend radii (see two versions in Fig. 5) has been proposed [9] to overcome this disadvantage. This design creates a gradient in flat racetrack coils quadrupoles that is close to the gradient in cosine theta quadrupoles by allowing conductors to be placed at a radius similar to the midplane radius of cosine theta quadrupoles. The design uses twice as much conductor as a conventional design. Therefore, such a design is attractive where only a few magnets are needed and a higher conductor cost can be tolerated in favor of high performance or where the use of flat racetrack coils with large bend radii is critical. As shown in Fig. 6, it is possible to obtain good field quality. The design allows flexible, cost-effective and systematic R&D - a feature that has been found useful in various R&D magnet programs based on flat racetrack coils.

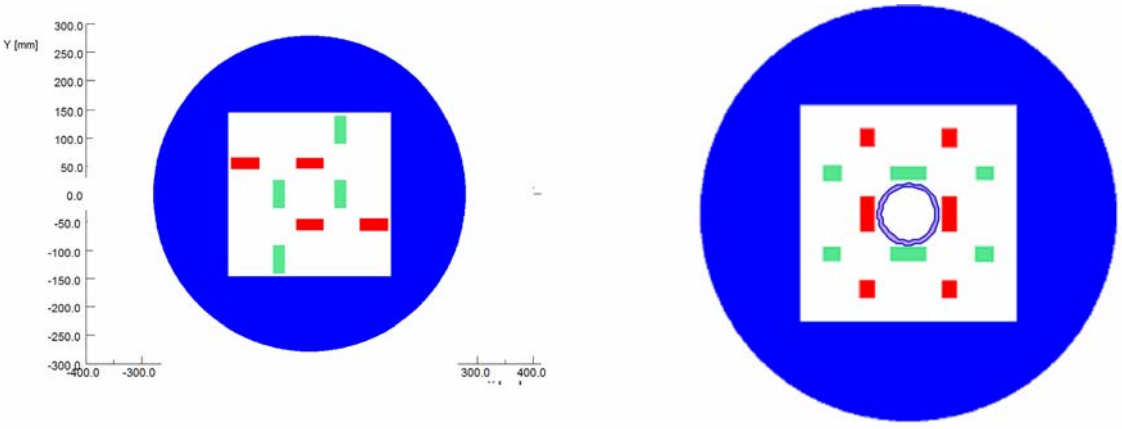

Fig. 5 Two versions of the modular quadrupole design. The one on the left is simpler and uses four sets of racetrack coils and one on the right is symmetric and uses eight sets of racetrack coils.

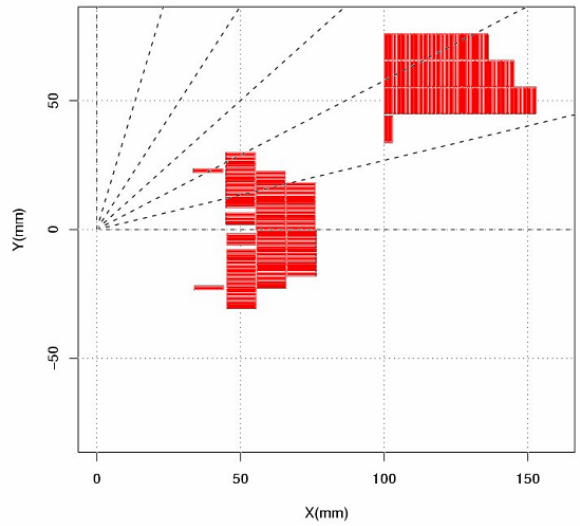

n	a_n	b_n
6	-0.0049	-0.0015
10	0.0006	0.0075
14	0.0018	0.0231
18	0.0000	0.0000

Fig. 6 A 90 mm aperture modular quadrupole design optimized for field quality. Harmonics are given at a reference radius of 30 mm (2/3 of coil radius). The magnet design was optimized with RACE2dOPT [8].

3. WIND & REACT AND REACT & WIND MAGNET TECHNOLOGIES

All known high field superconductors (such as Nb_3Sn, Nb_3Al and HTS) are brittle in nature. However, they are not brittle initially and become brittle only after the composite is reacted (heat treated) to turn them into a metallic compound that can become superconducting when cooled to low temperatures. There are two distinct approaches to make magnets with such conductors: “Wind & React” and “React & Wind”. In the “Wind & React” approach, the coil is wound before the reaction when the conductor is still ductile. The entire coil package consisting of conductor, insulation, wedges, end-spacers, and other structures, is then heat treated at high temperatures. This puts limitations on the types of materials that can be used in the coil package. Moreover, one must also deal with the differential thermal expansion of various materials in the coil package to make sure that they do not put excessive strain on the conductor. In the “React & Wind” approach only the conductor is heat treated before winding the coil. In this case, the major challenge is to find design and manufacturing processes that do not put excessive strain on the coil during the construction of the magnet. The issues and comparisons (advantages and disadvantages) between “React & Wind” and “Wind & React” are listed in Table 1. Most Nb_3Sn magnets to date have been built using the “Wind & React” approach as it offers a greater likelihood of success (at least in short R&D magnets) due to lower bending and

handling degradation. However, the "React & Wind" approach is considered to be more scalable for long magnets provided one can develop magnet designs that are "conductor friendly" and demonstrate this technology in successful magnets. The "React & Wind" technology is particularly important for HTS magnets where the reaction temperature is very high (~880 K) and the allowance for variation in this is very low (~0.5 K).

Table 1
Comparison between "Wind & React" and "React & Wind" technologies.

Issues	Wind & React	React &Wind
Use of "Brittle Super-conductors"	Since one does not have to work with the brittle superconductor, the "Wind & React" is the safest and the most popular choice for the demonstration of successful R&D magnets. (+)	Biggest challenge for "React & Wind". Brittle superconductor must go through all steps of coil manufacturing. That's why it is the least popular for R&D magnets. Design and automate all aspects of tooling to minimize potential for conductor degradation. (-)
Insulation and use of other material in coil	Limited choices (insulation is generally thicker), as they must withstand high reaction temperatures. (-)	Can use a variety of insulation and other materials in the coil, as they do not go through high reaction temperature. (+)
Length scale-up issues	Biggest challenge for "Wind & React". Integrated build-up of material in the ends and in transition region as coil gets longer due to differential thermal contraction. (-)	A successful demonstration of technology in short magnet directly applies to long magnets, as the coil does not go through high reaction temperature. This is the biggest strength and argument for "React & Wind". (+)
Industrialization	More new technologies (-)	Fewer new technologies. (+)
Biggest challenge for future	Length scale-up issues, particularly in designs with complex ends. (-)	Magnet and conductor designs to minimize the bending strain. (+)

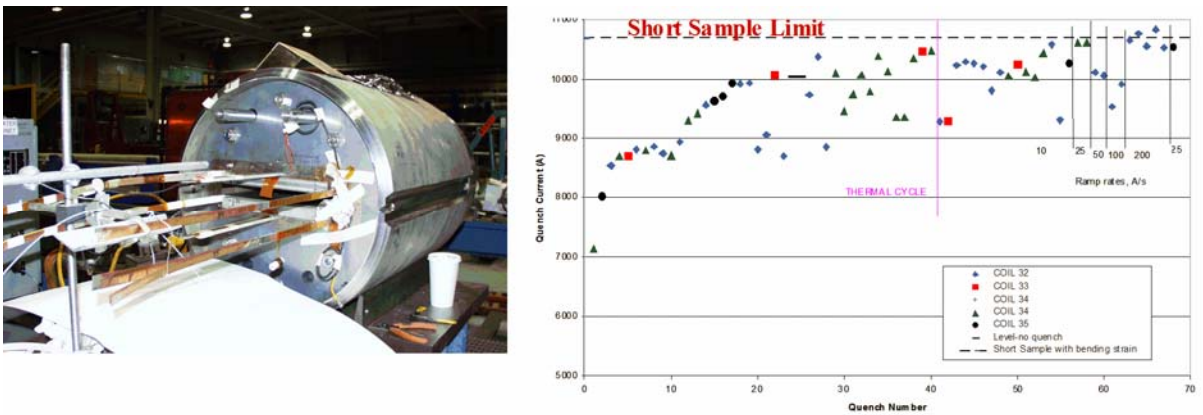

Fig. 7: React & Wind 32 mm aperture common coil dipole (left) that was recently built and tested at BNL. The magnet reached the computed short sample current (right).

4. TEST RESULTS OF REACT & WIND COMMON COIL DIPOLE AT BNL

Recently a "React & Wind" Nb_3Sn 32 mm aperture common coil dipole was built and tested at BNL. The detailed design of this magnet has been discussed elsewhere [10]. The magnet was made with a relatively lower performance MJR (modified Jelly Roll) conductor with $J_c(12T,4K) < 2000$ A/mm^2.

The magnet reached the computed short sample current of 10.8 kA and field of 10.3 T. This is a significant result as it demonstrates that it is possible to design and built a magnet in the 10+ T range using "React & Wind" technology. The construction, analysis and test results will be discussed in more detail elsewhere [11]. A conductor-friendly design with flat racetrack coils with large bend radii and the development of tooling (such as a new winding machine) that minimized the degradation of conductor played a major role in the success of this magnet. An interesting feature is the large open space (32 mm X 240 mm) that can be used for testing insert coils without disassembling the magnet.

5. HTS IN HIGH FIELD MAGNET DESIGNS

For a long time HTS has been considered as the conductor for future magnets either for achieving very high fields or operating at temperatures much higher than 4 K. However, recent test results at BNL in making several racetrack coils and an R&D magnet with HTS tape for the Rare Isotope Accelerator (RIA) [12] and 10-turn common coil R&D magnets with Rutherford cable [13] show that conductor, coil and magnet technology have now evolved to a stage that one can seriously consider HTS for accelerator magnets. The conductor is available in long lengths. Moreover, one can make a series of coils with a consistently good performance (see Fig. 8). Thirteen coils were made with Bi-2223 tape and were tested in a warm and cold iron designs. In cold iron test set-up, two, four and six were tested in series, whereas in warm iron design twelve coils were tested in series. The critical current of two, four, six and twelve coils was measured as a function of temperature in a magnetic structure (see Fig. 9). An important benefit of using HTS in magnets are that they can tolerate large energy deposition and that the temperature control of the cryogenic system can be relaxed to several degrees from a few tenths of a degree in conventional LTS magnets.

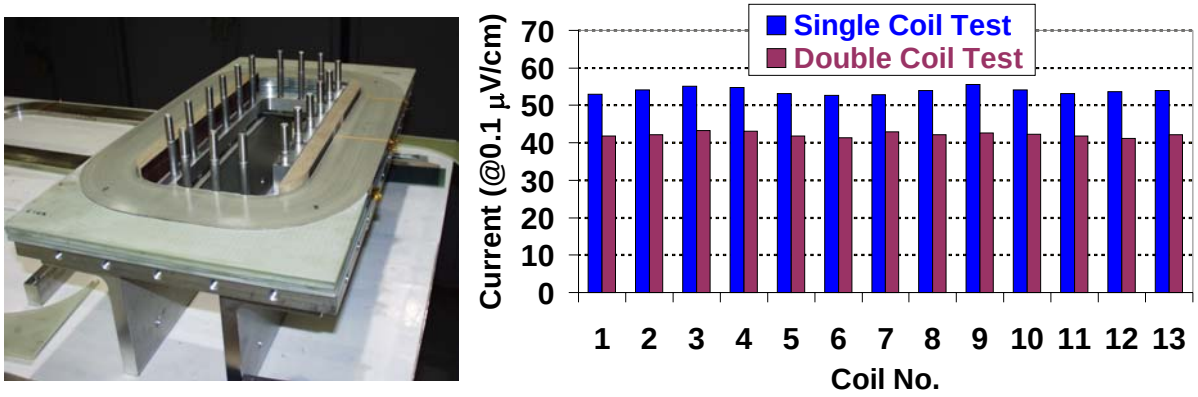

Fig. 8 Racetrack coils made with ~220 meter of HTS tape from American Superconductor Corporation (ASC). The performance of the 13 coils tested so far has been very uniform and consistent (right).

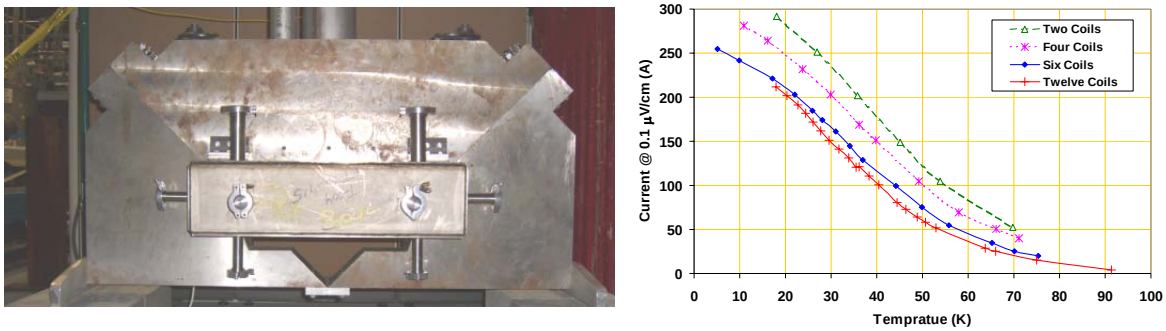

Fig. 9 Warm iron magnetic mirror HTS quadrupole for RIA's fragment separator region (left). Measured current carrying capacity of number coils (two, four, six and twelve) as a function temperature is shown on right.

For an LHC luminosity upgrade one can take advantage of the special high field characteristics of HTS. The RIA HTS quadrupole design is a super-ferric magnet design that is suitable for a lower field. At very high field, no LTS carries as much current as HTS does. Traditionally, accelerator magnets have been built with Rutherford cable operating at several kilo-amperes. BNL has built and tested several coils and R&D magnets [13] made with Bi-2212 Rutherford cable (see Fig. 10). The improvements in performance of Rutherford cable over time are also shown. It should be possible to develop high field accelerator magnets with flat tape as well; in particular as ramp rate requirements in high-energy machines are now much lower. Moreover, future YBCO tapes could be much wider and can carry several kilo-amperes current at any field. It is noted that as the development of HTS technology has been funded mainly for applications that do not need high current cable, a prudent approach would be to develop magnet designs and technology around the conductor.

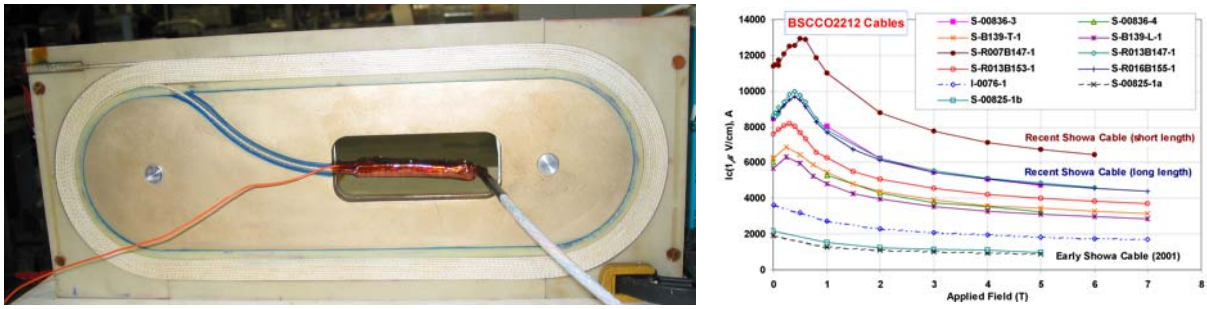

Fig. 10 On the left, an HTS coil made with Rutherford cable for a common coil dipole.On the right the measured current carrying capacity at 4 K as a function of field Rutherford cable tested between 2001 and 2003.

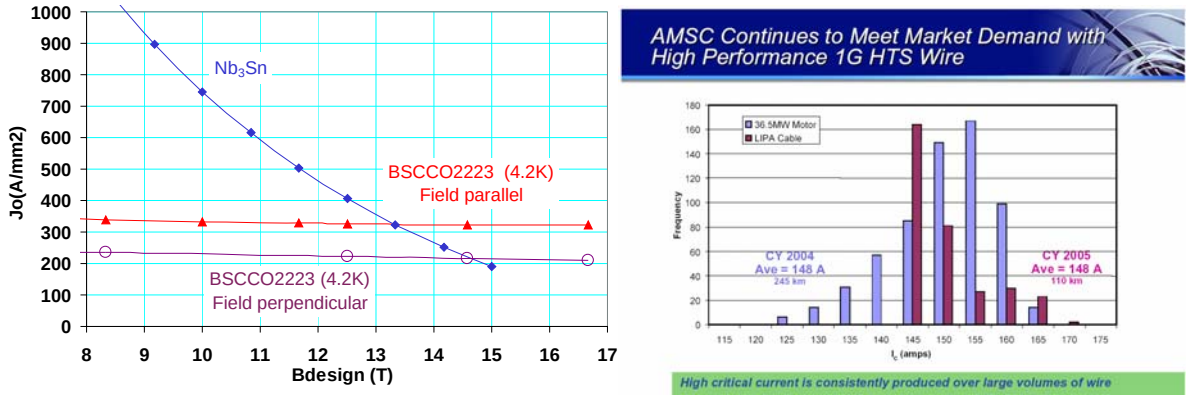

Fig. 11 On the left we see the overall current density in coil as a function design field (including peak field and margin) for commercially available HTS tape (Bi-2223) and Nb_3Sn Rutherford cable for designing LHC IR upgrade magnets. On the right we see the measured critical current at 77 K (self field) in AMSC HTS tape [14].

The right side of Fig. 11 shows that the current carrying capacity of HTS decreases slowly as a function of field so that at high fields HTS has more critical current density than that in conventional low temperature superconductors (LTS). The design field at which coils made with commercially available HTS will have higher engineering (or overall) current density than the Nb_3Sn being used in designing LARP quadrupoles is estimated. It is recalled that the design field (the field that machine builder can use in designing an accelerator) is generally 20% lower than the limiting field on the superconductor due to peak field (field enhancement) and margin requirements. Overall current density includes copper (in case of Nb_3Sn) or silver (in case of HTS) and insulation. A current density of 2400 A/mm^2 (12T, 4.2K) is assumed for Nb_3Sn and a critical current of 155 A (77K, self field) for Bi-2223. Both of these have been produced in higher performance versions, however, those

improvements do not significantly change the relative cross-over (~13.5 T for field parallel and ~14.5 T for field perpendicular) between Nb_3Sn and HTS (see Fig. 11). Even though HTS is more expensive than Nb_3Sn, for a few magnets a higher-cost conductor should be acceptable in favor of performance, as the conductor costs are a small fraction of the overall magnet development cost.

6. SUMMARY

A number of racetrack coil magnet designs with good field quality have been presented that can potentially be used in an LHC luminosity and/or energy upgrade. These include: common coil dipole, open midplane dipole, modular high gradient quadrupole and common coil magnet system. Racetrack coil geometry offers a high likelihood of success in making magnets with brittle conductors due to its simple, 2-d geometry. Because of large bend radii, these designs allow the use of both "Wind & React" and "React & Wind" technology. The "React & Wind" approach with racetrack coil geometry offers an attractive option for making "long" magnets with brittle superconductors. Test results of the BNL common coil dipole shows that one can successfully build magnets using "React & Wind" technology. Present day HTS provides higher engineering or overall current density in coils, compared to Nb_3Sn, in magnets that must operate above ~14 T.

The brief summary presented here is complementary to the presentation made at the workshop [15].

REFERENCES

[1] R.C. Gupta, A Common Coil Design for High Field 2-in-1 Accelerator Magnets, PAC'97 JACoW (1998) 3344.

[2] G. Danby et al., Proc.12th Int.Conf. on High Energy Accelerators, Fermilab (1983).

[3] R.C. Gupta, Common Coil Magnet System for VLHC, PAC'99 JACoW (1999) 3239.

[4] R. Gupta et al., Common Coil Magnet Program at BNL, ASC2000, IEEE Trans Appl. Supercond. 11 1 (2001) 2168.

[5] S. Russenschuck, ROXIE – A Computer Code for the Integrated Design of Accelerator Magnets, EPAC'98 JACoW (1998) 2017.

[6] R. Gupta et al., Optimization of Open Midplane Dipole Design for LHC IR Upgrade, PAC'05 JACoW (2005) 3055.

[7] N.V. Mokhov et al., Energy Deposition Limits in A Nb_3Sn Separation Dipole in Front of the LHC High-Luminosity Inner Triple, PAC'03 JACoW (2003) 1748.

[8] P. Thomson, RACE2dOPT and a series of other codes developed to optimize accelerator magnets, Private communication.

[9] R. Gupta, Modular Design and Modular Program for High Gradient Quadrupoles, to be presented at ASC2006, Seattle.

[10] J. Cozzolino et al., Magnet Engineering and Test Results of the High Field Magnet R&D Program at BNL, ASC2002, IEEE Trans Appl. Supercond. 13 2 (2003) 1347.

[11] R. Gupta et al., Common Coil Magnet Program at BNL, to be presented at ASC2006, Seattle.

[12] R. Gupta et al,, Test Results of HTS Coils and An R&D Magnet for RIA, PAC'05 JACoW (2005) 3016.

[13] R. Gupta et al., Status of High Temperature Superconductor Magnet R&D at BNL, MT-18, IEEE Trans. Appl. Supercond. (2004) 1198.

[14] G. Ferguson, American Superconductor Corporation, http://www.amsuper.com/.

[15] http://www.bnl.gov/magnets/Staff/Gupta/Talks/wamdo2006/gupta-wamdo2006.pdf

A PRELIMINARY CONSIDERATION OF A 1.5 TEV INJECTOR ACCELERATOR FOR THE LHC

H. Piekarz
FNAL, Batavia, USA
G. de Rijk and L. Rossi
CERN, Geneva, Switzerland

Abstract
The possibility of a 1.5 TeV pre-accelerator in the LHC tunnel is explored. This machine, the Low Energy Ring, uses VLHC type two-in-one super-ferric magnets (Pipetron). The existing LHC experiments are traversed through a beam pipe in common with the LHC.

1. MOTIVATION

A primary goal for the LER (Low Energy Ring) injector accelerator is to inject 1.5 TeV proton beams into the LHC, instead of the current injection scheme with 0.45 TeV beams from the SPS. At this new energy, the field harmonics [1] of the LHC magnets are sufficiently satisfactory to prevent the luminosity losses expected to appear when applying the transfer of lower energy SPS beams. In the long term, the LER injector accelerator would greatly facilitate the implementation of a machine, which doubles the LHC energy (DLHC).

2. ELECTED BOUNDARIES FOR THE LHCI DESIGN AND CONSTRUCTION

As presented in some detail in Chapter 13, it is expected that design and construction of the LER will take 5-6 years. In order to minimize the potential impact of the LER implementation process on the ongoing LHC physics program, the following LER design and construction criteria have been adopted:

- The LER accelerator will be installed in the LHC tunnel during regular LHC shutdowns.
- No new tunnel digging will be required.
- The current SPS-LHC beam injection scheme will remain intact and will be used "as-is" to inject beams into the LER ring. At any time, a reversal to the standard SPS-LHC injection and the LHC operations will be possible.
- The LER accelerator components will be designed and fabricated using as much as possible known technologies. So, only component design, followed by prototyping to verify performance and to facilitate procurement for mass production, will be used.

3. OUTLINE OF THE NEW INJECTION SCHEME FOR THE LHC ACCELERATOR COMPLEX

We propose to install the LER accelerator inside the LHC tunnel. This accelerator would accept 0.45 TeV proton beams from the SPS through the existing TI2 and TI8 transfer lines, and then accelerate these beams to 1.5 TeV, so as to better match the beam acceptance of the LHC magnets. The LER accelerator would be based on super-ferric, combined function magnets. These magnets were originally proposed for the VLHC Stage 1, a p-p collider in the US [2]. A basic property is that they require only minimal space in the accelerator tunnel. The magnet and its supporting systems (conductors, power supply, current leads, etc.) were recently successfully tested at Fermilab [3-7].

In the new LHC beam injection scheme, the proton bunch stacking and the formation of the full intensity beam is performed in the LER ring. The beam passes through the LHC accelerator beam pipe in several of LHC straight sections. This means that in some straight sections the LER and the LHC accelerators share the same beam pipe. This scheme is being proposed to eliminate costly digging of new bypass tunnels around the detectors.

Once the stacking of the clockwise and the counter-clockwise 0.45 TeV beams in LER is completed, the beams are accelerated to 1.5 TeV. At this top energy, the beam is passed into the entire LHC ring using a single transfer mode through one of the transfer lines. For this single transfer, only one set of the LER transfer line magnets is to be ramped down. The ramping down has to be done in a time period determined by the time interval between the tail and the head of the beam train. The other transfer lines (4 x 2 transfer lines in total) are switched off when the gap in the beam train passes. This idea of LER to LHC beam transfer is illustrated in Fig. 1.

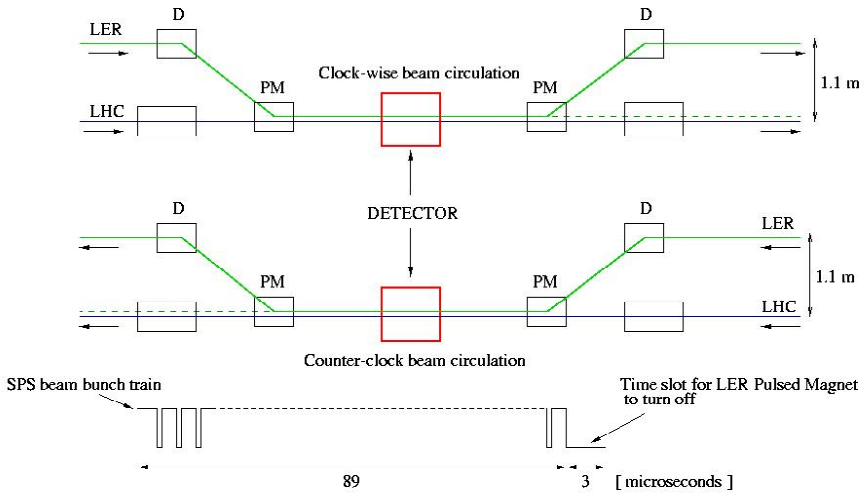

Fig. 1 The principle of the proposed LER - LHC beam transfer method. D stands for dipole magnet and PM stands for fast pulsing dipole magnet

The time slot for beam transfer is 3 μs, while the beam circulation time in the LHC ring is 89 μs. After the beam transfer into the LHC ring is completed, and the beam circulates in the LHC ring only, all the LER magnets (transfer lines and main arc) can be ramped down and remain on standby for the duration of the store (~10 h). This may help to reduce potential effects of the LER magnets fringe field on the operation of the LHC magnets at 7 TeV. Moreover, it will save on the refrigeration power used for operating the LER magnets.

The minimum allowable vertical separation between the LER and LHC rings is about 135 cm. In the IR regions, where the detectors reside, the total length of the straight sections is about 528 m. The available space, on each side of the detectors, at the LHC ring level that could be used for inserting the LER-LHC transfer-line magnets totals only about 80 m. This situation poses a great challenge for the transfer of the 1.5 TeV beam between the two rings. A possible conceptual LER-LHC transfer line design and arrangement of the transfer line magnets in the IR1 and IR5 regions are discussed in Chapters 8 and 9. The proposed conceptual LER-LHC injection scheme together with the LER ring arrangement is shown in Fig. 2.

At present the SPS beam is transferred to the LHC rings by using the TI2 (clockwise circulation) and the TI8 (counter-clockwise circulation) beam lines. A set of fast kicker magnets placed in the front straight sections of the IR2 (ALICE detector) and IR8 (LHCb detector) performs the beam transfer into the LHC ring. These kicker magnets use about half of the available space on one side of the straight sections. Consequently, if the LER beams are required to pass through the

LHC beam pipe at IR 2 and 8 (to make possible the operation of ALICE and LHCb with LER), the TI2 and TI8 lines must inject beams into the LER rings at a shorter distance than presently into the LHC. Such a scheme will also free some space for the transfer of the LER beams to the LHC ring in the front section of IR2 and IR8, but it will considerably complicate the TI2 and TI8 beam lines. The need to operate the LHCb and ALICE detectors with LER is physics driven, and if this is desired then modifications to the TI2 and TI8 beam lines must be considered. For now we propose a LER-LHC injection scheme that does not assume the ALICE and LHCb detectors operating with the upgraded LHC luminosity resulting from the LER implementation. Our scheme, however, allows to run these detectors with a standard LHC operation mode any time even after the LER installation and operation.

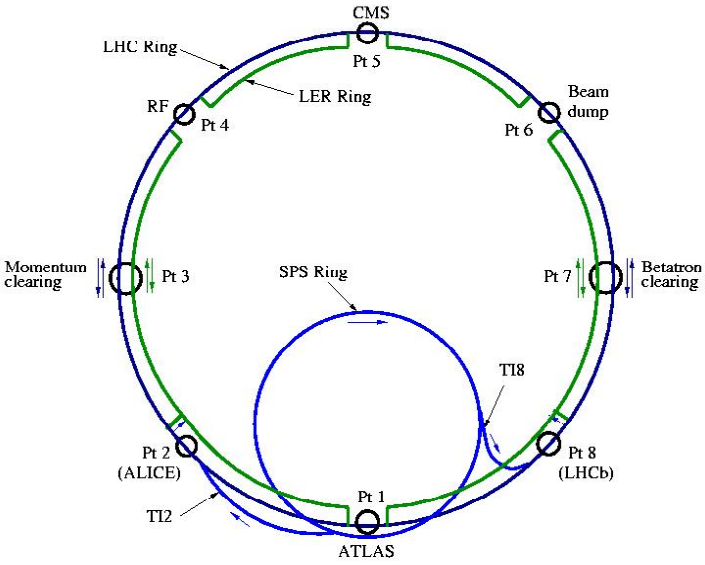

Fig. 2 A conceptual arrangement of the LER-LHC injection scheme

The beam from the TI2 transfer line enters the LHC ring at the short straight section just in front of IR2. It travels through the IR2, and is then transferred to the LER ring. It passes the IR3 area, and it is transferred into the LHC beam pipe only at IR4 where it will use the RF system of the LHC. After IR4 the LER beam goes back to its ring until it reaches IR5 where it shares the LHC beam pipe while passing through the CMS detector. It is again bumped into the LER ring until it reaches IR6 where it is bumped into the LHC beam pipe to use the beam dump facility. After IR6 it enters the LER ring again, passes IR7 and IR8, and re-enters the LHC beam pipe at IR1 (ATLAS). Immediately after IR1 it is bumped back into the LER ring, and will stay there until reaching IR4. The beam from TI8 has the same path in LHC/LER as the TI2 one, except that it enters the LER ring right after IR8 and it travels in counter-clock direction. We assume that LER will have its own momentum and betatron clearing systems in IR3 and IR7, respectively.

4. THE VLHC STAGE 1 MAGNET AND ITS MAIN CHARACTERISTICS

A conceptual design of the VLHC Stage 1 main arc dipole magnet is shown in Fig. 3. The magnet features two pole gaps between the top and the bottom half-cores. The magnetic field is induced by a current of up to 100 kA from a single transmission line conductor located in the centre of the half-core assembly. The field in the pole gaps is entirely shaped by the iron, facilitating the magnetic design. The VLHC Stage 1 magnet is a combined function gradient dipole with two half-cell versions, focusing and de-focusing, which are placed interchangeably along the accelerator ring. The magnet pole gap is 20 mm high, and the beam pipe is elliptical with an effective vacuum space of 18 mm (v) and 28 mm (h). During tests on a model magnet at FNAL, the magnetic field was measured using a 69 cm long, 15.2 mm diameter tangential coil, and with a Hall probe array of 102 sensors. The

characteristic measured dipole strength versus current is shown in Figure 4. In Figure 5 and 6 we show the measured quadrupole strength and the sextupole harmonic versus the dipole field (data analysis from [7]). The quadrupole strength reflects the design gradient of 4 %. The sextupole and other normal and skew field harmonics (in units at 10 mm) up to the order of 10 were found relatively small, not exceeding 2-3 units (or 0.02 %-0.03 %). The accuracy of the measurements is especially poor at low fields as the tangential coil design was optimized for the high fields.

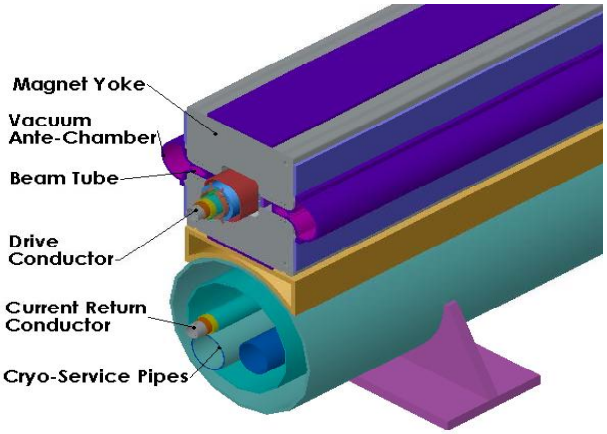

Fig. 3 The VLHC Stage 1 magnet conceptual design.

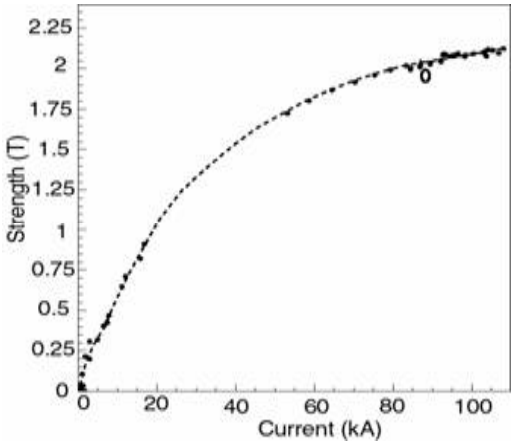

Fig. 4. The measured dipole field versus current. The circle shows the maximum current for VLHC operation.

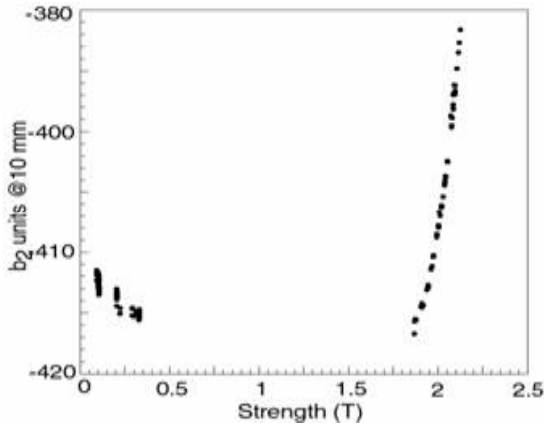

Fig. 5 The measured quadrupole strength as a function of the dipole field. The maximum dipole field for VLHC operation is 1.966 T.

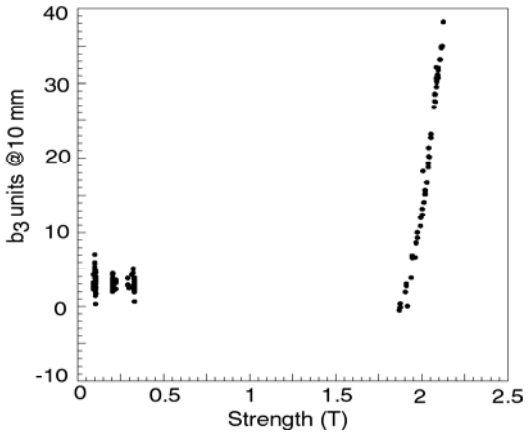

Fig. 6 The measured sextupole strength as a function of the dipole field.

5. ADAPTATION OF THE VLHC STAGE 1 MAGNET TO LER

5.1 Dipole field and gradient of the LER arc magnet

A preliminary design of the LER optics [8] used the VLHC combined function magnets with a goal to replicate the LHC optics and match the LHC footprint. The LER and LHC optics are shown in Figs. 7 and 8. The dispersion suppressers were modelled on the ones of the Main Injector at Fermilab with 66 % of the arc magnet length and 75 % of the arc cell length. A list of arc and dispersion suppression cells for LER that allow to exactly reproduce the LHC lattice is shown in Table 1.

Table 1
LER arc and dispersion suppressor cells

Cell Type	Cell Length (m)	Magnet Type	Magnet Length (m)	Number per Cell	B (T)	B' (T/m)
Arc	107	GF/GD	12	8	1.595	4.858
Dispersion suppressor	80	GSF/GSD	8	8	1.595	10.112

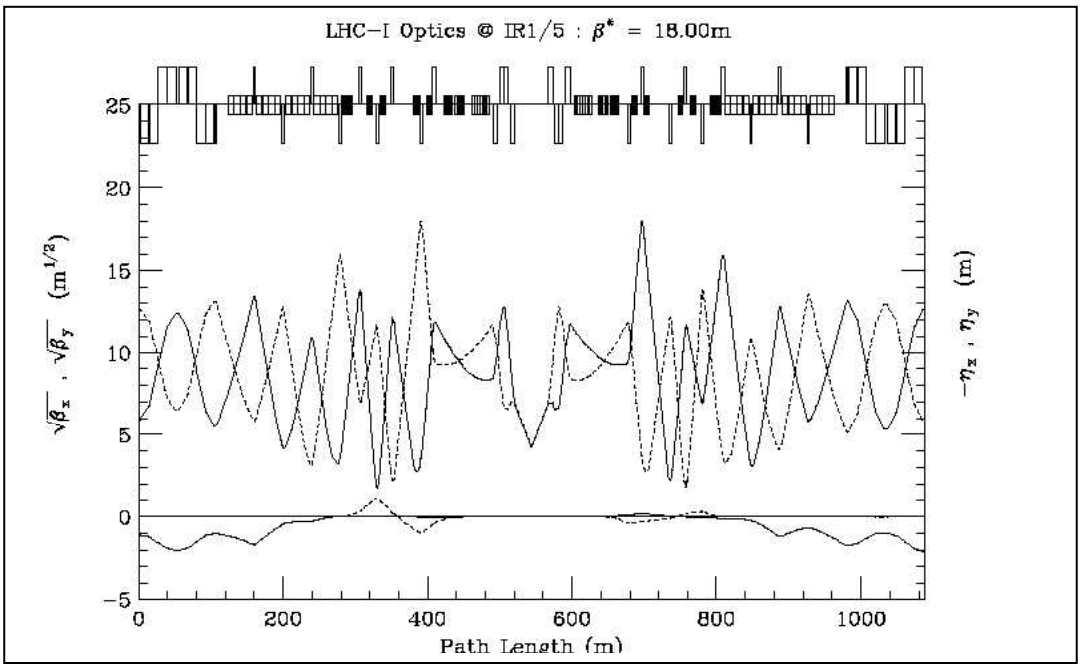

Fig. 7 The LER (LHC-I) optics at IR1, designed based on VLHC LF magnets.

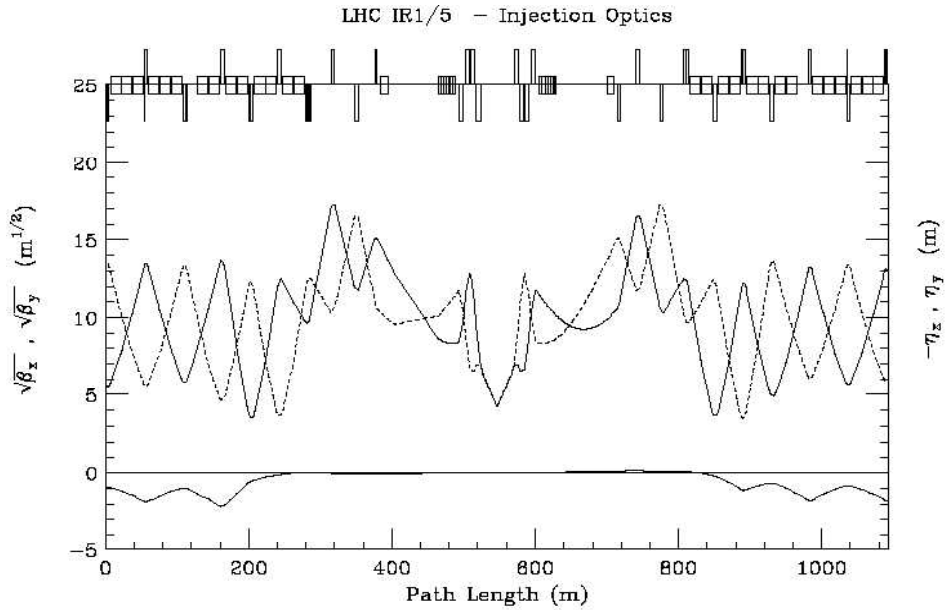

Fig. 8 The LHC optics at IR1.

At a LER field of 1.595 T the required magnet current is only 55 kA, considerably lower than the current for the VLHC (89 kA for 1.966 T). The required LER gradient corresponds to +/- 3 %, as opposed to +/- 4 % for the VLHC. The lower field and gradient improve the quality of the main arc magnets, as the operation is further away from the saturation region, which becomes very strong above 1.9 T. A preliminary list of the LER quadrupole parameters at IR1 and IR5 is shown in Table 2.

Table 2
LER quadrupole parameters for IR1 and IR5

Quad	L (mag) (m)	B' (left) (T/m)	B' (right) (T/m)
Q4	4.0	- 62.92	62.92
Q5	4.0	68.98	- 68.98
Q6	4.0	- 97.83	97.83
Q7	4.0	80.88	- 80.88
Q8	4.0	- 91.25	91.25
Q9	4.0	56.46	- 56.46
Q10	3.0	- 81.27	80.62
Q11	3.0	68.45	- 68.45
Q12	3.0	- 58.38	56.39
Q13	1.5	48.02	- 39.53

5.2 Beam separation in the LER magnet

The VLHC magnet was designed for a beam separation of 150 mm. The LHC beam separation is 194 mm. With a single beam transfer mode there is no need to equalize the beam separation for the two accelerators. Both the LER and LHC circulating beams use their own set of horizontal bending magnets to pass the beam in the straight sections. Minimizing the size of the magnet cores is important for magnet cost reduction as the cost of the iron yokes dominates the cost of the magnet.

5.3 Beam gap in the LER magnet

The VLHC magnet gap is 20 mm. The preliminary LER lattice design [8] suggests that a 20 mm gap may be sufficient, but more detailed lattice simulations, including a beam impedance and a beam instability study [9], are needed to reach a more binding conclusion. As the nominal operating current for the LER magnet is 55 kA, widening of the gap by 20 %-30 % is certainly feasible as the B-field response to the current is nearly linear below 1.6 T, and the conductor can operate up to 100 kA. However, in that case a new magnetic design with an enlarged iron yoke would be needed. A larger magnet yoke will also incur an increased magnet cost.

5.4 Return conductor for the LER magnet ring

The LER main-arc dipole magnets will be powered with a single transmission line conductor using a single power supply and a single set of current leads. The arrangement of the transmission line conductor as proposed for the VLHC (235 km circumference) is shown in Fig. 9. A possible arrangement of the quench detection and protection circuits is also indicated. The drive conductor loops through half of the accelerator circle, turns 180 degree back, runs as a return conductor the full circle, turns again 180 degree and then excites the remaining half of the accelerator magnets. This makes the continuing length of conductor to be ~ 470 km. This length will be ~52 km for LER. As the currents in the overlapping conductors run in opposite directions, the magnetic fringe field is strongly suppressed at far distances. This is important for the safety of low flying civil aircraft.

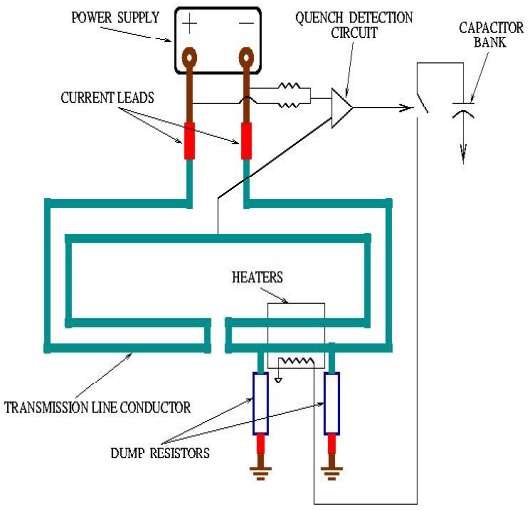

Fig. 9 Conceptual arrangement of the VLHC conductor.

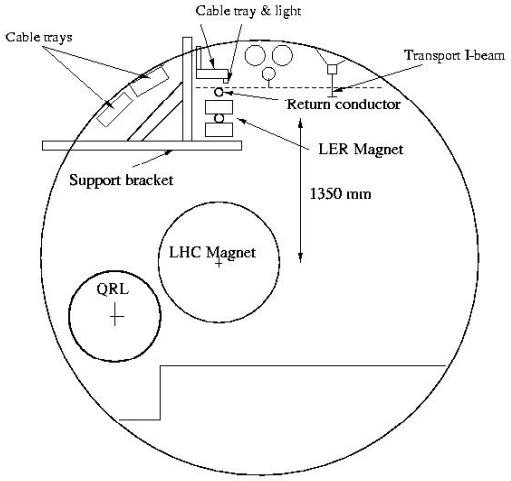

Fig. 10 A possible arrangement of the main arc LER magnet in the LHC tunnel.

The magnetic fringe field due to the return conductor sections inside the magnet is small, but in the areas between the magnets it is strong (1 T conductor self-field). The alternative is to use a drive conductor only, and to install heavy magnetic shielding (e.g. 4 cm steel plates) covering all the open sections of the conductor. This may be inconvenient at the magnet joints, especially at the cryogenic ones where access is needed for servicing. From the aviation safety point of view there would never be 100 % guarantee that the fringe fields are suppressed using “removable” shielding. The issue of the return conductor may be revisited again for the LER case as the accelerator circumference is 10 times smaller then the VLHC and likewise is the cost of the installation of the iron shielding.

Both the drive and the return conductors must bypass the detector areas. In case of a single conductor a heavy magnetic shield would have to be installed to protect the detectors and the personnel. The drive and the return conductors are separated vertically by 28 cm, and the cryostat pipe enclosing both of them is only 36 cm in diameter. This indicates how much space is needed in the area behind the detectors for the installation of the bypass conductor lines.

5.5 LER ring location in the LHC tunnel

The inspection of the LHC accelerator tunnel leaves only one possibility for the location of the LER magnet, and that is in the space above the LHC magnet as shown in Figure 10. In order to minimize the vertical distance between the LHC and LER rings the return conductor of the super-ferric magnet will be placed in the space above this magnet, rather then below as in the VLHC case. This new arrangement is shown in Figure 10. There is a 4 cm thick steel shield placed on top of the magnet to suppress any effect of a fringe field from the return conductor on the field in the LER magnet gap. There is also probably a need for a protection of the LHC magnet from the fringe field propagating below the LER magnet. Fringe field simulations are needed to determine the location and thickness of the magnetic shielding for the LHC magnet.

In Figure 11 and 12 the preliminary LER magnet locations and supports are shown for a typical LHC ring locations, with and without the cryogenic jumper. The magnet is supported from two crossing I-beams fastened to the top and side of the wall of the tunnel. The spacing is to be determined by an engineering analysis of the strength required to support the magnet weight of 500 kg/m. There are some obstacles for the LER magnets, typically located in straight sections IR1 through IR8. These

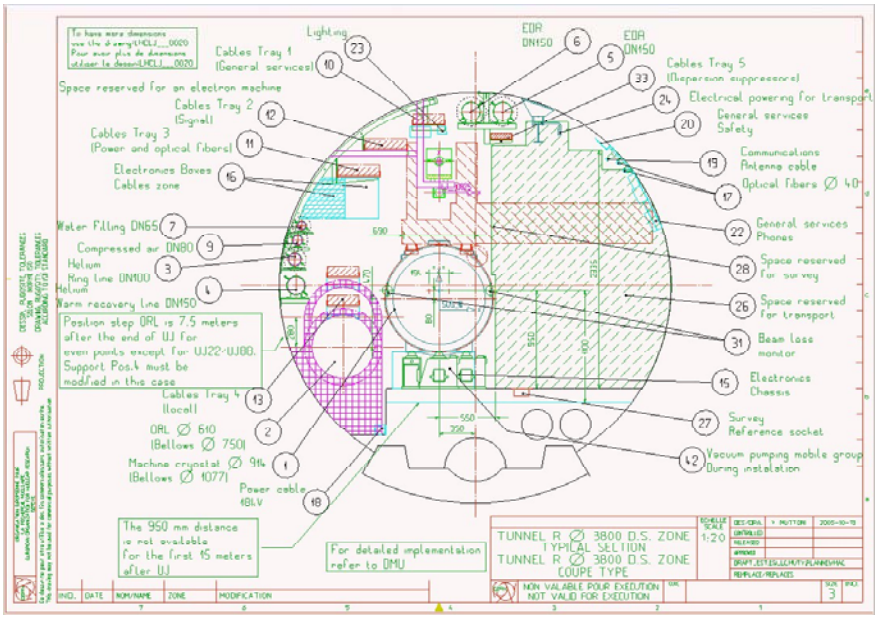

Fig. 11 Mounting of the LER magnet in a typical location in the LHC ring,

are mainly: (1) the LHC magnet power cables on the distribution boxes which are fed on top (~ 10 m long space at each side of each IR), (2) helium feeds from the top or from the sides at all IRs (~ 15 m space), and (3) the power cables for the accelerating cavities at IR4 (~ 50 m). A re-arrangement or bypassing of these obstacles does not appear to be an insurmountable task.

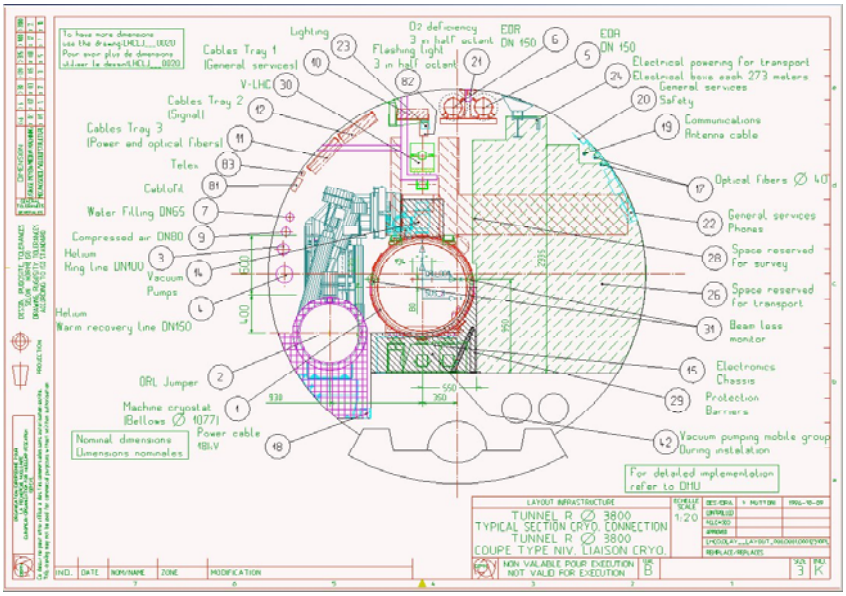

Fig. 12 Mounting of the LER magnet in a location with LHC magnet cryo-feed (jumper).

6. CRYOGENIC SUPPORT

The transmission line magnets use supercritical helium at 4.5 K, 4 bar, and 60 g/s flow rate. The total liquid inventory is ~ 50 000 l. The LHC QRL system at CERN can deliver 1700 g/s of supercritical helium, so the 60 g/s required for the LER magnets is in within the projected LHC operational needs.

It is thus conceivable that no new cryogenic plant needs to be built to support the LER operation. The LER magnets could tap into the QRL line at any convenient distance, e.g. each 1 km.

7. MAIN ARC MAGNET ASSEMBLY WORK AND ITS INSTALLATION IN THE TUNNEL

The half-cores and the transmission line conductors will probably be fabricated in an outside factory. The magnet assembly work, which is basically the laser welding of the half-cores into a magnet, can be done in an outside facility, or in an assembly hall at CERN. The assembled magnets would then be lowered down into the LHC tunnel, and placed on prepared I-beam supports. The conductor splicing, the closing of the helium flow connections, beam pipe installation, instrumentation connections, etc., would all be done in the tunnel. The tunnel work can proceed during any operation break of the LHC accelerator.

8. LER TO LHC BEAM TRANSFER DESIGN AT 1.5 TEV

Beam transfer from the LER ring into the LHC ring is the most challenging task of the LER proposal that needs to be very seriously dealt with. The injection scheme with one accelerator residing on the top of the other has been done before (e.g. Recycler and the Main Injector at Fermilab) but at considerably lower energies.

The vertical separation of the LER and LHC rings can be made to be 135 cm. This means that the 1.5 TeV beam needs to be bent down (or up) out of the LER (or LHC) ring, transported, and then bent into the LHC (or LER) ring over a vertical distance of 135 cm. About half of this distance, 67.5 cm, is needed to clear any LHC magnets. Once the LER beam has cleared these magnets it will not be difficult to transfer the beam into the LER ring. The operation of clearing the LHC magnets must take place necessarily within the available free space of the straight sections so the transfer line magnets can reside at the LHC ring level. Although the total length of the LHC straight section is about 528 m, such a free beam path is no longer than 100 m on each side of the detectors. As pointed out earlier we assumed no re-arrangement of the LHC magnets in the IR regions, so the completion and operation of the LHC accelerator proceeds as originally planned. A preliminary LER lattice design [8] was made to produce the footprint as close as possible to that of the LHC to preserve the best possible beam quality in the LER ring and in the LER-LHC beam transfer operation. Consequently, the LER-LHC transfer line magnets must use only the magnet free sections between D1 and Q5. The proposed design assumes that the beam transfer is made using 4 bends (Figure 13), each with a bending power of 84 Tm.

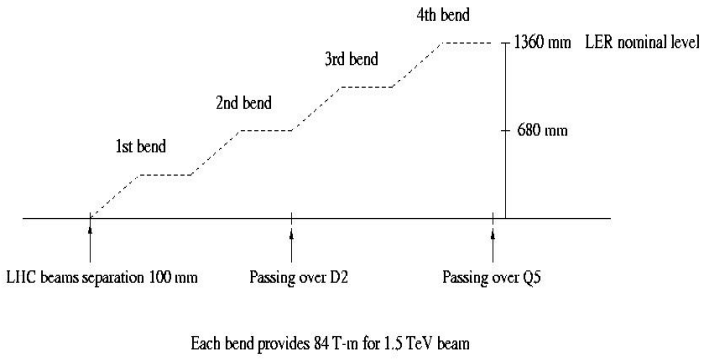

Fig. 13 A conceptual arrangement of the LHC to LER transfer line.

Two bends lift the LER beam to a level of 0.675 m to allow the transfer line magnets to pass over the D2 magnet of the LHC. The next two bends put the beam at 1.35 m above the LHC ring. The

1.35 m level becomes the nominal level of the LER ring. In the horizontal plane the LER beams separation of 150 mm will be achieved by rotating the vertically bending magnets in a plane that is perpendicular to the beam direction.

9. CONCEPTUAL DESIGN OF THE LER - LHC TRANSFER LINE MAGNETS

In the horizontal plane the clock-wise and counter-clock LHC beams have no separation at D1, but they are separated by 194 mm at D2. The first magnet pair of the first vertical bend section must be placed at a location that the clock and counter-clock beams are separated enough to allow for operating these magnets with a good magnetic field quality.

We assume that ~ 100 mm beam separation may be sufficient to design a good quality first magnet pair. Such a beam separation is near the middle of the D1–D2 distance of 86.6 m, and puts severe strain on achieving the two first bends. Their path may be slightly expanded, if needed, by placing a horizontally bending dipole, D1A, next to the exit of the D1. The D1A would be a permanent feature of the LHC. As the beams travel in opposite directions, and are inclined at the D1 (and at D1A) with opposite angles, a single dipole magnet will carry the task of bending both the LER and LHC beams off their original central LHC paths. The bending power of this magnet must be sufficient to increase the separation of the counter-rotating beams at the first LER vertical bend to at least 100 mm, but each beam must stay well within the 40 mm diameter of the LHC beam pipe. A set of two, short magnets of about 1 Tm will allow to kick each beam by ~ 10 mm sideways at the location of the first vertical bend (~ 18 m from the face of D1) thus providing the required minimum 100 mm LER beam separation for the magnet pair of the first vertical bend. The D1A dipole will also affect the LHC beams. Consequently, the field of the D2 dipole should be appropriately adjusted to a lower value to keep the LHC beams separated by 194 mm at D2. A preliminary LER-LHC transfer line magnet arrangement is shown in Fig. 14.

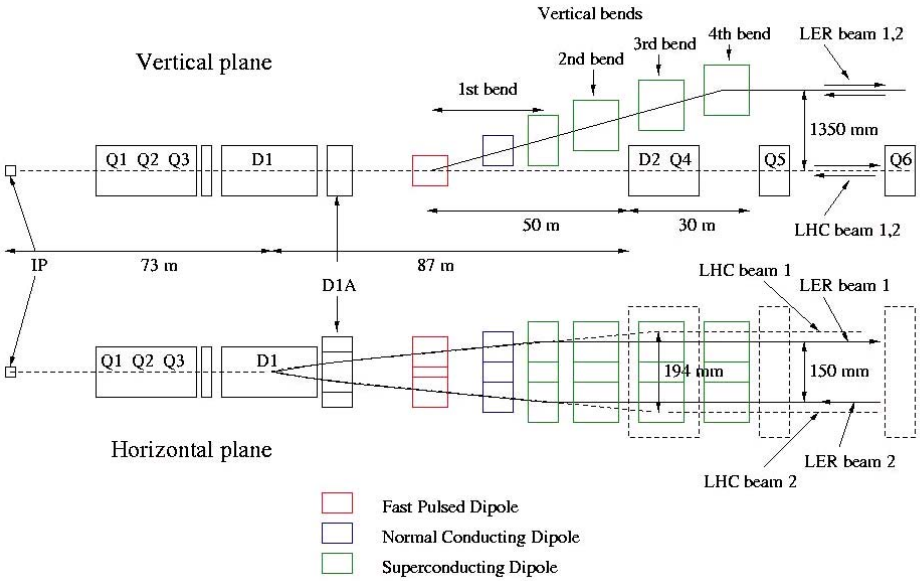

Fig. 14 A preliminary arrangement of the LER-LHC transfer line magnets.

The first vertical bend is arranged using three sets of magnets. The first set consists of fast pulsing pairs of single bore magnets which, when turned off, allow the clockwise beam to pass into the LHC ring. A drift space after the first set of magnets accommodates LER/LHC beam pipe separation. A second set consists of pairs of normal-conducting magnets, placed above the LHC beam pipe. The third set consists of two-bore, high-field superconducting magnets to complete the first bend. The 2nd, 3rd and 4th bends consists of two-bore, high-field superconducting magnets.

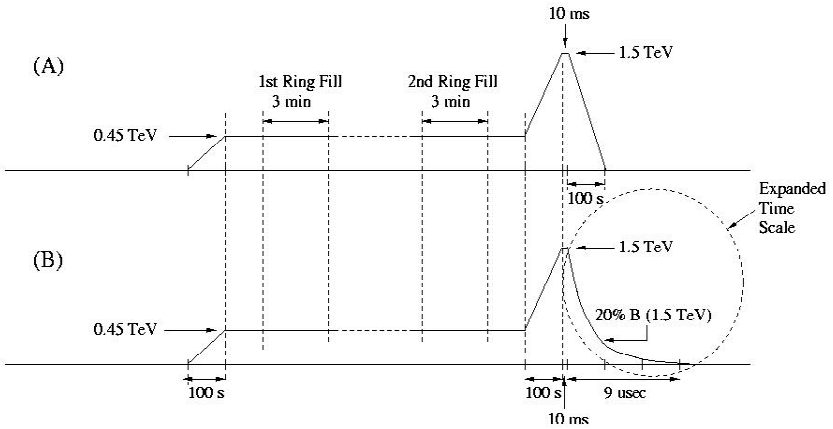

A - Ramping scheme for the LER arc and non-pulsed magnets of the LER-LHC transfer line

B - Ramping scheme for the fast pulsed magnets of the LER-LHC transfer line

Fig. 15 Timing sequence for the LER-LHC beam injection.

In order to understand the choice and arrangement of the magnets in the first bend consider the timing sequence of the SPS-LER-LHC beam transfer scheme. This is shown schematically in Fig. 15. When the SPS is ready for beam transfer, all LER magnets, including those in the transfer lines, are ramped to the required fields for the 0.45 TeV beam. A ramping time of 100 s is characteristic of the main arc LER magnets. The stacking of the first SPS beam begins and lasts about 3 min. Then the stacking of the 2nd SPS beam begins and lasts about 3 min. When the stacking of the second beam is complete the LER magnets ramp to 1.5 TeV (this takes 100 s). The 1.5 TeV beams may circulate for ~ 10 ms to stabilize, and then the fast pulsing LER-LHC transfer line is turned off forcing the beams to circulate in the LHC rings. At this point all remaining LER magnets are ramped down.

The operation of the fast pulsing magnets is more complicated due to the fact that for each beam the magnets on the opposite sides of the IR must work in tandem. This is illustrated in Fig. 16. When the tail of the LER beam has passed magnet PM2, this magnet has 3 μs to be turned off before the head of the LER bunch train returns. But PM1 must operate for an additional 89 μs until the entire LER bunch train has passed through PM2 and into the LHC. The PM magnets on each side of the IR have their counterparts of opposite timing sequence for the beam circulating in the opposite direction.

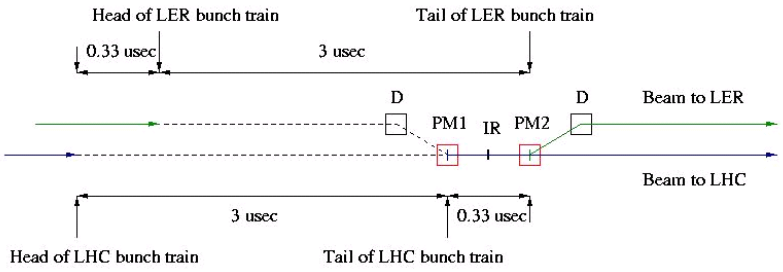

Fig. 16 Timing relation between head and tail of the LER and LHC beams passing through PM magnets.

The LER-LHC beam transfer procedure, as described above, requires the fast pulsing magnets to be ON during the SPS to LER transfer and ramping to 1.5 TeV of all magnets in both LER rings. Then they are turned off in a very short time (~ 3 μs) to force the beams to circulate in the LHC rings only. This is an unusual application of fast pulsing magnets. In accelerators, these magnets (known as "kickers") are mostly used to remove the circulating beam, e.g. for beam dumping. It means that they

are ramped up fast, stay ON until the beam is out, and can ramp down slowly to stand-by mode. Beam transfer from one accelerator to another, is typically done using a tandem of kicker and Lambertson magnets. The kicker magnet is used to move the beam in (or out) of the field-free zone in the Lambertson. In the LER application, a Lambertson magnet would have to stay ON during the LER beam stacking, and then follow the beam energy increase. The kicker magnet paired with the Lambertson, would force the LER beam into a field-free zone, and thus allow the beam passage into the LHC ring. The kicker would have to have a rise time of 3 μs, stay ON for 87 μs, and then decay in 3 μs so that its field would not interfere with the circulating LHC beam. This meanss that for LER-LHC beam transfer a design with a kicker and a Lambertson magnet may be difficult. Moreover, Lambertson magnets are difficult to design, and relying on the use of iron cores are limited to rather low fields. With the required vertical bend, the spatial closeness of the clockwise and counter-clockwise beams and a very limited free space between the D1 and D2 LHC dipoles, the application of Lambertson magnets for the beam transfer does not seem appropriate.

A fast pulsing vertical dipole set, with a ~ 10 Tm total bending power, must lift the LER beam by ~ 70 mm above the LHC nominal beam line using an overall beam path of ~ 17 m. The magnet aperture gap must accommodate the space needed for the LHC beam pipe (40 mm) and the magnet aperture width must accommodate the vertical deflection of the LER beam (up to 40 mm). The fast pulsing magnets have a horizontal B-field orientation to bend the beam in the vertical direction.

The proposed fast pulsing magnets must be powered with a single conductor in order to minimize the inductance. Typically, such magnets can be designed with an inductance of ~ 1 μH for the length of ~ 1 m. The lower the inductance, the lower the voltage generated when the magnet current supply is turned off, so the choice of magnet size and field are largely driven by the parameters of the power converter. Based on experience with the VLHC low field magnet, we concluded that we could use a 90 kA dc power unit for the fast pulsing magnet operation. With a 1 μH magnet inductance the expected voltage drop at a 3 μs turn-off is ~ 30 kV - plausibly manageable with a magnet length of 0.8 - 0.9 m, a beam drift spacing for magnet connections and a longer drift space for the separation of the LHC and LER beam pipes. With a 90 kA current source, the magnetic field decreases as the magnet aperture increases while accommodating increased vertical separation of the LER beam. In order to estimate the available field with 90 kA current we assumed a magnet based on the “intersecting ellipse” conductor geometry [10] as shown in Fig. 17.

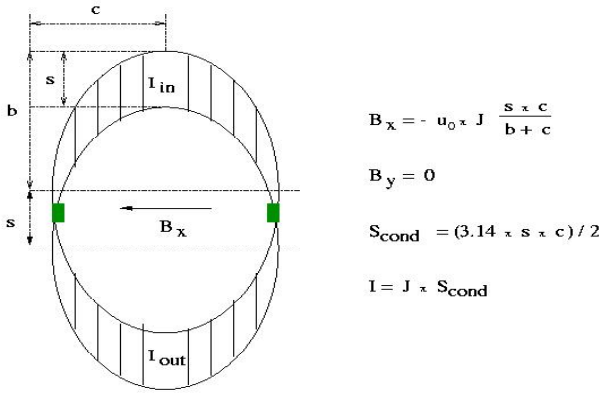

Fig. 17 Dipole magnet model approximation.

Using a formula from [10] (3.22, page 31) we derived the B-field for a 90 kA current but with a vertical beam separation of 10 mm, 20 mm, 30 mm and 40 mm and a magnet gap of 40 mm. The deduced B-fields are: 1.55 T, 1.40 T, 1.28 T and 1.17 T for the 10 mm, 20 mm, 30 mm and 40 mm LER-LHC beam separation, respectively. With these magnet B-fields we arranged the first section of the first bend of the transfer line magnets as presented in Table 3.

The cross-sectional area of the conductors in all magnets is 236 mm^2. With such a small conductor the power dissipation, even at 30 kA, makes it impossible to operate for the 10 minutes required for LER to LHC beam transfer. The solution is to make the conductors from OFHC copper (99.999 % pure), and to operate the magnet below 20 K. The resistance of a 1 m long magnet conductor is then ~ $2x10^{-8}$ Ω, and a preliminary analysis [11] using a mechanical design of the magnet as described below, suggests that a very small flow rate of supercritical liquid helium (less than 3 g/s) is sufficient to sustain magnet operation "indefinitely" at 30 kA, and for a reasonable time for operation, at 90 kA. A conceptual design of a fast pulsing magnet pair is shown in Fig. 18. The elliptically shaped magnet conductors are housed inside the cryo-pipe (austenitic steel, 0.65 mm) and outside the elliptical vacuum beam pipe. The elliptically shaped conductors will be assembled from multiple layers of thin copper plates to minimize the effect of eddy currents at high frequencies. In our application the fast pulsing magnets are ramped up slowly so only at power turn-off do eddy currents appear. This is of less concern, though, for the beam transfer operation.

Table 3
LER-LHC Transfer line vertical bending magnets

	B (T)	Magnet length (m)	nbr of magnets	Drift space (m)	Total magnet length (m)	vertical shift (cm)	total vertical shift (cm)	beam path (m)	magnet type
1st bend									
	1.55	0.8	2	0.2	1.8	1	1	1.8	FPD, 1 bore, pair
	1.40	0.8	2	0.2	1.8	1	2	3.6	FPD, 1 bore, pair
	1.28	0.7	3	0.3	3.0	1	3	6.6	FPD, 1 bore, pair
	1.17	0.7	3	0.3	3.0	1	4	9.6	FPD, 1 bore, pair
LER-LHC beam pipe separation				7.2		3	7	16.8	
	2.7	0.9	8	1.6	8.8	8	15	25.6	NCD, 1 bore, pair
drift space				2.4		1	16	27	
	7.2	0.8	6	1.8	6.6	17	33	33.6	SCD, 2 bore
drift space				1		1	34	34.6	
2nd bend									
	7.2	0.8	15	3	15	34	68	49.7	SDC, 2 bore
LER beam passes over face of D2									
3rd bend									
	7.2	0.8	15	3	15	34	102	64.7	SDC, 2 bore
4th bend									
	7.2	0.8	15	3	15	34	136	79.7	SDC, 2 bore
LER beam passes over face of Q5									

The insulation of the cryo-pipe from the conductors is provided by a 2 mm thick Nomex layer. Nomex is frequently used for electrical insulation in both warm and cold environments. A 2 mm thick Nomex layer withstands a pulsed voltage of > 60 kV. It is very hard, with no measurable compression observed in tests with 0.1 MPa pressure. At cryogenic temperatures its mechanical strength increases. The magnetic force between conductors pushes them apart, so the top of the conductors should be flattened and properly matched to the insulating Nomex, to the cryo-pipe wall behind and to the G11 support rings (subject of simulations). The beam pipe is made of 0.65 mm thick non/magnetic austenitic steel. Electrical insulation (60 kV) is provided by 10 layers of 25 μm Kapton tape. Liquid helium flows in the space between the cryo-pipe and the Nomex insulation, covering most of the conductor. Nomex is easy to machine, allowing the punching of numerous perforations to facilitate efficient cooling in spite of the small cross-sectional area of the liquid helium flow.

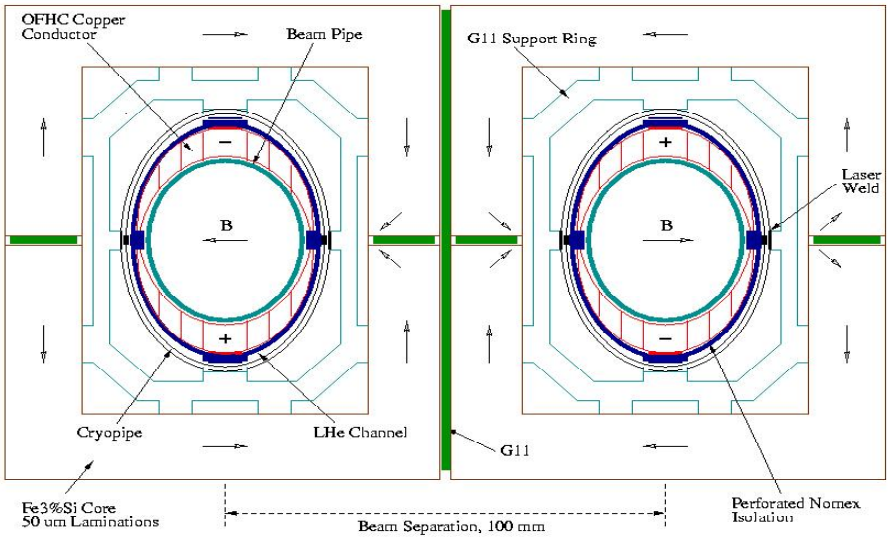

Figure 18. A conceptual design of a fast pulsing magnet pair.

Although the magnetic field in the gap is entirely generated by the conductor, stray field from the neighboring magnet will affect its quality. In order to minimize this effect, each magnet is embedded inside a pair of C-type cores. The cores are insulated from each other with G11 sheets. The cores are wound using a 50 μm Fe3%Si tape. Magnetic cores made from such tapes were recently successfully used in the production of fast (3 μs rise time) kicker magnets [12]. We roughly estimate that a 20 mm thick core is sufficient to minimize the stray fields to a manageable level. As the beams in the transfer line separate, the thickness of the core can be increased, if needed.

The magnet cryo-pipe will be covered with MLI for heat absorption and the whole magnet assembly will be placed inside the cryostat. This allows minimization of the current bus due to a low resistance of the OFHC copper in the cold state. This also minimizes the size of the power converter itself, which is largely determined by the size of the copper bars carrying the current. Parts of the rectifiers may need to be kept > 100 K, to ensure proper operation of the diodes. A design of a 90 kA power supply with components partially working at cold temperatures is being considered [13].

Turning-off the fast pulsing magnets in a time span of 3 μs is the most challenging part of the LER transfer line magnets proposal. As the resistance of the conductors is a small fraction of a μΩ, the turning off of the power supply will result in a long current decay time. A short decay time constant must be imposed on the system. An IGCT (Integrated Gate Commutating Thyristor) device installed in-line with the magnet leads, is typically used for such applications. IGCTs, however, are bulky, expensive and difficult to use in the cold environment. A new idea of enforcing fast magnet current decay that takes advantage of the cold environment around the magnet, is proposed. A possible conceptual design [13] of such a system is shown in Fig. 19.

In this design the power connections to the magnet as well as a portion of the power supply itself are placed in a cryogenic environment made of three zones. A 15 K zone contains the magnet conductors as described earlier. A 40 K zone is primarily to support the working of the HTS leads to the magnets. We anticipate that it may be possible to place the switcher cells inside a 100 K zone if diodes designed to operate at such temperatures are available. On one of the current leads to the magnet, there are 3 logically distinct systems: HTS, PT (power transformer) and SD (superconducting dump). In order to stop the magnet current, the PT accepts a reversed, 30 kV, 100 kA and 3 s long power signal. The superconductor heats-up, the HTS leads stop conducting and the current returns to the power supply through the SS substrate of the HTS and the shunt resistors. The key to success of this idea is the feasibility to use the SS substrate of the HTS as a dump resistor. The switcher cells have no connection to ground. Consequently, unloading of the current must take place within the

conductors in the power supply system. Simulations [13] indicate that the minimum resistance of SD should be ~ 0.2 Ω with SR at ~ 0.075 Ω. The HTS uses SS tape as a substrate but they also have a substantial amount of stabilizing silver that makes its resistance in a non-superconducting state very low [14]. NbTi conductor in a CuNi matrix, soldered onto the SS bar offers much higher resistance in a non-superconducting state [15] but requires operation at 4.5 K. In that case both the magnet and the accompanying superconducting dump resistor would have to operate at 4.5 K. The advantage of the CuNi/NbTi conductor is that it would minimize the size of the dump resistor. As supercritical helium is readily available in the tunnel, this should not be a problem.

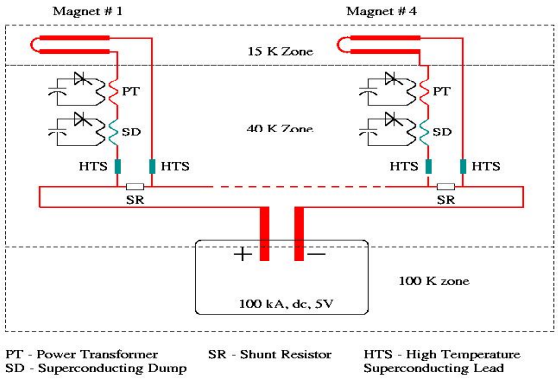

Fig. 19 Conceptual arrangement of a power converter for a cryogenic environment.

The application of a cryogenic environment to a fast pulsing magnet power converter also facilitates integration in the tunnel. Three to four fast pulsing dipoles of the LER-LHC transfer line would be housed in a common cryostat, with 2 power converter assemblies mounted on top. Possible vertical and horizontal arrangements of the normal conducting, cold magnets are shown in Fig. 20.

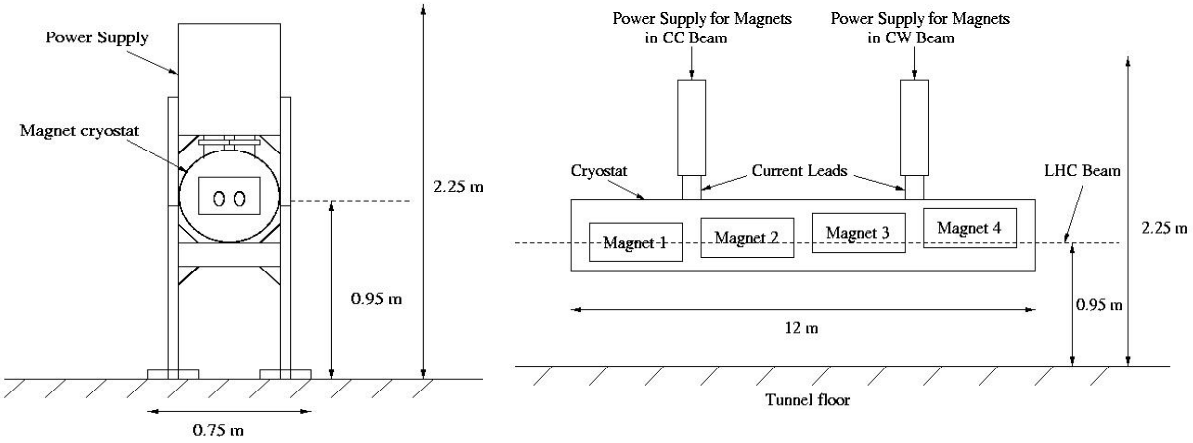

Fig. 20 Left: A vertical view of the fast pulsing dipole arrangement in the tunnel. Right: A side view of the vertical pulse magnet set in the tunnel. Note, the horizontal and vertical scales are not the same.

10. DETECTOR SAFETY WITH THE LER-LHC TRANSFER LINES

If the LER ring would bypass the IR regions, there would be no risk of detector damage due to a magnet failure during the LER-LHC beam transfer. For the LER beams to bypass the detectors in the straight section area would require a minimum bending angle of ~ 180 mrad. This would make it difficult to design successful transfer line beam optics that matches the LER footprint to the LHC. Probably the beam would have to be kicked off the LER ring much farther than 260 m (1/2 of straight section), increasing tunnel construction cost, now estimated at $20M - $25M) per 600 m of length.

In order to protect the detectors, additional steel collimators of at least 10 m length would be required between the first fast pulsing magnet set at the D1 LHC dipole and the first vertical fast pulsing magnet further downstream. CMS studies [16] indicate that with a total loss of a 7 TeV beam at a radius of 15 mm, the instantaneous fluence in the tracking detector is equivalent to 5 % - 10 % of the annual LHC operation dose. The maximum energy of the LER beam is 1.5 TeV, reducing considerably the radiation dose indicated and with additional collimators the dose due to the LER transfer line failure should be viewed as minor compared with possible failures of the standard LHC.

11. CROSSOVER MAGNETS AND BEAM DUMP

Beam crossover magnets based on the transmission line conductor were discussed in the VLHC Design Study [1], and the same proposal could be applied to the LER accelerator. The LER accelerator will utilize the RF and the beam dump systems of the LHC accelerator.

12. MAJOR COMPONENT COST ESTIMATE

The cost in 2001 $ includes 20 % contingency, and was estimated by scaling down by a factor of 10 from the VLHC proposal [1]. The cost of power converters, cooling water, etc. is included, but that of magnet support fixtures in the tunnel, and of some other necessary modifications (e.g. possible need for tunnel enlargement at the transfer line magnet locations) are not included.

Table 4
Cost estimate

	System	[$M]
1	Main arc magnets	80
2	Correctors and special magnets	12
3	Transfer line magnets	12
4	Installation (120 people @ 100K$/y)	24
5	Beam pipe vacuum system	15
6	Main arc magnet cryogenic support	7
	Grand Total	150

Table 5
Tentative schedule

	Activity	Time [Y]	Lapsed time [Y]
1	LER accelerator design, including transfer lines	1	1
2	Prototyping and testing transfer line magnets (and main arc dipole magnet, if needed)	2	2
3	Preparation of main arc magnet industrial production	1	2
4	Magnet production	3	5
5	Magnet installation in the tunnel	2	5
6	LER commissioning	1	6

13. SCHEDULE OF MAGNETS FABRICATION AND INSTALLATION IN THE TUNNEL

A task flow-chart is shown in Fig. 21, and the very tentative schedule (see Table 5) is very speculative. Items 1–3 and the items 4-5 can proceed simultaneously, but item 4 must follow items 1-2, so the magnet production cannot start sooner than 2 years from the time "zero". As soon as some main arc magnets are produced and tested, the installation in the LHC tunnel may begin.

The overall time for the LER completion work will depend on the number of months per year allowed for LER installation, and the number of crews working simultaneously on the installation in the tunnel. We assumed that 20 crews of 6 people should be able to install 40 magnets per week, or 1200 magnets in 30 weeks (~ 8 months). Hence with one 4-months break of the LHC operation per year, the LER installation in the tunnel may be completed in a period of two years. In summary, the LHC operation with the LER as injector could be ready in 6 years from the time "zero".

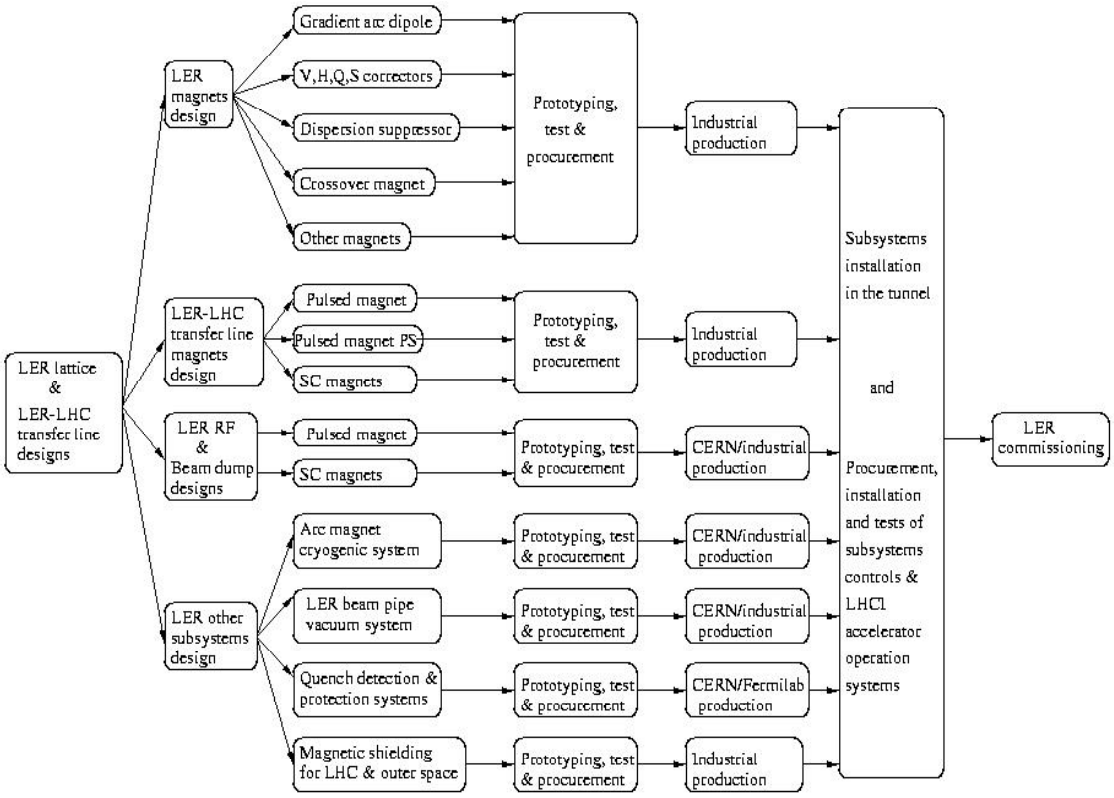

Fig. 21 A task flow-chart for the LER accelerator design and construction based in part on VLHC Stage1 construction schedule proposal [1].

14. CONCLUSIONS

We made a very preliminary overview of the feasibility of installing an injector accelerator ring (LER) in the LHC tunnel using VLHC Stage 1 super-ferric magnets. We believe that there are no insurmountable obstacles for such an undertaking. Transfer of the beam from the LER ring to the LHC is challenging, but should be feasible and cost effective due to a possible simplification involving a minor re-arrangement of the D1 LHC dipole. Further consideration of the LER accelerator sub-systems, the design of the transfer line magnets, re-design (if needed) of the main arc magnet, design of the corrector and other special magnets will require a full study of the LER lattice, the LER to LHC injection scheme, beam stability, and the interaction between LER and the LHC accelerators.

ACKNOWLEDGEMENTS

We greatly profited from several illuminating discussions with Gianluigi Arduini, Jean-Pierre Koutchouk, Yvon Muttoni, John Osborne, Germana Riddone of CERN, with Giorgio Ambrosio, William Foster, Steven Hays, John Johnstone, Vladimir Kashikhin, Michael Lamm , Tanaji Sen and Vladimir Shiltsev of Fermilab, and with Masayoshi Wake of KEK.

We are also greatly indebted to Steve Holmes, Robert Kephart and Peter Limon for inspiration and support.

REFERENCES

[1] LHC Design Report Vol 1, O. Brunning et al., CERN-2004-003, Section 4.7 Dynamic aperture.

[2] Design Study for a Staged VLHC, Fermilab-TM-2149 (2001).

[3] H. Piekarz, A Test of 2 Tesla Superconducting Transmission Line Magnet System, MT19, IEEE Trans. Appl. Supercond. 16 2 (2006) 342.

[4] S.L. Hays, The 100 kA DC Power Supply for a Staged Hadron Collider Superferric Magnet, MT19, IEEE Trans. Appl. Supercond. 16 2 (2006) 1626.

[5] Y. Huang, The Development of 100 kA Current Leads for Superconducting Transmission Line Magnet, MT19, IEEE Trans. Appl. Supercond. 16 2 (2006) 457.

[6] V.S. Kashikhin, Test Results of a 2 Tesla Transmission Line Magnet obtained with 102 Sensor Array of Hall Station, MT19, IEEE Trans. Appl. Supercond. 16 2 (2006) 1844.

[7] G. Velev, Field Quality Measurements of a 2 Tesla Transmission Line Magnet, MT19, IEEE Trans. Appl. Supercond. 16 2 (2006) 1840.

[8] J. Johnstone, Preliminary design of the LHCI lattice and the LHCI-LHC transfer line, work in progress (2006).

[9] V.l. Shiltsev, Preliminary study of the beam impedance and instabilities for the LER, work in progress (2006).

[10] Martin N. Wilson, Superconducting Magnets, ISBN 0 19 854810 9 (1983).

[11] Y. Huang, Cryogenic Analysis of the LER Fast Pulsing Magnet, work in progress (2006).

[12] M. Mayer, D. Fox, F. Castronuovo and U. Jansson, IEEE Transactions on Magnetics 40 2 (2004) 3051.

[13] S. Hays, Conceptual Design of the LER Pulsed Magnet Power Supply, work in progress (2006)

[14] L. Masur and J. Kellers, Development of Long Length HTS wire for Electrical Power Applications, American Superconductor Corporation, Two Technology Drive, Westborough, MA 01581, USA

[15] H. Piekarz and G.W. Foster, Design Study for VLHC, Sec. 5.2.4, Fermilab-TM-2149 (2001)

[16] CMS Technical Proposal, CERN/LHCC 94-3 (1994).

PROGRAM ON MAGNETS AND SUPERCONDUCTORS UNDER DOE SUPPORT: A GLOBAL VIEW

B. Strauss
Office of High Energy Physics, U.S. Department of Energy

Abstract
Several operational offices within the U.S. Department of Energy support superconductor and superconducting magnet development. Thanks to this support, regular progress has been made in the development of high performance superconducting material, and in that of the next generation of very high field accelerator magnets based on the use of brittle conductor.

1. INTRODUCTION

Both superconductor and superconducting magnet development are supported by several operational offices within the U.S. Department of Energy. The Office of Energy Transmission & Efficiency and the Office of Basic Energy Sciences are the main support for the development of high temperature superconductors (HTS). The Office of High Energy Physics (OHEP) is responsible for the program to develop next generation accelerator, beam line magnets and detector magnets.

2. HIGH TEMPERATURE SUPERCONDUCTORS (HTS)

The goals of this approximate $34 million annual budget are to develop HTS wire with 100 times the power capacity of conventional copper and aluminum cables and at a cost of $10/kiloamp-meter, to increase three to five times the amount of current carrying capacity of transmission cables within existing right-of-way and to develop HTS electric power equipment with one-half the energy losses and on-half the size of conventional units. Strategic research in this area is carried out primarily at national laboratories and universities and focuses on the underlying characteristics of HTS and associated technologies. Second generation (YBCO) development to improve coated conductors is done on a partnership with laboratories and industry. Utility applications are developed primarily by industry in partnership with various utility companies. The annual budget is about equally divided between each of the activities above.

3. DEVELOPMENT OF NEXT GENERATION MAGNETS FOR HEP

The Office of High Energy Physics (OHEP) funds a broad-based program to develop next generation accelerator, beam line, and detector magnets. The program necessarily includes the development of suitable superconductors and insulation.

3.1 Programs supported at the universities

Five university programs are supported. These are at Florida State University, The Ohio State University, The University of Wisconsin (soon to be at the National High Magnetic Field Laboratory), Texas A&M University, and NIST. Research topics range from optimization of liquid helium heat transfer at sub-lambda temperatures to the optimization of Nb_3Sn conductors and magnets. The annual budget for these activities is about $1.7 million. At the U.S. National Laboratories OHEP supports a broad program of development in superconducting technologies. Three laboratories, Fermilab, LBNL and BNL are supported within this program.

3.2 Programs supported at the U.S. national laboratories

The OHEP supports a broad program of development in superconducting technologies at the U.S. National Laboratories. Fermilab, LBNL and BNL are supported within this program.

3.2.1 Fermilab

Work at Fermilab is supported by the base funding of that laboratory and the local budget is determined by their director. In superconducting magnets their efforts are directed to support of magnets for the Tevatron, participation in the US LHC Accelerator Project and the development of high field magnets for future accelerators. For the LHC, Fermilab fabricated 18 interaction region quadrupole cold masses that were inserted into 9 cryostats. Fermilab also provided the cryostats for the quadrupole cold masses provided by KEK. The laboratory's base program has also supported development on shell-type Nb_3Sn quadrupoles.

3.2.2 Lawrence Berkeley National Laboratory

The effort at the Lawrence Berkeley National Laboratory has been to focus on exploring coil and structure design options while pushing the field limits of superconducting dipoles. This has been done on a well conceived set of model magnets consistent with a limited budget. In this program peak fields of 16 tesla have been achieved with stress levels of 180 MPa in the structure. The goal is the achievement of a 20 tesla dipole.

3.2.3 Brookhaven National Laboratory

At the Brookhaven National Laboratory work has been focused on developing react and wind technologies for Nb_3Sn magnets. Using this method a common coil racetrack magnet was constructed reaching 10 Tesla. BNL has been the center of high current short sample testing.

3.3 Small Business Innovation Research (SBIR) Program

OHEP leverages the Small Business Innovation Research (SBIR) program that is mandated by Congress. In fiscal year 2005 there were 10 Phase I grants at $100,000 each for development of Nb_3Sn, MgB_2 and advanced insulations. In addition there were nine active Phase II grants funded at $600,000 over two years in support of superconductor development.

3.4 LHC Accelerator Research Program (LARP)

All of these efforts have been used to leverage the LHC Accelerator Research Program (LARP) that presently funds superconductor magnet development at the level of $6 million per annum. The goal is to develop a four meter long, 210 T per meter, quadrupole prototype magnet. LARP has identified and is working on a program that makes use of the abilities of each of the national laboratories. Numerous technical challenges have been identified and are being resolved.

4. CONCLUSION

The ongoing programs have achieved the following goals:

- Nb_3Sn critical current performance of 2500 Acm^{-2} at 15 Tesla and 4.2 K;
- Development of co-processed ceramic insulations;
- Attainment of a 16 Tesla field in an Nb_3Sn dipole;
- Understanding of low field instabilities in Nb_3Sn magnets;
- Development of integrated design tools.

This provides a solid base for addressing the remaining problems in the quest for reliable very high field superconducting accelerator magnets. Intellectual cooperation with the CARE/NED effort of the European community is excellent and should ensure the necessary world-wide optimization of efforts.

Presentations
(slides)

* * * * *

Beam-Beam tune spread for round beams

tune shift from head-on collisions (primary IP's)

$$\xi_{HO} = \frac{N_b r_p}{4\pi\gamma\varepsilon}$$

limit on ξ_{HO} limits $N_b/(\gamma\varepsilon)$

tune shift from long-range collisions
n_{par} parasitic collisions around each IP

$$\xi_{LR} \approx \pm 2\, n_{par}\, \frac{\xi_{HO}}{(d_{sep}/\sigma)^2}$$

increases for closer bunches or reduced crossing angle

$$\frac{d_{sep}}{\sigma} \approx \theta_c \frac{s}{\sigma(s)} \approx \theta_c \sqrt{\frac{\beta^*}{\varepsilon}}$$

relative beam-beam separation for full crossing angle θ_c

	ξ_{HO} / IP	no. of IP's	ΔQ_{bb} total
SPS	0.005	3	0.015
Tevatron (pbar)	0.01-0.02	2	0.02-0.04
RHIC	0.002	4	~0.008
LHC (nominal)	0.0034	3	~0.01

high-lumi in IP1 and IP5 (ATLAS and CMS), halo collisions in IP2 (ALICE) and low-lumi in IP8 (LHC-b)

conservative value for total tune spread based on SPS collider experience

Performance limitations of the present LHC

and LHC luminosity upgrade paths

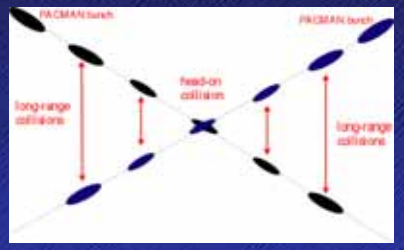

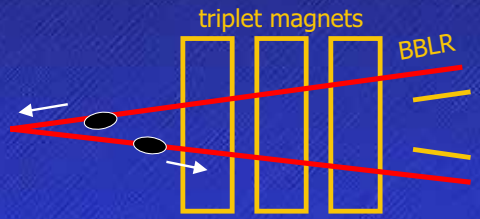

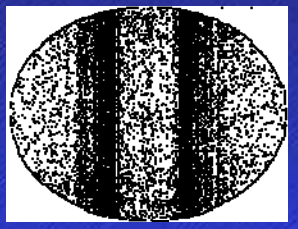

Beam-Beam tune footprints

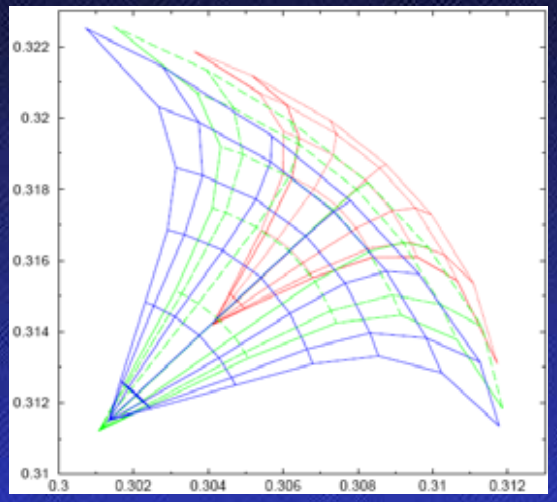

Tune footprints corresponding to betatron amplitudes extending from 0 to 6σ for LHC nominal (red-dotted), ultimate (green-dashed), and "large Piwinski parameter" configuration (blue-solid) with alternating H-V crossing only in IP1 and IP5.

Outline

- Beam-beam limit and nominal LHC performance
- Luminosity optimization and operational margins
- LHC upgrade paths and beam induced heat loads
- Catalog of beam performance limitations
  - IR aperture: flat beams and quad re-alignment
  - Magnet quench limits
  - Collimation, impedance, and beam intensity
  - Electron cloud effects
  - Feedback systems and emittance preservation

Minimum crossing angle

Beam-Beam Long-Range collisions:

- perturb motion at large betatron amplitudes, where particles come close to opposing beam
- cause 'diffusive' (or dynamic) aperture, high background, poor beam lifetime
- increasing problem for SPS, Tevatron, LHC, i.e., for operation with larger # of bunches

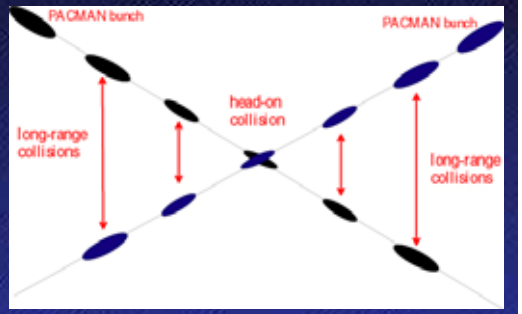

dynamic aperture caused by n_{par} parasitic collisions around two IP's

$$\frac{d_{da}}{\sigma} \approx \frac{\theta_c}{\sigma_\theta} - 3\sqrt{\frac{n_{par}}{32}\frac{N_b}{10^{11}}\frac{3.75\mu m}{\varepsilon_n}} \Rightarrow \frac{\theta_c}{\sigma_\theta} \approx 6 + 3\sqrt{\frac{I}{0.5A}\frac{3.75\mu m}{\varepsilon_n}}$$

$\sigma_\theta = \sqrt{\frac{\varepsilon}{\beta^*}}$ angular beam divergence at IP

higher beam intensities or smaller β^* require larger crossing angles to preserve dynamic aperture and shorter bunches to avoid geometric luminosity loss

$\Rightarrow$ baseline scaling: $\theta_c \sim 1/\sqrt{\beta^*}$, $\sigma_z \sim \beta^*$

LHC working points in collision

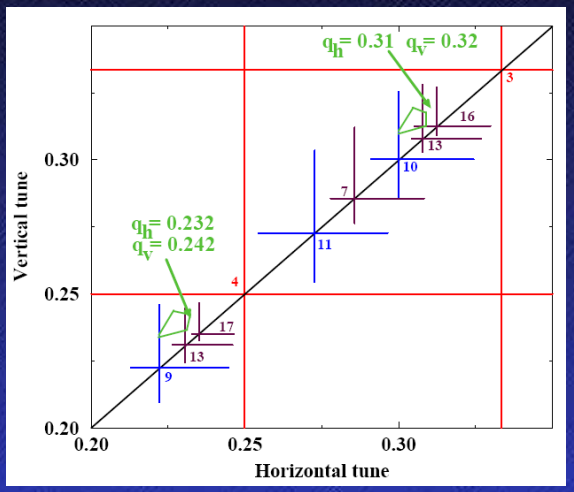

The beam-beam tune footprint has to be accommodated in between low-order betatron resonances to avoid diffusion and bad lifetime. More resonance-free space near the coupling resonance $\Rightarrow$ good coupling compensation may allow $\Delta Q_{bb} \sim 0.015$

Various LHC upgrade options

parameter	symbol [unit]	nominal	ultimate	shorter bunch	longer bunch
number of bunches	n_b	2808	2808	5616	936
protons per bunch	N_b [10^{11}]	1.15	1.7	1.7	6.0
bunch spacing	Δt_{sep} [ns]	25	25	12.5	75
average beam current	I [A]	0.58	0.86	1.72	1.0
normalized emittance	ε_n [μm]	3.75	3.75	3.75	3.75
longitudinal profile		Gaussian	Gaussian	Gaussian	flat
rms bunch length	σ_z [cm]	7.55	7.55	3.78	14.4
ß* at IP1&IP5	β^* [m]	0.55	0.50	0.25	0.25
full crossing angle	θ_c [μrad]	285	315	445	430
Piwinski parameter	$\theta_c \sigma_z/(2\sigma^*)$	0.64	0.75	0.75	2.8
peak luminosity	L [10^{34} cm^{-2} s^{-1}]	1.0	2.3	9.2	8.9
luminosity lifetime	τ_L [h]	15.5	11.2	6.5	4.5
events per crossing		19	44	88	510
luminous region length	σ_{lum} [mm]	44.9	42.8	21.8	36.2

Luminosity optimization

$\sigma^* = \sqrt{\varepsilon\beta^*}$ transverse beam size at IP $\quad \varepsilon_n = \gamma\varepsilon = \gamma\frac{\sigma^2}{\beta}$ normalized emittance

$$L = \frac{n_b f_{rev} N_b^2}{4\pi\sigma^{*2}} = \frac{\gamma}{4\pi\beta^*}\frac{N_b}{\varepsilon_n} I$$

peak luminosity for head-on collisions round beams, short Gaussian bunches

$I = n_b f_{rev} N_b$ total beam current
- long range beam-beam
- collective instabilities
- synchrotron radiation
- stored beam energy

N_b/ε_n beam brightness
- head-on beam-beam
- space-charge in the injectors
- transfer dilution

Collisions with full crossing angle θ_c reduce luminosity by a geometric factor F

$$F \cong 1/\sqrt{1+\left(\frac{\theta_c \sigma_z}{2\sigma^*}\right)^2}$$

maximum luminosity below beam-beam limit

☐ short bunches and minimum crossing angle (baseline scheme)

H-V crossings in two IP's ☐ no linear tune shift due to long range

total linear bb tune shift also reduced by F $\quad \Delta Q_{bb} = \xi_x + \xi_y \cong \frac{N_b r_p}{2\pi\varepsilon_n} F$

Luminosity with Flat Beams

Flat beams means aspect ratio $r \neq 1$ at the IP:

$$\varepsilon_x = \varepsilon_y = \varepsilon, \quad \beta_x^* \equiv r\beta^*, \quad \beta_y^* \equiv \beta^* / r, \quad r = \frac{\sigma_x^*}{\sigma_y^*} = \sqrt{\frac{\beta_x^*}{\beta_y^*}}$$

The X-ing plane is always the plane where the beam size is largest at the IP (*i.e.* smallest at the triplet):

- To gain aperture in the triplet (smaller X-ing angle and better matching of beam aspect ratio to beam-screen shape)
- To gain luminosity (geometric loss factor closer to unity)

$$L_{\text{flat}} = \frac{L_{\text{round head-on}}}{\sqrt{1+\left(\frac{\theta_c \sigma_z}{2r\sigma^*}\right)^2}}, \qquad \sigma^* = \sqrt{\sigma_x^* \sigma_y^*} = \sqrt{\varepsilon\beta^*}$$

Heat loads per beam aperture for various LHC upgrade options

parameter	symbol [unit]	nominal	ultimate	shorter bunch	longer bunch
protons per bunch	N_b [10^{11}]	1.15	1.7	1.7	6.0
bunch spacing	Δt_{sep} [ns]	25	25	12.5	75
average beam current	I [A]	0.58	0.86	1.72	1.0
longitudinal profile		Gaussian	Gaussian	Gaussian	flat
rms bunch length	σ_z [cm]	7.55	7.55	3.78	14.4
Average electron-cloud heat load at 4.6–20 K in the arc for R=50% and δ_{max}=1.4 (in parentheses for δ_{max}=1.3)	P_{ecloud} [W/m]	1.07 (0.44)	1.04 (0.59)	13.34 (7.85)	0.26 (0.26)
Synchrotron radiation heat load at 4.6–20 K	P_γ [W/m]	0.17	0.25	0.50	0.29
Image currents power at 4.6–20 K	P_Ω [W/m]	0.15	0.33	1.87	0.96
Beam-gas scattering heat load at 1.9 K for 100-h beam lifetime (in parentheses for a 10-h lifetime). It is assumed that elastic scattering (~40% of the total cross section) leads to local losses.	P_{gas} [W/m]	0.038 (0.38)	0.056 (0.56)	0.113 (1.13)	0.066 (0.66)

Flat beams

- Interesting approach, flat beams may increase luminosity by ~20-30% with reduced crossing angle
- Symmetric doublets studied by J. Johnstone (FNAL) require separate magnetic channels, *i.e.* dipole-first, Crab cavities or special quads
- Tune footprints are broader than for round beams, since there is only partial compensation of parasitic beam-beam encounters by the H/V crossing scheme. More work needed to evaluate nonlinear resonance excitation.
- Probably requires BB Long Range compensation
- Recently S. Fartoukh has found an interesting flat beam solution with anti-symmetric LHC baseline triplets

LHC performance limitations from IR optics constraints

- The triplet aperture is completely filled for nominal LHC conditions
- However there are two ways to better use the available aperture with "minimal" modifications:
  - Flat beams
  - IR quadrupole re-alignment

IR quadrupole re-alignment (R. Tomàs)

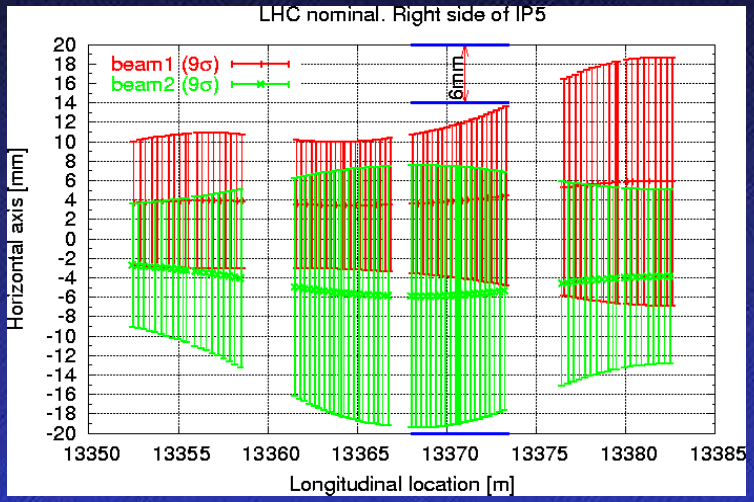

- Aperture gain of up to 6 mm by Q2 re-alignment
- Find optimum for aperture and/or energy deposition
- Present orbit correctors may not be strong enough

Beam aspect ratio vs triplet aperture

beam screen orientation for H/V scheme

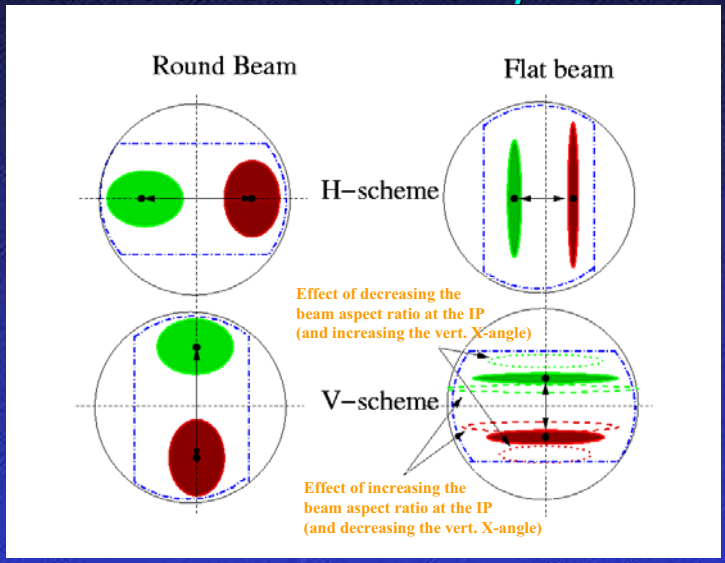

Find the optimum matching between beam-screen and beam aspect ratio

Magnet quench levels

follow-up of CARE-HHH-AMT workshop (P. Pugnat)

Review of past estimates for LHC dipoles (D. Leroy)

- **Continuous losses: 10 mW/cm³ or 0.4 W/m of cable produces $\Delta T < 0.2$ K with the insulation selected for MBs $\Rightarrow$ ~10^7 p/s at 7 TeV**
- **Transient losses: enthalpy margin ~1 mJ/cm³ from insulated conductor and ~35 mJ/cm³ from LHe (if $\Delta t_{loss} > 8$ ms)**

LHC & Magnet Operation (R. Schmidt & S. Fartoukh)

- During the ramp, quench margins of MB's & MQ' decrease significantly
- During the squeeze the margin of some quadrupoles in experimental insertions could decrease.

Quench Levels and Transient Beam Losses at HERA (K. Wittenburg)

- Empirical approach:
  - adiabatic approximation for quench level: 2.1 mJ/cm³ for $\Delta T_{cs} = 0.8$ K
  - cooling & MPZ concept taken as safety margins,
  - x16 the threshold in p/s for continuous loss rate (from Tevatron)
- Experiences & Lessons:
  - **Quenches occurred at about a factor 5 below expectation**
  - BLM's cannot protect against instantaneous losses

Pushing the LHC luminosity by 10-20%

Case	β_x^* [cm]	β_y^* [cm]	θ_c [μrad]	n_1 at triplet	geometric lumi loss [%]	L/L_{nom}
Nominal r=1, β^*=55 cm	55	55	285	~7	83.9	1.00
Flat r=2, β^*=55 cm	110	27.5	201	~7	95.1	1.13
Flat r=1.6, β^*=55 cm	88	34.4	225	~7.5	92.7	1.10
Flat r~1.7, β^*~51 cm	88	30	225	~7	92.7	1.18

All these cases are allowed by the nominal LHC hardware: layout, power supply, optics anti-symmetry, beam screen orientation in the triplets (only changing the present H/V scheme into V/H scheme)

Efficiency of the Cleaning System

- The LHC Cleaning System should allow to run the machine close to the quench limit of the super-conducting magnets for the specified lifetime:

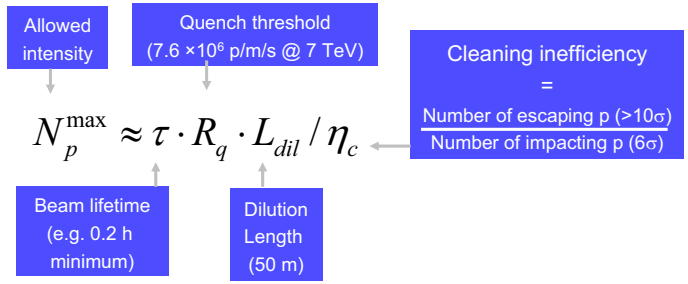

=> SIMPLIFIED DEFINITION OF QUENCH LIMIT !

=> Major role of the quench limit on maximum intensity of the machine !

G. Robert-Demolaize

Maximum allowed intensity

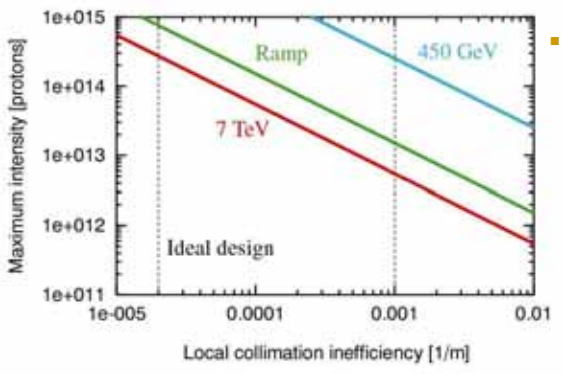

- To achieve LHC design intensity, we require the following local cleaning inefficiencies:

Injection $(\tau^{\mathrm{inj}} = 0.1\ \mathrm{h})$

$$\tilde{\eta}_c^{\mathrm{inj}} = 10^{-3} m^{-1}$$

Top energy $(\tau^{\mathrm{low}\beta} = 0.2\ \mathrm{h})$

$$\tilde{\eta}_c^{\mathrm{low}\beta} = 2 \times 10^{-5} m^{-1}$$

(assuming simplified quench limits).

=> used as input for quench limits in loss maps!

G. Robert-Demolaize

Conclusions for LHC IR magnets

- Heat loads associated to *pp* collisions are considerable in the experimental insertions, in particular in the low-beta triplets.
- Thermal properties of the coils of both types of low-beta quadrupoles were experimentally studied, and confirm a safety factor of 3 with respect to expected heat load for nominal luminosity.
- MQM and MQY quadrupoles have insulation schemes analogous to the MB. Similar thermal properties could be expected, but have not been experimentally verified.
- Magnets operating at 4.5 K are expected to have higher quench limits for transient losses, but lower for continuous losses than at 1.9K.

Magnet	Coil insulation	Operating temperature	Injection			Collision			Conditions/Reference
			Temperature margin	Heat reserve (transient losses)	Peak power density	Temperature margin	Heat reserve (transient losses)	Peak power density	
MB	2x50mu (50% overlap) + 73 mu (2 mm gap)	1.9 K	7 K	38 mJ/cm3	10 mW/cm3	1 K	0.8 mJ/cm3	5 mW/cm3	LPR 44; Meuris et al. (1999)
MQXA	2x25mu (50% overlap) + 60 mu (2 mm gap)	1.9 K	8.2 K	55 mJ/cm3		1.3 K	1.3 mJ/cm3	4 mW/cm3	Kimura et al, IEEE Tran SC., 9(1999)1097
MQXB	2x25mu (55% overlap) + 50 mu (2 mm gap)	1.9 K	8 K	50 mJ/cm3		1.2 K	1.2 mJ/cm3	0.4 mW/g	Mohkov et al., LPR 633
MQM	2x25mu (50% overlap) + 55 mu (2 mm gap)	1.9 K	7.5 K	50 mJ/cm3	10 mW/cm3	1 K	1.0 mJ/cm3	5 mW/cm3	
MQM	2x25mu (50% overlap) + 55 mu (2 mm gap)	4.5 K	6.5 K	75 mJ/cm3		1.2 K	5 mJ/cm3	2 mW/cm3	
MQY	2x25mu (50% overlap) +55 mu (2 mm gap)	4.5 K	6.5 K	75 mJ/cm3		1.4 K	5 mJ/cm3	2 mW/cm3	
MQTL	B-stage epoxy impregnated	4.5 K	6.5 K	75 mJ/cm3		2 K	5 mJ/cm3	1.0 mW/cm3	R.Wolf, Pr comm., 28 July 2004

Estimate of Quench Limits

Example of Results for transient losses (Available for all LHC magnet types)

Magnet type	Cable type	Op-T (K)	Enthalpy (mJoule/cm³)	
			Fast perturbation	Slow perturbation (no insulation)
			< 0.1 ms	> 100 ms
MB	Type-1	1.9	1.54	56.55
MB	Type-2	1.9	1.45	56.41
MQ	Type-3	1.9	4.24	70.53
MQMC	Type-4	1.9	1.51	49.97
MQML	Type-4	1.9	1.51	49.97
MQM	Type-7	1.9	1.51	49.97
MQM	Type-7	4.5	2.41	9.87
MQML	Type-4	4.5	2.41	9.87
MQY	Type-5	4.5	2.89	12.15
MQY	Type-6	4.5	3.80	15.31

from A. Siemko *et al.*, CERN LTC 19 October 2005

Overall System Status 7 TeV

- Status Chamonix 2005:

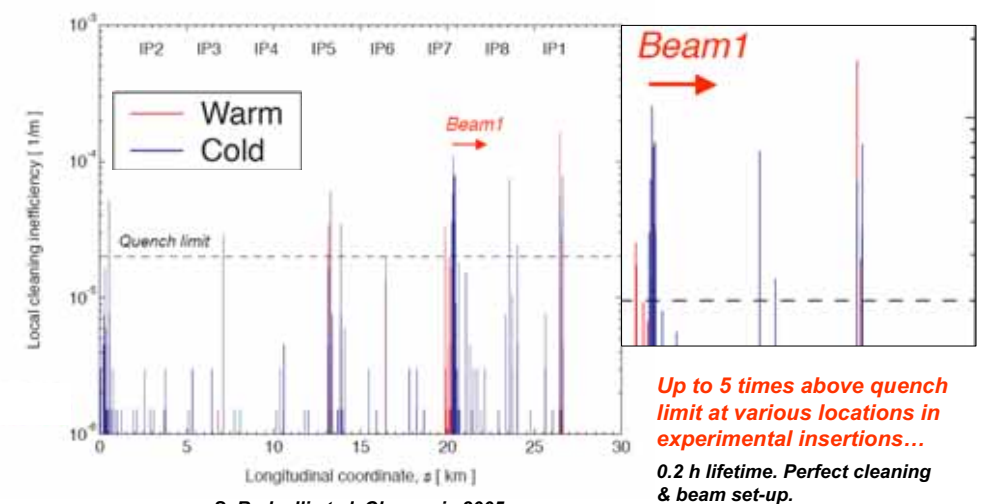

S. Redaelli et al, Chamonix 2005

Up to 5 times above quench limit at various locations in experimental insertions…

0.2 h lifetime. Perfect cleaning & beam set-up.

Latest 7 TeV Results with Collimation Full LHC System

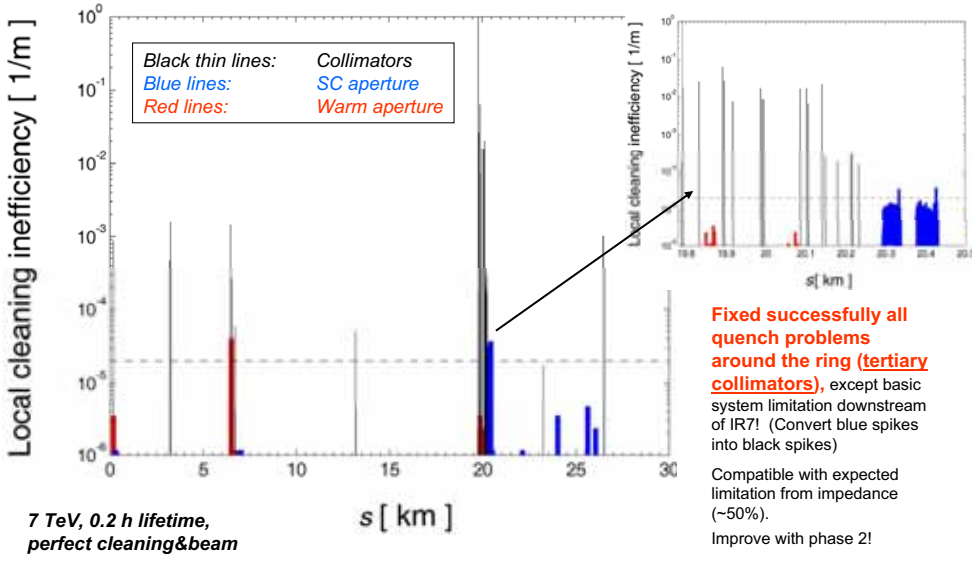

7 TeV, 0.2 h lifetime, perfect cleaning&beam

Fixed successfully all quench problems around the ring (tertiary collimators), except basic system limitation downstream of IR7! (Convert blue spikes into black spikes)

Compatible with expected limitation from impedance (~50%).

Improve with phase 2!

Phase 1 – Injection & Early Physics

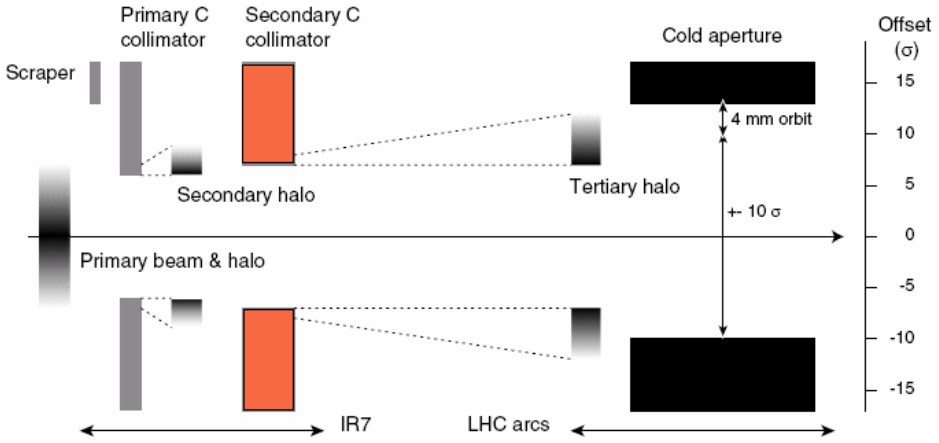

G. Robert-Demolaize

Phase 2 – Collision Optics

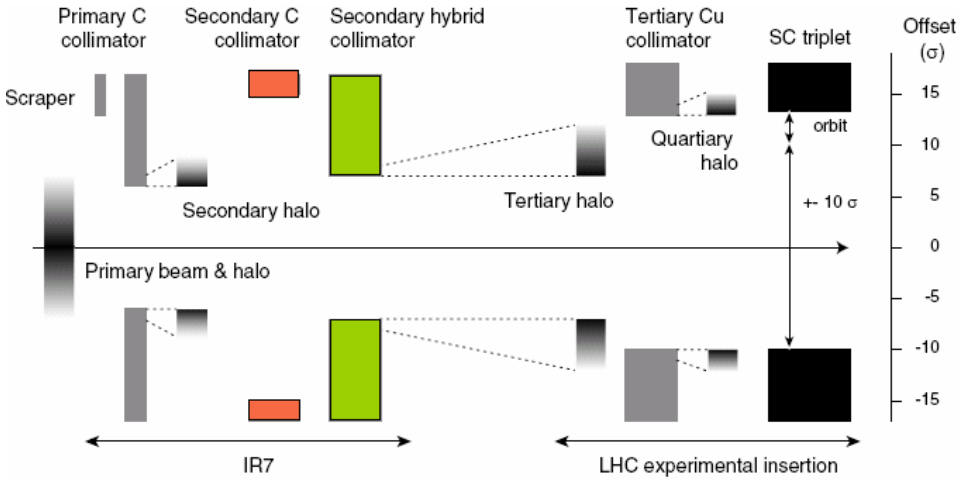

G. Robert-Demolaize

generalized formula: combine correct frequency dependence of Burov-Lebedev with nonlinear dependence on transverse coordinates from Piwinski, assuming that the two dependencies remain factorized

$$\Delta Q_y^{general} \approx \frac{\beta}{4\pi}\frac{N_b r_p L}{2\pi\gamma}\int_{-\infty}^{\infty}\frac{3}{2}Z_{BL,y}^{flat}(\omega)e^{-\omega^2\sigma_z^2/c^2}d\omega\left(\frac{3b^2}{\pi^2}\right)\frac{erf\left(\frac{b-y_{co}}{\sigma_y}\right)}{erf\left(\frac{b-y_{co}}{2^{1/2}\sigma_y}\right)^2}\int_{-\infty}^{\infty}\int_{-2b=4y_{co}}^{2b}G(X,Y)\frac{e^{-\frac{Y^2}{4\sigma_y^2}-\frac{X^2}{4\sigma_x^2}}}{4\pi\sigma_x\sigma_y}dYdX$$

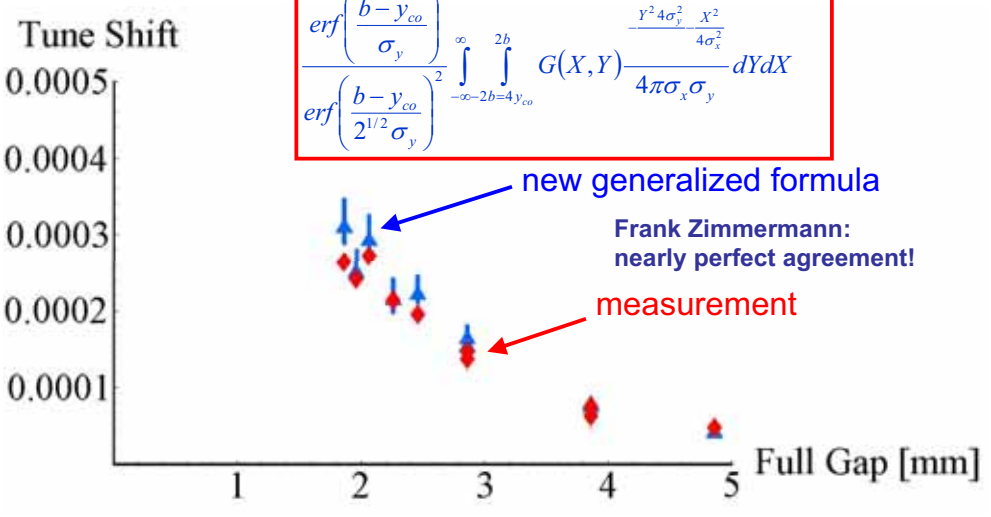

prototype LHC collimator installed in the SPS (R. Assmann)

LHC graphite collimators

- One may think that the classical "thick-wall" formula applies also for 2 cm thick graphite collimators about 2 mm away from the beam
- In fact it is not ⇒ The resistive impedance is ~ 2 orders of magnitude lower at ~ 8 kHz!

Usual regime: $d, \delta < a$

New regime: $d >> a, \delta \le d$

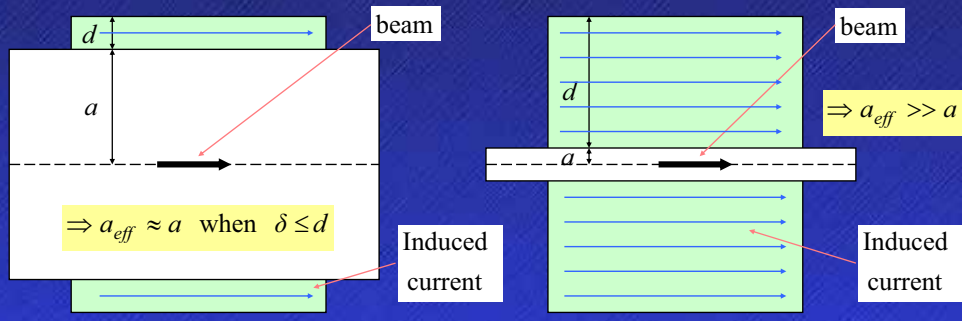

Collimator-Induced Tune Change (Changing Collimator Gap)

Gap: 2.1 51 mm

M. Gasior, R. Jones et al

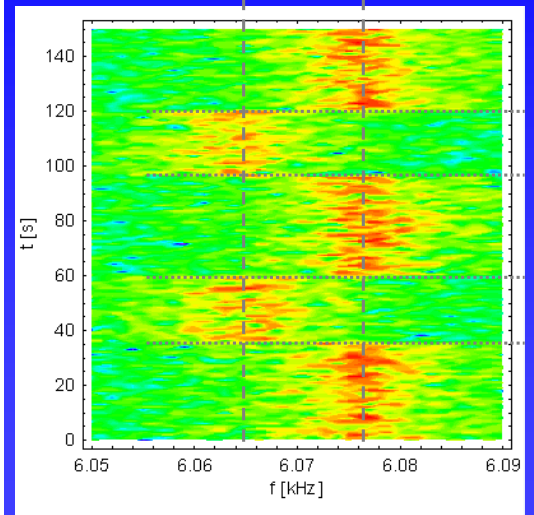

SPS tune depends on collimator gap!

Expected tune change observed within factor 2!

Impedance estimates are strongly confirmed by experiment!

F. Zimmermann et al

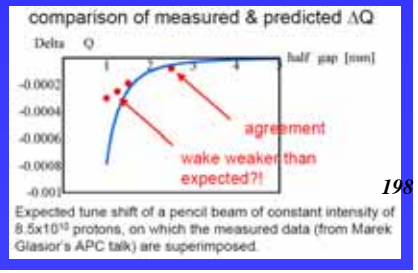

Expected tune shift of a pencil beam of constant intensity of 8.5x10¹⁰ protons, on which the measured data (from Marek Glasior's APC talk) are superimposed.

R. Assmann

Machine Protection and Collimation challenges

- Magnet quench limits need to be experimentally validated
  ⇒ Fresca test facility and LHC sector test
- Beam Loss Monitors need proper calibration for efficient machine protection ⇒ LHC sector test
- Learn how to set-up routinely a complicated three-stage collimation system ⇒ control beta-beating at ~10% level
- Phase-2 collimation system is not compatible with nominal LHC intensity at 7 TeV, if we want to stabilize the beams using Landau octupoles at zero chromaticity:
  - use low-noise transverse feedback and chromaticity to stabilize the beams?
  - octupoles are "passive" and more reliable ⇒ ideal to push machine performance and reduce experimental background levels
  - active feedback may increase emittance and reduce luminosity
  - investigate crystal assisted collimation and/or develop new low-impedance collimators (*e.g.,* longitudinally segmented or incorporating Cu stripes to carry low-frequency image currents?)

LHC stability diagram (maximum octupole strength) and collective tune shift for the most unstable coupled-bunch mode at 7 TeV (E. Metral, 2004)

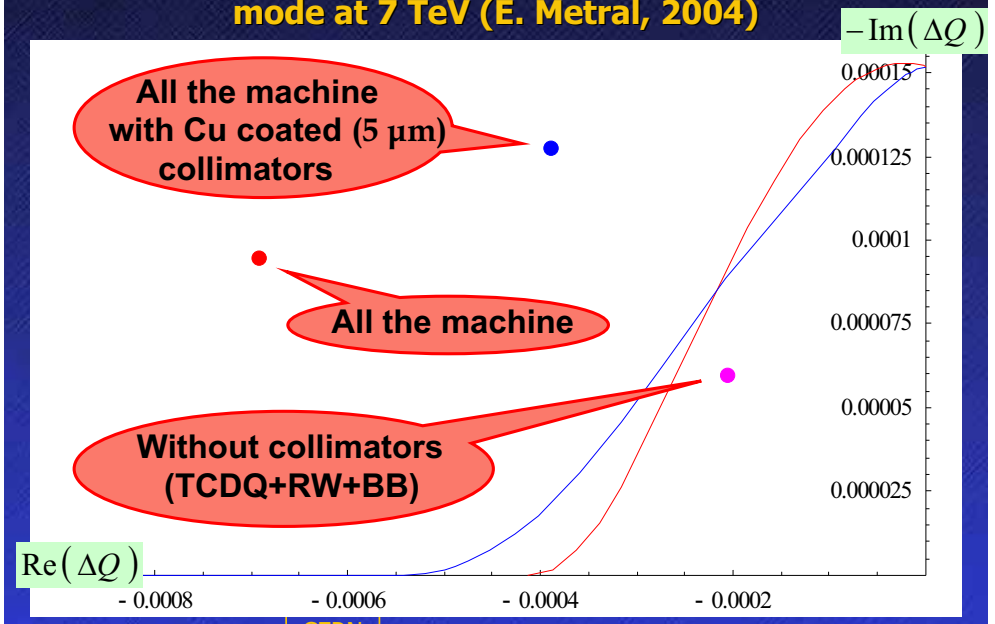

LHC strategy against Electron Cloud

1) warm sections (20% of circumference) **coated by TiZrV getter** developed at CERN; low secondary emission; if cloud occurs, ionization by electrons (high cross section ~400 Mbarn) aids in pumping & pressure will even improve

2) outer wall of beam screen (at 4-20 K, inside 1.9-K cold bor will have a **sawtooth surface** (30 μm over 500 μm) to reduce photon reflectivity to ~2% so that photoelectrons are only emitted from outer wall & confined by dipole field

3) pumping slots in beam screen are **shielded** to prevent electron impact on cold magnet bore

4) rely on **surface conditioning** ('scrubbing'); commissioning strategy; as a last resort doubling or tripling bunch spacing suppresses e-cloud heat load

unique vacuum sy

Stability diagrams (vertical plane) LHC at 7 TeV

Phase 2 collimators: ~70% of the nominal LHC intensity can be stabilized using Landau octupoles at zero chromaticity

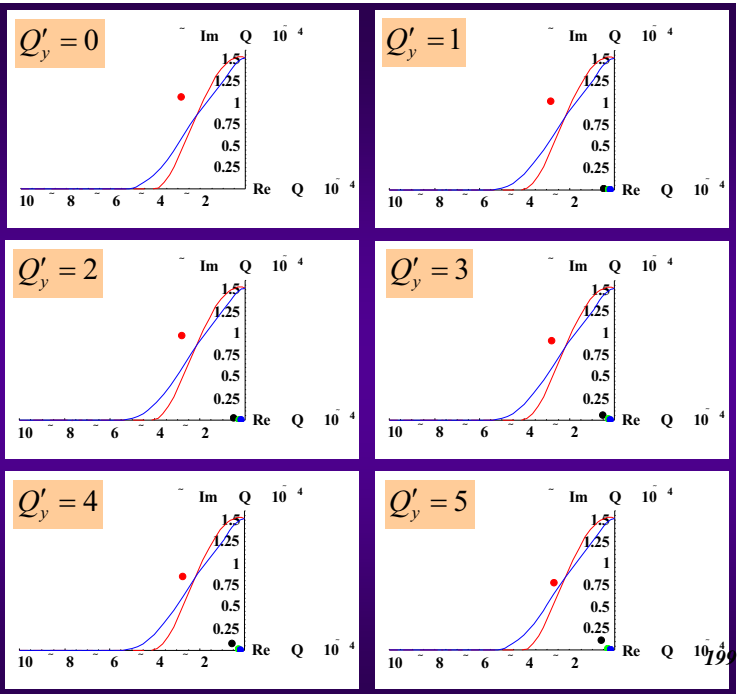

Instabilities & emittance growth caused by the electron cloud

1) **Multi-bunch instability** – not expected to be a problem can be cured by the feedback system
2) **single-bunch instability** – threshold electron cloud density ρ_0~4x10^{11} m^{-3} at injection in the LHC
3) **incoherent emittance growth**
   new understanding! (CERN-GSI collaboration)
   2 mechanisms:
   - **periodic crossing of resonance** due to e$^-$ tune shift and synchrotron motion (similar to halo generation from space charge)
   - **periodic crossing of linearly unstable region** due to synchrotron motion and strong focusing from electron cloud in certain regions, e.g., in dipoles

arc heat load vs. intensity, 25 ns spacing, 'best' model

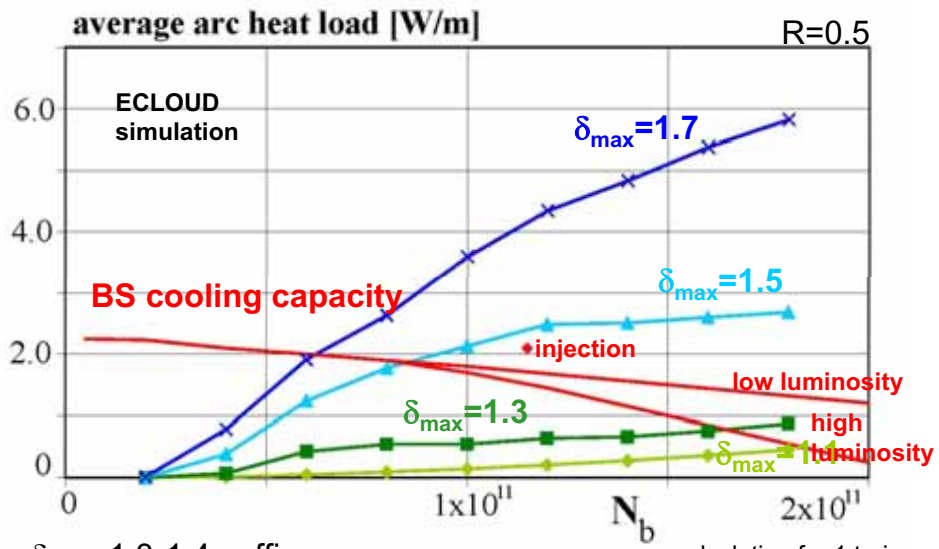

δ_{max}=1.3-1.4 suffices

calculation for 1 train
computational challenge!
higher heat load for quadrupoles in 2nd train under study

Resonance Trapping (G. Franchetti, GSI)

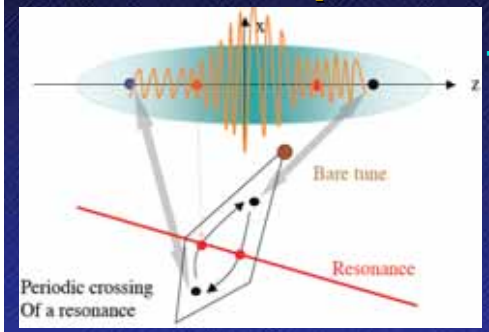

The same resonance trapping mechanism can explain slow emittance growth and beam losses observed with space charge in the PS (left) and with electron cloud in the SPS (below)

Particles with large synchrotron amplitudes reach larger and larger betatron amplitudes and are lost ⇒ bunch shortening

Particle losses are enhanced by chromaticity

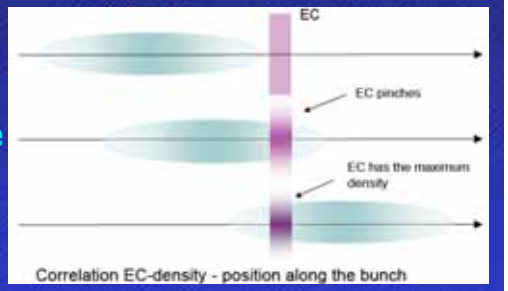

is "scrubbing" needed in LHC?

- still lacking experimental data, e.g., on $\varepsilon_{max}(\theta)$
  → *uncertainty in heat load prediction* of factor ~2
- also incomplete understanding of scrubbing (*COLDEX data vs. prediction*, RHIC, DAFNE)
- if δ_{max}~1.3 reached in commissioning, no scrubbing is needed for heat load and fast instabilities
- pressure should be ok too according to N. Hilleret
- one concern: *long-term emittance growth* and poor lifetime (observed in SPS after scrubbing)
- we still believe we need to prepare a scrubbing strategy in case it turns out to be necessary to go to δ_{max}~1.3 (e.g., tailor train spacings & train lengths at nominal bunch intensity)

200

LHC bunch train at injection in the SPS

Q_x=26.135
Q_y=26.185

ξ_x=0.15
ξ_y=0.1

V_{RF} ~ 3 MV
dampers on
coupling: 0.008

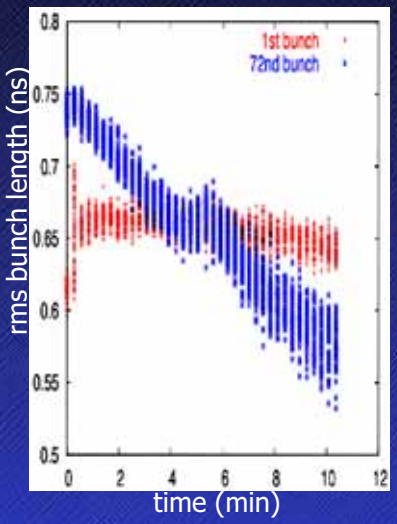

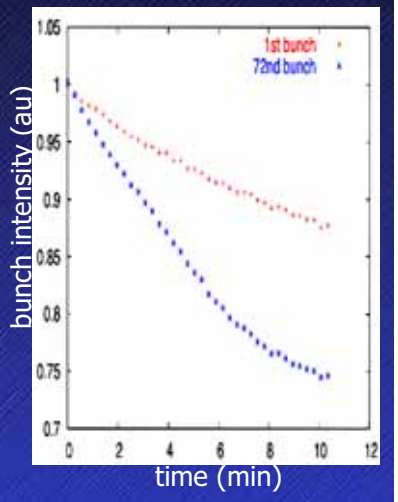

Evolution of bunch length and bunch population for the first and the last bunch in an LHC bunch train of 72 bunches. SPS measurements with electron cloud in Aug 2004. Courtesy G. Rumolo, G. Arduini, and F. Roncarolo.

single-bunch "TMC" instability

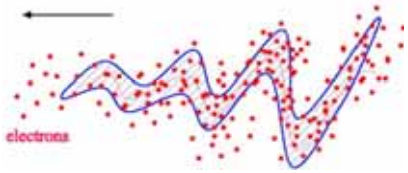

fast ε growth above e⁻ density threshold; slower ε growth below

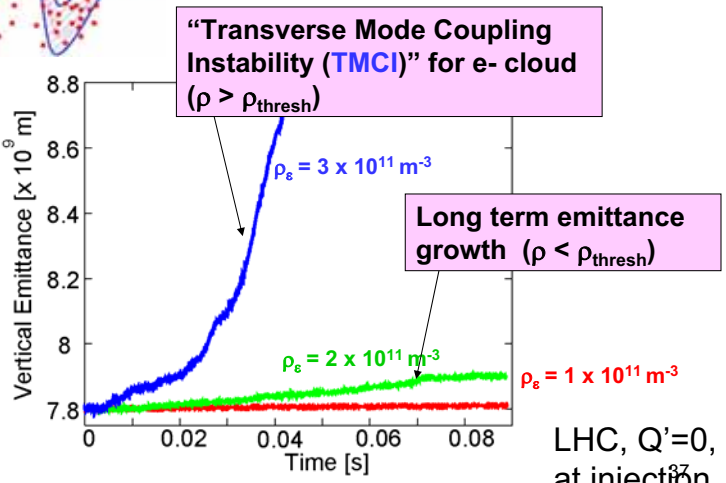

E. Benedetto

LHC, Q'=0, at injection

Frank Zimmermann, LHC Electron Cloud, GSI Meeting 30.03.2006

Tentative Conclusions

- Some "safety nets" in the original LHC conceptual design (low-impedance, stabilization by octupoles, full triplet aperture without beam screens) have been sacrificed to guarantee a more robust collimation system and a safer IR vacuum behaviour
- Machine downtime caused by magnet quenches may be initially frequent, until collimation and machine protection are fully mastered
- A shorter machine turnaround time implies reliable tables of quench levels, BLM calibrations, and a dynamic optics control (reference magnets)
- Emittance control will be challenging and may require crystal assisted collimation and/or new low-noise feedback systems.
- A longitudinal feedback may enable shorter bunches and reduce geometric luminosity loss for lower β^*.

Electron density vs LHC beam intensity

Challenge: how to go from δ_{max}~1.7 to 1.3?
Scrubbing should be done at nominal N_b (stripes)

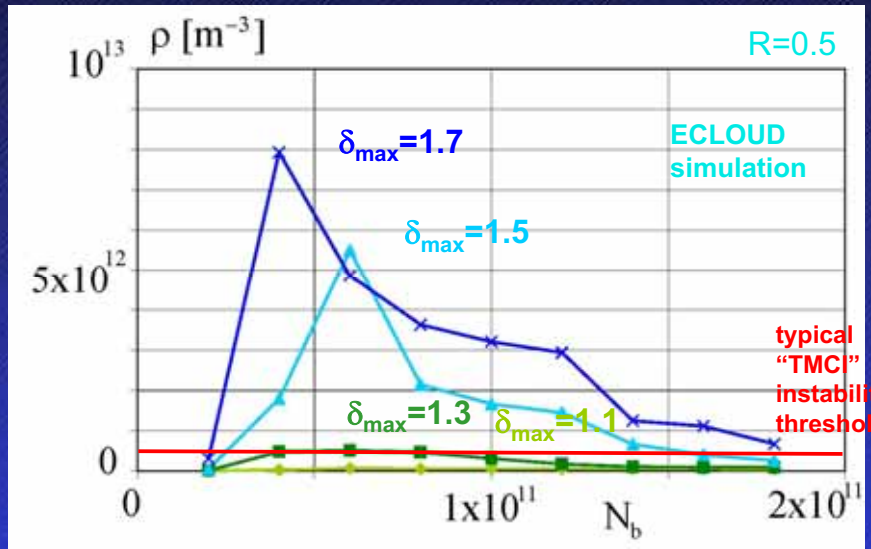

calculation for 1 bunch train

Additional Slides

Tentative Conclusions (continued)

- Reaching nominal LHC performance is challenging
- Some uncertainties remain in connection with electron cloud effects and vacuum behaviour of the cold arcs: exceeding nominal beam current may be impossible or take several years ⇒ operation with 75 ns bunch spacing would reduce e-cloud & long range beam-beam effects and maximize luminosity
- Operation with flat beams can help relaxing IR aperture constraints and/or increasing luminosity
- A re-alignment of the IR quads would further relax aperture constraints, increase luminosity, and minimize energy deposition in the magnet coils. This option should be considered also for the IR upgrade.

HERA operational experience

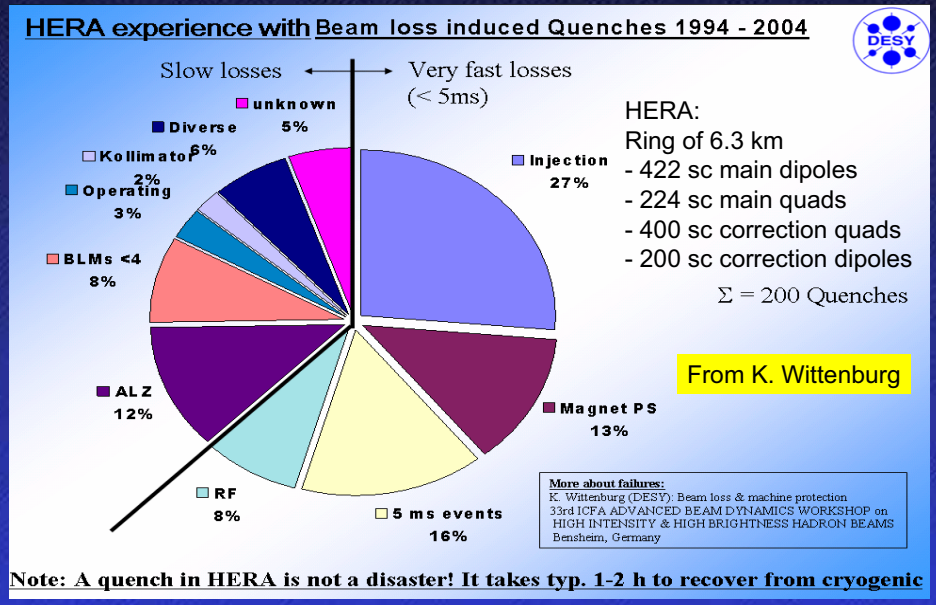

Tentative Conclusions for the LHC IR Upgrade

- We do need triplet spares and thus a back-up or intermediate IR upgrade option based on NbTi magnet technology. What is its luminosity reach?
- A vigorous R&D programme on Nb_3Sn magnets should start at CERN asap, complementary to the US-LARP programme, to reach an LHC luminosity of $\sim 10^{35}$ after 2015
- Alternative IR layouts (quadrupole-first, dipole-first, D0, flat beams, Crab cavities) will be rated in terms of technological and operational risks/advantages by the end of 2006

202

Vertical growth rate of head-tail modes in the LHC as a function of chromaticity at injection energy, for ~3000 bunches of nominal intensity

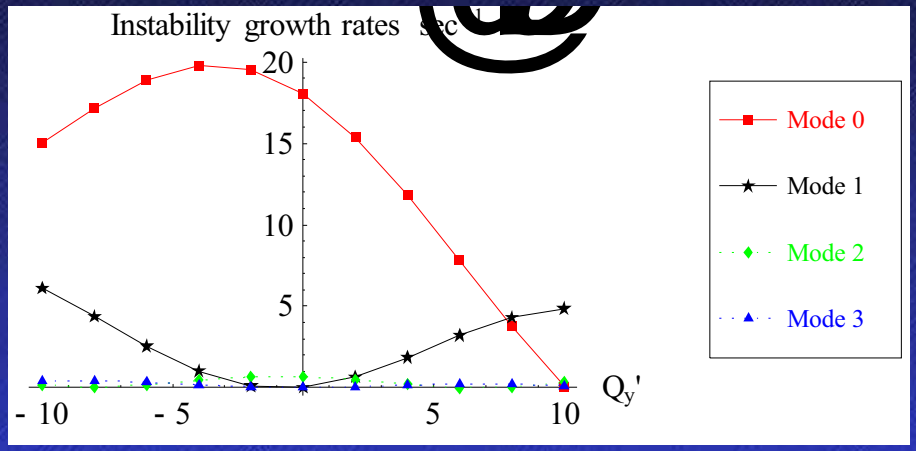

At injection head-tail modes with growth rates up to about 4 sec^{-1} are stabilized by lattice nonlinearities (assuming an amplitude detuning of 0.002 at 6 sigma). The rigid mode m=0 has to be stabilized by the transverse feedback.

Heat load in the Low-β Triplet

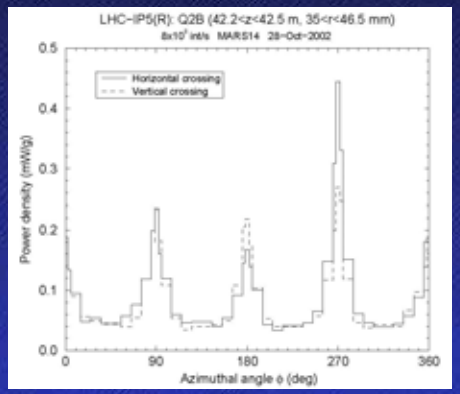

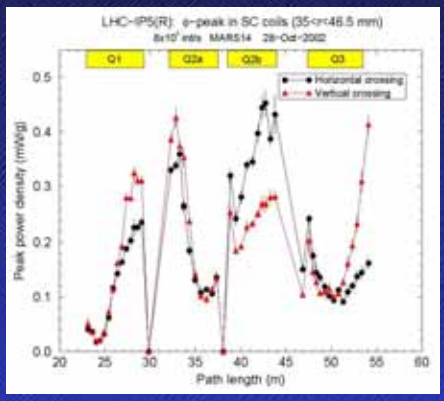

N. Mokhov et al, LHC Project Report 633

Peak power density: 0.45 mW/g

Stability diagrams (vertical plane) LHC at 7 TeV

Phase 1 collimators: ~50% of the nominal LHC intensity can be stabilized using Landau octupoles at zero chromaticity

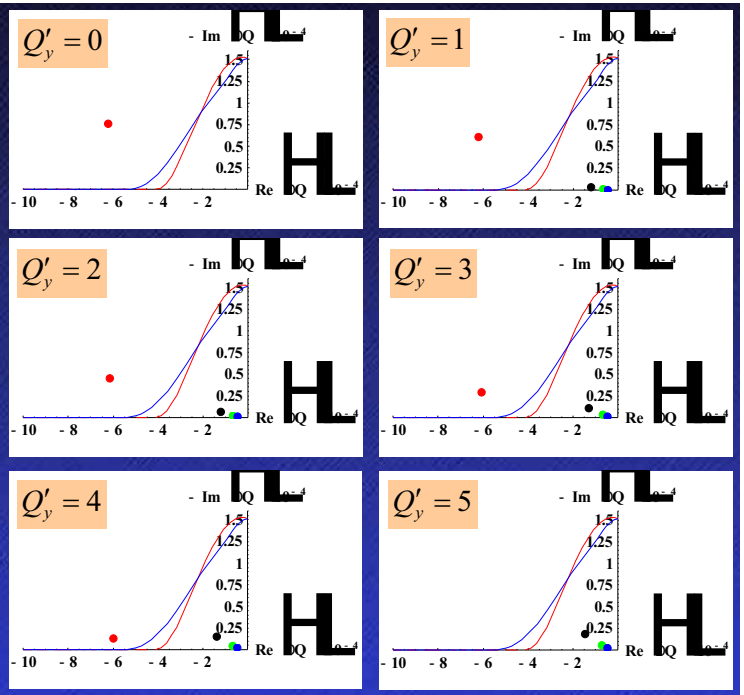

Trapped modes for tertiary LHC collimator chambers (A. Grudiev, 2006)

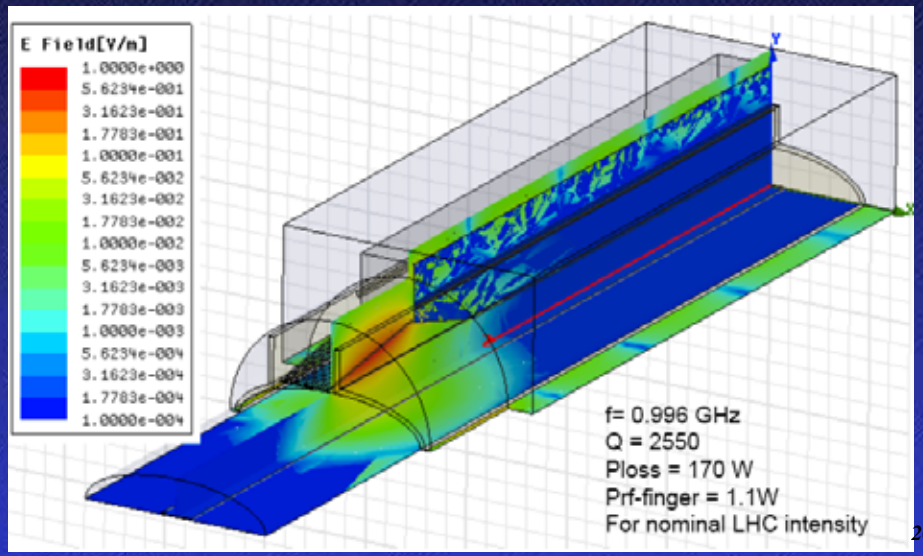

Upgrades considered, physics potential of the LHC at 10^{35} cm^{-2} s^{-1} (SLHC)

What improvements in the physics reach operating the LHC at a luminosity of ~ 10^{35} cm^{-2} s^{-1} with an integrated luminosity ~ 1000 fb^{-1}per year at $\sqrt{s} \approx 14$ TeV i.e. retaining present LHC magnets/dipoles -

➡ an upgrade at a relatively modest cost for machine (IR) + experiments (< ~ 0.5 GSF) for ~ 2013-15

a more ambitious upgrade (but ~ 2-3 GSF!) would be to go for a $\sqrt{s} \approx 25$ - 30 TeV machine (2018-20) changing LHC dipoles (~15T, Nb_3Sn?) - just mentioned here

For the 10^{35}cm^{-2} sec^{-1} case:
- expected modifications/adaptations of LHC and experiments/CMS,
- improvements in some basic SM measurements and in SM/MSSM Higgs reach
- improvements in reach at high mass scales, main motivations for an upgrade i.e exploit maximally the "existing" machine and detectors

WAMDO Workshop on Accelerator Magnet Design and Optimization, CERN April. 3 -6 th, 2006

Physics potential of an upgraded LHC (SLHC at ~10^{35} cm^{-2} s^{-1}), demands to detectors and machine

D. Denegri,
CE Saclay/DAPNIA/SPP

Nominal LHC and possible upgrade steps

Nominal LHC: 7 TeV beams,
- injection energy: 450 GeV, ~ 2800 bunches, spacing 7.5 m (25ns), bunch length 7.5 cm
- 1.1 *10^{11} protons per bunch, β^* at IP : 0.5 m $\Rightarrow$ 10^{34} cm^{-2} s^{-1} (lumi-lifetime ~10h)

Possible upgrades/steps considered:
- increase up to 1.7 *10^{11} protons per bunch (beam-beam limit) $\Rightarrow$ 2*10^{34} cm^{-2} s^{-1}
- increase operating field from 8.3T to 9T (ultimate field) $\Rightarrow$ $\sqrt{s} \approx 15$ TeV

minor hardware changes to LHC insertions or injectors:
- modify insertion quadrupoles (larger aperture) for $\beta^* = 0.5 \rightarrow 0.25$ m
- increase crossing angle 300 μrad → 424 μrad
- halving bunch spacing (12.5nsec)*, with new machine RF system
  $\Rightarrow$ L ≈ 5 * 10^{34} cm^{-2} s^{-1}

major hardware changes in arcs or injectors:
- SPS equipped with superconducting magnets to inject at ≈ 1 TeV $\Rightarrow$ L ≈ 10^{35} cm^{-2} s^{-1}
- new superconducting dipoles at B ≈ 15 Tesla for beam energy ≈ 13 TeV i.e. $\sqrt{s} \approx 25$ TeV

*12.5 nsec is more favorable for experiments, 10 or 15 nsec more favorable for the PS/SPS RF systems at 200 MHz, ultimately question of cost of electronics to experiments vs. to accelerators;

Probable/possible LHC luminosity profile - need for L-upgrade in a longer term

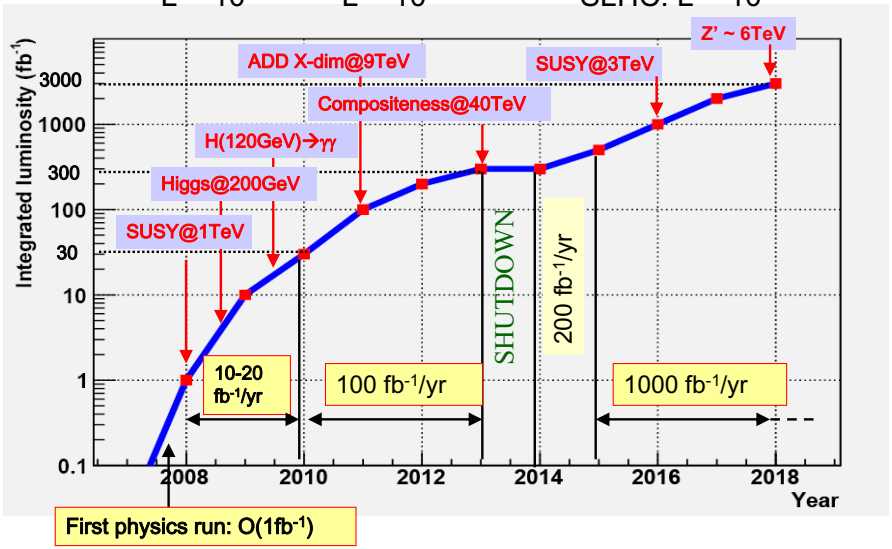

204

CMS yoke and forward detectors- modifications considered for SLHC

End cap yoke for SLHC, acceptance up to $|\eta| \sim 2$

Reinforced shielding inside forward muons, replacement of inner CSC and RPC's

Supplement YE4 wall with borated polythene

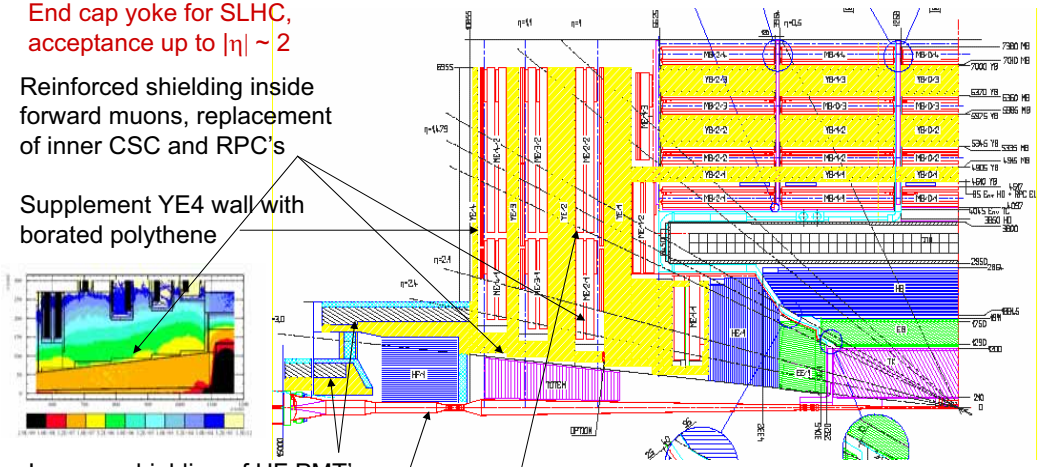

Improve shielding of HF PMT's

Possibly increase YE1-YE2 separation to insert another detector layer?

Free space in radius in the HF calo is : 14cm beam-pipe radius + 5cm clearance, the issue - if quads were to be located there or in the "TOTEM part", is the neutron albedo into CMS acceptable

Main CMS areas affected by luminosity upgrade

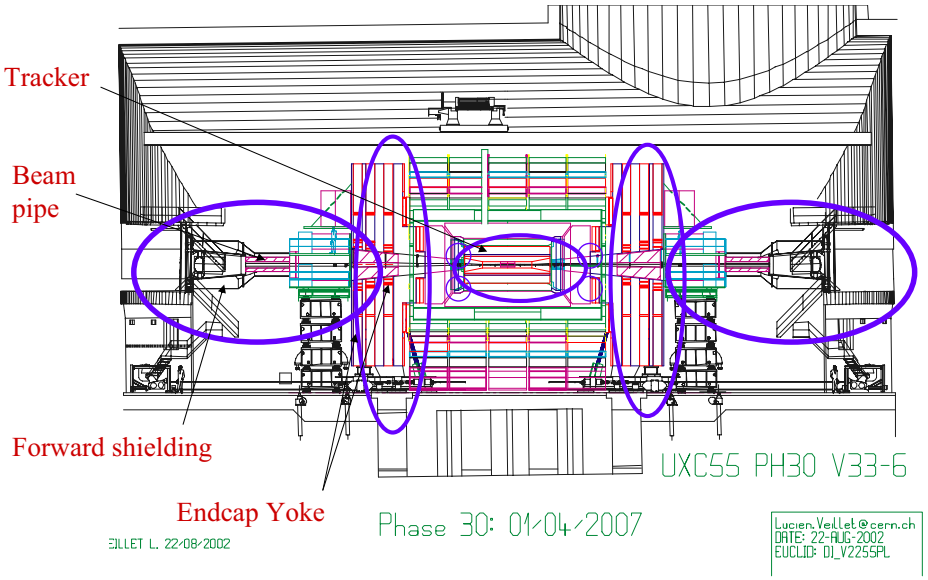

Experimental conditions at 10^{35} cm^{-2} s^{-1} (12.5ns) - considerations for tracker and calorimetry

~ 100 pile-up events per bunch crossing - if 12.5 nsec bunch spacing (with adequate/faster electronics, reduced integration time) -
compared to ~ 20 for operation at 10^{34}cm^{-2}s^{-1} and 25 nsec (nominal LHC regime),

➡ $dn^{ch}/d\eta$/crossing ≈ 600 and ≈ 3000 tracks in tracker acceptance

$H \rightarrow ZZ \rightarrow ee\mu\mu$, m_H = 300 GeV, in CMS

Generated tracks, p_t > 1 GeV/c cut, i.e. all soft tracks removed! I. Osborne

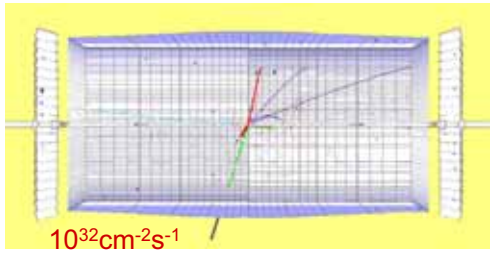

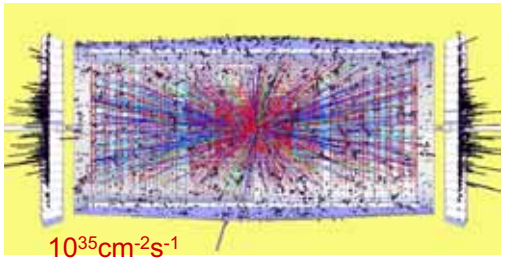

➡ If same granularity and integration time as now: tracker occupancy and radiation dose in central detectors increases by factor ~10, pile-up noise in calorimeters by ~ 3 relative to 10^{34}

Shielding between machine and HF

Basic functions of the shielding elements between the machine area and HF are:

-reduce the neutron flux in the cavern by 3 orders of magnitude

-reduce the background rate in the outer muon spectrometer (MB4, ME3,ME4) by 3 orders of magnitude

-reduce the radiation level at the HF readout boxes to a tolerable level

A.Ball

Rotating system is near the limits of mechanical strength (doubly hinged structure), new concept or supplementary system around existing RS needed for SLHC running,

time needed to open and close CMS would increase significantly (~1 week per shutdown)

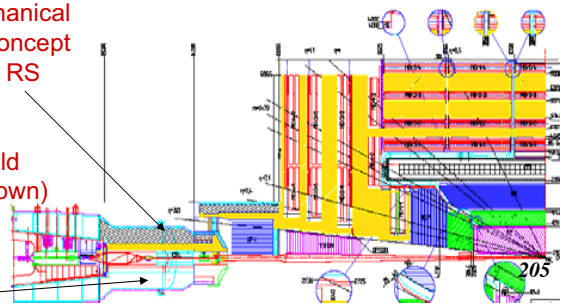

VFCAL (rapidity range 3 - 5), rad. damage

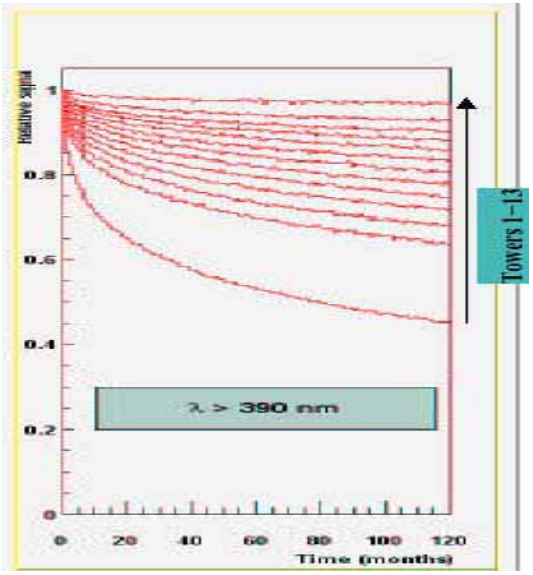

In CMS quarz fibers in iron ie Cerenkov calorimetry

Tower 1 loses 60% of light during LHC, down to 4% of original after 10 years of SLHC.

Tower 2 down to 23% after 10 years of SLHC. SLHC "kills" a few high eta towers.

Andre Gribushin

Inner CMS tracking for SLHC

From R.Horisberger

Pixels to much larger radius

Technology and Pixel size vary with radius

Not too large an extrapolation in sensor technology

Cost/Geometry optimization

QuickTime™ and a TIFF (LZW) decompressor are needed to see this picture.

Importance of VFCAL/feasability of forward jet tagging at 10^{35} cm^{-2} s^{-1}

Forward jet tagging needed to improve S/B in VB fusion/scattering processes pp → qqH, qqVV ….if still of interest in ~ 2015 , but could also be crucial if no Higgs found by then!

Fake fwd jet tag ($|\eta| > 2$) probability from pile-up (preliminary …)

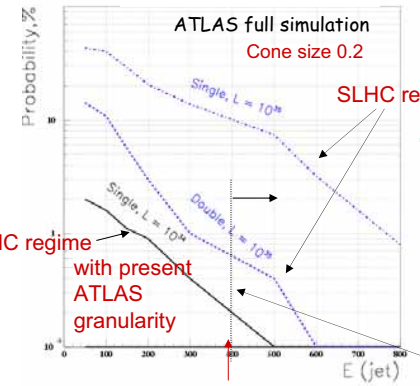

SLHC regime

LHC regime with present ATLAS granularity

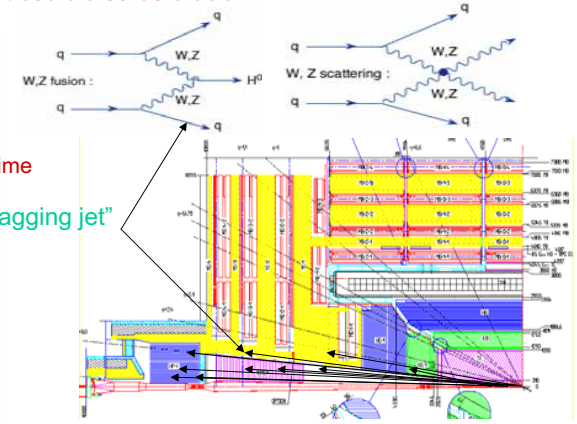

"tagging jet"

cut at > ~ 400 GeV

➡ Method should still work at 10^{35}: increase forward calo granularity, reduce jet reconstruction cone from 0.4 to ~ 0.2, optimise jet algorithms to minimize false jets

CMS inner tracking for SLHC

From R.Horisberger

Pixels to be used to much larger radius, from ~10 cm up to ~ 60 cm

Technology and pixel size vary with radius, not too large an extrapolation in sensor technology, cost geometry optimization:

3 pixel systems proposed:

- system 1 - for maximal fluence and rate, two layers between ~ 10 -15 cm
  . ~ 400 CHF/cm^2

- system 2 -large pixel system, two layers between ~ 15 - 30 cm
  . ~ 100 CHF/cm^2

- system 3 -large area macro-pixel system,~four layers between ~ 30 - 60 cm
  . ~ 40 CHF/cm^2

This 8 -layer system could eventually deal with up to 1200 tracks per unit of rapidity i.e. 10^{35} luminosity with 25 nsec bunch spacing.

206

Expectations for detector performances at 10^{35} cm^{-2} s^{-1} - overview

• Electron identification and rejections against jets, E_t = 40 GeV, ATLAS full simulation

L (cm^{-2} s^{-1})	Electron efficiency	Jet rejection
10^{34}	81%	10600±2200
10^{35}	78%	6600±1130

• Electron resolution degradation due to pile-up, at 30 GeV: 2.5% (LHC) → 3.5% (SLHC)

• b-jet tagging performance: rejection against u-jets for a 50% b-tagging efficiency

p_T (GeV)	R_u at 10^{34} cm^{-2}s^{-1}	R_u at 10^{35} cm^{-2}s^{-1}
30-45	33	3.7
45-60	140	23
60-100	190	27
100-200	300	113
200-350	90	42

Preliminary study, ATLAS
⇒performance degradation at 10^{35} factor of ~ 8 - 2 depending on E_t
⇒ increase (pixel) granularity!

• Forward jet tagging and central jet vetoing still possible - albeit at reduced efficiencies reducing the cone size to ≈ 0.2

probability of fake double forward tag is ~ 1% for E_{jet} > 300 GeV (|η| > 2)
probability of ~ 5% for additional central jet for E_t > 50 GeV (|η| < 2)

Foreseeable changes to detectors for 10^{35}cm^{-2}s^{-1} overview

changes to CMS and ATLAS :

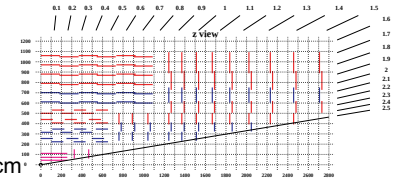

• Trackers, to be replaced due to increased occupancy to maintain performance, need improved radiation hardness for sensors and electronics
- present Si-strip technology is OK at R > 60 cm
- present pixel technology is OK for the region ~ 20 < R < 60 cm
- at smaller radii(<~10 cm) new techniques required

• Calorimeters: ~ OK
- endcap HCAL scintillators in CMS to be changed
- endcap ECAL VPT's and electronics may not be enough radiation hard
- desirable to improve granularity of very forward calorimeters - for jet tagging

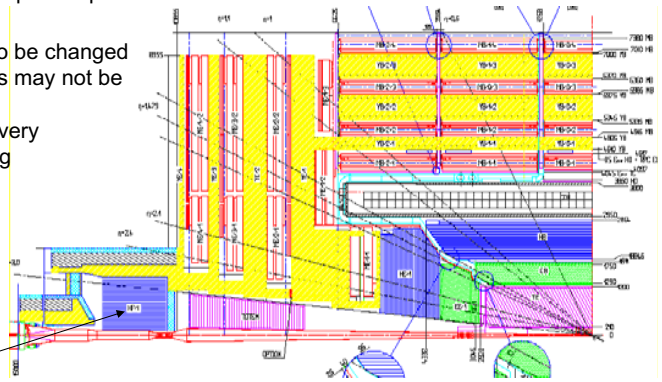

• Muon systems: ~ OK
- acceptance reduced to |η| <~ 2.0 to reinforce forward shielding

• Trigger(L1), to be replaced, L1(trig.elec. and processor) for 80 MHz data sampling

➡ VF calorimeter for "jet tagging"

ew physics, triple gauge boson couplings

In the SM TGC uniquely fixed, extensions to SM induce deviations

• At LHC the best channels are: Wγ → lνγ and WZ → lνll

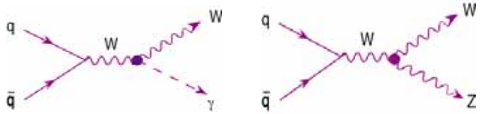

5 parameters describe these TGCs:
g_1^Z (1 in SM), $\Delta\kappa_z$, $\Delta\kappa_\gamma$, λ_γ, λ_z (all 0 in SM)
Wγ final state probes $\Delta\kappa_\gamma$, λ_γ and WZ probes g_1^Z, $\Delta\kappa_z$, λ_z

• TGCs: a case where a luminosity increase by a factor ~10 is better than a center-of-mass energy increase by a factor ~ 2

Correlations among parameters

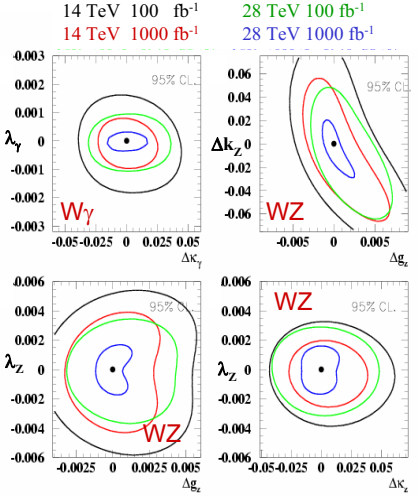

➡ SLHC can bring sensitivity to λ_γ, λ_z and g_1^Z to the ~ 0.001 level (of SM rad.corrections)

Cost expectations for CMS upgrade for SLHC

from J.Nash

Inner Tracker	25 - 30 MCHF
Outer Tracker	90 MCHF
Level 1 Trigger	15 MCHF
DAQ	10 MCHF
Other Front Ends	5 -10 MCHF
Additional Costs 10ns/15ns	20 - 30 MCHF
Infrastructure	15 MCHF

These costs do not include CERN staff required for upgrade work

$A/H \to \mu\mu$. /VLHC

$A/H \to \mu\mu$ - channel which most obviously should benefit from increased statistics at SLHC (and increased cm energy/ VLHC even more)

- easy to trigger -

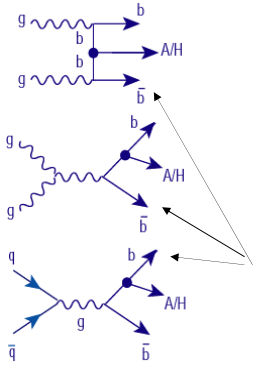

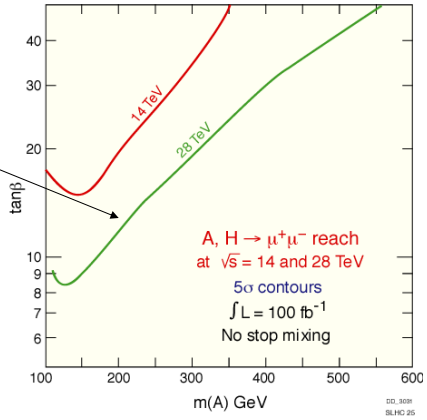

but as main production mechanism is associated bbA/H production, good b-tagging performance highly desirable, i.e. trackers with performances comparable to present ones would be required

Higgs physics - new modes/larger reach

Increased statistics would allow:

- to look for modes not observable at the LHC for example:

$H_{SM} \to Z\gamma$ (BR ~ 10^{-3}), $H_{SM} \to \mu^+\mu^-$ (BR ~ 10^{-4}) - the muon collider mode!
$H^\pm \to \mu\nu$

to check couplings; H_{SM}, $H^\pm$ etc masses well known by this time!

- extend significantly coverage of the MSSM parameter space, for example in:

$A/H \to \mu^+\mu^-$, $A/H \to \tau^+\tau^- \to \mu$, $A/H \to \tau^+\tau^- \to \mu/$ $+\tilde{\tau}$, $H^\pm \to \tau\nu$
$A/H \to \chi\chi \to$ $\tilde{\mu}$..

Specific example for a new mode:

$H_{SM} \to \mu^+\mu^-$ $120 < M_H < 140$ GeV, LHC (600 fb^{-1}) significance: < 3.5σ,
SLHC (two exps, 3000 fb^{-1}each) ~ 7σ

Higgs pair production and Higgs self coupling

Higgs pair production can proceed through two Higgs bosons radiated independently (from VB, top) and from trilinear self-coupling terms proportional to λ_{HHH}^{SM}

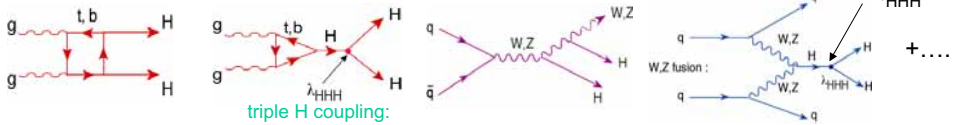

triple H coupling:
$\lambda_{HHH}^{SM} = 3m_H^2/v$

very small cross sections, hopeless at LHC (10^{34}), some hope at SLHC channel investigated, $170 < m_H < 200$ GeV (ATLAS):

$gg \to HH \to W^+W^-W^+W^- \to l^\pm\nu jj\ l^\pm\nu jj$
with same-sign dileptons - very difficult!

➡ total cross section and λ_{HHH} determined with ~ 25% statistical error for 6000 fb^{-1} provided detector performances are comparable to present LHC detectors

cross sections for Higgs boson pair production in various production mechanisms and sensitivity to λ_{HHH} variations

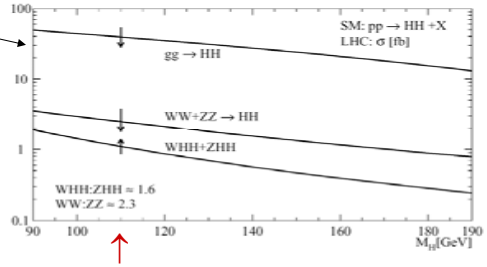

arrows correspond to variations of λ_{HHH} from 1/2 to 3/2 of its SM value

SLHC: improved reach for heavy MSSM Higgs bosons

The order of magnitude increase in statistics with the SLHC should allow to extend the discovery domain for massive MSSM Higgs bosons A,H,H±

example: $A/H \to \tau\tau \to$ lepton + τ-jet, produced in bbA/H

Peak at the 5σ limit of observability at the LHC greatly improved at SLHC, fast simulation, preliminary:

S. Lehti

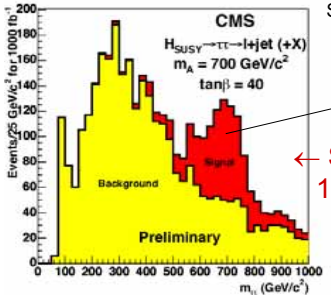

← SLHC 1000 fb^{-1}

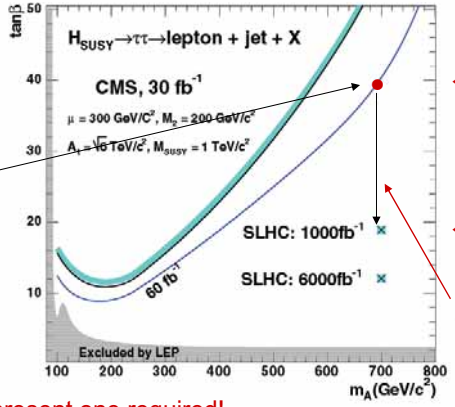

←LHC 60 fb^{-1}

←SLHC 1000 fb^{-1}

gain in reach

208

b-tagging performance comparable to present one required!

SUSY at SLHC - importance of statistics

"Reach" means a > 5σ excess of events over known (SM) backgrounds; discovering SUSY is one thing, understanding what is seen requires much more statistics!

Compare for ex. 100 fb^{-1} reach and sparticle reconstruction stat limited at 100 fb^{-1} at "point G" (tgβ = 20), as many topologies required, leptons, b-tagging…

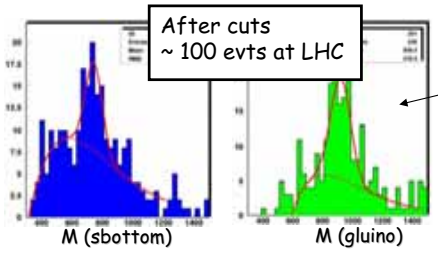

Reach vs luminosity, jets + E_t^{miss} channel

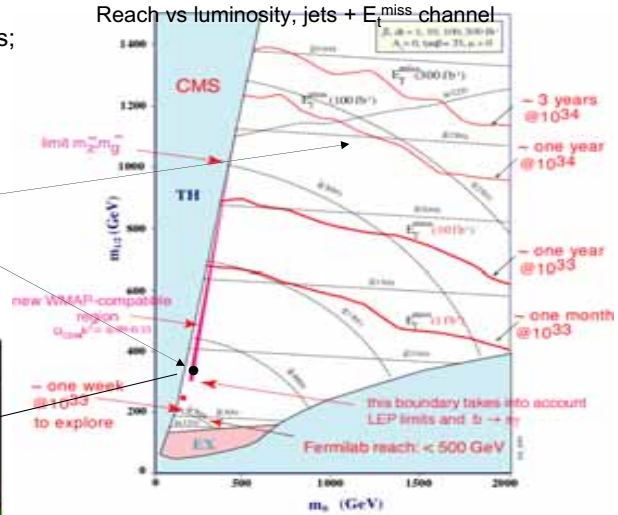

This is domain where SLHC statistics may be decisive! but LHC-type detector performance needed

WZ vector resonance in VB scattering

If no Higgs found, possibly a new strong interaction regime in V_LV_L scattering, this could become the central issue at the SLHC! For ex.:

Vector resonance (ρ-like) in W_LZ_L scattering from Chiral Lagrangian model
M = 1.5 TeV, leptonic final states, 300 fb^{-1} (LHC) vs 3000 fb^{-1} (SLHC)

lepton cuts: p_{t1} > 150 GeV, p_{t2} > 100 GeV, p_{t3} > 50 GeV; E_t^{miss} > 75 GeV

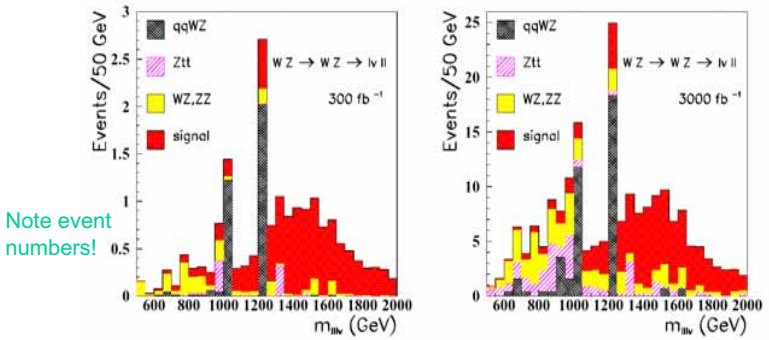

Note event numbers!

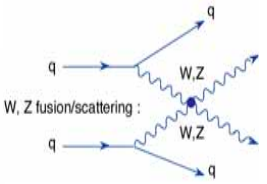

These studies require both forward jet tagging and central jet vetoing! Expected (degraded) SLHC performance is included

increased cm energy/ VLHC even better!!

at LHC: S = 6.6 events, B = 2.2 events

at SLHC: S/√B ~ 10

New gauge bosons, Z' → · ~ reach at SLHC

Additional heavy gauge bosons (W, Z-like) are expected in various extensions of the SM symmetry group (LR, ALR, E_6, SO(10)…..),

Examples of Z' peaks in some models:

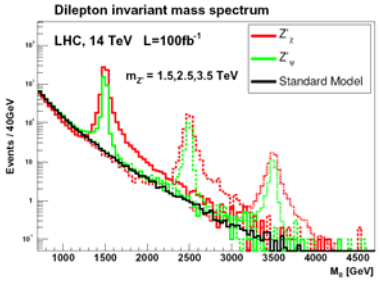

LHC discovery potential for Z' → ''μ ·

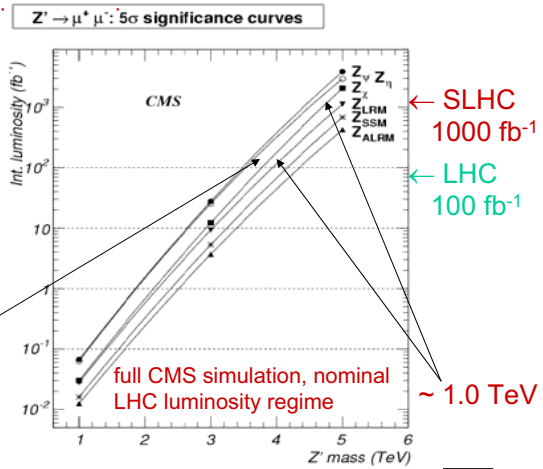

← SLHC 1000 fb^{-1}

← LHC 100 fb^{-1}

LHC reach ~ 4.0 TeV with 100 fb^{-1}

full CMS simulation, nominal LHC luminosity regime

~ 1.0 TeV

➡ gain in reach ~ 1.0 TeV i.e. 25-30% in going from LHC to SLHC

SUSY at SLHC/VLHC - mass reach

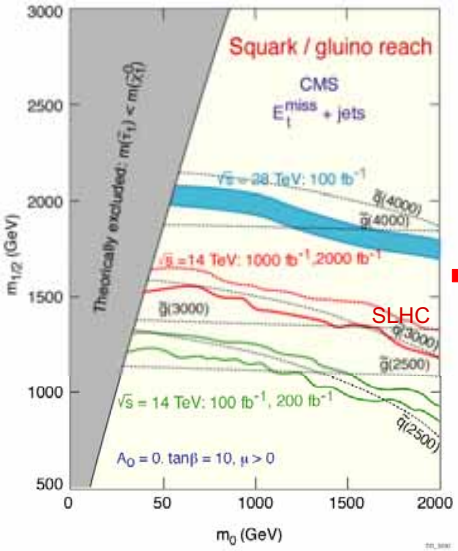

• Higher integrated luminosity brings increase in mass reach in squark, gluino searches, i.e. in SUSY discovery potential;
not too demanding on detectors as very high E_t jets, E_t^{miss} are involved, large pile-up not so detrimental

➡ with SLHC the SUSY reach is increased by ~ 500 GeV, up to ~ 3 TeV in squark and gluino masses
(and up to ~ 4 TeV for 30 TeV VLHC)

• the advantage of increased statistics should be in the sparticle spectrum reconstruction possibilities, larger fraction of spectrum, requires detectors of comparable performance to "present ones"

209

Notice advantage of a 28 TeV machine….

General remarks on desirability for detector upgrades, SLHC vs LHC (I)

• High mass/ TeV scale searches such as:
SUSY reach (squarks, gluinos), W', Z', Z_{KK}, R-S gravitons, LQ, extra dim monojets etc not much affected by higher pile-up, nor by some reduction in acceptance for leptons, $|\eta| < 2.5 \rightarrow |\eta| < 2.0$, as heavy objects are centrally produced;
excellent tracker still needed for muon momentum resolution, tracker isolation criteria; b and τ-tagging performance somewhat less important

• Important topics which would benefit greatly from the ~ 300 fb^{-1} to 3000 fb^{-1} increase, but depend on forward jet tagging and/or central jet veto, suffer from increased pile-up:
pp → qqH, qqVV (heavy Higgs, MSSM Higgs, resonant or non-resonant W_L , Z_L scattering - an alternative to Higgs mechanism for EWSB
direct slepton pair (→ 2 leptons), and chargino-neutralino (→ 3 leptons) pair production
precision measurements of TGC, QGC …….

These studies require maintaining present calorimetric angular coverage preferably with improved granularity especially in the forward region if "forward jet tagging" turns out to be important (if no Higgs found!), new detector techniques (quartz fibers and clading? or…) to sustain radiation damage

Extra dimensions, TeV^{-1} scale model

Theories with extra dimensions - with gravity scale ~ ew scale - lead to expect characteristic new signatures/signals at LHC/SLHC; various models: ADD, ABQ, RS…

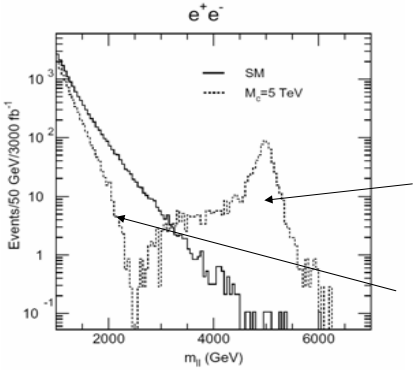

Example: two-lepton invariant mass

TeV^{-1} scale extra dim model (ABQ-type, one "small" extra dim. $R_c = 1/M_c$) with M_c = 5 TeV, 3000 fb^{-1}

peak due to first γ, Z excitation at ~ M_c ;

note interference between γ, Z and KK excitations $\gamma^{(\ )}$, $Z^{(n)}$, thus sensitivity well beyond direct peak observation from dσ/dM (background control!) and from angular distributions/ F-B asymmetry

➡ reach ~ 6 TeV for 300 fb^{-1} (LHC), ~ 7.7 TeV for 3000 fb^{-1} from direct observation
indirect reach (from interference) up to ~ 10 TeV at LHC, 100 fb^{-1}
~ 14 TeV for SLHC, 3000 fb^{-1}, e + μ

10σ

General remarks on desirability for detector upgrades, SLHC vs LHC (II)

• b-tagging capability - probably most difficult to maintain at 10^{35} at the present 10^{34} (expected) level of performance, but would be most desirable,
to increase the SUSY spectrum coverage, for stop, sbottom (especially in case of "inverted mass hierarchy" where these could be the only observable sparticles….),
for precision measurements on SM Higgs BR's,
to extend MSSM Higgs searches in bbA/H, tbH± etc final states
rare top decays (FCNC) t → u/c + γ/Z, rare $B^o_{s,d}$ decays……

• τ-tagging capability, even more demanding on tracker/impact parameter/sec vertex measurements,
for A/H → ττ , H± → τν;
for SUSY/stau spectroscopy (at large tgβ neutralinos largely decay to tau-stau);
GMSB with $\tilde{\tau}_1 \rightarrow \tau\ G_{3/2}$ (scenario with $\tilde{\tau}_1$NLSP)
$\tau^{\pm} \rightarrow 3\mu^{\pm}$, $\mu^+\mu^-e^{\pm}$, $\mu^{\pm}e^+e^-$…….

These topics require highest performance tracker, measurements close to beam pipe for impact parameter/sec. vertices, new tracking technologies needed for r < ~ 10 cm;
τ-related physics requires understanding hadronic τ triggering at high luminosity; these studies also require minimizing pile-up i.e. optimizing the product of b/τ-tagging efficiency and integrated luminosity!

Possible physics situation after 3-5 years of LHC running/ conceivable scenarios for SLHC

(view of D.Denegri)	I	II	III	IV	V
Detector (CMS) or machine requirements	Heavy bosons Extra dims, W',Z',KK recs. no SUSY	no Higgs no SUSY W,Z scat., BESS, TC	very massive SUSY, gluino,squark at 2 - 3 TeV	SUSY at ~ 0.5 - 1TeV A,H ~ 0.5 TeV	SM-Higgs, TGC ,QGC, SM tests, Triple-Higgs cpl.
Tracker: patt. rec; p	Excel. p-resol.	high perform.	high perform.	max.requirement	high perform.
Tracker: IP;b, τ-tag.	less need for b,τ	No effort	b, τ-tag. desirab.	optimal b, τ-tag	excel. b, τ-tag
Muons ($\|\eta\|$ < ~2.0?) (now $\|\eta\|$ < 2.4)	reduced acceptance OK	red. acc. OK	red. acc. OK	Largest acceptance possible.	Largest accept. possible.
ECAL ($\|\eta\|$ < ~ 2.0?)	red. accept for precis. meas.OK	red. acc ~ OK	OK	Largest accept possible	Largest accept. possible.
HCAL ($\|\eta\|$< ~ 3) E_T^{miss}	Some red. acc .OK	Full acceptance needed, f-jet-tag	Full accept.needed	Full accept .and perf. needed,E_T^{miss}	Full accept. and perf. needed, E_T^{miss}
VFCAL ($\|\eta\|$ from < 5 to < ~ 4.0 - 4.5?)	Reduc. accept. OK	Full acc.required Improve granular.	Not essential, Red. accept	Not so essential, Red. Acc. if need	Not so essential, Red. acc. if needed
Trigger/electronics bunch crossing	25 nsec ~ OK, minimal changes	25 nsec or 12.5 nsec	25 nsec or 12.5 nsec	Track. at L1, ~12.5 nsec needed minimize pile-up	Track. at L1, ~12.5 nsec needed minimize pile-up
Comments/Machine/ IR/bunch crossing	Max. int. Lumi. Max cm Energy Pile-up <~ 200	Max. int. Lumi Max cmEnergy Pile-up < 200	Max. int Lumi. Max cm Energy Pile-up < 200	Minimize pile-up <~100, stable run conditions Optimize b/τ tag eff.*Int luminosity	Minimize pile-up <~100, stable run conditions Optimize b/τ tag eff.*Int luminosity

210

Forward beam pipe

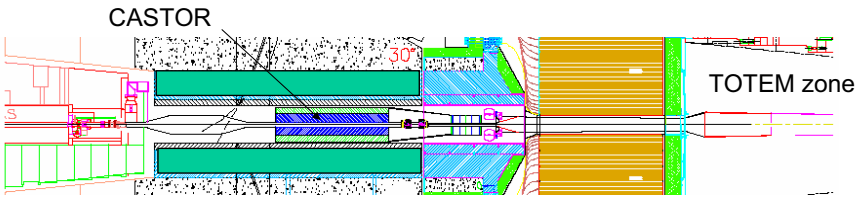

thin pipe 13-16 m believed good for 10^{34} pp
CASTOR & TOTEM easily installed/removed for special runs (eg heavy ion), interspersed with high lumi pp

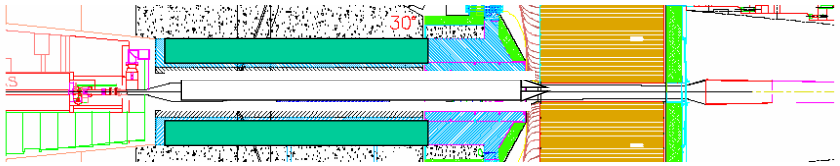

wide pipe (400mm) after HF and in its shadow

A.Ball

Conclusions on SLHC

In conclusion the SLHC ($\sqrt{s} \approx 14$ TeV, $L \approx 10^{35}$ cm^{-2} s^{-1}) would allow to extend significantly the LHC physics reach - whilst keeping the same tunnel, machine dipoles and a large part of "existing" detectors, however to exploit fully its potential inner/forward parts of detectors must be changed/hardened/upgraded, trackers in particular, to maintain performances similar to "present ones"; forward calorimetry of higher granularity would be highly desirable for jet tagging, especially if no Higgs found in the meantime!

Cost issues for 10ns or 15ns

ECAL

- Replacing EB electronics would be costly
- 3 MCHF - Off Detector
- 3 -10 MCHF New Front End electronics
  - Depends on scope of change
- 4 - 5 MCHF Remove/Dismount/Integrate/Install
- Total of 10 -18 MCHF for ECAL

Other detectors

- Changing Front End and Off-Detector components will likely be in the range of 1- 3 MCHF for each detector
- Estimate 10 MCHF for HCAL/Muons total

Asynchronous running

- Still need to evaluate the efficiency losses and cost implications in the off detector electronics

spares

Level 1 trigger at SLHC/muon pt resol. at L1?

The trigger/DAQ system of CMS will require an upgrade to cope with the higher occupancies and data rates at SLHC

One of the key issues for CMS is the requirement to include some element of tracking in the Level 1 Trigger

There may not be enough rejection power using the muon and calorimeter triggers to handle the higher luminosity conditions at SLHC

Using the studies for HLT applications gives an idea of what could be gained using elements of the tracker in the Level 1

Muon rates in CMS at 10^{34}

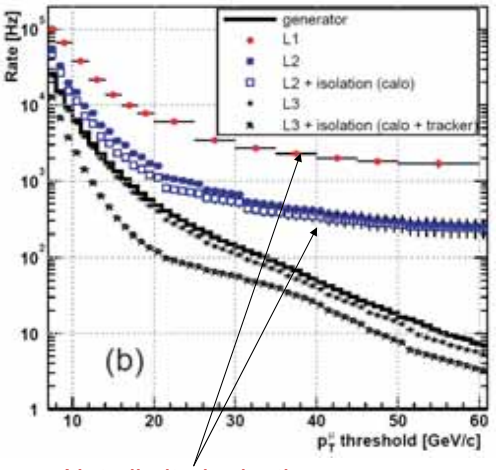

Note limited rejection power (slope) without tracker information!

Integrated Magnet Design

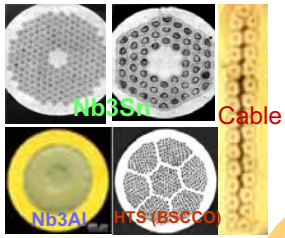

Electromagnetic analysis

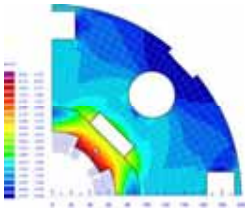

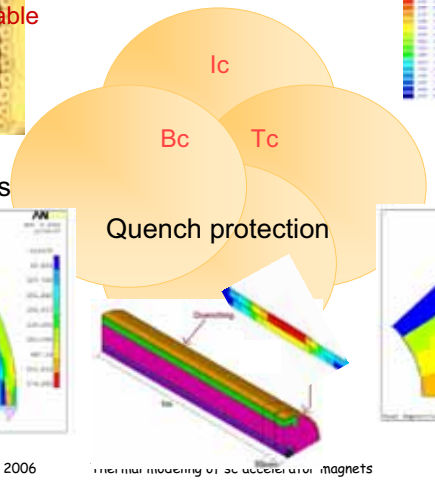

Mechanical analysis

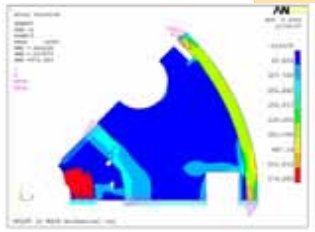

Thermal analysis

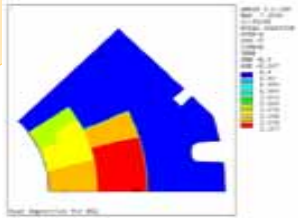

Thermal Modeling of SC Accelerator Magnets

I. Novitski, for the Fermilab-HFM Group

CERN, 3 – 6 April 2006

Thermal Analysis of IR Quads

99/02/20 14.29

Deposition studies to estimate the total radiation heat load to the system for adequate coil cooling and conductor quench margin.

A continuous heat load due to the beam-induced deposition released in IR magnet coils
(pp collisions and beam loss in the IR vicinity, estimated by MARS Monte-Carlo code, FLUKA)

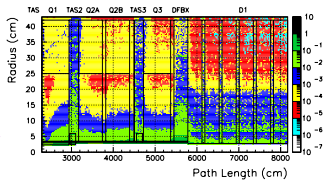

The beam induced energy deposition will cause the magnet coil temperature rise
(estimated by ANSYS, FEA)

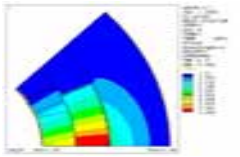

Heat will propagate from the coil (inner layer) through insulation to the helium channel around the beam tube, from the coil (outer layer) to the helium in space between collars or through the collars to the He around collar packs

Heat transfer through He to the heat exchanger located in the iron yoke hole
(Heat transfer analysis, analytical or code).

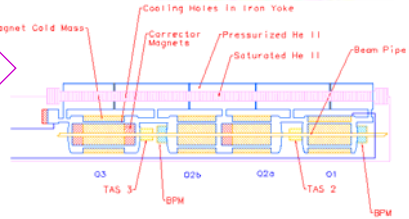

To prevent magnet quench, the cable turn temperature should be below the SC critical temperature
(delta Tc=F(conductor critical surface))

Outline

- **Introduction**
- **Temperature profile calculation**
  - Model
    - magnet designs and parameters
    - ANSYS thermal model
    - heat depositions
    - material properties and boundary conditions
  - Results
    - NbTi and Nb3Sn IRQ
- **Operation margin definition and calculation**
- **Quench limit**
- **Conclusions**

Radiation Heat Depositions

The MARS output data for energy deposition is tabulated.
MARS and ANSYS meshes are different.

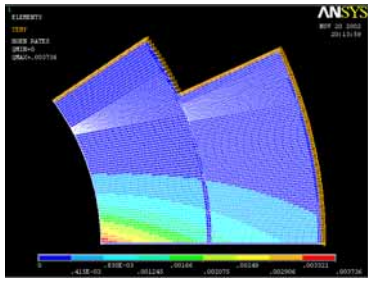

Contour plot of the applied heat load. There is strong dependence of radiation-induced heat depositions on radial and azimuthal coordinate.

The distribution of radiation-induced heat depositions in the coil was fitted by the following function found from the analysis of the heat deposition distribution in quadrupole calculated by MARS code:

$$P(r,\vartheta) = Po \cdot \exp\frac{-(r-Rin)}{Ro} \cdot \frac{\vartheta o}{\vartheta + \vartheta o}$$

where

r and θ are polar coordinates,

Rin is the coil inner radius,

Po is the energy deposition power on the coil inner surface,

Ro and θo are fitting parameters.

IRQ Magnet Design

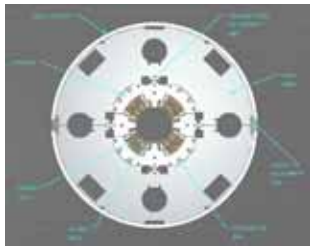

NbTi MQXB cross-section.

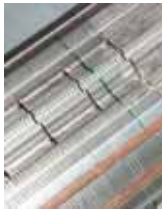

Periodic radial channels

- Two-layer NbTi and Nb3Sn coil with 70-mm and 90-mm bore, insulated with Kapton, supported by SS collar and surrounded by iron yoke.
- Cold mass is filled by pressurized superfluid He at T=1.9 K.
- External HeII heat exchanger connected with cold mass at each end.
- Annular channel between the beam pipe and the coil – *longitudinal and azimuthal heat transfer*
- Periodic radial channels in quad poles, porous collar and yoke blocks – *radial heat transfer*
- Longitudinal channels in the iron yoke – *longitudinal heat transfer to the heat exchanger*

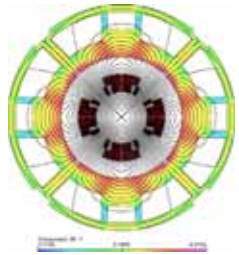

90-mm Nb3Sn quads cross-section.

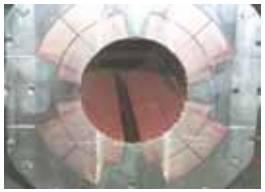

NbTi coil

IRQ Material Properties

Material properties:

- **Thermal conductivity at 1.9 K for different materials used in the magnet is summarized in Table.**
- **In this analysis it was assumed that the material properties are independent on temperature variation.**

Material	Thermal Conductivity at 1.9 K (W/m/K)
NbTi Inner Coil Azimuthal	0.018
NbTi Outer CoilAzimuthal	0.016
NbTi Inner Coil Radial	4.54
NbTi Outer Coil Radial	6.45
Copper (wedges)	140
Kapton (insulation)	0.005
Stainless Steel (collar)	0.1
Nb3Sn Inner/Outer Coil Azimuthal	0.046
Nb3Sn Inner/Outer Coil Radial	10.0
Bronze (wedges, poles)	0.8
S2-glass/epoxy (cable insulation)	0.03

ANSYS Thermal Model

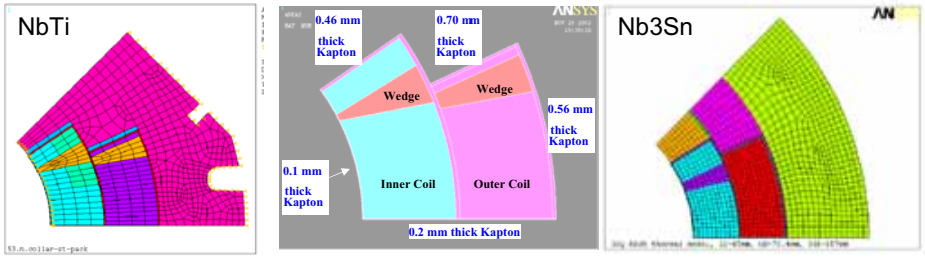

- Two-dimensional finite element thermal models of the collared-coil cross-sections were developed using ANSYS code.
- It includes the inner and outer coil layers which consist of insulated cables and wedges, the ground insulation, and the stainless steel collars.
- The materials used in the modeled geometry are shown with different colors.

Mid-plane Temperature

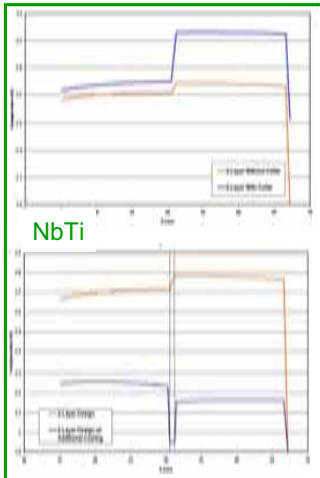

Temperature distribution along the NbTi coil mid-plane.

A **larger temperature rise** (especially **in the coil outer layer**) is **observed** for the case **when superfluid Helium does not penetrate inside the collar blocks**.

However, **the effect is relatively small** and general temperature profile remains the same with the coil T_{max} in the outer layer.

Interlayer cooling channel in two-layer coil **allows significant reduction of the temperature of both layers.**

The inner layer temperature decreases by ~450 mK and that of the outer layer by ~600 mK.

The coil T_{max} in this case moves to the coil inner layer.

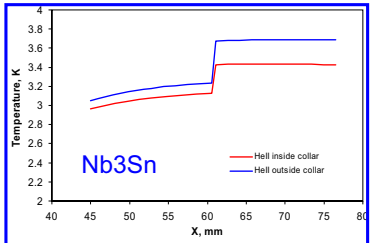

Temperature distribution along the Nb3Sn coil mid-plane.

As expected, a larger temperature rise is observed for the case where the 1.9 K boundary condition is applied at the collar external surface.

However, the effect is small and the general temperature profile remains the same.

IRQ Cooling Conditions

Coil cooling conditions:

- **Boundary conditions include constant HeII temperature of 1.9 K in the annular channel and on the outer surface of the coil (or collar), and zero heat flux through the coil mid- and pole planes.**
- **At the coil bore side, a constant heat transfer coefficient of 300 W/m²/K was applied (Kapitza resistance).**
- **HeII penetrates inside the collar blocks reaching the coil outer surface**
- **HeII does not penetrates inside the collar blocks surface**
- **Interlayer channel for HeII additional to penetrated case**

Summary of Thermal Analysis

The azimuthal temperature distribution in each layer is non-uniform and the radial temperature distribution in each layer is quite uniform in cases of NbTi and Nb3Sn IR quads, although both the radial and azimuthal distributions of radiation-induced heat deposition in the coil are non-uniform.

The temperature distribution for each turn is practically uniform.

In both cases the maximum turn temperature is in the coil mid-plane in the outer layer.

The turn temperature rise *dT* is determined by the average heating power *Pav* deposited in the turn

$$dT \sim k(Pav) \cdot Pav,$$

where coefficient *k(Pav)* characterizes the turn cooling conditions in the coil.

Coefficients *k(Pav)* for each turn in magnet coil can be determined from the calculated temperature profile and known heat deposition distribution.

If material properties do not depend on *dT*, *k=const*, which depends on magnet design and turn position in the coil.

Calculated Temperature Profile

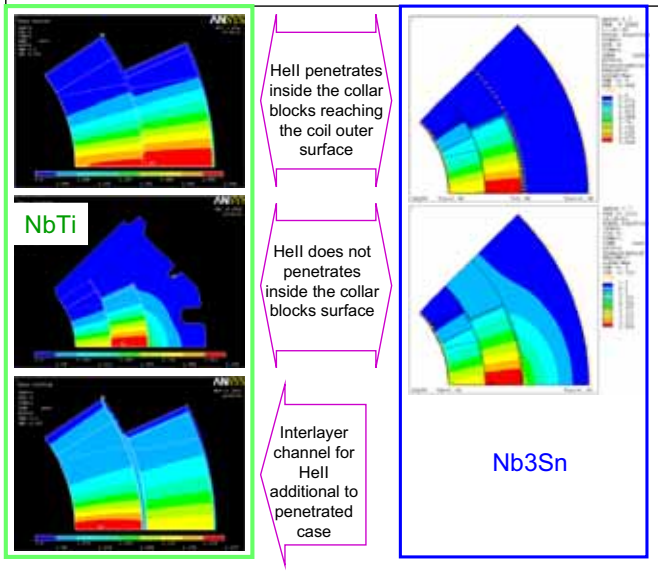

In both cases:

- The azimuthal temperature distribution in each layer is non-uniform due to low coil conductivity in this direction
- the radial temperature distribution in each layer is quite uniform.
- the maximum temperature is in the coil mid-plane if interlayer channels did not work.

215

Measurement and Calculation Comparison

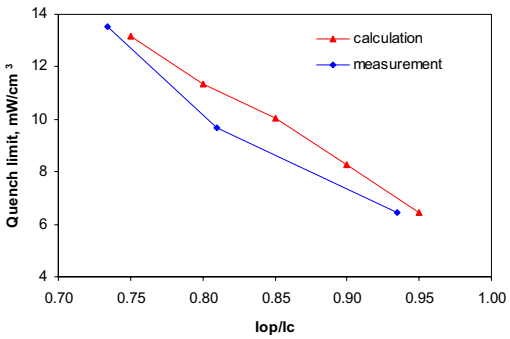

Measured and calculated quench limit for NbTi MQXB (inner-layer mid-plane turns) vs. the critical current margin at T_{op}=1.9 K.

- The experimental verification of the HGQ thermal model is based on measurements of the sensitivity of the magnet critical current to the AC loss heat deposition in the coil.
- Good correlation of measured and calculated data in case of blocked channels in the inner-layer insulation.
- Quench limit at Iop/Ic=0.85 and Top=1.9 K
  - -10 mW/cm^3 (calculation)
  - -9-9.5 mW/cm^3 (measurement)
- The experimental data confirm that MQXB IR quads provide the operation margin of ~2.5 wrt to the radiation heat deposition at the nominal LHC luminosity and Top=1.9-1.95K (3.6mW/cm3 deposited energy at the inner mid-plane turn)

Operation Margin Definition

Turn Operation Margin (*TOM*) in magnet is defined as follows:

$$TOM_i = dT_{c\_i}/dT_{t\_i}$$

where

dT_{c_i} is turn #i critical temperature margin (depends on superconductor *Ic(B,T)*, operation current and temperature and turn position in a coil)

dT_{t_i} is turn #i temperature rise (depends on turn position in a coil – Pav_i, cooling conditions)

It could be defined also as

$$TOM_i = Pav_{c\_i}/Pav_{t\_i}$$

where

$Pav_{c\_i} = dT_{c\_i}/k$ is turn #i quench limit

Pav_{t_i} is average heating power in turn #i (e.g. MARS data)

Magnet Operation Margin (*MOM*) is defined as follows:

$$MOM = min(TOM_1, \ldots TOM_N),$$

where

N is the number of turns in magnet.

The operating margin of IR quads with respect to the radiation-induced heat deposition is determined by the operation margin of inner-layer mid-plane turn.

Conclusions

NbTi MQXB:

- Quench limit at Iop/Ic=0.85 and Top=1.9 K is 10 mW/cm^3 (calculation) and 9-9.5 mW/cm^3 (measurement)
- Factor of 2.5 operation margin wrt radiation-induced heat deposition at nominal luminosity

Nb3Sn IRQ:

- Quench limit at Iop/Ic=0.85 and Top=1.9 K is 36 mW/cm^3 (calculation)
- Factor of 10 operation margin wrt radiation-induced heat deposition at nominal luminosity
- Thermal analysis requires knowledge of the following parameters:
  - Coil thermal conductivity measurements
  - Kapitza resistance for S2-glass/epoxy insulation
  - Temperature dependence of material properties
  - Sensitivity analysis (Bc2, Tc, stress, radiation, etc.)
- Experimental verification of the thermal analysis using Nb3Sn dipole models (available) or future IRQ models (work in progress)
- HeII heat exchanger for larger heat depositions in the magnets

IRQ Quench Limit

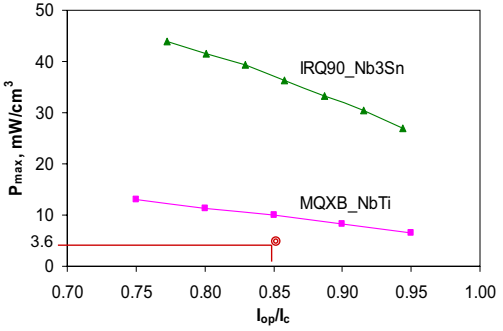

Calculated quench limit for Nb3Sn IRQ and NbTi MQXB (inner-layer mid-plane turns) wrt the radiation heat depositions vs. the critical current margin at T_{op}=1.9 K.

Quench limit depends on superconductor *Ic(B,T)*, operation current (critical current margin), operation temperature and turn position in a coil.

Quench limit at Iop/Ic=0.85 and Top=1.9 K

- 10 mW/cm^3 (NbTi MQXB)
- 36 mW/cm^3 (Nb3Sn IRQ)

Nb3Sn IR quads provide more than factor of 3 larger quench limit with respect to the radiation-induced heat depositions than NbTi IR quads (MQXB).

The effect of critical current margin is relatively small.

Part I: FLUKA

Authors: A. Fasso[1], A. Ferrari[2], J. Ranft[3], P.R. Sala[4]
[1] SLAC Stanford, [2] CERN, [3] Siegen University, [4] INFN Milan

Interaction and Transport Monte Carlo code

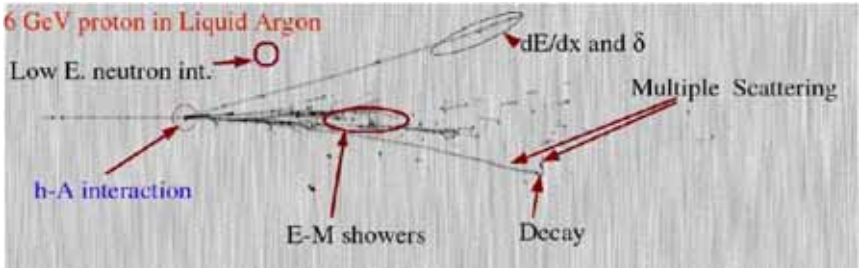

Web site: http://www.fluka.org

Energy deposition by radiation: the CERN experience with FLUKA

WAMDO Workshop
A.Ferrari, M.Magistris, A.Presland, M.Santana, A.Tsoulou,V.Vlachoudis
CERN Tue 4/4/2006

FLUKA Description

- FLUKA is a general purpose tool for calculations of particle transport and interactions with matter, covering an extended range of applications spanning from proton and electron accelerator shielding to target design, calorimetry, activation, dosimetry, detector design, Accelerator Driven Systems, cosmic rays, neutrino physics, radiotherapy etc.
- 60 different particles + Heavy Ions
  - Hadron-hadron and hadron-nucleus interaction 0-10000 TeV
  - Electromagnetic and μ interactions 1 keV – 10000 TeV
  - Nucleus-nucleus interaction 0-10000 TeV/n
  - Charged particle transport – ionization energy loss, mcs, higher order processes
  - Neutron multi-group transport and interactions 0-20 MeV
  - ν interactions
  - Transport in magnetic field
  - Combinatorial (boolean) and Voxel geometry
  - Double capability to run either fully analogue and/or biased calculations
- Maintained and developed under INFN-CERN agreement and copyright 1989-2006
- More than 1000 users all over the world

http://www.fluka.org

The "FLUKA team" (AB-ATB-EET)

- 4 staff + 2 fellows
- Past and present tasks:
  - n_TOF physics and engineering
  - CNGS physics, engineering, optimization, radiation protection
  - IR4 radiation damage and shielding
  - Machine protection elements (TCDQ, TDI, TCDD)
  - IR7 machine protection and damage to electronics
  - Code development
- In this talk:
  - Short introduction to FLUKA (mostly examples)
  - An example relevant for cold magnets: IR7

Negative muons at floating altitudes: CAPRICE94

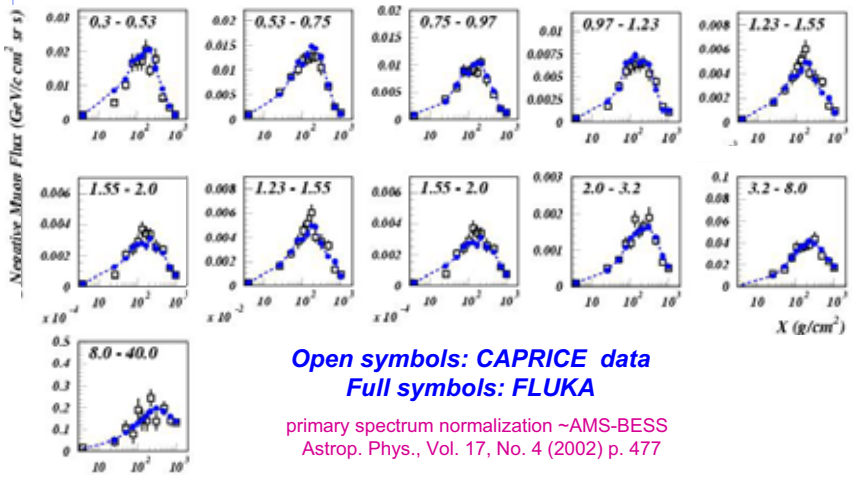

Open symbols: CAPRICE data
Full symbols: FLUKA

primary spectrum normalization ~AMS-BESS
Astrop. Phys., Vol. 17, No. 4 (2002) p. 477

FLUKA – Hadronic Models

Inelastic Nuclear Interactions

- Hadron-Nucleon
  - 5 GeV - ≈100 TeV Dual Parton Model (DPM)
  - >≈100 TeV DPMJET-III
  - 2.5 - 5 GeV Resonance production and decay model
- Hadron-Nucleus
  - < 5 GeV PEANUT : Sophisticated Generalized Intranuclear Cascade (GINC) pre-equilibrium
  - High Energy Glauber-Gribov multiple interactions Coarser GINC
- Nucleus-Nucleus
  - < 5 GeV/n modified version of rQMD-2.4
  - High Energy DPMJET-III

All models: Evaporation / Fission / Fermi break-up / Fragmentation
γ-deexcitation of the residual nucleus

Elastic Scattering and Charge exchange

- Phase shift based hadron-nucleon cross sections.
- Tabulated nucleon-nucleus cross sections

Hadron/muon fluxes in the atmosphere

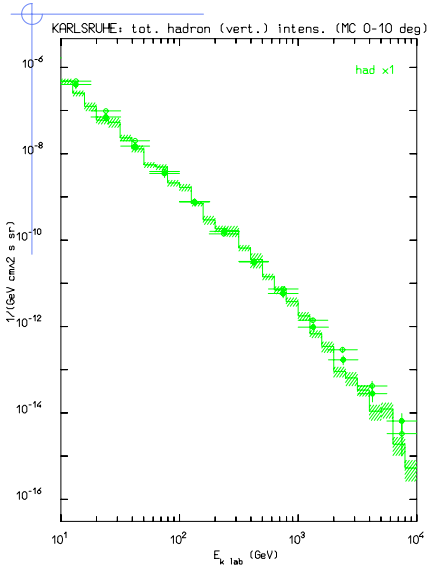

Hadron flux at sea level, KASKADE
H. Kornmayer et al, JPG 21, 439 (1995).

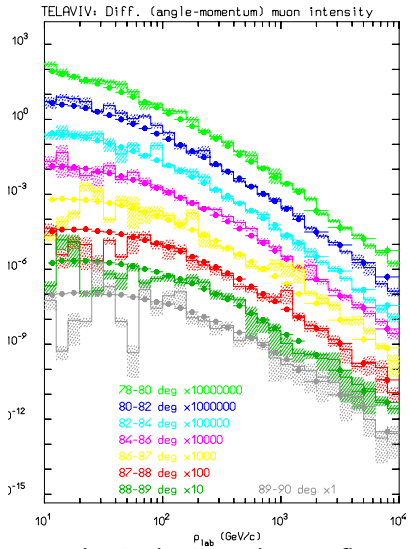

Tel Aviv horizontal muon flux: up to 10 TeV

Nonelastic hA interactions at high energies: examples

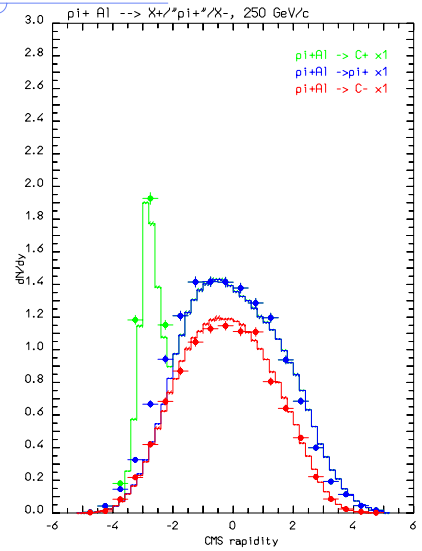

Rapidity distribution of charged particles produced in 250 GeV π^+ collisions on Aluminium
Data from Agababyan et al., ZPC50, 361 (1991).

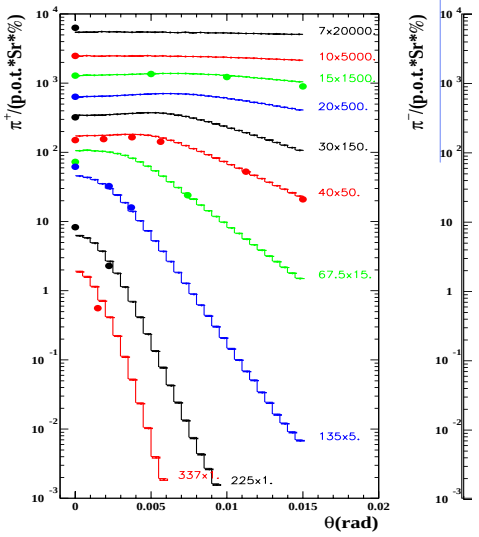

Double diff distribution for π^+ production from 450 GeV/c p on Be
H.W Atherton CERN 80-06
SPY : PLB 425, 208 (1998)

Cern Neutrino to Gran Sasso

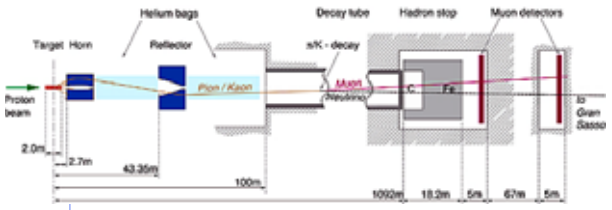

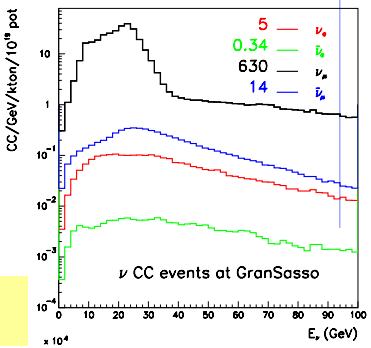

Engineering and physics: target heating, shielding, activation, beam monitors, neutrino spectra

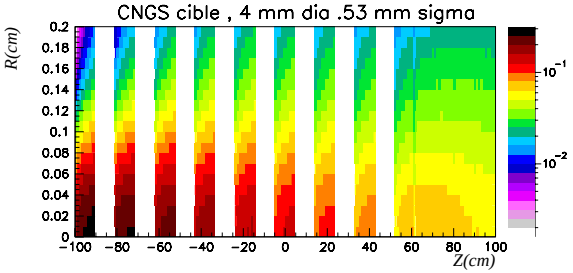

Energy dep. In CNGS target rods, GeV/cm³/pot

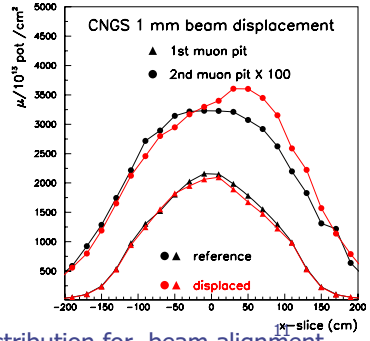

Muons in muon pits: horizontal distribution for beam alignment

Thin target examples

p + ^{80}Zr → p + X (80 MeV)

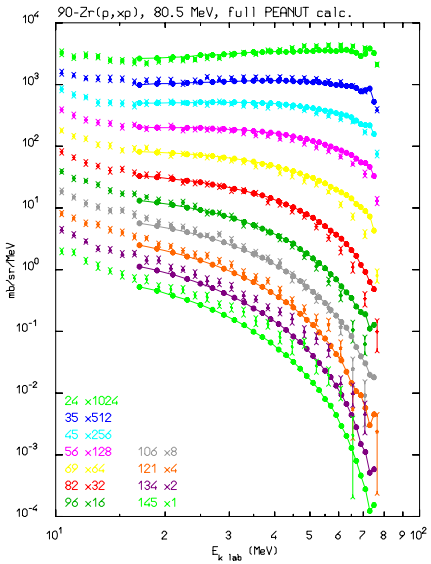

p + Al → π⁻ + X (4 GeV/c)

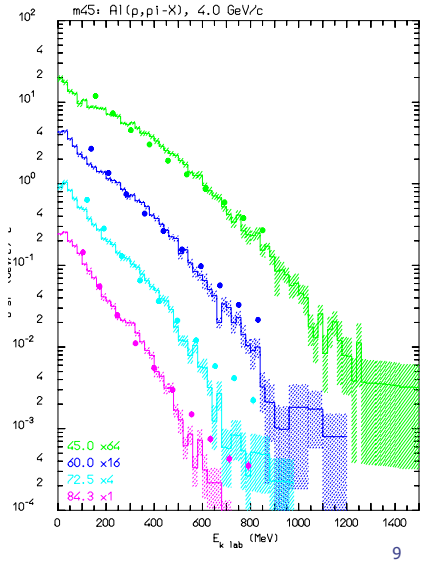

LHC Cleaning Insertions

Two warm LHC insertions are dedicated to beam cleaning

Collimation systems:
IR3: Momentum cleaning
IR7: Betatron cleaning

Normal operation:
- 0.2 hours beam lifetime
- 4×10^{11} p/s for 10 s
- Power = 448 kW

Quench limit: 5 mW/cm³

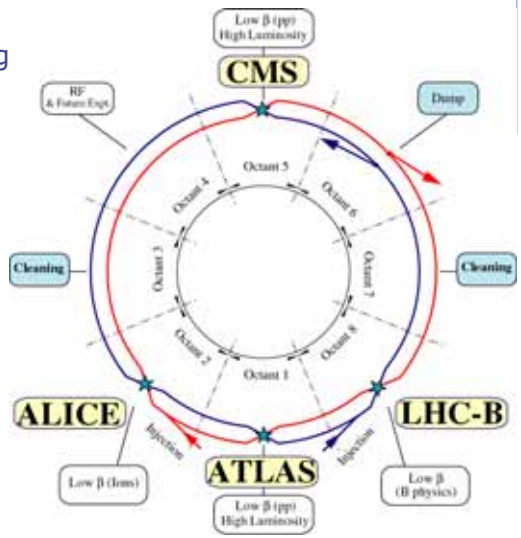

158 GeV/n fragmentation

Fragment charge cross section for 158 AGeV Pb ions on various targets. Data (symbols) from NPA662, 207 (2000), NPA707, 513 (2002) (blue circles) and from C.Scheidenberger et al. PRC, in press (red squares), histos are FLUKA (with DPMJET-III) predictions: the dashed histo is the electromagnetic dissociation contribution

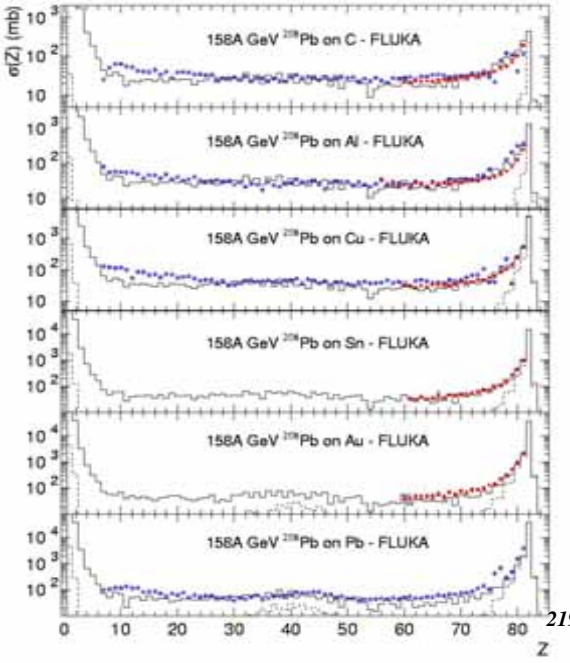

Geometry Implementation

- Dynamic FLUKA input generation with several ad-hoc scripts
- Detailed description of more than 20 prototypes
- Magnetic field maps: Analytic + 2D Interpolated
- Prototypes are replicated rotated and translated.
- Adjust the collimators planes during runtime!
- Dynamic generation of the ARC (curved section)
- Optics test: Tracking up to 5 σ, both vertical / horizontal, reproduce beta function. Central orbit reproduced to 1 μm after 1.5km

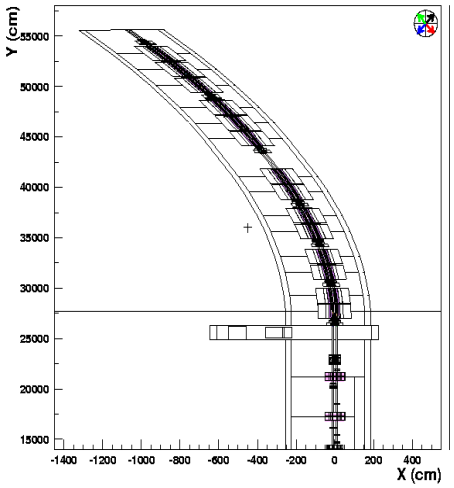

IR7: Overview

- Motivation
- Geometry and Simulation setup
- Studies:
  - Collimator robustness ⇒ Accident scenarios
  - Energy on the superconducting magnets ⇒ Active absorbers
  - Dose on warm magnets ⇒ Passive absorbers
  - Beam Loss Monitors ⇒ Signal in BLM's as a function of the loss point
- Summary

Warm magnets

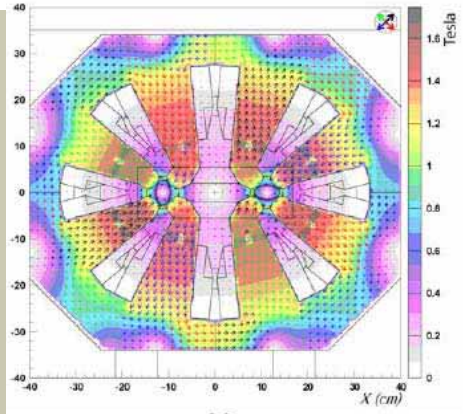

FLUKA geometry exported to PovRay,
a RayTracer for creating three-dimensional graphs.

IR7 layout

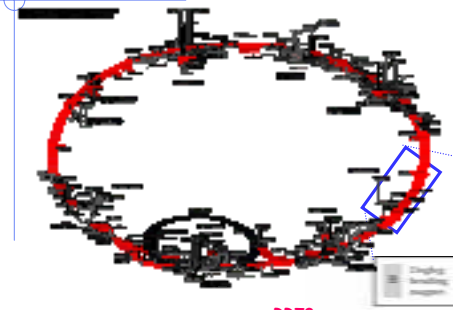

- LHC optics files
- Top beam energy
- Primary collimators: 6 σ
- Secondary collimators: 7 σ
- Absorbers: 10 σ

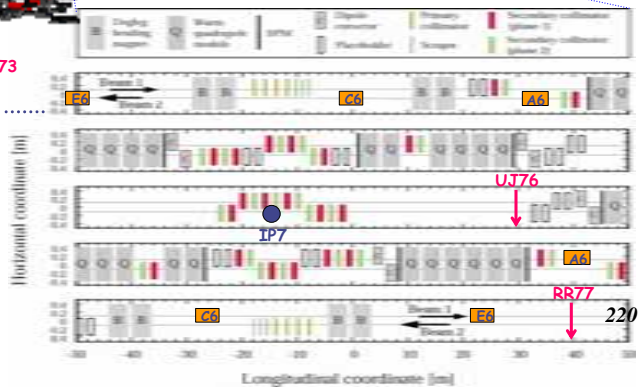

- IR7 Layout contains over 200 objects
- Warm section
- 2 Dispersion suppressors
- Collimators with variable positioning of the jaws

⇒ Challenging simulation work

IR7 Virtual Tour

Cold magnets

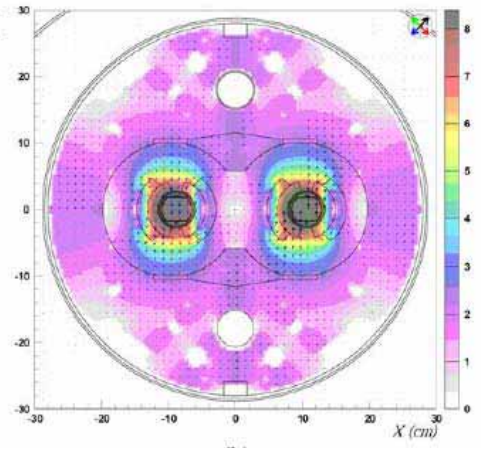

The superconducting dipoles (MB) are made out of 4 sections to account for the curvature of the real dipoles

Collimator robustness: C is the only viable choice

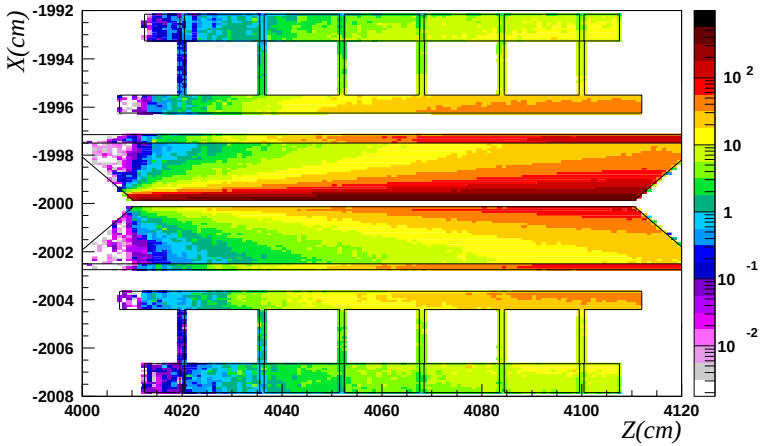

TT40 test beam: energy deposition (J/cm^3) for 3 10^{13} 450 GeV protons on the collimator prototype

Secondary collimators

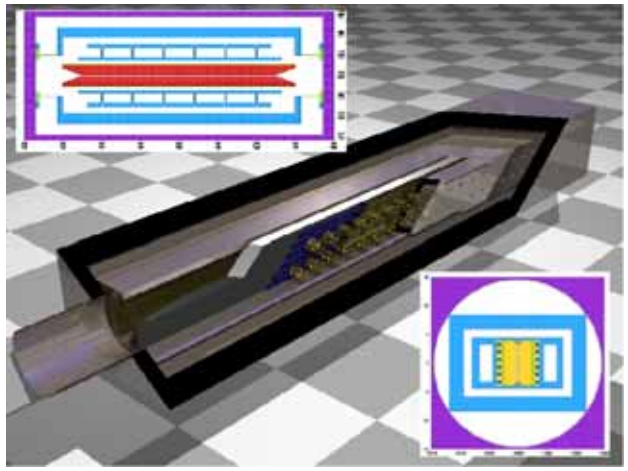

Peak Power deposition in MQTLHA6

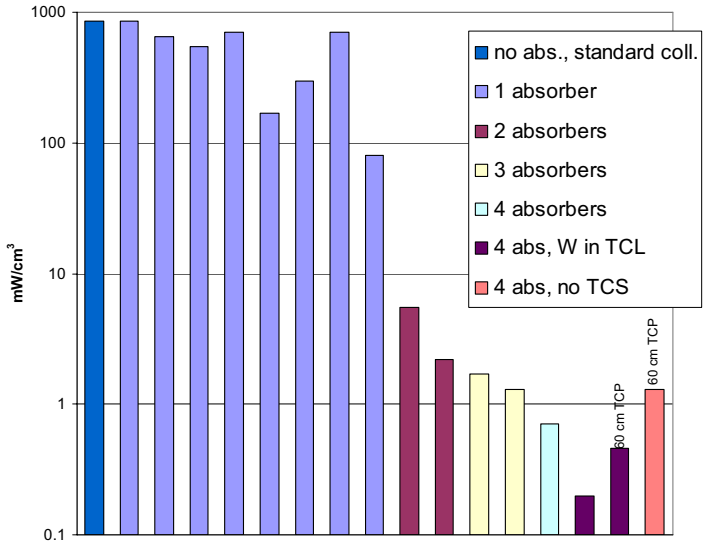

Primary Inelastic collisions map

- Generated by the SIXTRACK program (AB-ABP)
  - 3 scenarios: Vertical, Horizontal and Skew
  - Pencil beam of 7 TeV low-beta beam on primary collimators
  - Spread in the non-collimator plane: 200 μm
  - Recording the position and direction of the inelastic interactions
- FLUKA source: force an inelastic interaction on the previously recorded positions

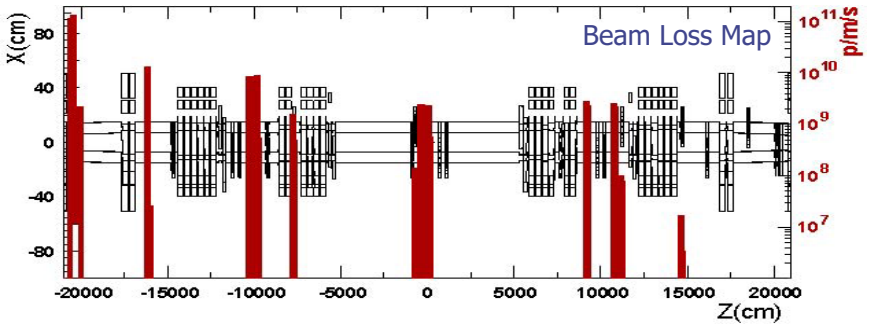

Current layout: horizontal losses

- A6v C6h E6v F6h A7h
- 60 cm long TCP jaws
- Tertiary halo
- W insert in active absorbers
- Passive absorbers for MBW's and MQW's protection

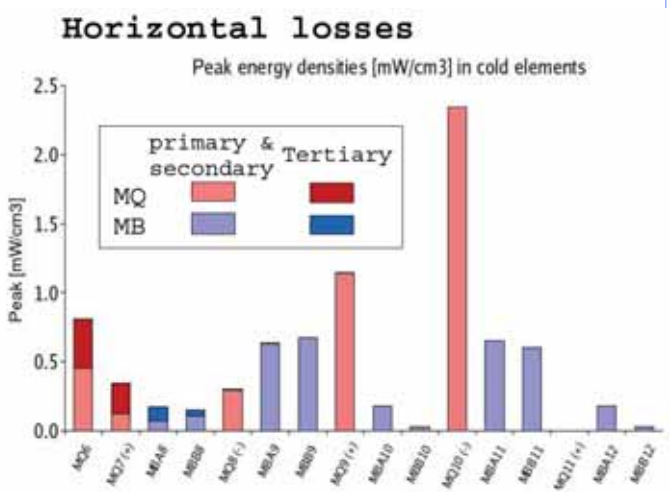

Active Absorber Layout

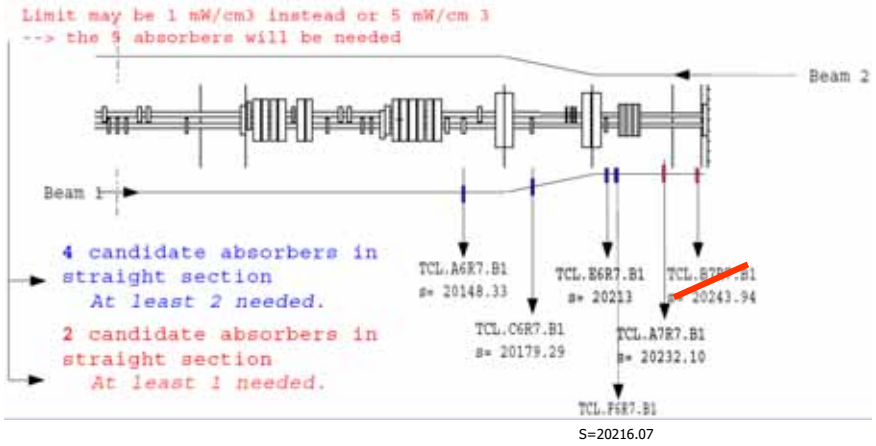

Simulation Accuracy

Sources of errors:

- Physics modeling:
  - Uncertainty in the inelastic p-A extrapolation cross section at 7 TeV lab (corresponding to √s = 115 GeV)
  - Uncertainty in the modeling used

  ⇒ Factor ~1.3 on integral quantities like energy deposition (peak included) while for multi differential quantities the uncertainty can be much worse
- Layout and geometry assumptions
  - It is difficult to quantify, experience has shown that a factor of 2 can be a safe limit
- Beam grazing at small angles on the surface of the collimators.
  - Including that the surface roughness is not taken into account ⇒ A factor of 2 can be a safe choice.
- Safety factor from the SIXTRACK program is not included!
- In the case of the final focus quadrupoles:
  - Uncertainty in the 7+7 TeV center-of-mass interactions (≈10000 TeV in the lab) ⇒ A factor of 1.4 can be a safe choice

Current layout: vertical losses

- A6v C6h E6v F6h A7h
- 60 cm long TCP jaws
- Tertiary halo
- W insert in active absorbers
- Passive absorbers for MBW's and MQW's protection

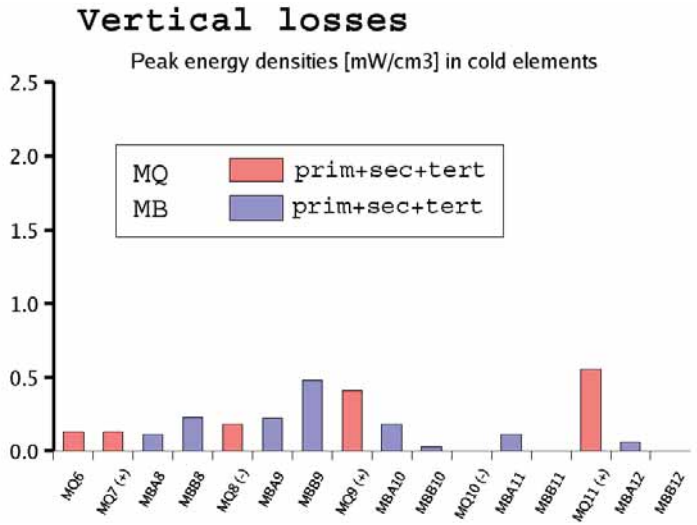

Conclusions

- FLUKA: developed jointly by INFN and CERN for a variety of applications
- Show case: detailed description of the IR7 setup, with dynamic generation of all the necessary input files using the latest optics.
  - Powerful tool used for various studies:
    - Energy deposition on Collimators, Warm Objects, Superconducting magnets
    - Si Damage calculations, Shielding studies for electronics
    - Ozone production…
  - Results for IR7:
    - With 5 absorbers (3 in the straight section, one at the beginning of the arc) we are below the quench limit of 5 mW/cm^3 assuming a safety factor of 2-3.
    - 3 passive absorbers are required in order to protect MBW's and MQW's

Impact of the passive absorber on the most exposed MQW

Most of the radiation passes through the beam pipe
=> The most important parameter is the inner radius.

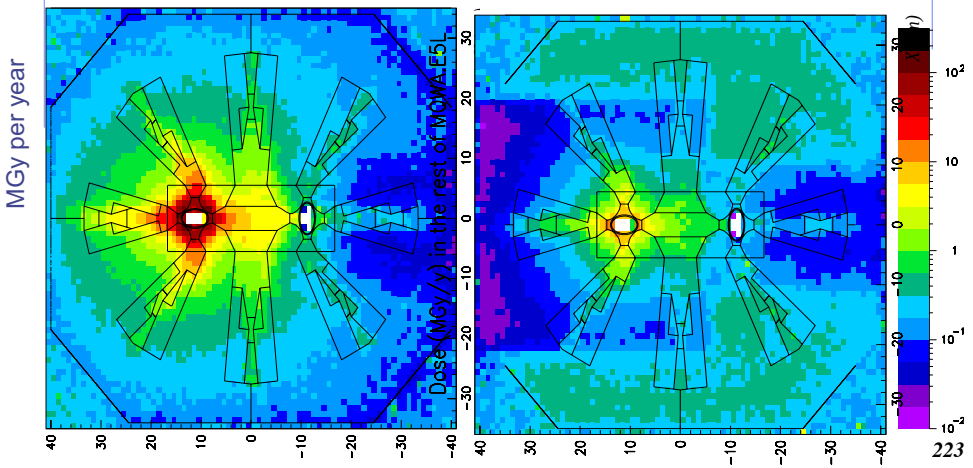

Constraint: 30 MGy over 10 years

END

EFDA EUROPEAN FUSION DEVELOPMENT AGREEMENT

Project Schedule

- **Milestones**
  - Project start: Oct 04
  - CFT for facility preparation: Oct 04
  - Conceptual design phase: Oct 04-June 05
  - CFT for strand procurement: May 05
  - CFT for cabling and jacketing: June 05
  - CFT for dipole construction: July 05
  - **Contracts ready for signature :Dec. 05**
  - Dipole procurement: March 06-Dec 07
  - Dipole facility commissioning: Spring 08

EFDA EUROPEAN FUSION DEVELOPMENT AGREEMENT

EFDA Dipole Project
E.Salpietro

- **Project overview**
  - Objectives, Schedule
- **System specifications**
- **System description**
  - Design concept, guidelines, main features
- **Performance analysis**
- **Project Status**

EFDA EUROPEAN FUSION DEVELOPMENT AGREEMENT

System Specifications

- Test well clear bore *(SULTAN samples)*

  Width x height = 144 mm x 94 mm
- Test well length *(SULTAN samples)*

  L=2850 mm
- DC Field

  B_{DC}=12.5 T (1% in-plane homogeneity)
- AC Field

  B_{AC} =±0.3 T (f~5 Hz, T~100 s)

EFDA EUROPEAN FUSION DEVELOPMENT AGREEMENT

Project overview

- **Objective**
  - Build a test facility to perform full size conductor tests in high background DC field (~12.5 T) and small pulsed AC field for (~0.3 T, f~10 Hz)
- **Applications**
  - ITER conductor tests (short term)
  - Backup of SULTAN (>20 years old)

Main parameters

Operating current	(kA)	16.80
Central magnetic field (DC, 3D)	(T)	12.50
Stored magnetic energy (3D)	(MJ)	15.20
Iron yoke outer diameter	(m)	1.20
Steel cylinder outer diameter	(m)	1.27
Total conductor length	(m)	1689
SC strand weight	(kg)	516
CU strand weight	(kg)	422
AC saddle coils		
Operating current	(A)	350
Turns		6x16
Central magnetic field (AC, 2D)	(T)	0.3
RRR		>300

System Specifications

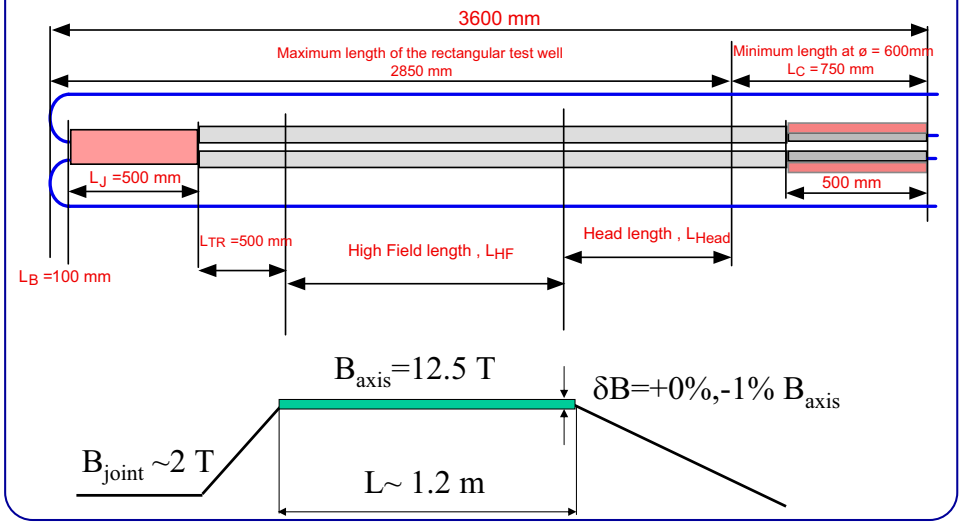

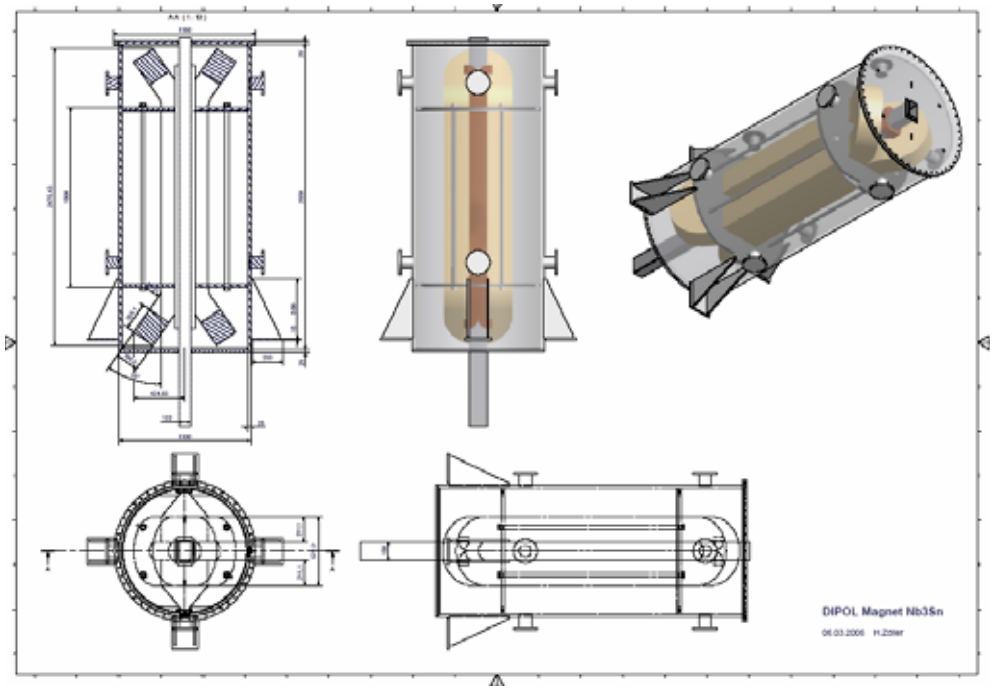

System description
Design concept

- **Test well**
  - Rectangular bore (SULTAN)
  - two-in-the-bore samples (SULTAN)
  - Cold bore (compactness)
- **DC coils (SC)**
  - Saddle shaped coils (compactness)
  - Layer wound (grading)
  - CIC conductor (stability)

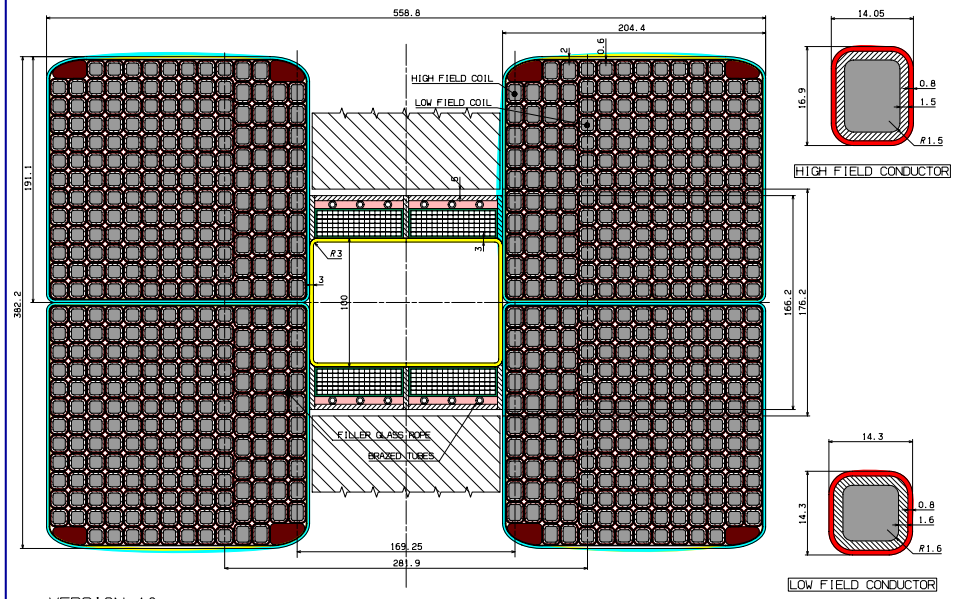

VERSION 10

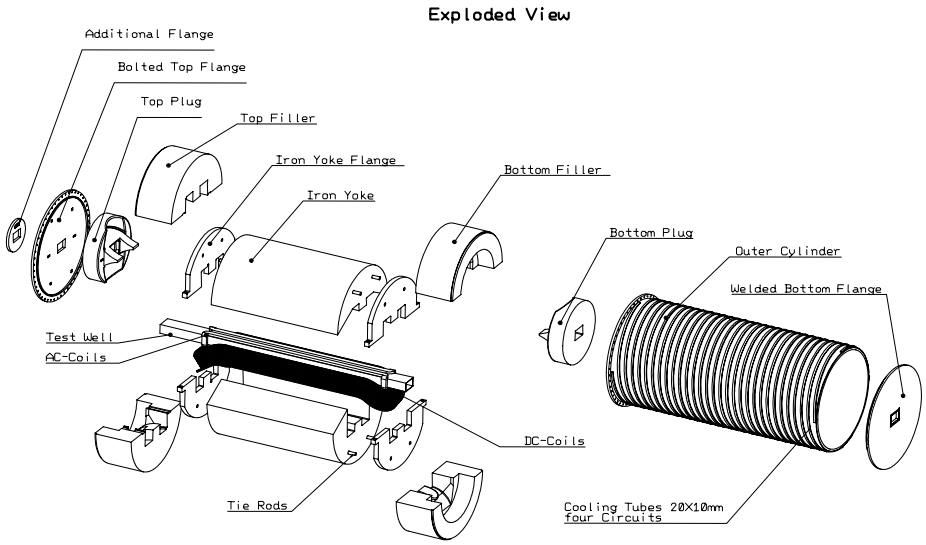

EFDA_DI-POLE
01.07.05

Peak magnetic field (T)	12.69	10.53	8.50	7.19	6.27	5.44	4.52
Current sharing temperature (K)	6.07	6.93	6.71	7.80	8.52	7.58	8.54
Hot spot temperature (K)	202	108	181	166	156	150	138
Void fraction	0.33	0.331	0.348	0.348	0.348	0.348	0.348
Coil horizontal turns (layers)	2	2	2	2	2	2	2
Coil horizontal turns (layers)	10	11	13	13	13	13	12
Insulation thickness (mm)	0.80	0.80	0.80	0.80	0.80	0.80	0.80
Jacket thickness (mm)	1.50	1.50	1.60	1.60	1.60	1.60	1.60
Insulated conductor width (mm)	14.05	14.05	14.30	14.30	14.30	14.30	14.30
Insulated conductor height (mm)	16.90	16.90	14.30	14.30	14.30	14.30	14.30
Insulation area (mm^2)	55	55	52	52	52	52	52
Jacket area (mm^2)	68	68	64	64	64	64	64
Cable space area (mm^2)	114	114	88	88	88	88	88
Helium flow area (mm^2)	38	38	31	31	31	31	31
Number of non copper strands	144	96	48	48	48	48	48
Number of copper strands	0	48	60	60	60	60	60
Non copper area (mm^2)	38	25	13	13	13	13	13
Copper area (mm^2)	38	51	45	45	45	44	44
Conductors unit lengths (m)	89	101	124	128	133	138	132
SC strand mass (kg)	123	92	57	59	61	63	61
CU strand mass (kg)	0	46	71	74	76	79	76
Wetted perimeter (m)	0.31	0.31	0.23	0.23	0.23	0.23	0.23
Hydraulic diameter (mm)	0.50	0.50	0.54	0.54	0.54	0.54	0.54

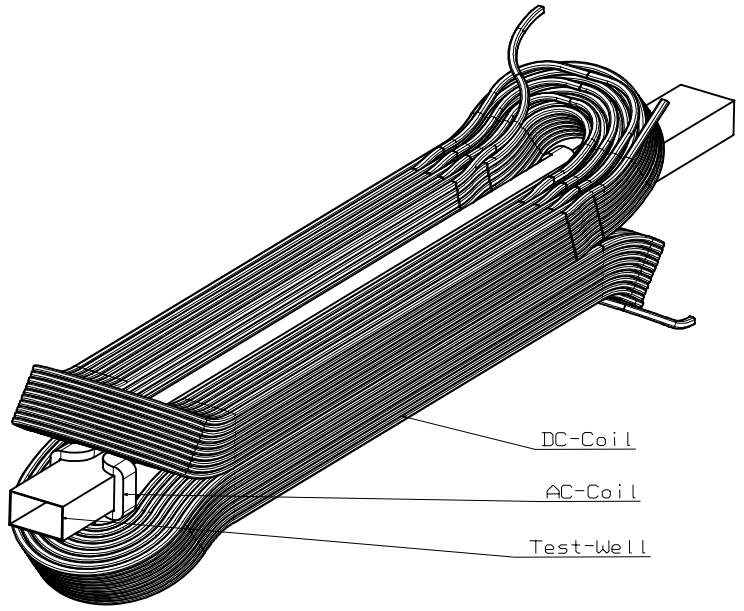

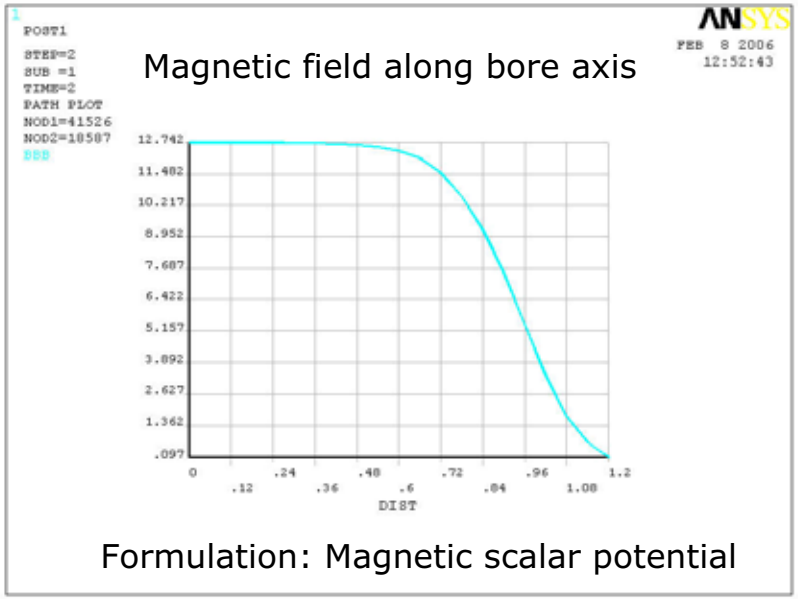

Magnetic field along bore axis

Formulation: Magnetic scalar potential

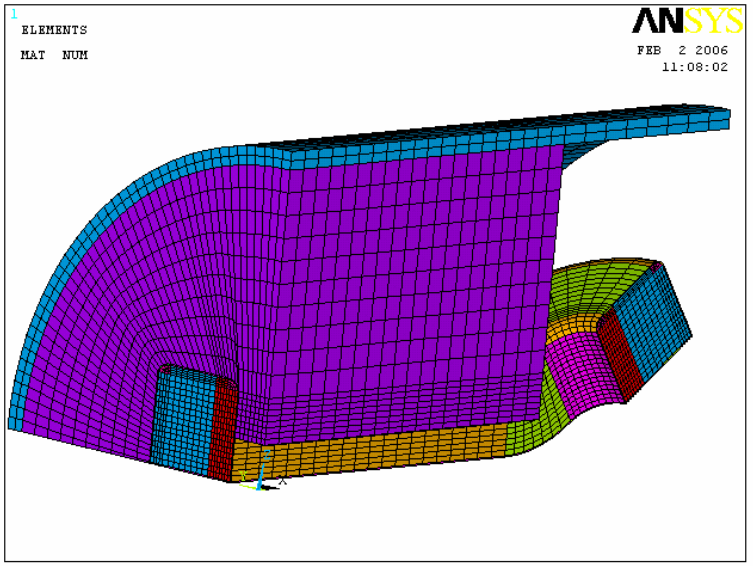

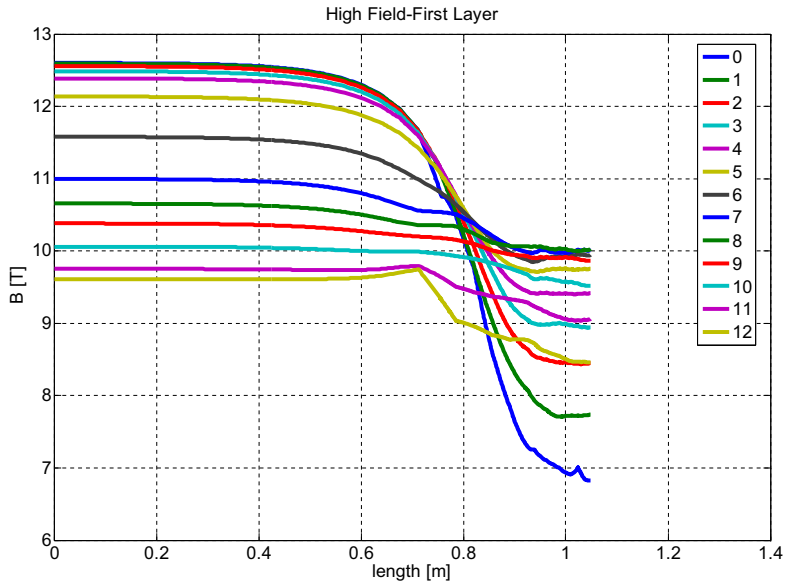

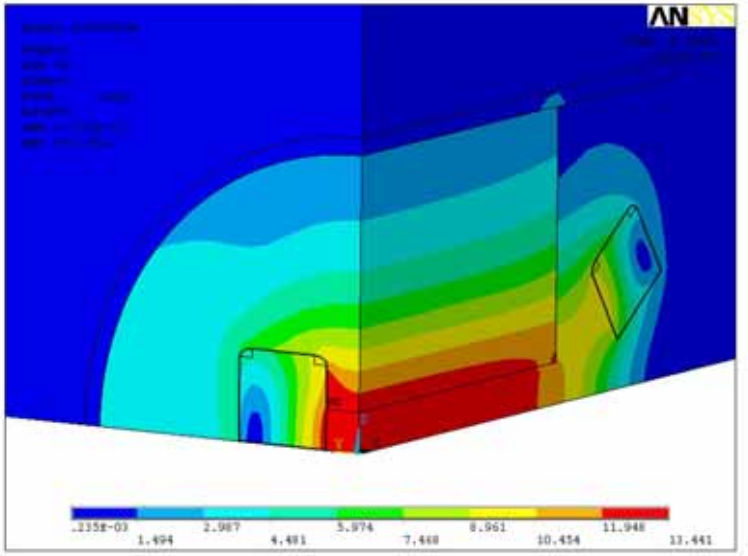

Formulation: Magnetic scalar potential

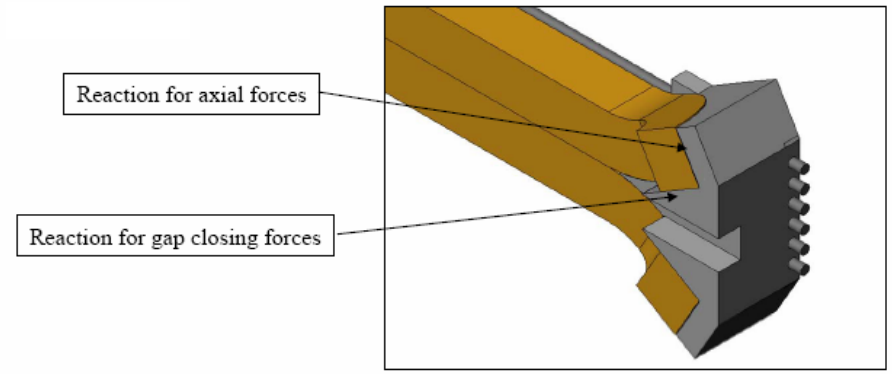

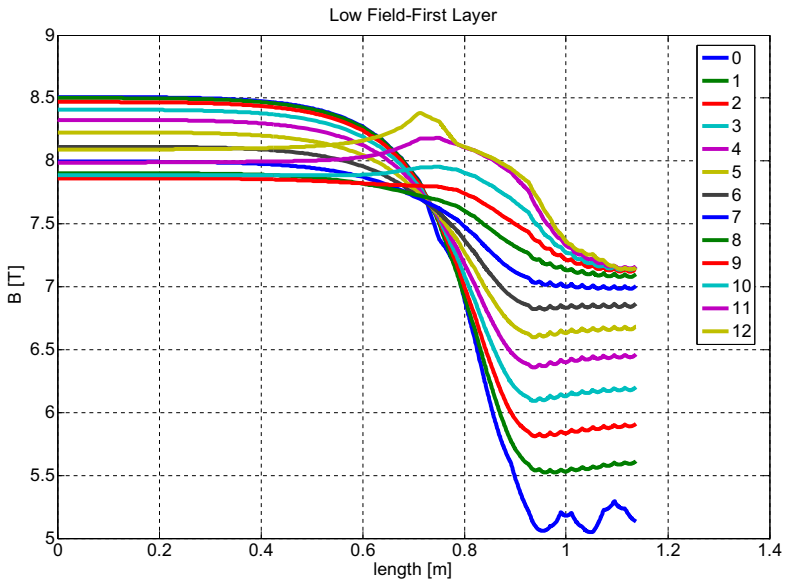

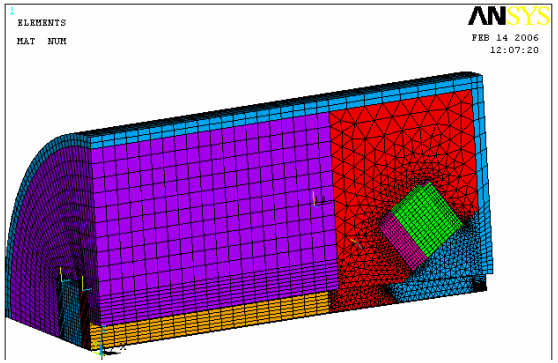

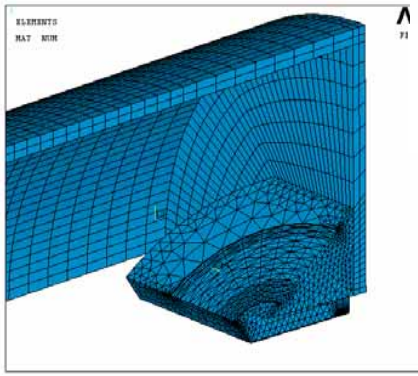

contact elements around wedge and between filler and iron filler impregnates cylinder

	Magnetic energy (MJ)	Field at bore centre (T)
EDGE ELEMENTS	15.50	12.620
MAGNETIC VECTOR POTENTIAL	15.50	12.723
SCALAR POTENTIAL	15.66	12.742

Forces on winding pack	Fx (MN)	Fy (MN)	Fz (MN)
EDGE	4 x 1.20	11.5	-5.40
MVP	4 x 1.80	12.0	-5.37
SP	4 x 1.86	12.0	-5.36
Forces on Iron	Fx (MN)	Fy (MN)	Fz (MN)
EDGE	4 x -0.60	-5.70	-1.90
MVP (Max stress tensor)	4 x -0.70	-5.50	-1.90
SP (Max stress tensor)	4 x -0.64	-5.50	-1.97

EFDA EUROPEAN FUSION DEVELOPMENT AGREEMENT

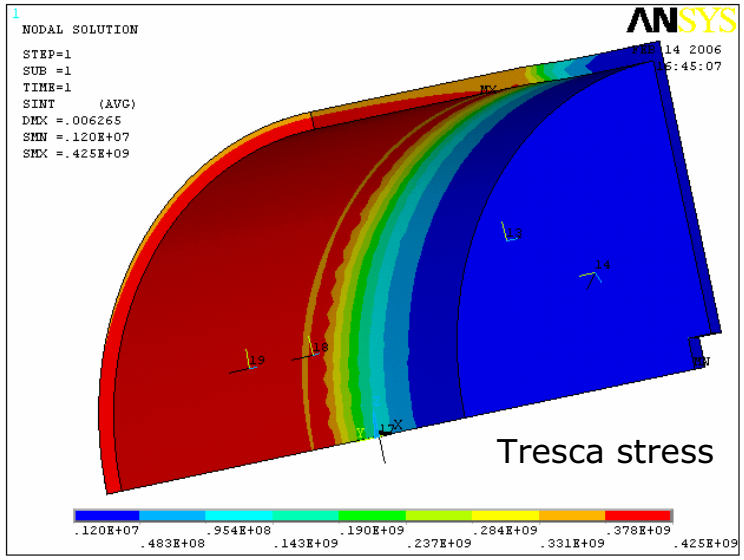

23

EFDA EUROPEAN FUSION DEVELOPMENT AGREEMENT

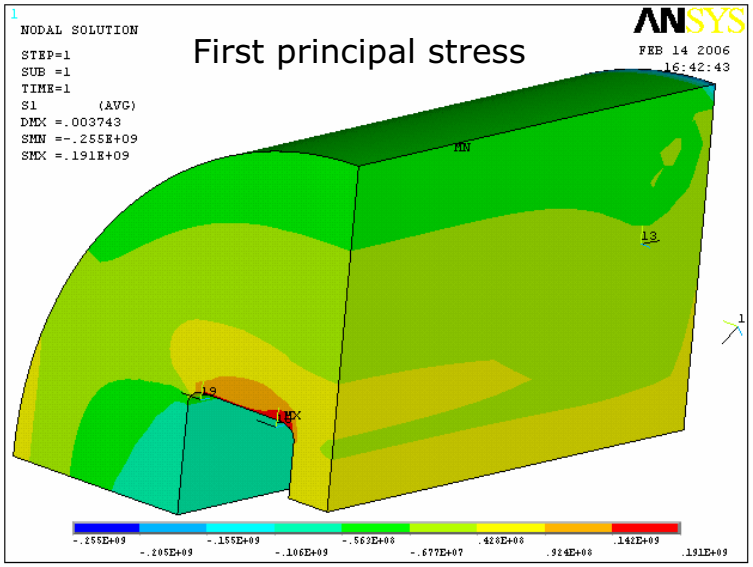

21

EFDA EUROPEAN FUSION DEVELOPMENT AGREEMENT

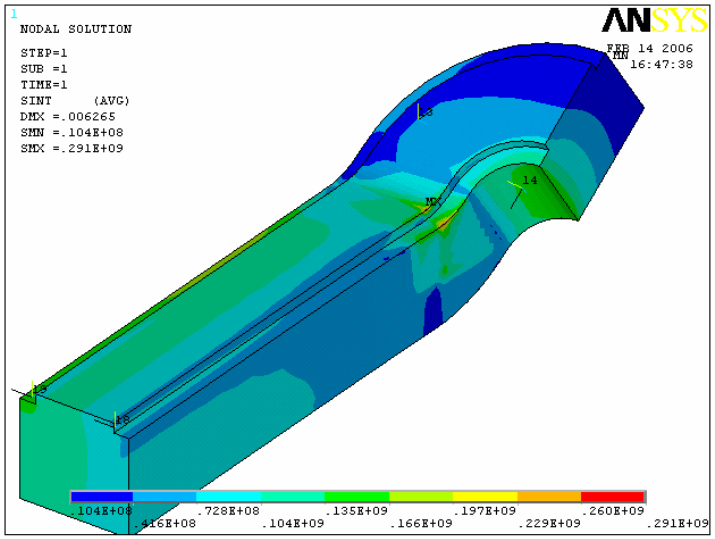

Tresca stress on smeared winding pack

24

EFDA EUROPEAN FUSION DEVELOPMENT AGREEMENT

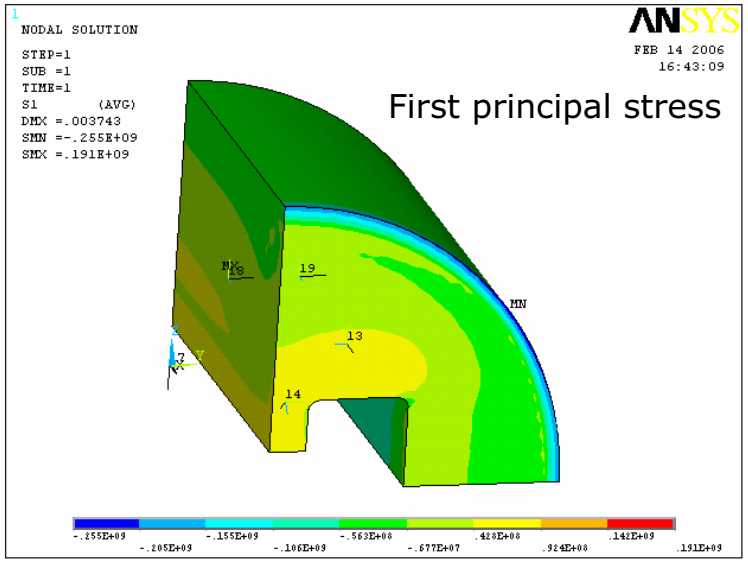

22

Iron yoke & Outer cylinder

- **Yoke**
  - MAGNETIL BC 5.8™ (LHC dipole), high saturation field, $\mu_0 M_{sat} \sim 2$ T;
  - Laminated iron plates insulated and impregnated

File & heat	*Temperature K*	*Young's Modulus GPa*	*Yield Strength MPa*	*Ultimate Tensile strength MPa*	*Uniform elongation %*	*Total elongation %*
Cernx-1	295	205	115	249	32	52
Cernx-2	7	200	-	723	0,5	0,5
Cernx-3	233	196	151	260	~25	~50
Cerny-1	295	200	123	282	26	44
Cerny-2	7	211	-	926	0,5	0,5
Cerny-3	90	210	642	653	5,9	20

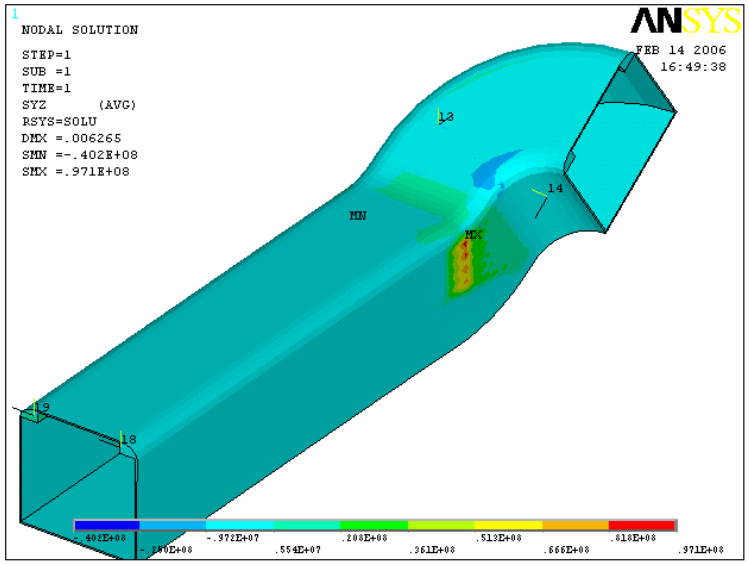

Shear stress on ground insulation

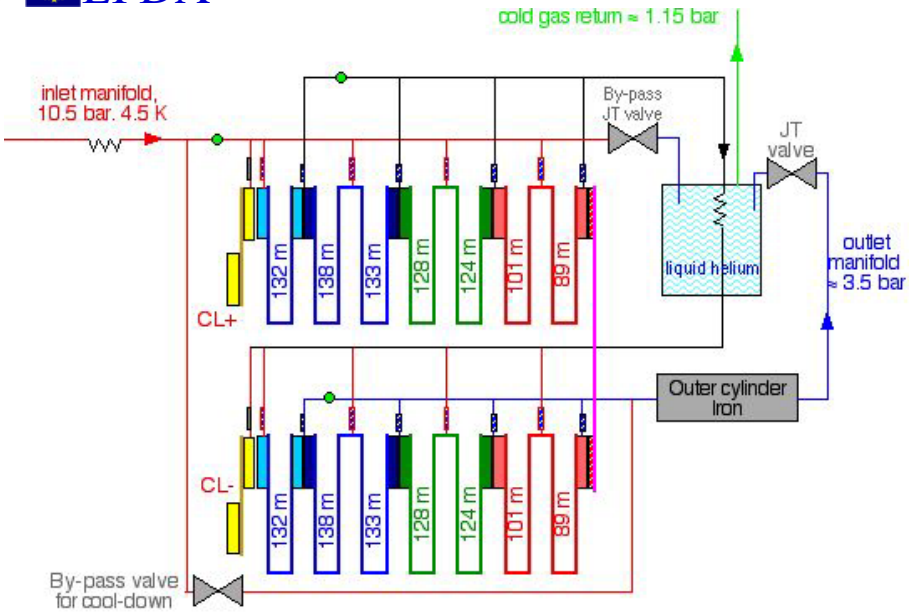

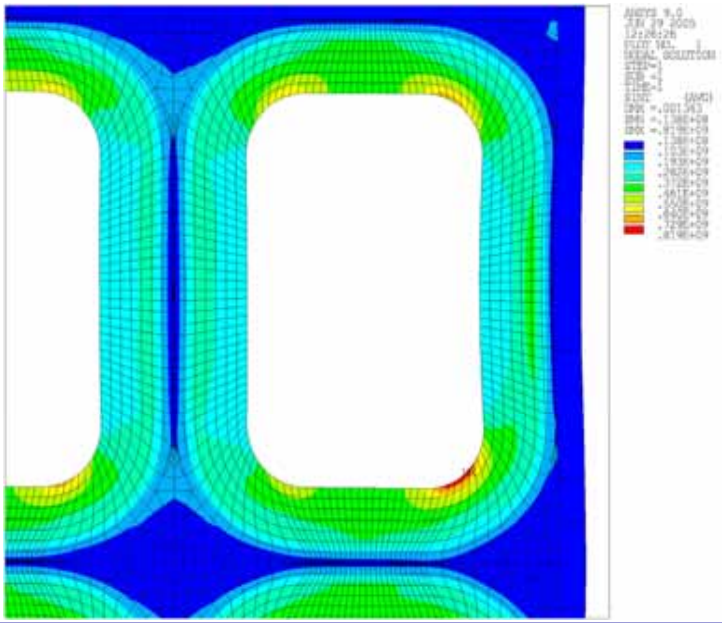

Quench detection

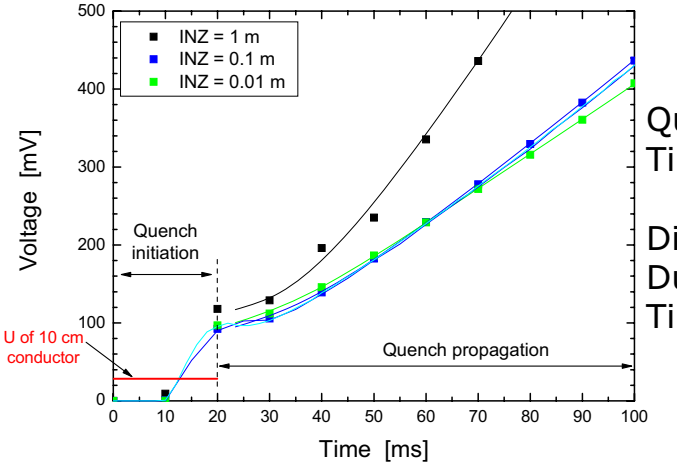

DESIGN

Quench detection
Time <200 ms

Discharge
Dump delay
Time <150 ms

Dipole cool-down: 20 g/s

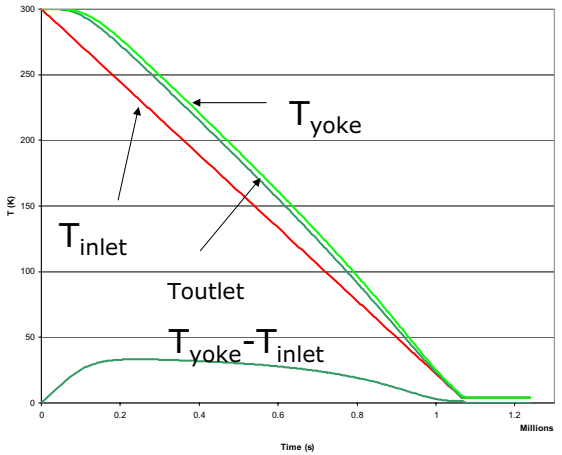

Quench analysis

Normal length: 1 m or 10 m
h_{ch}=1000 W/m^{2}K, h_{cj}=200 W/m^{2}K, h_{hj}=1000 W/m^{2}K

T(K)	HF	MF	LF
inlet	113	111	98
middle	**150**	**169**	**114**
outlet	117	106	72

p(bar)	HF	MF	LF
inlet	144	95	86
middle	**180**	**144**	**120**
outlet	137	125	114

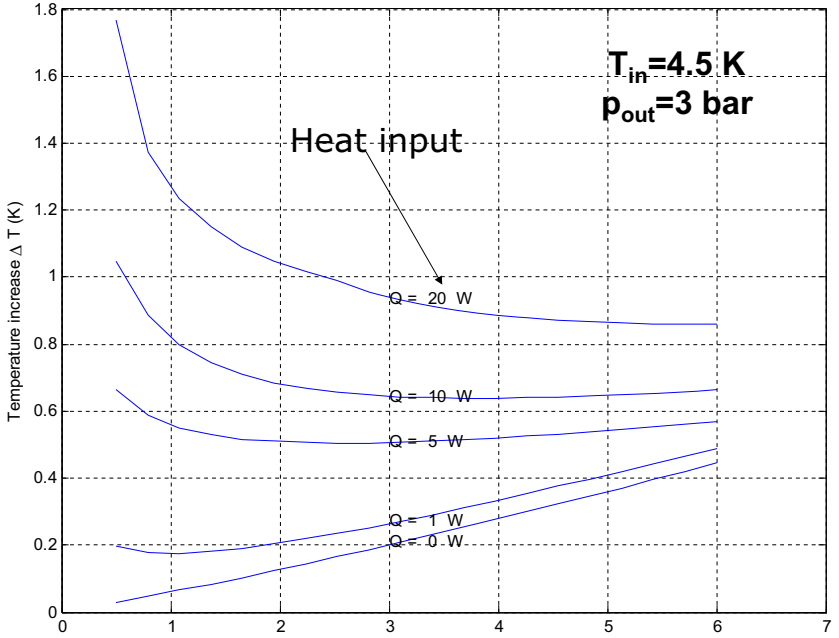

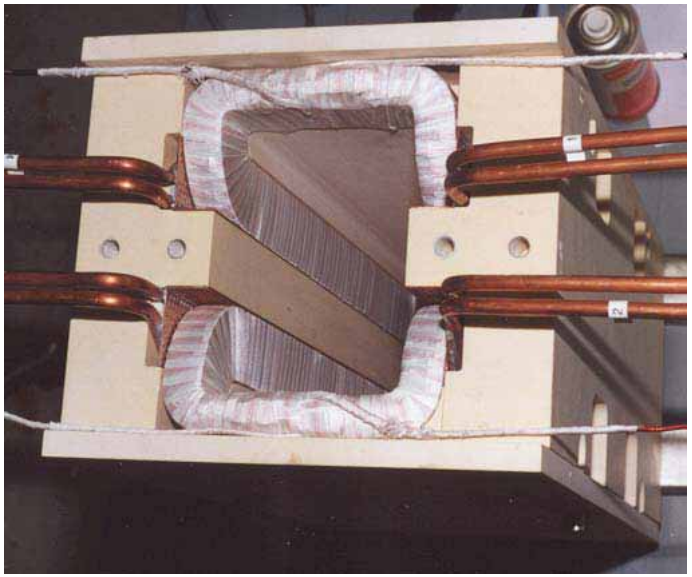

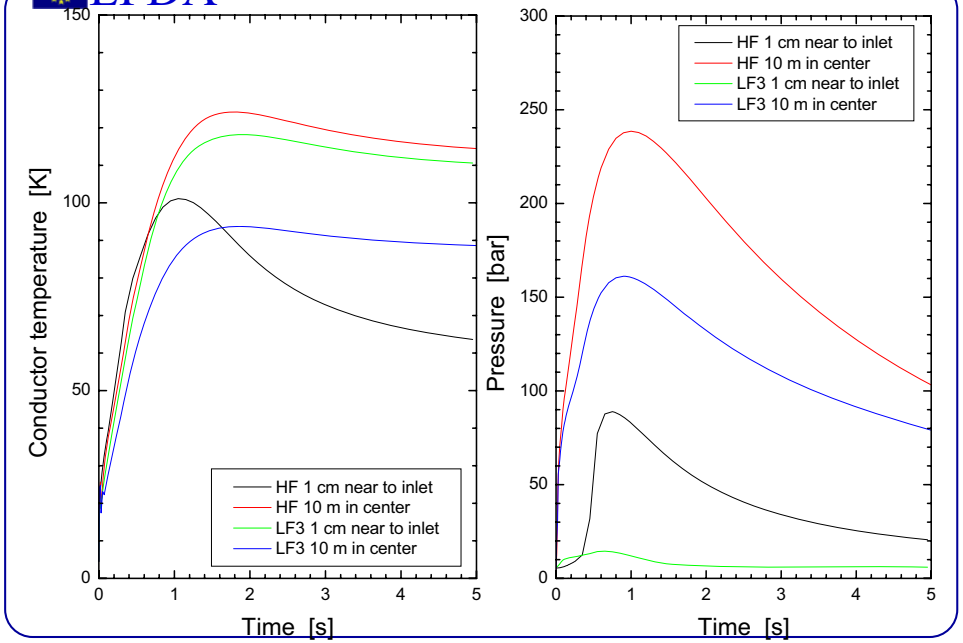

Project Status

- Preliminary Tests
- Jacket Shaping Test
- Strand Delivery
- Conductor Full Size Sultan Sample
- Iron Yoke Delivery
- Dummy Dipole

AC Coils

- Similar to SULTAN AC saddle coils
- Each saddle coil carries ~ 34 kA, 6x16 turns, ~ 350 A/turn each
- High purity (RRR>300) copper strands, each turn is insulated plus epoxy-reinforced glass insulation vs ground (no kapton)
- Cooled by conduction through tubes embedded in a thick copper bar

LF Jacket formed from circular tube: inner dimensions check

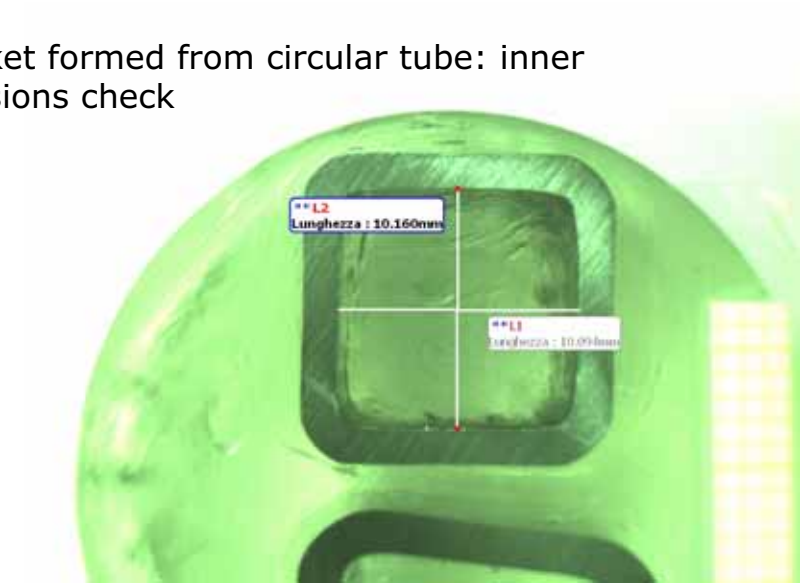

HIGH Jc STRAND

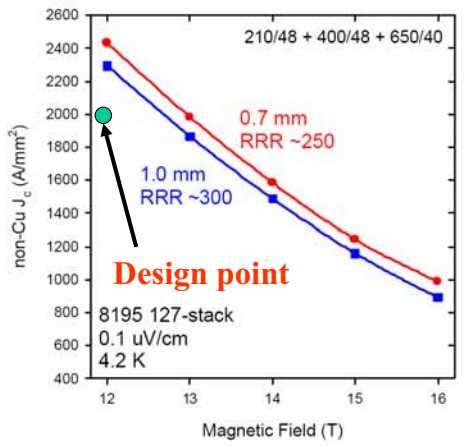

- D_{eff} about 60 µm
- Short HT
- RRR > 200
- Max conductor unit length ~ 150 m

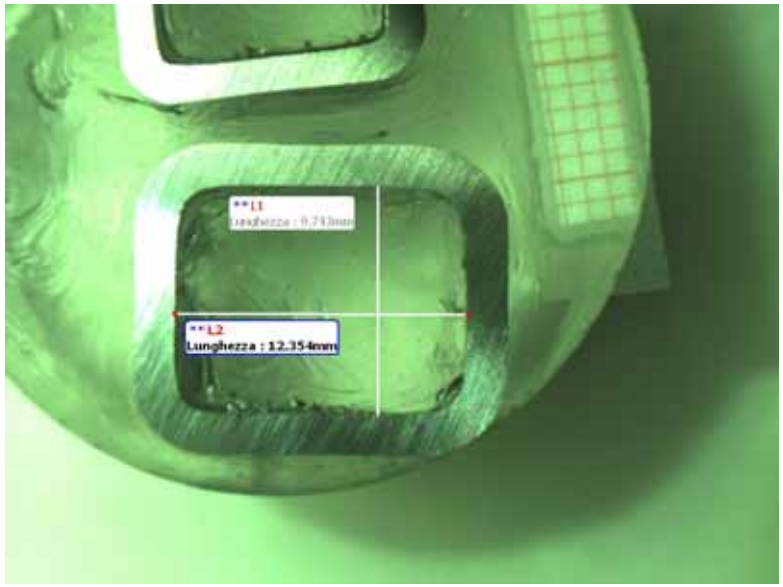

HF Conductor: Inner Dimensions Check

Dipole Strand -
Strain Dependence

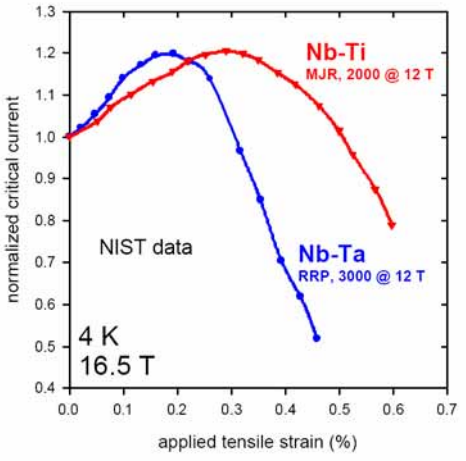

- Strain dependence better with Ti addition
- Impact on unit length to be checked
- Full characterisation going on
- Results expected in June

234

EFDA EUROPEAN FUSION DEVELOPMENT AGREEMENT

Dummy Dipole

Made with full size dipole cross section

Only half DC coil made with scrapped superconducting strands

Completion expected by the end of the 2006

EFDA EUROPEAN FUSION DEVELOPMENT AGREEMENT

Dipole Strand and Conductor

Dipole Strand: Oxford Instruments, Superconductivity

Due dates

- Delivery One (30 kg strand): **delivered**
- Delivery Two (120 kg strand): **9 months**
- Delivery Three (280 kg strand): **15 months**

Dipole Conductor : ENEA

- Procurement of the jacket material under way (available in May 2006)
- Conductor manufacture of prototype samples under way test expected in July

EFDA EUROPEAN FUSION DEVELOPMENT AGREEMENT

Strands and Conductors Developpement

- Advanced Nb_3Sn Strand Procurement
- Single Strands Characterization
- Sub size and Full-size Conductors Tests
- Dipole Conductor with advanced strand

EFDA EUROPEAN FUSION DEVELOPMENT AGREEMENT

Iron Yoke Delivery

- Iron Yoke for Dipole is Delivered
- Iron Yoke for Dummy with reduced width is being delivered

Single Nb_3Sn Strand SS jacketed

Results:

- Four techniques to apply bending strain on reacted samples tested
- Evaluation going on but "long twist pitch" case confirmed (i.e. bending has small effect at high longitudinal compression):

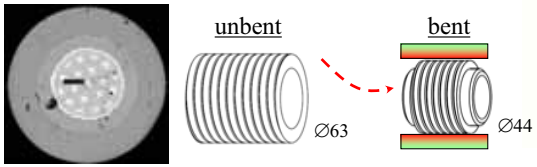

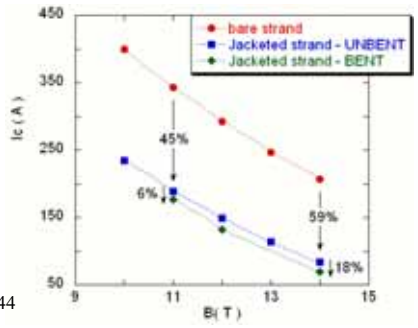

Advanced Nb_3Sn Strand Procurement – **Results**

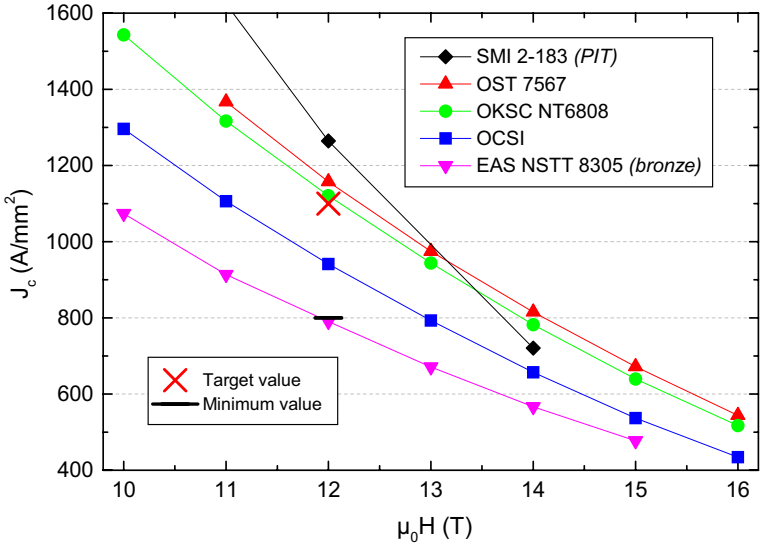

Activities on Subsize Conductors – **Objectives**

- Parametric study of strand and conductor relevant parameters (void fraction, twist pitch) on sub cable samples to gain more insight into the relation:

  strand performance ↔ conductor performance

- Assessment of the influence of the strand production process on residual strain after heat treatment of jacketed conductors by direct comparison ofthe sub size conductor performance
- Samples to be measured where tensile strain can be applied: FBI facility at FZK

Single Nb_3Sn Strands

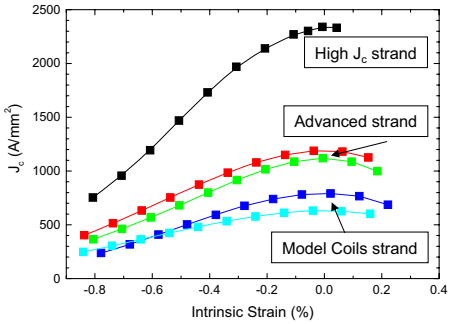

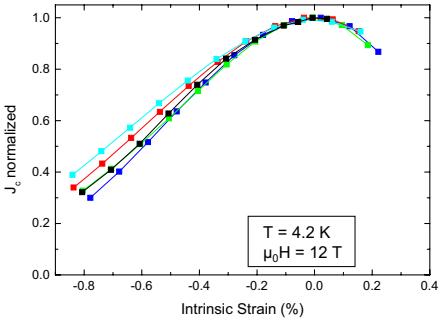

Advanced strands not more sensitive to strain than standard Nb_3Sn strands

236

Sub size Conductor Layout

- The bundle consists of 84 Nb_3Sn strands and 24 Cu wires
- The cable pattern is 3 x 3 x 3 x 4 = 108
- The rolled steel jacket has 1 mm thickness
- Outer dimension 18.4 x 7.7 mm
- Void fraction ≈ 35%
- Non-Cu area = 21.64 mm^2

Subsize Conductors

- Results of first measurements not conclusive:

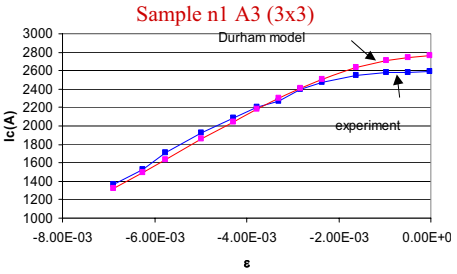

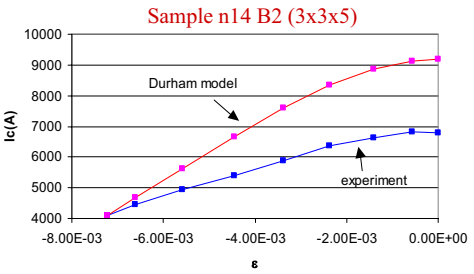

- Sample manufacture slightly revised to improve current distribution and cooling
- Manufacture (Batch 2) to be completed in April 2006 and delivery of reacted samples before summer
- Sample tests and evaluation until the end of 2006

- Critical current / Quench current: The conductor critical current close to strand current .At increasing current, the quench and critical current converge. After cycling minor degradation

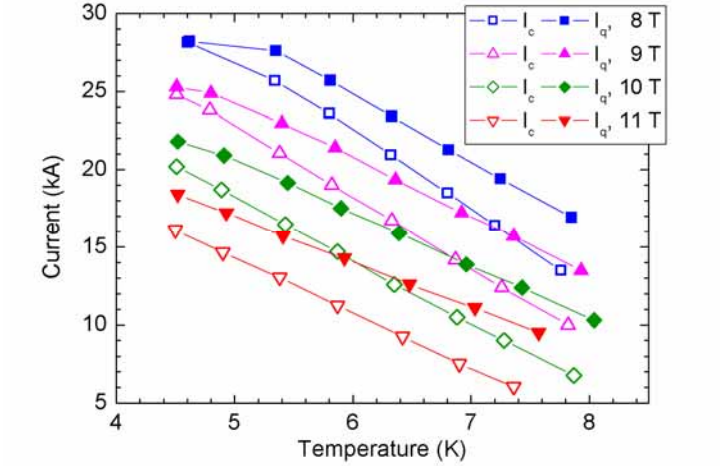

SULTAN Sample

- Standard hairpin sample, with helium inlet at the U-bend
- Termination EB welded, swaged and finally solder filled
- Instrumentation for voltage taps, temperature sensors and pressure taps

- N - Index: In the series of test before cyclic load, the n-index of the CICC is very close to the strand one

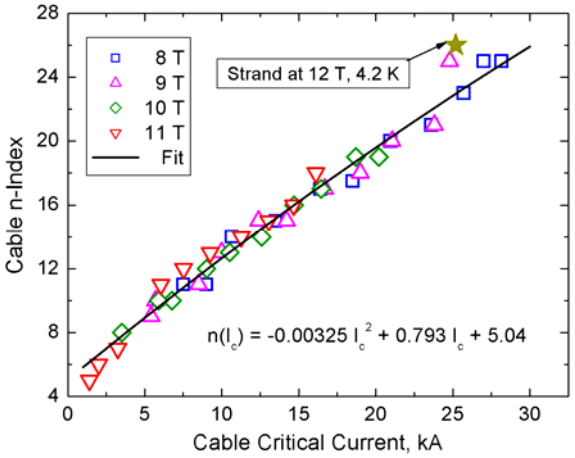

Full size Conductors

➢ **Assess the performance of advanced Nb_3Sn strand on ITER full size scale**

→ same CICC parameters as in the past (TFMC) to exclude other influences

➢ Sample I completed and tested: higher strand I_c transferred to conductor but with the (expected) BI effect

➢ Sample II manufacture almost completed: delivery expected by March

Magnet Science & Technology Division

- Highest (and highest quality) magnetic fields for NHMFL users
- 3-pronged approach
  - Pulsed
  - Powered
  - Persistent
    - LTS
    - LTS-HTS

Technologies for very high field solenoids at the NHMFL

J.R. Miller
Magnet Science & Technology Division, NHMFL
Workshop on Accelerator Magnet Design and Optimization
CERN, 3-6 April 2006

NHMFL Pulsed User Magnets: Directions

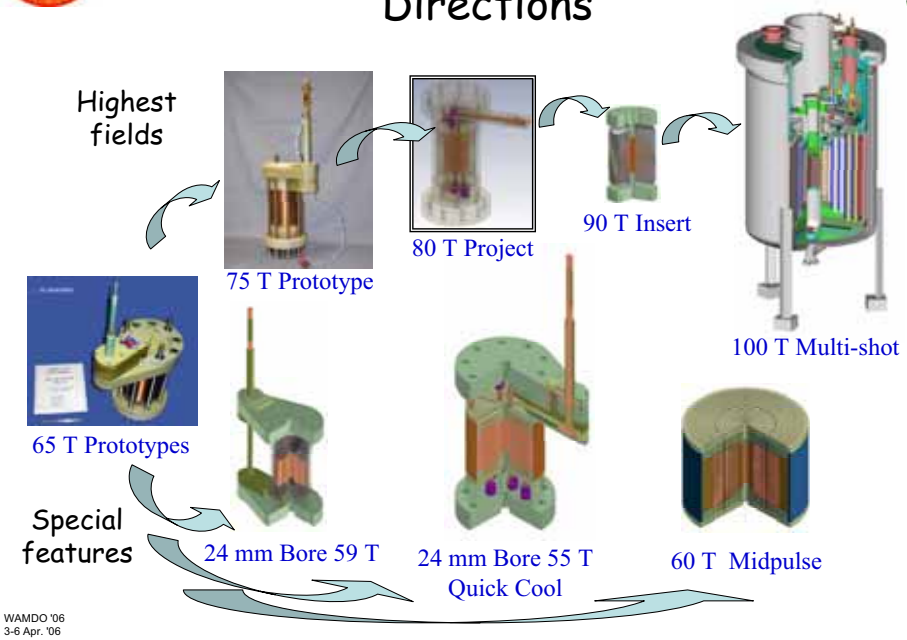

The National High Magnetic Field Laboratory

Providing state-of-the-art **pulsed**, **powered**, and **persistent** magnets at 3 locations for the worldwide user community engaged in basic research

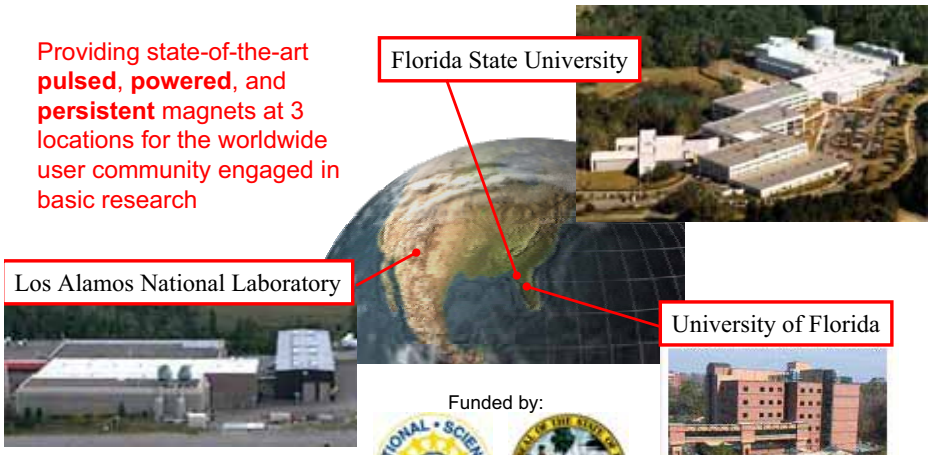

Funded by:

New opportunities introduced by HTS demo

25T combined field from the
NHMFL 20T LBR magnet
and the Oxford/NHMFL 5T HTS insert

NHMFL Persistent User Magnets: UWB 900 MHz NMR

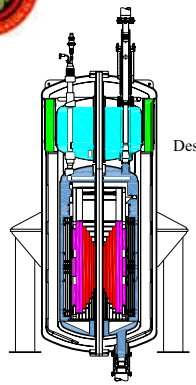

April 1999
Design Completed

July 2004-present
Magnet at 900MHz
- 40 MJ
- 21.1 T
- 105mm warm bore
- 10Hz/hr drift rate
- ~1ppb inhomogeneity

September 2002
Magnet delivered
& tested

HF grade
(type 1)

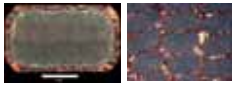

LF grade
(type 2)

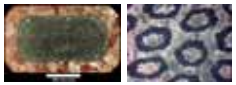

Bronze-route Nb_3Sn cond.

COHMAG: 30T, 1.3GHz NMR?

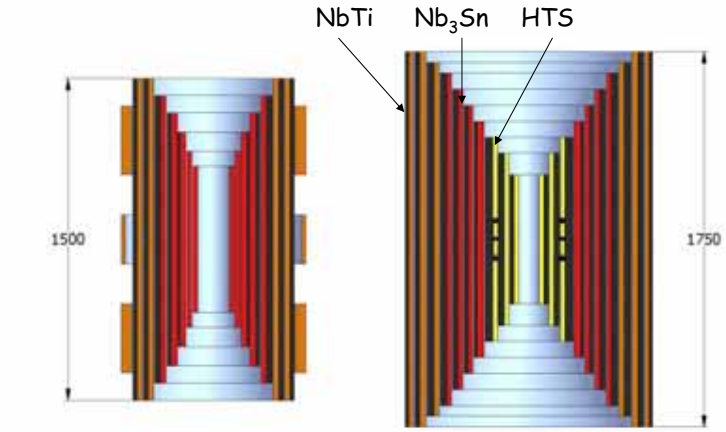

900 MHz, 1.8 K

30 T, 1.8 K

Very high field (21T) FT-ICR

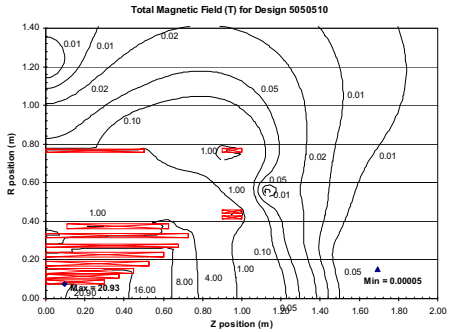

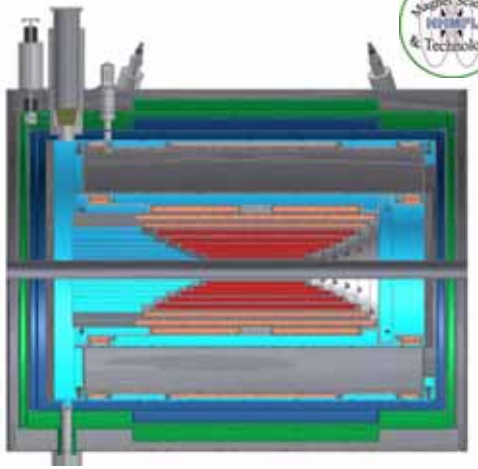

- Horizontal axis
- Active shielding (close access on one end)
- User-friendly cryogenics (indefinite hold time)
- Enhanced compactness, reliability, & safety
- Collaboration with commercial sector

240

Series-Connected Hybrid:

a new generation magnet system that dramatically expands the present frontier for science at high field

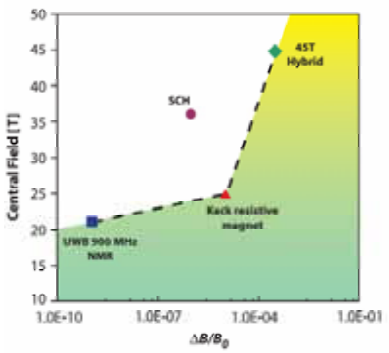

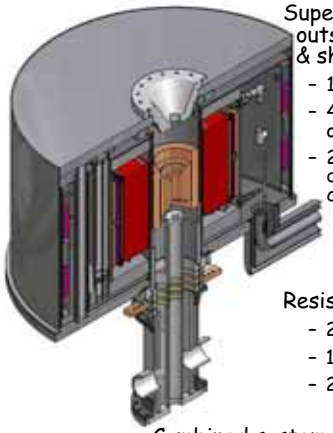

Superconducting outsert (main, shield, & shim coils)
- 14T contribution
- 4.5K forced-flow operation
- 2kV emergency discharge from full current

Resistive insert
- 22T contribution
- 12 MW
- 20 kA, 600 V

- Unique combination of performance parameters:
  - High field
  - High field quality
  - Larger bore
- Improved access (both from above and below)
- Greater availability

Combined system
- 36T central field
- ~1 ppm over 10mm DSV
- 52 MJ @ 20 kA
- Shielded to earth's field at 15 m

HTS conductor options

Bi 2223 tapes

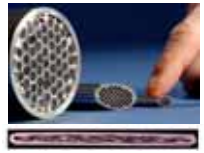

Courtesy AMSC*

Bi 2212 wires (round or aspected)

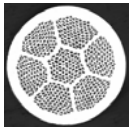

Courtesy OI-ST*

2nd generation YBCO tapes

Courtesy AMSC*

MgB_2 wires

Courtesy Hypertech Res.*

*use of images does not imply endorsement

Power/protection circuit and operations capability

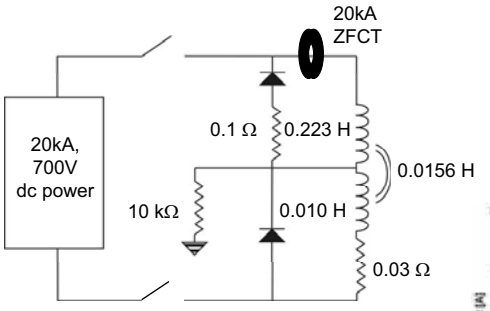

2kV emergency discharge

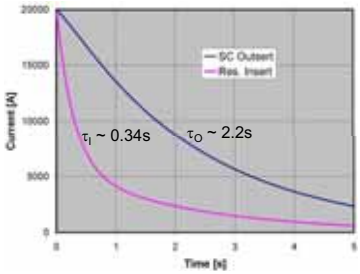

Max. speed up & down, 10s pause

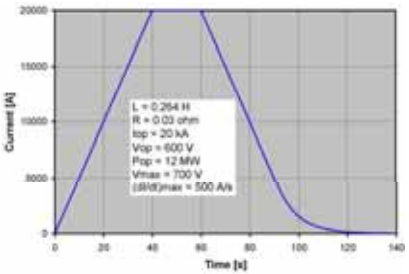

The magnet system can be "dumped" or ramped up and down at 500 A/s without exceeding current-sharing temperature

NHMFL Powered User Magnets: 45T Hybrid

Florida Poly-Bitter Technology

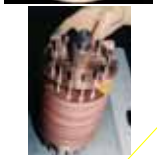

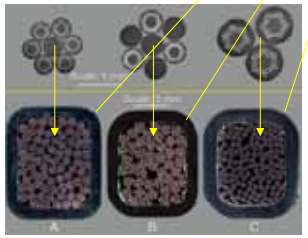

Nb_3Sn Nb_3Sn NbTi

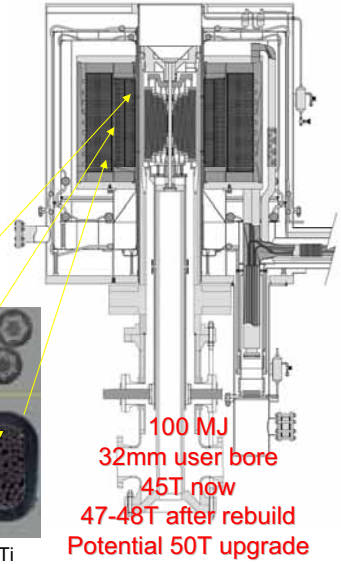

100 MJ
32mm user bore
45T now
47-48T after rebuild
Potential 50T upgrade

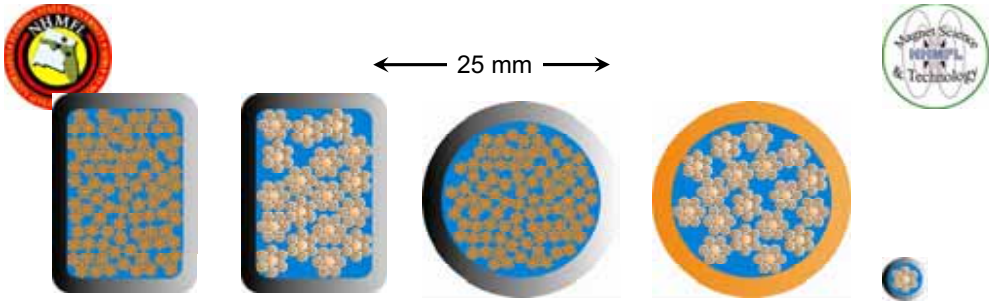

CICC technology for the outsert

Field quality enhanced by shimming

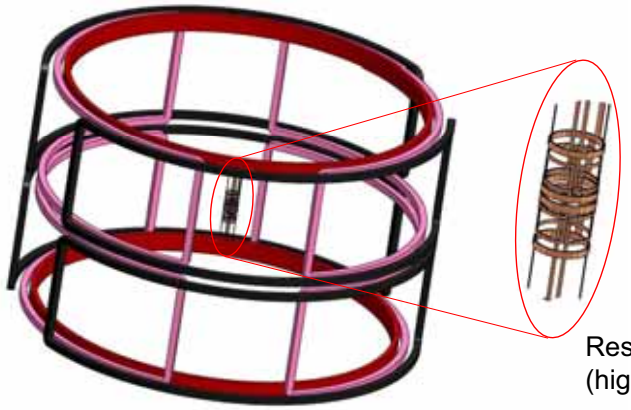

Superconducting shims (X, Y, & Z)

Based on attainable superconductor specifications

Parameter	specification
Wire diameter (mm)	0.610 ± 0.003
I_C (A) at 12T, 4.2K, 10 μV/m	> 248
n at 12T, 4.2K, 10 μV/m	> 25
Copper area (mm^2)	> 0.177*
R_{273}/R_{20} after heat treatment	> 100
Twist pitch (mm)	10.0 ± 1.5 right-hand twist
Hysteresis loss over 7-0-7-T cycle (kJ/m^3 of composite wire)	< 1200

* This corresponds to a copper fraction of approximately 0.588 in the composite strand

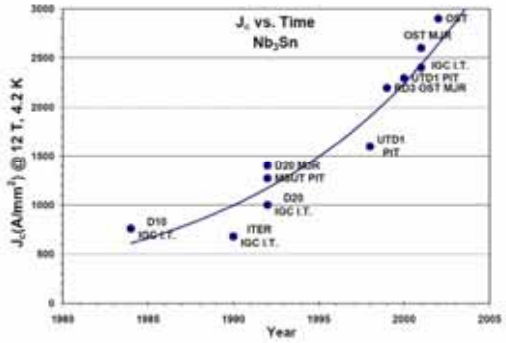

System requires ~ 1 t of wire

Specified I_C corresponds to $J_{C,non\text{-}Cu}$ ~ 2000 A/mm² at 12T, 4.2K (well within range established by US-HEP community)

Florida-Bitter technology for the insert

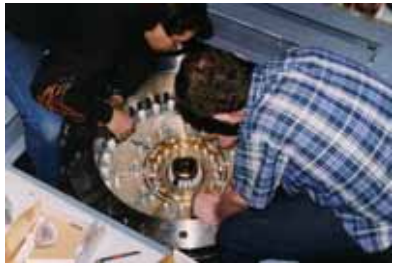

Improved cooling and reduced stress for higher power density, higher current density, and highest fields

Composition of coils in the 45T Outsert

(based on 1000 MPa yield in conduit
and 1000A/mm² at 12T, 4.2K in Nb_3Sn)

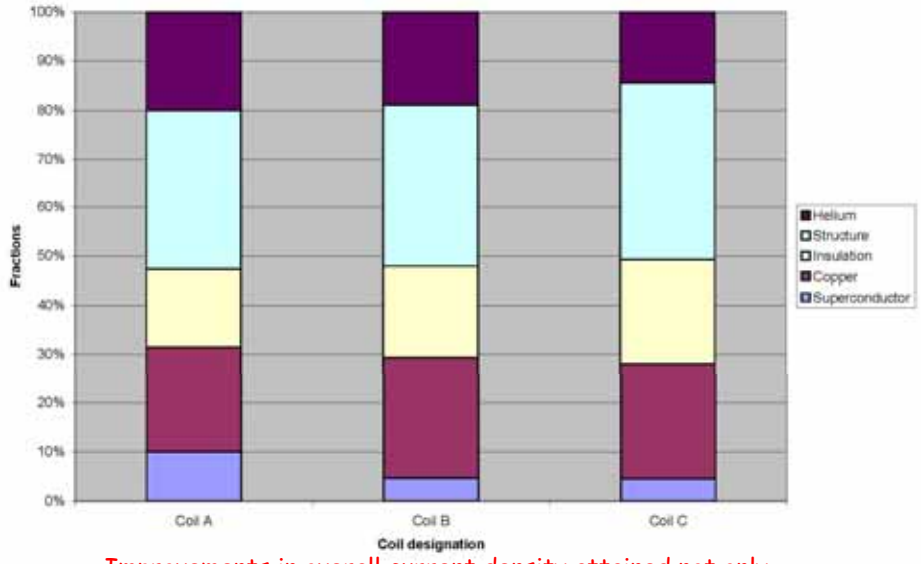

Improvements in overall current density attained not only by improvements in superconductor current density

Tests of commercial evaluation samples confirm availability of specified wire performance

OI-ST

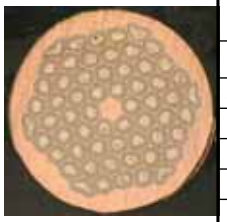

RRP, 60 subelements

Parameter	OI-ST	NHMFL specification	SMI-EAS
Wire dia. (mm)	0.6	0.610±0.003	0.6
I_C (A)	327	>248	276
n	30	>25	53
Cu area (mm²)	0.133	>0.177	0.150
R_{273}/R_0	?	>100	?
Twist pitch (mm)	?	10.0±1.5	25
Hyst. loss (kJ/m³)	≈2000	<1200	≈400

SMI-EAS

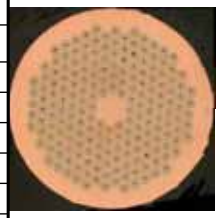

PIT, 192 subelements

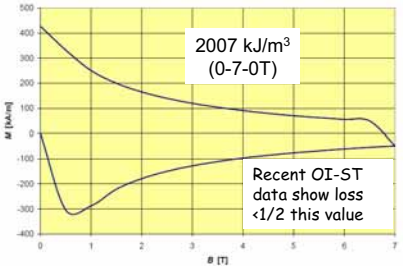

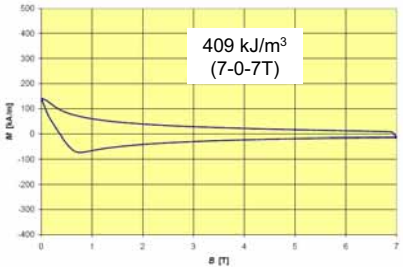

New conduit alloy exceeds our initial design requirements

Haynes 242, age-hardening Ni-Mo-Cr alloy

Strength & toughness

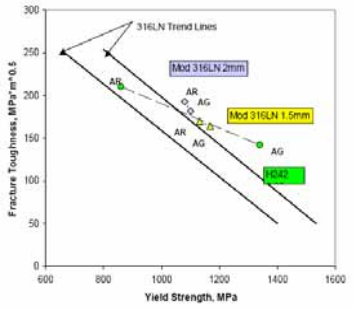

Modulus & thermal contraction

Alloy	295K Modulus GPa	1000 K to 300 K Ref T 300 K %	295 K to 4 K Ref T 300 K %	1000 K to 4 K Ref T 1000K %
Nb_3Sn [7]				0.76
Haynes 25 [1]	225	1.057	0.23	1.276
316 SS [2]	195	1.309	0.33	1.622
Incoloy 908 [5]	185	0.987	0.17	1.147
Haynes 242	229 [6]	0.91 [6]	0.2	1.1

Fatigue crack growth rate

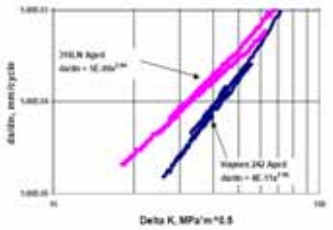

Strength of welds (preliminary)

Alloy	Condition	Base Yield Strength MPa	Weld Yield Strength MPa	Base Tensile Strength MPa	Weld Tensile Strength MPa
Haynes 25	As Rec'd	1002	1021	1667	1518
316LN (45T Hyb)	As Rec'd	1321	1334	1691	1646
316LN Cond	Aged	1201	1140	1616	1415
Haynes 242	Aged	1340	1116	1968	1648

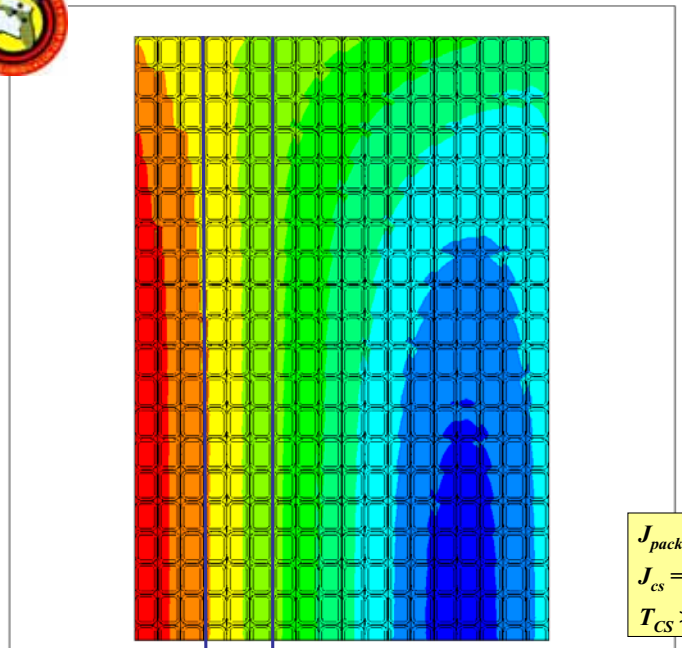

J_{pack} = 59.5 A/mm²
J_{cs} = 105 A/mm²
T_{CS} > 7.2 K

243

Revised version: enhanced compactness & maintainability

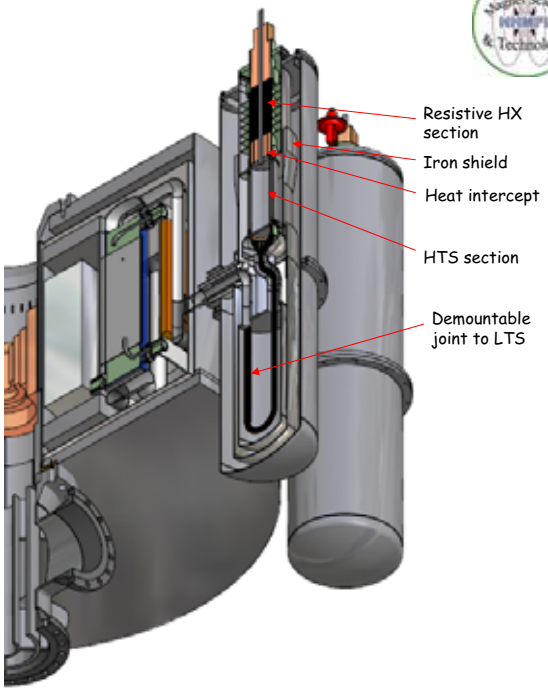

The greatest benefits are attained when all individual benefits are taken together

Material	Wall Thickness (mm)	Inner Radius (m)	Outer Radius (m)	Coil Length (m)	Turns / Layer	Layers
Stainless Steel	2.35	0.305	0.6101	0.942	42	18
Haynes 242	1.8	0.305	0.5894	0.8298	39	18

Conduit alloy	Mod. 316LN	Haynes 242	
Wall cross-section [mm^2]	140.4	104.4	-26%
Length of conductor [m]	2173	1973	-9%
Volume of jacket [m^3]	0.3052	0.2060	-32%
Mass of conduit [tonne]	2.44	1.84	-24%

Fabrication 20 kA current leads

- Resistive element formed by "jelly roll" of pierced Cu sheet around s.s. core tube
- No Cu removed by piercing: simultaneously reducing effective conduction cross-section and increasing heat-transfer surface
- Heat load to LN_2
  - Approx. 490 W/lead at full current
  - Approx. 260 W/lead during standby

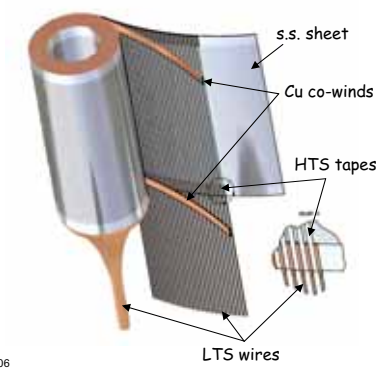

- HTS element formed by "jelly roll" of perforated s.s. sheet (constituting a protective shunt) with HTS tapes (Bi-2223 in Au-Ag matrix) bonded to it
- Cu co-wind at top and bottom for good current transfer
- Cu fillers between tapes at top & LTS wires inserted at bottom
- Heat load to LHe
  - 6.5 W/lead continuously

20 kA HTS current leads: an enabling technology

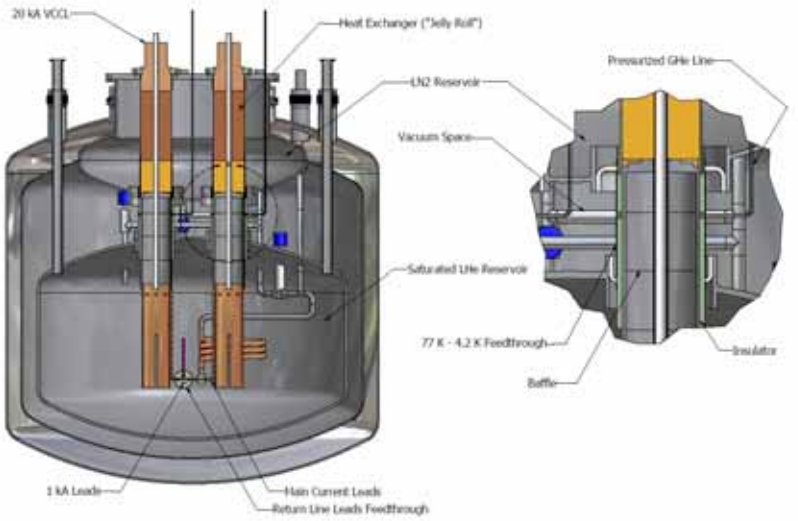

Summary

- Solenoidal magnet systems at the NHMFL operate at the frontiers of performance in all categories: pulsed, powered, and persistent.
- Ongoing development activities promise to push these frontiers even farther.
- These developments benefit substantially from collaboration with the HEP community.

Cryosystem configuration

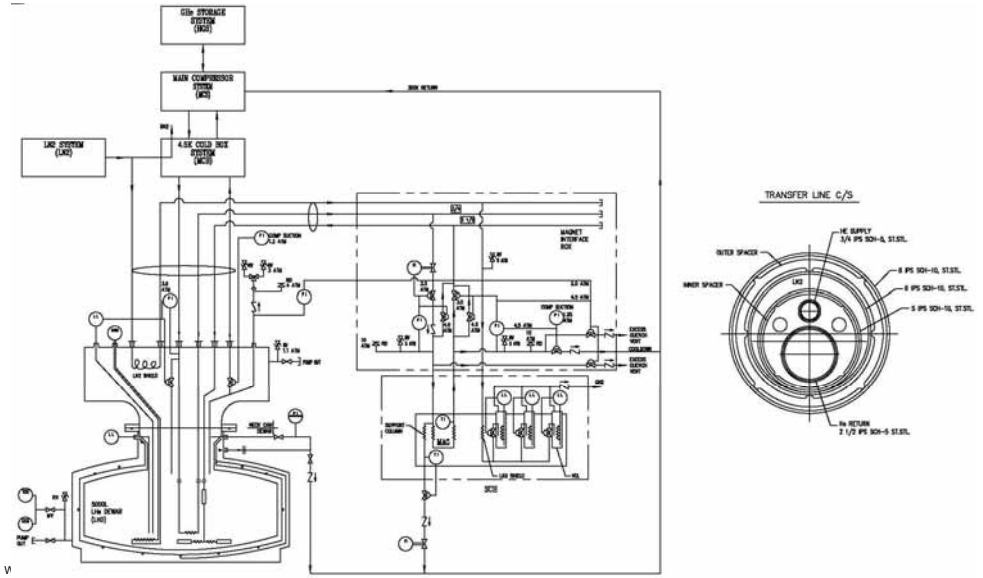

Heat loads to He, various scenarios

Ready, 0-current	
0-current xtat heat load [W]	23
Supply/return-line heat load [W]	20
Cryostat interface box [W]	10
Buffer/sub-cooler dewar [W]	30
Valves [W]	15
Total [W]	**98**

Steady-state, full-current	
Full-current xtat heat load [W]	28
Supply/return-line heat load [W]	20
Cryostat interface box [W]	10
Buffer/sub-cooler dewar [W]	30
Valves [W]	15
Total [W]	**103**

Ramping, various cycle times

Cycle time [min]	5	10	15	20	25	30
Mean AC heating [W]	241	121	80	60	48	40
Full-current xtat heat load [W]	28	28	28	28	28	28
Supply/return-line heat load [W]	20	20	20	20	20	20
Cryostat interface box [W]	10	10	10	10	10	10
Buffer/sub-cooler dewar [W]	30	30	30	30	30	30
Valves [W]	15	15	15	15	15	15
Total [W]	**344**	**224**	**183**	**163**	**151**	**143**

Superconductors

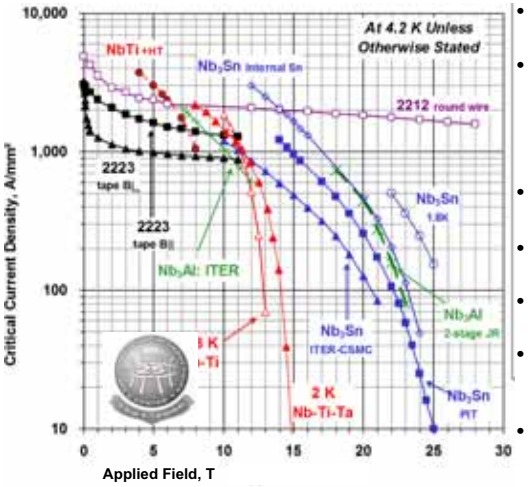

- Present generation accelerator magets Uses NbTi (Tc~9.5Kand Bc2(0)~14T)
- Practical superconductors for the second generation accelerator magnets:
  - Nb3Sn (Tc~18K, Bc2(0)~27T)
  - BSCCO-2212 (Tc~85K), BSCCO-2223 (Tc~110K)
- R&D superconductors:
  - Nb3Al, MgB2, YBCO
- Superconductor R&D is a key part of accelerator magnet R&D
- All these superconductors are brittle strain/stress sensitive
- These require new design and technological approaches, and new structural materials
- Present focus of core magnet R&D programs is on Nb3Sn

US Core Accelerator Magnet Programs

A.V. Zlobin, Fermilab

BNL magnet program

- BNL has been involved with SC magnet R&D since 1960s.
  - First experience with Nb3Sn magnets since middle 1960s.
- BNL has excellent infrastructure to perform magnet R&D which includes magnet fabrication and test facilities for both short and long magnets, capability for small production runs, and facilities for conductor testing
- Magnet Division: staff ~55, including 8 on the scientific staff
  - FY06: 12.5 heads (LARP, accelerator, ILC)
  - FY06 headcount is down, following RHIC & LHC construction

BROOKHAVEN NATIONAL LABORATORY

US core programs

- SC accelerator magnets are key elements of modern accelerators which allows advancing machine energy and luminosity
- Accelerator magnet R&D programs in U.S. are being performed by four groups at
  - *Brookhaven National Laboratory (BNL)*
  - *Fermi National Accelerator Laboratory (Fermilab)*
  - *Lawrence Berkeley National Laboratory (LBNL)*
  - *Texas A&M University (TAMU)*

BROOKHAVEN NATIONAL LABORATORY

BERKELEY LAB

- All these programs are focused on the development of next generation accelerator magnets with magnetic fields above 10 T and large operation margins and their technologies
- The magnet groups perform also magnet R&D in support of Labs missions and contribute to national and international projects which use SC accelerator magnets

R&W Nb3Sn dipole

- R&D focus on the R&W technology
- Proposed innovative block-type common coil design for hadron colliders compatible with R&W technology
- Recently fabricated and tested a common coil dipole model
  - 30-strand cable, OST MJR Nb3Sn 0.8-mm strand.
  - Four racetrack 620 mm long coils.
  - The usable coil aperture 32 mm.
  - Stainless steel collars applied a modest preload in the coil straight section and perpendicular to the cable surface.
  - The iron yoke and stainless steel shell limited coil strain in transverse direction.
- The model reached the expected conductor limit of 10.8 kA (peak/central field of 10.8/10.3 T).
- After a thermal cycle, the lowest quench was at 8.8 T.
- No dependence of quench current on ramp rate up to 200 A/s.

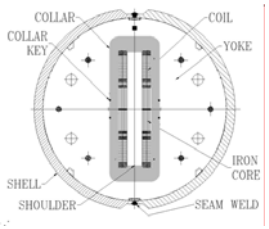

Present R&D directions

- R&D with NbTi
  - IR dipoles for LHC (recently completed)
  - Magnets for ILC IR
  - High ramp rate magnets for FAIR at GSI
- R&D with Nb3Sn
  - Common coil magnet design and R&W technology
  - LARP support: Long racetrack coils
- R&D with BSSCO
  - Quad in a high radiation environment (RIA fragmentation)
  - Energy-efficient magnets for new generation light source
- Looking ahead: advanced high-temperature superconductors
  - YBCO, MgB2

R&D with Nb_3Sn

- Design studies in support of LARP magnet work:
  - Open midplane dipole (D1)
- Advantages:
  - Low heat deposition and radiation dose in the coil
- Challenges:
  - obtaining good field quality,
  - minimizing peak fields on coils,
  - large vertical forces with no structure between the coils,
  - designing a support structure.

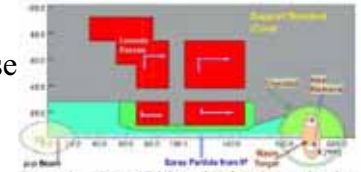

Figure 1: "Open Midplane Dipole" design that has essentially no conductor or structure at the midplane.

NbTi Magnet R&D

IR magnets with modest field requirements - e+e-

- CAD/CAM direct wind ⇔ IR magnets with multiple coils
- BEPC II IR, recently completed
- ILC large-crossing angle IR:
  - Optics for both entering and exiting beams
  - Recent: quadrupole with little external field ⇒ crossing angle reduced from 20 mrad to 14 mrad

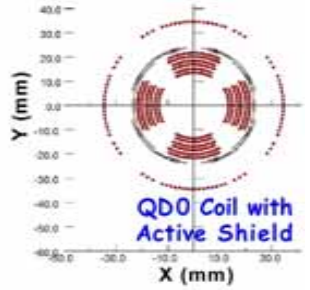

Fast ramping magnets for FAIR at GSI

- Modify standard Rutherford cable, insulation, magnet construction to tolerate high ramp rates (RHIC 0.06 T/s ⇒ GSI 4 T/s)
- Work on 1 m model dipole for GSI recently completed
- Application: upgrade high-energy injector (e.g., SPS)

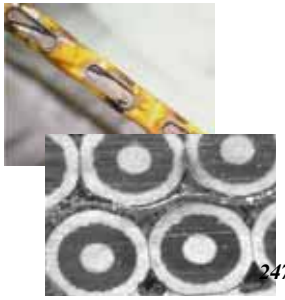

R&D directions

- **Tevatron Support**
- **Participation in the LHC Accelerator Project (LHC)**
- **Participation in LHC Accelerator Research Program (LARP)**
- **Development of High Field Magnets for future accelerators (HFM)** – the primary focus on Nb3Sn materials and technology development for 10-15 T accelerator magnets, and Nb3Sn technology scale up
- **Other Activities** –conceptual designs of quads for ILC Beam Delivery System and SC magnets for Main Linac, SC solenoids for ILC Positron Source and High Intensity Neutrino Beam Project (Proton Driver), SC magnet system for Muon Cooling Channel, etc.

R&D with BSCCO

- BSCCO: high temperature superconductor (HTS), brittle, tape
  - High Tc ⇒ tolerates larger temperature variation than LTS
  - brittle tape ⇒ planar coils (usually racetrack), DC magnet
- Application: RIA fragmentation quad (1st quad after target)
  - Superferric design - warm iron
  - only 2 coils - run with cryocooler
  - R&D goal: mirror quad (1 coil, ~ design gradient and forces)
  - R&D so far: successful test of first 25% of coils with iron

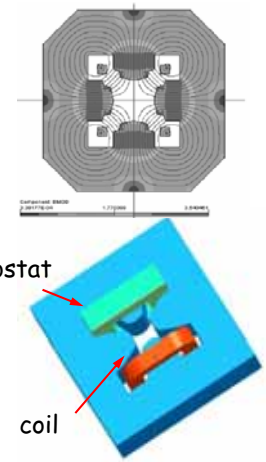

- Further in the future: "2nd generation HTS," YBCO - soon available in long lengths -- higher current, wider than BSCCO

NbTi magnets

- Study of the sextupole time dependence in Tevatron arc dipoles and discovery and repair of displaced cold masses due to support sags
  - *improvement of Tevatron performance in Run II*
- Development and fabrication of large-aperture NbTi quadrupoles for the LHC interaction regions
  - *18 IR Quad cold masses (MQXB) and cryostats 18 FNAL quads (MQXB) and 18 KEK quads (MQXA)*
- Development and successful test of a combined function superferric magnet with 100 kA SC transmission line and 100 kA Power Supply
  - *design is considered for some LHC upgrade scenarios*
- Design of IRQ for BTeV – *cancelled in 2005*

FNAL magnet program

Fermilab has been involved with SC magnet R&D for many years:
- Started with NbTi SC accelerator magnets in 1970s.
- Nb3Sn magnet R&D since 1998.

Fermilab has excellent facilities for magnet R&D

Magnet fabrication facilities:
- IB3 (16000 sq ft): short SC magnet R&D (L<2m)
- ICB (24000 sq ft): long SC magnets production (L<15-m)

Magnet test facilities:
- Vertical Magnet Test Facility (VMTF): L<4m, OD<0.6m
- Horizontal Magnet Test Facility (HMTF): L<15-m
  - T=1.9-4.5 K (1.5kW@4.5K 60W@1.8K), Imax=30 kA

Supporting Labs:
- SC R&D Lab - Short Sample Test Facility (17 T and 16 T)
- Cable Development Lab – 42-strand cabling machine
- Material Lab - mechanical and electrical tests, microscopy

The infrastructure is continually upgraded to meet program needs

Fermilab Technical Division

Staff: HFM+LARP (~21 FTE), other projects (~2-3 FTE)

Next steps

- Technology development using racetracks and mirror configurations
  - Strand and cable testing in magnet environment
  - Insulation and impregnation materials
- Technology scale up using PIT and RRP strand
  - well understood HFDM design and fabrication technology
  - Two steps: 2m and 4m
- Increase field level using RRP strand
  - 11-12 T – dipole design (HFDA)
  - 15 T – quadrupole design

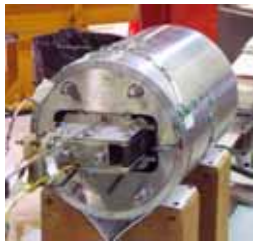

Nb3Sn magnets

- Studied both shell-type and block-type coils and W&R and R&W technologies
- Developed and tested 3 R&W racetracks and 40-mm double-aperture common coil dipole
  - *~75% of short sample limit*
- Developed and tested 5 W&R dipole models and 5 mirror configurations
  - *One mirror and two dipoles reached short sample limit and design field of 10 T*
- Studies of magnetic instabilities in modern Nb3Sn strands and cables and their effect on magnet quench performance
- Study of field quality reproducibility in Nb3Sn accelerator magnets, studies of Nb3Sn coil magnetization effect on magnet field quality and demonstration of its compensation with passive correction

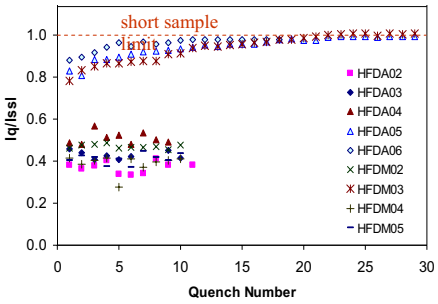

Materials R&D

- Extensive material R&D in support of magnet R&D
- Contribute to National conductor R&D programs sponsored by DOE
- Collaborate with industry:
  - **Nb_3Sn strands produced using different methods:**
    - **Internal Tin (IT, RRP) – OST, Supergenics (U.S.)**
    - **Powder in Tube (PIT) – SMI (Netherland)**
    - **Distributed Tin (DT) – Mitsubishi (Japan)**
  - **alternative superconductors:**
    - **Nb3Al – NIMS (Japan)**
    - **HTS (BSCCO) – AMSC, OST (U.S.)**
- Perform cable R&D in collaboration with BNL, LBNL, CERN:
  - **Different strand types (Cu, NbTi, Nb_3Sn, Nb3Al, Bi2212)**
  - **Different cable design: one and two stage cables**
  - **Mixed strand cable (Cu and SC)**
  - **Resistive interlayer core and copper stabilizer**
  - **Cable insulation**

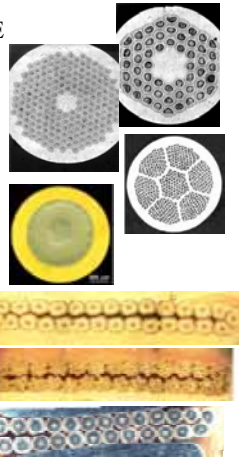

Material R&D Results

- Study of Nb3Sn strand and cable stability including deff and RRR effects
- Nb3Sn heat treatment optimization to achieve high Jc and RRR
- Cabling degradation studies for different Nb3Sn strands
  - *minimization of Ic degradation, strand improvement*
- Studies of cable sensitivity to transverse pressure
  - *stress limit for different Nb3Sn technologies and magnet designs*
- Study of ceramic insulation and binder
  - *coil fabrication technology improvement*

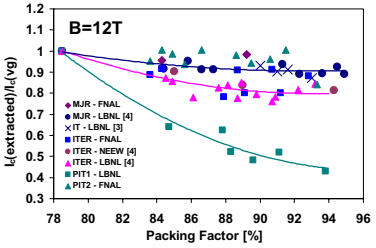

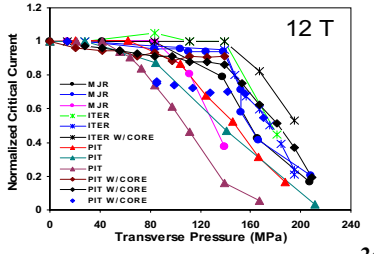

High Field Dipole Models

D20 (13.5 T) RD3b (14.5 T) HD-1 (16 T)

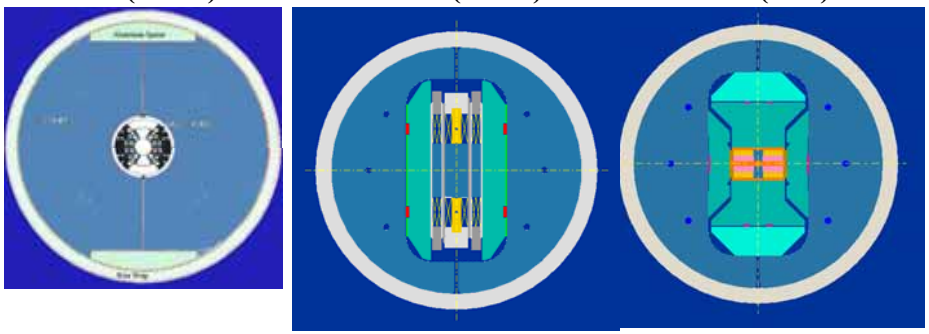

Cos θ Common Coil Block

Exploring coil and structure design options while pushing the field limits

LBNL magnet program

- LBNL has been involved with SC magnet R&D since 1970s.
  - Experience with Nb3Sn magnets since 1980s.
- LBNL has appropriate infrastructure to perform magnet R&D including model magnet fabrication and test facilities, and facilities for cable fabrication and conductor testing.
- Staff ~21 FTE (~13 FTE in the core program)

Technology R&D

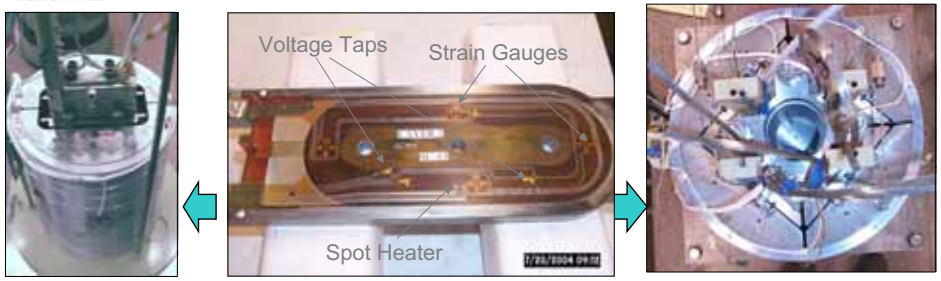

SM Dipole SC Coil SQ Quadrupole

- Sub-scale coils:
- Cost-effective, rapid turn-around tools for technology and instrumentation development
- R&D topics: conductor, cable, mechanics, materials, fabrication procedures, quench study
- Testing in both dipole (SM) and quadrupole (SQ) configurations, field range of 9-12 Tesla;
  - SM-01- Baseline
  - SM-02/03 - Mixed-strand
  - SM-04 - CTD/FNAL Ceramic Insulation
  - SM-05- Stress/temperature limits
  - SM-06 (2004) - Quench limits, new instrumentation

R&D directions

- **Materials**:
  - superconductors,
  - insulation,
  - structural
- **Cable R&D**
- **Technology**: focus on W&R
- **Coil designs**:
  - efficient, simple & cost-effective
  - Since 1997 focus on block-type coils
- **Structures** to handle large forces and stresses
  - Al shrinking cylinder and bladders
- **Design, analysis and diagnostics** tools
  - Full integration of CAD & analysis tools
  - Coupled magnetic, mechanical, and thermal analysis across different platforms
  - Modeling of the mechanical behavior of the 3D structure from assembly to excitation: coil end displacements and gaps
  - 3D quench propagation modeling, computation of the thermal stress

Materials Development

- Supporting high field conductor development through DOE/HEP
- Strand heat-treat optimization studies to achieve high RRR and improve stability thresholds
- Cable R&D using different strands (LTS, HTS)
- Cable optimization to minimize edge damage while retaining mechanical stability

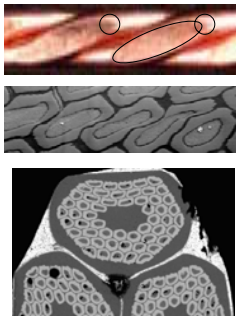

Next LBNL Dipole: HD2

High-Field Arc Dipoles

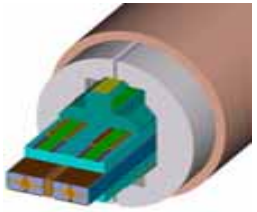

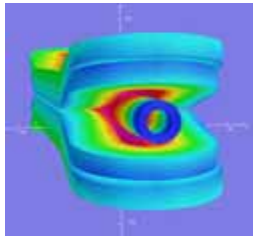

Design Features & Applications

- Target field above 15 Tesla
- Clear bore 35 mm
- Block coil configuration
- Geometric harmonics: 10^{-5}
- Suitable for HF cable testing
- Compatible with HTS inserts

High-field cable testing

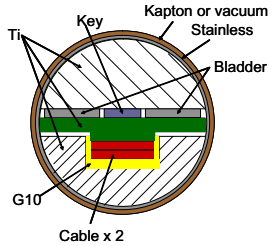

Parameter	Unit	HD1	HD2
Clear bore	mm	8	35
Coil field	Tesla	16.1	16.1
Bore field	Tesla	16.7	15.3
Max current	kA	11.4	15.2
Stored Energy	MJ/m	0.66	0.89
F_x (quadrant, 1ap)	MN/m	4.7	5.9
F_y (quadrant, 1ap)	MN/m	-1.5	-2.7
Ave. stress (h)	MPa	150	140

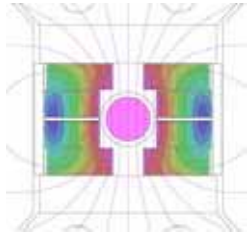

TAMU Magnet R&D

Accelerator Research Lab/TAMU

Facility for model magnet fabrication: winding, reaction, impregnation, assembly

Testing at LBNL

Staff: 8+students

- P. McIntyre, A. McInturff, A. Sattarov – physicists
- J. Byeon, P. Noyes, N. Pogue – grad students
- R. Blackburn, N. Diazcenko, T. Elliott, B. Henchel, D. Jaisle – techs

- Present R&D direction:
  - HFM design and technology
  - Magnets for Super-SPS
  - IR magnets for LHC Luminosity
  - Magnet to Triple LHC energy

Toward a 20 Tesla Dipole

- R&D to approach a 20 T dipole field:
  - Fine-tune Nb3Sn performance to its full potential
  - Develop design features for high-field coil inserts
  - Master HTS conductor and coil technologies

- Two steps are planned for FY07:
  - HTS wind-and-react coil fabrication
    - *test in background field of Nb3Sn coils*
  - High field cable testing in HD2

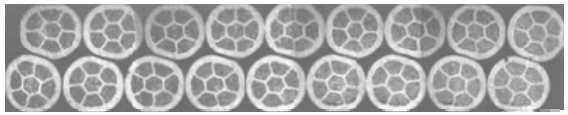

HTS cable

Design Studies for LHC upgrades

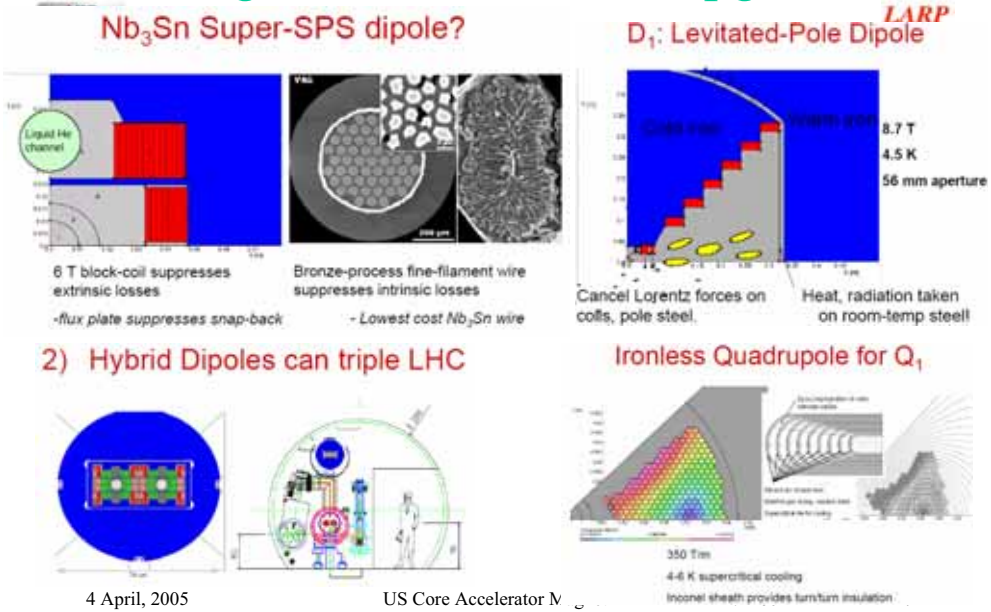

Magnet design and technology

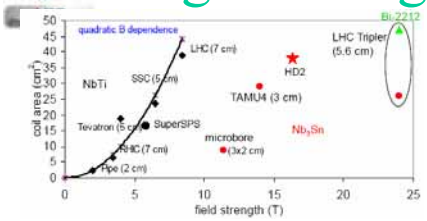

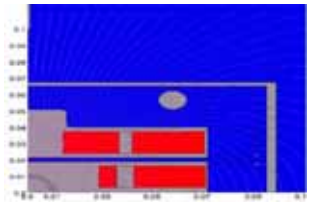

- Designs of 12-24+ T magnets
- Block coil design
- Stress management
- Superconductor: NbTi, Nb3Sn, Bi-2212
- Conductor optimization
  - conductor grading
  - SC and Cu strand mixing
- Flux plate to suppress the persistent-current effect in block-type magnets
- Coil pre-load with bladders

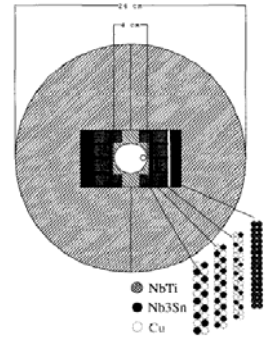

Figure 1. 12 Tesla block-coil dipole: optimized Nb_3Sn, NbTi.

Summary

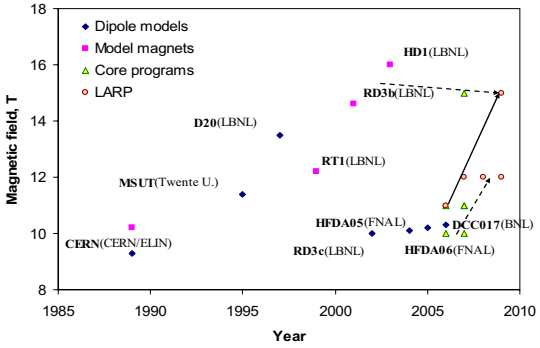

By 2009-2010 LARP and core magnet R&D programs are planning to explore field range of 10-15 T for Nb3Sn accelerator magnets and demonstrate the Nb3Sn technology scale up

- US have strong accelerator magnet R&D programs focused on the development of new generation accelerator magnets
- Excellent magnet fabrication and test facilities
- Strong magnet groups
- 10-16 T short models based on Nb3Sn superconductor
- This result is based on strong materials R&D

Testing of TAMU2

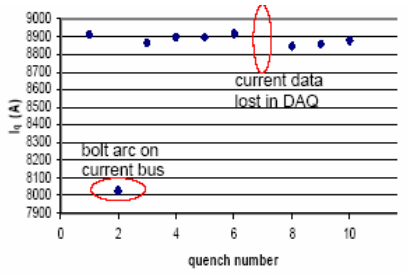

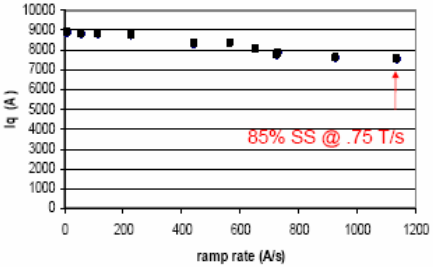

- Single-pancake model to evaluate stress management structure
- ~93% short sample first and every quench – *no training*
- low AC losses in coil up to ~2 T/s – suggests a better technology for rapid-cycling accelerators

DAPNIA

ILC Space of Parameters

E_{cm} = 500 GeV , L = 2 10^{34} cm^{-2} s^{-1} — 5.6 10^{34}

		nom	low N	lrg Y	low P	High L
N	$\times 10^{10}$	2	1	2	2	2
n_b		2820	5640	2820	1330	2820
$\varepsilon_{x,y}$	μm, nm	9.6, 40	10,30	12,80	10,35	10,30
$\beta_{x,y}$	cm, mm	2, 0.4	1.2, 0.2	1, 0.4	1, 0.2	1, 0.2
$\sigma_{x,y}$	nm	655 5.7	495, 3.5	495 8	452, 3.8	452, 3.5
D_y		18.5	10	28.6	27	22
δ_{BS}	%	2.2	1.8	2.4	5.7	7
σ_z	μm	300	150	500	200	150
P_{beam}	MW	11	11	11	5.3	11

DAPNIA

ILC Needs for High Field Magnets

I. ILC Design (in brief)

II. The Positron Source
   a) The helical undulator
   b) The positron collection

III. The Final Focus Systems
   a) The final doublet of quadrupole + sextupole
   b) The detector solenoid

DAPNIA

II. ILC Polarized Positron Source

Baseline Configuration : Helical undulator

Polarized e+ produced from conversion of polarized photons generated by the 250 GeV e- beam

+

Auxiliary (keep alive) source

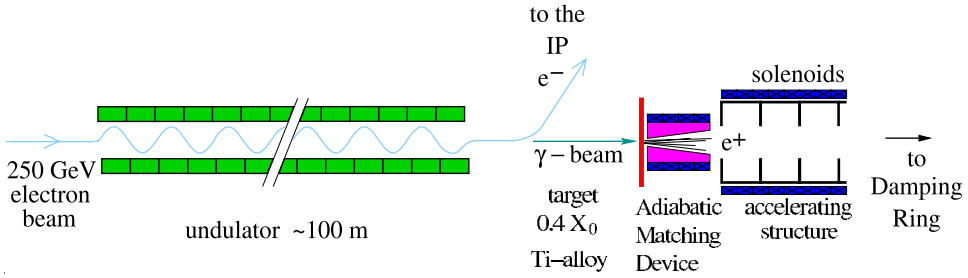

DAPNIA

I. The ILC Baseline Configuration

1st Stage : 500 GeV cm energy
2nd Stage : 1 TeV cm energy

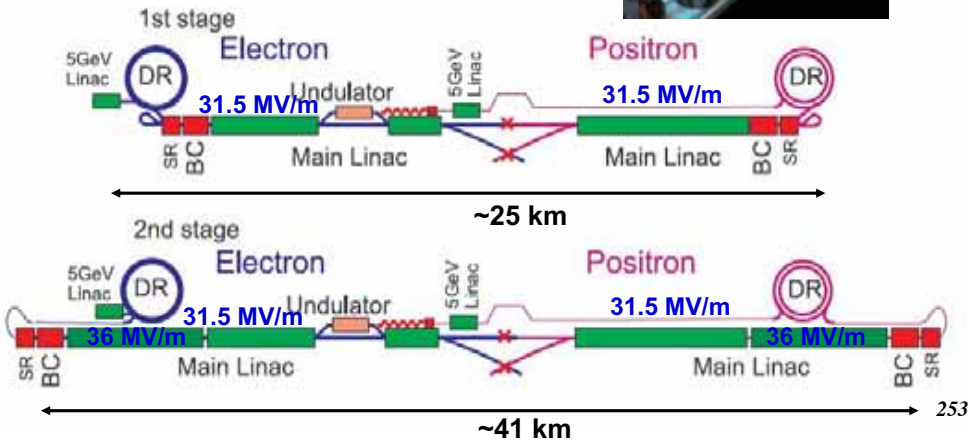

Positron Capture: Adiabatic Matching

DAPNIA

AMD concept for ILC
V.S.Kashikhin, FNAL,
V. Bharadwaj, SLAC

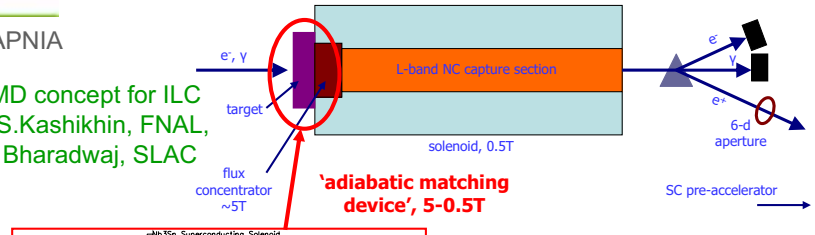

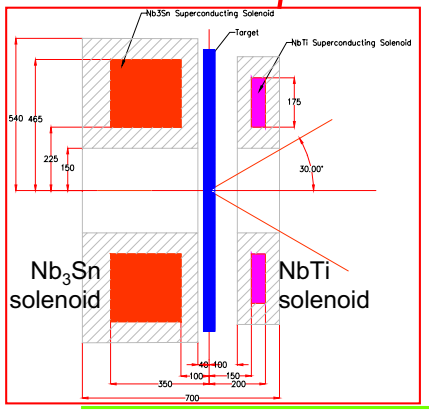

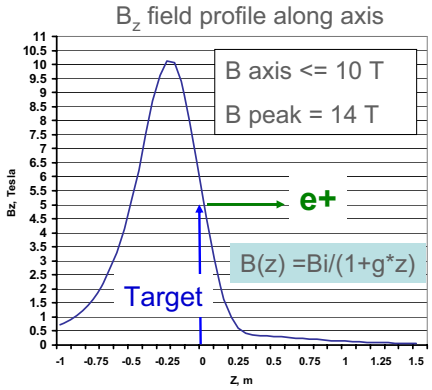

SC Helical Undulator Design

DAPNIA

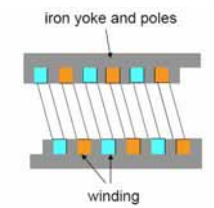

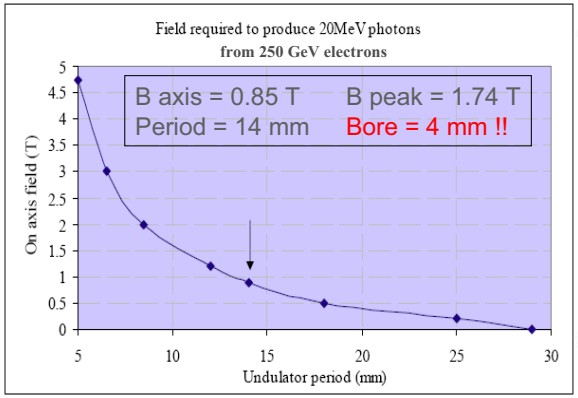

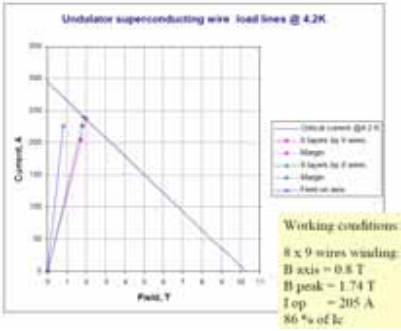

III. ILC Final Focus Systems

DAPNIA

Two Interaction Regions

- **Baseline Configuration :**
  20 mrad and 2 mrad crossing angles
- **Alternative Configuration :**
  Head-on collisions (0 mrad)

under study in view of advantages from the detector point of views (less background and easier tracking analysis)

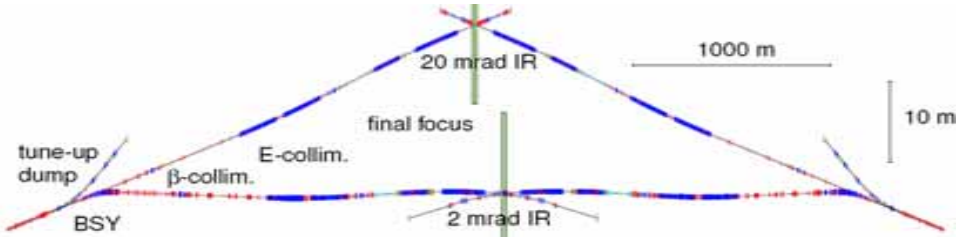

SC Helical Undulator Prototype

DAPNIA

UK HeLiCal Collaboration (CCLRC-RAL)

20 period NbTi Prototype

Undulator winding principle

Winding two helixes at a time

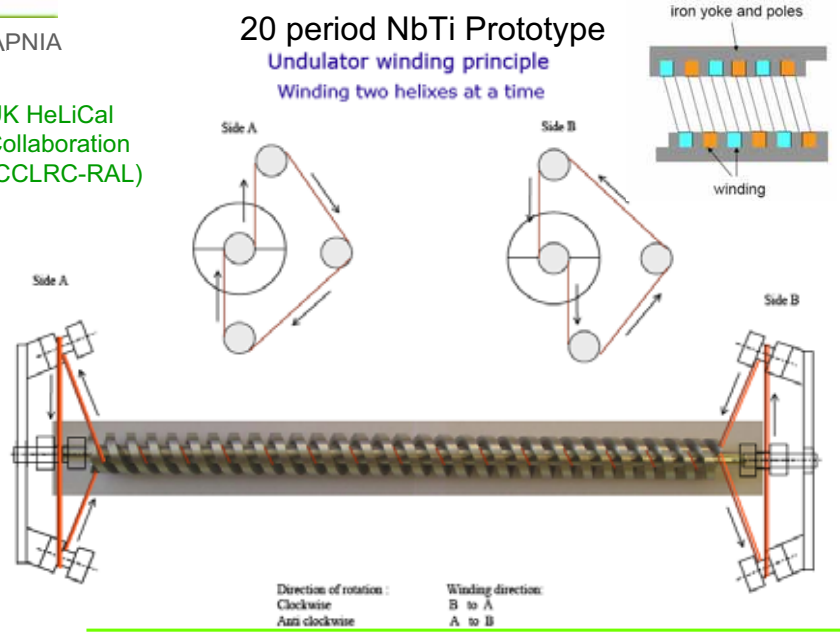

254

2 mrad Interaction Region

DAPNIA

Small crossing angle 2 mrad 'à la TESLA' :
requiring large aperture magnets (R_{bore} > 35mm)
to extract the disrupted spent beam+ beamstrahlung

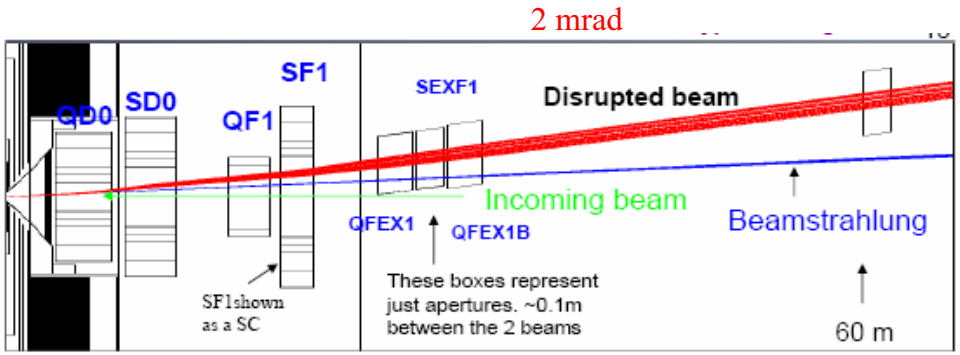

20 mrad Interaction Region

DAPNIA

Large crossing angle 20 mrad 'à la NLC':
allowing focalization + extraction optics
with compacts doublets (R_{bore} = 10 mm)

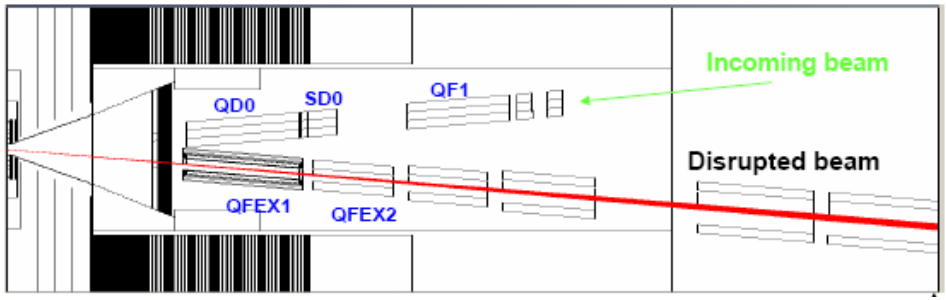

L*=3.5 m 18 m

2 mrad Interaction Region

DAPNIA

Final Doublet Specifications (QF1 is normal c[ting])

Magnet	Type	Bore [mm]	Field at Bore [T]	Length [m]
QD0	SC Quad.	70	5.6	2.5
SD0	SC Sext.	176	4.0	3.8
SF1	SC Sext.	224	2.1	3.8

QD0 ~ low-β LHC quad, but very large aperture sextupoles are challenging

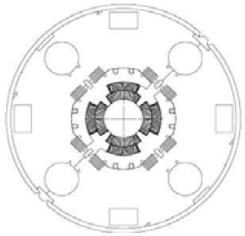

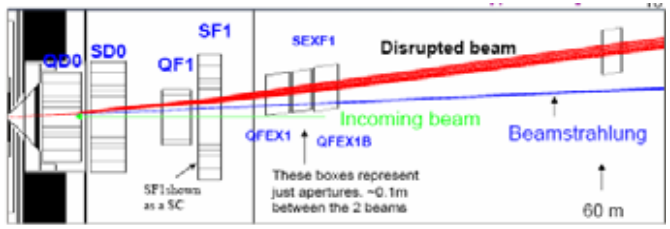

20 mrad Interaction Region

DAPNIA

Quadrupole NbTi
144 T/m 'serpentine'
B. Parker (BNL) and A. Seryi (SLAC)

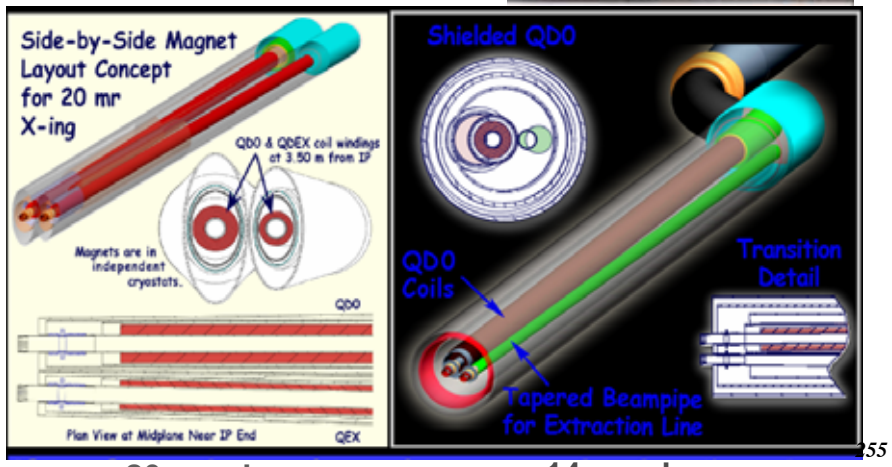

20 mrad 14 mrad

DAPNIA

0 mrad Interaction Region

SC Final Doublet Specifications

Magnet	Type	Bore [mm]	Field at Bore [T]	Length [m]
QD0	SC Quad.	56	6	1.5
SD0	SC Sext.	56	3.7	0.5
QF1	SC Quad.	56	6	2×0.5
SF1	SC Sext.	56	2.6	0.4

quads ~ Nb3Sn lattice LHC quad, sextupoles ~ NbTi lattice LHC sextupole

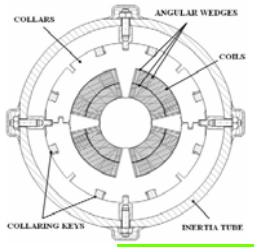

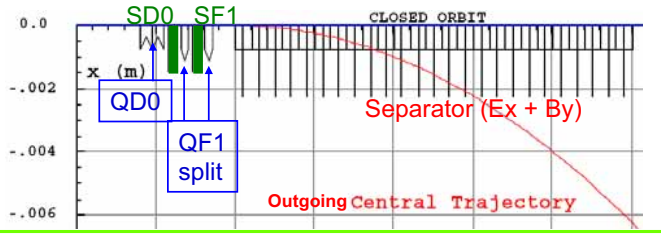

DAPNIA

0 mrad Interaction Region

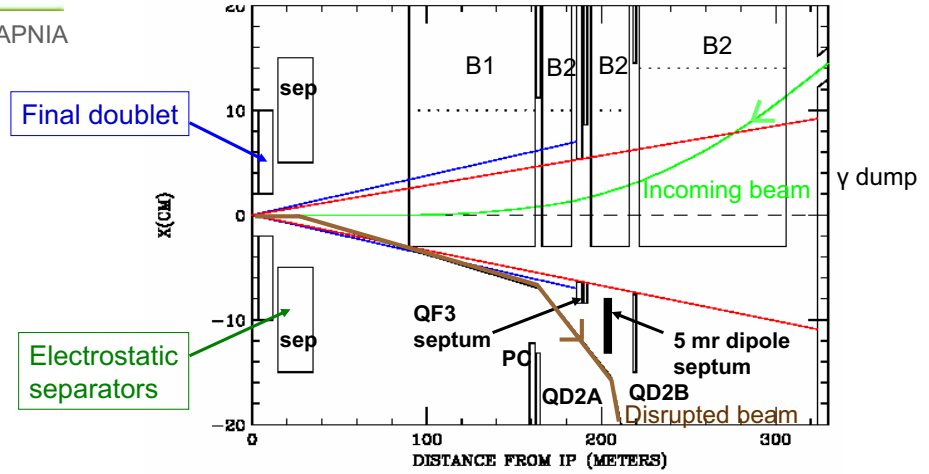

TESLA 'Head-on' scheme revisited : new extraction scheme based on LEP electrostatic separators at 25 kV/cm and QD2 off-axis quadrupole *(Lew Keller, SLAC)*

DAPNIA

0 mrad Interaction Region

The applied 4T Solenoid field imposes
1) Iron Free quadrupole QD
2) Nb3Sn technology

Lattice LHC quadrupole 250 T/m

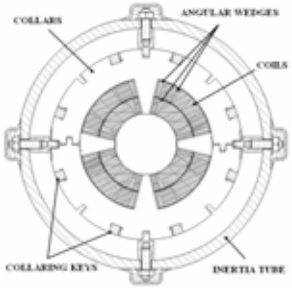

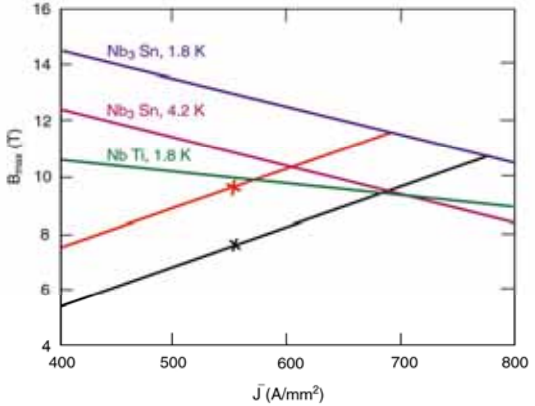

TESLA quadrupole inside the solenoid
$B_{max} = f(J_c)$

X Quadrupole alone (Ø 56 mm, G = 250 T/m)
X Quad + 4T solenoid

DAPNIA

e+e- Pair Background in the Vertex Detector

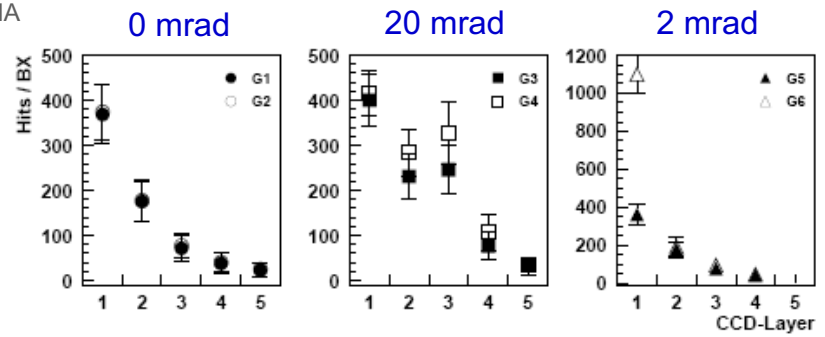

Number of hits per bunch crossing
on the vertex detector (CCD option)
for 6 different geometries

⇒ The head-on collision scheme provides better background and better low-angle detector coverage

256

DAPNIA

The Detector Solenoid

'Large Detector Concept' 4T solenoid inherited from 'CMS'

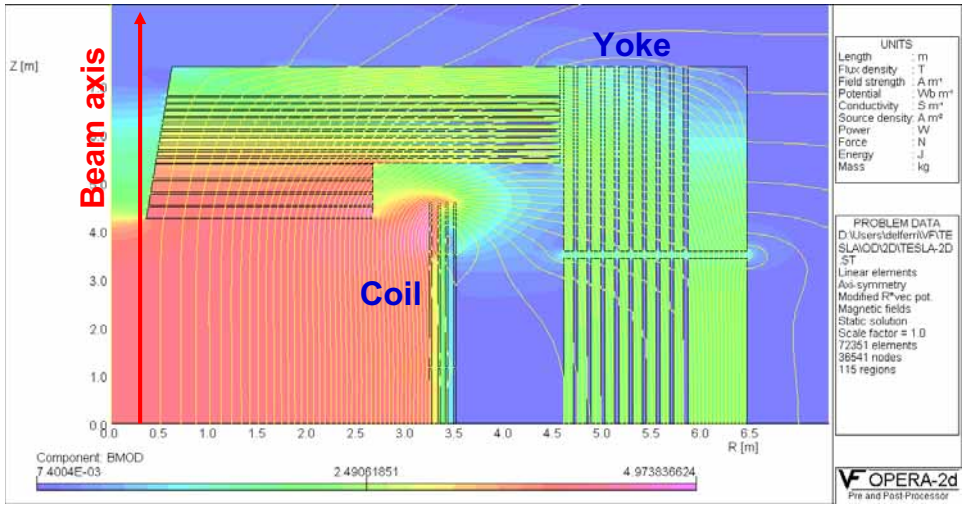

DAPNIA

Beam loss Modelisation

QD0 Quadrupole Volume in GEANT4 based BDSIM

- Ring 1: 200 segments
  3.4 < ~R < 3.5 cm
  Material: Aluminium
- Ring 2: 200 segments
  3.5 < ~R < 4 cm
  Material: NbTi
- Ring 3: 200 segments
  4 < ~R < 5 cm
  Material: NbTi
- Ring 4: 200 segments
  5 < ~R < 8 cm
  Material: NbTi
- Ring 5: 200 segments
  8 < ~R < 13 cm
  Material: NbTi
- Ring 6: 200 segments
  13 < ~R < 20 cm
  Material: NbTi

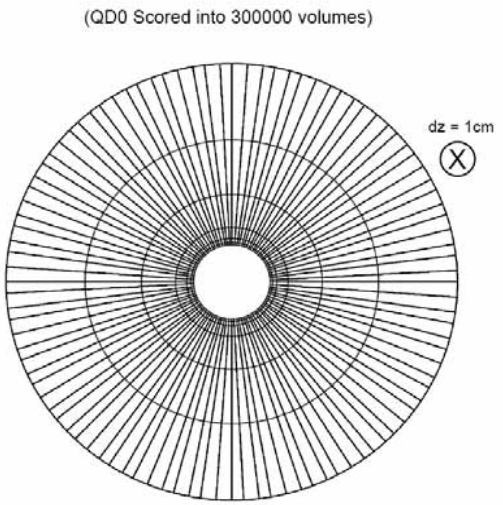

(J. Carter, RHUL)

DAPNIA

Field Calculations for 'LDC' Solenoid

B_z on axis

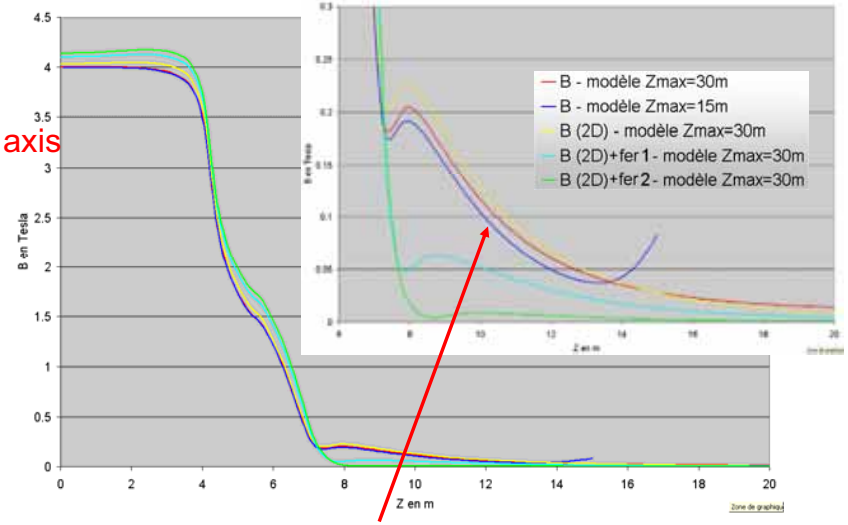

Fringe field on the axis (0.1 T @ 10 m) can be reduced by adding Iron on the caps

DAPNIA

Beam loss Modelisation

Heat deposition from spend beam dispersed in the off axis quadrupole, calculated with BDSIM

Peak power : 1.9 mW/g for nominal parameters
4 mW/g for high luminosity parameters (2 mrad IR)

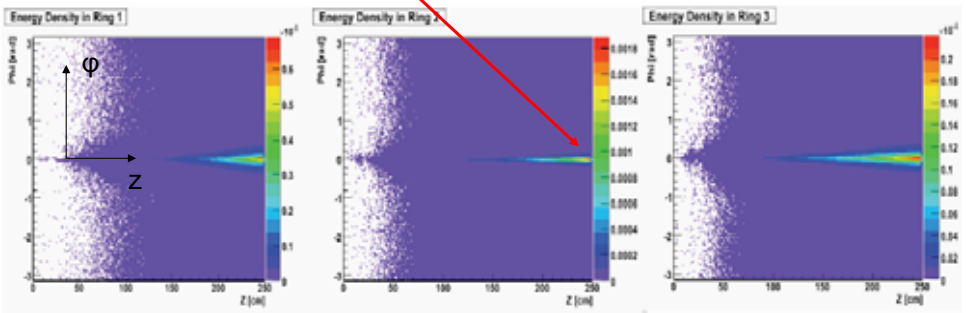

34 mm < R < 35 mm 35 mm < R < 40 mm 40 mm < R < 50 mm

(J. Carter, RHUL)

DAPNIA

Conclusions

- The ILC needs High Field Magnets in two sectors:
  1) the Positron Source (undulator + capture)
  2) the Final Focus Doublets (quadrupoles + sextupoles)

- The need for Nb3Sn magnets is identified for
  1) the 10 T positron capture AMD solenoid
  2) the final quadrupole of the head-on scheme, because of the applied 4T detector field

- The *local* chromatic correction requires SC *sextupoles* doublets in the final focus optics

- Based on a1998 TESLA study, the LHC quads field quality should be OK for the ILC (e.g. $a3 < 5\times10^{-5}$ @ R0=10 mm)

Design options for high field Nb_3Sn accelerator magnets

V. Kashikhin for HFM Group

April 5, 2006

Outline

- Some types of high field magnets:
  - shell type magnets - CERN, LBNL, Twente, KEK, FNAL
  - double dipole magnet – SSC, FNAL
  - active shielded - KEK, FNAL (AHF), BNL (ILC)
  - toroidal (motor) type - CERN (NED), FNAL (BTeV)
- Options in magnet technology
- Magnets for linear accelerators

Proposed concepts based on accelerator magnet design

Shell Type Superconducting Magnet Design 3 Layers

Design studies and practical experience with two-layer shell-type dipole magnets show that 12-13 T field is the upper limit for a 2-layer shell-type Nb_3Sn magnet with practical strand size and cable aspect ration. Thus, for achieving higher fields it is necessary to increase the coil width and respectively the number of layers.

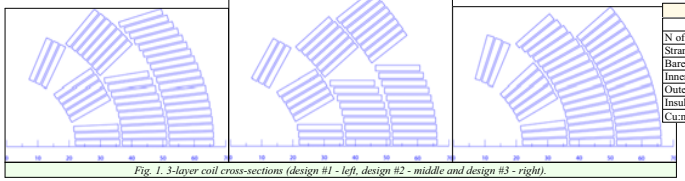

Fig. 1. 3-layer coil cross-sections (design #1 - left, design #2 - middle and design #3 - right).

TABLE I. CABLE PARAMETERS FOR THE 3-LAYER COILS.

Parameter	Unit	Coil #1	Coil #2	Coil #3
N of strands	-	28		
Strand diameter	mm	1.000		
Bare cable width	mm	14.232		
Inner cable edge	mm	1.687	1.800	1.688
Outer cable edge	mm	1.913	1.800	2.284
Insulation thickness	mm	0.254		
Cu:nonCu ratio	-	1.00		

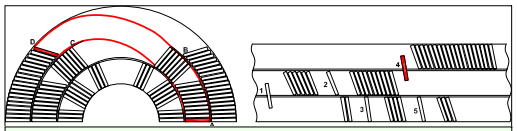

Fig. 3. 3-layer coil end design w/o the interlayer splices.

TABLE III. 3-LAYER MAGNET PARAMETERS.

Parameter	Coil #1	Coil #2	Coil #3
N of turns in the coil	94	90	90
Total coil area (Cu + nonCu), cm^2	42.70	40.886	40.886
Non-Cu J_c (12 T,4.2K), A/mm^2	2000	2000	2000
Bore quench field, T	13.268	13.157	13.186
Quench current Iq, kA	14.902	15.394	15.261
Peak field in the coil at Iq, T	13.873	13.73	13.769
Magnet inductance at Iq, mH/m	5.07	4.62	4.69
Stored energy at Iq, kJ/m	562.95	547.41	546.15
Lorentz Fx/quadrant at Iq, MN/m	4.027	3.957	3.936
Lorentz Fy/quadrant at Iq, MN/m	-1.942	-1.906	-1.889

TABLE II. SYSTEMATIC FIELD HARMONICS AT 10 MM RADIUS.

n	b_n at 1kA, 10^{-4}		
	Coil #1	Coil #2	Coil #3
3	0.0003	0.0003	-0.0040
5	0.0009	0.0017	-0.0557
7	0.0030	0.0068	-0.1849
9	-0.0146	-0.0157	0.0391

3-layer coil could be wound without interlayer splices with both leads positioned in the coil mid-plane. This approach potentially reduces the magnet fabrication time and cost, and improves reliability against failure of internal splices.

Shell Type Superconducting Magnet Design 4 Layers

A 4-layer coil allows simple conductor grading

In coil #4 the two outermost layers were designed using a narrower cable made of the same strand whereas in coils #5 and #6 they were designed using a cable with the same width but smaller strand diameter.

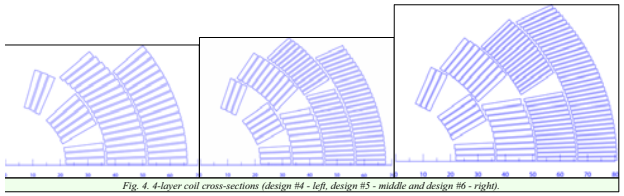

Fig. 4. 4-layer coil cross-sections (design #4 - left, design #5 - middle and design #6 - right).

TABLE VI. 4-LAYER MAGNET PARAMETERS.

Parameter	Coil #4	Coil #5	Coil #6
N of turns in the inner coil	58	58	60
N of turns in the outer coil	94	108	132
Total coil area (Cu + nonCu), cm^2	49.23	44.46	68.18
Non-Cu J_c (12 T,4.2K) inner coil, A/mm^2	2000	2800	2800
Non-Cu J_c (12 T,4.2K) outer coil, A/mm^2	2000	2000	2000
Bore quench field, T	14.49	14.98	15.96
Quench current Iq, kA	11.381	10.27	11.22
Peak field in the inner coil at Iq, T	15.048	15.81	16.45
Peak field in the outer coil at Iq, T	12.173	12.58	13.37
Magnet inductance at Iq, mH/m	13.25	15.54	20.04
Stored energy at Iq, kJ/m	858.1	819.5	1261.4
Lorentz Fx/quadrant at Iq, MN/m	5.32	5.39	6.74
Lorentz Fy/quadrant at Iq, MN/m	-2.66	-2.70	-3.57

The magnets can reach 13-16 T fields.

4-layer coil designs allow coil grading and potentially reaching 16 T field level.

The 16 T field was reached in graded 4-layer design using highest available Jc.

Taking into account the significant increase of the coil volume and required high Jc this field is probably maximum practical field for Nb_3Sn coils.

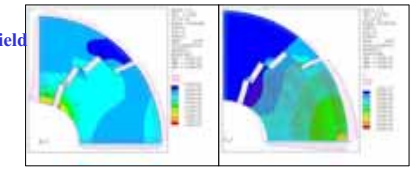

Multipole Magnet

The magnet assembled from 12 identical racetrack type superconducting coils and capable generate any combination of dipole, quadrupole and sextupole normal and skew magnetic fields. The coil groups are powered from separate power supplies. In the case of normal dipole, quadrupole and sextupole fields the total field is symmetrical relatively the magnet median plane and there are only five powered separately coil groups. This type multipole magnet was proposed for Fermilab BTeV project.

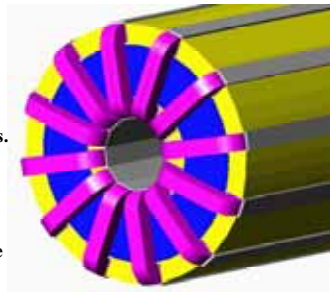

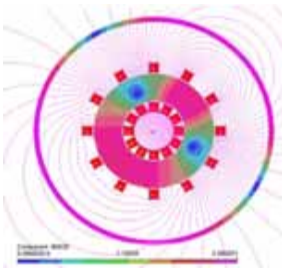

Multipole Magnets

Parameter	FNAL	RHIC	UNK	LHC	BTEV
Dipole field, T	0.62	0.58	0.59	0.11	0.6 max
Quadrupole gradient, T/m	9.84	2.72	4.37	60	20.8 max
Sextupole strength, T/m²	294.5	-	448		375
Operating current, A	50	50	20	100	35-77
Critical current @ 4.2K, 5T, A	160	130	54-69	228	160
Coil maximum field, T	1.5	-	1.3	3 -3.22	1.7
Coil inner diameter, mm	80	82.1	80	90	80
Outer cold mass diameter,mm	152		168	242	290
Conductor diameter, mm	0.5	0.33	0.3	0.5	0.5
Strand current density, A/mm²	255	585	283	510	255
Cu/NbTi ratio	-	2.5	1.7	2.0	2.0
Jc @ 4.2K, 5T, A/mm²	-	-	2000	3165	2200
Length, m	0.77	0.5	1.37	0 52	0.8 - 1.2

The combined function magnetic field is formed by 12 identical racetrack coils equally distributed. The rectangular coil cross-section was chosen to simplify the winding process. In common case each coil can be powered separately. A proper programming of power supplies can eliminate also all field deviations caused by manufacturing deviations, iron saturation effects, etc. The current of each N-th coil is the sum of the dipole, quadrupole and sextupole components:

$$I_N = I_{ND} + I_{NQ} + I_{NS}$$

Superconducting Double Dipole Magnet

Recent progress in Nb_3Sn superconductor technology provides the base for increasing magnet field in accelerator magnets up to 15-16 T. One of the novel approaches to the design of this magnet is to split the magnet winding into two separate dipole windings powered in series or separately. Each winding generates a homogeneous magnetic field in the magnet aperture. The inner dipole winding is based on the 2-layer Nb_3Sn coils previously developed and tested at Fermilab. The outer dipole winding is made of sub-sized Nb_3Sn cable and has about two times higher current density.

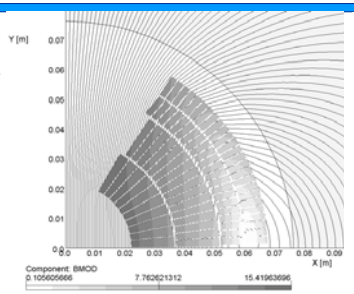

TABLE I
MAGNET PARAMETERS

Parameter	Air Core	Iron Core
Aperture magnetic field, T	15	15
Peak current, kA	15.2	12.6
Superconductor peak field, T		
Inner coil	15.5	15.4
Outer coil	13.3	13.4
Aperture diameter, mm	40	40
Outer winding OD, mm	136	136
Iron yoke OD, mm	-	560
Stored energy at 15 T, MJ/m	1.06	0.94
Inductance at 15 T, mH/m	9.2	11.8
Lorentz force (quadrant), MN/m		
Horizontal	4.8	5.7
Vertical	-5.7	-2.6
Superconducting Nb3Sn cable, mm		
Inner	14.23 x 1.91	
Outer	7.1 x 1.91	
Strand diameter, mm	1.0	1.0

$$B = k_{in}\ I_{in} + k_{ou}\ I_{ou}$$

I_{in}, I_{ou} - currents in inner and outer coils,

$k_{in} = B_{in} / I_{in}$, $k_{ou} = B_{ou} / I_{ou}$ – transfer functions

The total field harmonics in this case can be calculated

$$bn = (bn_{in}\ k_{in}\ I_{in} + bn_{ou}\ k_{ou}\ I_{ou}) / (k_{in}\ I_{in} + k_{ou}\ I_{ou})$$

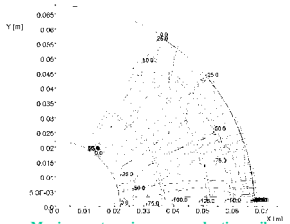

Maximum stress in superconducting coils at 15 Tesla ~ 150 MPa

TABLE III
IRON CORE MAGNET FIELD

Inner, A	Outer, A	Bo, T	b3	b5	b7
150	150	0.21	0.78	-7.3	0.8
1395	1395	1.997	0.78	-7.3	0.8
7950	7950	10.23	6.94	-8	0.67
12600	12600	15.02	3.6	-8.65	0.73
0	1398	1.17	0.12	-1.33	0.018
0	7938	6.2	8.55	-1.3	3.02
0	12600	9.02	6.6	-1.42	0.223
-139.6	1398	1.092	0	-0.25	-0.09
-793.8	7938	5.79	8.6	-0.13	-0.093
-1260	12600	8.41	7.*	-0.13	-0.1

Multipole Magnet

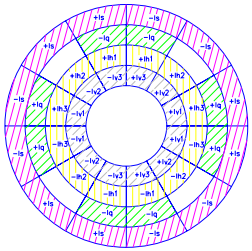

Dipole+Quadrupole+Sextupole Coil Currents:

$I_1 = I_{12} = I_{d1} + I_q + I_s$ $\quad I_{12} = -I_1$
$I_2 = I_{11} = I_{d2} - I_s$ $\quad I_{11} = -I_2$
$I_3 = I_{10} = I_{d3} - I_q - I_s$ $\quad I_{10} = -I_3$
$I_4 = I_9 = -I_{d3} - I_q + I_s$ $\quad I_9 = -I_4$
$I_6 = I_7 = -I_{d1} + I_q - I_s$ $\quad I_7 = -I_6$
$I_5 = -I_2$
$I_8 = -I_5$

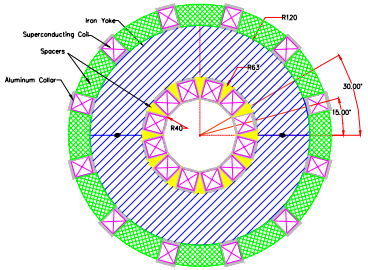

Proposed variant of multipole magnet has the following advantages:

- **only one type of multipole magnet for all needs**
- **possibility to generate any combination of dipole, quadrupole and sextupole normal and skew fields**
- **stable magnetic center and field quality**
- **simple coil manufacturing**
- **single strand continues coil, no inner splices**
- **good mechanical stability because of eliminating opposite forces in coils**
- **good coil cooling**
- **possibility of individual coil block test and training**
- **easy assembly, disassembly and repair**
- **Possibility to use Nb_3Sn superconductor and technology to increase maximum field and temperature margin**

Superconducting Double Dipole Magnet

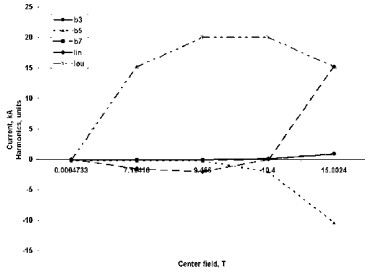

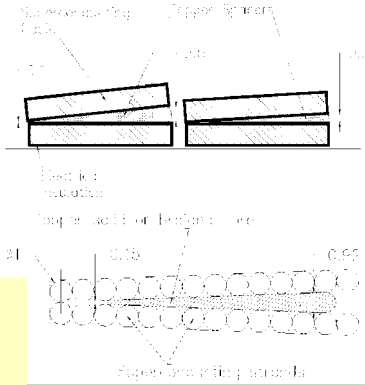

The proposed double dipole magnet has following advantages:
- **superconductor volume efficient, capable to reach 15 T magnetic field;**
- **solid, mechanically homogeneous coils;**
- **extra copper stabilizer combined with the rectangular cable;**
- **good field quality in large aperture when powered only the outer winding;**
- **field quality improving by using the inner coil for correction;**
- **simple coil configuration with low sensitivity to manufacturing deviations.**

As it follows from the previous analysis it is possible to manufacture the double dipole magnet with the field up to 15 Tesla on the base of existing Nb_3Sn magnet technology. Such type magnets can be used as stand alone magnets and for future accelerators.

Distributed spacers provide mechanically homogeneous structure

260

Quench Margin & Design Concept

Quench Margin

Both quadrupoles based on the NbTi conductor achieve the maximum operating gradients with 15-20% quench margin.

Using of Nb_3Sn cable in these magnets allows enhancement of the operating gradients by a factor of 1.5 with the same quench margin. The radiation losses produce an extra heat load of 0.3–1.0 mJ/g.

At 1.0 mJ/g deposition, the quench margin for NbTi coil has to be more than 25% and for Nb_3Sn coil only 10%.

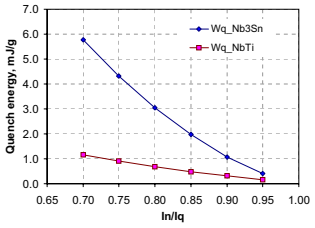

Design Concept

At the reasonable magnet current of 15-20 kA and several hundreds of turns in the windings, a traditional shell type coil would suffer from stress accumulation at the midplane and large random field harmonics coming from the variation of individual cable positions within the shells. Thus it was imperative to split the shells into a number of mechanically decoupled blocks, providing the stress management and individual positioning and support for each block. The winding mandrel is a cylinder with rectangular slots machined in longitudinal direction. For easier stacking and pre-stressing inside the slots, the cable is wound in the "hard bend" way with the long edge tangential to the mandrel. After the coil is wound and cured, the mandrel serves as the mechanical support structure for the coil. Simple bending experiments demonstrated that the Rutherford type cable with 28 strands, 1 mm in diameter can be hard-bent around ~50 mm round mandrel without the stability loss.

Large-Bore Quadrupoles (D=300mm)

Large-bore superconducting quadrupoles for LANL AHF project were designed.

The quadrupoles have two concentric windings connected in series and configured so that the outer winding fully cancels the outer fringing magnetic field. The active shielding eliminates fringing fields and Lorentz forces between adjacent quadrupoles, reduces magnet size and weight.

Parameter	NbTi	Nb_3Sn
Strand diameter, mm	1.000	
Number of strands	32	
Cable bare width, mm	16.214	
Cable bare thickness, mm	1.772	
Number of SC strands	32	8
Number of Cu strands	0	24
Copper to non-copper ratio	1.6	0.85
J_c(5T,4.2 K), A/mm^2	3000	-
J_c(12T,4.2 K), A/mm^2	-	2200

Parameter	Small- bore	Large- bore
Operating gradient, T/m	24.15	13.18
Magnetic length, m	3.0	4.3
Reference radius R_{ref}, mm	113.4	241.3
Field quality at R_{ref}	$<10^{-4}$	$<10^{-4}$
Main coil inner radius, mm	170.0	322.0
Screen coil inner radius, mm	276.0	513.5
Iron screen inner radius, mm	345.0	595.0
Iron screen thickness, mm	10.0	10.0
Number of turns in the main coil	232	508
Number of turns in the shield coil	104	220
Coil area, cm^2	174.4	378.0
Operating current, kA	14.10	11.77
Quench gradient with NbTi, T/m	28.25	15.80
Quench current with NbTi, kA	16.49	14.11
Peak field in the coil, T	6.1	6.3
Inductance, mH/m	9.91	49.41
Nominal stored energy, kJ/m	985.4	3420.7
Max. field in the iron screen, T	0.4	0.2

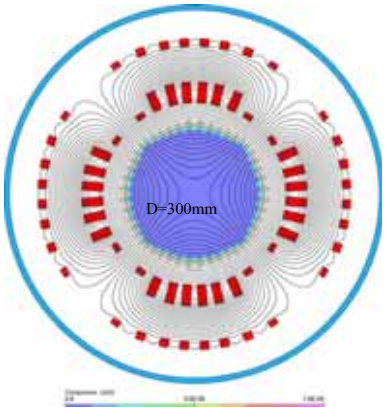

Active shield superconducting magnet was built and tested in Japan.

Active shields used in MRI Superconducting Solenoids

Options in Magnet Technology

Most Nb_3Sn magnet coils are vacuum impregnated with high viscosity epoxy.

Attractive alternative technology:

- Epoxy with fillers (boron nitride, rare-earth additions, etc.)
- Winding encapsulation under a high pressure to provide full epoxy penetration
- High thermal capacity and thermal conductivity resins and fillers
- High radiation resistant insulation – ceramics (FNAL), polyimids (FNAL plan) , epoxy+polyurethans (CERN/Efremov conventional correctors), etc.
- Magnet mechanical structure as closed mold for encapsulation
- High pressure impregnation as additional prestress for winding LBNL (S.Caspi), FNAL(Proposal)

Large-Bore Quadrupoles (D=600mm)

Magnet parameters

Parameter	Small- bore	Large- bore
Operating gradient, T/m	24.15	13.18
Magnetic length, m	3.0	3.0
Reference radius R_{ref}, mm	113.4	241.3
Field quality at R_{ref}	$<10^{-4}$	$<10^{-4}$
Main coil inner radius, mm	170.0	322.0
Screen coil inner radius, mm	276.0	513.5
Iron screen inner radius, mm	345.0	595.0
Iron screen thickness, mm	10.0	10.0
Number of turns in the main coil	232	508
Number of turns in the shield coil	104	220
Coil area, cm^2	174.4	378.0
Operating current, kA	14.10	11.77
Quench gradient with NbTi, T/m	28.25	15.80
Quench current with NbTi, kA	16.49	14.11
Peak field in the coil, T	6.1	6.3
Inductance, mH/m	9.91	49.41
Nominal stored energy, kJ/m	985.4	3420.7
Max. field in the iron screen, T	0.4	0.2

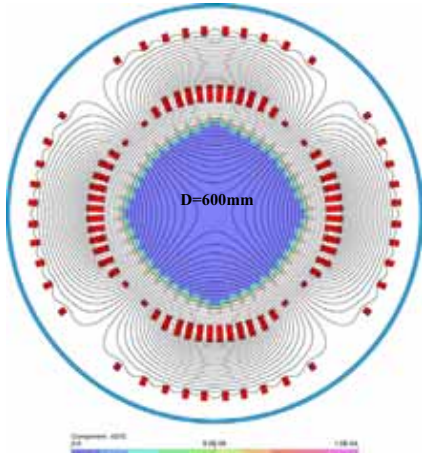

Magnets for ILC IR

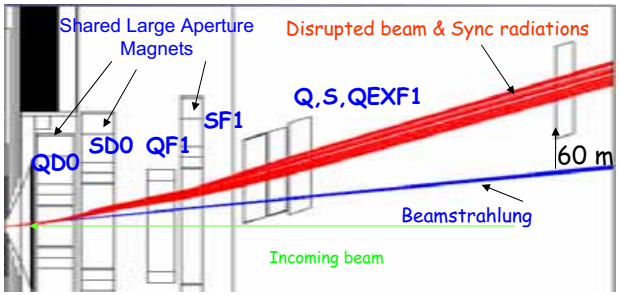

LHC IR Quadrupole

2 mrad IR Quadrupole

- Aperture 70 mm
- Effective length 2.5 m
- Gradient 160 T/m
- Magnetic center stability 1-5 μm
- Girder with 50 nm steps
- Removable magnet system for Detector exchange

Possible issues

- magnetic center motion (SC magnetization, Lorentz forces, mechanics, iron saturation and hysteresis, etc)
- Detector solenoidal field
- superconducting magnets moving carriage

Design options

- NbTi LHC IR Quadrupole (2 m models built and tested)
- Nb3Sn Quadrupole (LARP type)

but small filament size superconductor (bronze technology)

Options in Magnet Technology

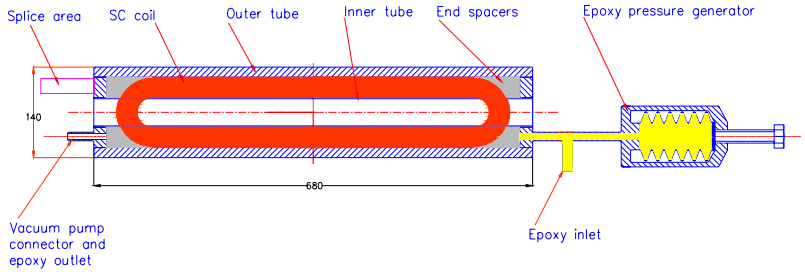

Inner and outer tubes with end flanges form the closed volume for impregnation/encapsulation. After the pumping out of the assembly, epoxy flows from an outer vessel in the inner winding volume. When the whole volume is filled in with epoxy, inlet and outlet valves/plugs should be closed. The additional pressure inside the assembly is provided by epoxy pressure generator. The inner tube with 2 mm wall thickness is capable to carry outer pressure no less than 60 Mpa.

Summary

Design options for Nb3Sn High Field Accelerator Magnets

- 15 T shell type 3-4 coil layers magnets
- 15 T Double dipole magnets
- Compact high field multipole magnets with racetrack coils
- Large-bore magnets with coils wound into the slots
- Distributed spacer homogeneously wound coils
- Rigid high pressure encapsulated coils
- High gradient and magnetic center stability quadrupoles

Magnets for ILC Main Linac

ILC Main Linac Quadrupole

- Low current (50 –100 A)
- Aperture 50 – 80 mm
- Gradient > 50 T/m
- Length ~ 0.6 m
- Magnetic center stability 1-5 μm
- Low fringing fields 1-10 μT

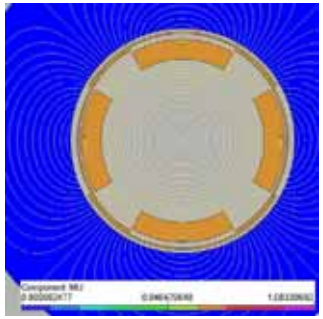

2-4 μm magnetic center displacement in quadrupole with dipole correctors

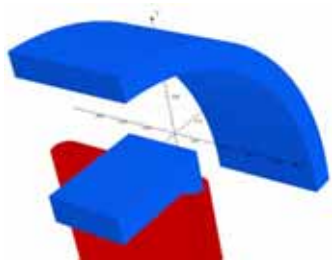

Dipole corrector 3D field calculations showed the 0.3% integrated field homogeneity at 30 mm aperture radius for this 150mm length corrector

Possible issues:

- magnetic center motion (SC magnetization, Lorentz forces, mechanics, iron saturation and hysteresis, etc)
- fringing field trapped in SCRF at cooling down and operation

Proposal – Separate main quadrupole and dipole correctors to eliminate coupling effects

Magnet Structure Concept

- Coil:
  - Nb3Sn Rutherford-type conductors in 2 layers.
  - Preliminary coil geometry from Daniel Leroy (CERN).
- Collars:
  - Relatively thin (low bending resistance), - spacers.
- Yoke:
  - Horizontal split.
  - Used to support collared-coil assembly (high stiffness).
- Outer-Cylinder:
  - Relatively high thermal contraction.
  - Ensures a good contact at the yoke / collar interface.

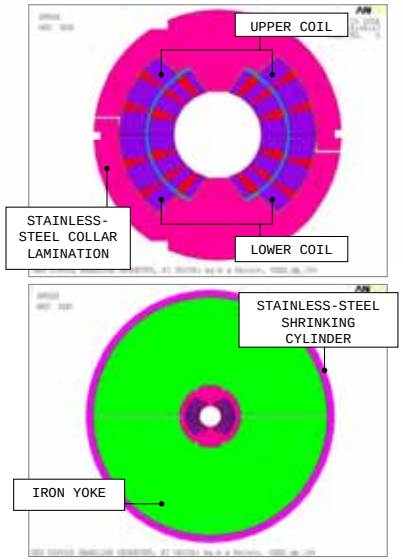

Progress in NED Mechanical Design

Peter Loveridge
P.Loveridge@rl.ac.uk

Engineering Analysis Group
Rutherford Appleton Laboratory

WAMDO - 2006

Current Model Strategy

- 2D Approach - end effects are ignored.
- Frictionless “surface-to-surface” contact is assumed between components.
- Multiple load-steps used to simulate complete load history:
  - Step 1: Collaring
    - An azimuthal pre-load is induced in the coil.
    - The use of keys to “lock” the collars in place is simulated.
  - Step 2: Yoke / Outer cylinder assembly
    - The “split” iron yoke and stainless-steel shrinking cylinder are assembled around collared coil at room temperature.
  - Step 3: Cooldown
    - The whole magnet structure is cooled from room temperature to 4.2 K.
  - Step 4: Powering
    - Lorentz forces are applied to the conductors.
- Force, displacement, and stress results may be evaluated at each step.

Introduction

- A structural Finite Element model of a next-generation accelerator dipole magnet is being developed at RAL:
  - Global model of complete magnet structure.
  - Single cable sub-model.
- Part of NED framework – MDO working group:
  - Working group charged with investigating and comparing preliminary designs for large bore (88 mm aperture), high field (15 Tesla), accelerator dipole magnets.
  - RAL efforts concentrated on cosine-theta, layer-type coil structure.
- Objective of preliminary mechanical design – to assess the mechanical implications:
  - Lorentz forces can be up to 5 times higher than in LHC dipole magnets.
  - Preliminary work only at this stage…
  - Status report:
    - Have modelled all the steps and basically understand the sequential behaviour.
    - The details are not yet optimised.

Step 1: Collaring

- Zero vertical displacement applied at coil mid-plane: valid providing the upper / lower coil interface is always in compression, - OK.

- Results:
  - Maximum stress in collar located at key-slot.
    - General stress level ~150 MPa.
    - 0.2 % P.S. ~ 1000 MPa (LHC collar @ 77K).
  - Vertical ovalisation of collared-coil occurs.
  - Average azimuthal stress at coil mid-plane = 25 MPa.

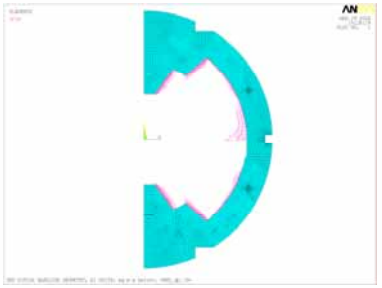

STEP 1: CONTACT FORCES

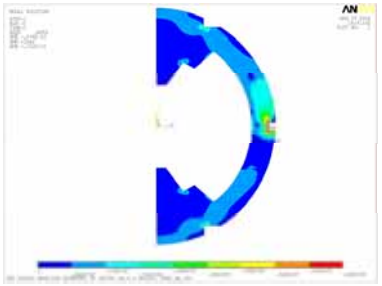

STEP 1: VON-MISES STRESS

Material Property Data

- This design depends strongly on the material properties (modulus at RT and 4.2 K, integrated thermal expansion):
  - Nb3Sn conductors:
    - Modelled as homogeneous material.
    - Data from "stack" compression tests carried out by SACLAY.
  - Stainless-steel collars / iron yoke:
    - LHC dipole material data used.
  - Cu Alloy Spacers:
    - SACLAY quadrupole design.
  - G10 interlayer spacer:
    - Literature.
  - KAPTON ground plane insulation:
    - Manufacturers data.
- NED working group have assembled a fully referenced material properties table for mechanical computations:
  - EDMS 683000 <https://edms.cern.ch/document/683000/2>

Step 2: Yoke + Cylinder Assembly

- Objectives:
  - Force collared coil assembly back into a more circular shape.
  - Prepare for cooldown phase.

- Method:
  - Yoke + Outer-cylinder are assembled at room-temperature.
  - Frictionless contact at the following interfaces:
    - Yoke / Collar
    - Yoke / Cylinder
    - Yoke-top / Yoke-bottom
  - There is a 1 mm nominal radial interference fit between the cylinder / yoke.
  - Key constraint released,

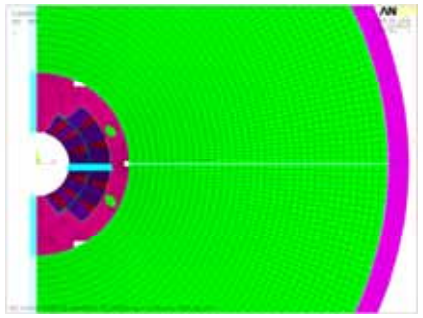

STEP 2: BOUNDARY CONDITIONS

Step 1: Collaring

- Objectives:
  - Apply a compressive azimuthal stress (~25 MPa) in the coil.

- Method:
  - Collar laminations to be assembled in pairs.
  - Front collar / Back collar modelled.
  - Collar pair connected by "spot-welds".
  - Frictionless contact modelled at the coil/collar interface.
  - Vertical collar displacement applied at the key slot: δY = ±200 μm

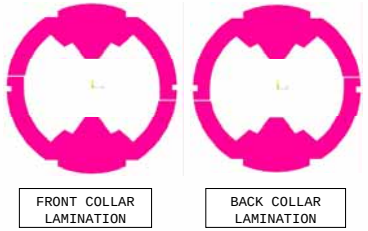

FRONT COLLAR LAMINATION

BACK COLLAR LAMINATION

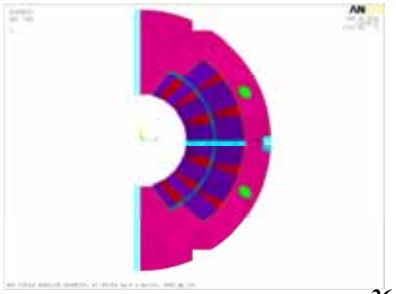

STEP 1: BOUNDARY CONDITIONS

Step 4: Powering

- Objectives:
  - Apply the magnetic forces to the conductors.
- Method:
  - Lorentz forces on the conductors calculated in ANSYS:
    - Non-linear iron b-h data.
    - Current density in conductor assumed to be constant.
    - Gives distribution of forces within each conductor.
  - Benchmark exercise carried out to verify the forces:
    - ANSYS, OPERA (VF), ROXIE.
    - Very good agreement (within1%).

$$F_{sum} = \sqrt{F_x^2 + F_y^2}$$

NUMBERING SCHEME

LORENTZ FORCES

Block Number	∑FX (MN/m)	∑FY (MN/m)	FSUM (MN/m)
1	1.58	-0.18	1.59
2	1.72	-0.29	1.75
3	1.33	-0.29	1.36
4	1.08	-0.21	1.10
5	0.18	-0.48	0.52
6	0.75	-1.22	1.43
7	1.24	-1.18	1.71
Total	7.88	-3.86	

Step 2: Yoke + Cylinder Assembly

- Results:
  - The collared-coil assembly is forced to conform to the shape of the yoke, - i.e. roughly circular.
  - Hoop-stress induced in cylinder due to interference fit:
    - ~ 370 MPa in this case.
  - Bending in the yoke begins to close the horizontal gap at the outer edge along a distance of ~ 90 mm.
  - Azimuthal stress at coil mid-plane not uniformly distributed:
    - This is something we clearly need to optimise since this effect is currently seen to propagate through to the subsequent steps.

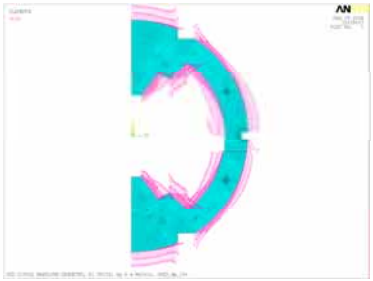

STEP 2: CONTACT FORCES

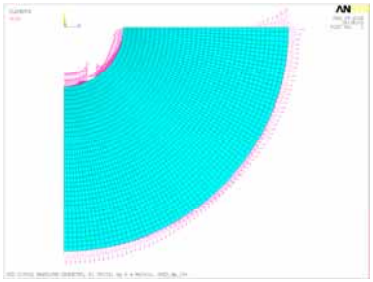

STEP 2: CONTACT FORCES

Step 4: Powering

- Results:
  - Yoke gap remains closed
  - Large horizontal Lorentz force components supported by the yoke
  - In this case a loss of contact occurs at the collar pole for the inner coil layer.

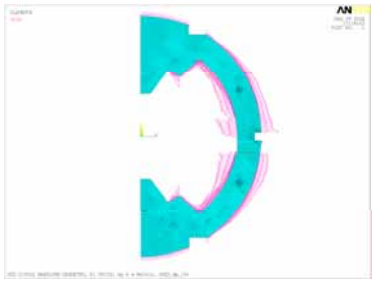

STEP 4: CONTACT FORCES

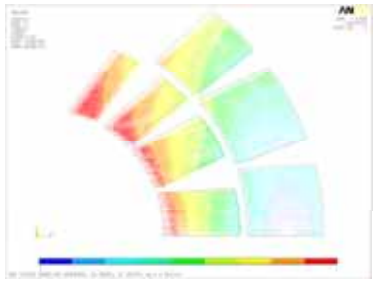

STEP 4: NORMALISED MAGNETIC FORCE VECTORS

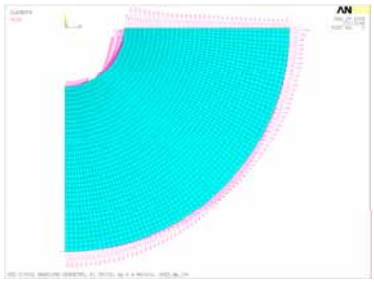

STEP 4: CONTACT FORCES

Step 3: Cooldown

- Objectives:
  - For the collared-coil to be well supported by the yoke after cooldown.
  - Pre-load the coil prior to powering.
- Method:
  - Entire assembly cooled from room-temperature to 4.2 K.
  - Calculate displacements due to thermal contraction.
- Results:
  - Yoke mid-plane gap closes all the way along.
  - Contact at collar / yoke interface.

THERMAL EXPANSION PROPERTIES

Material	Used On	Integrated Thermal Expansion (293-4.2 K)
Nb_3Sn Conductor	Insulated Cable Stack	3.9×10^{-3}
Stainless-steel	Collars Outer-cylinder	2.6×10^{-3}
'Magnetil' Steel	Yoke	2.1×10^{-3}

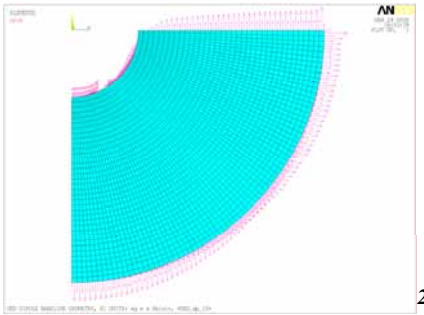

STEP 3: CONTACT FORCES

Further work

- Global Model Development:
  - Optimise magnet parameters in order to control the stress distribution in the coil.
  - Implement orthotropic material properties for cable:
    - Currently have isotropic material model based on “azimuthal” compression test data.
    - By simple rule-of-mixtures calculation the “radial” stiffness should be grater by a factor ~ 2.
  - Look in more detail at the collaring process, maybe use 2 sub-steps:
    - 1A – Assembly in press.
    - 1B – Insert key and release press load.
- Submodel Development:
  - Calculate sub-model results for each of the 4 load steps.
  - Link to NED insulation development work package, -S. Canfer, RAL.
  - Missing data:
    - strand material properties?
- 3D modelling..?

Global Model Summary

- RAL have developed a working mechanical model of a next generation accelerator dipole magnet.
- Multiple load steps ensure that the full load history is modelled:
  - 1. Collaring.
  - 2. Yoke + Cylinder Assembly.
  - 3. Cooldown.
  - 4. Powering.
- Results at each step are making sense and affect all subsequent steps.
- Many parameters still to optimise in order to minimise the peak azimuthal stresses at the coil mid-plane:
  - Preload applied to coil prior to powering.
  - Shape of iron at yoke/collar interface.
  - Shape of iron mid-plane gap.
  - Moduli for wedges / spacers in coil

Cable Submodel

- Objectives:
  - Compute peak stresses in cable strands.
  - Investigate stress state in cable insulation (compression, shear).
  - Link to insulation development programme.
- Method:
  - Cable submodel under development:
    - 40 strands
    - Orthotropic glass-fibre insulation
    - Epoxy filled gaps
    - Filling factor = 87%
  - Interpolate submodel boundary conditions from global model at each step.
- Results:
  - Work in progress...

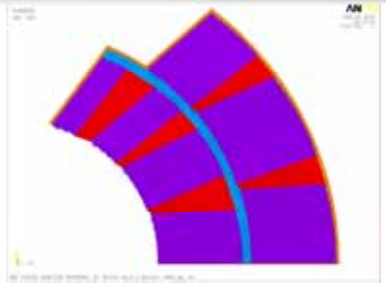

GLOBAL MODEL ELEMENT MESH

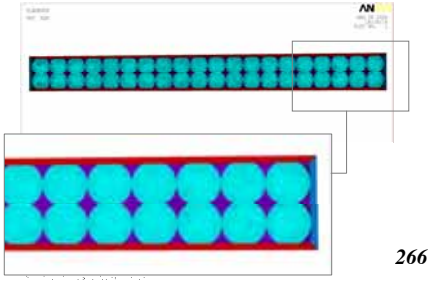

SUBMODEL ELEMENT MESH

Position of the Problem

Explore new designs (beyond cosθ) to push the limits :

- *High fields > 13 T-15T*
- *Large aperture > 130-160 mm*
- *Accelerator Field Quality*
- *Compact cross-section*
- *Reasonable volume, mass (and cost !)*

Limitations :

-Nb3Sn strand issues (Jc, stability, T margin, etc….)
-Large magnetic forces
-Cross-section stress distribution
-Strand stress sensitivity
-Non-linear mechanical behaviour of winding pack
-Need for prestress

$$F \approx B^2$$

Force an stress management using new designs

Progress at CEA Saclay
in the design of
High Field Magnets

P. Vedrine
H. Felice
CEA Saclay DSM/DAPNIA/SACM

Nb3Sn Cos 2θ Magnetic Forces

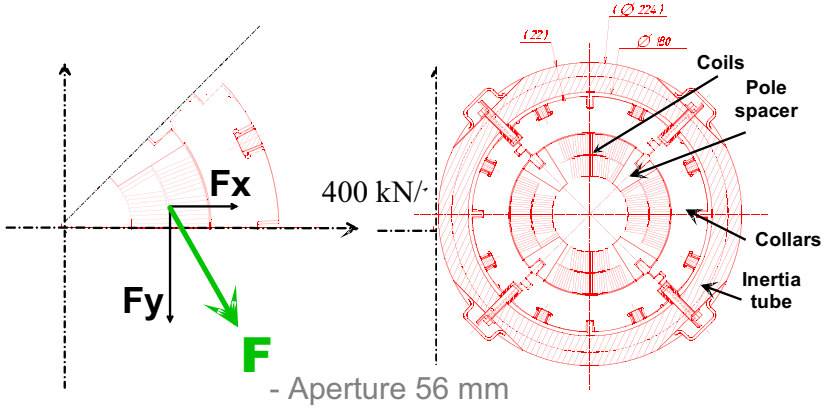

- Aperture 56 mm
- 220 T/m
- Peak field 8.6 T
- 11 800 A

Outline of Presentation

- Position of the Problem
- Force and stress management
- Preliminary Design Studies
- 2D Magnetic Design
- 2D Mechanical Design
- Experimental Apparatus for Prestress Studies
- Conclusion

WGMDO NED

Non-Linear Mechanical Characteristics

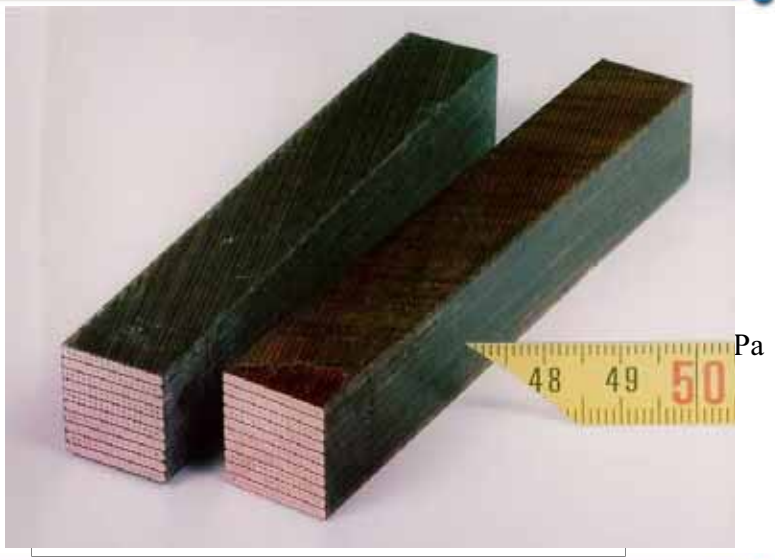

Pa

Non-Uniform Azimutal Stresses Distribution

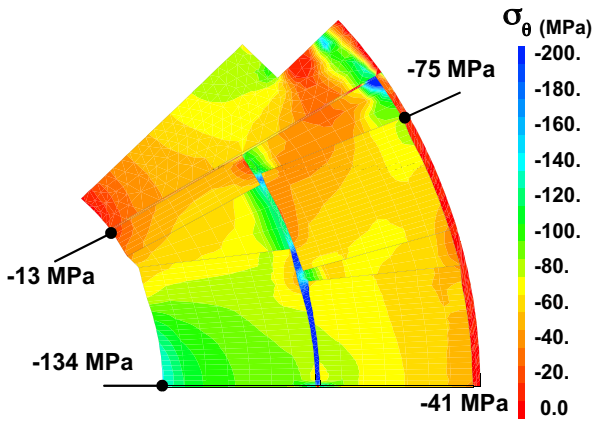

Need for Prestress

To avoid conductor displacements at full current
which may trigger quenches

High field (15T) Nb3Sn magnet ~ 150-200 MPa ~ 120-170 MPa

$$\sigma_{prestress} \approx \frac{2}{3} F_\theta + E \int_{300K}^{4K} \Delta\alpha dT$$

Low field (8T) NbTi magnet ~ 30 MPa ~ 30 MPa

Young modulus of Nb3Sn > 3 times Young Modulus of NbTi
Fully impregnated structure <> Polyimide insulated structure
Stability & margin temperature @ 4K >1.8 K

Can we accept some displacements during energization
and reduce the prestress ? : hypothesis to be tested

Strand Transverse Stress Sensitivity

150 MPa limit

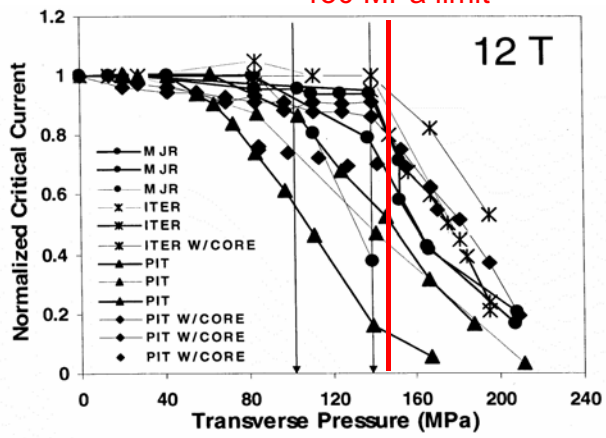

Courtesy of E. Barzi (FNAL)

Stress Management - Virial theorem

$$\int \sum_i \sigma_i dV = \int \frac{B^2}{2\mu_0} dV = U_m$$

Principal stresses

-Uniform (high) Tensile Stress Distribution ⇒ Avoid bending & compressive stresses

-Avoid Compressive Stress in the winding ⇒ Intercept forces near the conductor Structural « arches » or « web », ….

Force Management

Explore ways to reduce the effects of magnetic forces

$$\vec{F} = \frac{1}{\mu_0} \oint_{C1} (\vec{B}(\vec{B}.\vec{n}) - \frac{1}{2}(\vec{B})^2 \vec{n}) dl$$

Maxwell Tensor

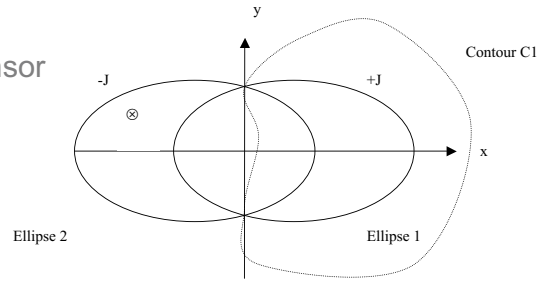

Stress Management

$$B \approx \mu_0 J \langle w \rangle \qquad \sigma_{cond} \approx JB \langle d \rangle$$

Typical size of winding pack — **Typical size of stress management cell**

$$\sigma_{cond} \approx \frac{B^2}{\mu_0} \frac{\langle d \rangle}{\langle w \rangle}$$

Goal : σ < 150 Mpa everywhere and every time

Play with the winding pack dimensions and structure (height, width, support structure)

Force Management

$$\vec{F}_x = \frac{1}{\mu_0} \oint_{Oy} (-\frac{1}{2}(\vec{B}_{y(x=0)})^2 o\vec{x}) dl \qquad \vec{F}_y = -\frac{1}{2\mu_0} \int \left| B_{y(y=0)} \right|^2 o\vec{y} dl$$

$$\vec{F}_{Xtot} = \vec{F}_{Xaperture} + \vec{F}_{Youtside} \qquad \vec{F}_{Ytot} = \vec{F}_{Yaperture} + \vec{F}_{Ywinding} + \vec{F}_{Youtside}$$

Reduce the winding pack height — Reduce the winding pack width

But contradictory with stress management

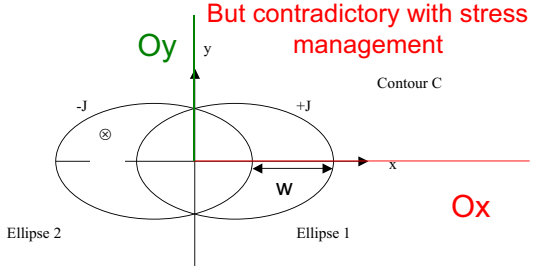

Parametric study (15T field – 130mm aperture)

$$S_{sup} = 2ab\left(2\arcsin\left(\frac{c}{2a}\right) + \frac{c}{a}\sqrt{1-\frac{c?}{4a?}}\right)$$

$J_e = 500\ A/mm^2$

$$H_{int}(z) = \frac{Jb}{a+b}c$$

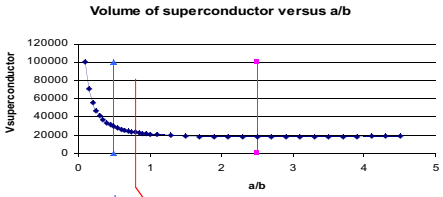

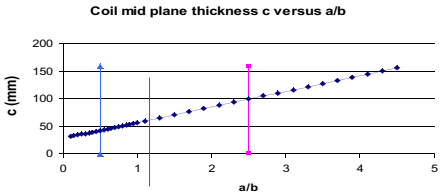

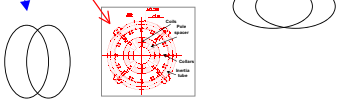

Cos θ

Preliminary Design Studies

Revisiting the old times

Cable Definition

NED strand

Number of strands : 38

Strand diameter : 1.25 mm

Height of the non insulated cable : 23.75 mm

Width of the non insulated cable : 2.31 mm

Insulation thickness : 0.2 mm

JcnonCu à 15T 4.2°K: 1500A/mm²

1350 A/mm² with 10% cabling degradation

dJc/dB = 500 A/mm²/T

Ellipses intersection – Uniform Field

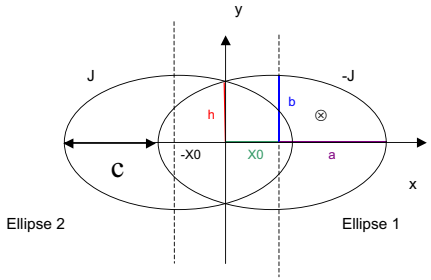

H = Hy + i Hx

$$H_{int}(z) = \frac{Jb}{a+b}c$$

Play with winding pack dimensions (height, width)

Intersection of ellipses with b > a - Ø130

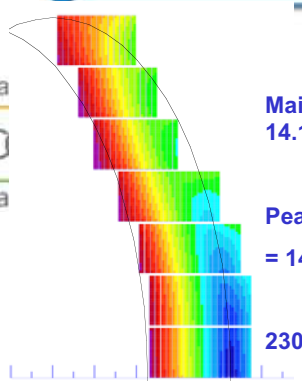

Main field = 14.12T

Peak Field = 14.64 T

230 turns

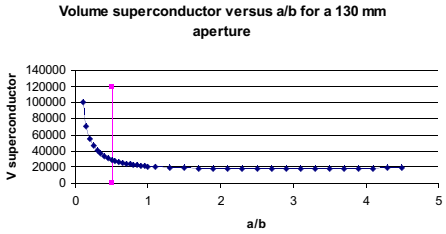

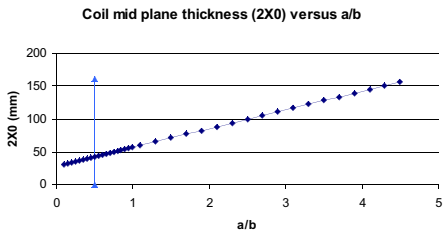

a = 86 mm

b = 172 mm a/b = 0.5

c = 42 mm

Intersection of ellipses with a > b - Ø130

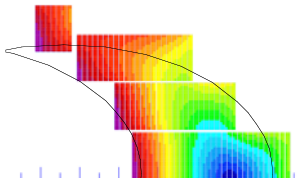

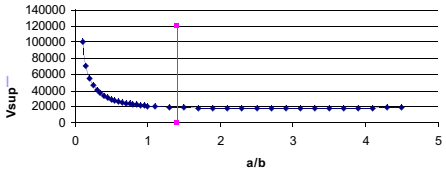

a = 104 mm

b = 74 mm a/b = 1.4

C = 68 mm

Main field =14.06T

Peak field = 15.5 T

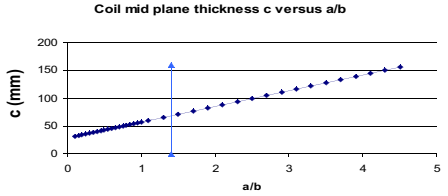

164 turns

Intersection of ellipses with b > a - Ø130

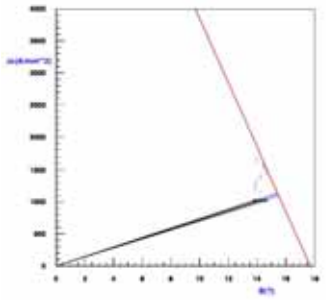

Minimum quench margin = 5.7%

L = 19.46 mH/m

E = 4.38 MJ/m

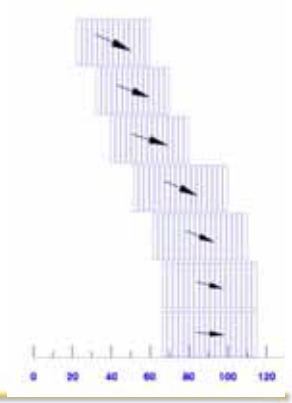

Fx = 31.18 MN/m

Fy = - 5.29MN/m

Stress on the mid plane = 108.4 MPa

Intersection of ellipses with a > b - Ø130

Minimum quench margin = 6.09%

L = 14.84 mH/m

E = 3.46 MJ/m

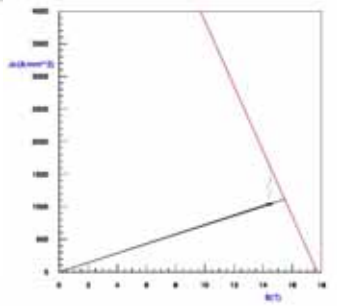

Fx = 19.83 MN/m

Fy = - 6.24 MN/m

Mean Stress on the mid-plane = 76 MPa

(no bending effect)

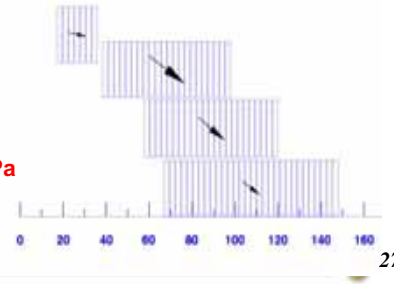

NED Conductor Characteristics

dapnia cea saclay

- Strand characteristics
  - strand diameter (Ds) = 1.25 mm
  - copper/ non copper ratio = 1.25
  - JcnonCu = 1500 A/mm² at 15T and 4.2 K
    = 1350 A/mm² with 10 % degradation
- Cable characteristics
  - Number of strands (Nbs) = 38
  - Width = 24.7 mm (L = 1.04 Nbs/2 Ds)
  - Thickness = 2.175 mm (e = 0.87 Ds * 2)
- Insulation thickness : 0.2 mm on each side of the conductor
- Interlayer space : at least 2 mm

Summary Ø130

dapnia cea saclay

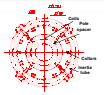

	Cos θ	a > b	a < b
Main field (T)	14.2	14.06	**14.12**
Peak field (T)	15.24	15.5	**14.64**
Fx (MN/m)		19.83	31.18
Fy (MN/m)	-9.9	-6.24	**-5.29**
P (MPa)	217	76	108.4
L (mH/m)	**8.37**	14.84	19.46
E (MJ/m)		3.46	4.38
Number of turns	100	164	230

Parameters

dapnia cea saclay

Peak/ Quench field (T)	15	
Quench margin (%)	10	
Copper/non copper ratio	1.25	
Harmonics		∅ 130 mm
		∅ 160 mm
Peak stress (MPa)	150	
Peak Temperature (K)	300	

dapnia cea saclay

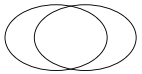

Magnetic design of a 15 T 130 – 160 mm Aperture Racetrack Coil Nb3Sn dipole magnet

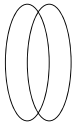

WGMDO NED

130 mm aperture – 15 T = quench field

Magnetic field aspect with quench margin = 0%

	Main field (T)	I (kA)	Peak field (T)	PF/MF	Quench margin (%)	L (mH/m)	E (MJ/m)
Ellipse	**14.74**	**22.399**	**15.46**	**1.049**	**0**	**16.64**	**4.8**
Cos θ	14.31	26.31	15.29	1.068	0	8.71	3.013
Slot	14.03	15.825	15.28	1.089	0	27.15	3.439
	13.92	21	15.3	1.099	0	15.22	3.356

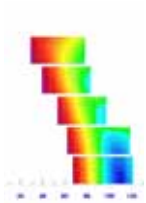

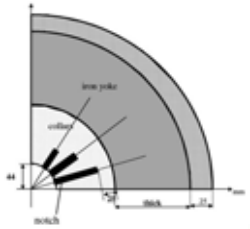

130 mm aperture – 15T = quench field

Coil geometric dimensions

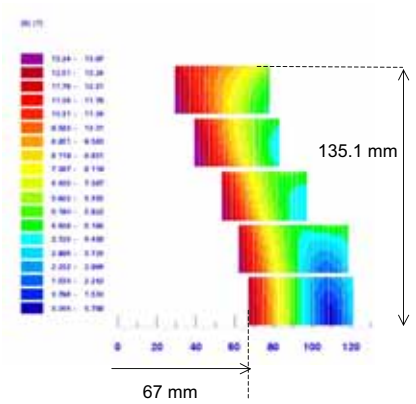

	96 turns
5	19 turns
4	**17 turns**
3	17 turns
2	22 turns
1	21 turns

130 mm aperture – 15 T = quench field

Electromagnetic forces aspect – comparisons QM = 0%

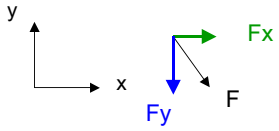

$$Px = \frac{\sum_{numbercond} Fx > 0}{S}$$

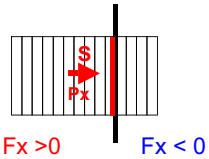

Design	Main Field (T)	I (kA)	Total Fx (MN/m)	Maximum average stress (MPa)
Ellipse	**14.74**	**22.399**	**28.36**	**141**
Cos θ	14.31	26.31	20.9	214.8
Slot	14.03	15.825	20.9	140.44
	13.92	21	19.8	139.02

130 mm aperture – 15 T = quench field

Yoke geometric dimensions

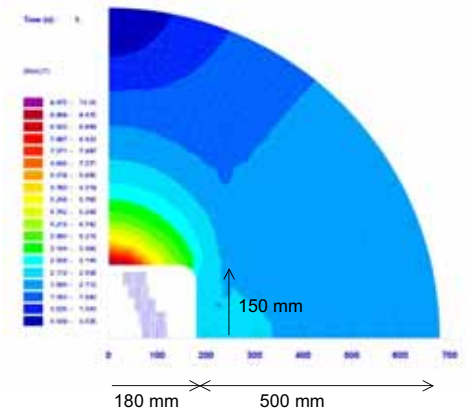

160 mm aperture – 15 T = quench field

quench margin = 10%

Design	Main field (T)	I (kA)	Peak field (T)	PF/MF	Quench margin (%)	L (mH/m)	E (MJ/m)
Ellipse	13.375	18.281	14.029	1.049	10.8	30.16	5

Design	b1	b3	b5	b7
Ellipse	10^4	0.09	-0.05	0.008

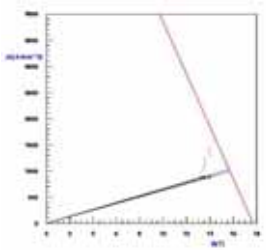

Total Fx (MN/m)	28.67
Fy (MN/m)	-5.59
Pxav max (MPa)	-124.3
Pyav max (MPa)	-90.4

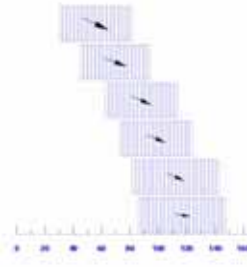

130 mm aperture – 15 T = quench field

Magnetic field aspect with quench margin = 10%

Design	Main field (T)	I (kA)	Peak field (T)	PF/MF	Quench margin (%)	L (mH/m)	E (MJ/m)
Ellipse	13.32	19.983	13.976	1.049	10.1	16.92	3.38

Design	b1	b3	b5	b7
Ellipse	10^4	0.004	0.004	-0.0008

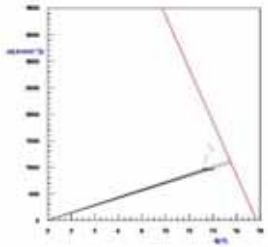

Total Fx (MN/m)	23.25
Fy (MN/m)	-4.3
Pxav max (MPa)	-115.1
Pyav max (MPa)	-79.5

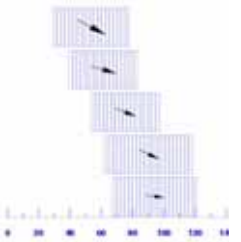

Ellipse Design Summary (QM 10%)

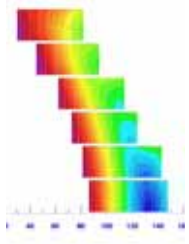

	B0 (T)	PF/B0	L mH/m	E MJ/m	Total Fx MN/m	Fy MN/m	Pxav max MPa	Pyav max MPa	Nbr turns
Ø 88	13.39	1.032	10.72	2.14	18.59	-3.45	-105.1	-63.8	78
∅130	13.32	1.049	16.92	3.38	23.25	-4.3	-115.1	-79.5	96
∅160	13.37	1.049	30.16	5	28.67	-5.59	-124.3	-90.4	127

160 mm aperture – 15T = quench field

Coil geometric dimensions

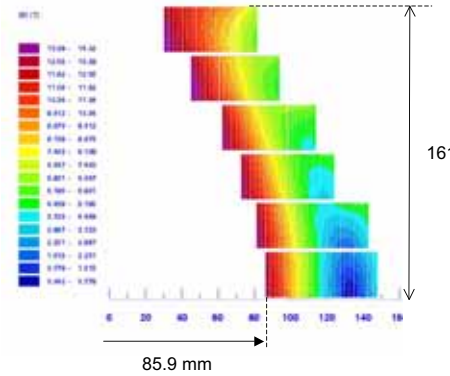

	127 turns
6	20 turns
5	**19 turns**
4	20 turns
3	20 turns
2	24 turns
1	24 turns

Mechanical properties

NED Material Table

Material	Used On	Elastic Modulus / GPa		Poissons Ratio	Integrated Thermal Expansion (293-4.2 K)
		4.2K	293K		
Nb_3Sn Conductor stack	Coil	42	30	0.3	3.9×10^{-3}
Cu Alloy	Wedges	110	110	0.3	3.6×10^{-3}
G10	Interlayer Spacer		4	0.35	6.0×10^{-3}
Kapton	Ground Plane Insulation		2.5	0.34	6.0×10^{-3}
Austenitic St/St	Laminations / Inertia Tube	215	205	0.3	2.9×10^{-3}
Magnetic Steel	Yoke	215	205	0.3	2.1×10^{-3}

Aspects revealed by the magnetic design

Advantages	Drawbacks	To investigate
- **Higher field** - **Good efficiency** with a low peak field on main field ratio - **Good homogeneity** - **Lower vertical Fy force** (compared to cosine theta design) - **Lower stresses**	- **Higher expended forces Fx** -**Higher stored energy** -**Higher inductance** -**Higher superconductor volume**	- **3D** : with coil ends - **Protection** because of the high inductance

General Model Mesh

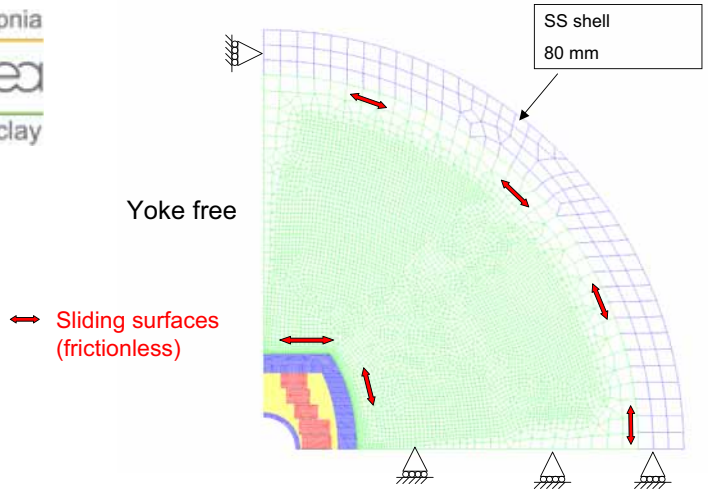

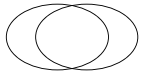

2D Mechanical Design

15 T, 130 mm Aperture

Nb3Sn Dipole Magnet

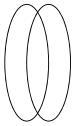

WGMDO NED

Stress Results

dapnia
cea
saclay

Sigxx prestress (MPa)

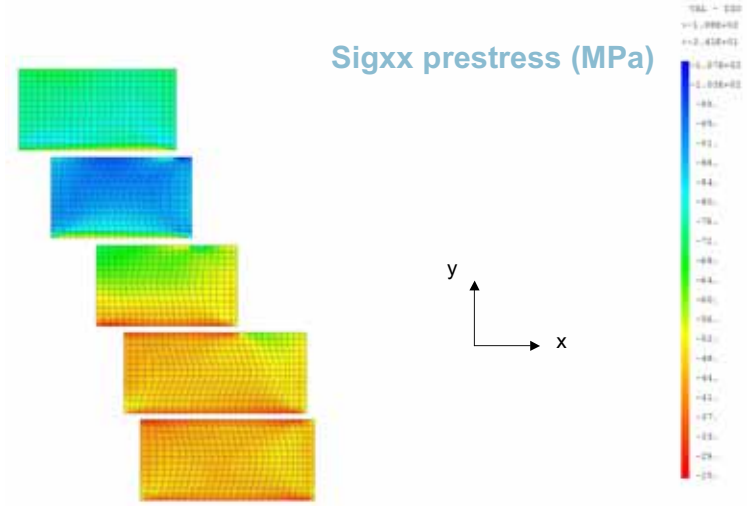

Coil Package Model Mesh

dapnia
cea
saclay

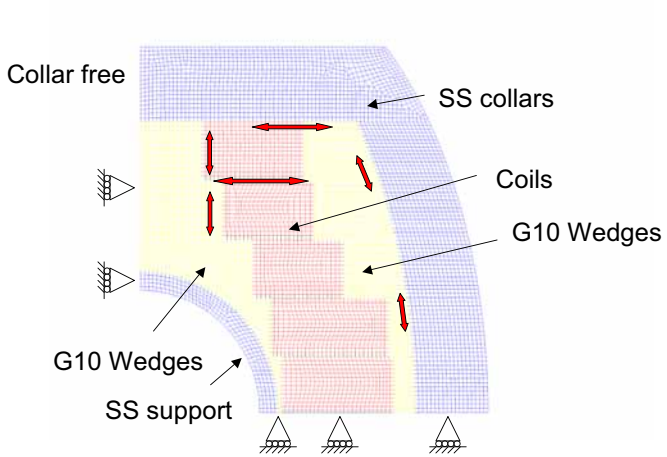

Sigxx cool down (MPa)

dapnia
cea
saclay

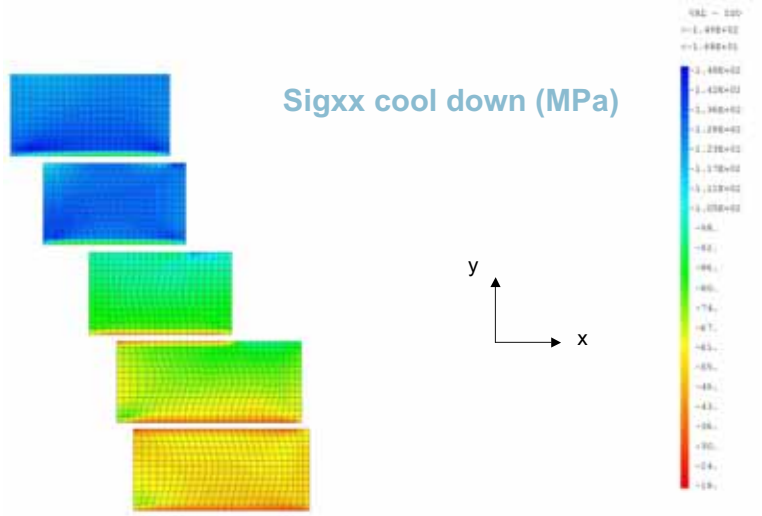

Applied Pre-stress

dapnia
cea
saclay

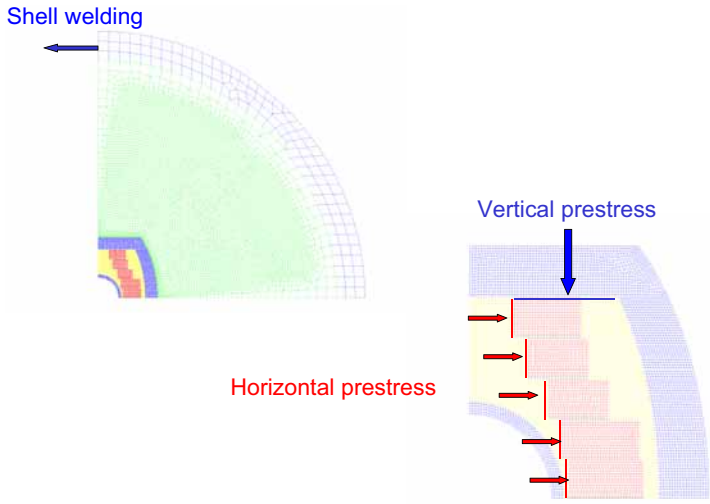

dapnia
cea
saclay

Sigyy cool down (MPa)

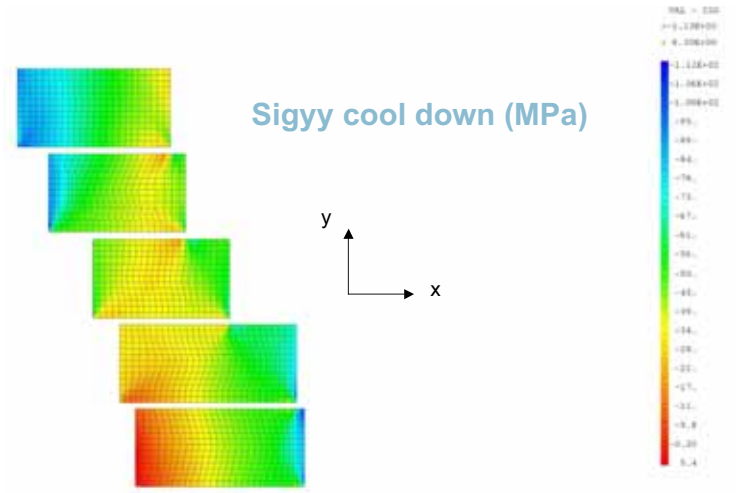

dapnia
cea
saclay

Sigxx operation (MPa)

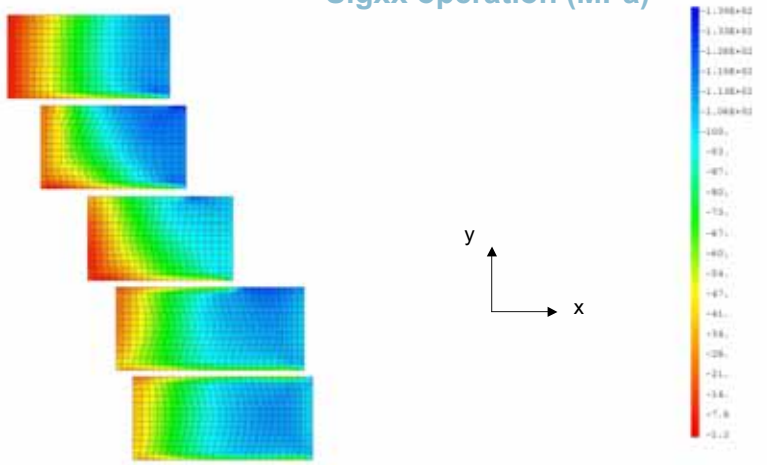

dapnia
cea
saclay

Sigyy operation (MPa)

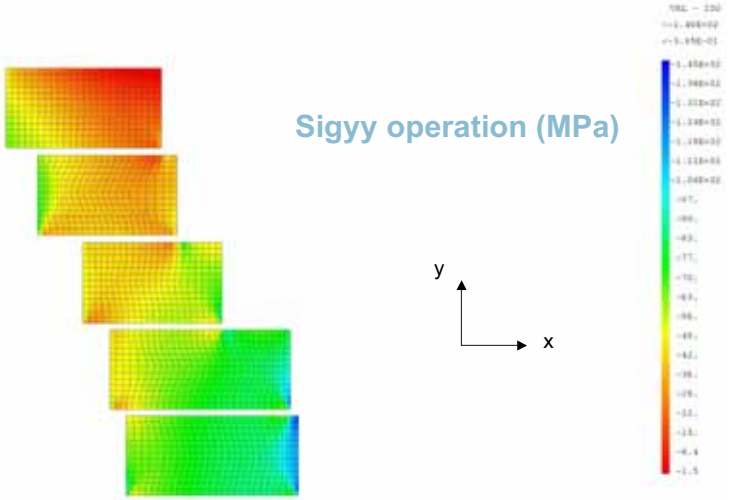

dapnia
cea
saclay

Sigyy prestress (MPa)

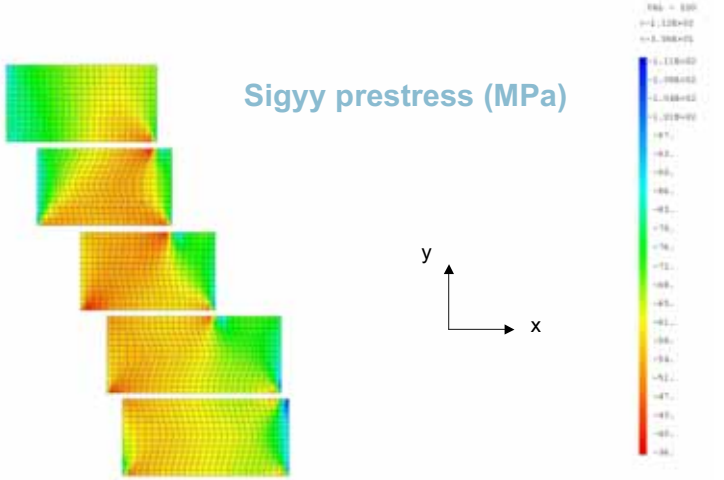

Experimental Apparatus for Prestress Studies: Subscale Dipole

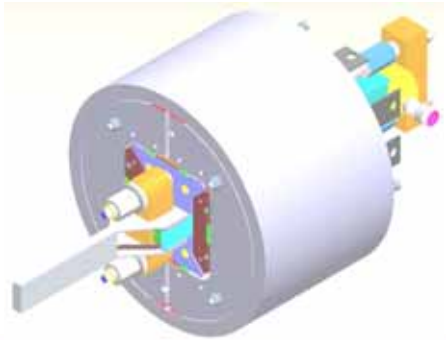

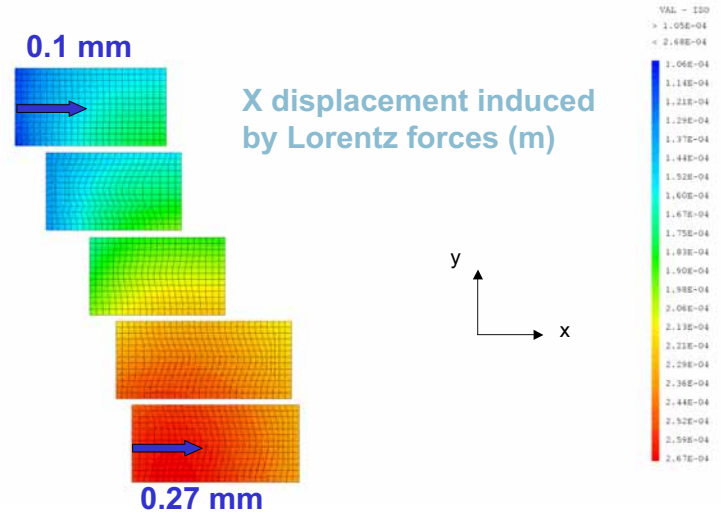

Experimental Apparatus: Subscale Dipole

Objectives

Degradation of the Nb3Sn performance with the mechanical stresses.

→ Understand the influence of a reduction of prestress (axial, azimutal/lateral, radial/horizontal) on training and quench performance :

studies are made on small Nb3Sn racetrack coils in a dipole configuration.

Context

Collaboration with LBNL (S. Caspi, P. Ferracin, S. Gourlay, R. Hafalia, G. Sabbi)

- Racetrack coil delivery: LBNL (Nb3Sn double pancakes)
- Design of a new external mechanical structure : collaboration between LBNL and Saclay
- Mechanical Structure Manufacturing: CEA Saclay
- Assembly : LBNL
- Tests : LBNL May/July 2006

Aspects revealed by the mechanical design

Advantages	Drawbacks	To investigate
- **Manageable vertical & horizontal stresses** - **in larger aperture** - **Reduce the need for intermediate supports** - **Lower vertical Fy force** (compared to other designs) **Lower and uniform stresses**	-**Large horizontal force** -**Stress issues transfer:** from y-direction to x-direction - **Need of an internal support** to prevent the coil from bending **Reduced aperture**	-**Optimization** of the coil package -**3D** : coil ends support, longitudinal prestress - **Optimization of the shell structure** -**Effect of the manufacturing process**

SD load line : CuAl island

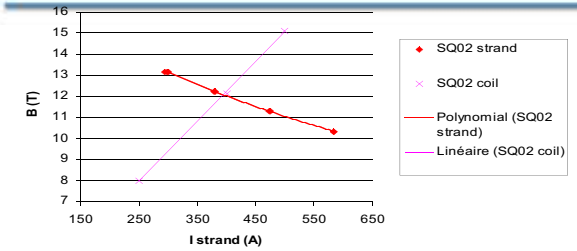

I_{ss} = 8000A
B_0 = 10.3 T
B_{end} = 12.13 T
$F_{z/end}$ = 80 kN
σ = 130 MPa

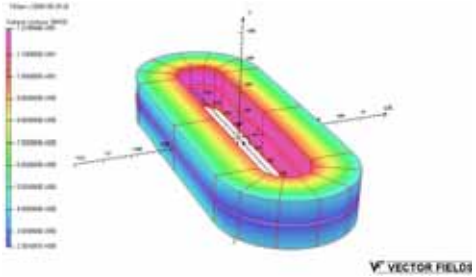

Inspired by the LBNL Subscale Magnet (SM)

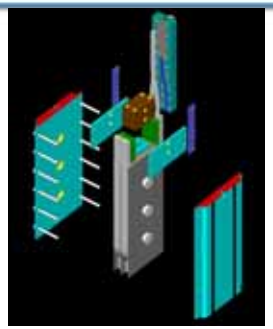

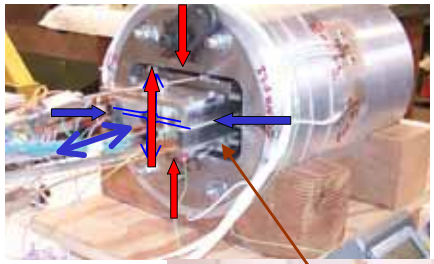

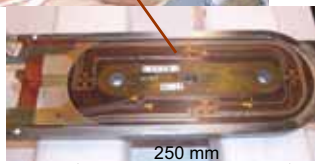

-Small "racetrack" coils Nb_3Sn (double pancake winding around an iron or CuAl pole piece)

-Tested in a common coil configuration: applied prestress in the vertical direction through bladders and keys

Add the possibility to test the coils in a dipole configuration

RR Hafalia et al, An Approach for Faster High Field Magnet Technology Development, IEEE Transactions on Applied Superconductivity, vol. 13, no 2, June 2003

SD load line : iron island

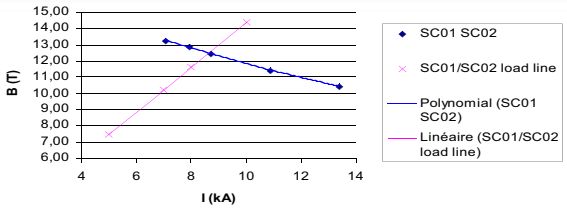

I = 8000A
B_0 = 11.1 T
B_{end} = 11.65 T
$F_{z/end}$ = 70 kN
σ = 130 MPa

I_{ss} = 8500A
B_{end} = 12,4 T

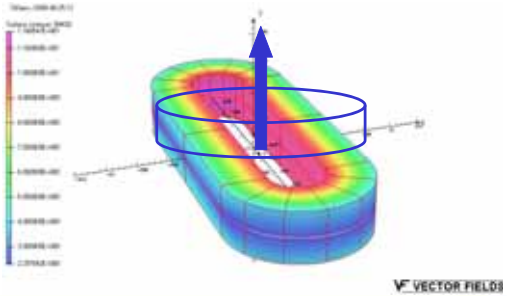

Subscale Dipole

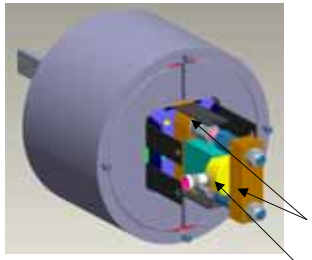

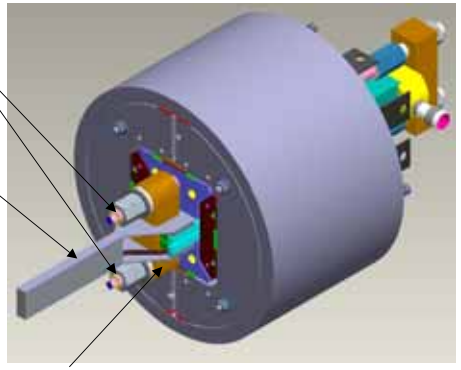

Conclusion

dapnia

cea

saclay

- Compact high field/large aperture accelerator magnet design are <u>also</u> limited by stress and force issues :
  - ➢ Proposition of new designs to manage the stress/force issues.
  - ➢ Reduction of the winding overall current density (either by reducing the conductor current density and/or introducing a structural network to intercept the forces)
- We need to understand the role of the prestress in Nb3Sn coils, in order to reduce the peak stresses.
  - ➢ Proposition of new experiments

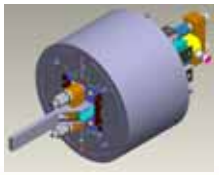

HFDA Magnet design

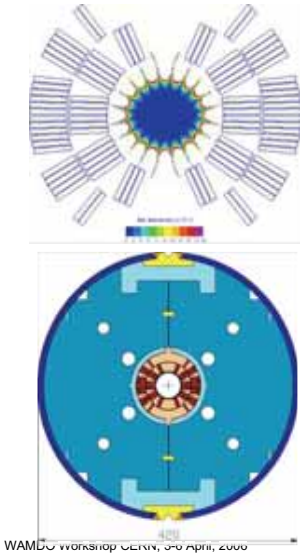

Common features:

- 2-layer shell-type coil;
- 43.5 mm bore, cold iron yoke;
- Same cable dimensions.

Major differences:

- HFDA02-04 → 1-mm MJR strand;
- HFDA05-06 → 1-mm PIT strand;
- HFDA02-03 → 25 μm stainless steel (SS) core between the strands;
- HFDA04-06 → no SS core.

Field quality of Nb_3Sn accelerator magnets

V. Kashikhin for High Field Magnet Group

April 6, 2006

Measurement convention

- A 250 mm probe was utilized in HFDA02-04/06 and a 43 mm probe was used in the HFDA05. All the probes are 25 mm in diameter.
- The field harmonics were represented by the following expansion:

$$B_y + iB_x = B_1 \times 10^{-4} \sum_{n=1}^{\infty} (b_n + ia_n)\left(\frac{x+iy}{r_0}\right)^{n-1}$$

- A probe centering correction was performed by zeroing the unallowed by the dipole symmetry a_8 and b_8.
- The main field was assumed to be pure normal (no skew dipole component) and a corresponding field angle was assigned.
- All harmonics are reported at r_0=10 mm.

Introduction

- Five nearly identical shell-type dipole models (HFDA02-06) were built and tested.
- One magnet, HFDC01, with common coil geometry was built and tested
- The test offered a unique opportunity of systematic study of the field quality in Nb_3Sn accelerator magnets.
- The field quality was measured under various conditions and compared with the theoretical predictions.

Corrective actions

Action:

- a thick steel plate was introduced between two half-coils of HFDA04 during the heat treatment.

Result:

- the normal quadrupole component was improved;
- the skew quadrupole got larger, possibly due to the opposite half-coil orientations with respect to the gravity vector during the coil heat treatment.

Action:

- the half-coils of HFDA05 and HFDA06 were reacted and impregnated individually with the same orientation relatively to the gravity vector.

Result:

- the harmonic measurements in HFDA05/06 (except for a_2 in 06) magnet showed the best geometrical field quality among HFDA models.

Geometrical harmonics

The geometrical harmonics were determined as the average values between up and down ramps at 3 kA in the body.

Geometrical field harmonics, 10^{-4}

n	HFDA02		HFDA03		HFDA04		HFDA05		HFDA06		HFDC01	
	a_n	b_n	a_n	b_n	a_n	b_n	a_n	b_n	a_n	b_n	a_n	b_n
2	-9.6	4.1	1.93	-7.13	12.56	0.75	-0.45	4.59	-8.22	-3.63	-3.27	0.16
3	-0.2	-4.0	0.81	-2.36	-0.25	8.28	0.90	1.16	1.10	3.78	0.23	9.70
4	-1.1	0.4	-0.75	-0.19	0.06	0.16	-1.97	0.79	-1.31	-1.52	-0.34	0.02
5	0.3	0.0	0.04	-0.53	0.11	-0.34	0.26	1.94	0.25	1.2	0.04	0.72
6	0.3	0.0	0.03	0.12	-0.01	0.02	-0.28	0.22	-0.39	-0.30	0.00	-0.01
7	-0.1	0.1	0.03	0.04	-0.03	0.49	0.03	0.29	0.08	0.17	-0.00	-0.06
9	-0.2	-0.2	0.04	-0.01	-0.07	-0.15	-0.01	0.10	-0.1	0.07	-0.00	-0.03

HFDA02-04/06 had large skew or normal quadrupole components.

Possible explanation → top-bottom or left-right asymmetry in the coils due to heat treatment of the assembled two half-coils with no initial prestress.

Persistent current effect

- The persistent current effect was similar and well predictable in HFDA02-04 made of 1-mm MJR strand.
- In order to reduce the persistent current effect, simple passive correctors based on thin iron strips were developed and successfully tested.
- The passive correction has effectively reduced the sextupole variation in the field range of 1.5-4 T during the field up-ramp from $19.4 \cdot 10^{-4}$ to $3.7 \cdot 10^{-4}$.

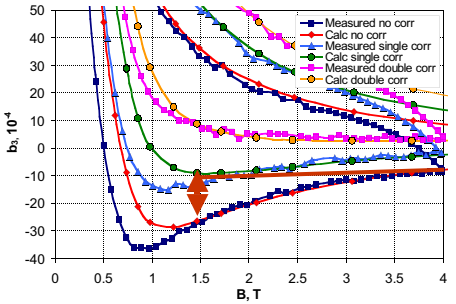

Iron strips

Slice studies

HFDA02 coil was cut in the straight section (with the yoke in place) and the block coordinates were measured by an optical inspection system.

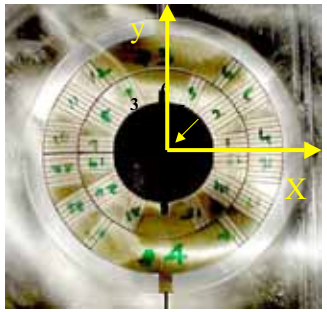

Block deviations from the nominal position

Block #	Radial, mm		Azimuthal, mm		Inclination, deg	
	Δ	σ	Δ	σ	Δ	σ
1	-0.375	0.11	0.102	0.173	0.877	0.476
2	-0.213	0.115	0.161	0.12	1.221	0.391
3	-0.19	0.076	-0.129	0.09	0.941	0.272
4	-0.288	0.09	0.113	0.122	0.444	0.691
5	-0.234	0.062	-0.252	0.129	1.22	0.367
6	-0.094	0.012	-0.285	0.092	0.511	0.22

Major findings:

- Radial position → systematic shift towards the center in all the blocks;
- Azimuthal position → significant random deviations from the nominal in all the blocks;
- Midplane gap → larger than the nominal by 200±150 μm.

0.7-mm MJR strand

Sextupole @10mm in HFDC01 magnets

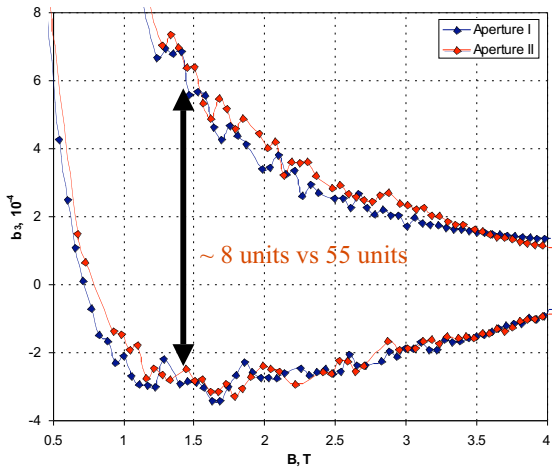

- **The persistent current effect was ~7 times lower in the HFDC01 common-coil magnet than in HFDA02-04 magnets due to the specific coil layout.**
- **However, the amplitude of field oscillations was lower by only a factor of ~1.5 that is consistent with 30% smaller d_{eff}.**
- **Thus the effect of flux jumps can not be reduced by simply correcting the persistent current effect.**

Flux jump effect

- Conductor instabilities are affecting also the field quality.
- While it may not be relevant for the short magnet development, a successful accelerator magnet needs to demonstrate the "accelerator" field quality along with the reliable quench performance.

Unallowed harmonics

Quadrupole in HFDA04 magnet

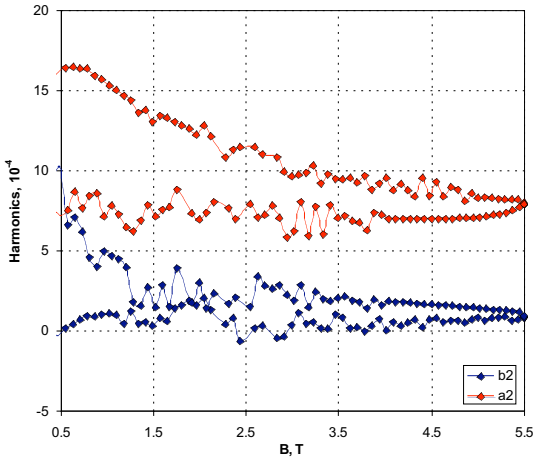

- **Large fluctuations in the normal and skew quadrupole components of HFDA04 dipole magnet are observed.**
- **The flux jumps can happen in any region of the coil under favorable conditions (when the stability criterion is violated).**
- **They are not necessarily complying with the magnetic field symmetry (e.g. dipole) and can produce fluctuations in allowed and unallowed harmonics.**

1-mm MJR/PIT strands

Sextupole @10mm in HFDA magnets

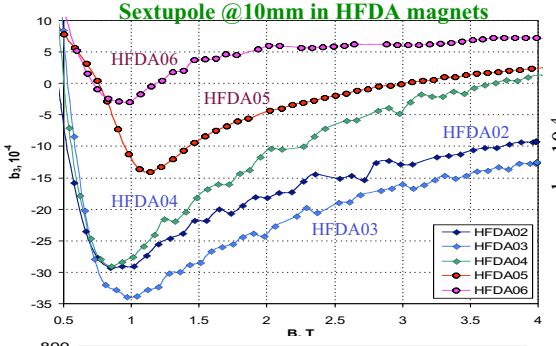

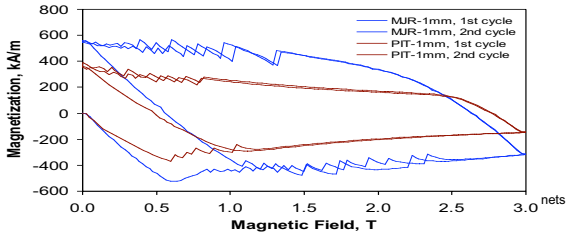

Noise in the sextupole

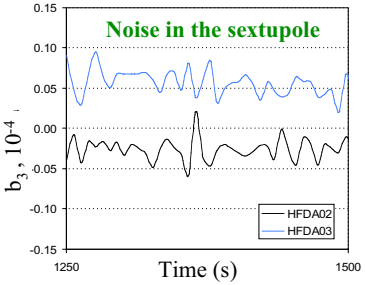

- **What looks like "noise" in HFDA02-04 measurements is actually reflection of the flux jumps in the field quality.**
- **The noise level was ~50 times lower as shown in the plot above.**

Sextupole decay

- The decay measurements were performed at constant currents around 1.5 T field after a pre-cycle with 20 A/s.
- There was no significant b_3 variation during 30 minutes in HFDA02-04, though a periodic oscillation in HFDA04 and HFDA06 was observed.
- There was a distinct sextupole variation in HFDA05 that decayed by 8 units during the first 30 minutes at current plateau.
- More data are needed to constrain a model for the dynamics effects in Nb3Sn magnets

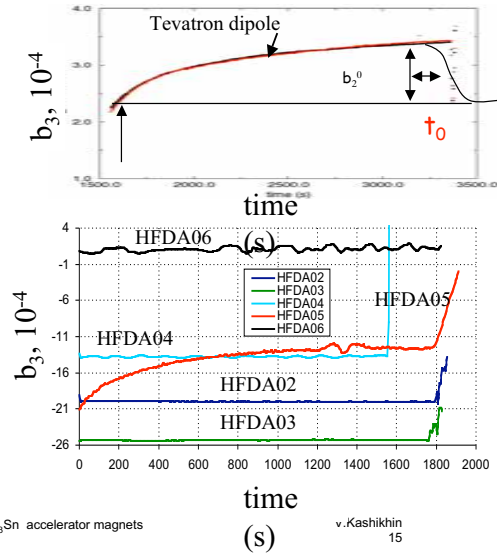

Reproducibility

HFDA02/05 consecutive cycles

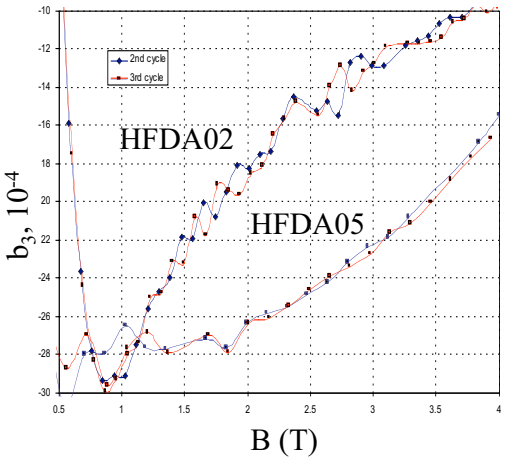

- The field quality is presented for two consecutive current cycles in HFDA02/05 magnet.
- Harmonic fluctuations are not repeatable from cycle to cycle.
- They can not be predicted or measured in order to apply corresponding correction using passive or active correction system.
- The only way to improve the field quality is to reduce the flux jump amplitude.

Conclusion

- Five nearly identical short Nb_3Sn dipole models were fabricated and tested at Fermilab. First systematic studies of field quality in Nb3Sn magnets were performed.
- The geometrical harmonics were determined by the magnet fabrication tolerances. Noticeable improvements of the low-order geometrical harmonics were achieved after some optimization of the coil fabrication process. There is also a room for further improvements.
- The persistent current effect was well predictable in all the magnets. A passive correction technique was developed and successfully tested.
- The measured amplitude fluctuations of the low-order harmonics in the models due to flux jumps is in the order of 1-2 units. These random fluctuations may not effect the beam dynamics (need to be confirmed by AP) , they will reduce the accuracy of the field quality measurements.
- The large eddy current effect observed in HFDA05 and 06 magnet is due to low interstrand contact resistance. It can be reduced by using a stainless steel core in the cables with high RRR.
- Magnetic measurements are a powerful method for magnet diagnostics – they will provide important information for LARP magnet R&D

Eddy current effect

- Coil magnetization in HFDA05/06 was different for the first three magnets.
- A similar behavior was observed in SSC dipole DCA312 with a low interstrand resistance.
- Major difference between the first three and the last two magnets: RRR_{HFDA04}~5, RRR_{HFDA05}~110.
- Δb_3 extrapolated to dI/dt=0 is consistent with the expected persistent current effect.

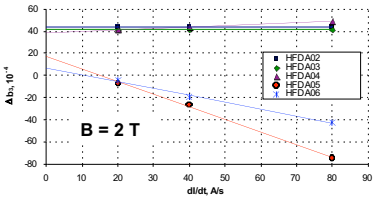

HFDA02-04

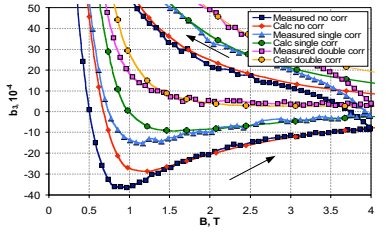

HFDA06

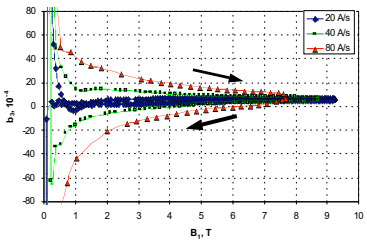

Backups

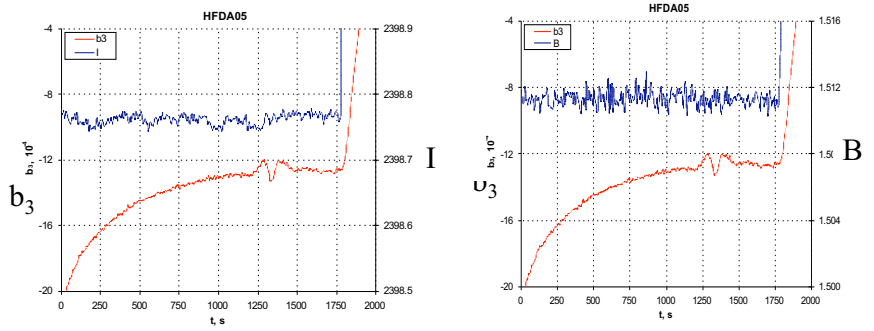

b_3 I b_3 B

Time (s)

HFDA06

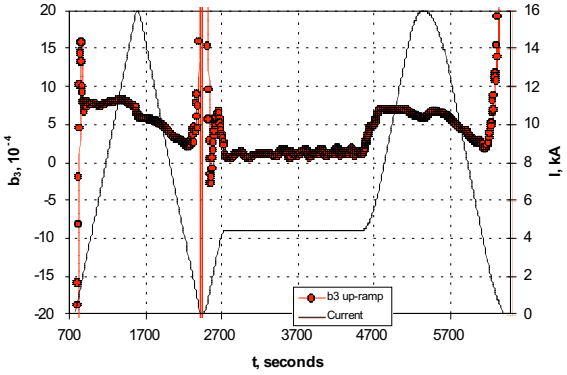

Outline

- **The Problem**
  - Various Instability Manifestations
  - Observations to be Explained and Harmonized
- **Explanations/Models**
  - Underlying Unity of the Problem
  - Break-up into three Regimes for Present system
  - Application of Models
- **Solutions/Comments**
  - RRR vs d_{eff}
  - RRR Solution in a potted magnet (*Heat diffusion vs time constant)*
  - Prediction of I_s?

REGIMES OF INSTABILITY IN Nb_3Sn CONDUCTORS

[or]

RRR vs d_{eff}

M.D. Sumption, E.W. Collings
Funded by DOE HEP Grant DE-FG02-95ER40900

WAMDO, Geneva, April 2006

Manifestations of Instability

- Low Field
- High Field
- Intermediate Field

Importance of Strand Stability and relationship to the Magnet Load Line

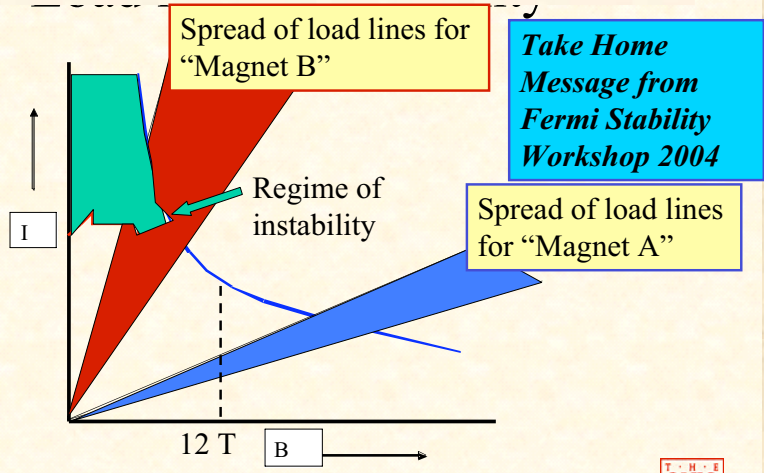

Low Field *M-H* Observations/Questions

- **Observation 1:** Fine (Partial) FJ near origin
- **Observation 2:** Larger FJ at slightly higher fields, for less stable strands the FJ can be complete
- **Observation 3:** From S&B, Magnetization limit (of $J_c d_{eff}$ limit, not strongly (hardly) influenced by cooling (see ***No***; Sumption, IEEE, ***Yes, Slightly;*** Goldfarb, IEEE)
- **"Ron Scanlan Criterion for Stability":** Partial FJ OK, full FJ "not OK"
- **Question 1:** What is the origin and upshot of tendency for Fine and Partial FJ near the origin, larger ones further out?
- **Question 2:** How good is the Ron Scanlan Stability Criterion – which is, in it's new form, ***Steve Gourlay's Question – how do I predict I_s?***

Low Field Flux Jumping in *M-H* loops

Two varieties—seen at OSU, NIST, Fermi

(a) Strands with Complete FJ

(b) Strands with Partial Flux Jumps

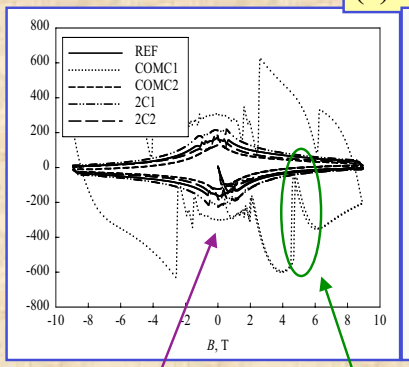

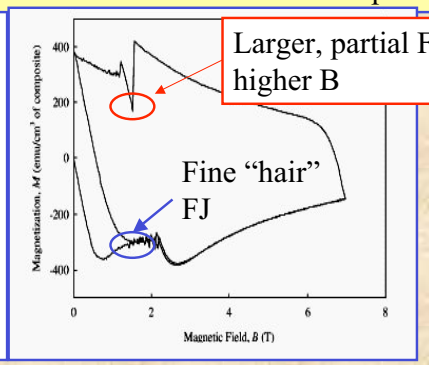

Larger, partial FJ at higher B

Fine "hair" FJ

Fine "hair" FJ at lower fields

Near complete FJ at higher fields

High Field *I-V* with very small over-voltage limits –Marginal stability

Seen by all measuring J_c in High Performance Sn – Fermi, LBNL, BNL, OSU, NIST, others

Obs 4: Strand quenches during early part of *I-V* SC transition

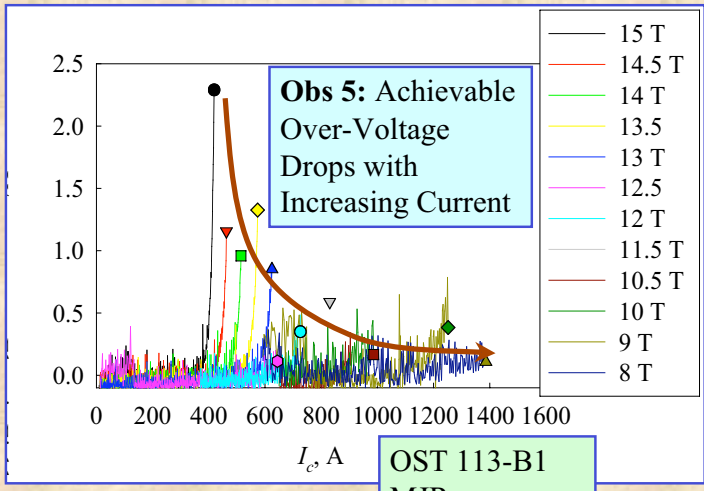

Obs 5: Achievable Over-Voltage Drops with Increasing Current

OST 113-B1 MJR

Magnetization ($\propto J_c d_{eff}$) Limit

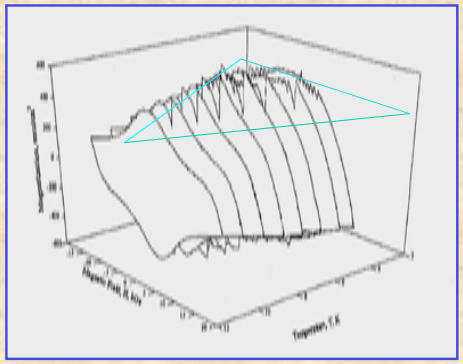

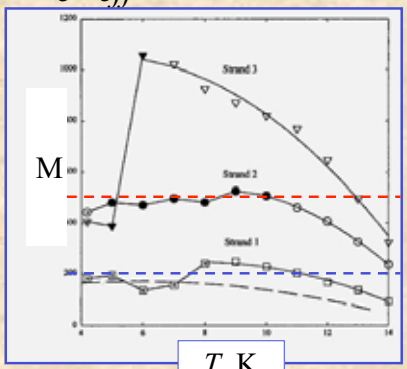

Straight from Swartz and Bean, above some limiting magnetization, Flux jumping occurs – limit may vary for various wires

$$M_{\max} = \left(\frac{0.2}{3\pi}\right)\sqrt{10^9\left(\frac{3}{\pi}\right)\beta_{sc}T^3\Delta T_0}$$

Sumption, Collings, IEEE Trans. Mag 11, 2001

Not strong Function of cooling

Or – $M \propto J_c d_{eff}$ – *so as* $J_c \uparrow$, $d_{eff} \downarrow$

Observations/Questions

- **Q1:** What is the origin Fine and Partial FJ near the origin, larger ones further out?
- **Q2:** What level of FJ indicates dangerous Instability – ***how do I predict I_s?***
- **Q3:** How relevant are high Field Instabilities to I_s and stability generally?
- **Q4:** How can we have dangerous Instabilities in *I-V* at *B* where no *M-H* FJ exist?
- **Q5:** How are the various instabilities connected? Are they Dynamic, Adiabatic?
- **Q6:** How do we predict and/or improve I_s.

Observation 7: Dangerous Instabilities in I-V at field where no *M-H* FJ exist

Intermediate Regime

Flux Jumping Below 2.5 T

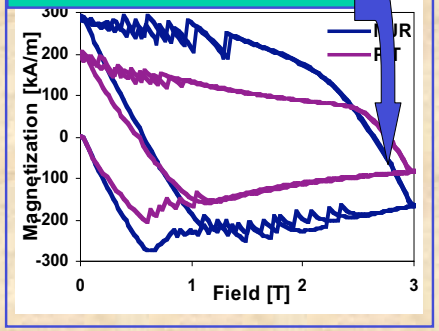

Observed initially at Fermilab (Barzi)

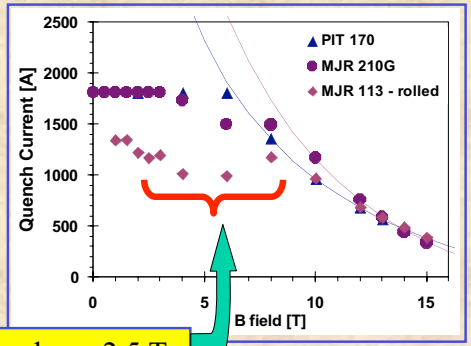

E. Barzi from NIMS 2004

But, Instabilities above 2.5 T

-- up to 8 T, then OK

The Three Regimes

Low Field Regime: ***Magnetic Flux Jump Dominated, <u>Frequently Partial Flux Jumping</u>***

Influence of transport current secondary, shows up in *M-H* loop measurements – Frequently partial Flux jumping ("Scanlan" Crit)

High Field Regime: ***Current Dominated***

Controls *I-V* Measurements, Determines difference between so-called "stable" and "unstable" strands during 12 T J_c measurement

Intermediate Field Regime: ***Strong Field and Current Interaction – Frequently <u>Full Instability</u>***

Not the only magnet instability source, but for strand driven magnet instabilities, this is the ***Origin of "unexpected" Instabilities*** in Nb_3Sn Magnets

V vs *B* Type Instabilities at both low and Intermediate fields

Low Field *I-V* Instabilities Flux Change Dominated

High Field *I-V* Instabilities No apparent FJ in *M-H* only- - mixed current/*B* event

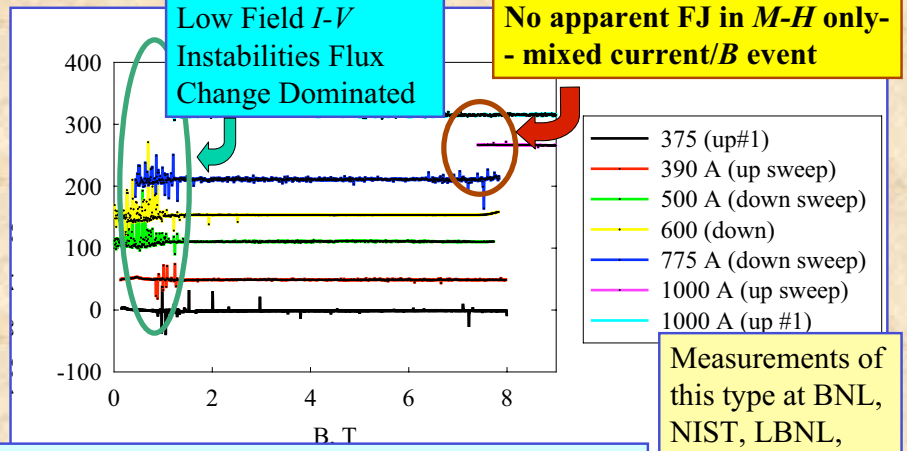

Measurements of this type at BNL, NIST, LBNL, OSU

Observation 8: Partial FJ-IV intermediate field Instabilities can also exist (where no M-H FJ does)

Low field Regime-I

- At low fields, Nb_3Sn strands are usually far away from real FJ stability – too far for cooling to help. Thus, low field FJ while not ***necessarily adiabatic, might as well be – the energies are too great.*** (see below)
- However, the heat capacity is large in this regime – allowing partial flux jumps. The series of partial Flux jumps which define the low field M-H loops limit the flux motion induced energy
- This, this regime can be adequately treated (in retrospect) with a Swartz and Bean mode, but with enthalpy considered, which leads to the existence of a ***partial flux jump regime***

One Problem, Three limits

- These three cases are various limiting cases of an underlying electromagnet instability
- Not Related at all to the traditional Stekly Stability Criterion
- The Basic Problem is this, in the presence of small *Q* perturbations:

Heat Gen = Heat Capacity + Cooling

Heat Generation term comes ultimately from Electric Fields acting on currents – either *directly* or as *flux motion*

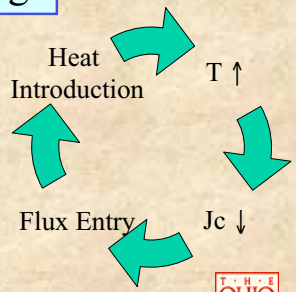

Low Field Instability II

- **Q1:** What is the origin Fine and Partial FJ near the origin, larger ones further out?

  a – at lower fields T_c is higher, thus the Enthalpy to T_c is greater -- allowing FJ to recover.

  b- at higher fields, J_c is dropping faster, T_c is reduced, FJ more catastrophic.
- **Q2:** What level of FJ indicates dangerous Instability – ***how do I predict I_s?***
- ***We must keep our eyes on the steepest load line. Fields-currents below this are not relevant – leads us to intermediate regime***

Higher Field Regime (Strand Testing)

$$JA_{SC}\delta E < Ph_i\delta T$$

$$\left[E_{1-V} + d_{eff}\frac{dB}{dt}\right]\left(\frac{nd}{4h_i}\right)\frac{dJ}{dT} < 1$$

Heat Generation

Must assume non-adiabatic conditions -- otherwise strands run in non-zero *E*-regime will generate heat to quench always

Klimenko, Mints, Martovetsky Formulation

Predicts achievable over-voltages

Magnetic term "ignored" at higher fields

Q3: How relevant are high Field Instabilities to I_s ?– *A: Connected, but not very predictive*

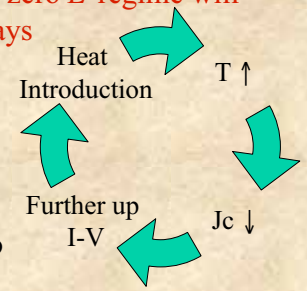

Starting Point – Heat Balance

$\Delta Q_s + \Delta Q_g$ = Heat Capacity term + Cooling term

Heat Perturbation

Heat Generated by Flux incursion

Heat absorbed by strand (delta T)

Heat removed by cryogen

In order to get a tractable solution , this is frequently simplified –

Vadim, Zlobin (following Hancox, others) have ignored cooling term, but integrated Heat Generation and Heat capacity over temperature range – brings out enthalpy effects and defines limited stability regime

A second approach (following Wilson) assumes averages, does not integrate – but includes dynamic effects

Intermediate Regime

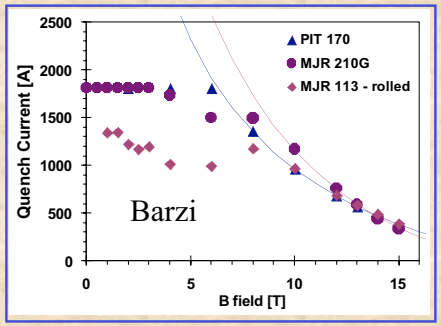

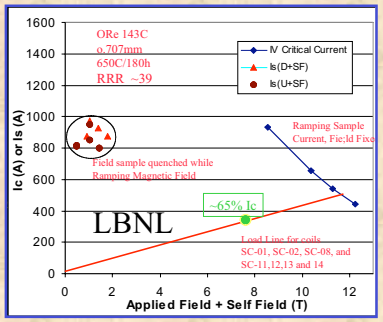

It will turn out to be useful to consider

1. Enthalpy considerations, following **Vadim and Zlobin** (Fermi – after Hancox), especially in the 0-4 T range.
2. Dynamic stabilization effects – especially at 4 -8 T, say

Which is more important may depend on the slope of the steepest load line

Enthalpy Approach – Fermilab

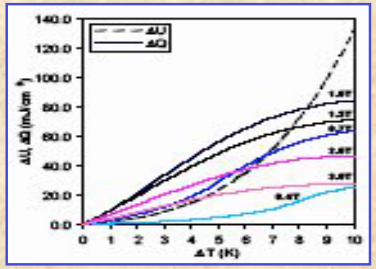

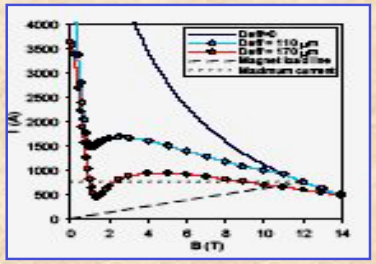

- Fermi focusses on adiabatic approach, includes enthalpy
- Follows Hancox, others, parallels YBCO work by Mints, Muller, allows map of full and partial FJ regimes
- Fermilab approach is Engineering approach, aimed not at new physics, but making quantitative predictions.
- Good point – describes very low field regime and partial instability
- Not descriptive for observed RRR influences – must include dynamics

Intermediate Field Regime II

- Field and Current Driven Instability
- Must include influence of Enthalpy: **Vadim Kashikhin, Zlobin, e.g., IEEE --5LB02 ASC**
- Must include **Dynamic Effects** – to describe RRR-Induced Stability Improvement in Strands (Cooley, BNL)

Question: What's the influence of RRR vs d_{eff}

Results: Slab Conductor, with Cu stabilization layers, with current

$$\beta_s = \frac{\mu_0 \lambda^2 J_c^2 \left(d_{eff}/2\right)^2}{\gamma C \Delta T} = \frac{3}{(1+3i)}\left\{1 + \frac{4}{\pi^2}(1+i)^2 v\right\}$$

Here $i = I/I_c$, and v is a cooling parameter

Centerline shift (increases flux motion and energy

Time constant increase due to longer current decay

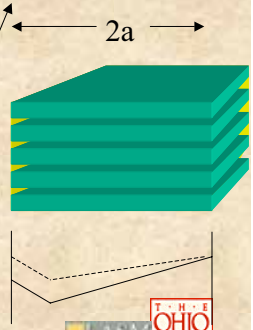

Partial Instabilities and Enthalpy

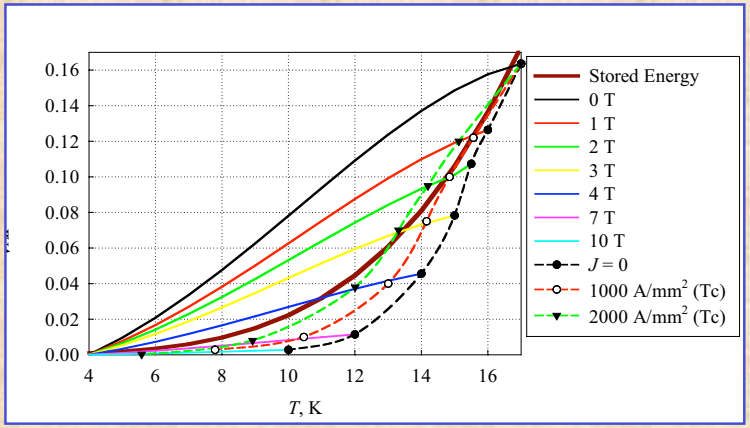

Fermi-like calculations – showing growth of instability with current

Time constants $\Delta Q_s + \frac{\mu_0 \lambda J_c \lambda \Delta J_c a^2}{3} = \gamma C \Delta T + \frac{h \tau_J \Delta T}{a}$

Note: When the SC currents are reduced, eddy currents in the Cu flow to continue shielding; τ_J is the time is takes for eddy currents in the Cu to decay.

For a slab this is given by $\tau = \frac{4a^2}{\pi^2 D}$

But for a MF strand, a shielding time constant is quite different

$$\tau = \frac{\mu_0}{2\rho_{eff}}\left(\frac{L_p}{2\pi}\right)^2 \qquad \frac{1}{\rho_{eff}} = \frac{1}{\rho_t} + \frac{w}{a\rho_m} + \frac{aw}{\rho_m}\left(\frac{2\pi}{L_p}\right)^2$$

$$\rho_{eff} \approx \rho_m$$

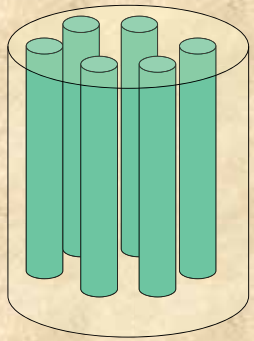

The inter-bundle time constant is dominant

Simple approach (Wilson): Slab-no current

$$\underset{1}{\Delta Q_s} + \underset{2}{\frac{\mu_0 \lambda J_c \lambda \Delta J_c a^2}{3}} = \underset{3}{\gamma C \Delta T} + \underset{4}{\frac{h \tau_J \Delta T}{a}}$$

1 Heat Perturbation

2 Heat Generated by Flux incursion

3 Heat absorbed by strand (delta T)

4 Heat removed by cryogen

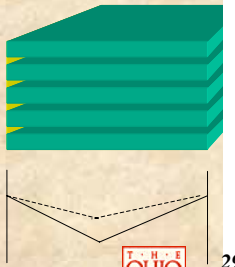

ΔJ_c is the change in J_c due to the heat pulse

a is the slab width

γC = volumetric specific heat

h = heat transfer coefficient

τ_J = time constant for shielding current decay

Influence of RRR vs d_{eff} for various cooling Conditions

Then for ***high h*** (liquid Helium bath), $h = 5 \times 10^4$ J/K m, and $\beta < 3$ **RRR** for stability

For ***Lower h***, 1000 J/K m, $\beta <$ **(3/40)(40+RRR)**

- d_{eff} control is vital, but at least out to RRR = 50, this seems to be very beneficial. If h drops significantly below 1000 J/K m, this would be less true.
- ***RRR within the strand is important, not just at perimeter***

Result for MF strand

$$\beta_s = \frac{\mu_0 \lambda^2 J_c^2 \left(d_{eff}/2\right)^2}{\gamma C \Delta T} = \frac{3}{}\left\{1 + \frac{\upsilon}{4\pi^2}\right\} \qquad \upsilon = \frac{h\mu_0}{\gamma C \rho_{\text{int } er}} L_p^2$$

$$\upsilon = \frac{40}{4\pi^2} RRR$$

Then for ***high h*** (liquid Helium bath), $h = 5 \times 10^4$ J/K m, and $\beta < 3$ RRR for stability

For ***Lower h***, 1000 J/K m, $\beta <$ (3/40)(40+RRR)

Adding Transport Current

$$\beta_s = \frac{\mu_0 \lambda^2 J_c^2 \left(d_{eff}/2\right)^2}{\gamma C \Delta T} = \frac{3}{(1+3i)}\left\{1 + \frac{4}{\pi^2}(1+i)^2 \upsilon\right\}$$

$$\beta_s = \frac{F\mu_0 \lambda^2 J_c^2 \left(d_{eff}/2\right)^2}{\gamma C \Delta T} = \frac{3}{(1+3i)}\left\{1 + \frac{\upsilon}{4\pi^2}\right\}$$

Re-work v term

Drop second i-term, decay time not enhanced

Add geometrical factor to deposition term

Thermal Transport -- h, "h_i", h_{ins}

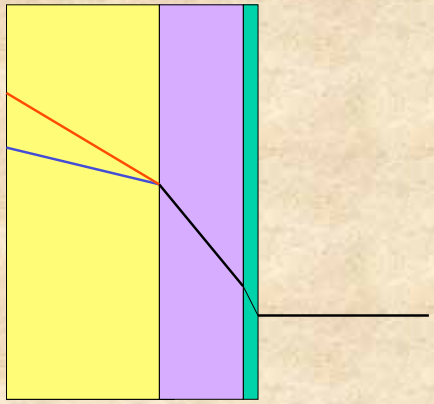

- Yellow is Cu
- Green Is surface boundary
- Purple is insulation
- Red is low RRR
- Blue is high RRR

"Cylindrical" Expression Results

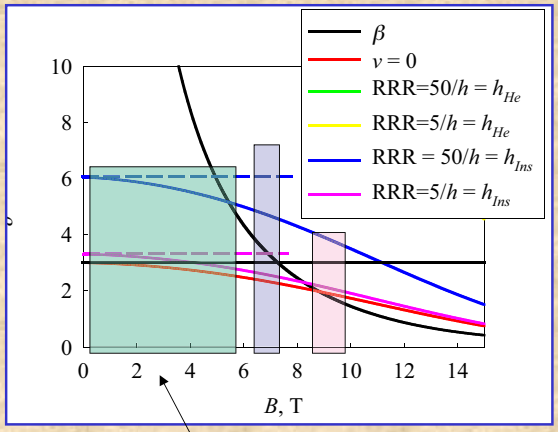

Enthalpy-related partial FJ regime

J_c = 3000 A/mm² 12 T

d_{eff} = 100 μm

B_{c2} = 25 T

f'= 15T/1588 A/mm²

Partial FJ vs catastrophic instability not addressed here – but is needed. In general, higher field events more catastrophic

Scheme for Display and Analysis

- We would like to perhaps plot on a load line graph, I vs B
- Wilson's eq is in β vs i, where $i = I/I_c$, which is doubly inconvenient, since the x-variable involves $i=I/I_c(b)$
- *However, if we set $B=fI$ or $f'J$ (a magnet load line), then we have B as the x-variable, from B and the load line I, and from J(B) the Ic.* ***This results in a usable relation.***

BNL, A. Ghosh

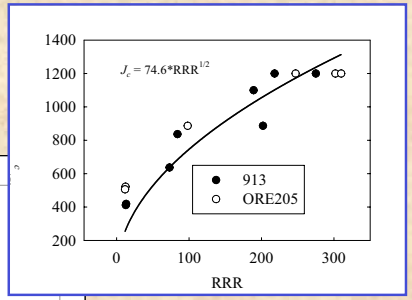

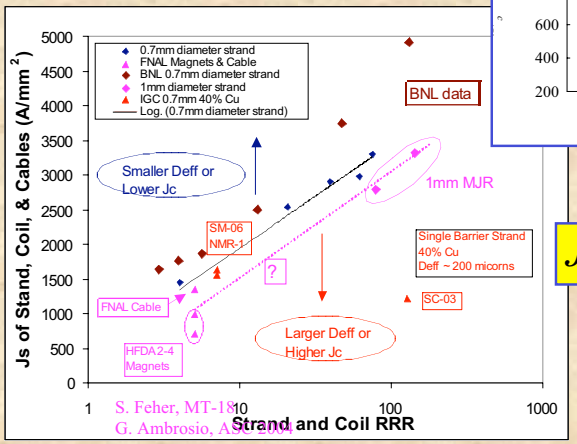

$J_s \propto (1/d_{eff})*RRR^{1/2}$

--but this simplification ignores onset of partial FJ regime --

Some Parameters

First, add in Kramer relation for J_c, set $a = R$

$$J_c = \frac{ConstB_{c2}B_{c2}^{\nu-1}}{B} b^{0.5}(1-b)^2 = Const'\frac{(1-b)^2}{b^{0.5}}$$

A 12 T J_c of 3000 A/cm² give C = 7690 A/mm²

$$J_c = \frac{C}{(B/B_{c2})^{1/2}}\left(1-\frac{B}{B_{c2}}\right)^2$$

Now use T_c-T_b = 18(1-b) - 4

λ=0.40

d_{eff} = 100 μm

B_{c2} = 25 T

f'= 15T/1588 A/mm²

Now, to make this relevant, set *B = fJ*

Resolving β vs B (or i) and I vs B

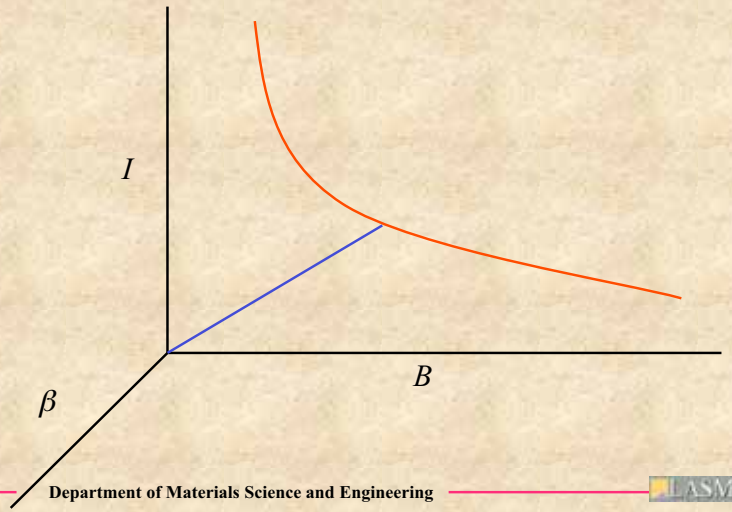

CONCLUSIONS

(1) RRR-induced dynamic stability is important – lets us squeeze out an important margin

(2) d_{eff} minimization important, especially at very low fields – BUT d_{eff} is a stand-in for magnetization

(3) RRR up to 100 is beneficial (only limited by magneto-resistance)

(4) RRR needs to be high *within the strand* – not just on the outside

(3) Flattening the J_c vs B curve would be beneficial –add Ti, push B_{c2} instead of pinning for HFM – perhaps also HT at higher T?

β For various load lines

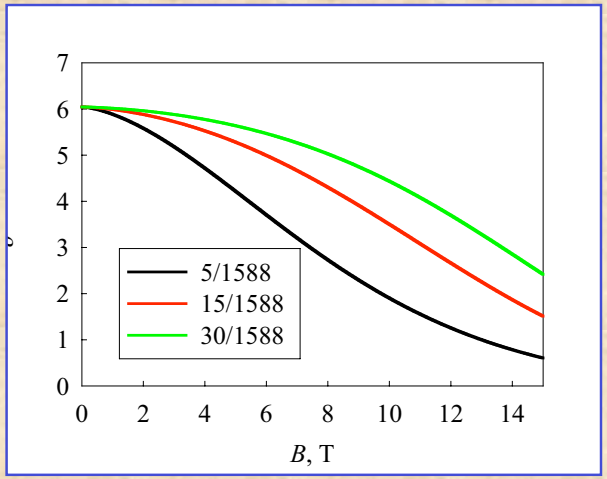

Appendix

More on Comparisons

- Since the adiabatic part of the prefactor is very close to experiment, the difference is due to a too-simplistic picture of the shielding currents – after all the filament array is relatively coarse, and current paths may not be everywhere uniform
- Nevertheless, if we de-rate for this effect, we get a useful description of the RRR effect which should have predictive power.
- Then
- Jc = 1500 A/mm2(1+RRR/20)

Load Line Again
Load lines and Stability

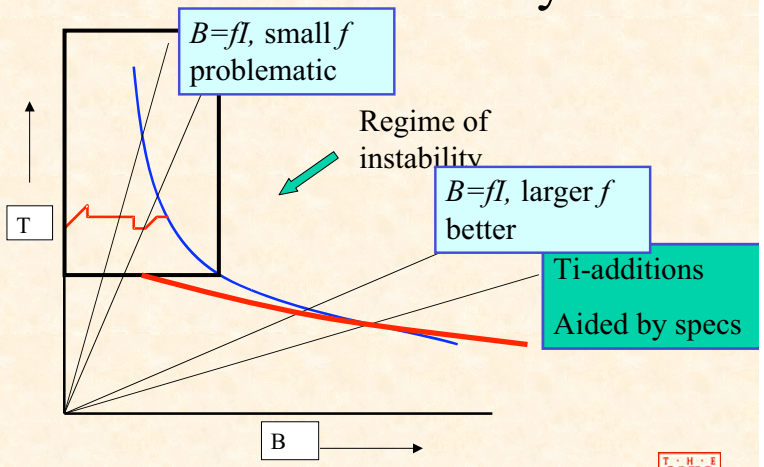

What would be useful to know

- There is utility in modifying these analytic expressions to give even more quantitative numbers – but they also allow us to make sure all relevant terms are included in analysis
- Corrections for the geometrical aspects of the flux-entry term are needed
- Emphasis on what will result in a catastrophic event, vs a partial flux jump

Comparison to Experimental Results

Starting with $\beta_s = \frac{F\mu_0\lambda^2 J_c^2 (d_{eff}/2)}{\gamma C \Delta T} = \frac{3}{(1+3i)}\left\{1+\frac{\upsilon}{4\pi^2}\right\}$ And $\upsilon = \frac{40}{4\pi^2} RRR$

We would estimate $J_{lim} \cong (1.5 \times 10^9\ A/m^2) RRR^{1/2} = 1.5 \times 10^3\ RRR^{1/2}$

Note that in the absence of the RRR effect, we would estimate a value of 1500 A/mm^2

This seems very optimistic about the influence of RRR.

How does this compare to experiment?

Thermal equilibrium

- $d_{strand}/d_{fil} > D_{mag,c}/D_{thermal,f}$ – so the strands can "get all the heat out" during the decay – ***no fat filament effects***

- The strands are not at the same temperature everywhere on the same time scale as the Cu, so ***at any given time J_c is non-uniform – but this can be treated on a average basis***

τ and the fourth term

- Typical values for τ are 10 msec for RRR = 100, and 0.5 msec for RRR = 5
- Looking at the "fourth term" we find that (based on the cooling of a cylindrical object)

$$\gamma CV\frac{dT}{dt} = \Delta Th[SurfaceArea]$$ Thus

$$\Delta Q_s + \frac{\mu_0 \lambda J_c \lambda \Delta J_c a^2}{3} = \gamma C \Delta T + \frac{h\tau_J \Delta T}{R}$$

Higher field requires new superconductor, handling immense stress loads

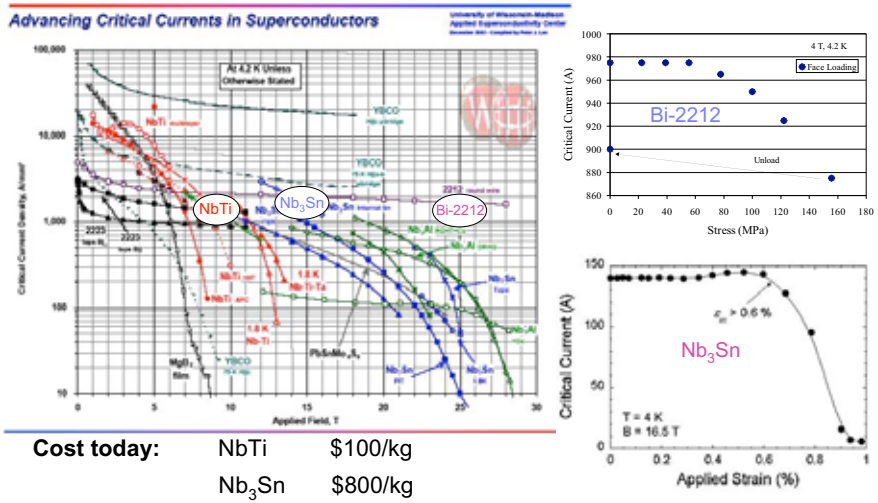

Cost today: NbTi $100/kg

Nb_3Sn $800/kg

Bi-2212 $1,800/kg

LHC-T
Tripling the LHC

Raymond Blackburn, Joong Byeon, Nick Diaczenko, Tim Elliott, Bill Henchel, Andrew Jaisle, Alfred McInturff, Peter McIntyre, Patrick Noyes, Dior Sattarov

Texas A&M University

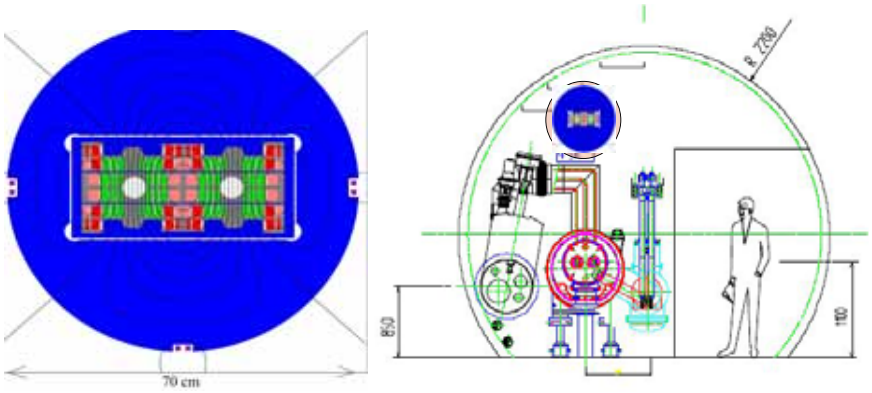

Nb_3Sn dipole technology at Texas A&M:
stress management, flux plate, bladder preload

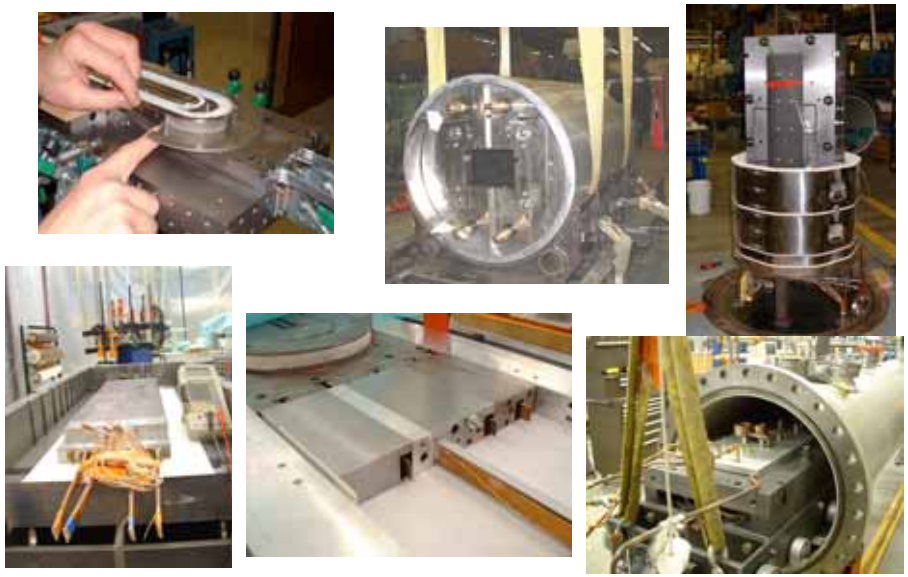

Evolution of the gluon spectrum

Assumptions:

- Luminosity grows x3 with adiabatic damping
- Luminosity needed to produce a given number of particles of mass m (assuming gauge couplings constant) scales with m^2
- So twice the mass scale requires 4/3 the luminosity.

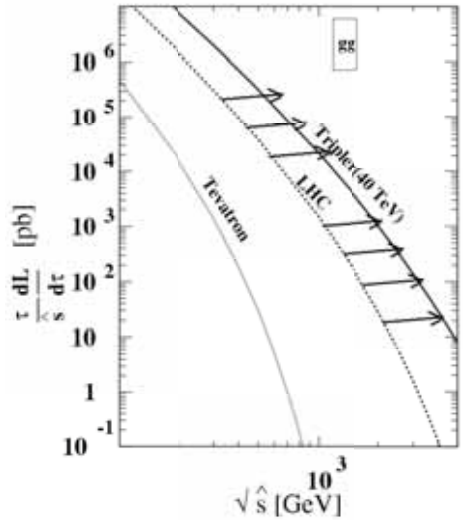

Triple the energy – double the mass reach

Dutta 2004

Ultra-clean S-glass insulation

- S-glass insulation woven directly onto cable.
- Remove organics from the insulated cable in detergent wash, DI rinse.
- Apply fine spray of Palmitic acid on cable edges for lubrication

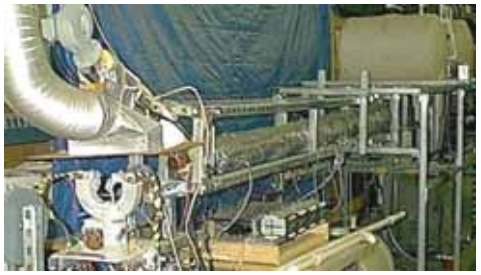

Use high-field superconductor, limit coil stress

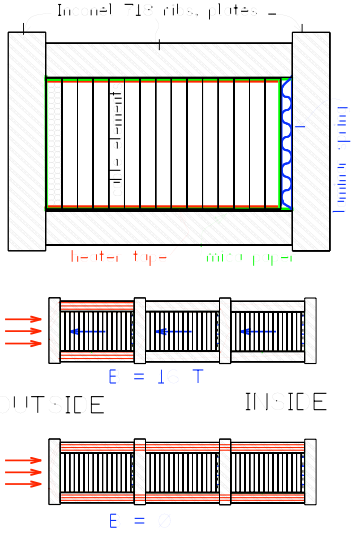

Bending ends on a pancake

- Windings are made as racetracks.
- Wind controlled gap between turns at ends → tightens to lock at desired bend angle.
- Allow block to flare slightly in bend region.
- Coil package is flexible, ends are easily bent by hand.
- Mechanical model was wound with planar coils, bent to angle as shown.

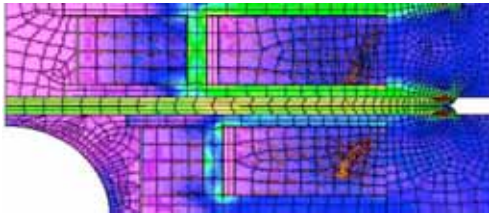

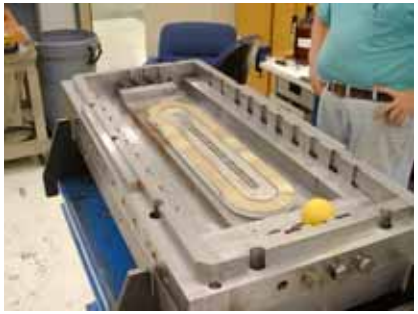

Each winding block is supported as a piston within its cell of structure:

•The laminar spring ensures decoupling of compressive stress between blocks.

•Mica paper ensures release of shear stress on all boundaries.

•Preload is delivered to ~1.2 x max Lorentz loading,

to structure but not block.

Compressive stress in each block cycles ~10 MPa → 110 MPa.

Bladder preload in action

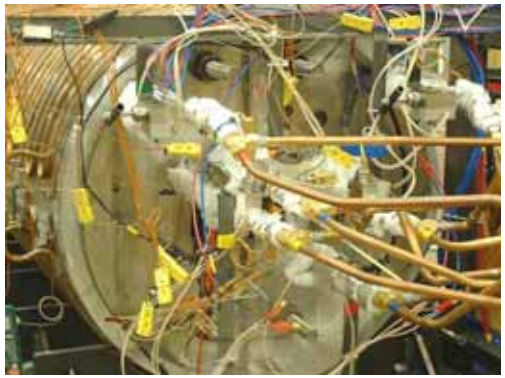

Heat entire dipole to 80 C.

Evacuate bladders, fill with Wood's metal

Preloaded to 2,000 psi using hand pumps.

Sustain pressure while magnet is cooled using water jacket.

If you want to disassemble dipole, just reverse the procedure.

Reaction bake @ 650 C

Argon atmosphere purge manifolded throughout coil.

Same furnace can bake 875 C in O_2 purge for Bi-2212 and maintain separate purges of Ar in Nb3Sn, O_2 in Bi-2212 windings.

We can react a 3 m long dipole in this furnace.

Friction Lock of Axial Load

- Top/bottom bladders deliver uniform loading of *structure* against flux return.
- Axial component of Lorentz stress is friction-locked to flux return, and to stress shell.
- Minimum requirement on end support.

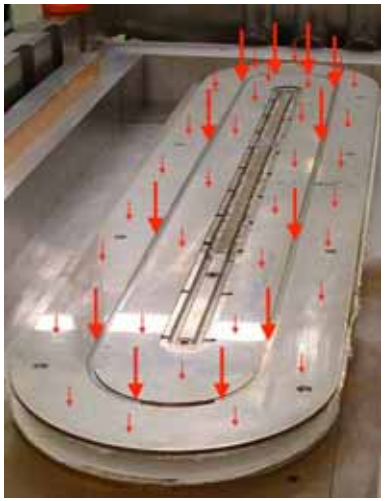

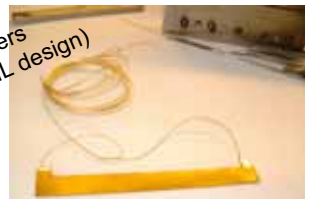

Flat strain transducers (CERN/FNAL/LBNL design)

Bladder preload in TAMU2

TAMU2 = single-layer model dipole embodying stress management, bladder preload

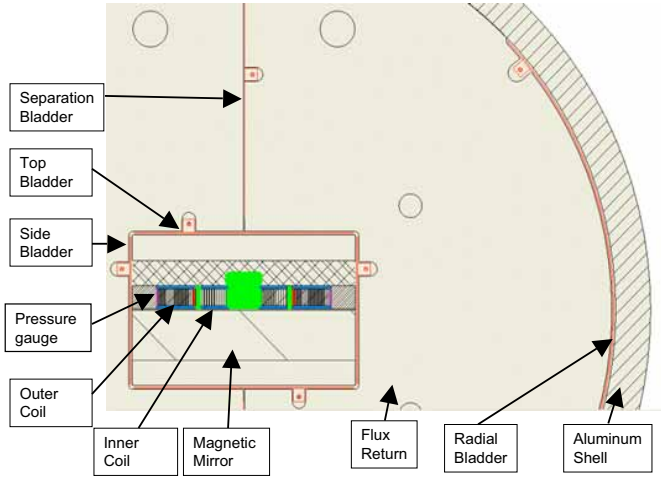

Testing of TAMU2: no training

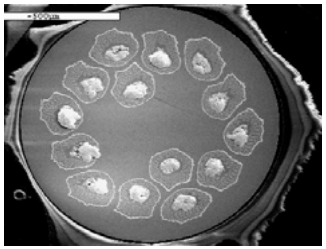

ITER strand

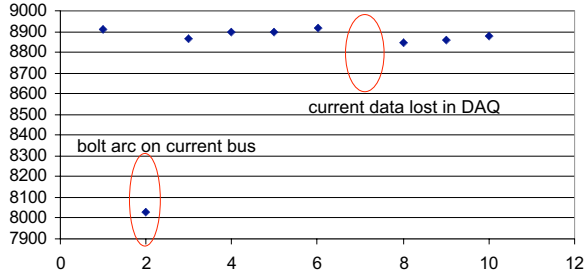

7T single-layer magnetic mirror model

- First quench at 8920 A
  - 93%-98% of edge-on short sample
  - All quenches start on innermost return end

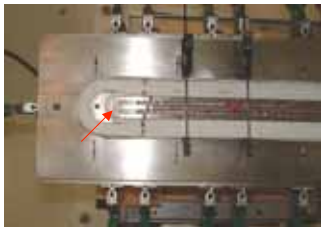

Nb_3Sn/NbTi Splices

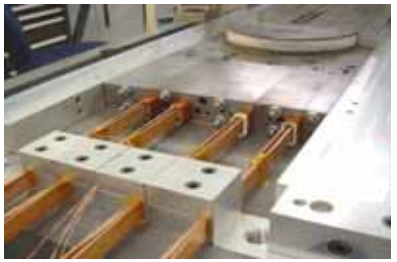

Preparing the cable ends

One joint assembled with heater module

Cross-section of practice splices

Extend to 24 Tesla:
Bi-2212 in inner (high field) windings, Nb_3Sn in outer (low field) windings

Dual dipole (ala LHC)

Bore field	**24 Tesla**
Max stress in superconductor	**130 MPa**
Superconductor x-section:	
Nb_3Sn	**26 cm²**
Bi-2212	**47 cm²**
Cable current	**25 kA**
Beam tube dia.	**50 mm**
Beam separation	**194 mm**

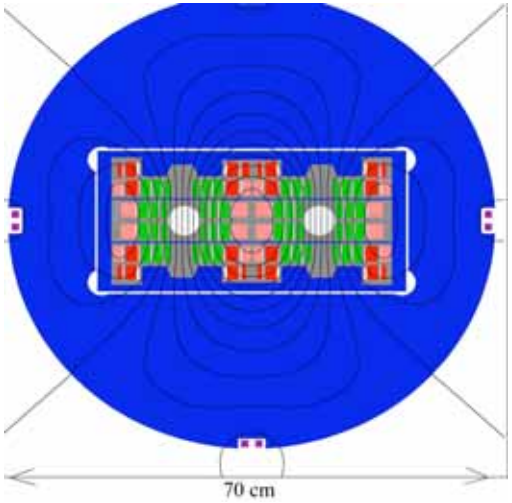

Vacuum Impregnation

Coil in coffin, fitted for epoxy supply/purge, being inserted into retort

Impregnated coil with leads and test connections

Block-coil geometry strongly suppresses the re-distribution of magnetization by boundary-induced currents

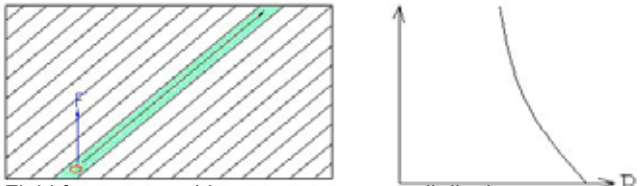

Field face-on to cable: cos θ, common coil dipoles

$$\vec{F} = \left(\vec{u} \cdot \vec{\nabla}\right)\vec{B}$$

Field edge-on to cable: block-coil dipole

- Ramp field hi→lo, induce magnetization current loops in subelements
- Cycle dipole at injection to reduce mangetization, set on charging side of hysteresis
- Dwell at fixed field for injection – magnetization loops migrate under gradient force

Control flux return size using NbTi trim

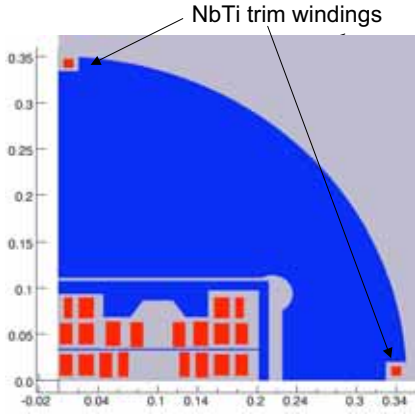

Field strength on steel boundary @ full field: 100 G max 5 cm from surface

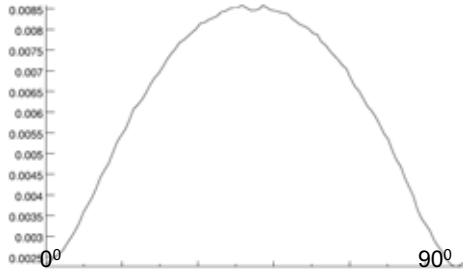

We must tame Bi-2212 for coil technology

- Nb_3Sn windings must be reacted at 650 C in argon atmosphere for a week.
- Bi-2212 windings must be reacted at 870 C in O_2 atmosphere, ~10 minute excursion to partial melt, ΔT ~2 C
- How to do both on one coil???
  - Wind Bi-2212 inner windings, do heat treat @ 870 C.
  - Control fast excursion to partial melt using modulation of pO_2
    - Isothermal melt processing (Holesinger)
  - Wind Nb_3Sn outer windings, do second heat treat @ 650 C.
  - Stress management structure isolates purge gas in the two windings.
  - React the Nb_3Sn with Ar purge, hold O_2 purge on Bi-2212.

Flux plate suppresses multipoles from persistent currents, snap-back

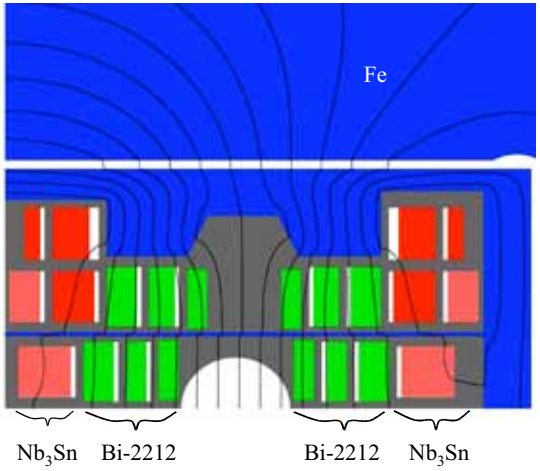

Accelerator Issues

- Synchrotron radiation: power/length $\tilde{P} \propto E^4 I / \rho^2$

  critical energy $E_c \propto E^3 / \rho$

LHC: E = 7 TeV P = 0.22 W/m E_c = 44 eV (hard UV) scatters, desorbs

LHC Tripler: E = 20 TeV P = 14 W/m E_c = 1.2 keV (soft X-ray) absorbs!

– Use photon stop:

Instead of intercepting photons at ~10 K along dipole beam tube, intercept between dipoles room-temperature finger.

– Soft X-rays actually easier to trap that hard UV

or

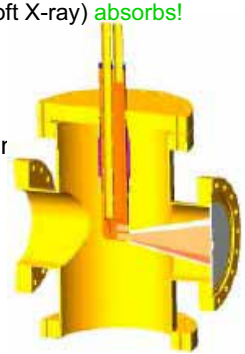

Photon Stop

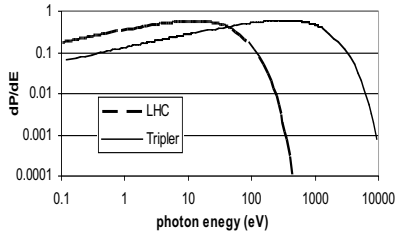

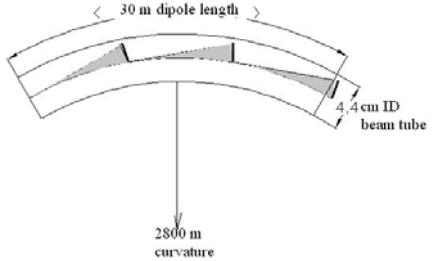

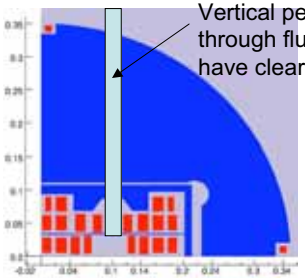

Vertical penetration through flux return (coils have clearance)

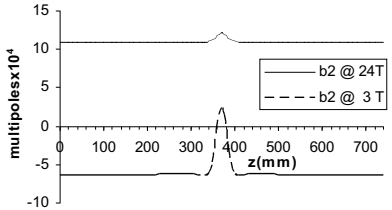

Effect on $\langle b_3 \rangle$ ~10^{-5} cm^{-2}

OST has achieved three vital milestones for LHC-T during the last year!

- At the last LTSW I presented the LHC Tripler concept and said it needed Bi-2212 wire with 500 A in a 0.8 mm wire at high field – 40% more than existed.
  – OST is coming close!

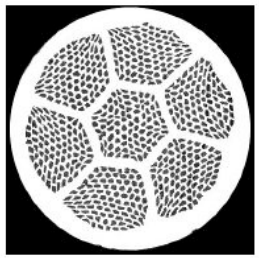

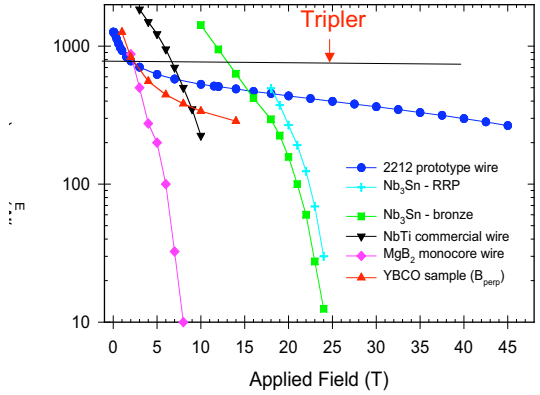

- The challenge to react Bi-2212 wire: partial melt needs fast excursion with 2 C uniformity/control.
  – OST has improved the heat treat so that ±3 C is OK.
  – More work in progress.

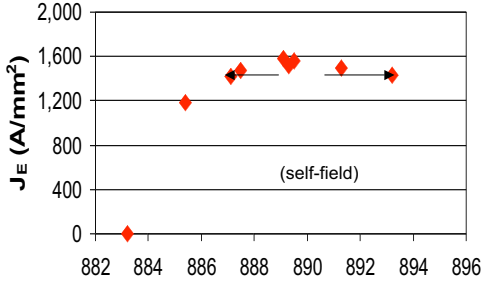

- The insulation must withstand 875 C bake.
  – Ceramic braid now approaching thickness needed.

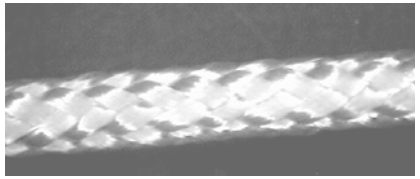

Inject from Super-SPS

- For luminosity upgrade of LHC, one option is to replace the SPS and PS with a rapid-cycling superconducting injector chain.
- 1 TeV in SPS tunnel → 1.25 T in hybrid dipole: flux plate is unsaturated, x5 suppression of snap-back multipoles at injection.
- SuperSPS needs 5 T field, ~10 s cycle time for filling Tripler → > 1 T/s ramp rate

Photon stop rotates: clears aperture at injection energy, collects light at collision energy

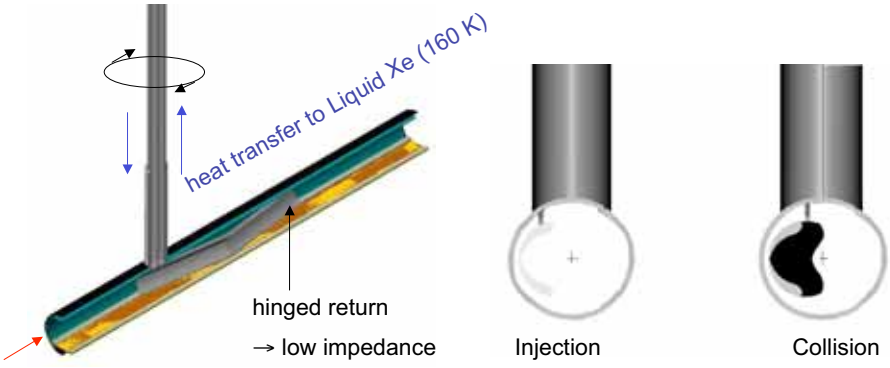

160 W/stop collected @ 1 W/cm^2

Same refrigeration power for Tripler as for LHC

Again block-coil geometry is optimum

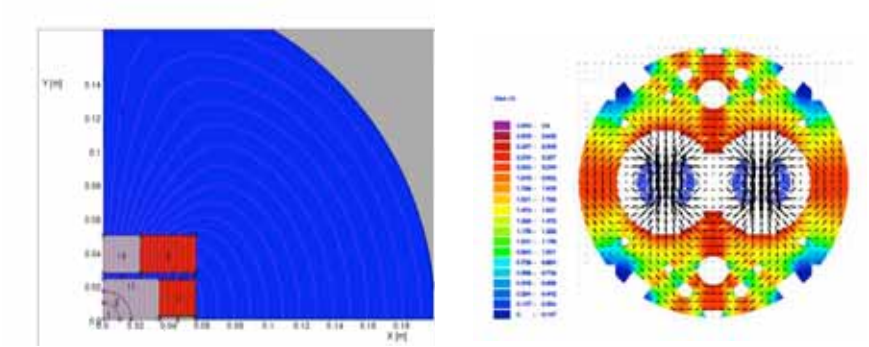

In block-coil dipole, cables are oriented vertically:

$$\vec{B} \| \hat{n}$$

Result: minimum induced current loop, minimum AC losses

In cos θ dipole, cables are oriented on an azimuthal arch:

$$\vec{B} \perp \hat{n}$$

Result: maximum induced current loop, maximum AC losses

Electron cloud effect

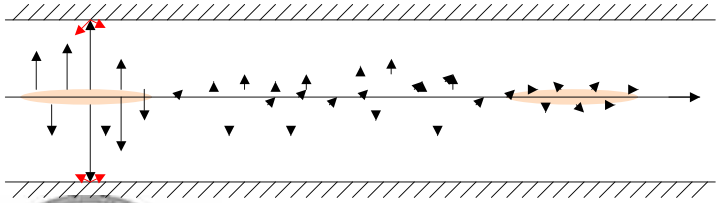

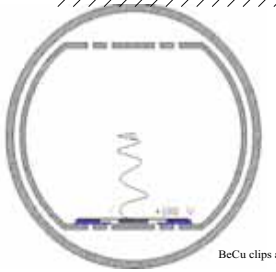

- •dominates heat load ~2 W/m,
- •drives long-term emittance growth
- •Suppress electron multipacting by locating an electrode on bottom of beam screen.(1 mm thick).
- •Bias electrode +100 V, suppress all secondary electrons, kill electron cloud effect.

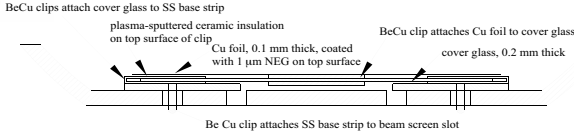

Magnets are getting more efficient!

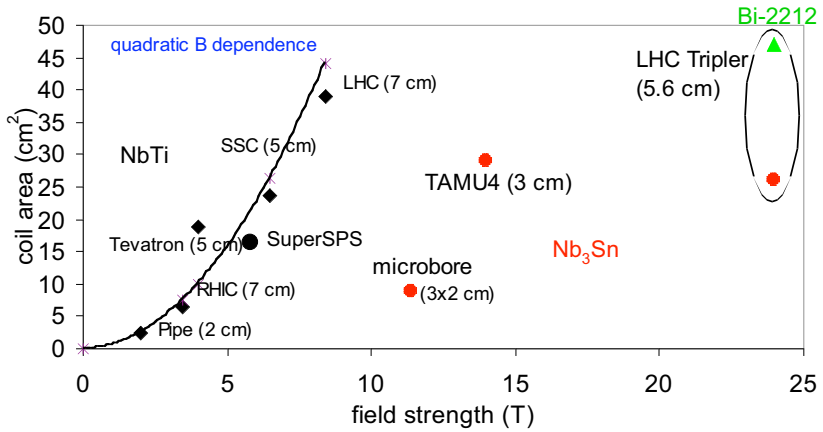

Preliminary design for Super-SPS dipole

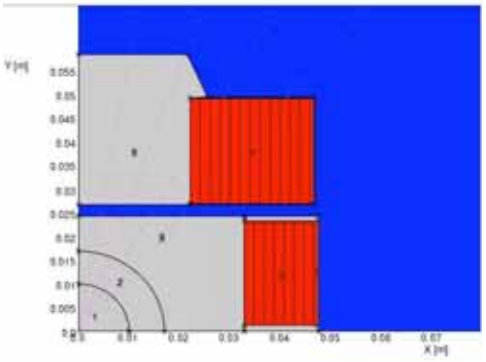

6 T short-sample field (to allow for AC loss degradation)

LHC NbTi strand (wider cable to optimize geometry, minimize inductance)

We are modeling AC losses, expect to be low.

Flux plate suppresses multipoles from persistent currents, AC-induced currents

Recent tests of TAMU2 demonstrate robust ramp behavior.

Requirements on filament size may be significantly relaxed compared to cos θ

LHC Tripler Cost?

1. *superconductor*

- Nb_3Sn:
  - performance needed: $j_{non\text{-}Cu}$ = 3200 A/mm^2 @ 12 T
  - Tripler needs 400 tons
  - I asked OST to estimate cost in that quantity
  - $800/kg → $320 M
- Bi-2212:
  - performance needed: j_{eng} = 850 A/mm^2 @ 25 T
  - Tripler needs 1000 tons
  - I asked OST to estimate cost in that quantity
  - $1,800/kg → $1,800 M

Ramp rate studies

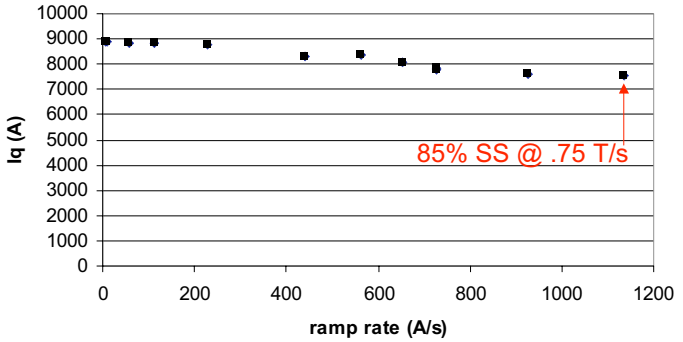

Power supply was unable to ramp faster than ~1 kA/s because of small load inductance (single-layer coil)

Accelerator R&D:
Skunk Works for the Future of HEP

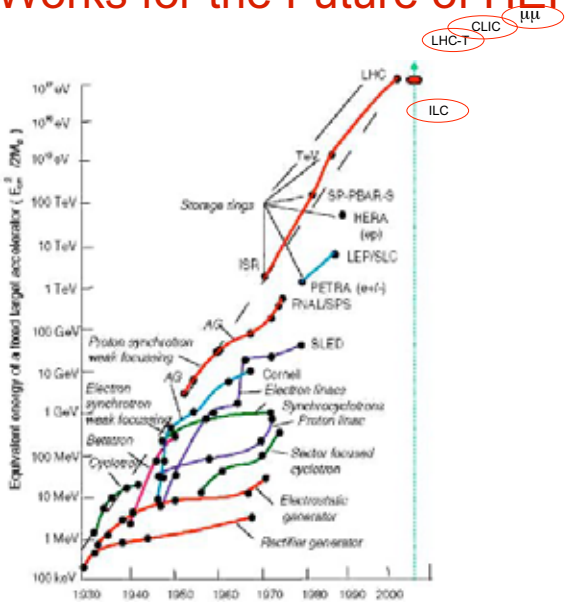

2. Fabrication

- Compare to LHC magnets:

	LHC	LHC-T		projected conductor cost
Cold mass diameter	570	800	mm	
Total mass	2,000	3,900	kg/m	
Beam tube diameter	57	50	mm	
Coils:				
Total turns/bore	82	160		
Conductor area:				
NbTi (2100 A/mm^2 @ 9 T, 1.9 K)	18		cm^2	\$100/kg
Nb_3Sn (3000 A/mm^2 @ 12 T, 4.2 K)		27	cm^2	\$800/kg
Bi-2212 (400 A/mm^2 @ 24 T, 4.2 K)		47	cm^2	\$1,800/kg
Coil current	12,000	33,000	A	
Stored energy (both bores)	0.5	10	MJ/m	

ICE estimating: costs scale with # turns, total mass

940 M → 1,900 M

Total magnet cost: \$4,000 M

Conclusions

- Stress management can facilitate the fabrication of Bi-2212 windings and Nb_3Sn windings in the same coil.
- Recent developments with Bi-2212 move it close to the starting point for LHC-T coil development.
- With photon stops it should be possible to collect synchrotron light at high reservoir temperature so that refrigeration is not a dominant expense.
- Block-coil dipole with flux plate may be attractive choice for Super SPS injector.
- *If we begin now vigorous R&D on hybrid dipoles, we might be able to mature them in time for the end of high-luminosity LHC running – then CERN would have it as an option for upgrade.*